Synthèse, caractérisation et modélisation de matériaux en couches minces pour l'optique en vue d'applications

Julien Cardin

UNIVERSITÉ
CAEN
NORMANDIE

CIMAP

HABILITATION A DIRIGER DES RECHERCHES

Synthèse, caractérisation et modélisation de matériaux en couches minces pour l'optique en vue d'applications

présentée le 15 décembre 2015 par

Dr. Julien Cardin

Jury

Yann Boucher, Maître de conférences, HDR, ENIB, Brest, FOTON
Christian Dufour, Professeur des universités, Université de Caen, CIMAP
Fabrice Gourbilleau, Directeur de recherche CNRS, Caen, CIMAP
Dominique Leduc, Maître de conférences, HDR, Université de Nantes, GEM
Alexandre Vial, Professeur à l'Université de technologie de Troyes, LNIO

Centre de Recherche sur les Ions, les Matériaux et la Photonique (CIMAP)
Université de Caen Normandie

SOMMAIRE

Remerciements page 5

Curriculum vitae page 6

Synthèse des travaux page 15

Sélections de Publications page 101

Remerciements

Je tiens à remercier en premier lieu les membres du Jury qui ont accepté de participer à mon jury d'habilitation : Mr Yann Boucher, Maître de conférences à l'École nationale d'ingénieurs de Brest (ENIB), Alexandre Vial, Professeur à l'Université de technologie de Troyes (UTT), Dominique Leduc, Maître de conférences à l'Université de Nantes, Christian Dufour, Professeur des universités à l'Université de Caen Normandie (UNICAEN) et enfin Fabrice Gourbilleau, Directeur de Recherche au CNRS. Je leur exprime toute ma gratitude pour leur travail et pour toutes les remarques constructives qu'ils ont apportées à mon manuscrit.

Je remercie les doctorants et post-doctorants qui, par leur travail et leurs questions, ont contribué aux résultats présentés ici et avec lesquels j'ai réellement pris plaisir à travailler : Khalil Hijazi, Céline Lecerf, Sébastien Cueff, Larysa Khomenkova, Pratibha Nalini Ramesh Sundar, Chuan-Hui liang, Yong-tao An, Matthieu Roblin, Alexandre Fafin, Lucile Dumont, Florian Ehré, Hichem Ben Ammar, Patrick Benzo, Jennifer Weimmerskirch, Nicolas Guth.

J'adresse mes sincères remerciements au directeur du Laboratoire CIMAP actuel M Amine Cassimi et au directeur précédent M Serge Bouffard pour leurs encouragements constants. Je remercie le responsable de l'équipe NIMPH, Fabrice Gourbilleau pour la confiance et le soutien qu'il m'a accordés tout au long de ces années.

Un grand merci également à mes collègues de l'équipe NIMPH pour leur travail et leur bonne humeur : Philippe Marie, Patrick Voivenel, Cédric Frilay, Mickael Boisserie, Sylvain Foubert, Xavier Portier, Christian Dufour, Christophe Labbé, Franck Lemarié ainsi qu'à mes collègues (trop nombreux pour être cités) des autres groupes du CIMAP.

Les résultats que nous avons obtenus au cours de ces années n'existeraient pas sans le travail de nos collègues du service administratif du laboratoire CIMAP : Mesdames Christiane Malot, Delphine Hasley et Lucie Bercker. Qu'elles en soient ici remerciées. Je remercie également les tutelles que nous avons multiples : l'Université de Caen Normandie, l'Ensicaen, le CNRS et le CEA. Mes remerciements vont enfin à tous les collègues d'autres laboratoires ou entreprises avec lesquels nous avons eu, nous avons et nous aurons la chance de collaborer. Merci aux collègues du CEMES à Toulouse, de l'Institut des Sciences Chimiques de Rennes, de l'IEMN à Lille, de l'IMN et du GEM à Nantes, du LSI à l'Ecole Polytechnique, du Lab. Foton à Lannion, le CRISMAT, le LCS et le LCMT à Caen.

Merci à Amanda, Frida et Victor simplement d'être là. Enfin je remercie mes proches qui sont parfois loin, pour leur constant soutient. Merci, Tack så mycket, Danke schön.

Julien Cardin
76 rue Jacques Prevert
14280 Saint Contest
Tél. : (+33) 6 83 80 38 63
Email : julien.cardin@free.fr
Site : https://www.researchgate.net/profile/Julien_Cardin/

Né le 17 mai 1974 (41 ans)
A Lauterach (Autriche)
Nationalité Française
PACSÉ, 2 enfants

Formation

2000 – 2004	Université de Nantes, ex-Institut de Recherche en Électronique et Électrotechnique de Nantes Atlantic ex-IREENA (IETR). Doctorat de physique du solide. Mention très honorable avec félicitations du jury.
1999 – 2000	Université de Nantes. Diplôme d'études approfondies (DEA) Physique du Solide et des Surfaces.
1997 – 1999	Université de Nantes. Maîtrise et licence de physique, mention physique du solide.
1996 – 1997	Université Technique de Berlin. Étudiant Erasmus en physique à la TU Berlin.

Expériences Professionnelles

Depuis 2007	Ingénieur de Recherche (2^{nd} classe, BAP C) au laboratoire CIMAP CNRS/CEA/ENSICAEN/Université de Caen Basse-Normandie, Caen, France.
2005-2007	Associé de Recherche (contrat post-doctoral) à l'Institut Royale de Technologie (Kungliga Tekniska Högskolan KTH), Stockholm, Suède.
2003-2004	Attaché Temporaire à l'enseignement et à la Recherche (ATER) à l'Université de Nantes, France.
2000-2004	Doctorant à l'Institut de Recherche en Electronique et Electrotechnique de Nantes Atlantique ex-IREENA (IETR), Université de Nantes, France.

Domaines Scientifiques

- ◇ Croissance de matériaux complexes (hybrides, dopés, organiques, inorganiques, nanostructurés) en film mince par méthodes chimiques (sol-gel) ou physiques (pulvérisation cathodique magnétron).
- ◇ Spectroscopie optique de matériaux sous forme de films minces ou de dispositifs pour des applications en photonique (laser, amplificateur optique, modulateur de lumière...) en énergie (photovoltaïque...) et en capteur (SERS...).
- ◇ Modélisation des interactions rayonnement-matière de l'échelle nanométrique (champ proche, nanoparticules) à l'échelle macroscopique (milieu effectif, milieu à gain) dans des systèmes allant du film mince au dispositif. Les méthodes développées ou employées sont de natures analytiques (analyse modale, méthodes matricielles) ou numériques (approximation dipolaire discrète, différences finies, ADE).

Activités d'enseignement

Depuis 2015 Création d'un cours en Thermodynamique hors équilibre ("énergies renouvelables") à l'École nationale supérieure d'ingénieurs de Caen (ENSICAEN), 3 année, filière énergie, Caen, France.
▷ *14 heures eq. TD par an.*

Depuis 2013 Création d'un cours et de Travaux dirigés et enseignement sur le calcul scientifique avancé et l'initiation au Visual Basic sous Excel à l'école nationale supérieure d'ingénieurs de Caen (ENSICAEN), 1 année, filière Matériaux et Chimie, Caen, France.
▷ *30 heures eq. TD par an.*

Depuis 2011 Création des travaux pratiques et enseignement en Thermodynamique hors équilibre ("énergies renouvelables") à l'École nationale supérieure d'ingénieurs de Caen (ENSICAEN), 3 année, filière énergie, Caen, France.
▷ *32 heures eq. TD par an.*

2008 à 2010 Création d'un cours et enseignement de l'option Photonique en Master d'électronique et automatisme à l'École nationale supérieure d'ingénieurs de Caen (ENSICAEN), Caen, France.
▷ *20 heures eq. TD sur 2 ans.*

2001 à 2004 Création d'un cours et enseignement sur les techniques de mesures optiques en Licence professionnelle «Capteur, Instrumentation et Métrologie» IUT de Mesures physiques, Université de Nantes, Saint-Nazaire, France.
▷ *45 heures eq. TD sur 3 ans.*

2001 à 2003 Travaux pratiques de physique et Mécanique, IUT Science et génie des matériaux, IUT de Nantes, France.
▷ *144 heures eq. TD sur 2 ans.*

2000 à 2004 Activités d'enseignement en physique de TD et TP, Premier cycle, Université de Nantes, France.
▷ *105 heures eq. TD sur 4 ans.*

2000 à 2003 Activités d'enseignement en physique de TD et TP, DUEF Formation continue, Université de Nantes, France.
▷ *36 heures eq. TD sur 3 ans.*

Activités d'encadrement

Doctorat

CIMAP, Caen, France.

- Co-encadrement de thèse de Mme Lucile Dumont, soutenance prévu en 2016.
- Co-encadrement de thèse de M. Alexandre Fafin, soutenance prévu en 2014.
- Co-encadrement de thèse de M. Chuan-hui Liang, thèse soutenue en novembre 2013.
- Participation aux travaux de thèse de M. Matthieu Roblin, thèse soutenue en septembre 2013.
- Co-encadrement de thèse de Mme Pratibha N.R. Sundar, thèse soutenue en septembre 2012.
- Participation aux travaux de thèse de Mme Céline Lecerf, thèse soutenue en septembre 2011.
- Participation aux travaux de thèse de M. Khalil Hijazi, thèse soutenue en septembre 2010.

KTH, Stockholm, Suède.

- Participation aux travaux de thèse de M. Andrzej Gajda 2005-2007.

	EX-IREENA (IETR), Nantes, France. • Participation aux travaux de thèse de M. Thomas Schneider 2003-2004.
Master	CIMAP, Caen, France. • Co-encadrement du stage de M1 recherche de M. François Ternet 2012-2013. • Co-encadrement du stage de M2 recherche de M. Alexandre Fafin 2010-2011. • Co-encadrement du stage de M1 recherche de M. Alexandre Fafin 2009-2010.
	EX-IREENA (IETR), Nantes, France. • Co-encadrement du M1 recherche de M. Joël Bazoma 2010-2011. • Encadrement du TER de Maitrise de physique de Mme Eléna Borissenko 2002-2003. • Participation à l'encadrement du DEA de de M. Ludovic Godet 2001-2002.
Licence	CIMAP, Caen, France. • Encadrement de M. Erick Ramón Baca, échange avec l'Université de Guanajuato, Mexique 2013-2014. • Encadrement de projet Ensicaen sur la conversion de fréquence (3 étudiants) 2011. • Encadrement de projet Ensicaen sur le photovoltaïque (3 étudiants) 2010. • Encadrement de M. Adrien Baloche, Calibration spectrale, DUT Mesures Physiques 2009. • Encadrement de M. Dorian Bayart, Métrologie de faisceau laser, DUT Mesures Physiques 2008.
	EX-IREENA (IETR), Nantes-Saint Nazaire, France. • Encadrement de Mme Nathalie Delaunay, Licence "Capteur, Instrumentation et Métrologie". ▷ *Stage confidentiel industrie sur les capteurs à fibre optique appliqués à l'instrumentation en construction naval pour un appels d'offre de la DCN.*

Activités administratives

2008-2010	Membre élu du conseil de Laboratoire du CIMAP, Caen, France.
2002	Membre étudiant élu au conseil scientifique de la Faculté des sciences de l'Université de Nantes, France.

Langues

· Anglais : Niveau Maîtrise, Niveau C2 dans le Cadre Européen.
· Allemand : Niveau Avancé ou Indépendant, Niveau B2 dans le Cadre Européen.
· Suédois : Niveau Intermédiaire ou de Survie, Niveau A2 dans le Cadre Européen.
· Russe : Niveau Introductif ou Découverte, Niveau A1 dans le Cadre Européen.

Activités de revues

· OSA : Optics express, Optics letters.
· Elsevier : Optics and Lasers in Engineering.
· IEEE : Photonics Technology Letters.

Communications :

Publications	Actes	Actes& Résumés	Oraux	Affiches	Brevets
Comité de lecture		-	-	-	-
39	8	7	12	15	1

Publications avec comité de lecture

1. SiN_x :Tb^{3+}-Yb^{3+}, an efficient downconversion layer compatible with silicon solar cell process, L. Dumont, **J. Cardin**, P. Benzo, M. Carrada, C. Labbé, A.L. Richard, D.C. Ingram, W.M. Jadwisienczak, F. Gourbilleau, Solar Energy Materials and Solar Cells, 145(2), 84–92, 2016.
2. The Copper Fluorene phosphonate Cu(PO3-C13H9).H2O : A layered antiferromagnetic hybrid, N. Hugot, M. Roger, J.-M. Rueff, **J. Cardin**, O. Perez, V. Caignaert, B. Raveau, G. Rogez, P.-A. Jaffrès, European Journal of Inorganic Chemistry, DOI : 10.1002/ejic.201501041, 2015.
3. Photochemical preparation of silver nanoparticles supported on zeolite crystals, M. Zaarour, M. El-Roz, B. Dong, R. Retoux, R. Aad, **J. Cardin**, C. Dufour, F. Gourbilleau, J.-P. Gilson, S. Mintova, Langmuir, 30 (21), 6250–6256, 2014.
4. Theoretical investigation of the more suitable rare earth to achieve high gain in waveguide based on silica containing silicon nanograins doped with either Nd3+ or Er3+ ions, A. Fafin, **J. Cardin**, C. Dufour, F. Gourbilleau, Optics Express 22 (10), 12296-12306, 2014.
5. Annealing effects on the photoluminescence of terbium doped zinc oxide films, A. Ziani, C. Davesnne, C. Labbé, **J. Cardin**, P. Marie, C. Frilay, S. Boudin, X. Portier, Thin Solid Films 553, 52-57, 2014.
6. Correlation between matrix structural order and compressive stress exerted on silicon nanocrystals embedded in silicon-rich silicon oxide, G. Zatryb, A. Podhorodecki, J. Misiewicz, **J. Cardin**, F. Gourbilleau, Nanoscale Research Letters 8 (1), 1-7 1, 2013.
7. Structural and optical characterization of pure Si-rich nitride thin films, O. Debieu, R.P. Nalini, **J. Cardin**, X. Portier, J. Perrière, F. Gourbilleau, Nanoscale Research Letters 8 (1), 1-13 1, 2013.
8. Modeling of the electromagnetic field and level populations in a waveguide amplifier : a multi-scale time problem, A. Fafin, **J. Cardin**, C. Dufour, F. Gourbilleau, Optics Express 21 (20), 24171-24184, 2013.
9. Highly Efficient Infrared Quantum Cutting in Tb3+-Yb3+ Codoped Silicon Oxynitride for Solar Cell Applications, Y.T. An, C. Labbé, **J. Cardin**, M. Morales, F. Gourbilleau, Advanced Optical Materials, 2013.
10. Evidence of two sensitization processes of Nd3+ ions in Nd-doped SiOx films, C.-H. Liang, **J. Cardin**, C. Labbé, F. Gourbilleau, Journal of Applied Physics, 114 (3), 033103, 2013.
11. Sensitization of Er3+ Infrared Photoluminescence Embedded in a Hybrid Organic-Inorganic Copolymer containing Octahedral Molybdenum Clusters, Y. Molard, C. Labbé, **J. Cardin**, S. Cordier, Advanced Functional Materials, 2013.
12. Effect of the Si excess on the structure and the optical properties of Nd-doped Si-rich silicon oxide, C.-H. Liang, O. Debieu, Y.-T. An, L. Khomenkova, **J. Cardin**, F. Gourbilleau, Journal of Luminescence, 132 (12), 3118-3121, 2012.
13. SiOx/SiNy multilayers for photovoltaic and photonic applications, R.P. Nalini, L. Khomenkova, O. Debieu, **J. Cardin**, C. Dufour, M. Carrada, F. Gourbilleau, Nanoscale Research Letters, 7 (1), 124, 2012.
14. Enhancing The Optical And Electrical Properties of Si-based Nanostructured Materials, R.P. Nalini, P. Marie, **J. Cardin**, C. Dufour, P. Dimitrakis, P. Normand, M. Carrada, F. Gourbilleau, Energy Procedia, 10, 161-166, 2011.
15. Effects of the thickness on the properties of erbium-doped silicon-rich silicon oxide thin films, S. Cueff, C. Labbé, **J. Cardin**, K. Hijazi, J.-L. Doualan, O. Jambois, B. Garrido, R. Rizk, physica status solidi (C), 8 (3), 1027-1032, 2011.

16. Texture effect of neodymium doped gallium oxide thin films on their optical properties, C. Lecerf, P. Marie, **J. Cardin**, F. Jomard, X. Portier, Optical Materials, 3 (7),1131-1134, 2011.
17. On the nature of the stretched exponential photoluminescence decay for silicon nanocrystals, G. Zatryb, A. Podhorodecki, J. Misiewicz, **J. Cardin**, F. Gourbilleau, Nanoscale research letters, 6 (1), 106, 2011.
18. New Si-based multilayers for solar cell applications, R.P. Nalini, C. Dufour, **J. Cardin**, F. Gourbilleau, Nanoscale research letters, 6 (1), 156, 2011.
19. Electromagnetic modeling of waveguide amplifier based on Nd 3+ Si-rich SiO 2 layers by means of the ADE-FDTD method, C. Dufour, **J. Cardin**, O. Debieu, A. Fafin, F. Gourbilleau, Nanoscale research letters, 6 (1),1-5, 2011.
20. Effect of the Nd content on the structural and photoluminescence properties of silicon-rich silicon dioxide thin films, O. Debieu, **J. Cardin**, X. Portier, F. Gourbilleau, Nanoscale research letters, 6 (1), 1-8, 2011.
21. Cathodoluminescence and photoluminescence comparative study of erbium-doped silicon-rich silicon oxide, S. Cueff, C. Labbé, B. Dierre, J. Cardin, L. Khomenkova, F. Fabbri, T. Sekiguchi, R. Rizk, Journal of Nanophotonics, 5 (1), 051504, 2011.
22. Effect of annealing and Nd concentration on the photoluminescence of Nd3+ ions coupled with silicon nanoparticles, O. Debieu, D. Bréard, A. Podhorodecki, G. Zatryb, J. Misiewicz, C. Labbé, **J. Cardin**, and F. Gourbilleau, Journal of Applied Physics, 108 (11), 113114, 2010.
23. Influence of neodymium concentration on excitation and emission properties of Nd doped gallium oxide nanocrystalline films, A. Podhorodecki, M. Banski, J. Misiewicz, C. Lecerf, P. Marie, **J. Cardin**, X. Portier, Journal of Applied Physics, 108 (6), 063535, 2010.
24. Efficient energy transfer from Si-nanoclusters to Er ions in silica induced by substrate heating during deposition, S. Cueff, C. Labbé, **J. Cardin**, J.-L. Doualan,L. Khomenkova,K. Hijazi,O. Jambois,B. Garrido,R. Rizk, Journal of Applied Physics, 108 (6), 064302, 2010.
25. Thermal stability of high-k Si-rich HfO2 layers grown by RF magnetron sputtering, L. Khomenkova, X. Portier, **J. Cardin** and F. Gourbilleau, Nanotechnology, 21, 285707, 2010.
26. High Energy Excitation Transfer from Silicon Nanocrystals to Neodymium Ions in Silicon-Rich Oxide Film, A. Podhorodecki, J. Misiewicz, F. Gourbilleau, **J. Cardin**, and C. Dufour, Electrochemical Solid-State Letters., 13, K26-K28, 2010.
27. Optically active Er3+ ions in SiO2 codoped with Si nanoclusters, D. Navarro-Urrios, Y. Lebour, O. Jambois, B. Garrido, A. Pitanti, N. Daldosso, L. Pavesi, **J. Cardin**, K. Hijazi, L. Khomenkova, F. Gourbilleau, R. Rizk, Journal of Applied Physics, 106 (9), 93107, 2009.
28. Towards an optimum coupling between Er ions and Si-based sensitizers for integrated active photonics, K. Hijazi, R. Rizk, **J. Cardin**, L. Khomenkova and F. Gourbilleau, Journal of Applied Physics, 106 (2), 24311, 2009.
29. Towards an enhanced coupling between the Er ions and Si nanoclusters, L. Khomenkova, F. Gourbilleau, **J. Cardin** and R. Rizk, Physica E : Low-dimensional Systems and Nanostructures, 41 (6), 2009.
30. Enhanced fraction of coupled Er in silicon-rich silicon oxide layers grown by magnetron co-sputtering, K. Hijazi, L. Khomenkova, F. Gourbilleau, **J. Cardin** and R. Rizk, Journal of Luminescence, 129 (12), 1886-1889, 2009.
31. Structural and optical characteristics of Er-doped SRSO layers deposited by the confocal sputtering technique, K. Hijazi, L. Khomenkova, **J. Cardin**, F. Gourbilleau and R. Rizk, Physica E : Low-dimensional Systems and Nanostructures, 41 (6), 2009.
32. Long lifetime and efficient emission from Er3+ ions coupled to Si nanoclusters in Si-rich SiO2 layers, L. Khomenkova, F. Gourbilleau, **J. Cardin**, O. Jambois, B. Garrido and R. Rizk, Journal of Luminescence, 129 (12), 1519–1523, 2009.

33. Growth and characterization of gallium oxide thin films by radiofrequency magnetron sputtering, P. Marie, X. Portier and **J. Cardin**, Physica Status Solidi (A), 205 (8), 1943-1946, 2008.
34. Determination of refractive index, thickness, and the optical losses of thin films from prism-film coupling measurements, **J. Cardin** and D. Leduc, Applied Optics, 47, 894-900, 2008.
35. A method to retrieve optical and geometrical characteristics of three layer waveguides from m-lines measurements, T. Schneider, D. Leduc, C. Lupi, **J. Cardin**, H. Gundel, and C. Boisrobert, Journal of Applied Physics, 103, 063110, 2008.
36. Optical characterisation of a three layer waveguide structure by m-lines spectroscopy, T. Schneider, D. Leduc, **J. Cardin**, C. Lupi, H. Gundel, Ferroelectrics, 352 (1), 50-60, 2007.
37. Optical properties of PZT thin films deposited on a ZnO buffer layer, T. Schneider, D. Leduc, **J. Cardin**, C. Lupi, N. Barreau, H. Gundel, Optical Materials, 29 (12), 1871-1877, 2007.
38. Optical characterization of PZT thin films for waveguide applications, **J. Cardin**, D. Leduc, T. Schneider, C. Lupi, D. Averty, H. Gundel, Journal of the European Ceramic Society, 25 (12), 2913-2916, 2005.
39. Wet Chemical Etching of Pb(Zr,Ti)O3 Ferroelectric Thin Films for Optical Waveguide Application, H. Gundel, **J. Cardin**, D. Averty, L. Godet, D. Leduc, and C. Boisrobert, Ferroelectrics, 288 (1), 303-313, 2002.

Actes de congrès avec comité de lecture

1. Modeling of optical amplifier waveguide based on silicon nanostructures and rare earth ions doped silica matrix gain media by a finite-difference time-domain method : comparison of achievable gain with Er3+ or Nd3+ ions dopants, **J. Cardin**, A. Fafin, C. Dufour, F. Gourbilleau, Proc. of SPIE, Physics and Simulation of Optoelectronic Devices XXIII, 935709, 2015
2. Effect of annealing treatment on Nd-SiOx thin film properties, C.-H. Liang, **J. Cardin**, L. Khomenkova, F. Gourbilleau,Proc. SPIE 8431, Silicon Photonics and Photonic Integrated Circuits III, 84311Y, Juin 2012.
3. Optical and structural properties of SiO2 co-doped with Si-nc and Er3+ ions, S. Cueff, C. Labbé, B. Dierre, **J. Cardin**, L. Khomenkova, F. Fabbri, T. Sekiguchi, R. Rizk, Proc. of SPIE, 7766, 77660Z, 2010.
4. Impact of the annealing temperature on the optical performances of Er-doped Si-rich silica systems, S Cueff, C Labbé, **J. Cardin** and R. Rizk, IOP Conference Series : Materials Science and Engineering, 6, 012021, 2009.
5. Photoluminescence Activity of Neodymium-doped Gallium Oxide Thin films, C. Lecerf, P. Marie, C. Frilay, **J. Cardin**, X. Portier, MRS Proceedings, Fall meeting, Boston, Janvier 2008.
6. Widely tunable directional coupler filters with 1D photonic crystal, B. Jaskorzynska, Z.J. Zawistowski, M. Dainese, **J. Cardin**, L. Thylen, Proc. of 7th International Conference on Transparent Optical Networks 1, 136-139, 2005.
7. Pb(Zr,Ti)O3 ceramics thick films for optical device applications, **J. Cardin**, D. Leduc, C. Boisrobert, and H. Gundel, Proc. of SPIE, Advanced Organic and Inorganic Optical Materials 3, 5122, 374-379, 2003.
8. Synthesis and characterization of polymers for nonlinear optical applications, V. Boucher, **J. Cardin**, D. Leduc, R. Seveno, R. Le Ny, H. Gundel, C. Boisrobert, S. Legoupy, F. Legros, V. Montembault, F. Odobel, C. Monnereau, E. Blart, D. Bosc, A. Goullet, and J.Y. Mevellec, Proc. of SPIE, Advanced Organic and Inorganic Optical Materials 3, 5122, 209-212, 2003.

Actes de congrès et résumé

1. Rare Earth-Doped Si-Based Thin Films, F. Gourbilleau, A. Fafin, P. Benzo, L. Dumont, **J. Cardin**, C. Labbe, C. Dufour, Proceeding of 225th ECS Meeting, Orlando, Etats Unis, Mai 2014.
2. **(Invité)** Rare Earth Sensitization in Si-Based Structures for Photonic Applications, F. Gourbilleau, C.-H. Liang, Y.-T. An, A. Fafin, **J. Cardin**, L. Khomenkova, C. Labbé, M. Morales, C. Dufour, Proceeding of ECS Meeting 223rd, Mai 2013.
3. Imagerie en champ proche optique à 1,55μm de guides d'onde plasmoniques par rétro-injection sur laser à fibre, M. Roblin, S. Girard, H. Gilles, M. Laroche, **J. Cardin**, C. Dufour et U. Luders, Optique-Marseille-2011, 2011
4. Near-field optical imaging of plasmonic devices using heterodyne optical feedback on Er doped DFB fiber laser, M. Roblin, S. Girard, H. Gilles, M. Laroche, **J. Cardin**, C. Dufour, U. Luders, Laser Science/ Frontiers in Optics, 2011.
5. Near-field optical imaging of plasmonic waveguides using heterodyne optical feedback on Er doped DFB fibre laser, M. Roblin, S. Girard, H. Gilles, M. Laroche, **J. Cardin**, C. Dufour, Lasers and Electro-Optics Europe (CLEO EUROPE/EQEC), 2011.
6. **(Invité)** Doped Rare Earth-Si Based Nanostructures for Photonic Applications, F. Gourbilleau, O. Debieu, **J. Cardin**, C.-H. Liang, C. Dufour, Proceeding of 219th ECS Meeting, 2011
7. Optical and Electrical Properties of Si-Based Multilayer Structures for Solar Cell Applications, R.P. Nalini, **J. Cardin**, K.R. Dey, X. Portier, C. Dufour, F. Gourbilleau, Proceeding of 219th ECS Meeting, 35 (4), 273-285, 2011.

Communication orales

1. Modeling of optical amplifier waveguide based on silicon nanostructures and rare earth ions doped silica matrix gain media by a Finite difference time domain method : comparison of achievable gain with Er3+ or Nd3+ ions doped waveguide, **J. Cardin**, A. Fafin, C. Dufour, F. Gourbilleau, SPIE OPTO, San Francisco, États Unis, 7-12 Février 2015.
2. **(Invité)** Modélisation de la réponse optique de nano-cristaux métalliques ou semi-conducteurs en matrice diélectrique, **J. Cardin**, Ecole thématique du GdR Nacre, St Aygulf, France, Septembre 2014.
3. **(Invité)** Modeling of gain material and light management for photonics, photovoltaic and lightning applications, **J. Cardin**, OLEDs, OPVs, LEDs and materials for organic electronics and photonics, Chilworth Manor, Southampton, Royaume-Uni, Septembre 2014.
4. **(Invité)** Modeling of gain and plasmonic material for photonics, photovoltaics and lightning applications : 2D and 3D approaches, **J. Cardin**, A. Fafin, C. Dufour, C. Labbé, and F. Gourbilleau, MEET workshop, Villers-sur-Mer, France, Septembre 2013.
5. Nanostructured Silicon and Rare Earth Based Gain Media for Compact Infra-red Light Source : Experimental and Theoretical Investigations, **J. Cardin**, A. Fafin, C.-H. Liang, C. Dufour, O. Debieu, C. Labbé, P. Pirasteh-Charrier, J. Charrier, Y. Dumeige, Y. Boucher, F. Gourbilleau, ICMAT 2013 Materials Research Society of Singapore (MRS-S), Singapour, Juin-Juillet 2013.
6. Development of New Kinds of Plasmonics Materials Through Swift Heavy Ion Shaping Technique, **J. Cardin**, C. Dufour, V. Khomenkov, A. Fafin, I. Monnet, G. Rizza, P.-E. Coulon, A. Slablab, D. Mailly, C. Ulysse, X. Lafosse, S. Perruchas, T. Gacoin, ICMAT 2013 Materials Research Society of Singapore (MRS-S), Singapour, Juin-Juillet 2013.
7. Modeling plasmonic properties of nanoparticles for photovoltaic applications, **J. Cardin**, A. Fafin, F. Gourbilleau and C. Dufour, Workshop du GDR Nacre du projet MEET Recent development on Photovoltaic : Nanoparticles and Plasmonic, Cabourg, France, Avril 2013.

8. Modelling of waveguide amplifier based on Nd3+ doped silicon rich silicon oxyde (SRSO) by a ADE-FDTD method, **J. Cardin**, C. Dufour, A. Fafin, F. Gourbilleau, MRS fall meeting Boston, Symposium : BB, Boston, États Unis, Novembre 2012.
9. Modelling of waveguide amplifier based on Nd3+ doped silicon rich silicon oxyde (SRSO) by a ADE-FDTD method, **J. Cardin**, C. Dufour, A. Fafin, F. Gourbilleau, E-mrs fall meeting, Symposium : J, Varsovie, Pologne, Septembre 2011.
10. Optical characterization of PZT thin films for waveguide applications, **J. Cardin**, D. Leduc, T. Schneider, C. Lupi, D. Averty, and H. Gundel, Electroceramics IX, Cherbourg, France, 2004.
11. Couches minces de titanate de plomb (PZT) pour l'optique guidée, **J. Cardin**, D. Leduc, et H. Gundel, Journées des couches minces ferroélectriques, Pessac, France, 2003.
12. PZT ferroelectric ceramic thin films for optical device applications, **J. Cardin**, D. Leduc, C. Boisrobert, and H. Gundel, Advanced Optical Materials and Devices, AOMD-3, Riga, Lettonie, 2002.

Affiches

1. A theoretical investigation of the optical gain in waveguide based on a silica matrix containing silicon nanograins and doped either with Nd3+ or with Er3+ ions, A. Fafin, J. Cardin, C. Dufour, F. Gourbilleau, EMRS Spring meeting, 2015.
2. Terbium doped Silicon Nitride films for Light Emitting Diodes applications, P. Benzo, L. Dumont, **J. Cardin**, C. Labbé and F. Gourbilleau, eMRS, Lille, France, mai 2014.
3. Study of Tb3+-Yb3+ doped Silicon Nitride frequency conversion layers for Solar Cell Applications, L. Dumont, P. Benzo, **J. Cardin**, C. Labbé, I-S Yu, F. Gourbilleau, eMRS, Lille, France, mai 2014.
4. Annealing effects on the photoluminescence of terbium doped zinc oxide thin films, A. Ziani, C. Davesnne, C. Labbé, P. Marie, **J. Cardin**, C. Frilay, P. Voivenel and X. Portier, eMRS, Strasbourg, France, mai 2013.
5. Optical response of ion shaped gold nanoparticules embedded within a silica matrix. A theoretical description based on finite difference time domain scheme, A. Fafin, **J. Cardin**, A. Slablab, P.E. Coulon, G. Rizza and C. Dufour, Optics and photonics days, Besançon, France, novembre 2012.
6. Modélisation de la réponse optique de nanoparticules d'or incluses dans une matrice de silice, A. Fafin, **J. Cardin**, C. Dufour, A. Slablab, P.E. Coulon, G. Rizza, GDR Nacre, Toulouse, France, octobre 2012.
7. Rare earth doped Zinc oxide thin films for optoelectronic applications, C. Davesnne, A. Ziani, **J. Cardin**, C. Labbe, P. Marie, C. Frilay, P. Voivenel, L. Méchin, X. Portier, Proceeding of : European Workshop on nano Transparent Conductive Materials, Janvier 2012.
8. Which observables to characterize multi-polar plasmon resonances in a gold nanowire embedded in a silica matrix, A. Fafin, **J. Cardin**, F. Gourbilleau, P.-E. Coulon, A. Slablab, G. Rizza and C. Dufour, Emrs, Strasbourg, France, mai 2012.
9. Electromagnetic modeling of plasmonic properties of gold nanoparticles embedded within a dielectric matrix deformed by swift heavy ions **J. Cardin**, A. Fafin, F. Gourbilleau, P.-E. Coulon, A. Slablab, G. Rizza, C. Dufour, Meta12, Paris, France, avril 2012.
10. Étude d'un guide d'onde à base de Silice Enrichie en Silicium dopée Nd3+ par une méthode ADE-FDTD, **J. Cardin**, C. Dufour, O. Debieu et F. Gourbilleau, Journées nationales d'optique guidée, Besançon, France, 2010.
11. Nd-doped (Si-rich SiO2/SiNx) Multilayers Approach for Efficient Electrically Excited Device, O. Debieu, P. Nalini, **J. Cardin**, C. Dufour and F. Gourbilleau; MRS Boston Fallmeeting, USA, 2010.

12. Effect of the Matrix (SiOx, SiOxNy, and SiNx) on the Optical Properties of Nd3+ ions O. Debieu, J. Perriere, **J. Cardi**n and F. Gourbilleau, MRS Boston Fall-meeting, USA 2010.
13. Computing the Gain of a Waveguide Amplifier Based on Nd3+ doped Silicon Rich Silicon Oxide Layers by Means of the ADE-FDTD Method, **J. Cardin**, C. Dufour O. Debieu and F. Gourbilleau ; MRS Boston Fall-meeting, USA, 2010.
14. First synthesis and characterizations of polymers for non-linear optical application, V.Boucher, **J. Cardin**, D.Leduc, R.Seveno, R. Le Ny, H.Gundel, C.Boisrobert, S.Legoupy, F.Legros, F.Huet, V.Montembault, L.Fontaine, F.Odobel, J.P.Pradere, D.Bosc, A.Goullet, J.Y.Mevellec, Advanced Optical Materials and Devices, AOMD-3, Riga, Lettonie, 2002.
15. Couches minces ferroélectriques de PbxZryTi1-yO3 pour des applications optiques, **J. Cardin**, R. Seveno, D. Leduc, C. Boisrobert et H. Gundel, Journées des couches minces ferroélectriques, Maubeuge, France, 2001.

Brevet

1. Brevet Européen Ref. No : Eur. Pat. Appl. n°EP13305040, Date : 01/2013 intitulé :"Nanocomposite hybrids containing rare earth ions and clusters of transition elements as sensitizers for applications in photonics".

Synthèse, caractérisation et modélisation de matériaux en couches minces pour l'optique en vue d'applications

Table des matières

pages

1 Introduction 19

1.1 Contexte général : Etat de l'art des matériaux pour l'optique 19

2 Travaux expérimentaux en spectroscopie des matériaux et applications 23

2.1 Guide d'onde planaire à base de matériaux non-linéaires optiques 23

2.1.1 Caractérisation M-lines de matériaux en film mince 25

2.1.2 Développement d'un coupleur directionnel accordable à base de polymère électro-optique et de cristaux photonique 1D 38

2.2 Etude des matériaux luminescents 43

2.2.1 Matrices hôtes 43

2.2.2 Centre émetteur/luminophore 44

2.2.3 Le silicium nanostructuré 46

2.2.4 Les terres rares 48

2.2.5 Couplage entre nanoparticule de silicium et terre rare 51

2.2.6 Fabrication/synthèse des matériaux à base de silicium 54

2.2.7 Sélection de travaux 56

3 Travaux théoriques sur l'interaction rayonnement optique/matière dans les processus luminescents ou résonants 63

3.1 Modélisation par différences finies dans le domaine temporel (FDTD) et système d'équations différentielles auxiliaires (ADE) 63

3.1.1 Milieu dispersif : application aux résonances plasmoniques 69

3.1.2 Milieu à gain : application aux guides d'onde dopés 79

3.2 Modélisation de matériaux stratifiés luminescents 83

4 Conclusion et perspectives 87

4.1 Conclusion 87

4.2 Perspectives 87

Références 89

Chapitre 1

Introduction

1.1 Contexte général : Etat de l'art des matériaux pour l'optique

Depuis une cinquantaine d'années, le développement de matériaux aux propriétés optiques particulières accompagne celui d'applications dans des domaines technologiques variés comme dans l'éclairage (lampes, DEL, OLEDS), les afficheurs (LCD, OLED écrans), l'énergie (photovoltaïque), les procédés industriels (découpe laser, lithographie), la médecine (ophtalmologie, endoscopie, chirurgie), les télécommunications optiques (fibre, amplificateur optique), les technologies de l'information (disque optique, imprimante laser, caméras) et la défense (imagerie IR, furtivité, guidage).

L'usage de ces matériaux dans ces applications est gouverné par leurs propriétés et leurs caractéristiques. Ces matériaux peuvent avoir des propriétés passives ou bien actives. Les propriétés optiques passives sont par exemple : la réflectivité, la transmittivité, l'absorptivité, les propriétés modales d'un guide d'onde constitué de films minces, les propriétés de diffusion de nanostructures en films minces, les propriétés de modification de la polarisation.

Les propriétés actives diffèrent selon leur nature et la nature de la grandeur extérieure appliquée. Parmi celles-ci on trouvera les effets électro-optiques et magnéto-optiques qui permettent de moduler l'indice de réfraction par application d'un champ électrique ou magnétique et ainsi d'exercer un contrôle de la phase d'une onde traversant ce milieu. Les matériaux luminescents excités de différentes manières (photoluminescence, électroluminescence...) trouvent de nombreuses applications dans les sources lumineuses (laser, DEL, lampes).

De nombreux autres phénomènes optiques surviennent en interaction avec les matériaux et il serait difficile de tous les décrire dans cette introduction. Citons toutefois les grandes catégories telles que les phénomènes basés sur la diffraction, la dispersion chromatique, les interférences, les anisotropies optiques, les phénomènes de diffusion, les effets photo-induits (électrique, thermique, Zeeman, Stark, réfractifs, dissociation, ionisation, ...) et les effets non-linéaires optiques (génération de seconde (SHG) et troisième harmonique (THG)).

Afin d'étudier les propriétés optiques de ces matériaux, il est nécessaire de mettre en œuvre des méthodes de caractérisation diverses. On pourra citer les méthodes basées sur l'imagerie optique (microscopie en champ proche optique), l'interférométrie (réflectrométrie en lumière incohérente OLCR), les techniques de spectroscopies (photoluminescence, photoluminescence d'excitation, M-lines), les techniques basées sur la polarisation (ellipsométrie, réflectométrie), la photométrie, la colorimétrie, l'holographie. Outre l'aspect fondamental que peuvent apporter ces techniques de caractérisation, elles permettent de quantifier et de qualifier les matériaux optimaux pour la mise au point d'applications.

Enfin les méthodes et outils de calculs et de modélisation permettent de pousser plus avant la compréhension des phénomènes physiques étudiés. Elles sont basées sur des descriptions plus ou moins complexes des interactions lumière-matière allant de l'optique géométrique à l'optique quantique en passant par l'optique ondulatoire, l'électromagnétisme, l'optique des milieux anisotropes et/ou non-linéaires...Leurs implémentation peut être complètement analytique (calcul d'optique géométrique) ou totalement numérique (FDTD). Outre l'aspect descriptif et explicatif de ces méthodes, celles-ci apportent un soutien important à la réalisation d'applications à partir de matériaux optiques optimisés. Le cercle

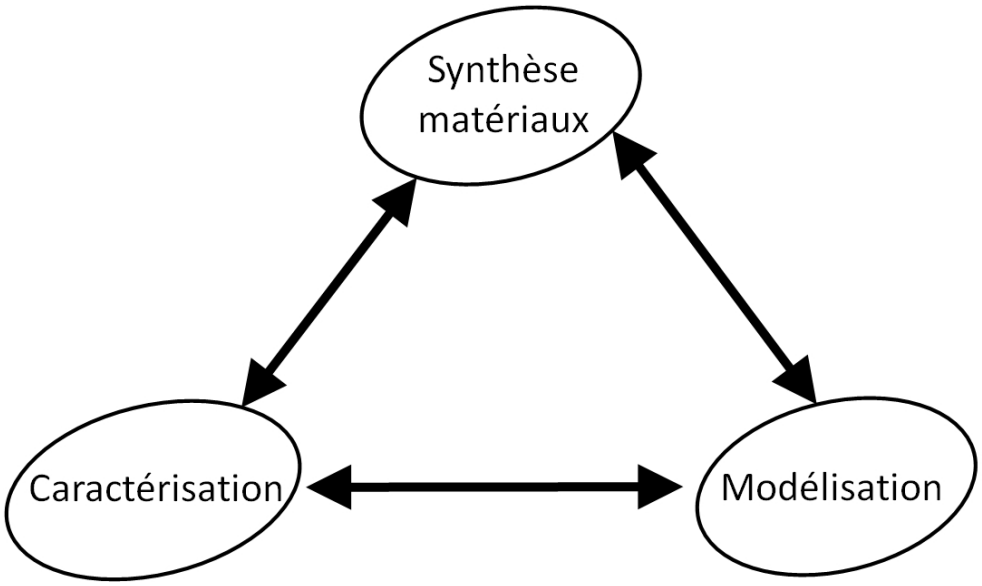

FIGURE 1.1 – cercle vertueux

vertueux de l'étude et de la mise en œuvre des matériaux pour l'optique serait la combinaison de la synthèse de ces matériaux, de leur caractérisation et de l'implémentation des méthodes et outils de calculs et de modélisation.

Les travaux réalisés ces dernières années m'ont amené à combiner ces trois aspects : synthèse de matériaux, caractérisations et modélisation. A propos de la synthèse de matériau, j'ai utilisé la synthèse par voie chimique pendant ma thèse (film mince de PZT) et mon postdoc (film mince polymère). A Caen, les méthodes de synthèse utilisées sont des méthodes physiques comme la pulvérisation cathodique magnétron. Mes activités directes

sont actuellement plus centrées sur la caractérisation et la modélisation des matériaux optiques, réalisés au sein de l'équipe NIMPH ou étudiés par l'intermédiaire de collaborations.

Dans la suite du manuscrit, je vais détailler les travaux post-doctoraux expérimentaux et théoriques réalisés en Suède, à Caen et en collaboration avec des laboratoires partenaires. Certains sujets ayant fait l'objet de publications détaillées seront brièvement abordés d'autres sujets ayant fait l'objet de moins de publications seront plus densément développés.

Chapitre 2

Travaux expérimentaux en spectroscopie des matériaux et applications.

2.1 Guide d'onde planaire à base de matériaux non-linéaires optiques.

Les matériaux étudiés dans ces travaux post-thèse sont issus pour certains de mon travail de thèse sur les matériaux ferroélectriques en couche mince de zirconate-titanate de plomb (PZT) mais également de projets de recherches amorcés pendant ma thèse sur les polymères électro-optiques. Ces matériaux étaient développés dans le but de réaliser des applications basées sur l'optique guidée et sur les effets non-linéaires optiques. De plus, des études sur des films de ZnO, issus de collaboration avec N. Barreau (Equi. CESES, IMN, Nantes), ont également été réalisées. Ces films ont été fabriqués dans la perspective de servir d'électrodes transparentes pour le développement de cellules solaires CIGS en film mince ou d'électrodes de commande sur des systèmes électro-optiques.

La densité de polarisation électrique $\vec{P}$ peut se voir comme la réponse d'un matériau soumis à l'interaction d'une radiation électromagnétique (lumière) avec celui-ci. Cette densité de polarisation est donnée par la relation générale (2.1) décrivant sa dépendance au champ électrique $\vec{E}$ ainsi qu'aux coefficients de susceptibilité électrique $\chi^{(i)}$ développés à l'ordre i.

$$\vec{P} = \epsilon_0 \left(\chi^{(1)} \vec{E} + \chi^{(2)} \vec{E}\vec{E} + \chi^{(3)} E\vec{E}E + \ldots \right) \tag{2.1}$$

Les susceptibilités $\chi^{(1)}$ sont des grandeurs tensorielles qui donnent la mesure de la rigidité des liaisons électroniques avec le réseau nucléaire. Plus "souple" sera la liaison, plus les électrons pourront s'éloigner des noyaux et par conséquent donner lieu à une polarisation plus importante. Les termes d'ordre 2 et plus ne sont exaltés que pour des champs électriques de forte amplitude (10^{+11} $V.m^{-1}$) nécessitant souvent l'usage de lasers. Les termes d'ordre pair (2, 4) existent seulement dans les matériaux ne présentant pas de centre de symé-

trie. Des études théoriques ainsi que des observations expérimentales ont établi que plus grande est la délocalisation électronique, plus grandes seront les valeurs des susceptibilités non-linéaires $\chi^{(n)}$ avec $(n > 1)$.

Parmi les matériaux non-linéaires optiques (NLO), on trouve des composés de nature inorganique ou organique. Pour les premiers, le niobate de lithium ($LiNbO_3$) est un représentant des matériaux NLO inorganiques cristallins les plus étudiés. Le PZT en tant que matériau ferroélectrique fait également partie de cette catégorie, avec notamment des études sur les composés dopés au lanthane [1]. Pour les polymères électro-optiques orientés, les propriétés optiques non linéaires, contrairement à celles des composés inorganiques, sont dues à la délocalisation électronique dans les molécules et polymères conjugués (liaison/orbitales π-électrons) [2]. La flexibilité de synthèse de la chimie organique est un avantage certain dans la production de matériaux organiques non-linéaires optiques. Cependant ceux-ci présentent des inconvénients majeurs tels que la faible résistance au flux laser et le photoblanchiment qui en font des produits à plus courte durée de vie que les matériaux non-linéaires optiques inorganiques [3].

Ces non-linéarités de la réponse électronique à une interaction optique peuvent se manifester expérimentalement de différentes manières : (i) l'effet électro-optique (EO) qualifie la dépendance de l'indice de réfraction au champ électrique, (ii) la génération de seconde harmonique ou mélange à quatre ondes, (iii) les diffusions inélastiques optiques Raman, Brillouin et Stokes. L'effet électro-optique (EO) peut être exploité pour moduler la phase, la polarisation, ou l'intensité d'une onde électromagnétique, et se trouve à la base du traitement d'un signal optique dans de nombreux composants comme les modulateurs électro-optiques. La réalisation de ces derniers sous forme de guide d'onde à partir de films minces (de l'ordre du μm) réduit considérablement leur taille et leur coût. La configuration guidée permet d'obtenir une propagation de l'onde sur une longueur nécessaire à l'interaction (EO) ($>10\lambda$). De plus, de par le confinement des modes guidés dans la structure guidante planaire, des densités d'énergie importantes peuvent être atteintes et ceci avec des facteurs de recouvrement optique η qui peuvent être grands (proches de 1). Pour rappel, les deux configurations de la modulation électro-optique sont représentées sur la figure(2.1). Dans le cas d'applications en optique guidée, la configuration transversale (figure(2.1)a) est privilégiée. Dans ce cas la tension nécessaire à l'obtention d'un déphasage de π (V_π) dépend alors du facteur géométrique $\frac{d}{L}$. Cette configuration guidée, de faible épaisseur d, permet donc de minimiser les tensions de polarisation appliquées pour commander l'effet électro-optique.

De plus, la micro-nano structuration des films minces ouvre également la voie à la réalisation de composants actifs, électriquement accordables, complexes comme des filtres ou des composants à bandes interdites photoniques accordables. Néanmoins la mise en œuvre de ces films dans des applications utilisant l'effet électro-optique reste un challenge. Les difficultés étant de différentes natures : (i) conservation de l'ordre cristallin/moléculaire à l'origine de l'effet EO (ii) intégration avec des matériaux de natures différentes (conducteur, semi-conducteur, organique/inorganique) (iii) toxicité des composés chimiques (Plomb, Lithium,...)

Avant le design et la réalisation de ces structures guide d'onde à effet électro-optique,

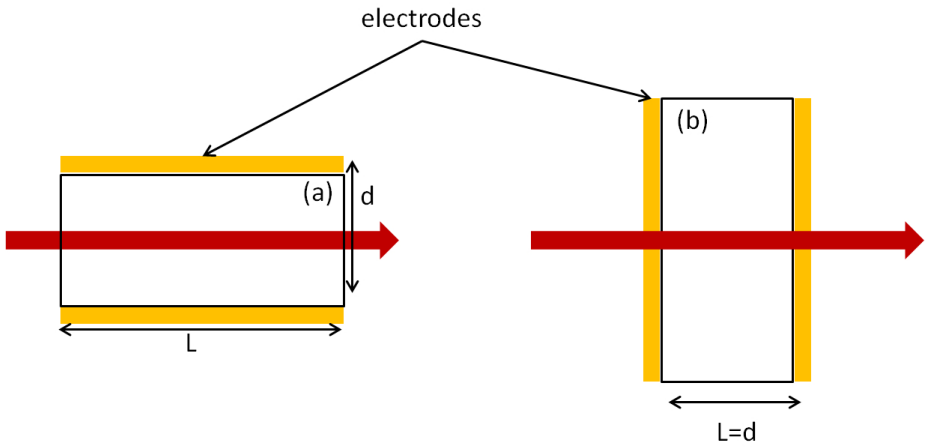

FIGURE 2.1 – Deux configurations possibles pour l'effet EO (Pockels) (a) configuration transversale (b) configuration longitudinale.

la connaissance approfondie des indices de réfraction et des épaisseurs des matériaux mis en œuvre est nécessaire. Pour rappel, la connaissance de l'indice complexe avec une grande précision est primordiale lorsque l'on souhaite développer une application basée sur l'optique guidée dans laquelle les sauts d'indice sont parfois aussi faibles que 10^{-3} à 10^{-4} [4]. L'intégration de matériaux multiples pour la réalisation de guides d'onde peut elle aussi se révéler complexe. En effet, les propriétés des matériaux individuels ne se retrouvent pas nécessairement à l'identique dans les structures composites qui forment le guide d'onde. Il est donc parfois nécessaire de pouvoir accéder à la connaissance des indices de réfraction n_1, $\tilde{n}_2 = n_2 + ik_2$, n_3 et des épaisseurs d_1, d_2, d_3 de systèmes multi-couches intermédiaires à la réalisation de guide d'onde modulateur électro-optique. La connaissance de l'absorption des matériaux mis en œuvre est également cruciale à la bonne réalisation/optimisation de la structure. L'objectif de réaliser la mise en œuvre de ces matériaux non-linéaires optiques en couche mince dans des applications basées sur l'optique guidée planaire nous a conduit à souhaiter caractériser les propriétés optiques linaires que sont les parties réelle et imaginaire de l'indice de réfraction. Nous souhaitions également pouvoir déterminer avec précision les épaisseurs des couches minces individuellement et dans les empilements réalisés pour le dispositif. Ce besoin de déterminer les indices de réfraction, les épaisseurs ainsi que l'absorption de matériaux en film mince de mono- bi- et tricouche m'a conduit à m'intéresser à la technique de spectroscopie M-lines.

2.1.1 Caractérisation M-lines de matériaux en film mince.

Dans le cadre de ma thèse, j'ai été amené à mettre en œuvre la technique de caractérisation M-lines ou spectroscopie de lignes noires, sur des échantillons de zirconate-titanate de plomb (PZT) développés pour des applications basées sur l'optique guidée (modulateur électro-optique d'intensité ou de phase). Cette technique présente l'avantage de permettre la détermination de l'indice de réfraction avec une précision de l'ordre de celle de l'indice

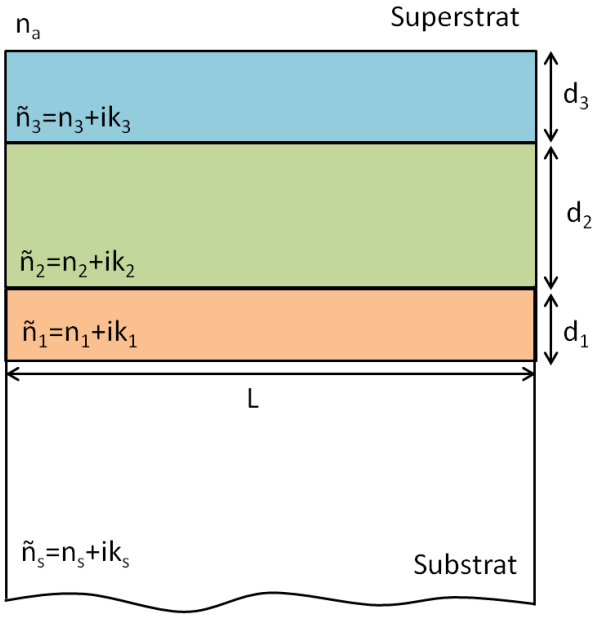

FIGURE 2.2 – Schéma de principe d'un guide d'onde à trois couches à effet EO (Pockels) en configuration de l'effet EO transversal.

du prisme (10^{-3}-10^{-4}) et la détermination de l'épaisseur à quelques nanomètres près. A contrario de l'ellipsométrie spectroscopique, cette technique ne nécessite pas de modèle de dispersion de l'indice de réfraction des matériaux étudiés mais un modèle modal de propagation. Cette technique développée aux Bell labs dans les années 1970 [5–8] est basée sur l'excitation sélective de modes de propagation dans une structure planaire guidante. Les modes excités peuvent être de nature guidée totalement ou à pertes (lorsqu'une interface de la couche caractérisée permet des fuites par réfraction). Pratiquement, ceci est réalisé par un couplage par champ évanescent obtenu lors d'une réflexion totale frustrée dans un prisme d'indice n_p quasiment au contact de la structure planaire à caractériser (Figure (2.4). La variation d'angle d'incidence de l'onde incidente de vecteur d'onde $k_0 = \frac{2\pi}{\lambda_0}$, avec λ_0 la longueur d'onde dans le vide, permet de parcourir une plage de constante de propagation $0 < \beta = n_p.\sin\theta k_0 < n_p k_0$. La mesure s'effectue généralement à l'air, donc l'indice supérieur est $\tilde{n}_a = 1$. Selon que l'indice de réfraction de la couche mince $\tilde{n}_c$ est supérieur ou inférieur à celui du substrat $\tilde{n}_s$, et selon les valeurs de la constante de propagation β, plusieurs régimes de guidage sont possibles : des modes guidés ou bien des modes à pertes radiatives de substrat (Figure 2.3). Un mode d'ordre m et de constante de propagation β^m est excité sélectivement lorsque l'accord de phase entre ce mode et l'onde incidente est réalisé. Connaissant la longueur d'onde de travail et l'indice de réfraction du prisme, cet angle θ^m interne au prisme est relié à la constante de propagation du mode β^m.

$$\beta(n_p, \theta^m, k_0) = \beta^m \tag{2.2}$$

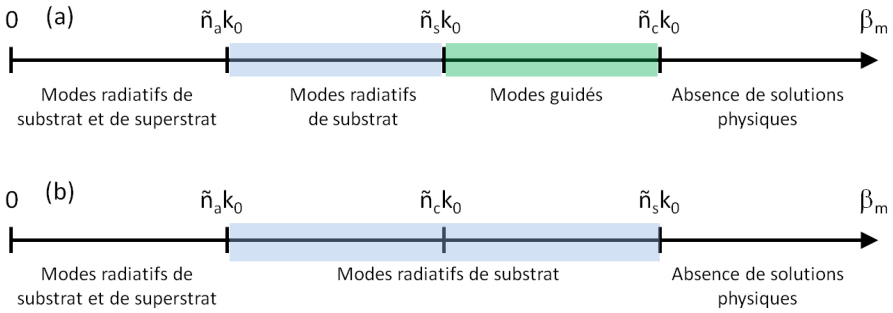

FIGURE 2.3 – Différents régimes de guidage selon les valeurs des indices de réfraction et les valeurs de constante de propagation : (a) Pour $\tilde{n}_a k_0 < \tilde{n}_s k_0 < \tilde{n}_c k_0$ selon la valeur de β les modes sont guidés ou à pertes radiatives de substrat (b) Pour $\tilde{n}_a k_0 < \tilde{n}_c k_0 < \tilde{n}_s k_0$, quelle que soit la valeur de β, les modes sont à pertes radiatives de substrat.

Les considérations de choix de prisme (angle et indice) sont détaillés dans ma thèse [9] et dans les travaux précurseurs [5, 6, 8]. Deux configurations de mesure sont couramment

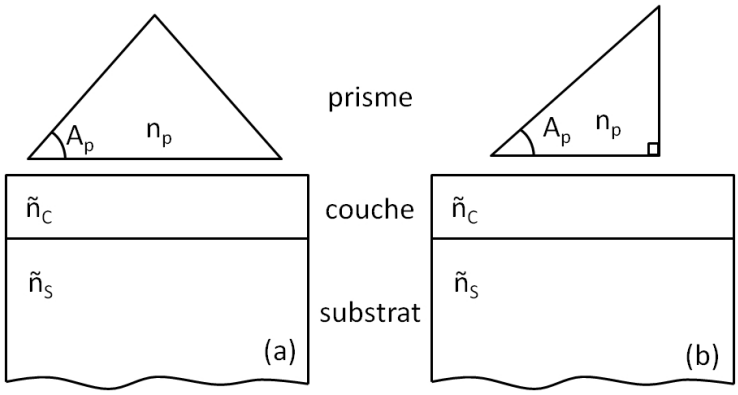

FIGURE 2.4 – M-lines en configuration : (a) en transmission et (b) en réflexion .

utilisées comme indiqué sur la figure 2.4 selon que l'on souhaite utiliser le mode transmission ou réflexion. Dans le cas d'une monocouche à saut d'indice, selon la configuration de mesure on obtient un spectre M-lines en transmission ou en réflexion (figure (2.5). Sur cette figure, la position des maxima (R) ou des minima (T) permet de déterminer l'angle d'incidence sur la face d'entrée du prisme ϕ_m qui conduit à la détermination de la constante de propagation du mode β^m excité par la relation :

$$\beta^m = n_p . \sin\theta_m k_0 = \tilde{n}_c . \sin\psi_m k_0 = k_0 \left(\sin\phi_m \cos A_p + \sqrt{n_p^2 - \sin^2\phi_m} \sin A_p \right) \qquad (2.3)$$

L'approche classique considère une monocouche sans perte d'indice $\tilde{n}_c$ d'épaisseur d sur substrat sans perte considéré comme semi-infini. Dans le cas où la couche mince est moins réfringente que le substrat, il s'agira de résoudre numériquement les équations des modes à perte ("leaky modes") [10, 11]. Dans le cas contraire, il s'agira de résoudre les équations

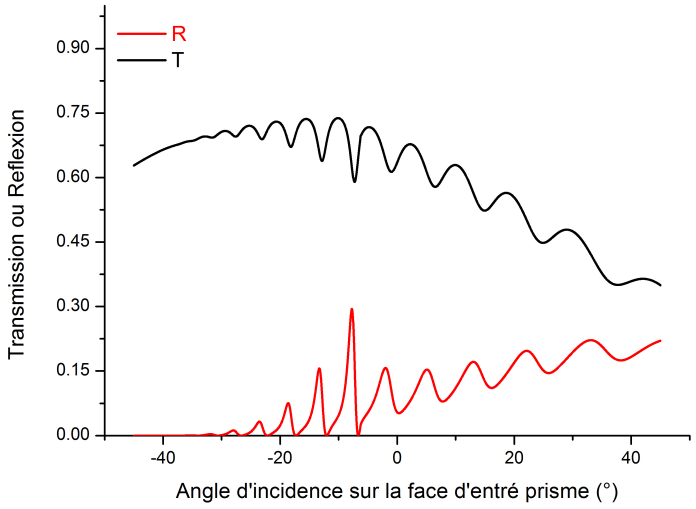

FIGURE 2.5 – Spectre M-lines d'une couche mince d'indice 1,8+0,01i de 2,7μm sur un substrat de type verre d'indice 1,50+0,00001i, longueur d'onde 632,8nm, prisme Ap=45°.

des modes guidés [8]. Selon la polarisation de l'onde incidente de mesure, les équations de dispersion des guides d'onde plan seront choisis TE ou TM. Comme la résolution numérique de ces équations nécessite deux modes minimum, les mesures comportant un nombre de modes Nm supérieurs à deux entrainent une surdétermination qui conduira à C^2_{Nm} couples de solution ($\tilde{n}_c$, d). Une procédure d'optimisation pourra alors être menée afin de réduire la dispersion des résultats. A la conclusion de mes travaux de thèse en 2004, j'avais mis au point différentes approches originales qui permettaient l'obtention des solutions (n_c, d) optimisées avec leurs incertitudes généralisés :

- ➤ Critère d'indexation des modes permettant d'attribuer l'ordre des modes mesurés [9, 12],
- ➤ Optimisation par simplex des couples de solution (n_c, d) [9],
- ➤ Calcul des erreurs sur ($\tilde{n}_c$, d) [12].

Détermination du coefficient d'extinction par la méthode M-lines.

La méthode M-lines conventionnelle permet la détermination de l'épaisseur et l'indice de réfraction (partie réelle) de films minces. A partir des angles des pics relevés sur les spectres expérimentaux, on résout numériquement l'équation de dispersion des guides d'onde plan correspondant à l'expérience (modes guidés ou à perte et polarisation TE/TM). En 1973, R. Ulrich et R. Torge mentionnaient le lien entre la largeur des pics M-lines et l'absorption dans les films minces mesurés [8]. En effet, plus l'absorption augmente et plus le facteur de qualité des pics M-lines diminue, ceci pouvant conduire à la quasi disparition de ces derniers. Partant de cette constatation expérimentale, nous avons cherché à savoir s'il était possible,

à partir de mesures M-lines, de déterminer le niveau de perte dans les couches minces étudiées. Le calcul numérique de la figure (2.6) illustre la modification des spectres M-lines obtenus avec différentes valeurs de coefficient d'extinction. Lorsque ce dernier augmente,

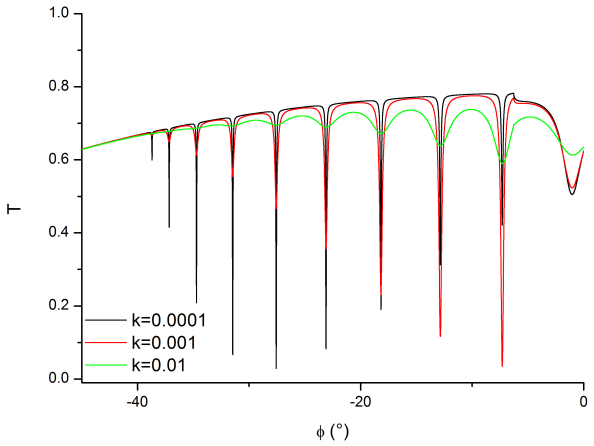

FIGURE 2.6 – Spectre M-lines d'une couche mince d'indice 1,8+ik de 2,7μm sur un substrat de type verre d'indice 1,50+0,00001i, longueur d'onde 632,8nm, prisme Ap=45°.

on observe une diminution du facteur de qualité de ces pics M-lines conduisant à leur élargissement. Pour rendre compte de cet élargissement (ou diminution de leur facteur de qualité) il fallait une technique qui permette de modéliser les spectres dans leur totalité. Nous avons donc utilisé une approche basée sur les matrices de transfert pour modéliser les spectres expérimentaux.

Nous avons développé une méthode d'analyse de mesure M-lines basée sur l'analyse de la réflectivité totale du système formé par le prisme et l'ensemble constitué du gap d'air de la couche mesurée et du substrat. L'apport de cette méthode est la détermination de grandeurs supplémentaires par rapport à la méthode conventionnelle. En effet, en plus de la partie réelle de l'indice de la couche mince mesurée n_c, on détermine le coefficient d'extinction k_c de celle-ci, ce qui permet de calculer le coefficient d'absorption $\alpha_c = \frac{4\pi k_c}{\lambda}$. Avec cette méthode, nous considérerons des films homogènes, isotropes et de rugosité négligeable devant la longueur d'onde. Cette méthodologie développée dans l'article [13] est basée sur deux aspects importants :

- La modélisation qui consiste à calculer la réflectivité angulaire du système formé par le prisme, le gap d'air, le film et le substrat par une méthode de matrice de transfert [14, 15]. La réflectivité théorique décrivant les spectres M-lines est une fonction des grandeurs suivantes : l'angle A_p et l'indice n_p du prisme, l'épaisseur e et l'indice $\tilde{n}_a$ du gap d'air, l'épaisseur d et l'indice $\tilde{n}_c$ de la couche mince et l'indice $\tilde{n}_s$ du substrat.
- Le modèle de réflectivité présenté précédemment aboutit à une description numérique non-linéaire de la réflectivité avec de nombreux paramètres (A_p, n_p, e, $\tilde{n}_a$, d,

$\tilde{n}_c$, $\tilde{n}_s$). De plus, il s'agit d'un modèle avec des contributions expérimentales (fonction de transfert) et analytiques (Matrices). Le choix d'une méthode numérique déterministe comme par exemple Newton-Raphson se serait révélé problématique. Nous avons donc développé une méthode numérique basée sur un algorithme évolutionnaire (algorithme génétique) pour permettre les ajustements des réflectivités angulaires expérimentales par la réflectivité théorique précédemment décrite.

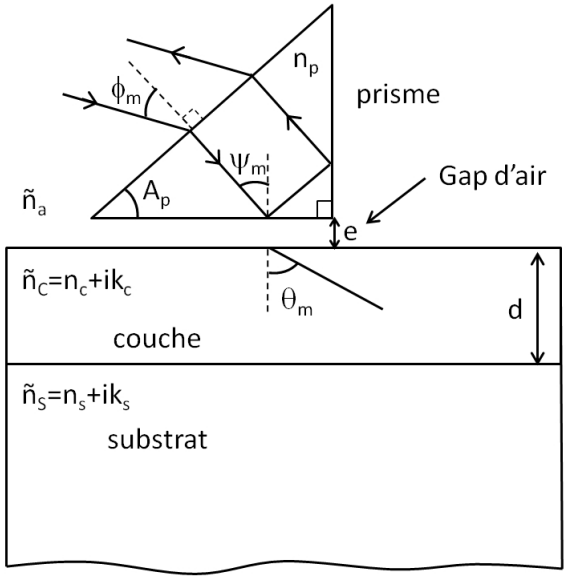

FIGURE 2.7 – Configuration de mesure M-lines dans le cas du prisme droit (mesure en réflexion) avec le prisme d'angle A_p et d'indice n_p, le gap d'air d'épaisseur e et d'indice $\tilde{n}_a$, la couche mince d'épaisseur d et d'indice $\tilde{n}_c$, le substrat d'indice $\tilde{n}_s$.

Pour permettre une bonne détermination des grandeurs recherchées à partir de mesures expérimentales, il est nécessaire de considérer une fonction expérimentale phénoménologique dans les calculs. Celle-ci est déterminée par un rapport de la réflectivité expérimentale sur la réflectivité théorique du prisme à vide (c'est-à-dire sans échantillon en contact). De plus, une estimation statistique de la propagation de l'incertitude a été menée au moyen de la méthode évolutionnaire d'ajustement. Cette méthode consiste à ré-échantillonner des erreurs sur les mesures selon une distribution choisie (Gaussienne) et de les réintroduire dans la méthode évolutionnaire afin de déterminer l'intervalle de confiance des résultats obtenus. Cette technique, proche des techniques de Monte Carlo, est appelée Bootstrap [16].

Cette méthode d'analyse a été employée avec succès sur des films de nature différente. il s'agissait de films de résine photosensible (S1818), de films d'oxyde de zinc dopé Aluminium (ZnO :Al) déposé par pulvérisation cathodique magnétron [17] et de films d'oxyde d'indium-étain commercial (ITO) [18]. Les mesures ont été réalisées avec un système M-lines commercial de la société Metricon [19] en polarisation TE à 632,8 nm. Les résultats des ajustements par la méthode évolutionnaire sont reportés dans les tableaux 2.1 et 2.2 ci-dessous. Le tableau 2.1 comporte les résultats obtenus par la méthode classique de résolution de l'équation modale de dispersion (EMD), ainsi que par la méthode évolutionnaire

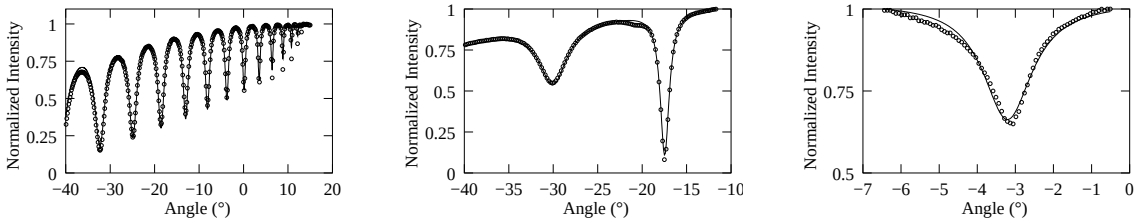

(a) Film de S1818 sur substrat de silicium

(b) Film de ZnO :Al sur substrat de verre

(c) Film d'ITO sur substrat de verre

FIGURE 2.8 – Spectres M-lines mesurés (∘) et ajustés (−) en mode TE.

utilisant l'algorithme génétique (AG). Le tableau 2.2 ne comporte que les valeurs obtenues par la nouvelle méthode évolutionnaire puisque ces paramètres ne sont pas décrits par les approches classiques pour les modes guidés ou à pertes.

	n		d (μm)	
Echantillon	AG	EMD	AG	EMD
S1818 #1	1.640 ± 2.10^{-3}	1.6401 ± 1.10^{-4}	3.407 ± 9.10^{-3}	3.80 ± 2.10^{-2}
S1818 #2	1.638 ± 2.10^{-3}	1.6381 ± 1.10^{-4}	3.408 ± 9.10^{-3}	3.41 ± 2.10^{-2}
S1818 #3	1.639 ± 2.10^{-3}	1.6387 ± 1.10^{-4}	3.281 ± 9.10^{-3}	3.28 ± 2.10^{-2}
ZnO #1	1.9310 ± 4.10^{-4}	1.934 ± 1.10^{-3}	0.870 ± 3.10^{-3}	0.839 ± 3.10^{-3}
ZnO #2	1.9270 ± 4.10^{-4}	1.930 ± 1.10^{-3}	0.904 ± 3.10^{-3}	0.832 ± 3.10^{-3}
ZnO #3	1.8600 ± 4.10^{-4}	1.861 ± 1.10^{-3}	0.587 ± 3.10^{-3}	0.554 ± 3.10^{-3}
ITO	1.80 ± 3.10^{-2}	1.78 ± 3.10^{-2}	0.17 ± 2.10^{-2}	0.18 ± 2.10^{-2}

TABLE 2.1 – Caractéristiques des différents films minces obtenues par l'algorithme génétique (AG) et par la résolution de l'équation modale de dispersion (EMD).

Dans le cas du S1818 et du ZnO, les spectres obtenus se composent respectivement de modes à pertes et de mode guidés. Les spectres sont ajustés de façon satisfaisante par le modèle numérique. Les valeurs de n_c et d'épaisseur d sont relativement en accord entre les deux méthodes EMD et AG. Les pertes obtenues sous la forme du coefficient d'extinction sont en accord avec celles communément admises pour la photorésine S1818 et le ZnO.

Le troisième type de mesure réalisée sur une couche fine d'oxyde d'indium-étain ITO déposé sur verre révèle un avantage supplémentaire de notre méthode sur l'approche classique. En effet, dans celle-ci la résolution numérique impose de mesurer deux modes (guidés ou à pertes) au moins afin de pouvoir résoudre les équations numériquement. Or l'approche consistant à ajuster la réflectivité par l'algorithme génétique permet d'obtenir les paramètres n_c, k_c, d et e pour une mesure ne comportant qu'un seul mode. Les valeurs obtenues sont en accord avec celles communément admises pour l'ITO.

Outre le bon accord avec les méthodes classiques de résolution des équations de dispersion, cette méthode permet donc de déterminer des grandeurs supplémentaires comme le

Echantillon	k	e (μm)
S1818 #1	$0.0028 \pm 7\,10^{-4}$	$0.105 \pm 5\,10^{-3}$
S1818 #2	$0.0012 \pm 7\,10^{-4}$	$0.145 \pm 5\,10^{-3}$
S1818 #3	$0.0021 \pm 7\,10^{-4}$	$0.152 \pm 5\,10^{-3}$
ZnO #1	$0.00067 \pm 6\,10^{-5}$	$3.3\,10^{-2} \pm 2\,10^{-3}$
ZnO #2	$0.00071 \pm 6\,10^{-5}$	$1.7\,10^{-3} \pm 2\,10^{-3}$
ZnO #3	$0.00260 \pm 6\,10^{-5}$	$2.7\,10^{-2} \pm 2\,10^{-3}$
ITO	$0.015 \pm 1\,10^{-2}$	0.19 ± 0.17

TABLE 2.2 – Caractéristiques des différents films minces obtenues par l'algorithme génétique (AG).

coefficient d'extinction k_c représentatif des pertes du milieu. De plus cette méthode évolutionnaire permet d'obtenir des résultats dans des cas particuliers où la méthode classique fait défaut comme le cas des films très minces supportant un seul mode. L'approche matricielle utilisée pour la modélisation de la réflectivité nous a ouvert la voie à d'autres types d'analyse pour les systèmes bicouches et tricouches, que je vais expliciter par la suite.

Publications

- J. Cardin, D. Leduc, Determination of refractive index, thickness, and the optical losses of thin films from prism-film coupling measurements, Applied optics, 47(7), 894-900, 2008.

Méthode M-lines adaptée pour l'analyse des bicouches et tricouches

La réalisation de système/application planaire à base de couches minces multiples nécessite la caractérisation des structures multicouches à différentes étapes. En effet au cours de l'élaboration d'un système multicouches, on peut être amené à caractériser les structures intermédiaires au cours du processus de fabrication. C'est pourquoi partant du formalisme des matrices de transfert utilisé pour la modélisation de la réflectivité dans l'approche par un algorithme génétique, nous avons proposé des formulations d'équation de dispersion des guides d'ondes plan dans le cas de systèmes bicouches et tricouches formés de matériaux différents. Ces travaux ont été réalisés dans le cadre des travaux de thèse de Mr Thomas Schneider qui a poursuivi mon sujet de recherche de thèse à l'Université de Nantes. Ils ont fait l'objet de plusieurs publications [17, 20, 21].

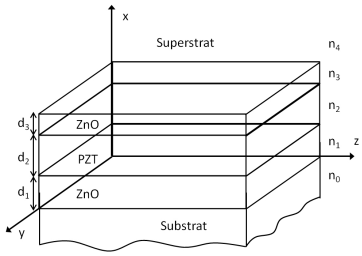

FIGURE 2.9 – Schéma d'un guide d'onde plan tricouches.

Nous avons limité l'étude au cas sans perte avec les indices de réfraction réels suivant :

$$n_2 > n_1, n_3 > n_0, n_4 \tag{2.4}$$

La méthode est basée sur la méthode des matrices de transfert dans le formalisme de F. Abeles [14] et sur une approche de modélisation des systèmes multicouches de matériaux d'indices de réfraction différents présentés par Chilwell et al [22]. Cette description matricielle permet de relier les amplitudes des champs aux interfaces supérieure et inférieure d'un film mince. Les films minces seront considérés comme linéaires, non-magnétiques, homogènes, isotropes, d'épaisseur d_i et d'indice de réfraction $\tilde{n}_i = n_i$ (sans perte optique $k_i = 0$).

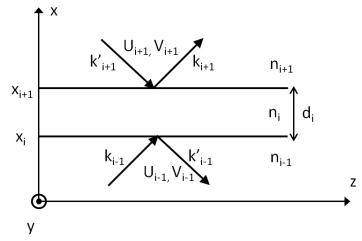

FIGURE 2.10 – Champs incident et réfléchi dans les milieux i-1 et i+1.

Il est possible de lier les amplitudes des champs $\begin{pmatrix} U_{i-1} \\ V_{i-1} \end{pmatrix}$ dans le milieu $i-1$ au point x_i à l'amplitude des champs $\begin{pmatrix} U_{i+1} \\ V_{i+1} \end{pmatrix}$ dans le milieu $i+1$ au point x_{i+1} par la relation 2.5 avec la matrice transfert de la forme suivante (Eq. 2.6) :

$$\begin{pmatrix} U_{i+1} \\ V_{i+1} \end{pmatrix} = M_i \begin{pmatrix} U_i \\ V_i \end{pmatrix} \quad (2.5) \qquad M_i = \begin{pmatrix} \cos(\kappa_i d_i) & \frac{i}{\gamma_i}\sin(\kappa_i d_i) \\ i\gamma_i \sin(\kappa_i d_i) & \cos(\kappa_i d_i) \end{pmatrix} \quad (2.6)$$

Nous considérerons dans le milieu d'indice n_i, l'onde de vecteur d'onde dans le vide k_0 et la constante de propagation β qui est la composante selon Oz du vecteur d'onde dans le milieu i. La composante transverse du vecteur d'onde dans le milieu i selon Ox κ_i s'obtient par la relation suivante $\kappa_i^2 = (n_i^2 k_0^2 - \beta^2)$. Selon le signe de κ_i^2, on exprime cette composante en fonction de la grandeur $a = \sqrt{|n_i^2 k_0^2 - \beta^2|}$:

- ➤ $\kappa_i^2 > 0$ alors $\kappa_i = a$
- ➤ $\kappa_i^2 < 0$ alors $\kappa_i = -ia$

Le tableau (2.3) donne les correspondances du paramètre γ_i dépendant de la polarisation.

Polarisation	γ_i
TE	$\frac{\kappa_i}{k_0}$
TM	$\frac{k_0 n_i^2}{\kappa_i}$

TABLE 2.3 – Paramètre γ_i dépendant de la polarisation.

En considérant un guide multicouches comme un empilement de N couches différentes (Fig. 2.9), la relation reliant les amplitudes des champs E et H dans le superstrat à celles des champs dans le substrat est issue du produit des matrices M_i représentant chaque film (Eq. 2.7).

$$\begin{pmatrix} U_{sup} \\ V_{sup} \end{pmatrix} = \prod_{i=1}^{N} M_i \begin{pmatrix} U_{sub} \\ V_{sub} \end{pmatrix} = M_{tot} \begin{pmatrix} U_{sub} \\ V_{sub} \end{pmatrix} \quad (2.7)$$

Dans ces travaux, nous souhaitions étudier uniquement les solutions modes guidés. C'est pourquoi après avoir écrit le système matriciel (Eq.2.7) nous devons considérer des conditions de champ évanescent aux interfaces avec le substrat et le superstrat pour établir le système d'équations décrivant le guide multicouches. La condition de nullité du déterminant de ce système conduit à l'équation (2.8) :

$$\gamma_4 m_{11} + \gamma_4 \gamma_0 m_{12} + m_{21} + \gamma_0 m_{22} = 0 \quad (2.8)$$

Les coefficients m_{ij} sont les éléments de la matrice M_{tot}. Cette équation générale décrit la

dispersion des modes guidés du système guide d'ondes tricouches 2.9 (en polarisation TE) :

$$\begin{aligned} a_2\, d_2 \quad &+ \arctan\left[\ \frac{i\gamma_0\,\gamma_1 + \gamma_1^2\tan(\omega\mu_0\gamma_1\, d_1)}{\gamma_1\,\gamma_2 - i\gamma_0\,\gamma_2\ \tan(\omega\mu_0\gamma_1\, d_1)}\ \right] \\ &+ \arctan\left[\ \frac{i\gamma_3\,\gamma_4 + \gamma_3^2\ \tan(\omega\mu_0\gamma_3\, d_3)}{\gamma_2\,\gamma_3 - i\gamma_2\,\gamma_4\ \tan(\omega\mu_0\gamma_3\, d_3)}\ \right] -\ m\,\pi = 0 \end{aligned} \tag{2.9}$$

Selon la nature de l'onde dans la couche i, les valeurs de γ_i peuvent être réelles ou imaginaires. Une analyse dans le plan complexe pourrait être nécessaire pour étudier les solutions de ce système (équation 2.9). Cependant, basé sur des arguments physiques nous pouvons séparer le problème en plusieurs sous-problèmes élémentaires. Les conditions de l'équation 2.4 sont à l'origine de quatre conditions de guidage distinctes par l'ordre des modes explicités ci-dessous :

- Les modes d'ordre les plus faibles ($0 \leq m < m_1$) se propagent seulement dans la couche centrale #2. Les champs décrivant ces modes sont évanescents dans toutes les couches autres que la couche #2 (seul $\gamma_2 \in \mathbb{R}$). L'équation de dispersion générale (2.9) devient :

$$\begin{aligned} a_2\, d_2 -\ &\arctan\left[\ \frac{a_0\, a_1 + a_1^2\tanh(a_1\, d_1)}{a_1\, a_2 + a_0\, a_2\tanh(a_1\, d_1)}\ \right] \\ &- \arctan\left[\ \frac{a_3\, a_4 + a_3^2\tanh(a_3\, d_3)}{a_2\, a_3 + a_2\, a_4\tanh(a_3\, d_3)}\ \right] -\ m\,\pi = 0 \end{aligned} \tag{2.10}$$

- L'ordre des modes augmentant jusqu'à un mode $m_1 \leq m < m_2$, deux cas sont possibles :
  - Dans le cas où $n_3 > n_1$ l'onde est guidée dans les couches #2 et #3 et l'équation 2.9 devient :

$$\begin{aligned} a_2\, d_2 -\ &\arctan\left[\ \frac{a_0\, a_1 + a_1^2\tanh(a_1\, d_1)}{a_1\, a_2 + a_0\, a_2\tanh(a_1\, d_1)}\ \right] \\ &- \arctan\left[\ \frac{a_3\, a_4 - a_3^2\tan(a_3\, d_3)}{a_2\, a_3 + a_2\, a_4\tan(a_3\, d_3)}\ \right] -\ m\,\pi = 0 \end{aligned} \tag{2.11}$$

  - Dans le cas où $n_1 > n_3$ l'onde est guidée dans les couches #1 et #2 et l'équation 2.9 devient alors l'Eq. 2.12.

$$\begin{aligned} a_2\, d_2 -\ &\arctan\left[\ \frac{a_0\, a_1 + a_1^2\tan(a_1\, d_1)}{a_1\, a_2 + a_0\, a_2\tan(a_1\, d_1)}\ \right] \\ &- \arctan\left[\ \frac{a_3\, a_4 - a_3^2\tanh(a_3\, d_3)}{a_2\, a_3 + a_2\, a_4\tanh(a_3\, d_3)}\ \right] -\ m\,\pi = 0 \end{aligned} \tag{2.12}$$

- Les modes d'ordre supérieur ($m_2 \leq m$) se propagent dans les trois couches du guide

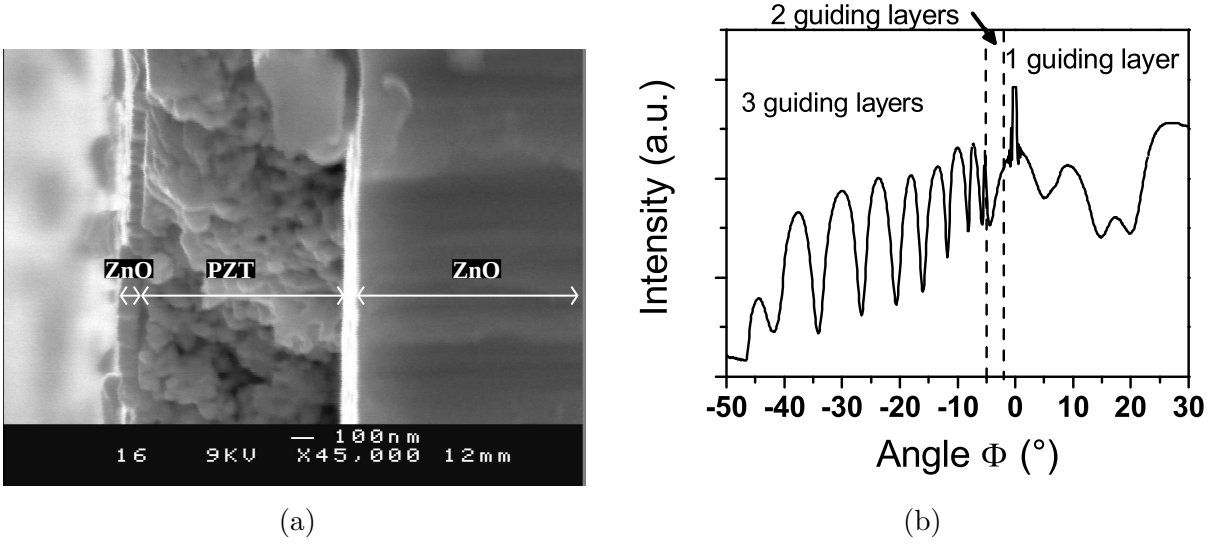

(a) (b)

FIGURE 2.11 – (a) Image MEB d'un guide d'onde planaire à trois couches (b) Spectre M-lines obtenu avec l'échantillon observé en MEB (figure 2.11a) mesuré à 29 mm du centre du substrat en mode TE [21]

d'onde, l'équation de dispersion devient alors :

$$\begin{aligned} a_2\, d_2 - \ \arctan\left[\ \frac{a_0\, a_1 - a_1^2 \tan(a_1\, d_1)}{a_1\, a_2 + a_0\, a_2 \tan(a_1\, d_1)}\ \right] \\ - \arctan\left[\ \frac{a_3\, a_4 - a_3^2 \tan(a_3\, d_3)}{a_2\, a_3 + a_2\, a_4 \tan(a_3\, d_3)}\ \right] - \ m\,\pi = 0 \end{aligned} \tag{2.13}$$

La résolution de ces équations est détaillée dans les travaux de T. Schneider et al. [17,20,21,23]. Dans le cas présent, la structure tricouches étudiée est représentée sur la figure 2.9. Il s'agissait d'un projet de réalisation d'un dispositif modulateur électro-optique. Le système était composé d'une couche de PZT déposée sur une couche de ZnO et surmontée d'une couche de ZnO. Les indices des couches sont supposés supérieurs à ceux du substrat et du superstrat. Le matériau utilisé pour la réalisation des électrodes transparentes est du ZnO dopé aluminium, dont l'indice de réfraction donné par la littérature est égal à 1,988 à 632,8 nm [24]. Le matériau constituant le cœur de la couche guidante est du PZT de composition brute $Pb_{1.4}(Zr_{0.4}Ti_{0.6})O_3$ dont l'indice est compris entre 2,22 et 2,25 [9] à 632,8nm.

Cette étude a mis en évidence plusieurs choses concernant la méthode d'analyse et la synthèse des matériaux multicouches :

➤ La méthode d'analyse M-lignes des guides planaires trois couches donne des résultats en accord avec ceux obtenus par la méthode d'analyse M-lines à deux couches. Les différences observées entre les valeurs obtenues avant et après le dépôt de la troisième couche restent inférieures à l'incertitude de la technique de mesure ainsi

qu'à la variabilité induite par la technique d'élaboration.

➤ Une augmentation de l'indice de réfraction du PZT de 2,2227±5.10^{-4} à 2,3610±5.10^{-4} entre un dépôt sur verre (Corning 1737F) et un dépôt sur ZnO sur le même substrat de verre a été observé. Ce comportement met en évidence un changement structural induit par la croissance sur le film de ZnO.

➤ L'indice de réfraction de la couche inférieure de ZnO est quasi constant. Il reste compris entre 1,9667±6.10^{-4} et 1,991±5.10^{-3}. Au contraire, l'indice de réfraction de la couche supérieure de ZnO montre de fortes variations de 2,015±8.10^{-3} à 2,123±8.10^{-3}. Cette variabilité pourrait provenir de la co-existence de deux phases cristallines différentes dans les couches minces de ZnO d'épaisseur inférieure à 500 nm [25].

	n_1	d_1 (μm)	n_2	d_2 (μm)	n_3	d_3 (μm)
2 couches	1,978	1,11	2,360	1,02		
3 couches	1,979	1,09	2,368	0,96	1,987	0,13

TABLE 2.4 – Mesure des grandeurs caractéristiques d'un guide d'ondes avant et après ajout de la troisième couche de superstrat de ZnO.

Publications

- T. Schneider, D. Leduc, J. Cardin, C. Lupi, N. Barreau, and H. Gundel, Optical properties of PZT thin films deposited on a ZnO buffer layer, Optical Materials, 29(12), 1871-1877, 2007.
- T. Schneider, D. Leduc, J. Cardin, C. Lupi, and H. Gundel, Optical characterisation of a three layer waveguide structure by M-lines spectroscopy, Ferroelectrics, 352(1), 50-60, 2007.
- T. Schneider, D. Leduc, C. Lupi, J. Cardin, H. Gundel, and C. Boisrobert, A method to retrieve optical and geometrical characteristics of three layer waveguides from M-lines measurements, Journal of Applied Physics, 103(6), 063110-063110, 2008.

2.1.2 Développement d'un coupleur directionnel accordable à base de polymère électro-optique et de cristaux photonique 1D.

J'ai réalisé un séjour postdoctoral à l'Institut Royal de Technologie (Kungliga Tekniska Högskolan, KTH) à Stockholm en Suède au sein du laboratoire d'Optique et Photonique (KTH/ICT/Optics and Photonics/FMI) sous la direction du Professeur Bozena Jaskorzynska. L'objectif de mes recherches était la réalisation et le développement de nouveaux dispositifs optiques intégrés actifs basés sur les matériaux à base de Silicium (Silicium et Silice amorphe déposés par PECVD) et de matériaux actifs comme des polymères ou des cristaux liquides à effets électro-optiques. Au sein de ce laboratoire, j'ai co-développé le concept de coupleur directionnel optique possédant la propriété d'être un filtre accordable en longueur d'onde et mis en place le développement de films de polymère électro-optique. Ce dispositif composé d'un guide d'onde à réflexion de Bragg (BRW) et d'un guide d'onde

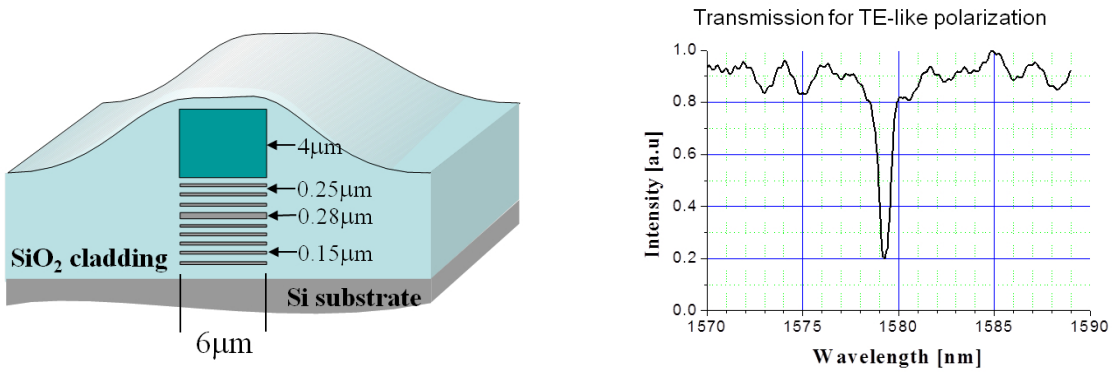

FIGURE 2.12 – Le coupleur directionnel réalisé à partir d'un guide d'onde à réseau de Bragg et d'un guide d'onde canal enterré dans de la silice (à gauche). Transmission optique mesurée dans le guide d'onde en silice dans la plage spectrale du couplage (à droite).

canal conventionnel forme un filtre sélectif en longueur d'onde compatible avec le couplage à faible perte par fibre optique. La largeur de bande transmise à travers le dispositif est de l'ordre de 2 à 3 nm à mi-hauteur (figure 2.12).

L'objectif de rendre cette structure accordable en longueur d'onde nous a conduits à modéliser ce coupleur directionnel en simulant la présence d'un matériau électro-optique dans deux configurations possibles (Figure 2.13). En s'appuyant sur le formalisme des matrices de transfert [15], de l'analyse modale développée par Visser et al. [26] et sur le concept de coupleur directionnel de Alferness et al. [27], nous avons pu déterminer les conditions de couplage entre les modes du guide canal et les modes du guide à réflexion de Bragg ainsi que les propriétés de réflexion, de transmission et de dispersion de ces structures. L'optimisation d'un coupleur directionnel repose sur le compromis entre la largeur de bande $\Delta\lambda_{-3dB}$ et l'accordabilité de celui-ci. Ce travail a notamment permis de montrer que, dans le cas d'une variation d'indice de réfraction du cœur du guide à réflexion

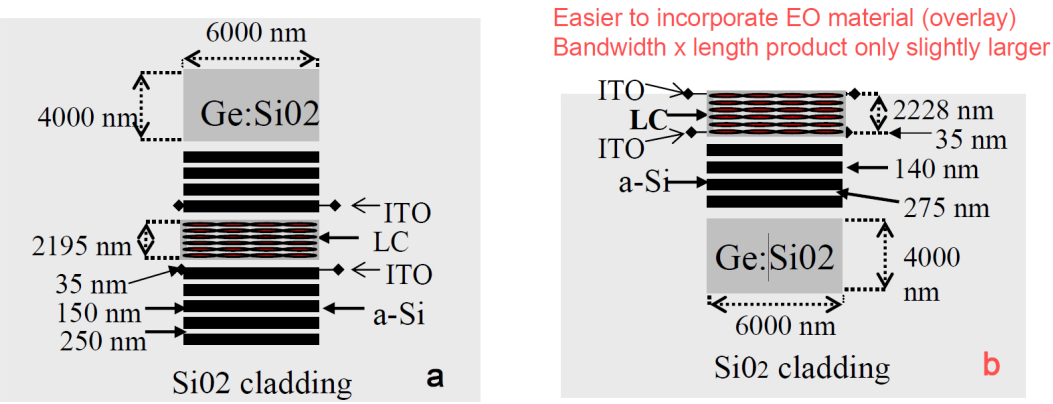

FIGURE 2.13 – Vue en coupe du coupleur directionnel accordable : a) avec un guide à réseau de Bragg complet b) avec un simple réseau de Bragg.

de Bragg de Δn=0,006, il était possible d'obtenir une accordabilité spectrale de la bande transmise à travers le dispositif de 120 nm [28].

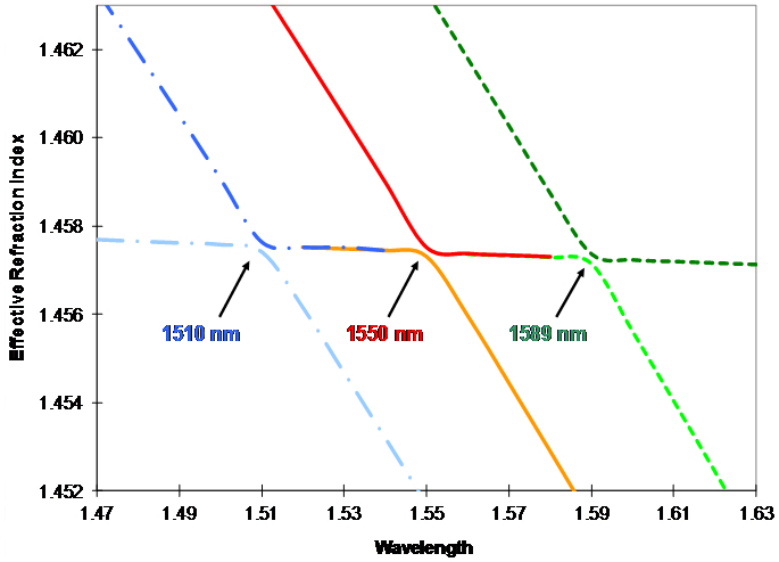

FIGURE 2.14 – Dispersion des modes du coupleur dans la plage spectrale du couplage.

Dans le but de réaliser un dispositif accordable basé sur ce principe, j'ai proposé l'utilisation de matériaux polymères possédant des propriétés électro-optiques (EO) avec des structures Si/SiO_2 amorphes déposées par PECVD. J'ai ainsi initié les études avec un matériau de référence dans un système "guest-host", le polyméthylméthacrylate (PMMA) dopé par le colorant Disperse Red 1 (DR1) et un polymère thermoréticulable synthétisé par F. Odobel et al. [29,30]. Ce dernier est plus performant du point de vue de la stabilité dans le temps et de l'effet électro-optique. Afin d'obtenir une susceptibilité non linéaire

quadratique non nulle et donc un effet électro-optique dans les films de polymère, j'ai mis en place un dispositif de polarisation sous champ couronne ("Corona poling") en configuration triode avec chauffage et régulation du courant couronne [31]. J'ai pu vérifier l'efficacité de ce dispositif pour polarisation sous champ couronne des polymères électro-optiques par des mesures de biréfringence induite de l'ordre de $\|n_o - n_e\| = 10^{-2}$ dans les films minces de PMMA-DR1. Ces matériaux uniaxes positifs présentent une symétrie $C_{\infty v}$, c'est à dire une infinité de plans de symétrie colinéaires avec l'axe du poling (en général perpendiculaire aux interfaces du film). L'ellipsoïde des indices est présenté sur la figure 2.15 et est décrit

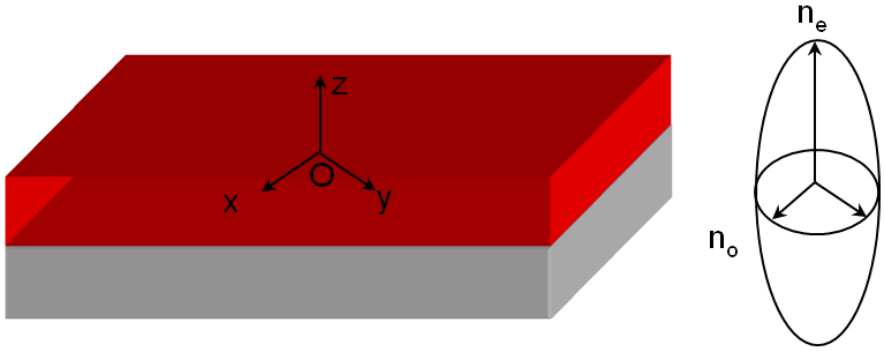

FIGURE 2.15 – Film de PMMA-DR1 orienté sous champ avec son ellipsoïde des indices de réfraction.

par l'équation 2.14. Le tenseur électro-optique (r_{ij}) des polymères Guest-host en notation réduite est représenté (équation2.15)

$$\frac{x^2}{n_o^2} + \frac{y^2}{n_o^2} + \frac{z^2}{n_e^2} = 1 \qquad (2.14) \qquad (r_{ij}) = \begin{pmatrix} 0 & 0 & r_{13} \\ 0 & 0 & r_{13} \\ 0 & 0 & r_{33} \\ 0 & r_{13} & 0 \\ r_{13} & 0 & 0 \\ 0 & 0 & 0 \end{pmatrix} \qquad (2.15)$$

Suivant la direction selon les axes Ox(Oy) et Oz, les variations d'indice obtenues sont donnés par l'équation (2.16) :

$$\begin{aligned} n_x = n_y &= n_o - \tfrac{1}{2} n_0^3 r_{13} Ez \\ n_z &= n_e - \tfrac{1}{2} n_e^3 r_{33} Ez \end{aligned} \qquad (2.16)$$

Afin d'avoir une connaissance plus approfondie de ces matériaux électro-optiques organiques pour permettre la simulation du dispositif plus avant, j'ai mis en place un banc de caractérisation des effets électro-optiques de films minces. Ce banc de caractérisation fonctionne en mode transmission dans des structures Fabry-Pérot réalisées à partir de films minces de polymère électro-optique munis d'électrodes semi-transparentes métalliques [32]. Des impulsions électriques alternatives sont appliquées au modulateur ainsi constitué qui est mis en rotation par rapport à son axe vertical. Un faisceau laser incident est transmis à travers le modulateur, son intensité est modulée par effet EO. Celle-ci est enregistrée

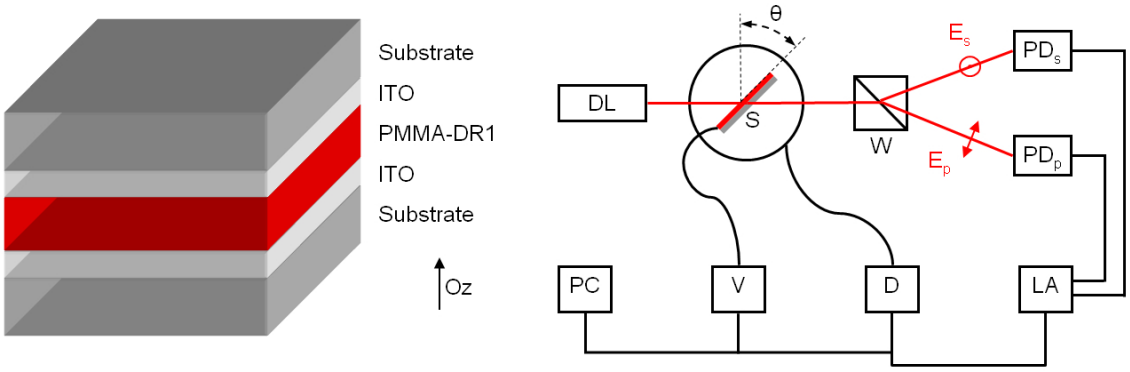

FIGURE 2.16 – Montage interférométrique de type Fabry-Pérot : DL Diode Laser, S Echantillon, W prisme Wollaston, PDs PDp Photodiode pour la polarisation S et P, LA Détection synchrone, D Moteur, V Tension AC, PC Ordinateur, P Polariseurs.

par l'intermédiaire d'une détection synchronisée sur les impulsions électriques alternatives. Les analyses par le formalisme des matrices de transfert et par une méthode numérique d'ajustement du type Simplex [33] de ce signal modulé en fonction de l'angle d'incidence conduisent à la détermination des coefficients électro-optiques r_{13} et r_{33} du polymère caractérisé. Dans le cas du PMMA-DR1 (figure 2.17), nous avons obtenu des valeurs en accord

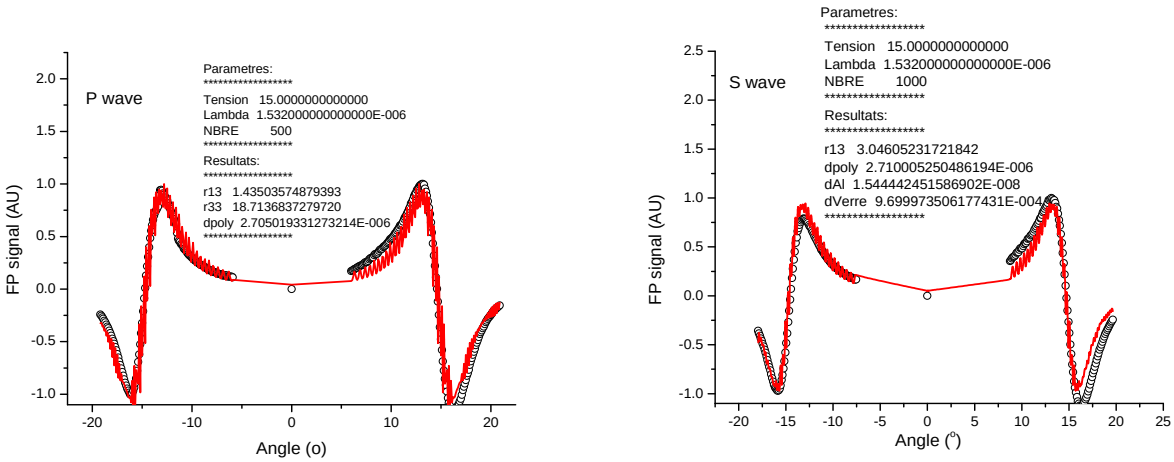

FIGURE 2.17 – Transmissions modulées expérimentales et leurs ajustements conduisant à la détermination des coefficients r_{13} et r_{33}.

avec la littérature (r_{13} =1 à 4 $pm.V^{-1}$ et r_{33} =10 à 30 $pm.V^{-1}$).

Publications

- V. Boucher, J. Cardin, D. Leduc, R. Seveno, R. Le Ny, H. W. Gundel, C. Boisrobert, S. Legoupy, F. Legros, V. Montembault, F. Odobel, C. Monnereau, E. Blart, D. Bosc, A. Goullet, and J. Y. Mevellec, Synthesis and characterization of polymers for nonlinear optical applications, Proc of SPIE on Advanced Optical Materials and Device (AOMD-3), vol 5122, pages 206-209, 2003.
- B. Jaskorzynska, Z. J. Zawistowski, M. Dainese, J. Cardin, and L. Thylen, Widely tunable directional coupler filters with 1d photonic crystal, In Transparent Optical Networks, IEEE Proceedings of 2005 7th Int. Conf., vol 1, pages 136-139, 2005.

2.2 Etude des matériaux luminescents.

Les interactions lumière - matière se partagent entre les phénomènes de diffusion (élastique et inélastique) et les phénomènes à absorption comme la luminescence. La luminescence est une émission de photons ultraviolets, visibles ou infrarouges à partir d'une espèce excitée électroniquement. Elle se produit dans de nombreux matériaux inorganiques (verre dopé terres rares) comme organiques (noyaux aromatiques : naphtalène, anthracène) et dans les trois phases solide, liquide, gazeuse de la matière. Les différents types de luminescence sont classés selon leur mode d'excitation (voir Tableau (2.5) ci-dessous :

Nom	**formes d'excitation**
Photoluminescence (fluo. et phosph.)	Absorption de lumière (photons)
Electroluminescence	courant ou champ électrique
Cathodoluminescence	faisceau d'électrons
Thermoluminescence	flux de chaleur (excitation antérieure)
Radioluminescence (scintillation)	rayonnement ionisant (RX, α, β, γ)
Chemiluminescence	réaction chimique (ex. oxydation)
Triboluminescence	friction mécanique
Sonoluminescence	son (ultrason)
Bioluminescence	processus biochimique

TABLE 2.5 – Les différents types de luminescence d'après [34].

La photoluminescence est une luminescence où le mode d'excitation est réalisé par l'absorption d'un photon, ce qui conduit l'espèce luminescente dans un état électronique excité. La désexcitation électronique s'accompagne d'une émission de photons qui est soit une fluorescence soit une phosphorescence.

Nous allons particulièrement discuter des propriétés de photoluminescence de matériaux solides en films minces dans lesquels on peut distinguer une matrice hôte (par exemple un oxyde ou un semi-conducteur) contenant le luminophore (par exemple un puits quantique ou un ion de terre rare).

2.2.1 Matrices hôtes.

La matrice hôte contient le luminophore ; elle permet son excitation par voie optique dans le cas de la photoluminescence et favorise son excitation et son émission. Selon les propriétés de la matrice hôte (mécanique, chimique, thermique. . .), celle-ci favorise également la mise en forme pour la réalisation d'applications spécifiques (ex : matrices polymères thermodéformables). En général, les matrices hôtes performantes doivent présenter certaines caractéristiques spécifiques favorisant la photoluminescence :

➤ Une faible absorption devant le gain sur la plage spectrale comprenant les longueurs d'onde de pompage ainsi que celles d'émission.

- ➤ Les canaux de désexcitation non-radiatifs doivent être limités devant les voies radiatives. Ces sources de déclin non-radiatifs ont de multiples origines (densité et énergie de phonons, défauts...)
- ➤ Les matrices jouent parfois le rôle de sensibilisateur en exacerbant l'excitabilité des luminophores qu'elles contiennent via des mécanismes d'excitation indirecte (transferts d'énergie vers les populations de luminophores). Il s'agit d'un cas particulier où les matrices doivent être absorbantes sur la gamme spectrale d'excitation.

Les matrices étudiées au CIMAP sont des matériaux semi-conducteurs ou isolants principalement de nature inorganique que l'on peut regrouper dans les catégories ci-dessous :

- ➤ Les matrices de silice non stœchiométrique (SiO_x) contenant un excès de Si pouvant conduire, après un recuit adapté, à des nanostructures de Si,
- ➤ Les matrices de nitrure de silicium non stœchiométrique (SiN_x),
- ➤ Les oxydes transparents conducteurs à grand gap comme Ga_2O_3 et ZnO,
- ➤ Des matrices organiques de type polyméthacrylate de méthyle (PMMA),
- ➤ Quelques composés ont été étudiés sous forme liquide pour des études spécifiques.

2.2.2 Centre émetteur/luminophore.

Les centres émetteurs/luminophores présentent pour caractéristiques communes des niveaux d'énergie électroniques qui peuvent être discrets comme dans le cas des terres rares ou densément rassemblés en bandes d'énergie dans les matériaux massifs comme les semi-conducteurs. Le diagramme de Perrin-Jablonski (Figure 2.18) représente de manière schématique les mécanismes d'absorption et de désexcitation survenant dans un processus de photoluminescence.

- ➤ L'absorption de photons incidents (pompage optique) conduit les électrons vers un état excité. C'est le phénomène le plus rapide des processus présentés avec des temps caractéristiques de 10^{-15}s. Plusieurs mécanismes sont alors possibles pour dépeupler ces états excités vers des états de plus basse énergie :
  - ➤ Une transition non-radiative vibrationnelle (TRNV) qui entraîne un dépeuplement des états excités en fournissant de l'énergie à la matrice hôte par génération de phonons. Ce phénomène présente des temps caractéristiques de 10^{-10} à 10^{-12} s.
  - ➤ Une transition non-radiative directe (TNRD) sans conversion d'état de spin (état singulet $\rightarrow$ état singulet). Les temps caractéristiques sont de l'ordre de 10^{-11} à 10^{-9} s.
  - ➤ Une désexcitation radiative de type fluorescence avec des temps caractéristiques de l'ordre de 10^{-10} à 10^{-7}s.
  - ➤ Une transition non-radiative indirecte (TNRI) avec conversion d'état de spin (état singulet $\rightarrow$ état triplet). Les temps caractéristiques sont de l'ordre de 10^{-10} à 10^{-8} s.
  - ➤ Une transition radiative de type phosphorescence avec des temps caractéristiques de l'ordre de 10^{-6} à 1 s.

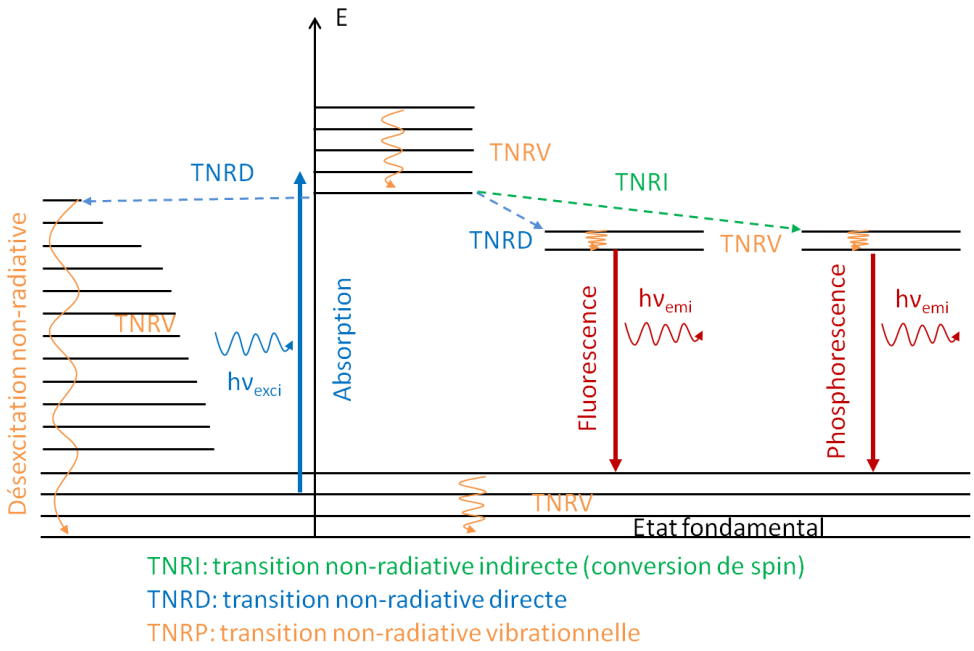

FIGURE 2.18 – Diagramme de Perrin-Jablonski.

Il est d'usage de distinguer expérimentalement les deux processus luminescents par un temps de déclin plus long pour la phosphorescence que pour la fluorescence. Cependant certaines phosphorescences présentent des durées de vie comparables à celles de la fluorescence, donc la distinction des deux phénomènes par la seule durée de vie n'est pas suffisante. L'émission de phosphorescence de par les transferts/transports d'énergie conduisant à la conversion de spin sera généralement de plus basse énergie que celle de fluorescence. Une photoluminescence sera observée lorsque les processus radiatifs seront majoritaires devant les non-radiatifs, ce qui se traduit par la relation 2.17 donnant l'efficacité de recombinaison radiative en fonction des probabilités de recombinaison radiative W_r et non-radiative W_{nr}.

$$\eta = \frac{W_r}{W_r + W_{nr}} \tag{2.17}$$

Les matériaux luminescents sont souvent des matériaux présentant une bande interdite d'énergie, dont la largeur est supérieure à l'énergie moyenne des phonons présents dans la matrice. C'est la raison pour laquelle, à l'état massif, les métaux ne luminescent pas alors qu'à l'état subnanométrique (r<0,5 nm longueur d'onde de Fermi) une luminescence est observée [35]. Celle-ci est due à leur nouvelle structure électronique présentant des niveaux d'énergie discrets avec un espacement entre les niveaux d'énergie supérieur à l'énergie d'activation thermique k_BT.

2.2.3 Le silicium nanostructuré.

Le silicium étant massivement utilisé en micro-électronique, c'est un matériau abondant et à la technologie bien maîtrisée. Afin de développer des applications mêlant microélectronique et photonique/optique, de nombreuses recherches ont été entreprises afin d'exalter les propriétés optiques du silicium dont la luminescence. Cependant, à l'état massif le silicium est un semi-conducteur à gap indirect dans lequel les recombinaisons radiatives entre bande de conduction et bande de valence s'accompagnent nécessairement de l'émission ou de l'absorption d'un phonon pour assurer la conservation de l'impulsion. La faible probabilité d'occurrence de ce processus radiatif assisté par phonon rend les transitions non-radiatives vibrationnelles prépondérantes dans le mécanisme de désexcitation des niveaux électroniques du silicium. La figure 2.19 représente schématiquement le phénomène d'absorption et d'émission de photons dans les semi-conducteurs à gap direct et indirect. Par conséquent, la luminescence du silicium est de plusieurs ordres de grandeur moins effi-

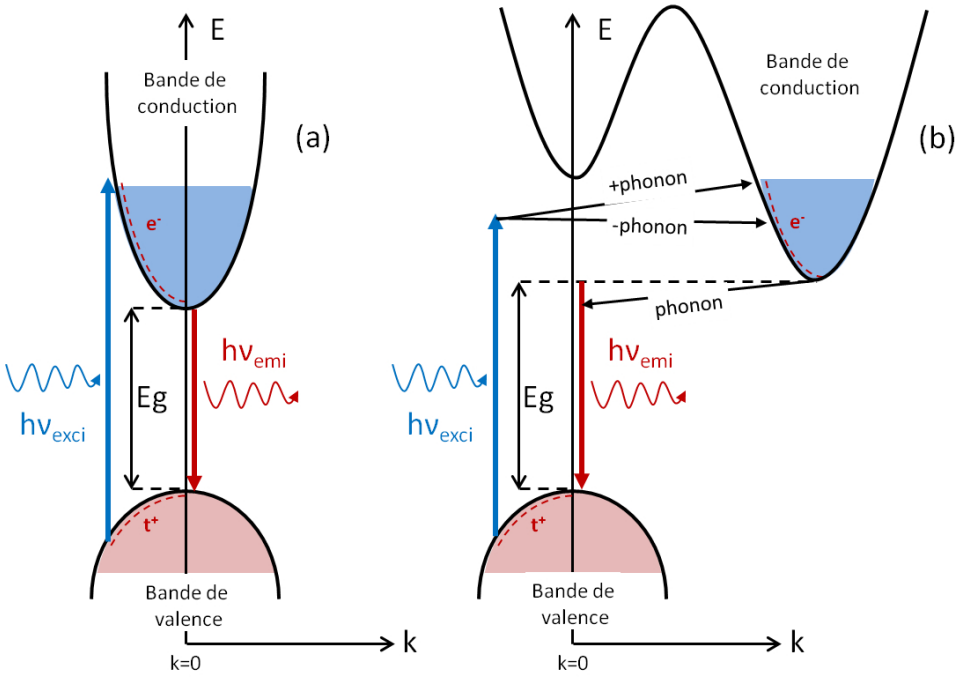

FIGURE 2.19 – Représentation schématique des phénomènes d'absorption et d'émission de photons dans les semi-conducteurs à (a) gap direct et (b) indirect.

cace que dans un matériau à gap direct comme l'InP. L'efficacité de recombinaison radiative du silicium massif est $\eta_{Si} \approx 10^{-6}$ [36].

Dans les années 1990, les travaux de L.T. Canham [37] ont montré que le silicium nanostructuré (appelé silicium poreux) présentait des propriétés de luminescence exaltée par rapport au silicium massif, et ceci à température ambiante. Par la suite, des travaux sur des nanoparticules de silicium (Nps-Si) en matrice diélectrique ont montré également des propriétés de luminescence importantes avec une plus grande stabilité dans le temps

due à la réduction de l'oxydation par rapport au silicium poreux. Ces nanoparticules de silicium présentent une luminescence avec une bande large dont l'énergie du maximum évolue selon la relation $E_{max}^{PL} \approx \frac{1}{d^p}$ avec d le diamètre de la nanoparticule et la puissance p [38]. Par exemple, Zacharias et al. [39] ont montré une variation de cette énergie dans une plage 1,25 à 1,55 eV pour une variation de diamètre d de 3,8 à 2 nm et avec une valeur de p=0,6 (Figure 2.20). Récemment, une efficacité quantique externe de 30 à 70% et interne

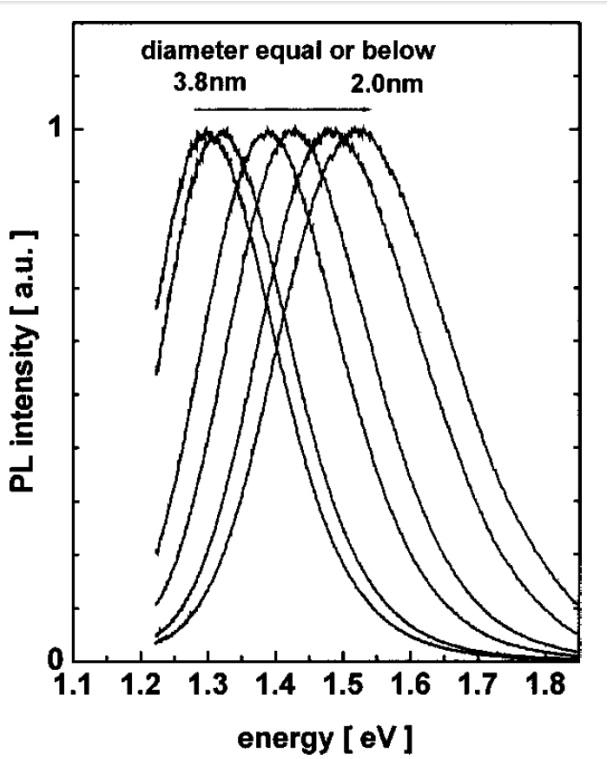

FIGURE 2.20 – Spectres de photoluminescence normalisés montrant un décalage vers le bleu corrélé avec la taille des cristaux [39].

tendant vers 100% a été obtenue sur des nanocristaux de silicium passivés par des ligants en solution, par le groupe de J. Linnros [40] en Suède.

Cette propriété de luminescence exaltée dans les nanostructures de silicium par rapport au silicium massif est communément attribuée au phénomène de confinement quantique des excitons (paire électron-trou) formés lors de l'absorption d'un photon dans les nanostructures. Le confinement quantique excitonique apparaît soit lorsque la taille de l'objet confinant devient plus petite que le rayon de l'exciton dans un matériau massif (rayon de Bohr de l'exciton), soit lorsque cette taille limite le libre parcours moyen de diffusion de l'exciton dans une ou plusieurs dimensions. Selon que l'on ait un confinement dans une, deux ou trois dimensions, on parle d'un puits quantique, d'un fil quantique ou d'une boîte quantique. Dans le cas des nanostructures de silicium, le confinement quantique induit également une augmentation de l'énergie de la bande interdite ainsi que du rayon de courbure des bandes, provoquant une relaxation des règles de sélection qui conduit à une plus grande

efficacité de recombinaison radiative. On dit couramment que le silicium nanostructuré est un matériau à gap quasi direct. Cependant, des observations plus détaillées de la luminescence des nanostructures de silicium ont montré : (i) des temps de déclin de PL longs comparés à ceux d'un semi-conducteur à gap direct, (ii) un fort couplage de la luminescence avec les phonons, (iii) une largeur spectrale importante et (iv) un temps de recombinaison radiatif non-exponentiel. Ces observations conduisent à une explication alternative de l'efficacité de luminescence des nanostructures de silicium. En effet, les nanostructures de silicium limiteraient le transport excitonique de par la barrière de potentiel formée par l'interface Si/SiO_2. Le transport excitonique étant fortement réduit, ceci conduit à une réduction drastique de la probabilité de recombinaison non-radiative W_{nr} sur des défauts, ce qui a pour conséquence une augmentation de l'efficacité de recombinaison radiative $\eta = \frac{W_r}{W_r+W_{nr}}$. Cette dernière explication est minoritaire dans la communauté mais apporte cependant des éléments d'interrogation significatifs au débat scientifique.

Dans les travaux effectués au CIMAP de Caen, nous observerons principalement des nanostructures de types boîtes quantiques, sous forme de nanoparticules de silicium (Nps-Si). Celles-ci sont fréquemment fabriquées par la synthèse de matrices de SiO_x non-stœchiométriques contenant un excès de silicium par rapport à la stœchiometrie de la silice (x < 2). Un traitement thermique approprié permet, par la suite la migration et l'agglomération de l'excès de Si sous forme de Nps-Si.

2.2.4 Les terres rares.

Les terres rares sont des éléments métalliques remarquables de par leur structure électronique : en effet, leur couche interne $4f^n$ (1<n<14) est incomplète, tandis que les couches externes $5s$ et $5p$ sont, quant à elles, entièrement remplies. Les terres rares utilisées pour leurs propriétés d'émission dans des matrices d'oxyde ou de nitrure sont dans un état d'oxydation III+ qui est le plus stable. Les configurations électroniques dans l'état fondamental et l'état III+ des principales terres rares étudiées dans ces travaux sont répertoriées dans le tableau 2.6 :

Nom	Symbole	Configuration électronique	
		fondamental	III+
Néodyme	Nd	[Kr]-$4d^{10}4\vec{f}^{4}5s^{2}5p^{6}5d^{0}6s^{2}$	[Kr]-$4d^{10}4\vec{f}^{3}5s^{2}5p^{6}5d^{0}6s^{0}$
Europium	Eu	[Kr]-$4d^{10}4\vec{f}^{7}5s^{2}5p^{6}5d^{0}6s^{2}$	[Kr]-$4d^{10}4\vec{f}^{6}5s^{2}5p^{6}5d^{0}6s^{0}$
Terbium	Tb	[Kr]-$4d^{10}4\vec{f}^{9}5s^{2}5p^{6}5d^{0}6s^{2}$	[Kr]-$4d^{10}4\vec{f}^{8}5s^{2}5p^{6}5d^{0}6s^{0}$
Erbium	Er	[Kr]-$4d^{10}4\vec{f}^{12}5s^{2}5p^{6}5d^{0}6s^{2}$	[Kr]-$4d^{10}4\vec{f}^{11}5s^{2}5p^{6}5d^{0}6s^{0}$
Ytterbium	Yb	[Kr]-$4d^{10}4\vec{f}^{14}5s^{2}5p^{6}5d^{0}6s^{2}$	[Kr]-$4d^{10}4\vec{f}^{13}5s^{2}5p^{6}5d^{0}6s^{0}$

TABLE 2.6 – Configuration électronique des terres rares étudiées.

De cette anomalie de remplissage des couches électroniques résultent les propriétés particulières qui font l'intérêt de ces éléments. Cette propriété, qui est un inconvénient

pour la séparation des terres rares par voie chimique, devient un avantage pour le dopage. En effet, les terres rares peuvent s'insérer de manière quasi identique dans des matrices hôtes de compositions chimiques différentes. Leurs propriétés optiques, étant liées aux transitions entre les niveaux électroniques de la couche $4f$ protégée de l'extérieur par les couches pleines $5s$ et $5p$, ont un comportement plus proche de celui des atomes libres (comme dans les gaz) que de celui des atomes insérés dans un cristal. Ainsi les niveaux d'énergie des ions terres rares dans un solide ne vont pas s'organiser en bandes comme dans tout autre solide, mais restent sous forme discrète à position moyenne prévisible et fixe.

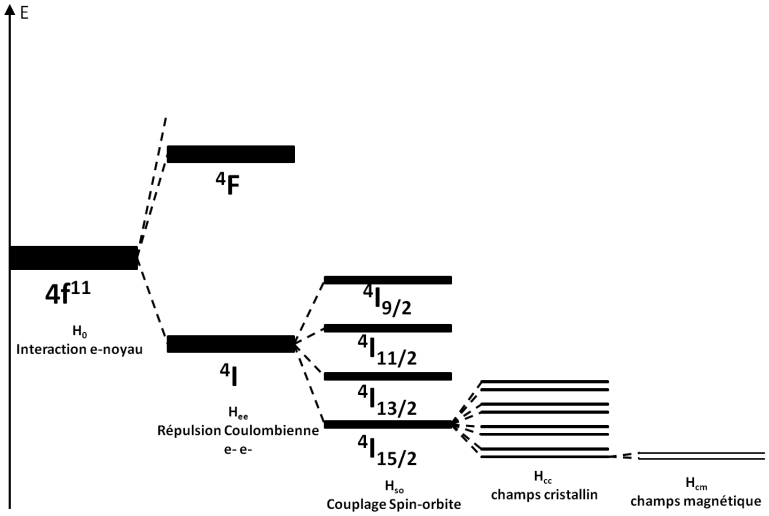

FIGURE 2.21 – Niveaux d'énergie de l'ion Er^{3+} en fonction des interactions électroniques considérées décrites par leur Hamiltonien respectif.

Le degré de dégénérescence des niveaux électroniques $4f^n$ des ions de terre rare est donné par la combinaison C_{14}^n avec n variant de 0 à 14. La dégénérescence peut être partiellement ou totalement levée par les interactions suivantes, décrites par un Hamiltonien spécifique :

- ➤ Interactions électrons-noyau, H_0,
- ➤ Interaction Coulombienne de répulsion électron-électron, H_{ee},
- ➤ Interaction spin-orbite, H_{so},
- ➤ Interaction avec le champ cristallin, H_{cc}.

Les niveaux d'énergie de l'ion libre sont caractérisés par les nombres quantiques correspondants donnés en notation spectroscopique suivante :

$$^{2S+1}L_J \tag{2.18}$$

avec $\vec{L} = \sum \vec{l}$ le moment orbital total et le moment $\vec{S} = \sum \vec{s}$ total de spin, desquels résulte par sommation le moment total $\vec{J} = \vec{S} + \vec{L}$ ($|L - S| \leq J \leq |L + S|$).

Comme mentionné préalablement, l'écrantage des électrons de la couche $4f$ par les couches externes pleines $5s2$ et $5p^6$ réduit très fortement l'influence du champ cristallin.

Cette propriété fait que les niveaux d'énergie d'un ion de terre rare au sein d'un matériau hôte dépendra très peu de la nature et de la qualité du site. On considéra donc souvent que les niveaux d'énergie d'un ion de terre rare au sein d'un matériau hôte sont identiques aux niveaux d'énergie de l'ion libre (c'est-à-dire soumis aux interactions électron-noyau, électron-électron et couplage spin-orbite). La qualité de la matrice hôte, contrairement au cas des autres ions dans un solide (semi-conducteur), n'a que peu d'influence sur les propriétés optiques. Ces ions sont ainsi peu sensibles au désordre, même au désordre extrême d'un verre.

L'influence du champ cristallin sur l'ion de terre rare n'est détectable que dans un matériau cristallin refroidi à basse température [41]. Il se manifesterait par une levée supplémentaire de la dégénérescence due à l'effet Stark provoquant l'apparition de sous-niveaux dont l'écartement est fonction du champ local et de la symétrie du site de la terre rare. Les transitions des ions terres rares trivalents, habituellement mis en jeu dans les émissions qui nous intéressent, ont lieu dans la configuration $4f^n$, c'est-à-dire entre états de même parité. De ce fait, elles sont interdites au premier ordre pour les émissions dipolaires électriques et permises au premier ordre pour les transitions dipolaires magnétiques par la Règle de Laporte [42]. Les transitions magnétiques et électriques dans les ions de terre rare sont cependant observables avec des probabilités équivalentes. Ceci est dû à une relaxation des règles de sélection liée à un mélange de parité avec des configurations de parité opposée et d'énergies plus élevées [43].

La transition entre niveaux d'énergie a une probabilité d'occurrence Γ, qui peut être calculée en utilisant la théorie de Judd-Ofelt [44]. Cette probabilité de transition entre deux niveaux est fonction de la probabilité de transition radiative Γ_r et de la probabilité de transition non-radiative Γ_{nr}, suivant la relation (2.19).

$$\Gamma = \Gamma_r + \Gamma_{nr} \tag{2.19}$$

A température ambiante, la durée de vie globale τ est mesurable. Celle-ci est liée à la probabilité de transition $\Gamma = \frac{1}{\tau}$. Des mesures à basse température, quelques K, sont nécessaires pour mesurer directement la durée de vie radiative $\tau_r = \frac{1}{\Gamma_r}$.

Des mécanismes limitant la photoluminescence des ions de terre rare peuvent intervenir dans des matrices fortement dopées ou codopées par ceux-ci. Lorsque la concentration en ions terres rares augmente dans une matrice hôte, des interactions ion-ion se produisent qui viennent diminuer l'intensité de luminescence. Le phénomène se manifeste généralement pour une distance entre deux ions inférieure à 2 nm, ceci conduit à une concentration des ions de quelque 10^{21} cm^{-3}. Les mécanismes responsables de cette diminution de la luminescence sont la relaxation croisée, l'absorption dans l'état excité, la migration d'énergie [43, 45].

Des mécanismes coopératifs à plusieurs ions de terre rare se produisant par transfert d'énergie peuvent également survenir conduisant à des mécanismes de conversion de fréquence comme les phénomènes de upconversion, de downconversion, addition de photons par transfert d'énergie... [43, 45].

2.2.5 Couplage entre nanoparticule de silicium et terre rare.

Les ions de terre rare (TR^{3+}), incorporées dans une matrice diélectrique comme la silice, présentent une faible section efficace d'absorption ($\sigma_{abs} \approx 10^{21} cm^2$). L'obtention d'une luminescence et donc d'un gain optique important sous un pompage modéré est donc problématique. Une solution à cette difficulté est de contourner la faible section efficace d'absorption par l'utilisation d'une excitation indirecte via une interaction donneur-accepteur (nanoparticule de silicium/TR^{3+}). On parle également d'utilisation d'un sensibilisateur de la terre rare. Les mécanismes d'excitation indirecte via une interaction donneur-accepteur présentent la caractéristique commune de nécessiter un accord des énergies mises en jeux entre le donneur et l'accepteur. Dans le cas d'un transfert radiatif (figure 2.22), l'énergie du pic d'émission du donneur doit coïncider avec l'énergie du pic d'absorption de l'accepteur, l'intégrale de recouvrement doit être non nulle.

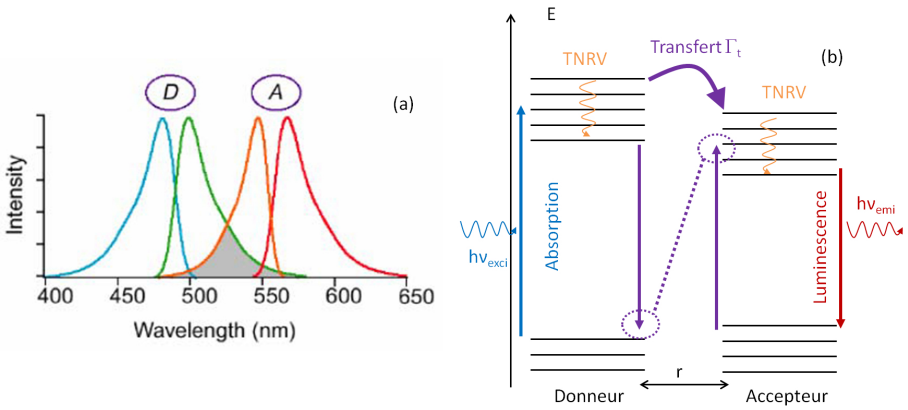

FIGURE 2.22 – (a) Bandes d'absorption et d'émission du donneur et de l'accepteur (b) Système donneur-accepteur typique.

Pour ce type d'interaction, deux mécanismes impliquant la distance nanoparticule-terre rare r sont couramment décrits :

- ➤ L'interaction d'échange électronique ou une interaction dipôle-dipôle. L'interaction d'échange présente un taux de transfert qui suit une loi en $\Gamma_t \approx \frac{r}{r_0}$ avec le rayon de Bohr effectif r_0.
- ➤ L'interaction dipôle-dipôle est régie par la théorie de Förster du couplage (FRET : Förster Resonant Energy Transfer) qui décrit le taux de transfert par une loi du type $\Gamma_t \approx \frac{1}{r^6}$.

Le rayon de Bohr effectif des ions de terre rare r_0<0,3Å [46] est petit devant les dimensions des nanoparticules de silicium (quelques nm). Le rayon de Förster des Nps-Si est quant à lui de l'ordre de 10 nm [47]. Par conséquent, l'interaction par échange Np-Si)/TR^{3+} sera négligeable devant l'interaction dipôle-dipôle (Förster). Le transfert Np-Si/TR^{3+} se faisant par couplage de Förster dans une région proche (< 10nm) des nanoparticules de silicium, il est nécessaire d'atteindre une distribution optimale des ions de terre rare dans la proximité des Nps-Si pour maximiser le transfert et par conséquent l'efficacité de lu-

minescence du système. Du fait que la section efficace d'absorption directe des Nps-Si de plusieurs ordres de grandeur supérieure à celle des ions de terre rare ($10^{-15}cm^2$ contre $10^{-21}cm^2$), l'excitation indirecte par les Nps-Si permet d'atteindre une section efficace effective des ions de terre rare augmentée de plusieurs ordres de grandeur. Outre ce fait, l'élargissement du gap des Nps-Si permet de limiter le transfert inverse de la terre rare vers les Nps-Si. De plus, la bande d'absorption des Nps-Si étant spectralement plus large que celle des ions de terre rare, ceci relâche la contrainte sur la finesse spectrale des sources de pompage optique.

La figure 2.23 représente le schéma de bande illustrant le couplage d'une Np-Si vers les ions Nd^{3+} et Er^{3+}. Le couplage entre la Np-Si et les ions de terre rare se fait respectivement depuis le niveau $^4I_{\frac{9}{2}}$ pour le Nd^{3+} et $^4I_{\frac{15}{2}}$ pour le Er^{3+}.

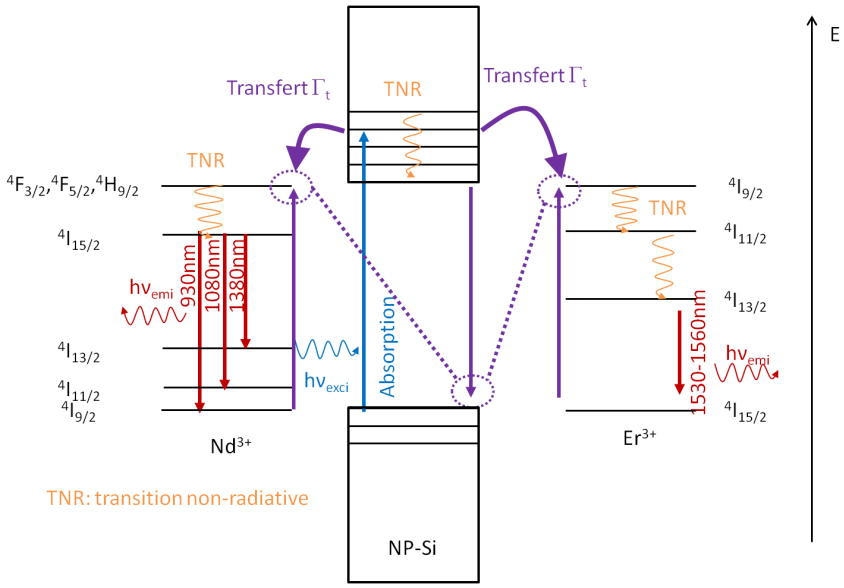

FIGURE 2.23 – Schéma de bande illustrant le couplage d'une Np-Si vers les ions Nd^{3+} et Er^{3+}.

Dans le cas d'une matrice contenant des nanostructures de silicium et des ions néodyme partiellement couplés, nous pouvons observer sur la figure 2.24 un spectre de photoluminescence comportant la luminescence des nanoparticules de silicium et de l'ion de terre rare Nd^{3+}.

Le transfert entre les nanoparticules de silicium et les ions de terre rare est parfois décrit de manière phénoménologique par un coefficient de transfert K exprimé en $cm^3.s^{-1}$. Les équations (2.20) décrivent la variation temporelle de l'état excité N^* et de l'état fondamental N des niveaux électroniques de Nps-Si considérées comme un système à deux niveaux :

$$\begin{cases} \frac{dN^*}{dt} &= \sigma\phi\,(N - N^*) - \frac{N^*}{\tau_r^{nr}} - KN^*N_0^{TR^{3+}} \\ \frac{dN}{dt} &= -\sigma\phi\,(N - N^*) + \frac{N^*}{\tau_r^{nr}} + KN^*N_0^{TR^{3+}} \end{cases} \tag{2.20}$$

Les valeurs de K ont été déterminées grossièrement pour le couplage Np-Si/Er^{3+} seulement.

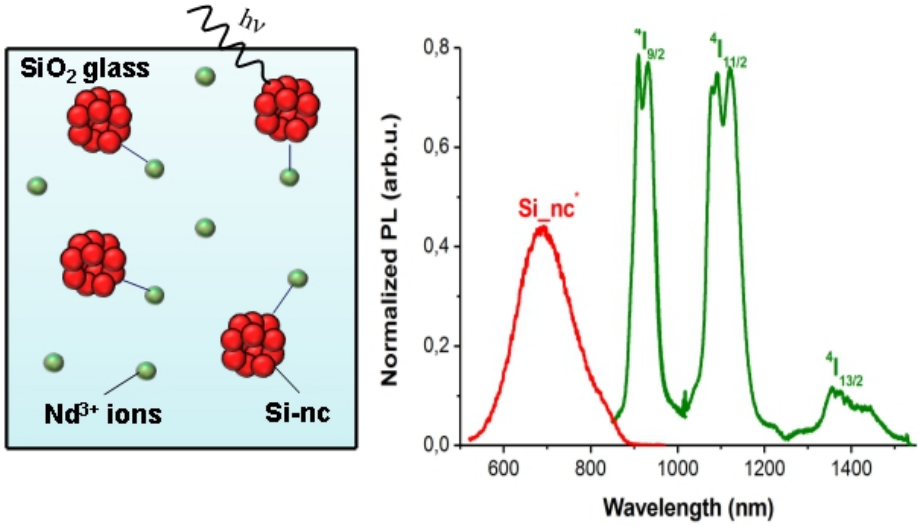

FIGURE 2.24 – Illustration du transfert d'énergie des Nps-Si vers les ions Nd^{3+} et spectre de photoluminescence montrant la luminescence des Nps-Si (en rouge) et du néodyme provenant du niveau ${}^4F_{\frac{3}{2}}$ (en vert) à 920 1060 et 1400 nm.

Les valeurs obtenues sont dans l'intervalle 2.10^{-14} et 3.10^{-15} $cm^{-3}.s^{-1}$ [48]. Les interactions donneur-accepteur dépendant de la distance, un modèle inspiré de celui de Pacifici [48] mais incluant l'effet de la distance de séparation a été développé par Garrido et al. [49]. Les auteurs utilisent pour cela un coefficient de couplage (K1) entre Nps-Si et TR^{3+} qui est fonction de la distance entre le donneur et l'accepteur. Ces phénomènes de couplage sont plus longuement décrits pour les ions erbium dans les travaux de Kenyon et al. [50], de Fuji et al. [51] et des travaux postérieurs [52–57]. Pour le couplage Np-Si :Nd^{3+}, ces phénomènes sont beaucoup moins documentés avec toutefois des études plus récentes suivantes [58–63].

2.2.6 Fabrication/synthèse des matériaux à base de silicium.

Les matériaux en film mince étudiés sont, sauf mention contraire, obtenus par une technique de pulvérisation radio-fréquence magnétron réalisée au CIMAP. Ce processus se divise en trois grandes étapes : la préparation, la pulvérisation et le recuit. La préparation comprend le nettoyage des substrats par différentes techniques (Éthanol, HF, nettoyeur plasma) qui ont un impact significatif sur la qualité et les propriétés finales des échantillons. La pulvérisation est déclinée dans la configuration verticale classique et confocale sur des bâtis de dépôt différents. Après le dépôt proprement dit, les films sont ensuite découpés puis recuits en appliquant un traitement thermique adapté afin d'atteindre les propriétés souhaitées/optimisées. Les principales caractéristiques de ces trois étapes de fabrication sont répertoriées dans le schéma (Figure 2.25) suivant :

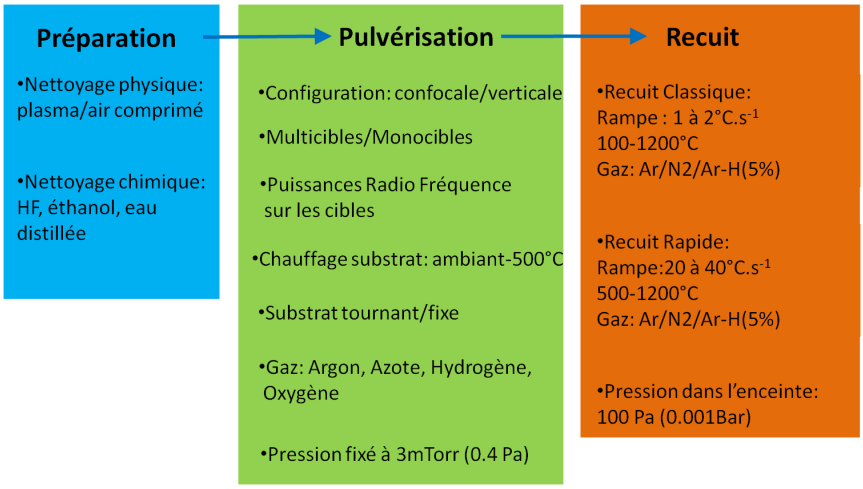

FIGURE 2.25 – Présentation synthétique du processus de fabrication avec ses principaux paramètres/degrés de liberté.

Les techniques de caractérisation utilisées sont répertoriées sur la figure (2.26). Les

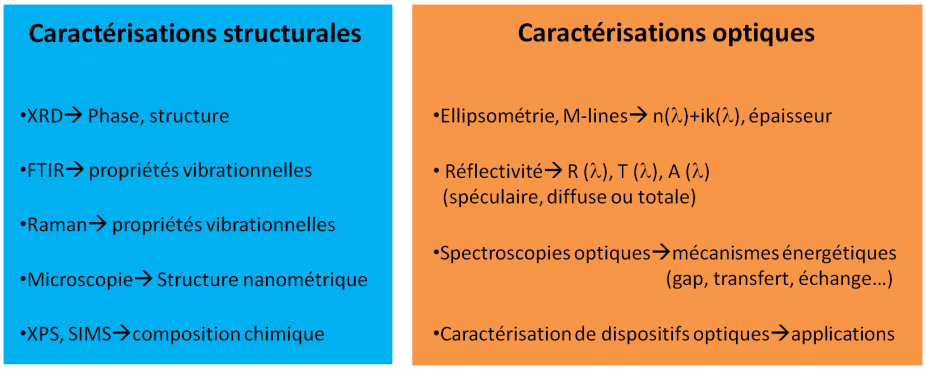

FIGURE 2.26 – Présentation synthétique des techniques de caractérisation.

descriptions des conditions de préparation, dépôts par pulvérisation, des traitements ther-

miques et des techniques de caractérisation sont détaillées dans les travaux de thèse auxquels j'ai pu participer ces dernières années :

- Matrices de SiO_x dopées terre rare (Er, Nd), il s'agit des travaux de thèse de M Khalil Hijazi [64], M Sébastien Cueff [36] et de M Chuan-Hui Liang [65],
- Matrices de SiN_x dopées terre rare (Er, Nd), cela est détaillé dans les travaux de thèse de M Chuan-Hui Liang [65],
- Matrices de SiO_x et SiN_x en super-réseau de pas nanométrique, des détails se trouvent dans les travaux de thèse de Mme Ramesh Pratibha Nalini Sundar [66],
- Matrices de SiN_x et SiN_xO_y dopées terre rare (Tb,Yb), des descriptions sont données dans les travaux de thèse de Mmes Yong-Tao An [67] et Lucile Dumont(en cours),
- Matrices de Ga_2O_3 et ZnO dopées terre rare (Nd,Eu), les travaux de thèse de Mme Céline Lecerf [68] et M Christian Davesnne [69] développent la description des dépôts.

2.2.7 Sélection de travaux.

Cette sélection de travaux a pour but de montrer les thématiques auxquelles j'ai pu contribuer sur les matériaux développés au laboratoire CIMAP dans l'équipe NIMPH ou étudiés dans le cadre de collaborations.

Matrice SiO_x

Les films de silice enrichie en silicium ont été développés par pulvérisation radio-fréquence magnétron en plasma réactif en étudiant le rôle de la variation du taux d'hydrogène. L'incorporation du Silicium en excès a été contrôlée par la variation du taux relatif d'hydrogène de 10% à 50% dans un mélange argon-hydrogène. Les films ont été déposés sans chauffage intentionnel des substrats et avec une densité de puissance de 0,75 $W.cm^2$. Tous les échantillons ont ensuite été recuits à 1100°C pendant 1 h sous un flux de diazote afin de favoriser la précipitation de l'excès de Si et induire la formation de Np-Si. Nous avons démontré les aspects spécifiques suivants :

➤ Le déclin de la luminescence des Nps-Si dans la silice à 750 nm a été étudié. Celui-ci peut être décrit par une fonction exponentielle étirée (Stretched exponential). L'algorithme de Stehfest nous a permis de calculer la densité de probabilité du taux de déclin ce qui a conduit à démontrer l'élargissement de cette densité de probabilité du taux de déclin, avec le désordre observé dans les échantillons [70].

Publications

- G Zatryb, A Podhorodecki, J Misiewicz, J Cardin, F Gourbilleau, On the nature of the stretched exponential photoluminescence decay for silicon nanocrystals, Nanoscale Research Letters, 6(1) :106, 2011.

Matrice SiO_x : Er

Les films de silice enrichie en silicium dopée avec des ions erbium ont été développés par pulvérisation rf magnétron en plasma réactif. Ces films ont été optimisés en vue de maximiser le transfert des Nps-Si vers le ions Er^{3+} et ainsi de maximiser l'émission à 1530-1560 nm. Nous avons démontré les aspects spécifiques suivants :

➤ Une fraction des ions Er^{3+} couplés au Nps-Si atteignant la valeur de 26% de la quantité totale d'erbium dans le cas le plus favorable [71–73]. Seule cette fraction d'erbium couplé pourra contribuer au gain optique dans une application à base de ce matériau.

Publications

- K Hijazi, R Rizk, J Cardin, L Khomenkova, F Gourbilleau. Towards an optimum coupling between Er ions and Si-based sensitizers for integrated active photonics, Journal of Applied Physics, 106(2) :024311-024311, 2009.

- K Hijazi, L Khomenkova, F Gourbilleau, J Cardin, R Riz, Enhanced fraction of coupled Er in silicon-rich silicon oxide layers grown by magnetron co-sputtering, Journal of Luminescence, 129(12) :1886-1889, 2009.
- D Navarro-Urrios, Y Lebour, O Jambois, B Garrido, A Pitanti, N Daldosso, L Pavesi, J Cardin, K Hijazi, L Khomenkova, F Gourbilleau, R Rizk, Optically active Er3+ ions in SiO2 codoped with Si nanoclusters. Journal of Applied Physics, 106(9) :93107,2009.

➤ L'amélioration des propriétés de luminescence induite par le chauffage du substrat pendant les phases de dépôt a été démontrée [74]. Les effets de ce recuit induit durant la croissance ont été comparés à ceux résultant de traitement thermique comparable classique effectué après un dépôt à la température ambiante. Il a été démontré que la première approche permet l'amélioration de l'efficacité de photoluminescence de l'erbium par un facteur 4.

Publications

- S Cueff, C Labbé, J Cardin, J-L Doualan, L Khomenkova, K Hijazi, O Jambois, B Garrido, R Rizk, Efficient energy transfer from Si-nanoclusters to Er ions in silica induced by substrate heating during deposition, Journal of Applied Physics, 108 :064302, 2010.

Matrice SiO_x : Nd

Les films de silice enrichie en silicium dopée au ions de néodyme ont été développés par pulvérisation rf magnétron en plasma réactif. Ces films ont été optimisés en vue de maximiser le transfert des Nps-Si vers le Nd^{3+} et ainsi l'émission à 920 1060 et 1400 nm. Nous avons démontré les aspects spécifiques suivants :

➤ Dans ce travail, sur la base d'expériences de photoluminescence [61], la preuve expérimentale d'un transfert d'énergie des Nps-Si vers les ions Nd^{3+} à plus haute énergie [4.40eV(280 nm) et 3.54eV(350 nm)] que le mécanisme classique de transfert d'énergie [1.6eV(770nm)] a été apportée. Ce transfert à haute énergie provoquant la transition des niveaux ${}^4I_{\frac{9}{2}} \rightarrow {}^4D_{\frac{3}{2}}, {}^4D_{\frac{5}{2}}$ semble plus efficace que le transfert classique à plus basse énergie provoquant la transition ${}^4I_{\frac{9}{2}} \rightarrow {}^4F_{\frac{3}{2}}, {}^4F_{\frac{7}{2}}$.

Publications

- A Podhorodecki, J Misiewicz, F Gourbilleau, J Cardin, C Dufour, High energy excitation transfer from silicon nanocrystals to neodymium ions in silicon-rich oxide film, Electrochemical and Solid-State Letters, 13(3) :K26-K28, 2010.

➤ Des films minces de SiO_x dopé par des ions Nd^{3+} ont été étudiés en fonction de la température de recuit et la concentration en ions Néodyme. L'augmentation de

l'intensité de luminescence du Néodyme avec la concentration de terre rare jusqu'à un seuil de concentration a été démontrée. Pour les fortes concentrations de Nd la formation d'agrégats d'oxyde de néodyme a également été mise en évidence [75, 76].

Publications

- O Debieu, D Bréard, A Podhorodecki, G Zatryb, J Misiewicz, C Labbé , J Cardin, F Gourbilleau, Effect of annealing and nd concentration on the photoluminescence of Nd^{3+} ions coupled with silicon nanoparticles, Journal of Applied Physics, 108(11) :113114, 2010.
- O Debieu, J Cardin, X Portier, F Gourbilleau, Effect of the Nd content on the structural and photoluminescence properties of silicon-rich silicon dioxide thin films, Nanoscale Research Letters, 6(1) :1-8, 2011.

➤ Deux processus d'émission dans une matrice SiO_x ont été mis en évidence selon la plage de température des recuits réalisés. Pour une température de recuit (T_r) <1000°C il s'agit d'émission issue d'une population de défauts alors que pour T_r>1000°C l'émission est le résultat de recombinaisons d'excitons formés dans les nanostructures de silicium. Les processus de sensibilisation des ions Nd^{3+} dans ces matériaux SiO_x : Nd suivent cette dualité. Pour les films recuits à basse température (T_r<1000°C), il s'agit de sensibilisation par les défauts ou des agrégats atomiques. Pour les films recuits à haute température (T_r>1000°C), il s'agit de sensibilisation par les nanoparticules de silicium [63].

Publications

- C-H Liang, J Cardin, C Labbé, F Gourbilleau, Evidence of two sensitization processes of Nd3+ ions in Nd-doped SiOx films, Journal of Applied Physics, 114(3) :033103, 2013.

Multicouches/super-réseau SiO_x/SiN_x

Des structures multicouches de Silice enrichie en silicium (SiO_x) alternées avec deux types de matériaux diélectriques, la silice stœchiométrique SiO_2 ou le nitrure de silicium non-stœchiométrique SiN_x ont été réalisées par un procédé de co-pulvérisation magnétron réactive. Ce matériau était développé dans la perspective d'applications dans des dispositifs photovoltaïques.

➤ Une augmentation significative de la densité de nanoparticules de silicium (10^{19}np-si.cm^{-3}) dans la sous-couche de SiO_x est obtenue en utilisant une sous-couche de SiN_x à la place de celle de SiO_2. L'amélioration des propriétés d'absorption, de photoluminescence et de conductivité a également été démontrée [77–80].

Publications

- R Pratibha Nalini, C Dufour, J Cardin, F Gourbilleau, New Si based multilayers for solar cell applications, Nanoscale Research Letters, 6(1) :156, 2011.
- R Pratibha Nalini, L Khomenkova, O Debieu, J Cardin, C Dufour, M Carrada, F Gourbilleau, SiOx/SiNy multilayers for photovoltaic and photonic applications, Nanoscale Research Letters, 7(1) :124, 2012.

Matrice SiN_x

Des films de SiN_x sans hydrogène ont été déposés sur des substrats de Silicium et de Silice amorphe par deux méthodes de pulvérisation magnétron, la méthode réactive et la co-pulvérisation de cibles de Si_3N_4 et Si. Ces échantillons ont été recuits sous atmosphère d'azote pour prévenir l'incorporation d'oxygène.

➤ La spectroscopie infra rouge par transformée de Fourier (FTIR : Fourier Transform Infrared Spectroscopy) nous a permis de démontrer l'absence d'oxygène et d'azote dans les films après recuit. Pour un recuit d'une heure à 1100°C des Nps-Si ont été formées avec des dimensions comprises entre 3 et 6 nm pour $x \leq 0{,}8$. La photoluminescence (PL) visible a été obtenue uniquement pour $x > 0{,}9$ démontrant ainsi que la luminescence n'est pas issue des états confinés dans la nanoparticule de silicium cristallin, mais de niveaux d'énergie électronique liés à des défauts localisés dans la matrice ou à la queue de bande des bandes d'énergie de la matrice [81].

Publications

- O Debieu, R Pratibha Nalini, J Cardin, X Portier, J Perrière, F Gourbilleau, Structural and optical characterization of pure si-rich nitride thin films, Nanoscale Research Letters, 8(1) :1-13, 2013.

Oxyde transparent conducteur et terre rare

Pour des applications dans le domaine des diodes électroluminescentes, nous nous sommes intéressés aux oxydes conducteurs transparents à grand gap du type β-Ga_2O_3 et ZnO dopés aux ions de terre rare, tels que l'ion Nd^{3+} ou le Tb^{3+}. Ces matériaux ont été déposés par pulvérisation magnétron puis recuits lors d'une étape postérieure.

➤ Les propriétés optiques des films d'oxyde de gallium dopé au néodyme ont été analysées. L'influence de la concentration des ions Nd^{3+} sur les mécanismes d'excitation/émission de ceux-ci et le rôle de la matrice d'oxyde de gallium ont été étudiés dans les références suivantes [68, 82, 83]

Publications

- C Lecerf, P Marie, J Cardin, F Jomard, and X Portier. Texture effect of neodymium doped gallium oxide thin films on their optical properties. Optical Materials, 33(7) :1131-1134, 2011.

- A Podhorodecki, M Banski, J Misiewicz, C Lecerf, P Marie, J Cardin, X Portier, Influence of neodymium concentration on excitation and emission properties of Nd doped gallium oxide nanocrystalline films, Journal of Applied Physics, 108 :063535, 2010.

➤ Les propriétés spectroscopiques de films d'oxyde de zinc dopé terbium ont été étudiées. Les changements structurels, les propriétés optiques et la photoluminescence associée ont été analysés en fonction du traitement thermique. Une variation de la contrainte bi-axiale interne à la couche mince, de compressive à extensive en fonction de la température de recuit (400 à 1000°C), a notamment été mise en évidence. A la température de 600°C une photoluminescence maximale des ions Tb^{3+} dans la matrice est obtenue [84].

Publications

- A Ziani, C Davesnne, C Labbé, J Cardin, P Marie, C Frilay, S Boudin, and X Portier, Annealing effects on the photoluminescence of terbium doped zinc oxide films, Thin Solid Films, 553 :52-57, 2014.

Matériaux hybrides organique-inorganique luminescents.

Un copolymère hybride luminescent à base d'une matrice de poly(méthacrylate de méthyle) (PMMA) comportant des agrégats octaédriques de Molybdène (Mo_6) et des ions Er^{3+} a été étudié dans le cadre d'une collaboration avec l'Institut des Sciences Chimiques de Rennes. Ces agrégats de Molybdène présentent des propriétés de photoluminescence dans le rouge (720nm) avec des efficacités quantiques pouvant atteindre jusqu'à 60% [85].

➤ Ces nouveaux matériaux hybrides homogènes et transparents présentent une photoluminescence Er^{3+} à 1540 nm qui est jusqu'à six fois plus intense en présence d'agrégats de Mo_6 qu'en absence de ceux-ci. Le rôle des agrégats de Mo_6 comme sensibilisateur des ions de terre rare a été démontré et fait l'objet de publications et d'un brevet déposé [86–89].

Publications

- Y Molard, C Labbé, J Cardin, and S Cordier. Sensitization of er3+ infrared photoluminescence embedded in a hybrid organic-inorganic copolymer containing octahedral molybdenum clusters, Advanced Functional Materials, 23(38) :4821-4825, 2013.
- Y. Molard, C. Labbé, J. Cardin, S. Cordier, and M. Amela-Cortes. A material comprising an host matrix, rare earth ions and a metal atom cluster as sensitiser, Brevet EP2754707, 2013.

Oxyde à forte permittivité pour l'électronique HfO_xSi_y.

Les couches minces de $HfSi_xO_y$ ont été développées par pulvérisation cathodique magnétron. Ces matériaux à forte constante diélectrique peuvent être utilisés pour des applications en micro-électronique, par exemple pour des oxydes de grille de transistor.

➤ Les études de la fonction diélectrique de ces matériaux composites au moyen des théories de milieu effectif ont conduit à la description des variations de stœchiométrie et ont permis de décrire les phases dans ces matériaux [90].

Publications

- L Khomenkova, Xavier Portier, J Cardin, and F Gourbilleau. Thermal stability of high-k Si-rich Hfo2 layers grown by rf magnetron sputtering, Nanotechnology, 21 :285707, 2010.

Chapitre 3

Travaux théoriques sur l'interaction rayonnement optique/matière dans les processus luminescents ou résonants

L'objectif de ce chapitre est de présenter les méthodes théoriques mises en œuvre dans mes travaux ces dernières années dans lesquels une contribution significative a été amenée. Un travail conséquent a été réalisé sur la méthode des différences finies dans le domaine temporel (finite-difference time-domain method, FDTD) couplée à des équations différentielles auxiliaires (Auxiliary differential equation, ADE) appliquée aux milieux à gain et aux nanostructures métalliques pour l'étude des résonances plasmoniques. En outre, la méthode ADE-FDTD a également été adaptée aux études menées au laboratoire CIMAP dans l'équipe Lasers, Instrumentation Optique et Applications (LIOA) sur la microscopie en champ proche optique dans le cadre des travaux de thèse de M Matthieu Roblin [91–93]. De plus, les méthodes matricielles déjà abordées dans ce manuscrit ont été étendues au cas de milieux stratifiés contenant des centres émetteurs pour apporter un support à l'interprétation des expériences de photoluminescence.

3.1 Modélisation par différences finies dans le domaine temporel (FDTD) et système d'équations différentielles auxiliaires (ADE).

La modélisation par la technique des différences finies dans le domaine temporel peut être schématisée sur la figure (3.1). A t_0, dans un volume de calcul restreint par des conditions aux limites, on définit des conditions initiales sur les grandeurs décrites par l'électromagnétisme (champs, courant, polarisation). La méthode FDTD permet de calculer l'évolution entre un instant t_0 et un temps $t>t_0$ des grandeurs électromagnétiques dans cet

espace de calcul.

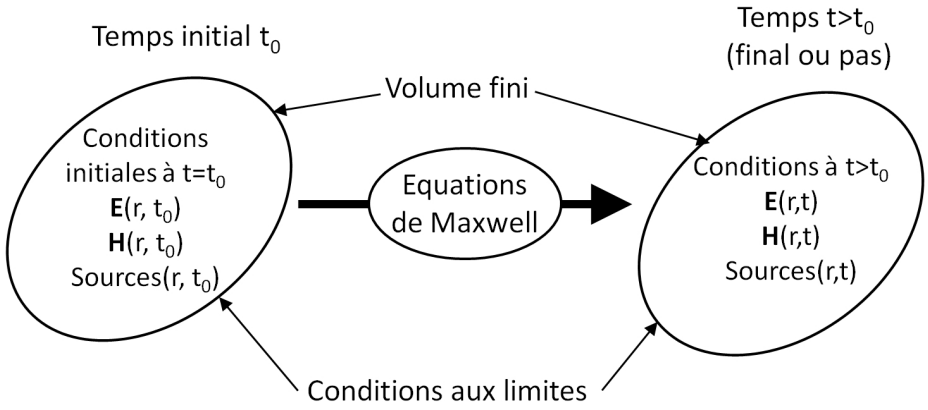

FIGURE 3.1 – Schéma de principe illustrant l'évolution dans le temps du champ électromagnétique régie par les équations de Maxwell à l'intérieur d'un domaine de l'espace délimité par les conditions aux limites et présentant des sources électromagnétiques.

Equations de Maxwell

Dans les milieux linéaires, homogènes et isotropes (l.h.i), les équations de Maxwell sont définies dans la forme symétrisée [94] suivante :

$$\begin{aligned} \frac{\partial \vec{H}}{\partial t} &= -\frac{1}{\mu} \operatorname{rot} \vec{E} - \frac{\sigma^m}{\mu} \vec{H} \\ \frac{\partial \vec{E}}{\partial t} &= +\frac{1}{\epsilon} \operatorname{rot} \vec{H} - \frac{\sigma^e}{\epsilon} \vec{E} \end{aligned} \tag{3.1}$$

Les champs électrique $\vec{E}$ et magnétique $\vec{H}$ sont liés entre eux par les équations comportant la permittivité électrique ϵ, la perméabilité magnétique μ, la conductivité électrique σ^e et une grandeur non physique dite de conductivité magnétique σ^m. Cette dernière sera mise à zéro dans les zones de l'espace de calcul physique mais se révélera très utile dans les zones des conditions aux limites de celui-ci.

La méthode des différences finies dans le domaine temporel repose sur une réécriture des équations de Maxwell précédentes dans un schéma aux différences finies. Cette réécriture doit permettre de faire apparaître de manière explicite les valeurs des champs les plus avancées dans le temps en fonction des valeurs précédentes.

Par exemple, dans le cas de l'équation de Maxwell Faraday :

$$\frac{\partial \vec{H}}{\partial t} = -\frac{1}{\mu} \operatorname{rot} \vec{E} - \frac{\sigma^m}{\mu} \vec{H} \tag{3.2}$$

La réécriture dans un schéma aux différences finies implique un changement de notation. Nous utiliserons celle de A. Taflove [94] communément admise (équation 3.3). Ainsi la

composante selon Ox du champ électrique $\vec{E}$ au point de coordonnées d'espace x_i, y_j, z_k et à l'instant t_n s'écrit en fonction des pas d'espace (Δx, Δy, Δz) selon les trois directions et le pas de temps (Δt) :

$$E_x\left(x_i, y_j, z_k, t_n\right) = E_x\left(i\Delta x, j\Delta y, k\Delta z, n\Delta t\right) = E_x|_{i,j,k}^{n} \tag{3.3}$$

En substituant les dérivées spatiales et temporelles par leurs différences finies, la composante du champ $\vec{H}$ selon Ox devient :

$$\frac{H_x|_{i,j,k}^{n+\frac{1}{2}} - H_x|_{i,j,k}^{n-\frac{1}{2}}}{\Delta t} = \frac{1}{\mu_{i,j,k}}\left(\frac{E_y|_{i,j,k+1}^{n} - E_y|_{i,j,k}^{n}}{\Delta z} - \frac{E_z|_{i,j+1,k}^{n} - E_z|_{i,j,k}^{n}}{\Delta y} - \sigma_{i,j,k}^{m} H_x|_{i,j,k}^{n}\right) \tag{3.4}$$

avec l'approximation suivante :

$$H_x|_{i,j,k}^{n} = \frac{H_x|_{i,j,k}^{n+\frac{1}{2}} + H_x|_{i,j,k}^{n-\frac{1}{2}}}{2} \tag{3.5}$$

On obtient finalement l'expression de la composante recherchée H_x suivante :

$$H_x|_{i,j,k}^{n+\frac{1}{2}} = \left(\frac{1-\frac{\sigma_{i,j,k}^{m}\Delta t}{2\mu_{i,j,k}}}{1+\frac{\sigma_{i,j,k}^{m}\Delta t}{2\mu_{i,j,k}}}\right) H_x|_{i,j,k}^{n-\frac{1}{2}} + \left(\frac{\frac{\Delta t}{\mu_{i,j,k}}}{1+\frac{\sigma_{i,j,k}^{m}\Delta t}{2\mu_{i,j,k}}}\right) \cdot \left(\frac{E_y|_{i,j,k+1}^{n} - E_y|_{i,j,k}^{n}}{\Delta z} - \frac{E_z|_{i,j+1,k}^{n} - E_z|_{i,j,k}^{n}}{\Delta y}\right) \tag{3.6}$$

De la même manière on obtient les composantes pour le champ électrique $\vec{E}$ dont voici la composante selon l'axe Oy :

$$E_y|_{i,j,k}^{n+1} = \left(\frac{1-\frac{\sigma_{i,j,k}^{e}\Delta t}{2\epsilon_{i,j,k}}}{1+\frac{\sigma_{i,j,k}^{e}\Delta t}{2\epsilon_{i,j,k}}}\right) E_y|_{i,j,k}^{n} + \left(\frac{\frac{\Delta t}{\epsilon_{i,j,k}}}{1+\frac{\sigma_{i,j,k}^{e}\Delta t}{2\epsilon_{i,j,k}}}\right) \cdot \left(\frac{H_x|_{i,j,k}^{n+\frac{1}{2}} - H_x|_{i,j,k-1}^{n+\frac{1}{2}}}{\Delta z} - \frac{H_z|_{i,j,k}^{n+\frac{1}{2}} - H_z|_{i-1,j,k}^{n+\frac{1}{2}}}{\Delta x}\right) \tag{3.7}$$

Par rapport à l'expression analytique des composantes des champs $\vec{E}$ et $\vec{H}$, ces expressions discrétisées par différences finies sont une approximation avec une erreur à l'ordre deux. L'observation attentive de ces équation (3.6) et (3.7) permet de visualiser l'entrelacement des composantes des champs $\vec{E}$ et $\vec{H}$ dans le temps et dans l'espace qui justifie le choix de l'algorithme de Yee [95] pour le calcul des champs discrétisés.

Algorithme de Yee

La méthode des différences finies dans le domaine temporel (FDTD) repose sur l'utilisation de l'algorithme de Yee [95] qui s'appuie sur plusieurs points pour résoudre dans le temps et l'espace les équations de Maxwell discrétisées :

- Dans l'espace les composantes des champs $\vec{E}$ et $\vec{H}$ sont positionnées sur deux grilles décalées avec un placement des composantes des champs respectifs qui assure la validité de l'expression locale des équations de Maxwell (figure 3.2).

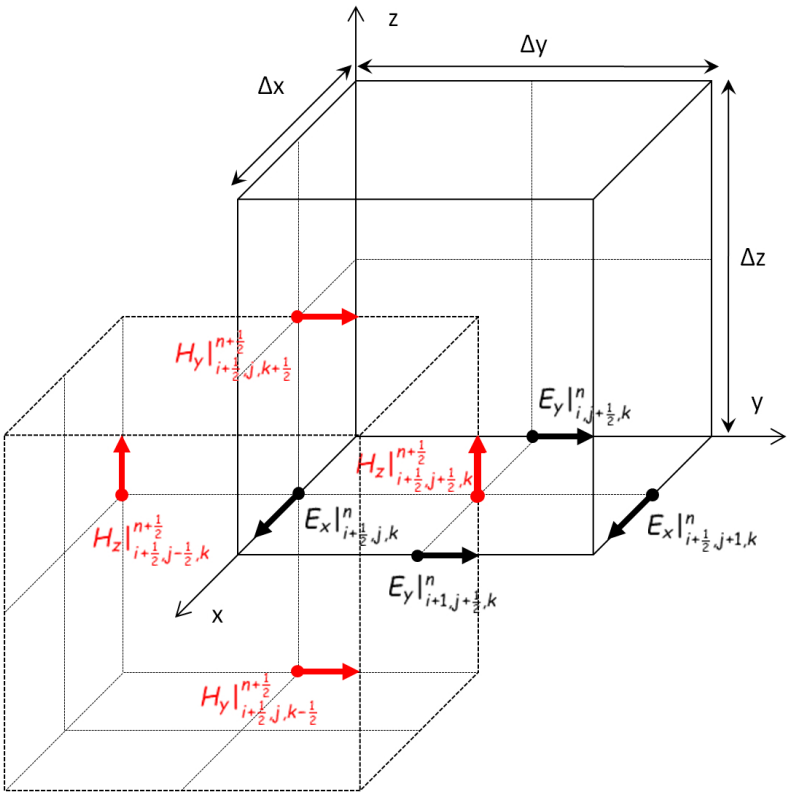

FIGURE 3.2 – Cellules de Yee sur deux grilles décalées montrant la disposition respective des composantes des champs $\vec{E}$ et $\vec{H}$.

- Le calcul des champs $\vec{E}$ et $\vec{H}$ est alterné dans le temps. La détermination des valeurs du champ $\vec{E}$ dans tout l'espace à l'instant $n+1$ se fait en fonction des valeurs du champ $\vec{H}$ dans tout l'espace à l'instant $n+\frac{1}{2}$ et des valeurs précédentes de $\vec{E}$ à l'instant n. De même, les valeurs du champ $\vec{H}$ à l'instant $n+\frac{1}{2}$ se font en fonction des valeurs du champ $\vec{H}$ à l'instant n et des valeurs précédentes de $\vec{H}$ à l'instant $n-\frac{1}{2}$.

La discrétisation induisant une erreur à l'ordre deux, des conditions particulières sur le choix des pas d'espace et de temps doivent être respectées pour assurer la stabilité de la méthode et diminuer les effets de la dispersion numérique.

Stabilité et dispersion numérique.

Les conditions de stabilité de la méthode FDTD présentées dans la littérature [94,96–98] sont discutées dans le manuscrit de thèse de Alexandre Fafin [99]. A trois dimensions, avec des pas spatiaux quelconques Δx, Δy et Δz, la condition de stabilité liant ces derniers avec le pas de temps s'écrit (équation 3.8) :

$$\Delta t = \frac{S}{c\sqrt{\left(\frac{1}{(\Delta x^2)}+\frac{1}{(\Delta y^2)}+\frac{1}{(\Delta z^2)}\right)}} \tag{3.8}$$

Avec S le nombre de Courant-Friedrich-Lewy [100] dit nombre de Courant qui doit être défini tel que $0 < S < 1$ pour assurer la convergence lors de la résolution de systèmes d'équations différentielles par une méthode des différences finies. Définissons les nombres $N_\lambda^{x(y,z)}$ comme le nombre de cellules par longueur d'onde selon une direction donnée $x(y,z)$. La discrétisation dans l'espace et le temps conduit à des vitesses de phase des ondes différentes selon la direction de propagation. La différence la plus importante se faisant entre la vitesse selon un axe principal v_p^{prin} (par exemple l'axe Ox) et celle selon un axe diagonal v_p^{diag}. Dans le cas d'une cellule carrée, c'est-à-dire $N_\lambda^x = N_\lambda^y = N_\lambda^z = N_\lambda$ le rapport des vitesses évolue selon l'équation 3.9 [94].

$$\frac{v_p^{diag}}{v_p^{prin}} = \frac{\sqrt{3}\arcsin\left(\frac{1}{S}\sin\frac{\pi S}{\sqrt{3}N_\lambda}\right)}{\arcsin\left(\frac{\sqrt{3}}{S}\sin\frac{\pi S}{\sqrt{3}N_\lambda}\right)} \tag{3.9}$$

Ce rapport tend vers 1 lorsque le nombre N_λ tend vers de grande valeur ($\to \infty$). Ceci justifie le choix généralement admis de $N_\lambda > 10$. Un nombre N_λ suffisamment grand doit donc être choisi avec cependant la limite majeure qu'un nombre élevé entraînera une augmentation de l'occupation mémoire et un temps de calcul important. Le choix de la dimension de la cellule unité par rapport à la longueur d'onde de travail joue donc un rôle important dans la méthode FDTD [101]. Dans le cas où des milieux d'indice différents sont considérés le choix de N_λ se fera alors pour la longueur d'onde la plus courte, c'est-à-dire dans le milieu le plus réfringent.

Conditions aux limites.

Les conditions aux limites absorbantes (CLA) de l'espace fini de calcul dans les méthodes FDTD sont d'une importance majeure. Outre la limitation nécessaire de l'espace de calcul, elles permettent la prise en compte de certaines spécificités des problèmes physiques à traiter. Par exemple les conditions périodiques permettent de modéliser des structures périodiques en définissant une cellule élémentaire représentative du système total étudié. La plupart des problèmes de l'électromagnétisme étudiés par FDTD vont mettre en œuvre des champs rayonnés ou diffusés. Les exigences que les conditions aux limites absorbantes doivent satisfaire dépendent fortement de leurs emplacements par rapport à la source du champ :

- ➤ Les CLA placées loin de la source, doivent être capables d'absorber des ondes planes homogènes.
- ➤ Les CLA placées dans le voisinage de la source, doivent être capables d'absorber les ondes évanescentes non homogènes.

Le développement des conditions aux limites dans les problèmes basés sur la FDTD a conduit à différentes approches (Engqvist et Majda [102], Mur [103]) détaillés dans les ouvrages de références [94, 98, 104]. En 1994, J.-P. Bérenger introduisit sa méthode split PML (perfectly matched layer) [105] basée sur l'ajout aux limites de l'espace de calcul d'une couche absorbante à l'impédance adaptée. Cette couche PML possède des conductivités électrique σ^e et magnétique σ^m fictives de telle sorte que le champ électromagnétique à la traversée de ce milieu non-physique soit absorbé tout en subissant un minimum de réflexion. Les méthodes sur les conditions aux limites se sont diversifiées avec notamment les méthodes Uniaxial PML, covolutional PML, Near PML [94,104]. Au vue de ces qualités, nous avons fait le choix de la méthode baptisée split PML par Bérenger. Le détail de celle-ci se trouve dans le manuscrit de thèse de Mr Alexandre Fafin [99]. Pour rappel, le schéma (figure 3.3) montre l'organisation de la split PML entourant la zone FDTD. La split PML est basée sur :

- ➤ Une absorption dans la zone PML assurée par une variation non abrupte de la conductivité électrique ou magnétique,
- ➤ l'adaptation de l'impédance entre les cellules de la PML et à la frontière PML/FDTD par une loi reliant les conductivités électriques σ^e et magnétiques σ^m.
- ➤ la séparation de chaque composante des champs dans la zone PML en sous composantes normale et transverse par rapport à la frontière FDTD/PML. Ceci permet d'assurer la condition d'incidence normale de chaque sous-composante dans la zone PML concernée.
- ➤ Une couche de conducteur électrique parfait (PEC : perfect electric conductor) entourant la PML qui permet de réaliser le calcul des champs dans toute la zone PML (dérivée spatiales s'appuyant sur les bords PEC). Celle-ci réfléchit les champs résiduels déjà absorbés sur un aller, ce qui permet une absorption sur le trajet retour.

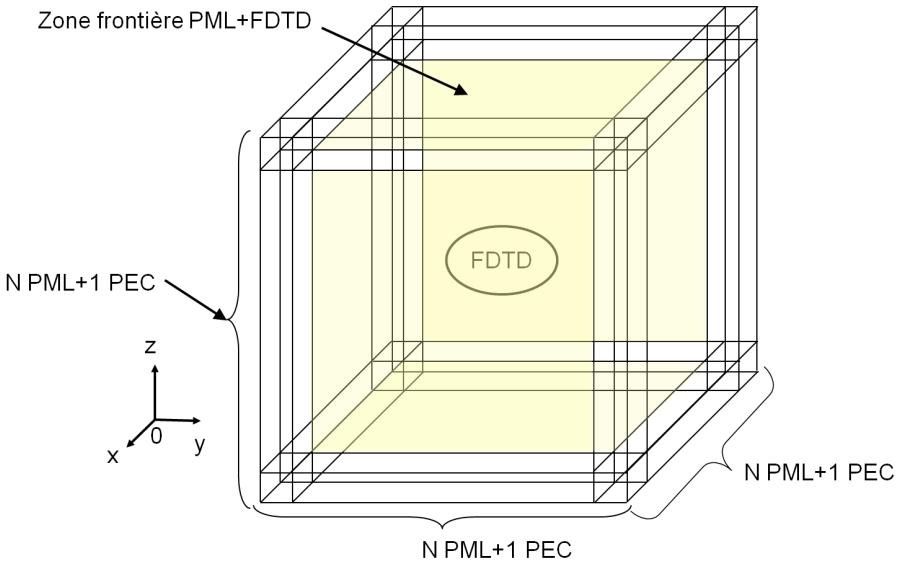

FIGURE 3.3 – Schéma en trois dimensions de la zone de calcul, qui comprend la zone FDTD entourée de N cellules de PML elle-même entourée d'une couche d'un conducteur électrique parfait [PEC : perfect electric conductor (E= 0 et H = 0)].

Les Sources électromagnétiques.

Les sources dans la méthode FDTD sont abondamment décrites dans la littérature [94, 98, 106], dans les travaux de thèse de Mr Alexandre Fafin [99] et de Mr Matthieu Roblin [93]. Les types de sources principalement utilisés dans nos travaux sont rappelés :

- ➤ Sources dures/Sources molles : approche qui consiste à imposer localement dans l'espace un champ qui peut être électrique ou magnétique et qui suit une fonction temporelle. Suivant que l'on autorise la superposition des champs ou non, nous aurons une source molle ou dure,
- ➤ Technique de séparation des champs totaux et diffusés (total field/scattered field TF/SF). Cette technique permet d'atténuer le champ arrivant en bord de boîte sur les PML et de créer des ondes planes d'orientation quelconque.
- ➤ Source modale par une méthode de différence finie dans le domaine fréquentiel (FDFD) présenté par Fallahkhair et al [107]. Cette technique implique l'utilisation de matrices creuses de dimensions importantes nécessitant des techniques de calcul adaptées notamment pour déterminer les valeurs et vecteurs propres [93, 108, 109].

3.1.1 Milieu dispersif : application aux résonances plasmoniques.

Les équations de Maxwell présentées jusqu'à maintenant ne permettent de traiter que des milieux possédant une permittivité ϵ et une perméabilité μ indépendantes de la longueur d'onde (milieu statique). Pour rendre compte de la fonction diélectrique de matériaux comme par exemple les métaux nobles, des modèles de Debye, Lorentz, et Drude ont été

implémentés [110–113]. En principe, un modèle de dispersion peut être décrit par la combinaison d'un modèle de Debye et de Lorentz comme cela a été appliqué avec succès dans la description de fonctions diélectriques de 11 métaux sur une large gamme spectrale de 0,1 à 6 eV [114]. Cette propriété n'a été utilisée dans les méthodes FDTD que plus tardivement par A. Vial et al [115]. Le modèle utilisé par [114] considère 5 oscillateurs de Lorentz. Nous avons adopté la même convention. Rakic et al [114] affirme qu'un modèle de Brendel et Bormann (BB) convient mieux que le modèle de Drude-Lorentz (DL) pour modéliser la permittivité de 11 métaux sur une plage d'énergie large. La figure 3.4 représente l'évolution des parties réelle et imaginaire de l'indice de réfraction issue de déterminations expérimentales et collectés par Palik [116] ajustées par le modèle DL par Rakic et par un algorithme génétique déjà employé dans la méthode M-lines [13]. Au vu de l'ajustement de l'indice de l'or, on peut raisonnablement s'interroger sur la procédure d'ajustement utilisée dans cette comparaison des modèles DL et BB.

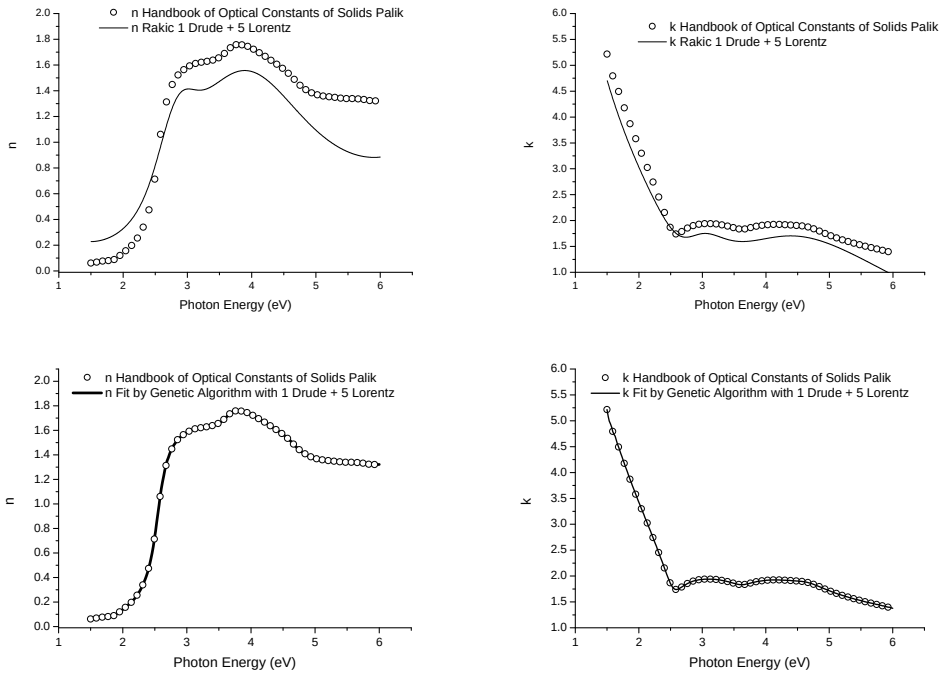

FIGURE 3.4 – Parties réelle et imaginaire de l'indice de réfraction de l'or [116] ajusté par le modèle de DL (en haut) paramètres de Rakic [114] (en bas) paramètres issus de l'algorithme génétique [13]

Cette approche de Drude-Lorentz est détaillée dans le manuscrit de thèse de M Alexandre Fafin [99]. La permittivité diélectrique relative complexe peut s'exprimer sous la forme suivante :

$$\epsilon_r(\omega) = \epsilon_r^f(\omega) + \epsilon_r^b(\omega) \tag{3.10}$$

Cette expression sépare de manière implicite les effets intra-bandes f (free electrons) des

effets inter-bandes b (bound electrons). La contribution intra-bande ϵ_r^f de la fonction diélectrique étant décrite par un modèle de Drude 3.11. La contribution inter-bande ϵ_r^b de la fonction diélectrique est décrite par un modèle de Lorentz 3.12.

$$\epsilon_r^f(\omega) = 1 - \frac{\omega_p^2}{\omega\left(\omega - i\Gamma_0\right)} \qquad (3.11) \qquad \epsilon_r^b(\omega) = \sum_{j=1}^{k} \frac{f_j \omega_p^2}{\omega_j^2 - \omega^2 + i\omega\Gamma_j} \qquad (3.12)$$

Les paramètres du terme de Drude et des k oscillateurs sont ω_p la fréquence plasma, le taux d'amortissement (damping constant) Γ_i, la fréquence ω_j et la force d'oscillateur f_j.

La densité de polarisation $\vec{P}(\omega)$ du métal soumis à un champ électrique devient :

$$\vec{P}(\omega) = \epsilon_0 \chi(\omega)\vec{E}(\omega) = \epsilon_0 \left[\epsilon_r(\omega) - 1\right] \vec{E}(\omega) \qquad (3.13)$$

La mise en œuvre d'une permittivité relative dans la méthode FDTD est réalisée au moyen de l'établissement d'équations différentielles auxiliaires appelées couramment ADE (Auxiliary Differential Equations). Dans le cadre de la modélisation de la dispersion chromatique dans les méthodes ADE-FDTD, celle-ci peut être établie à partir de la densité de polarisation [117] ou de la densité de courant [118]. Nous avons choisi l'utilisation de la densité de polarisation pour établir les équations du système ADE, plusieurs écritures sont alors possibles :

La densité de polarisation peut se décomposer en six termes, un terme de Drude $\vec{P}_0^D$ et cinq termes de Lorentz $\vec{P}_k^L$. La densité de polarisation de Drude $\vec{P}_0^D$ conduit à l'établissement de l'équation différentielle de la forme suivante :

$$\frac{d^2\vec{P}_0(t)}{dt^2} + \Gamma_0 \frac{d\vec{P}_0(t)}{dt} = \epsilon_0 \omega_p^2 \vec{E}(t) \qquad (3.14)$$

Pour $k = 1$ à 5, les densités de polarisation de Lorentz $\vec{P}_k^L$ permettent l'établissement de l'équation différentielle de la forme suivante :

$$\frac{d^2\vec{P}_j(t)}{dt^2} + \Gamma_j \frac{d\vec{P}_j(t)}{dt} + \omega_j^2 \vec{P}_j(t) = \epsilon_0 f_j \omega_p^2 \vec{E}(t) \qquad (3.15)$$

Afin de mettre en œuvre le modèle de dispersion dans la méthode ADE-FDTD, il est nécessaire de procéder à une réécriture de l'équation de Maxwell-Ampère afin de faire apparaître de façon explicite les densités de polarisation.

$$\frac{\partial \vec{E}}{\partial t} = \frac{1}{\epsilon_0} \operatorname{rot} \vec{H} - \frac{\sigma}{\epsilon_0}\vec{E} - \frac{1}{\epsilon_0} \frac{\partial\left(\vec{P}_0^D + \sum_{k=1}^{5} \vec{P}_k^L\right)}{\partial t} \qquad (3.16)$$

A cette étape, les équations de Maxwell-Ampère (3.16) et les équations différentielles de la densité de polarisation de Drude (3.15) et de Lorentz (3.14) sont discrétisées par la méthode des différences finies.

Il existe diverses manières de poser le système ADE pour décrire la dispersion des matériaux. Le choix doit être fait au vu de la nature des observables souhaitées et des performances de la méthode numérique qui en découle. Quelques approches sont :

- L'écriture explicite de l'équation de Maxwell-Ampère faisant apparaître la densité de polarisation peut se faire de différentes manières. Par exemple on peut mettre en évidence de manière explicite la conductivité électrique statique σ^e.

$$\chi(\omega)^D = \frac{\omega_p^2}{-\omega^2 + i\omega\Gamma_0} = -\frac{\omega_p^2}{\Gamma_0(i\omega + \Gamma_0)} + \frac{\sigma^e}{i\epsilon_0\omega} \tag{3.17}$$

- Le couplage par la densité de courant $\vec{J}$ par une écriture de l'équation de Maxwell-Ampère faisant apparaître celle-ci (Thèse Matthieu Roblin [93])
- Le modèle de dispersion de Drude à points critiques proposé par Alexandre Vial et al. [119] qui semble permettre une bonne description des fonctions diélectriques de l'aluminium et du chrome avec un nombre réduit de paramètres.
- Le modèle d'oscillateur décrivant les métaux et les semi-conducteurs de Deinega et al. [118]. Sur une plage spectrale équivalente, celui-ci permet d'ajuster les fonctions diélectriques de l'or et l'argent avec un plus faible nombre de paramètres que Drude-Lorentz.

Application

Dans le cadre de l'ANR ShaMan n°ANR-09-BLAN-0334-03, nous avons été sollicités par l'équipe de Giancarlo Rizza du Laboratoire des Solides Irradiés (LSI) de l'Ecole Polytechnique pour réaliser l'étude des propriétés optiques de nanoparticules métalliques d'or (Nps-Au) incluses dans des matrices diélectriques de silice, celles-ci étant nanostructurées par irradiation d'ions au grand accélérateur national d'ions lourds (GANIL) de Caen. Selon la fluence des ions, le volume initial de matière et la durée d'irradiation, la forme des Nps-Au peut varier. La technique expérimentale utilisée pour fabriquer des nanosphères

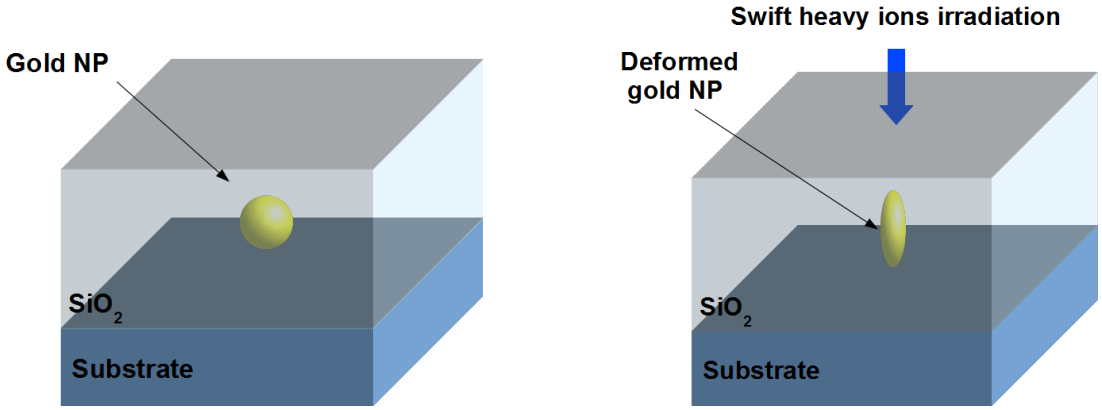

FIGURE 3.5 – Schéma de principe montrant l'étape avant et après la déformation obtenue par irradiation des Nps-Au par un faisceau Kr d'énergie 74MeV.

d'or incluses dans une matrice de silice et l'irradiation par ions lourds qui modifie leurs formes sont décrites dans la thèse de A. Fafin [99] et les publications de l'équipe de G

Rizza [120, 121]. Les objets obtenus par cette technique peuvent prendre des formes diverses et multiples. Nous nous sommes focalisés sur une famille d'objets à symétrie de révolution comprenant des octaèdres, des bâtonnets ou encore des fils. Ces nanoparticules

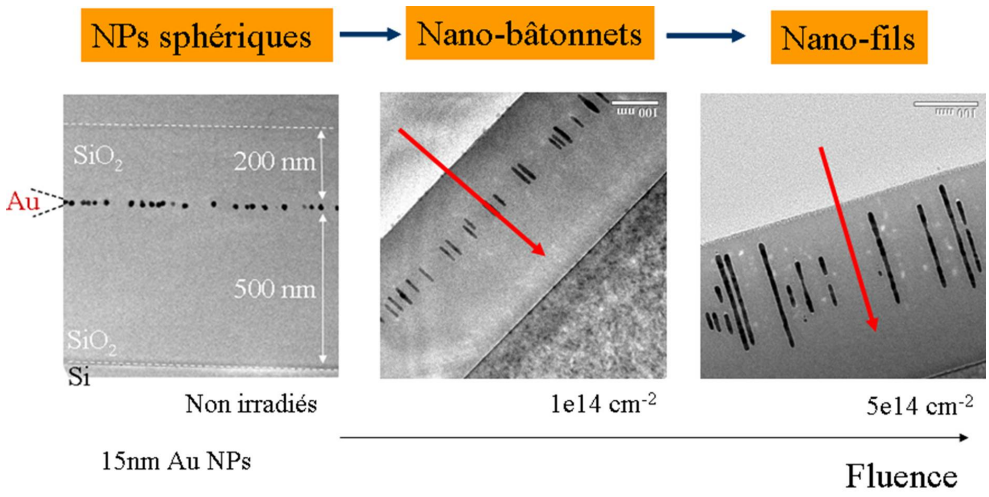

FIGURE 3.6 – Transformation des nanoparticules sphériques en nano-bâtonnets puis en nano-fils alignés et orientés dans la direction du faisceau d'ions. [120–123]

d'or ont été étudiées par spectroscopie de pertes d'énergies des électrons (electron energy loss spectroscopy, EELS). La technique EELS consiste à disperser en énergie un faisceau électronique traversant un objet pour analyser la présence de résonance de perte d'énergie électronique. Selon la gamme d'énergie perdue, on caractérise l'excitation de niveaux de cœur (>50), entre 50 et 10 eV il s'agit d'excitation inter et intra-bandes et pour des énergies entre 0 et 10 eV il s'agit de la partie plasmon. Nous étudierons uniquement la partie plasmon du spectre EELS entre 0,5 et 5 eV. A une résonance donnée, la distribution spatiale de ces pertes d'énergie présente une structuration spatiale particulière, considérée par la littérature, comme des résonances plasmoniques [124–126]. Notre objectif étant de réaliser la simulation numérique par ADE-FDTD des nano-objets d'or soumis à une excitation optique, d'identifier des résonances de plasmon et de comparer celles-ci avec celles obtenues par spectroscopie EELS. Cette spectroscopie optique détaillée dans le manuscrit de thèse de Mr Alexandre Fafin [99] repose sur l'excitation par une onde plane polychromatique (0-3 eV) des nanostructures d'or avec trois angles d'incidence (0°, 45° et 90°) par rapport au grand axe des nanostructures. Nous avons ensuite procédé à des enregistrements de plusieurs observables à différentes positions des objets analysés comme le rapport de champ total sur champ incident $\frac{E}{E_0}$ et les charges de polarisation à travers la divergence de la densité de polarisation $-\operatorname{div} \vec{P}$. Pour certains angles, les variations de ces observables en fonction de l'énergie laissent apparaître des résonances plasmoniques. A ces résonances, des enregistrements à deux dimensions du rapport $\frac{E}{E_0}$ ont été dressés suivant une coupe longitudinale le long du grand axe des structures (figure 3.8).

Ces résonances identifiées par spectroscopie optique ont été comparées avec celles obtenues par EELS. Nous avons observé un très bon accord entre les énergies de résonance

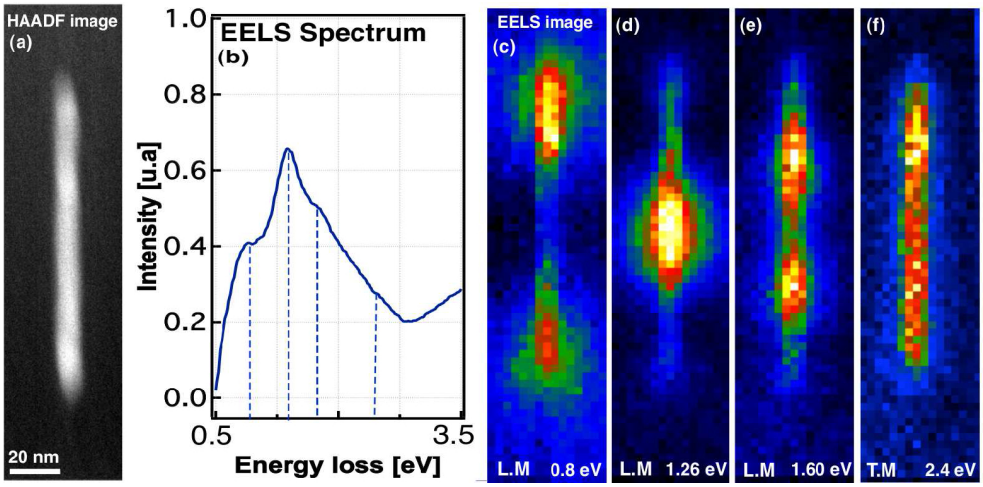

FIGURE 3.7 – (a)Image HAADF d'une nanoparticule d'or de rapport d'aspect R = 12. (b) Spectre EELS correspondant. (c-f) Images EELS à différentes énergies : 0,8 eV, 1,26 eV, 1,60 eV et 2,4 eV. Figure adaptée du travail de l'équipe de G. Rizza.

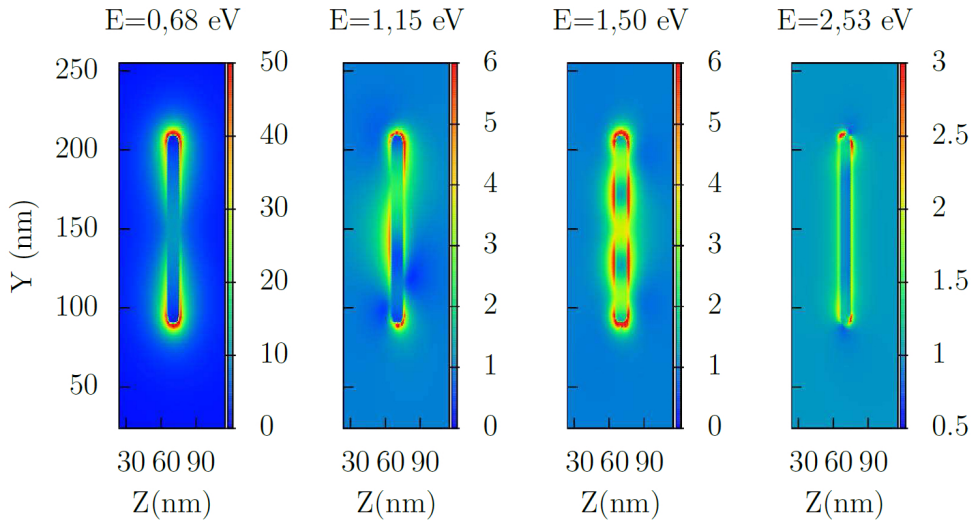

FIGURE 3.8 – Carte 2D du rapport $\frac{E}{E_0}$ d'un nanofil d'or de rapport d'aspect R = 12 obtenue par ADE-FDTD.

observées par EELS et par cette technique ADE-FDTD comme en témoignent les résultats pour un nanofil d'or de 120 nm de longueur et de 10 nm de diamètre suivant (tableau 3.1).

Type	ADE-FDTD (eV)	EELS (eV)	Diff. relative
Longitudinal	0.70	0.80	13%
	1.15	1.26	9%
	1.50	1.60	6%
Transversal	2.40	2.40	0%

TABLE 3.1 – Energie de résonances déterminées par ADE-FDTD et par spectroscopie EELS pour un nanofil d'or de longueur L = 120 nm et de diamètre D = 10 nm.

Cette technique de spectroscopie optique numérique met en jeu des observables différentes de celles utilisées dans la spectroscopie EELS. Cependant la résonance de plasmon identifiée par les deux techniques semble bien correspondre au même phénomène physique. Les écarts constatés peuvent se justifier par les différences sur la géométrie réelle et simulée et par des écarts entre les indices de réfraction modélisés pour l'or et de la matrice et les indices de réfraction expérimentale. A chaque énergie de résonance trouvée par la méthode ADE-FDTD, nous présentons le rapport $\frac{E}{E_0}$ dans le plan (xOz) passant par le centre du fil (figure 4.12). Les cartes à 0,68 eV et 1,50 eV sont issues du calcul où $\theta = 0°$ alors que celles à 1,15 eV et 2,53 eV sont issues du calcul où $\theta = 45°$. La résonance à 0,68 eV présente un caractère dipolaire électrique de par la structuration de son champ électrique. Les résonances à d'autres énergies correspondent à des modes d'ordre supérieur. La résonance à 2,4 eV (figure 3.9) correspond à un mode transverse puisque l'amplitude du champ électromagnétique est uniforme le long du fil.

La variation longitudinale du rapport $\frac{E}{E_0}$ à l'intérieur du fil le long de l'axe x passant par le centre de masse du fil pour $\theta = 45°$ a également été enregistrée (figure 3.9). Le rapport $\frac{E}{E_0}$ à 0,68 eV présente un ventre, celui à 1,15 eV deux ventres et celui à 1,50 eV trois ventres. Ces structures sont décrites dans la littérature comme le résultat de l'excitation d'ondes plasmon-polariton de surface (SPP) stationnaire de type Fabry-Pérot (FP) par le rayonnement de champ lointain [127, 128]. Les nanostructures d'or se comportent comme un résonateur Fabry-Pérot dont la condition de résonance longitudinale sur la phase est donnée par l'équation suivante [129–131] :

$$\beta.L + \phi = m\pi \tag{3.18}$$

β est la constante de propagation, L est la longueur du fil, ϕ est un terme de phase global représentatif de tous les déphasages induits par les réflexions aux extrémités du nanofil et par des éventuels objets déphasants sur le chemin optique et m est l'ordre du mode de résonance. Il prend des valeurs entières. L'analyse par le modèle de FP permet d'établir le lien entre la distance inter-ventre λ_{eff} dans la thèse de A. Fafin [99] et la constante de propagation β. Cette démarche permet d'obtenir la constante de propagation pour chaque résonance observée par ADE-FDTD. Une démarche comparable [99] permet

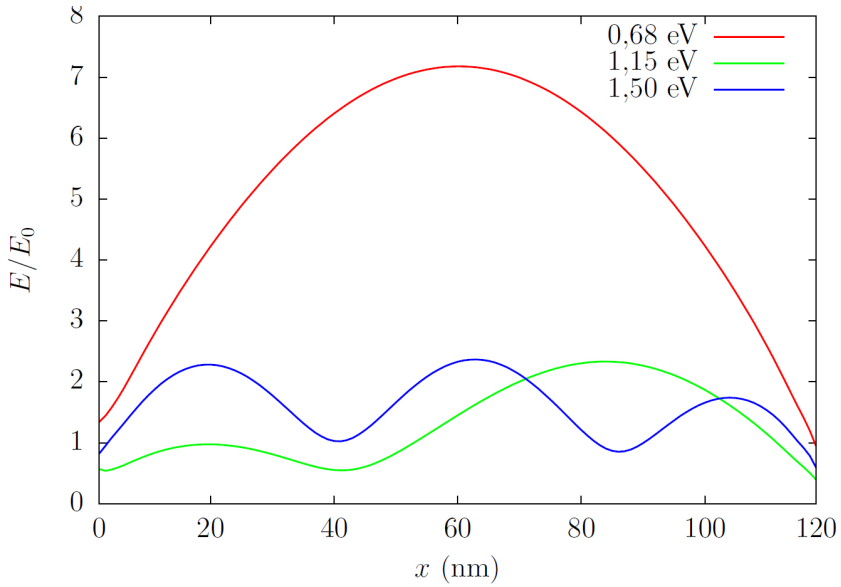

FIGURE 3.9 – Rapport $\frac{E}{E_0}$ à l'intérieur du fil le long de l'axe x passant par le centre de masse du fil dans le plan (xOz), pour une incidence de l'onde plane de 45°.

d'établir les constantes de propagation pour chaque résonance établie par spectroscopie EELS. Parallèlement à ces études expérimentales et numériques une étude analytique a été menée en assimilant les structures à des cylindres parfaits de rayon ρ en métal intégrés dans un diélectrique tel que représenté sur la figure 3.10.

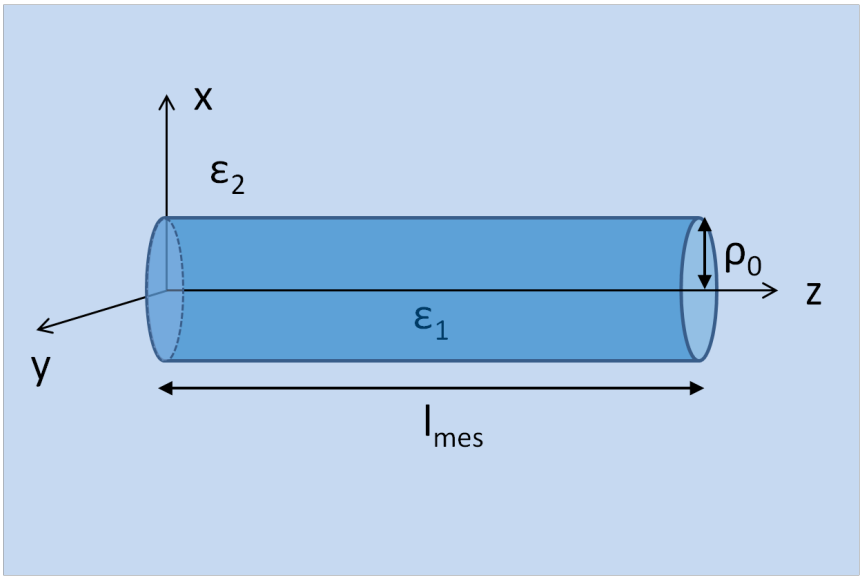

FIGURE 3.10 – Cylindre de permitivité ϵ_1 de longueur l_{mes} et de rayon ρ_0 dans une matrice diélectrique de permitivité ϵ_2

La dispersion des modes TEM d'ordre m peut être calculée en $\rho = \rho_0$ par la recherche des solutions de l'équation transcendante [132], [133] des modes guidés de la structure cylindrique (équation 3.19) :

$$\begin{aligned}&\left[\frac{1}{\kappa_1\rho_0}\frac{J^{'}(m,\kappa_1\rho_0)}{J(m,\kappa_1\rho_0)} - \frac{1}{\kappa_2\rho_0}\frac{H^{'}(m,\kappa_2\rho_0)}{H(m,\kappa_2\rho_0)}\right]\left[\frac{k_1^2}{\kappa_1\rho_0}\frac{J^{'}(m,\kappa_1\rho_0)}{J(m,\kappa_1\rho_0)} - \frac{k_2^2}{\kappa_2\rho_0}\frac{H^{'}(m,\kappa_2\rho_0)}{H(m,\kappa_2\rho_0)}\right]\\&-m^2\beta^2\left(\frac{1}{(\kappa_1.\rho_0)^2} - \frac{1}{(\kappa_2.\rho_0)^2}\right)^2 = 0\end{aligned} \tag{3.19}$$

Avec κ_1 et κ_2 les composantes transverses des vecteurs d'onde k_1 et k_2 dans les milieux 1 et 2. J et J$^{'}$ sont respectivement la fonction de Bessel J et sa dérivée. H et H$^{'}$ sont respectivement la fonction de Hankel H et sa dérivée. Les modes TM (TE) sont caractérisés par un champ magnétique (électrique) qui est perpendiculaire à l'axe du cylindre. Afin de comparer cette étude analytique aux calculs effectués par ADE-FDTD, nous restreindrons notre étude aux seuls modes TM c'est à dire avec le champ magnétique (électrique) perpendiculaire à l'axe du cylindre. Pour $m = 0$ on résout alors l'équation suivante (équation 3.20) :

$$\left[\frac{k_1^2}{\kappa_1\rho}\frac{J^{'}(0,\kappa_1\rho)}{J(0,\kappa_1\rho)} - \frac{k_2^2}{\kappa_2\rho}\frac{H^{'}(0,\kappa_2\rho)}{H(0,\kappa_2\rho)}\right] = 0 \tag{3.20}$$

Pour l'ensemble des objets à symétrie cylindrique étudiés dans ce projet ANR, nous avons reporté sur la figure (3.11) les couples de solutions (β,E) obtenues par EELS et ADE-FDTD ainsi que la relation de dispersion en mode TM des modes supportés par un cylindre infiniment long (Figure 3.20) de rayon $\rho = 5$ nm . Un excellent accord est obtenu entre cette relation de dispersion et les mesures de (β,E) obtenus par EELS et déterminés par ADE-FDTD.

La condition de Fabry-Pérot supplémentaire relative à la longueur finie du cylindre (équation 3.18) signifie que pour un cylindre de longueur l_{mes} nous n'aurons plus un continuum de vecteurs d'ondes possibles mais des valeurs discrètes. En récrivant l'équation 3.18 comme sous la forme de l'équation (3.21).

$$\beta = \frac{p.\pi - \phi}{l_{mes}} \tag{3.21}$$

On s'aperçoit, en faisant une hypothèse sur la phase, que la résolution simultanée de ces deux équations 3.20 et 3.21 permet d'obtenir des couples de solutions (β,E) qui permet d'établir les formes analytiques des champs autour du nano-objet. Il est alors possible de comparer celles-ci aux solutions numériques obtenus par ADE-FDTD et aux mesures par EELS.

Nous avons réalisé la comparaison des résultats obtenus par spectroscopie EELS avec les résultats obtenus par la méthode ADE-FDTD. L'objectif était de déterminer numériquement les conditions pour observer des résonances de type plasmonique afin d'identifier les structures observées pour les résonances de pertes d'énergie électronique. Enfin la courbe de dispersion déterminée expérimentalement et numériquement est reproduite par un modèle analytique. La relation de dispersion d'un cylindre infiniment long de rayon $\rho = 5$ nm donnée par le modèle analytique en mode TM, les mesures EELS et des résultats obtenus

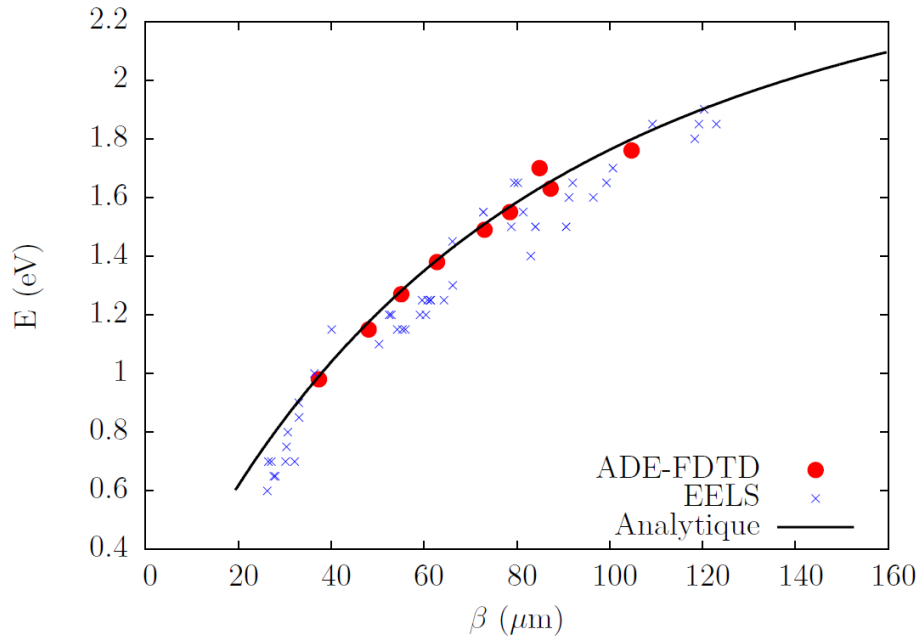

FIGURE 3.11 – Comparaison de la relation de dispersion entre un modèle analytique d'un cylindre infiniment long de rayon $\rho = 5$ nm (mode TM), les mesures EELS et les résultats obtenus par ADE-FDTD pour des nanofils de même rayon.

par ADE-FDTD pour des nanofils de même rayon ρ_0 sont présentées sur la figure 3.11. Cette figure montre l'excellent accord obtenu entre ces trois approches [134, 135].

Présentations orales

- J Cardin, A Fafin, F Gourbilleau, P-E Coulon, A Slablab, G Rizza, and C Dufour, Electromagnetic modeling of plasmonic properties of gold nanoparticles embedded within a dielectric matrix deformed by swift heavy ions. In META Conference, META12, Paris, France, 2012.
- J Cardin, C Dufour, V Khomenkov, A Fafin, I Monnet, G Rizza, P-E Coulon, A Slablab, D Mailly, C Ulysse, X Lafosse, S Perruchas, and T Gacoin. Development of new kinds of plasmonics materials through swift heavy ion shaping technique. In 7th International Conference on Materials for Advanced Technologies (ICMAT 2013), MRS Singapour, 2013.

3.1.2 Milieu à gain : application aux guides d'onde dopés.

Dans le cadre de l'ANR PNANO DAPHNES n°ANR-08-NANO-005, nous nous sommes intéressés à la modélisation d'un guide d'onde dont le cœur est un milieu à gain pour la réalisation d'un amplificateur optique intégré. L'objectif de modéliser la propagation d'un champ électromagnétique dans un guide d'onde optique actif basé sur la méthode des différences finies dans le domaine temporel (FDTD) nous a conduits à développer la méthode FDTD pour rendre compte de matériaux diélectriques actifs qui peuvent absorber ou émettre des champs électromagnétiques. Ce développement a été réalisé par le couplage des équations de Maxwell à un système d'équations différentielles auxiliaires (ADE) décrivant les densités de polarisation liées aux transitions autorisées et les populations des niveaux électroniques considérés. Le modèle d'oscillateur décrivant une transition est donné par l'équation (3.22) :

$$\frac{d^2\vec{P}_{ij}(t)}{dt^2} + \Delta\omega_{ij}\frac{d\vec{P}_{ij}(t)}{dt} + \omega_{ij}^2\vec{P}_{ij}(t) = \kappa\Delta N_{ij}(t)\vec{E}(t) \tag{3.22}$$

avec les paramètres suivants :

- $\Delta\omega_{ij} = \gamma_r + \gamma_{nr} + \frac{2}{T_2}$ largeur à mi-hauteur de la transition fonction du taux de transition radiatif, non-radiatif et du temps de déphasage
- ω_{ij} fréquence de la transition
- $\kappa = \frac{6\pi\epsilon_0 c^3}{\omega_{ij}^2\tau_{ij}n}$ constante de transition
- $\Delta N_{ij} = N_i - N_j$ différence de population entre les niveaux i et j
- $\vec{P}_{ij}$ densité de polarisation (densité de moment dipolaire par unité de volume)

Les populations des niveaux électroniques considérés sont décrites par des équations de population (équations 3.23,3.24).

Nanoparticules de Silicium

$$\frac{dN_{Si}^*(t)}{dt} = \underbrace{+\frac{1}{\hbar\omega_{Si}}\vec{E}(t)\frac{d\vec{P}_{Si}(t)}{dt}}_{\text{pompage optique}} \underbrace{-\frac{N_{Si}^*(t)}{\tau_{Si}|_{nr}^r}}_{\text{émission spontanée}} \underbrace{-KN_{Si}^*(t)N_0(t)}_{\text{transfert d'énergie}} \tag{3.23}$$

Population du niveau $^4\mathbf{F}_{\frac{3}{2}}$ de l'ion $\mathbf{Nd^{3+}}$

$$\begin{aligned}\frac{dN_3(t)}{dt} = &\overbrace{+\frac{1}{\hbar\omega_{32}}\vec{E}(t)\frac{d\vec{P}_{32}(t)}{dt}}^{\text{émission stimulée}} + \overbrace{\frac{1}{\hbar\omega_{31}}\vec{E}(t)\frac{d\vec{P}_{31}(t)}{dt}}^{\text{émission stimulée}} \\ &\underbrace{+\frac{1}{\hbar\omega_{30}}\vec{E}(t)\frac{d\vec{P}_{30}(t)}{dt}}_{\text{émission stimulée}} + \underbrace{\frac{N_4(t)}{\tau_{43}|_{nr}}}_{\text{transition non-radiative}} \underbrace{-\frac{N_3(t)}{\tau_{32}|_{nr}^r} - \frac{N_3(t)}{\tau_{31}|_{nr}^r} - \frac{N_3(t)}{\tau_{30}|_{nr}^r}}_{\text{émission spontanée}}\end{aligned} \tag{3.24}$$

Application

Notre objectif était de modéliser la propagation d'un champ électromagnétique dans un guide d'onde avec une couche contenant des centres absorbeurs et émetteurs comme des ions de terre rare Nd^{3+} ou Er^{3+} et des nanoparticules de silicium. Plus particulièrement, nous voulions déterminer les grandeurs caractéristiques du système comme les champs, les populations des niveaux, dans un régime stationnaire en fonction de paramètres initiaux tels que la concentration de centre émetteur, la géométrie, la configuration et la propagation de la pompe et du signal. Afin de modéliser ces régimes stationnaires dans un guide d'onde d'une couche contenant des centres émetteurs et absorbeurs, nous devions tenir compte de l'évolution temporelle des champs électromagnétiques et des populations des niveaux électroniques. Dans un guide contenant des nanoparticules de silicium et les ions néodyme, la durée de vie typique des niveaux électroniques est d'environ quelques ms, alors que la période caractéristique du champ électromagnétique est de l'ordre de la fs. Le choix d'un pas temps commun pour traiter ces différentes échelles de temps, entraînerait un long temps de calcul prohibitif (environ 10^{+15} itérations). Une solution possible pour surmonter ce problème de temps multi-échelle a été proposée par notre équipe en 2011 [136], en appliquant la méthode dite du facteur d'échelle temporel ou "time scaling" qui consiste à multiplier les équations différentielles décrivant les populations par un facteur d'échelle (10^6) de sorte que la convergence des niveaux de la population est accélérée. Malgré la réduction du nombre d'itérations de temps requise de 6 ordres de grandeur, cette technique ne diminuait pas suffisamment le temps de calcul et pouvait conduire à des instabilités numériques pour les facteurs d'échelle plus élevés.

Par conséquent, nous avons développé un nouvel algorithme ADE-FDTD (figure 3.12) à deux boucles qui permet de calculer la distribution de champ électromagnétique, les niveaux populations électroniques, et le gain dans le guide dans le régime stationnaire [137, 138].

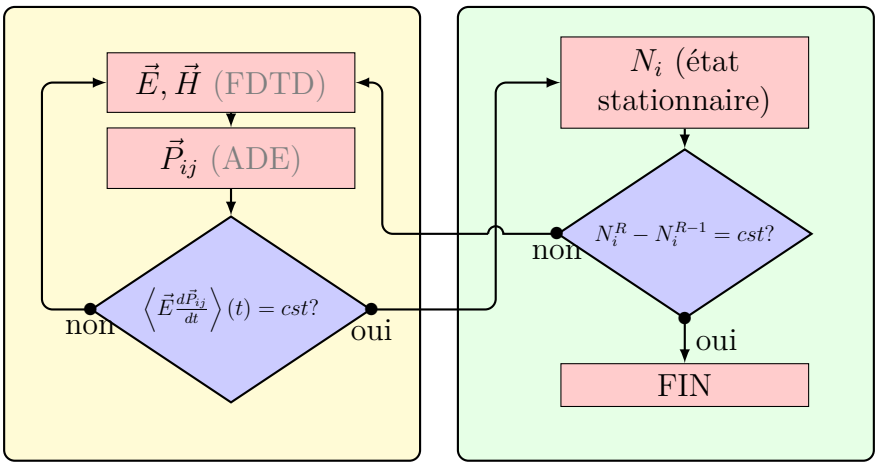

FIGURE 3.12 – Schéma de principe de l'algorithme ADE-FDTD à deux boucles.

Les spécificités de l'algorithme ADE-FDTD à double boucle sont rappelées ci-dessous

- ➤ Séparation de calcul des processus rapides (champs, densité de polarisation) et des processus lents (population des niveaux)
- ➤ Calibration des oscillateurs de Lorentz sur des données expérimentales (sections efficaces) avec comme degré de liberté les paramètres d'oscillateur ($\Delta\omega_{ij}$, ω_{ij}, constante de transition κ) mais également leur nombre (Princ. de superposition)

Ces travaux ont été largement développés et documentés dans les publications [137–139] ainsi que dans les travaux de thèse d'A. Fafin [99]. Une étude comparative de la réalisation de gain est effectuée dans un amplificateur optique guide d'onde dont la couche active est constituée par une matrice de silice contenant des nanograins de silicium agissant comme sensibilisateur soit des ions néodyme (Nd^{3+}), soit des ions d'erbium (Er^{3+}). Nous avons étudié le régime des états stationnaires des niveaux électroniques des ions de terres rares et des nanograins de silicium ainsi que du champ électromagnétique pour les différentes puissances de pompage. En outre, la distribution du gain linéique réalisable a été estimée dans cette gamme de pompage à partir des populations des niveaux dans leur état stationnaire par l'équation (3.25).

$$g_{dB/cm}(x,y,z) = \frac{10}{ln10}\left[\sigma_{em}N_{high}(x,y,z) - \sigma_{abs}N_{low}(x,y,z)\right] \tag{3.25}$$

Le guide d'onde dopé Nd^{3+} montre un gain brut par unité de longueur à 1064 nm pouvant atteindre 30 dB.cm^{-1}. Dans les mêmes conditions de pompage, le guide d'onde dopé avec des ions Er^{3+} présente un gain linéique maximum de 2 dB.cm^{-1} à 1532 nm. Compte tenu des pertes déterminées expérimentalement sur ce type de guide d'onde, nous avons démontré un gain net positif significatif pouvant être atteint dans le guide d'onde dopé avec l'ion Nd^{3+}.

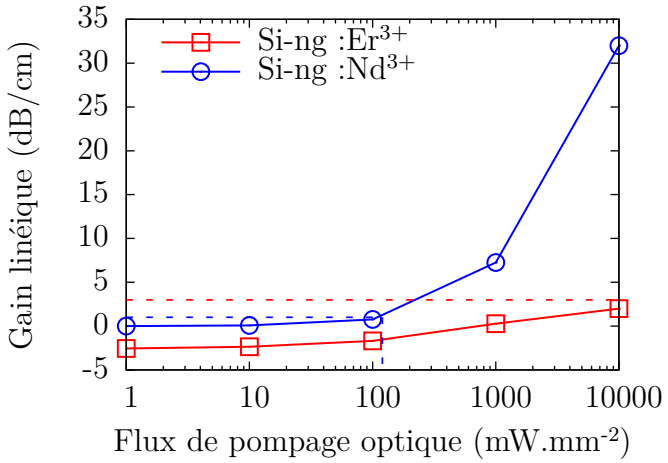

FIGURE 3.13 – Gain linéique enregistré au centre de la couche active au début du guide d'onde à la position x = 4.5 μm and y = 8.55 μm and z = 0. Les pertes expérimentales [140, 141] sont reportées en tiret pointillé.

L'algorithme développé est stable et applicable aux matériaux de gain avec des émetteurs optiques ayant une large gamme de durées de vie comme par exemple d'autres ions de

terre rare. La méthode est généralisable à d'autres modes d'excitation comme par exemple le pompage électrique avec la modélisation de l'injection de courant et le transport des porteur de charges [142].

Publications

- A Fafin, J Cardin, C Dufour, and F Gourbilleau. Modeling of the electromagnetic field and level populations in a waveguide amplifier : a multi-scale time problem, Optics Express, 21(20) :24171-24184, 2013.
- A Fafin, J Cardin, C Dufour, and F Gourbilleau. Theoretical investigation of the more suitable rare earth to achieve high gain in waveguide based on silica containing silicon nanograins doped with either Nd^{3+} or Er^{3+} ions, Optics Express, 22(10) :12296-12306, 2014.
- J Cardin, A Fafin, C Dufour, and F Gourbilleau. Modeling of optical amplifier waveguide based on silicon nanostructures and rare earth ions doped silica matrix gain media by a finite-difference time-domain method : comparison of achievable gain with Er^{3+} or Nd^{3+} ions dopants, In SPIE OPTO, pages 935709-935709, International Society for Optics and Photonics, 2015.

3.2 Modélisation de matériaux stratifiés luminescents.

Le but de ce travail est d'étudier les propriétés d'émetteurs inclus dans un film mince d'épaisseur d et d'indice de réfraction n_2. Les émetteurs sont pompés optiquement par une onde incidente de façon similaire à une configuration expérimentale d'un banc de photoluminescence. Nous allons examiner la couche mince telle que représentée sur la figure (3.14).

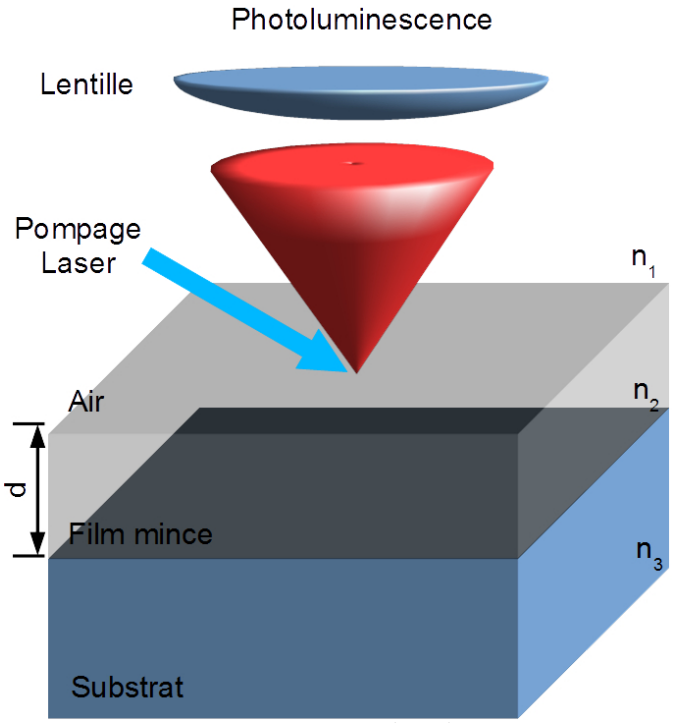

FIGURE 3.14 – thin layer

Basé sur le formalisme matriciel classique décrit par P. Yeh [15], le formalisme des matrices de transfert étendues proposé par Weber et al. [143] et détaillé par Y.G. Boucher [144] et le formalisme décrivant les termes sources de champs électromagnétique de Benisty et al [145], un modèle numérique de luminescence dans les milieux stratifiés a été développé. Les milieux sont décrits par des fonctions de dispersion issues de l'analyse par ellipsométrie spectroscopique. Ce modèle rend compte de plusieurs phénomènes mis en jeu dans les interactions de photoluminescence :

- La propagation de la pompe dans un système stratifié qui permet de rendre compte de la variation de l'absorption de la pompe avec l'épaisseur des films minces traversés. On peut observer notamment l'établissement d'ondes stationnaires et l'absorption de la pompe avec l'épaisseur.
- La population d'émetteurs est décrite par un jeu d'équations de population décrivant phénoménologiquement les mécanismes d'absorption et d'émission avec le décalage de Stokes. Les caractéristiques spectrales de l'émission sont décrites par des fonctions mathématiques couramment utilisés en spectroscopie (Lorentz,Voigt...).

- ➤ L'émission de chaque émetteur est décrite par la composition de l'émission de trois dipôles électriques. Ceci permet de rendre compte de l'isotropie ou de l'éventuelle anisotropie de l'émission de ces derniers.
- ➤ Le calcul est réalisé au moyen d'une discrétisation sur l'épaisseur, sur les angles et les longueurs d'onde. Les champs obtenus pour chaque pas de longueur d'onde, d'angle et d'épaisseur issus de ce calcul sont intégrés pour obtenir les observables comparables à l'expérience, c'est-à-dire l'intensité de photoluminescence.

Ces travaux faisant l'objet d'une publication en cours de préparation ne seront pas plus détaillés dans le manuscrit, mais pourront faire l'objet de développements à l'occasion de la soutenance.

Oxynitrure de silicium codopé Tb^{3+}-Yb^{3+} pour couche mince à conversion de fréquence optique pour applications aux cellules solaires.

Les cellules solaires silicium présentent une limite d'efficacité intrinsèque calculée par Shockley et Queisser de 29%, qui est quasiment atteinte en laboratoire [146]. Parmi les différentes approches pour améliorer l'efficacité des cellules solaires, des approches par les mécanismes de conversion de fréquence sont possibles. Ces mécanismes permettent de réaliser une photogénération de porteurs de charge plus efficace dans les cellules solaires au silicium par la modification du spectre solaire. Cette étude se concentre sur le processus de conversion descendante (down-conversion :DC) qui repose sur la conversion des photons UV en photons infrarouges avec une énergie juste au-dessus de la bande interdite. Ce mécanisme maximise le nombre de porteurs photogénérés avec une énergie proche de celle de la bande interdite de la cellule solaire $E \approx E_g$, au détriment des porteurs de plus haute énergie $E = E_g + \Delta E$.

Dans les cellules solaires (CS) classiques, les porteurs ayant une énergie très au-dessus de la bande interdite de la cellule solaire perdent une partie de leur énergie ΔE par transfert à la matrice par excitation de phonons. C'est un mécanisme de perte d'énergie pour la conversion PV. De surcroît, ce mécanisme de thermalisation conduit à une surchauffe de la cellule, qui entraîne une diminution de son efficacité de conversion et de sa durée de vie.

Une conversion descendante (DC) peut réduire les processus de thermalisation des porteurs photogénérés par absorption de photons (UV) et conversion en deux photons IR d'énergie supérieure à celle de la bande interdite de la cellule solaire en silicium. Dexter [149] a montré que ce système présente un intérêt potentiel avec un rendement quantique de conversion descendante (DC) supérieur à 100%. Par la suite, différents auteurs ont mis en évidence un rendement quantique interne allant de 120% à 199% à l'aide de différentes matrices et de combinaisons d'ions de terres rares (RE) [150–152]. Pour des raisons de simplicité, la combinaison à deux ions de terre rare a été choisie pour notre étude.

Afin d'obtenir un mécanisme DC compatible avec la cellule solaire silicium, deux ions de terres rares, Tb^{3+} et Yb^{3+}, ont été choisis en raison de leur configuration énergétique qui permet la conversion descendante (DC) vers une énergie en accord avec celle de l'énergie de la bande interdite du silicium. Pour assurer la compatibilité de la matrice contenant les ions Tb^{3+} et Yb^{3+} avec les cellules solaires silicium, notre équipe étudie le co-dopage

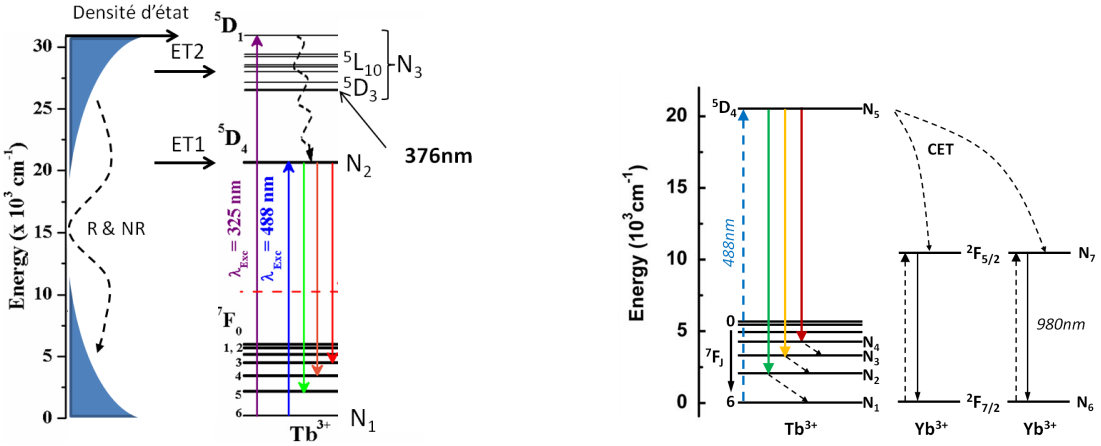

FIGURE 3.15 – Schéma de principe de l'excitation de l'ion Tb^{3+} dans les matrices de SiN_x [147] (à gauche) Description schématique des niveaux d'énergie mis en jeu dans le transfert Tb^{3+} :Yb^{3+} [148] (à droite)

de films de SiO_xN_y et SiN_y par les ions Tb^{3+} et Yb^{3+}. Ces matrices présentent l'avantage d'une section efficace d'absorption plus importante que celle des ions de terres rares (10^{-17}-10^{-18} cm^2 [153] au lieu de 10^{-20} cm^2 [154]). Cette absorption par ces matrices permet par la suite une excitation indirecte des terres rares par un mécanisme de transfert d'énergie efficace vers les ions Tb^{3+}. La transition des niveaux $^5D_4$ vers $^6F_7$ de l'ion Tb^{3+} correspond à une énergie de 2,53 eV (490 nm) qui est approximativement le double de l'énergie de la transition $^2F_{\frac{5}{2}}$ vers $^2F_{\frac{7}{2}}$ des ions Yb^{3+}, correspondant à une énergie de 1,26 eV (980 nm). Cette configuration énergétique permet le processus de découpage quantique par l'absorption d'un photon UV par un ion Tb^{3+}, un transfert d'énergie coopératif (TEC) de l'ion Tb^{3+} vers deux ions Yb^{3+} environnants [155] qui se désexcitent par l'émission de deux photons infrarouges à 980 nm. Les photons émis par les ions Yb^{3+} à 980 nm (1,26 eV) ont une énergie légèrement supérieure à celle de la bande interdite de CS de silicium (1,1 eV) et sont donc absorbés avec une énergie de thermalisation réduite par celle-ci. Contrairement au couple d'ions Pr^{3+} : Yb^{3+}, l'absence d'un niveau d'énergie intermédiaire de l'ion Tb^{3+} empêche la relaxation inverse de deux ions Yb^{3+} excités vers un ion Tb^{3+} [156]. Le principe d'utilisation d'une couche à conversion de fréquence en amont d'une cellule solaire est de disposer cette couche supplémentaire en surface de la cellule solaire qui par le mécanisme du découpage quantique interne permet de modifier la répartition spectrale du spectre incident sur la cellule. La méthode de modélisation de matériaux luminescents présentée section (3.2) a été mise en œuvre pour l'analyse de l'efficacité de ces couches à conversion de fréquence descendante dans deux études publiées dernièrement [148, 157] :

- La méthode a été employée pour déterminer l'efficacité quantique externe additionnelle de 2% apportée par la couche mince à conversion de fréquence descendante. Elle a permis d'estimer la fraction de l'émission des ions Yb^{3+} effectivement couplés dans le silicium sous-jacent (cellule solaire) et de décrire l'indicatrice d'émission.
- La méthode a également été appliquée afin de modéliser des spectres de photolu-

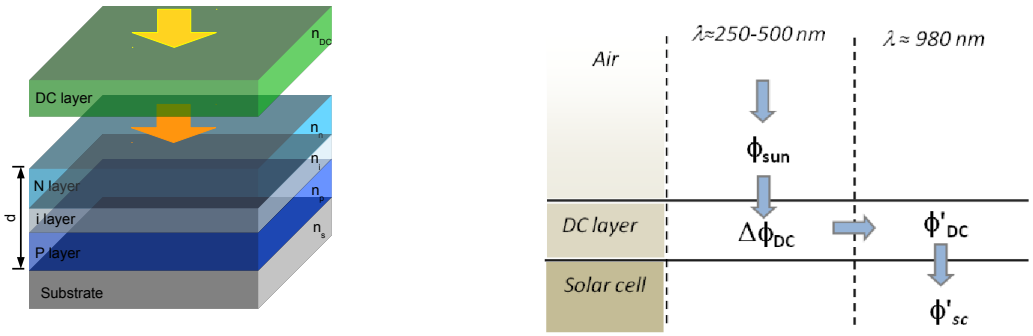

FIGURE 3.16 – Principe d'utilisation d'une couche mince à conversion de fréquence optique pour l'utilisation sur une cellule solaire (à gauche). Principe d'utilisation d'une couche mince à conversion de fréquence optique pour l'utilisation sur une cellule solaire (à droite).

minescence dans les matériaux de la couche à conversion de fréquence, de l'air, et du silicium. Les rendements d'extraction dans les trois milieux considérés, définis comme le rapport de la puissance optique dans un milieu sur la puissance optique totale émise, ont été calculés. La comparaison de ces rendements avec les mesures expérimentales de PL a permis de déterminer l'efficacité du couplage de l'émission DC vers le silicium.

Publications

- Y-T An, C Labbé, J Cardin, M Morales, and F Gourbilleau, Highly efficient infrared quantum cutting in Tb^{3+}-Yb^{3+} codoped silicon oxynitride for solar cell applications, Adv. Optical Mater., Vol. 1, Iss. 11, 855, 2013.
- L Dumont, J Cardin, P Benzo, M Carrada, C Labbé, AL Richard, DC Ingram, WM Jadwisienczak, and F Gourbilleau. SiN_x :Tb^{3+}-Yb^{3+}, an efficient down-conversion layer compatible with silicon solar cell process, Solar Energy Materials and Solar Cells, accepté pour publication.

Chapitre 4

Conclusion et perspectives

4.1 Conclusion

Les travaux présentés dans ce manuscrit illustrent la variété des sujets abordés autour des propriétés optiques des matériaux depuis une dizaine d'années. Ces travaux se partagent entre investigations expérimentales et théoriques. Les études expérimentales des propriétés optiques linéaires, non-linéaires et luminescentes ont été réalisées sur des matériaux inorganiques et organiques. Les matériaux organiques étudiés sont par exemple des matrices de type PMMA dopées par des chromophores [29]. Ces matrices organiques peuvent être également des matrices hôtes dopées par des luminophores comme par exemple les agrégats de Molybdène luminescents [86]. Les matériaux inorganiques étudiés sont de nature conductrice comme les TCO (Ga_2O_3, ZnO), semi-conductrice comme les SiN_x et isolante comme la silice SiO_2. Nombre de ces matériaux organiques et inorganiques, conducteurs ou isolants ont été dopés par les ions de terre rare (Er, Nd, Tb, Yb, Eu). Enfin des travaux plus récents issus de collaborations m'ont amené à étudier les propriétés optiques d'agrégats métalliques stabilisés dans des zéolithes en solution [158].

Parallèlement à ces activités expérimentales, je développe des méthodes de modélisation qui sont appliquées à l'interprétation d'expériences [13, 17] ou bien à l'étude et au développement d'applications à partir des matériaux [137, 139]. A travers des collaborations soutenues par l'ANR et le LABEX EMC3, j'ai pu développer mon expertise sur la modélisation des propriétés optiques des objets nanométriques semi-conducteurs ou métalliques inclus dans une matrice diélectrique par des méthodes comme le DDA et la méthode ADE-FDTD. Cette expertise a été mise à contribution dans le cas des particules d'or déformées par faisceau d'ions. L'analyse des propriétés plasmoniques de ces dernières a été réalisée avec un très bon accord entre les résultats expérimentaux et nos résultats théoriques [135].

4.2 Perspectives

Les perspectives s'articulent autour du développement de matériaux pour la photonique et l'énergie. Le développement de matériaux à gain pour la réalisation d'un amplificateur

optique ou d'un laser tout silicium à base de matrice de SiO_x ou SiN_x contenant des nanostructures de silicium et dopé par des ions de terre rare semble être une activité amenée à ralentir. En effet, l'efficacité importante des émetteurs à base de matériaux III-V et leur intégration sur Silicium pour des applications photoniques rendent moins intéressant le développement de sources laser ou d'amplificateurs à base de silicium qui sont aujourd'hui moins efficaces. Ces dernières années, des travaux sur le développement de matériaux pour l'énergie et notamment pour le photovoltaïque se sont accrus, aidés en cela par les sources de financement (région, labex, ANR). Ces travaux s'articulent autour du développement de semi-conducteurs nanostructurés pour les cellules solaires [159]. Plus récemment les films minces à conversion de fréquence basse pour des applications dans le photovoltaïque ont été développés dans des matrices à base de silicium [148, 157]. Les perspectives à court et moyen termes sont de poursuivre ces travaux en explorant les différentes matrices et combinaisons de luminophores. Les perspectives s'articulent également autour de plusieurs collaborations sur les propriétés de luminescence :

- ➤ Lab. CRISMAT (J.M. Rueff) sur des matrices luminescentes hybrides organique-inorganique.
- ➤ Lab LCS (S. Mintova) sur les composés nano et subnanométriques métalliques en matrice zéolithe
- ➤ LCMT (B. Witulski) collaboration sur les émetteurs organiques pour OLED (je suis référent de la thèse de Thu-Hong Doan au LCMT)

Beaucoup de travaux effectués sur la méthode ADE-FDTD et sur la méthode matricielle décrivant l'émission en milieux stratifiés restent à valoriser par des publications au cours des années futures. Le développement supplémentaire de méthodes de modélisation mis en œuvre dans l'équipe NIMPH se fera en adéquation avec les orientations expérimentales futures de l'équipe (films minces pour l'énergie, dynamique des porteurs EMC...). J'ai proposé récemment un nouveau sujet de recherche sur l'étude des propriétés thermique/optique de films minces pour le refroidissement radiatif passif. Des demandes de financement ont été récemment couronnées de succès, puisque deux financements ont été obtenus pour l'année à venir (Projet DAYCOOL soutenus par le Labex EMC3 et un PEPS CNRS énergie).

Références

[1] G.H. Haertling. Ferroelectric ceramics : history and technology. *J. Am. Ceram. Soc.*, 82(4) :797–818, 1999.

[2] D. Bosc, F. Foll, B. Boutevin, and A. Rousseau. Synthesis of a novel difunctional nlo azo-dye chromophore and characterizations of crosslinkable copolymers with stable electrooptic properties. *Journal of applied polymer science*, 74(4) :974–982, 1999.

[3] L. Dalton, A. Harper, A. Ren, F. Wang, G. Todorova, J. Chen, C. Zhang, and M. Lee. Polymeric electro-optic modulators : from chromophore design to integration with semiconductor very large scale integration electronics and silica fiber optics. *Industrial & engineering chemistry research*, 38(1) :8–33, 1999.

[4] G. Keiser. *Optical fiber communications*. McGraw-Hill Science, Engineering & Mathematics, 1983.

[5] P.K. Tien, R. Ulrich, and R.J. Martin. Modes of propagating light waves in thin deposited semiconductor films. *Applied Physics Letters*, 14(9) :291–294, 1969.

[6] P.K. Tien and R. Ulrich. Theory of prism-film coupler and thin-film light guides. *Journal of the Optical Society of America*, 60(10) :1325–1337, October 1970.

[7] P.K. Tien. Light waves in thin films and integrated optics. *Applied Optics*, 10(11) :2395–2413, 1971.

[8] R. Ulrich and R. Torge. Measurement of thin film parameters with a prism coupler. *Applied Optics*, 12(12) :2901–2908, 1973.

[9] J. Cardin. *Elaboration et caractérisation de couches minces ferroélectriques pour des applications optiques.* PhD thesis, Université de Nantes, France, 2004.

[10] R.T. Kersten. The prism-film coupler as a precision instrument part i. accuracy and capabilities of prism couplers as instruments. *Opt. Acta*, 22(6) :503–513, 1975.

[11] R.T. Kersten. The prism–film coupler as a precision instrument. part ii. measurements of refractive index and thickness of leaky wave guides. *Opt. Acta*, 22(6) :515–521, 1975.

[12] J. Cardin, D. Leduc, T. Schneider, C. Lupi, D. Averty, and H.W. Gundel. Optical characterization of pzt thin films for waveguide applications. *Journal of the European Ceramic Society*, 25(12) :2913–2916, 2005.

[13] J. Cardin and D. Leduc. Determination of refractive index, thickness, and the optical losses of thin films from prism-film coupling measurements. *Applied optics*, 47(7) :894–900, 2008.

[14] F. Abelès. La théorie générale des couches minces. *J. Phys. Radium*, 11(7) :307–309, 1950.

[15] P. Yeh. *Optical waves in layered media*, volume 95. Wiley Online Library, 1988.

[16] A.C. Davison and D.V. Hinkley. *Bootstrap methods and their application*, volume 1. Cambridge university press, 1997.

[17] T. Schneider, D. Leduc, J. Cardin, C. Lupi, N. Barreau, and H.W. Gundel. Optical properties of pzt thin films deposited on a zno buffer layer. *Optical Materials*, 29(12) :1871–1877, 2007.

[18] http ://www.pgo-online.com/.

[19] http ://www.metricon.com/.

[20] T. Schneider, D. Leduc, J. Cardin, C. Lupi, and H.W. Gundel. Optical characterisation of a three layer waveguide structure by m-lines spectroscopy. *Ferroelectrics*, 352(1) :50–60, 2007.

[21] T. Schneider, D. Leduc, C. Lupi, J. Cardin, H.W. Gundel, and C. Boisrobert. A method to retrieve optical and geometrical characteristics of three layer waveguides from m-lines measurements. *Journal of Applied Physics*, 103(6) :063110–063110, 2008.

[22] J. Chilwell and I. Hodgkinson. Thin-films field-transfer matrix theory of planar multilayer waveguides and reflection from prism-loaded waveguides. *JOSA A*, 1(7) :742–753, 1984.

[23] T. Schneider. *Elaboration, étude et analyse par spectroscopie M-lines de guides d'ondes composites multicouches*. PhD thesis, PhD thesis, Université de Nantes, 2006.

[24] W.L. Bond. Measurement of the refractive indices of several crystals. *Journal of Applied Physics*, 36(5) :1674–1677, 1965.

[25] S.-S. Lin and J.-L. Huang. Effect of thickness on the structural and optical properties of zno films by rf magnetron sputtering. *Surface and Coatings Technology*, 185(2) :222–227, 2004.

[26] T.D. Visser, H. Blok, and D. Lenstra. Modal analysis of a planar waveguide with gain and losses. *Quantum Electronics, IEEE Journal of*, 31(10) :1803–1810, 1995.

[27] R.C. Alferness and R.V. Schmidt. Tunable optical waveguide directional coupler filter. *Applied Physics Letters*, 33(2) :161–163, 1978.

[28] B. Jaskorzynska, Z.J. Zawistowski, M. Dainese, J. Cardin, and L. Thylén. Widely tunable directional coupler filters with 1d photonic crystal. In *Transparent Optical Networks, 2005, Proceedings of 2005 7th International Conference*, volume 1, pages 136–139. IEEE, 2005.

[29] V. Boucher, J. Cardin, D. Leduc, R. Seveno, R. Le Ny, H. W. Gundel, C. Boisrobert, S. Legoupy, F. Legros, V. Montembault, F. Odobel, C. Monnereau, E. Blart, D. Bosc, A. Goullet, and J. Y. Mevellec. Synthesis and characterization of polymers for nonlinear optical applications. In *3rd international conference on Advanced Optical Materials and Device (AOMD-3)[http ://www. fpd. lu. lv/AOMD3/]*, volume 5122, pages 206–209, 2003.

[30] C. Monnereau. *Synthèse de nouveaux matériaux organiques et organo-métalliques pour l'optique non-linéaire du deuxième-ordre*. PhD thesis, Nantes, 2005.

[31] J.A. Giacometti and J.S.C. Campos. Constant current corona triode with grid voltage control. application to polymer foil charging. *Review of scientific instruments*, 61(3) :1143–1150, 1990.

[32] P. Nagtegaele, E. Brasselet, and J. Zyss. Anisotropy and dispersion of a pockels tensor : A benchmark for electro-optic organic thin-film assessment. *JOSA B*, 20(9) :1932–1936, 2003.

[33] J.A. Nelder and R. Mead. A simplex method for function minimization. *The computer journal*, 7(4) :308–313, 1965.

[34] B. Valeur and M.N. Berberan-Santos. *Molecular fluorescence : principles and applications*. John Wiley & Sons, 2012.

[35] J. Zheng, P.R. Nicovich, and R.M. Dickson. Highly fluorescent noble metal quantum dots. *Annual review of physical chemistry*, 58 :409, 2007.

[36] S. Cueff. *Transfert d'énergie entre nanoclusters de Silicum et Erbium dans des matrices oxydes et nitrures de Si : applications à des diodes électroluminescentes*. PhD thesis, Université de Caen Basse Normandie, 2011.

[37] L.T. Canham. Silicon quantum wire array fabrication by electrochemical and chemical dissolution of wafers. *Applied Physics Letters*, 57(10) :1046–1048, 1990.

[38] C. Delerue, G. Allan, and M. Lannoo. Theoretical aspects of the luminescence of porous silicon. *Physical Review B*, 48(15) :11024, 1993.

[39] M. Zacharias, J. Heitmann, U. Scholz, R.and Kahler, M. Schmidt, and J. Bläsing. Size-controlled highly luminescent silicon nanocrystals : A sio/sio2 superlattice approach. *Applied Physics Letters*, 80(4) :661–663, 2002.

[40] F. Sangghaleh, I. Sychugov, Z. Yang, J.G.C. Veinot, and J. Linnros. Near-unity internal quantum efficiency of luminescent silicon nanocrystals with ligand passivation. *ACS nano*, 9(7) :7097–7104, 2015.

[41] R. Peretti. *Saturation spectrale de gain dans les amplificateurs à fibres dopées erbium : largeurs homogène et inhomogène et approche des nanomatériaux*. PhD thesis, Université Claude Bernard-Lyon I, 2008.

[42] O. Laporte and W.F. Meggers. Some rules of spectral structure. *Review of Scientific Instruments*, 11(5), 1925.

[43] F. Auzel. *Propriétés optiques des terres rares*. Ed. Techniques Ingénieur, 1980.

[44] B.M. Walsh. *Judd-Ofelt theory : principles and practices.* Springer, 2006.

[45] G. Liu and B. Jacquier. *Spectroscopic properties of rare earths in optical materials*, volume 83. Springer Science & Business Media, 2006.

[46] A. Al Choueiry. *Nanoparticles de silicium et ion erbium pour lámplification optique.* PhD thesis, Université Claude Bernard-Lyon I, 2007.

[47] J. Heitmann, M. Schmidt, M. Zacharias, V.Y. Timoshenko, M.G. Lisachenko, and P.K. Kashkarov. Fabrication and photoluminescence properties of erbium doped size-controlled silicon nanocrystals. *Materials Science and Engineering : B*, 105(1) :214–220, 2003.

[48] D. Pacifici, G. Franzò, F. Priolo, F. Iacona, and L. Dal Negro. Modeling and perspectives of the si nanocrystals–er interaction for optical amplification. *Phys. Rev. B*, 67(24) :245301, Jun 2003.

[49] B. Garrido, C. García, S.-Y. Seo, P. Pellegrino, D. Navarro-Urrios, N. Daldosso, L. Pavesi, F. Gourbilleau, and R. Rizk. Excitable er fraction and quenching phenomena in er-doped sio_2 layers containing si nanoclusters. *Physical Review B*, 76(24) :245308, 2007.

[50] A.J. Kenyon, P.F. Trwoga, M. Federighi, and C.W. Pitt. Optical properties of PECVD erbium-doped silicon-rich silica : evidence for energy transfer between silicon microclusters and erbium ions. *Journal of Physics : Condensed Matter*, 6(21) :L319, 1994.

[51] M. Fujii, M. Yoshida, Y. Kanzawa, S. Hayashi, and K. Yamamoto. 1.54 μm photoluminescence of Er^{3+} doped into Sio_2 films containing si nanocrystals : Evidence for energy transfer from Si nanocrystals to Er^{3+}. *Applied Physics Letters*, 71(9) :1198–1200, sep 1997.

[52] G. Franzo, V. Vinciguerra, and F. Priolo. The excitation mechanism of rare-earth ions in silicon nanocrystals. *Applied Physics A*, 69(1) :3–12, 1999.

[53] P.G. Kik and A. Polman. Erbium-doped optical-waveguide amplifiers on silicon. *MRS bulletin*, 23(4) :48–54, 1998.

[54] G. Franzo, D. Pacifici, V. Vinciguerra, F. Priolo, and F. Iacona. Er^{3+} ions-si nanocrystals interactions and their effects on the luminescence properties. *Applied Physics Letters*, 76(16) :2167–2169, 2000.

[55] S.-Y. Seo, M.-J. Kim, and J. H. Shin. The nd-nanocluster coupling strength and its effect in excitation/de-excitation of nd[sup 3+] luminescence in nd-doped silicon-rich silicon oxide. *Applied Physics Letters*, 83(14) :2778–2780, 2003.

[56] F. Gourbilleau, C. Dufour, M. Levalois, J. Vicens, R. Rizk, C. Sada, F. Enrichi, and G. Battaglin. Room-temperature 1.54 μm photoluminescence from er-doped si-rich silica layers obtained by reactive magnetron sputtering. *Journal of applied physics*, 94(6) :3869–3874, 2003.

[57] G.W. Adeola, O. Jambois, P. Miska, H. Rinnert, and M. Vergnat. Luminescence efficiency at 1.5 μm of er-doped thick sio layers and er-doped sio/sio_2 multilayers. *Applied physics letters*, 89 :101920, 2006.

[58] K. Watanabe, H. Tamaoka, M.Fujii, K. Moriwaki, and S. Hayashi. Excitation of nd^{3+} and tm^{3+} by the energy transfer from si nanocrystals. *Physica E : Low-dimensional Systems and Nanostructures*, 13(2) :1038 – 1042, 2002.

[59] A.N. MacDonald, A. Hryciw, Q. Li, and A. Meldrum. Luminescence of Nd-enriched silicon nanoparticle glasses. *Optical Materials*, 28(6) :820–824, 2006.

[60] A. Meldrum, A. Hryciw, A.N. MacDonald, C. Blois, T. Clement, R. DeCorby, J. Wang, and Q. Li. Interaction between rare-earth ions and amorphous silicon nanoclusters produced at low processing temperatures. *Journal of luminescence*, 121(2) :199–203, 2006.

[61] A. Podhorodecki, J. Misiewicz, F. Gourbilleau, and C. Cardin, J.and Dufour. High energy excitation transfer from silicon nanocrystals to neodymium ions in silicon-rich oxide film. *Electrochemical and Solid-State Letters*, 13(3) :K26–K28, 2010.

[62] D. Bréard, F. Gourbilleau, C. Dufour, R. Rizk, J.L. Doualan, and P. Camy. Spectroscopic studies of Nd^{3+}-doped silicon-rich silicon oxide films. *Materials Science and Engineering : B*, 146(1-3) :179–182, 2008.

[63] C.-H. Liang, J. Cardin, C. Labbé, and F. Gourbilleau. Evidence of two sensitization processes of Nd^3+ ions in Nd-doped SiOx films. *Journal of Applied Physics*, 114(3) :033103, 2013.

[64] K. Hijazi. *Contribution à lóptimisation du couplage Erbium–Nanograins de silicium pour des dispositifs photoniques compacts*. PhD thesis, UNIVERSITE DE CAEN BASSE-NORMANDIE, 2009.

[65] C.-H. Liang. *Propriétés optique des films minces à base de Si dopé Nd : vers un amplificateur optique*. PhD thesis, Université de Caen Basse Normandie, 2013.

[66] P. N. Ramesh Sundar. *Films minces à base de silicium nanostructuré pour des cellules photovoltaiques de troisième génération*. PhD thesis, Université de Caen Basse Normandie, 2012.

[67] Y.-T. An. *Films minces dopés terres rares à base de Silicium pour un effet de découpage de photons dans les cellules solaires*. PhD thesis, Université de Caen Basse Normandie, 2013.

[68] C. Lecerf. *Elaboration et caractérisations de films d'oxyde de gallium dopés terres rares*. PhD thesis, Université de Caen Basse Normandie, 2011.

[69] C. Davesnne. *Elaboration et caractérisation de films de ZnO dopé pour des applications optoélectroniques*. PhD thesis, Université de Caen Basse Normandie, 2014.

[70] G. Zatryb, A. Podhorodecki, J. Misiewicz, J. Cardin, F. Gourbilleau, et al. On the nature of the stretched exponential photoluminescence decay for silicon nanocrystals. *Nanoscale research letters*, 6(1) :106, 2011.

[71] K. Hijazi, L. Khomenkova, F. Gourbilleau, J. Cardin, and R. Rizk. Enhanced fraction of coupled er in silicon-rich silicon oxide layers grown by magnetron co-sputtering. *Journal of Luminescence*, 129(12) :1886–1889, 2009.

[72] K. Hijazi, R. Rizk, J. Cardin, L. Khomenkova, and F. Gourbilleau. Towards an optimum coupling between er ions and si-based sensitizers for integrated active photonics. *Journal of Applied Physics*, 106(2) :024311–024311, 2009.

[73] D. Navarro-Urrios, Y. Lebour, O. Jambois, B. Garrido, A. Pitanti, N. Daldosso, L. Pavesi, J. Cardin, K. Hijazi, L. Khomenkova, F. Gourbilleau, and R. Rizk. Optically active er3+ ions in sio2 codoped with si nanoclusters. *Journal of Applied Physics*, 106(9) :93107, 2009.

[74] S. Cueff, C. Labbé, J. Cardin, J.-L. Doualan, L. Khomenkova, K. Hijazi, O. Jambois, B. Garrido, and R. Rizk. Efficient energy transfer from si-nanoclusters to er ions in silica induced by substrate heating during deposition. *Journal of Applied Physics*, 108 :064302, 2010.

[75] O. Debieu, D. Bréard, A. Podhorodecki, G. Zatryb, J. Misiewicz, C. Labbé, J. Cardin, and F. Gourbilleau. Effect of annealing and nd concentration on the photoluminescence of nd3+ ions coupled with silicon nanoparticles. *Journal of Applied Physics*, 108(11) :113114, 2010.

[76] O. Debieu, J. Cardin, X. Portier, and F. Gourbilleau. Effect of the nd content on the structural and photoluminescence properties of silicon-rich silicon dioxide thin films. *Nanoscale research letters*, 6(1) :1–8, 2011.

[77] R.P. Nalini, J. Cardin, K.R. Dey, X. Portier, C. Dufour, and F. Gourbilleau. Optical and electrical properties of si-based multilayer structures for solar cell applications. *ECS transaction*, 2011.

[78] R.P. Nalini, C. Dufour, J. Cardin, and F. Gourbilleau. New si-based multilayers for solar cell applications. *Nanoscale research letters*, 6(1) :156, 2011.

[79] P. Nalini, R.Pand Marie, J. Cardin, C. Dufour, P. Dimitrakis, P. Normand, M. Carrada, and F. Gourbilleau. Enhancing the optical and electrical properties of si-based nanostructured materials. *Energy Procedia*, 10 :161–166, 2011.

[80] R.P. Nalini, L. Khomenkova, O. Debieu, J. Cardin, C. Dufour, M. Carrada, and F. Gourbilleau. Siox/siny multilayers for photovoltaic and photonic applications. *Nanoscale Research Letters*, 7(1) :124, 2012.

[81] O. Debieu, R.P. Nalini, J. Cardin, X. Portier, J. Perrière, and F. Gourbilleau. Structural and optical characterization of pure si-rich nitride thin films. *Nanoscale research letters*, 8(1) :1–13, 2013.

[82] C. Lecerf, P. Marie, J. Cardin, F. Jomard, and X. Portier. Texture effect of neodymium doped gallium oxide thin films on their optical properties. *Optical Materials*, 33(7) :1131–1134, 2011.

[83] A. Podhorodecki, M. Banski, J. Misiewicz, C. Lecerf, P. Marie, J. Cardin, and X. Portier. Influence of neodymium concentration on excitation and emission properties of nd doped gallium oxide nanocrystalline films. *Journal of Applied Physics*, 108 :063535, 2010.

[84] A. Ziani, C. Davesnne, C. Labbé, J. Cardin, P. Marie, C. Frilay, S. Boudin, and X. Portier. Annealing effects on the photoluminescence of terbium doped zinc oxide films. *Thin Solid Films*, 553 :52–57, 2014.

[85] M. Amela-Cortes, S. Cordier, N.G. Naumov, C. Mériadec, F. Artzner, and Y. Molard. Hexacyano octahedral metallic clusters as versatile building blocks in the design of extended polymeric framework and clustomesogens. *Journal of Materials Chemistry C*, 2(46) :9813–9823, 2014.

[86] Y. Molard, C. Labbé, J. Cardin, and S. Cordier. Sensitization of er3+ infrared photoluminescence embedded in a hybrid organic-inorganic copolymer containing octahedral molybdenum clusters. *Advanced Functional Materials*, 23(38) :4821–4825, 2013.

[87] Y. Molard, C. Labbé, J. Cardin, S. Cordier, and M. Amela-Cortes. A material comprising an host matrix, rare earth ions and a metal atom cluster as sensitiser, 2013.

[88] Y. Molard, C. Labbé, J. Cardin, and S. Cordier. Des nano-composites hybrides organiques/inorganiques pour le transport de l'information. Bulletin d'information du CNRS En direct des laboratoires, 2013.

[89] Y. Molard, C. Labbé, J. Cardin, and S. Cordier. Sources de lumière nano-composite organique/inorganique, pour le transport de l'information. Bulletin d'information du CEA Vie des labos, 2013.

[90] L. Khomenkova, X. Portier, J. Cardin, and F. Gourbilleau. Thermal stability of high-k si-rich hfo2 layers grown by rf magnetron sputtering. *Nanotechnology*, 21 :285707, 2010.

[91] M. Roblin, S. Girard, H. Gilles, M. Laroche, J. Cardin, C. Dufour, and U. Luders. Near-field optical imaging of plasmonic devices using heterodyne optical feedback on er doped dfb fiber laser. In *Laser Science*. Optical Society of America, 2011.

[92] M. Roblin, S. Girard, H. Gilles, M. Laroche, J. Cardin, and C. Dufour. Near-field optical imaging of plasmonic waveguides using heterodyne optical feedback on er doped dfb fibre laser. In *Lasers and Electro-Optics Europe (CLEO EUROPE/EQEC), 2011 Conference on and 12th European Quantum Electronics Conference*, pages 1–1. IEEE, 2011.

[93] M. Roblin. *Modélisation numérique et imagerie optique en champ proche par rétro-injection laser de guides d'onde plasmoniques*. PhD thesis, Université de Caen, 2013.

[94] A. Taflove, S.C. Hagness, et al. *Computational electrodynamics : the finite-difference time-domain method*. Artech House Norwood, MA, 1995.

[95] K. Yee. Numerical solution of initial boundary value problems involving maxwell's equations in isotropic media. *Antennas and Propagation, IEEE Transactions on*, 14(3) :302–307, 1966.

[96] M.S. Min and C.H. Teng. The instability of the yee scheme for the "magic time step". *Journal of Computational Physics*, 166(2) :418–424, 2001.

[97] A. Taflove and Morris E. Brodwin. Numerical solution of steady-state electromagnetic scattering problems using the time-dependent Maxwell's equations. *IEEE Transactions on Microwave Theory and Techniques*, 23(8) :623–630, 1975.

[98] D.M. Sullivan. *Electromagnetic simulation using the FDTD method*. John Wiley & Sons, 2013.

[99] A. Fafin. *Modélisation numérique de l'interaction onde-matière dans des matériaux nanostructurés à base de terres rares ou de nanoparticules métalliques pour la photonique ou la plasmonique*. PhD thesis, Université de Caen, 2014.

[100] R. Courant, K. Friedrichs, and H. Lewy. Über die partiellen differenzengleichungen der mathematischen physik. *Mathematische Annalen*, 100(1) :32–74, 1928.

[101] P.G. Petropoulos. Stability and phase error analysis of fd-td in dispersive dielectrics. *Antennas and Propagation, IEEE Transactions on*, 42(1) :62–69, 1994.

[102] B. Engquist and A. Majda. Absorbing boundary conditions for numerical simulation of waves. *Proceedings of the National Academy of Sciences*, 74(5) :1765–1766, 1977.

[103] G. Mur. Absorbing boundary conditions for the finite-difference approximation of the time-domain electromagnetic-field equations. *Electromagnetic Compatibility, IEEE Transactions on*, (4) :377–382, 1981.

[104] J.-P. Bérenger. Perfectly matched layer (pml) for computational electromagnetics. *Synthesis Lectures on Computational Electromagnetics*, 2(1) :1–117, 2007.

[105] J.-P. Bérenger. A perfectly matched layer for the absorption of electromagnetic waves. *Journal of computational physics*, 114(2) :185–200, 1994.

[106] J.B. Schneider, C.L. Wagner, and O.M. Ramahi. Implementation of transparent sources in fdtd simulations. *Antennas and Propagation, IEEE Transactions on*, 46(8) :1159–1168, 1998.

[107] A.B. Fallahkhair, K.S. Li, and T.E. Murphy. Vector finite difference modesolver for anisotropic dielectric waveguides. *Journal of Lightwave Technology*, 26(11) :1423–1431, 2008.

[108] P.R. Amestoy, I.S. Duff, J. Koster, and J.-Y. L'Excellent. A fully asynchronous multifrontal solver using distributed dynamic scheduling. *SIAM Journal on Matrix Analysis and Applications*, 23(1) :15–41, 2001.

[109] P.R. Amestoy, A. Guermouche, J.-Y. L'Excellent, and S. Pralet. Hybrid scheduling for the parallel solution of linear systems. *Parallel Computing*, 32(2) :136–156, 2006.

[110] M.C. Beard and C.A. Schmuttenmaer. Using the finite-difference time-domain pulse propagation method to simulate time-resolved thz experiments. *The Journal of Chemical Physics*, 114(7) :2903–2909, 2001.

[111] F.L. Teixeira, W.C. Chew, M. Straka, M.L. Oristaglio, and T. Wang. Finite-difference time-domain simulation of ground penetrating radar on dispersive, inhomogeneous, and conductive soils. *Geoscience and Remote Sensing, IEEE Transactions on*, 36(6) :1928–1937, 1998.

[112] S.K. Gray and T. Kupka. Propagation of light in metallic nanowire arrays : Finite-difference time-domain studies of silver cylinders. *Physical review B*, 68(4) :045415, 2003.

[113] M. Futamata, Y. Maruyama, and M. Ishikawa. Local electric field and scattering cross section of ag nanoparticles under surface plasmon resonance by finite difference time domain method. *The Journal of Physical Chemistry B*, 107(31) :7607–7617, 2003.

[114] A.D. Rakic, A.B. Djurišic, J.M. Elazar, and M.L. Majewski. Optical properties of metallic films for vertical-cavity optoelectronic devices. *Applied Optics*, 37(22) :5271–5283, 1998.

[115] A. Vial, A.-S. Grimault, D. Macías, D. Barchiesi, and M.L. de la Chapelle. Improved analytical fit of gold dispersion : Application to the modeling of extinction spectra with a finite-difference time-domain method. *Phys. Rev. B*, 71 :085416, Feb 2005.

[116] E.D. Palik and G. Ghosh. *Handbook of optical constants of solids : five-volume set*. Academic press, 1998.

[117] A.S. Nagra and R.A. York. Fdtd analysis of wave propagation in nonlinear absorbing and gain media. *Antennas and Propagation, IEEE Transactions on*, 46(3) :334 –340, mar 1998.

[118] A. Deinega and S. John. Effective optical response of silicon to sunlight in the finite-difference time-domain method. *Optics letters*, 37(1) :112–114, 2012.

[119] A. Vial and T. Laroche. Comparison of gold and silver dispersion laws suitable for fdtd simulations. *Applied Physics B : Lasers and Optics*, 93(1) :139–143, 2008.

[120] G. Rizza, E.A. Dawi, A.M. Vredenberg, and I. Monnet. Ion engineering of embedded nanostructures : From spherical to facetted nanoparticles. *Applied Physics Letters*, 95(4) :043105, 2009.

[121] G. Rizza, P.-E. Coulon, V. Khomenkov, C. Dufour, I. Monnet, M. Toulemonde, S. Perruchas, T. Gacoin, D. Mailly, X. Lafosse, C. Ulysse, and E.A. Dawi. Rational description of the ion-beam shaping mechanism. *Phys. Rev. B*, 86 :035450, Jul 2012.

[122] G. Rizza. Façonner la matière à l'échelle nanométrique par irradiation de faisceaux d'ions, 2011.

[123] G. Rizza, F. Attouchi, P.-E. Coulon, S. Perruchas, T. Gacoin, I. Monnet, and L. Largeau. Rayleigh-like instability in the ion-shaping of au–ag alloy nanoparticles embedded within a silica matrix. *Nanotechnology*, 22(17) :175305, 2011.

[124] J. Nelayah, M. Kociak, O. Stéphan, F.J.G. de Abajo, M. Tencé, L. Henrard, D. Taverna, I. Pastoriza-Santos, L.M. Liz-Marzán, and C. Colliex. Mapping surface plasmons on a single metallic nanoparticle. *Nature Physics*, 3(5) :348–353, 2007.

[125] V. Myroshnychenko, J. Rodríguez-Fernández, I. Pastoriza-Santos, A.M. Funston, C. Novo, P. Mulvaney, L.M. Liz-Marzán, and F.J.G. de Abajo. Modelling the optical response of gold nanoparticles. *Chem. Soc. Rev.*, 37(9) :1792–1805, 2008.

[126] U. Hohenester, H. Ditlbacher, and J.R. Krenn. Electron-energy-loss spectra of plasmonic nanoparticles. *Physical review letters*, 103(10) :106801, 2009.

[127] L. Douillard, F. Charra, Z. Korczak, R. Bachelot, S. Kostcheev, G. Lerondel, P.-M. Adam, and P. Royer. Short range plasmon resonators probed by photoemission electron microscopy. *Nano letters*, 8(3) :935–940, 2008.

[128] J. Dorfmüller, R. Vogelgesang, R.T. Weitz, C. Rockstuhl, C. Etrich, T. Pertsch, F. Lederer, and K. Kern. Fabry-pérot resonances in one-dimensional plasmonic nanostructures. *Nano letters*, 9(6) :2372–2377, 2009.

[129] T. Søndergaard and S. Bozhevolnyi. Slow-plasmon resonant nanostructures : scattering and field enhancements. *Physical Review B*, 75(7) :073402, 2007.

[130] T. Søndergaard, J. Beermann, A. Boltasseva, and S.I. Bozhevolnyi. Slow-plasmon resonant-nanostrip antennas : Analysis and demonstration. *Physical Review B*, 77(11) :115420, 2008.

[131] D. Rossouw, M. Couillard, J. Vickery, E. Kumacheva, and GA Botton. Multipolar plasmonic resonances in silver nanowire antennas imaged with a subnanometer electron probe. *Nano letters*, 2011.

[132] B.E. Sernelius. *Surface modes in physics*. Wiley-Vch, 2011.

[133] C.A. Pfeiffer, E.N. Economou, and K.L. Ngai. Surface polaritons in a circularly cylindrical interface : surface plasmons. *Physical review B*, 10(8) :3038, 1974.

[134] J. Cardin, A. Fafin, F. Gourbilleau, P.-E. Coulon, A. Slablab, G. Rizza, and C. Dufour. Electromagnetic modeling of plasmonic properties of gold nanoparticles embedded within a dielectric matrix deformed by swift heavy ions. In *META Conference, META12*, 2012.

[135] J. Cardin, C. Dufour, V. Khomenkov, A. Fafin, I. Monnet, G. Rizza, P.-E. Coulon, A. Slablab, D. Mailly, C. Ulysse, X. Lafosse, S. Perruchas, and T. Gacoin. Development of new kinds of plasmonics materials through swift heavy ion shaping technique. In *7th International Conference on Materials for Advanced Technologies (ICMAT 2013), Jun 2013, Suntec, Singapore*, Singapour, Singapore, June 2013. MRS Singapore.

[136] C. Dufour, J. Cardin, O. Debieu, A. Fafin, and F. Gourbilleau. Electromagnetic modeling of waveguide amplifier based on nd3+ si-rich sio2 layers by means of the ade-fdtd method. *Nanoscale research letters*, 6(1) :1–5, 2011.

[137] A. Fafin, J. Cardin, C. Dufour, and F. Gourbilleau. Modeling of the electromagnetic field and level populations in a waveguide amplifier : a multi-scale time problem. *Optics Express*, 21(20) :24171–24184, 2013.

[138] A. Fafin, J. Cardin, C. Dufour, and F. Gourbilleau. Theoretical investigation of the more suitable rare earth to achieve high gain in waveguide based on silica containing silicon nanograins doped with either nd 3+ or er 3+ ions. *Optics Express*, 22(10) :12296–12306, 2014.

[139] J. Cardin, A. Fafin, C. Dufour, and F. Gourbilleau. Modeling of optical amplifier waveguide based on silicon nanostructures and rare earth ions doped silica matrix gain media by a finite-difference time-domain method : comparison of achievable gain with er3+ or nd3+ ions dopants. In *SPIE OPTO*, pages 935709–935709. International Society for Optics and Photonics, 2015.

[140] D. Navarro-Urrios, F.F. Lupi, N. Prtljaga, A. Pitanti, O. Jambois, J.M. Ramírez, Y. Berencén, N. Daldosso, B. Garrido, and L. Pavesi. Copropagating pump and probe experiments on Si-nc in SiO_2 rib waveguides doped with Er : The optical role of non-emitting ions. *Applied Physics Letters*, 99(23) :231114, 2011.

[141] Parastesh P., J. Charrier, Y. Dumeige, Y.G. Boucher, O. Debieu, and F. Gourbilleau. Study of optical losses of Nd^{3+} doped silicon rich silicon oxide for laser cavity. *Thin Solid Films*, 520(11) :4026 – 4030, 2012.

[142] K.J. Willis, S.C. Hagness, and I. Knezevic. Multiphysics simulation of high-frequency carrier dynamics in conductive materials. *Journal of Applied Physics*, 110(6) :063714–063714, 2011.

[143] J.P. Weber and S. Wang. A new method for the calculation of the emission spectrum of dfb and dbr lasers. *Quantum Electronics, IEEE Journal of*, 27(10) :2256–2266, 1991.

[144] Y.G. Boucher. Theoretical investigation of amplified spontaneous emission in an active structure by extended (3x3) transfer matrix formalism : the case of a non-uniform longitudinal distribution of emitters. *Journal of the European Optical Society-Rapid publications, vol. 1 06027*, 1 :6027, 2006.

[145] H. Benisty, R. Stanley, and M. Mayer. Method of source terms for dipole emission modification in modes of arbitrary planar structures. *JOSA A*, 15(5) :1192–1201, 1998.

[146] William Shockley and Hans J Queisser. Detailed balance limit of efficiency of p-n junction solar cells. *Journal of applied physics*, 32(3) :510–519, 1961.

[147] J. Bauer. Optical properties, band gap, and surface roughness of si3n4. *physica status solidi (a)*, 39(2) :411–418, 1977.

[148] Y.-T. An, C. Labbé, J. Cardin, M. Morales, and F. Gourbilleau. Highly efficient infrared quantum cutting in tb3+- yb3+ codoped silicon oxynitride for solar cell applications. *Advanced Optical Materials*, 2013.

[149] D.L. Dexter. Possibility of luminescent quantum yields greater than unity. *Physical Review*, 108(3) :630, 1957.

[150] Q. Duan, F. Qin, D. Wang, W. Xu, J. Cheng, Z. Zhang, and W. Cao. Quantum cutting mechanism in tb3+-yb3+ co-doped oxyfluoride glass. *Journal of Applied Physics*, 110(11) :113503, 2011.

[151] Q.Y. Zhang, C.H. Yang, Z.H. Jiang, and X.H. Ji. Concentration-dependent near-infrared quantum cutting in gdbo3 : Tb3+, yb3+ nanophosphors. *Applied physics letters*, 90(6) :1914, 2007.

[152] J.J. Eilers, D. Biner, J.T. Van Wijngaarden, K. Krämer, H.-U. Güdel, and A. Meijerink. Efficient visible to infrared quantum cutting through downconversion with the er3+–yb3+ couple in cs3y2br9. *Applied physics letters*, 96(15) :151106, 2010.

[153] S. Yerci, R. Li, S.O. Kucheyev, T. Van Buuren, S.N. Basu, and L. Dal Negro. Energy transfer and 1.54 m emission in amorphous silicon nitride films. *Applied Physics Letters*, 95 :031107, 2009.

[154] R. Paschotta, J. Nilsson, P.R. Barber, J.E. Caplen, A.C. Tropper, and D.C. Hanna. Lifetime quenching in yb doped fibres. *Optics Communications*, 136(5-6) :375–378, 1997.

[155] P. Vergeer, T.J.H. Vlugt, M.H.F. Kox, M.I. Den Hertog, J.P.J.M. Van der Eerden, and A. Meijerink. Quantum cutting by cooperative energy transfer in $yb_xy_{1-x}po_4$:tb^{3+}. *Physical Review B*, 71(1) :014119, 2005.

[156] Q.J. Chen, W.J. Zhang, X.Y. Huang, G.P. Dong, M.Y. Peng, and Q.Y. Zhang. Efficient down-and up-conversion of pr^{3+}-yb^{3+} co-doped transparent oxyfluoride glass ceramics. *Journal of Alloys and Compounds*, 513 :139–144, 2012.

[157] L. Dumont, J. Cardin, P. Benzo, M. Carrada, C. Labbé, A.L. Richard, D.C. Ingram, W.M. Jadwisienczak, and F. Gourbilleau. Sinx :tb^{3+}-yb^{3+}, an efficient down-conversion layer compatible with silicon solar cell process. *Solar energy materials and solar cells*, 145(2) :84–92, 2016.

[158] M. Zaarour, M. El-Roz, B. Dong, R. Retoux, R. Aad, J. Cardin, C. Dufour, F. Gourbilleau, J.-P. Gilson, and S. Mintova. Photochemical preparation of silver nanoparticles supported on zeolite crystals. *Langmuir*, 30(21) :6250–6256, 2014.

[159] R.P. Nalini. *Si nanostructures thin films for 3rd generation of solar cells*. PhD thesis, Université de Caen, 2012.

Sélections de Publications

▷Widely Tunable Directional Coupler Filters with 1D Photonic Crystal. page 101
▷Optical properties of PZT thin films deposited on a ZnO buffer layer. page 105
▷A method to retrieve optical and geometrical characteristics of three layer waveguides from m-lines measurements. page 112
▷Determination of refractive index, thickness, and the optical losses of thin films from prism-film coupling measurements. page 119
▷Towards an optimum coupling between Er ions and Si-based sensitizers for integrated active photonics. page 126
▷Optically active Er^{3+} ions in SiO_2 codoped with Si nanoclusters. page 134
▷Efficient energy transfer from Si-nanoclusters to Er ions in silica induced by substrate heating during deposition. page 139
▷Thermal stability of high-k Si-rich HfO_2 layers grown by RF magnetron sputtering. page 145
▷Influence of neodymium concentration on excitation and emission properties of Nd doped gallium oxide nanocrystalline films. page 157
▷High Energy Excitation Transfer from Silicon Nanocrystals to Neodymium Ions in Silicon-Rich Oxide Film. page 163
▷Effect of the Nd content on the structural and photoluminescence properties of silicon-rich silicon dioxide thin films. page 166
▷Electromagnetic modeling of waveguide amplifier based on Nd^{3+} Si-rich SiO_2 layers by means of the ADE-FDTD method. page 174
▷SiO_x/SiN_y multilayers for photovoltaic and photonic applications. page 179
▷Effect of the Si excess on the structure and the optical properties of Nd-doped Si-rich silicon oxide. page 185
▷Evidence of two sensitization processes of Nd^{3+} ions in Nd-doped SiO_x films. page 189
▷Correlation between matrix structural order and compressive stress exerted on silicon nanocrystals embedded in silicon-rich silicon oxide. page 197
▷Modeling of the electromagnetic field and level populations in a waveguide amplifier : a multi-scale time problem. page 204
▷Sensitization of Er^{3+} Infrared Photoluminescence Embedded in a Hybrid Organic-Inorganic Copolymer containing Octahedral Molybdenum Clusters. page 218
▷Highly Efficient Infrared Quantum Cutting in Tb^{3+} ?Yb^{3+} Codoped Silicon Oxynitride for Solar Cell Applications. page 223
▷Theoretical investigation of the more suitable rare earth to achieve high gain in waveguide based on silica containing silicon nanograins doped with either Nd^{3+} or Er^{3+} ions. page 231
▷Photochemical Preparation of Silver Nanoparticles Supported on Zeolite Crystals. page 242
▷Modeling of optical amplifier waveguide based on silicon nanostructures and rare earth ions doped silica matrix gain media by a finite-difference time-domain method : comparison of achievable gain with Er^{3+} or Nd^{3+} ions dopants. page 249

Widely Tunable Directional Coupler Filters with 1D Photonic Crystal

Bozena Jaskorzynska (1)*, Zygmunt Jacek Zawistowski (2), Matteo Dainese (1)
Julien Cardin (1), Lars Thylén(1)
(1) Royal Institute of Technology (KTH), Department of Microelectronics and Information Technology, Kista Photonics Research Center (KPRC), Electrum 229, SE - 164 40 Kista, Sweden*
Tel: +46 8 790 40 62, Fax: +46 8 790 40 90, e-mail: bj@imit.kth.se
(2) Institute of Fundamental Technological Research, Polish Academy of Sciences, Department of Theory of Continuous Media, Swietokrzyska 21, 00-049 Warszawa, Poland, e-mail: zzawist@ippt.gov.pl

ABSTRACT
We present two concept examples for adding a wide range tunability to Si/SiO_2 devices involving a photonic crystal element. They are based on a directional coupler filter of two different geometries, where one of the arms is a Bragg Reflection Waveguide (BRW) used for the bandwidth improvement. The tuning relies on changing the properties of the BRW core. As an illustration we consider the smectic A* liquid crystal as the core material and show that ca 100 nm tuning range is achievable by the core index variations of 0.006 under applying electric field of 5 V/μm.
Keywords: optical filters, directional couplers, Bragg reflection waveguides, photonic crystal, liquid crystals, electrical tuning.

1. INTRODUCTION

Devices employing photonic crystals (PhC's) provide unique dispersion properties that can be utilized for realizing delay lines, dispersion compensators, enhanced efficiency wavelength converters and amplifiers, or narrow bandwidth filters and lasers. Most of the reported so far PhC based components, however, are not tunable, especially those made in silicon. Adding a tuning mechanism is desired for dynamically reconfigurable WDM networks, where the wavelength allocation is changed as the needs of the network change. It is of particular interest to add a wide range dynamic tuning to PhC devices in the low-cost, but passive Si/SiO_2 technology compatible with optoelectronics and the transmission fibres. This can e. g. be achieved by including micro-electro-mechanical systems (MEMS) elements, or by incorporating electro-optic materials, such as polymers or liquid crystals (LC's). Here, as an example of a device providing a wide continuous tuning and benefiting from the dispersion properties of a PhC element for the bandwidth narrowing, we consider an extension of our earlier proposed and demonstrated [1, 2] directional coupler filter where one arm is a Bragg Reflection Waveguide (BRW), i.e. a 1D PhC waveguide. The extended concept relies in essence, on making the BRW core tunable. In the presented example we simulated tunability of the core refractive index, for which we choose the smectic A* LC's, having the response time in the sub-microsecond regime [3], i.e. three orders of magnitude shorter than that of nematic LC's or of the thermo-optic phase shifters. However, the concept and the conclusions are also applicable to the case when the core width is tuned, with e. g. MEMS.

We consider and compare two geometries. One being a direct extension of [2] and presented in [4], where the silicon core is replaced by LC, and a new design where one of the BRW claddings is removed and the LC forms an overlay of the coupler. The latter is much easier for practical implementation and still, as we show, preserves similar performance when properly designed.

2. FILTER GEOMETRIES AND PRINCIPAL OF OPERATION

The filters we consider are both directional couplers with dissimilar arms [5]. Their cross sections are depicted in Fig. 1. One of the arms is a conventional (index guided) channel waveguide with a $GeSiO_2$ ($n_2 = 1.465$) core buried in a silica glass ($n_1 = 1.4558$). It is single mode in a wide wavelength range around 1.55 μm. The other arm is a LC core with two (Fig. 1a), or one (Fig. 1b) Bragg Reflector claddings consisting of alternating layers of amorphous silicon ($n_2 = 3.55$) and silica. The layer thicknesses, different for each of the cases, are given in Fig. 1. Only transverse electric (TE) waves are considered for which the extraordinary refractive index of the LC core (smectic A* BDH764E with a 45 deg pretilt in the plane parallel to the Bragg layers – see [4]), is tuned from its off-state value $n = 1.5657$ by -/+0.006, which is only a half of the refractive index change possible for this liquid crystal. This corresponds to -/+ 5 V/μm variations of the electric field applied between ITO electrodes placed at both sides of the LC core. The LC core can be regarded as a defect in 1D PhC formed by the Bragg layers. The whole, vertically etched structure is buried in a silica glass cladding, however in the case (1b) there is no glass on the top.

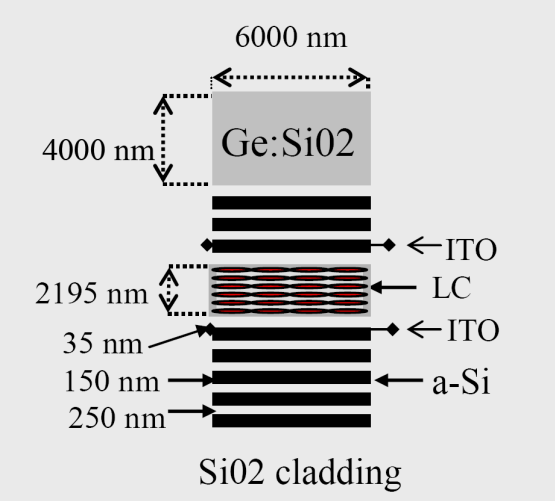

Figure 1a. Cross-section of the directional coupler filter with the"full BRW" arm.

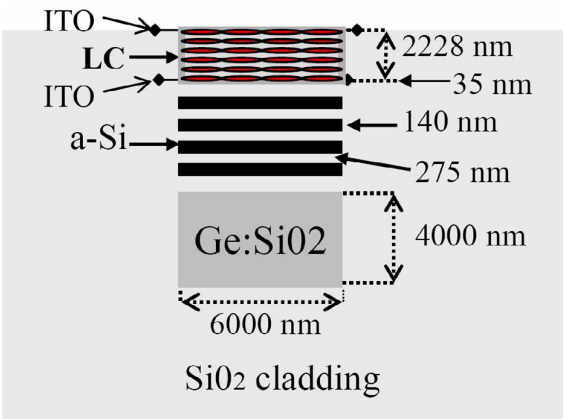

Figure 1b. Cross-section of the filter with the "LC overlay BRW" arm.

The filters are designed so that when no electric field is applied (the off-state), the signal around the central wavelength of 1550 nm launched into the conventional arm, is cross-coupled to the PhC arm over the coupling length L, defined as the beating length for the two lowest supermodes of the coupler:

$$L = \pi/(\beta_2 - \beta_1), \tag{1}$$

where β_1 and β_2 are the propagation constants of the supermodes. Light at all other wavelengths stays in the conventional arm. The central wavelength of the filter is determined by the phase synchronism (transverse resonance) condition [5, 6]. The filter bandwidth $\Delta\lambda_{-3dB}$ is inverse proportional to the coupler length L, and to the differential dispersion σ of the two waveguides in isolation [5]:

$$\Delta\lambda_{-3dB} \approx \frac{0.796\lambda}{L\sigma} \text{ where } \sigma = \frac{d\overline{N}}{d\lambda} - \frac{dN}{d\lambda} \text{ and } \overline{N}, N \text{ effective indices of the respective waveguides.} \tag{2}$$

Since the conventional $GeSiO_2/SiO_2$ arm is a low contrast waveguide of weak dispersion, to narrow the bandwidth a given coupler length the dispersion of the other arm should be maximized. Conventional waveguides possible with low index electro-optic materials, such as polymers or liquid crystals, are also low contrast and weakly dispersive. Whereas, in PhC waveguides (including BRW's) where light confinement at frequencies within the photonic band gap is possible for an arbitrarily low index core [7], high dispersion can be achieved by the PhC cladding design. By applying the BRW waveguide as one of the coupler arm we obtained a fourfold bandwidth-length product improvement without an extensive effort on the optimization. The main issue for the further analysis is determination of the tuning range.

3. PERFORMANCE ANALYSIS AND RESULTS

For approximate analysis of the tuning properties we used 1D formalism of Ref. 8, based on the scattering matrix method for stratified media, combined with the effective index method to account for the lateral confinement. In order to determine the tuning range we have analyzed the performance of the filter with respect to the following criteria:

- The cross-coupling to the same mode should occur over the whole tuning range.
- The difference between the propagation constants of the supermodes, determining the coupling length (1), should not vary too much with wavelength since it results in extinction-ratio variation.
- Relative dispersion slopes for the two supermodes should not exhibit strong variation either, so that the filter bandwidth variation is kept within acceptable limits.

For directional couplers there is a well known [6] trade off between the bandwidth $\Delta\lambda_{-3dB}$ and the intrinsic tuning rate $d\lambda/dn$:

$$\frac{d\lambda}{dn} = \frac{1}{A\sigma} = \frac{1}{\sigma}\frac{dN}{dn}, \tag{3}$$

since both scale inverse proportional with the differential dispersion. There is some room though for their simultaneous optimization by minimizing A, the factor not shown in [6]:

$$A(\lambda, n, N) = \frac{N}{n} + \frac{\lambda\sqrt{n^2 - N^2}}{2\pi dn}\frac{\partial\phi}{\partial N}. \quad (4)$$

Where d is the BRW core width, and ϕ is the phase shift under reflection from the Bragg cladding, which can be influenced by the choice of the layer thickness and when applicable, also the layer material. Since N lies in the range of the total internal reflection at the glass/Si interfaces the phase shift strongly depends on N, especially when it is chosen so that the incidence angles are close to the critical one. The simultaneous optimization can also be achieved by increasing the coupler length.

Having the above guidelines in mind we have made a preliminary optimization, where we compromised the bandwidth-length product in favor of the tuning range and its quality. In Fig. 2 we show an example of the tuning rate dependence on the Si layer thickness, for the coupler with a LC overlay (Fig. 1b). The curves are shown for several values of the silica layer thickness. The circle shows the chosen pair of the thicknesses for the Bragg cladding, which allowed increase of the tuning rate at the least degradation of the bandwidth, and of the filter performance over the total tuning range.

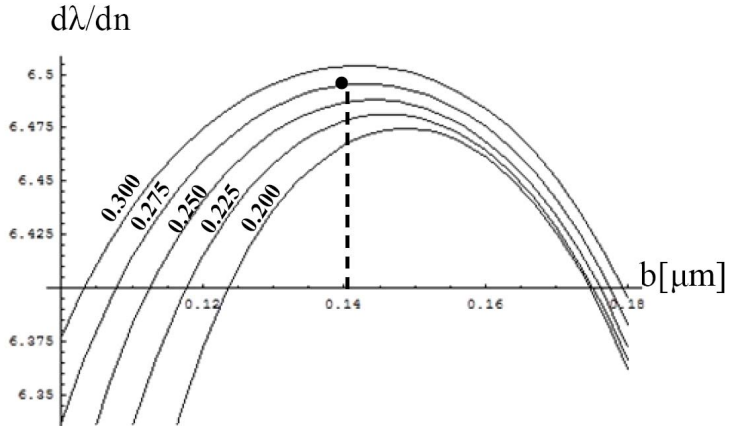

Figure 2. Dependence of the tuning rate on a Si layer thickness b, for different thicknesses of the silica layer. The circle indicates the choice made for the „overlay" case of Fig. 1b.

The latter is illustrated in Fig. 3, where the dispersion curves of the coupler are shown at the off-state and the extremes of the tuning range for both of the considered filters. For coupler 1a, the variations of the coupling length (1) over the range 1510 nm – 1589 nm, do not exceed 19%, hence the resulting variations of the amplitude are below 3%. The bandwidth (2) variations from its off-set value of 1.2 nm (at 7.4 mm length) are below 6% over the whole tuning range. For the filter with a LC overlay (Fig. 1b) a slightly better performance was obtained, probably because we have put more effort on its optimization.

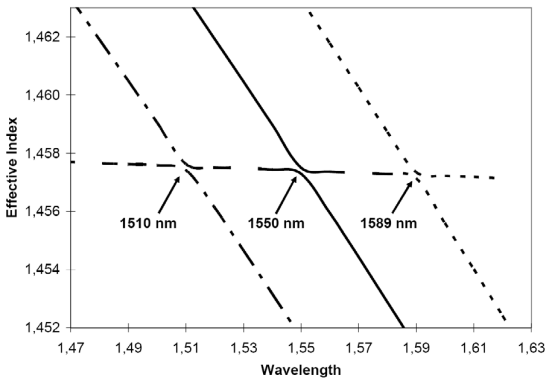

Figure 3a. Supermode dispersion at the off-state (1550 nm) and the extremes of the tuning range for ±Δn0.006 (±ΔE5 μ/Vm) for filter (1a).

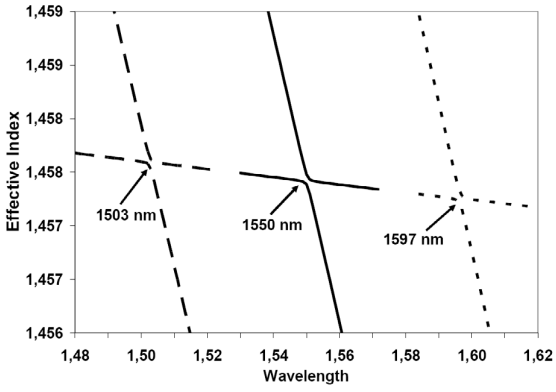

Figure 3b. Supermode dispersion at the off-state (1550 nm) and the extremes of the tuning range for ±Δn0.006 (±ΔE5 μ/Vm) for filter (1b).

The variations of the coupling length from its off-state value of 8.95 mm, and the resulting amplitude variations are in that case below 11% and 1.5%, respectively. Larger tuning range: 1503 nm – 1597 nm was obtained for the same value -/+ 5 V/μm of the applied field. Although the slope of the dispersion varies a bit more, the resulting bandwidth variations from its off-state value of 1.05 nm are still kept below 11%. Both of the filters are

designed for coupling between the fundamental (0-order) mode in the conventional arm and the first-order mode in the BRW arm. We have checked that the cross-coupling to the higher modes does not occur in a much wider wavelength range than the tuning ranges we show here.

4. SUMMARY

We analysed two design ideas for widely tunable filters based on directional couplers in which one arm is a conventional waveguide and the other is a BRW with a core formed by a commercially available smectic A* liquid crystal. We have checked that by applying BRW instead of a conventional waveguide with a LC core and silica cladding, a fourfold bandwidth narrowing is readily achievable for the same coupler lengths. We showed that tuning ranges of ca 90 nm around the 1.55 μm wavelength under applying the electric field of less than 5 V/μm, are feasible for both of the considered filters. Both of them show similar performance. Although for the filter with an overlay the bandwidth-length product is slightly worse, 1.05 nm x 8.95 mm to compare with 1.2 nm x 7.4 mm obtained for the full BRW case, it has better stability to the tuning variations, larger tunabilty range, and is easier to fabricate. We sketched the optimization guidelines and made a preliminary optimization in which the compromise was made between the bandwidth-length product and the tuning rate, with a focus on obtaining a wide tunability range. The presented designs and guidelines are readily applicable for other tuning mechanisms, e.g. where the BRW core width is tuned with MEMS.

ACKNOWLEDGEMENTS

This work is included in COST P11 action and the European Network of Excellence PHOREMOST. The support from the Swedish Research Council (VR), the Swedish Foundation for Strategic Research (SSF), and the (Polish) State Committee for Scientific Research (KBN), is gratefully acknowledged.

REFERENCES

[1] M. Dainese, M. Swillo, L. Thylen, M. Qiu, L. Wosinski, B. Jaskorzynska, and V. Shushunova, „Narrow band coupler based on one-dimensional Bragg reflection waveguide", *in Proc. OFC 2003*, Atlanta, USA, March 2003, paper MF39.

[2] Valeriya Shushunova, Marcin Swillo, Bozena Jaskorzynska, Min Qiu and Lars Thylén, „Separation of Optical Modes in a Coupler on the Basis of the Bragg One-Dimensional Grating", *J. Appl. Spectroscopy* vol. **70,** pp. 298-302 (2003).

[3] Anat Sneh, Hristina m. Johnson, Jian-Yu Liu, „High_Speed Wavelength Tunable Liquid Crystal Filter", *IEEE Photonics Technol. Lett*. **7**, pp. 379-381 (1995).

[4] Zygmunt Jacek Zawistowski, Bozena Jaskorzynska, „Electrically tunable filter based on directional coupler with 1D photonic crystal arm infiltrated with smectic liquid crystal", Proc. of *6th Int. Conf. on Transparent Optical Networks and European Symposium on Photonic Crystals, (ICTON/ESPC)*, Wroclaw, July 2004, vol. 2, pp. 127-130.

[5] D. Marcuse, „Bandwith of forward and backward coupling directional couplers", *J. Lightwave Techn*., **5**, pp. 1773-1777 (1987).

[6] R.C. Alferness and R.V. Schmidt „Tunable optical waveguide directional coupler filter", *Appl. Phys. Lett*. **33**, pp. 161 – 163 (1978).

[7] P.Yeh, A.Yariv, C.S. Hong, „Electromagnetic propagation in periodic stratified media", *J. Opt. Soc. Am*., **67**, pp 423-448 (1977).

[8] T.D. Visser, H. Blok, D. Lenstra, „Modal analysis of a planar waveguide with Gain and Losses", *J. Quantum Electronics*, **31**, pp.1803-1810 (1995).

Available online at www.sciencedirect.com
ScienceDirect
Optical Materials 29 (2007) 1871–1877
OPTICAL Materials
www.elsevier.com/locate/optmat

Optical properties of PZT thin films deposited on a ZnO buffer layer

T. Schneider [a], D. Leduc [a,*], J. Cardin [a], C. Lupi [a], N. Barreau [b], H. Gundel [a]

[a] Université de Nantes, Nantes Atlantique Universités, IREENA, EA1770, Faculté des Sciences et des Techniques, 2 rue de la Houssinière – BP 9208, Nantes F-44000, France
[b] Université de Nantes, Nantes Atlantique Universités, IREENA, EA1770, Faculté des Sciences et des Techniques, 2 rue de la Houssinière – BP 9208, Nantes F-44000, France

Received 13 June 2006; received in revised form 12 October 2006; accepted 12 October 2006
Available online 5 December 2006

Abstract

The optical properties of lead zirconate titanate (PZT) thin films deposited on ZnO were studied by *m*-lines spectroscopy. In order to retrieve the refractive index and the thickness of both layers from the *m*-lines spectra, we develop a numerical algorithm for the case of a two-layer system and show its robustness in the presence of noise. The sensitivity of the algorithm of the two-layer model allows us to relate the observed changes in the PZT refractive index to the PZT structural change due to the ZnO interface of the PZT/ZnO optical waveguide.

Keywords: *m*-Lines; Composite waveguides; PZT

1. Introduction

PZT ferroelectric thin films exhibit interesting optical properties, such as large electro-optic effects (Pockels, Kerr), a high refractive index, and a high transparency at visible and infra red wavelength. These properties are promising for the realization of different applications in the field of integrated optics as sensors or components for optical communications (optical shutter, waveguide, filter). In order to obtain active devices profiting from the electro-optic properties, electrodes have to be integrated. Most commonly they are made of transparent conductive materials like doped ZnO or indium tin oxide (ITO) when the absorption of light is a critical factor. The present paper studies a bilayer made of PZT and a transparent ZnO bottom electrode. It is generally known, that the crystallization behavior of ferroelectric thin films strongly depends on the structural properties of the substrate and hence may be influenced by the existence of an interface layer. This has been shown particularly for the case of PZT thin films elaborated on metal substrates using different conducting oxide interface layers [1]. In the case of the PZT/ZnO waveguide, we are interested in the relation between the PZT structural change and the optical properties of the films. For this purpose we developed a characterization method for a two layer planar waveguide based on prism coupler spectroscopy (or *m*-lines).

m-Lines spectroscopy [2–4] is widely used in order to determine the refractive index and the thickness of single layer homogeneous films. The refractive index profile of inhomogeneous waveguide can also be reconstructed with *m*-lines spectroscopy by using methods based on WKB approximation [5,6]. These methods are well suited in the case of guides where the index profile can be described by an a priori known continuous function. The case of multilayer guides where the index profile contains abrupt discontinuities, however, is less investigated. Dispersion equations of guided modes for the two layer guides were initially introduced by Tien et al. [7] and several experiments were performed [8–11]. The reconstruction of the film parameters in these measurements were made with the help of an optimization method, the simplex algorithm

* Corresponding author. Tel.: +33 2 51 12 55 33.
E-mail address: dominique.leduc@univ-nantes.fr (D. Leduc).

0925-3467/$ - see front matter © 2006 Elsevier B.V. All rights reserved.
doi:10.1016/j.optmat.2006.10.015

in general, that minimizes the differences between the measured effective indices and the calculated ones from the dispersion equations. In our approach, we choose to directly solve the system of dispersion equations. This requires to determine the roots of a system of nonlinear equations with five unknowns (the refractive index and the thickness of the two layers and the order of the first mode in the spectrum). The first section of the present paper is devoted to the study of the efficiency of this method. We will especially examine the influence of the noise in order to estimate the accuracy of the results. Then in the second section, we will apply the method in order to firstly characterize the ZnO layer and secondly the two-layer waveguides.

2. Characterization of two layers films using *m*-lines spectroscopy

2.1. Two layer dispersion equations

The analysis of *m*-lines spectra requires to know the dispersion equation for the studied guide. Because of its compactness, the transfert matrix method [12] is well suited for analysing multilayer waveguides. The geometry of the guide is shown in the Fig. 1. The layer j has a refractive index n_j and a thickness d_j. The layer 0 corresponds to the substrate and the layer 3 to the superstratum. In our case, $n_0 = 1.5169$ and $n_3 = 1$ at 632.8 nm wavelength. For TE modes, the electrical field in the layer j has only one component along the (Oy) axe: $E_{jy}(x,z) = A_j e^{i\gamma x} e^{i\beta_m z} + B_j e^{-i\gamma x} e^{i\beta_m z}$ and the tangential component of the magnetic field is $H_{jz} = i(\omega\mu_0)^{-1} dE_{jy}/dx$. In these expressions, ω is the angular frequency and β_m is the propagation constant of the mth guided mode. It is usually written as $\beta_m = kN_m$, where k is the wavevector modulus in vacuum and N_m the effective index. The x component of the wavevector, γ_j, gives the nature of the waves in the layer j: $\gamma_j = k(\omega\mu_0)^{-1}|n_j^2 - N^2|^{1/2}$ for travelling waves and $\gamma_j = ik(\omega\mu_0)^{-1}|n_j^2 - N^2|^{1/2}$ for evanescent waves. In the following, we will call $a_j = k|n_j^2 - N^2|^{1/2}$.

A transfert matrix M_j is associated to each layer

$$M_j = \begin{pmatrix} \cos(\omega\mu_0\gamma_j d_j) & \frac{i}{\gamma_j}\sin(\omega\mu_0\gamma_j d_j) \\ i\gamma_j \sin(\omega\mu_0\gamma_j d_j) & \cos(\omega\mu_0\gamma_j d_j) \end{pmatrix} \quad (1)$$

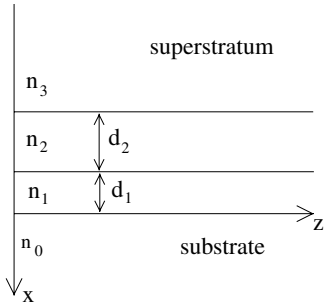

Fig. 1. Two layer waveguide.

The tangential component of the electric and the magnetic fields E_y and H_z must be continuous at the interface to satisfy boundary conditions. These conditions and the condition for obtaining guiding lead to the equation

$$\begin{pmatrix} 1 \\ -\gamma_3 \end{pmatrix} E_{3y} = M_2 M_1 \begin{pmatrix} 1 \\ \gamma_0 \end{pmatrix} E_{0y} = M \begin{pmatrix} 1 \\ \gamma_0 \end{pmatrix} E_{0y} \quad (2)$$

which has solutions only for

$$\gamma_3 m_{11} + \gamma_3\gamma_0 m_{12} + m_{21} + \gamma_0 m_{22} = 0 \quad (3)$$

where m_{ij} are the components of the matrix M.

The refractive index of PZT is known to be higher than that of ZnO ($n_2 > n_1$). Two kinds of guided waves are possible in this case:

- guided waves in layer 2, evanescent waves in the other layers

$$a_2 d_2 - \arctan\left(\frac{a_3}{a_2}\right) - \arctan\left[\frac{a_1^2 \tanh(a_1 d_1) + a_0 a_1}{a_1 a_2 + a_0 a_2 \tanh(a_1 d_1)}\right] - m\pi = 0 \quad (4)$$

- guided waves in layer 1 and layer 2, evanescent waves in the substrate and in the superstratum

$$a_2 d_2 - \arctan\left(\frac{a_3}{a_2}\right) + \arctan\left\{\frac{a_1}{a_2}\tan\left[a_1 d_1 - \arctan\left(\frac{a_0}{a_1}\right)\right]\right\} - m\pi = 0 \quad (5)$$

Eqs. (4) and (5) are the dispersion equations for the two layer waveguide.

2.2. Data analysis

The characterization of a two layer waveguide requires to determine five unknowns: the refractive indices and thicknesses of both layers and the order (m_1) of the first mode appearing in the *m*-lines spectrum. Very often, the latter parameter is neglected and the first mode in the spectrum is assumed to be the fundamental mode. The low order modes, however, are more difficult to excite since they require an high incidence angle and often spectra without the fundamental mode are observed. Therefore it seems indicated not to make any assumption on the order of the first mode and to consider it as an unknown. In order to determine all the unknowns, at least 5 modes in the *m*-lines spectrum have to be identified. In general, i.e. when the thicknesses of the layer 1 and layer 2 and the differences between the refractive indices of the different layers are large enough, a spectrum contains $M > 5$ modes.

One difficulty consists in associating the correct equation to each mode. As shown by Eqs. (4) and (5), the effective index of a mode depends on the type of guiding, either in one or in two layers. Hence a rupture in the spectrum corresponding to the transition between these two types

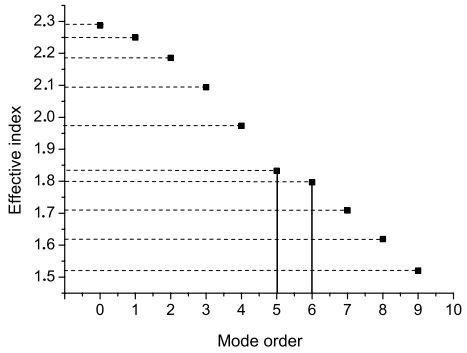

Fig. 2. Effective indices of the guided modes of a two layer film defined by $n_1 = 1.9$, $d_1 = 1$ μm, $n_2 = 2.2$ and $d_2 = 1.4$ μm.

has to be determined. In the following we will call m_2 the order of the first guided mode in two layers. Given that the dispersion equations are transcendental, it is not possible to derive a general analytical expression for m_2. Numerical simulations with noisy data, however, showed that m_2 is the value of m such that $|N_m - N_{m-1}| > |N_{m+1} - N_m|$ (see Fig. 2). This criterion results in a correct value of m_2 in the case of two thirds of the simulated waveguides. For almost all the other cases, the mismatch is equal to +1. Only one hundred of simulations from more than two millions lead to different results. Then, in our data analysis protocol, we first assume that m_2 obeys the criterion stated above and try then to solve the dispersion equations. If the program does not converge, we subtract one from the value of m_2 given by the criterion and again try to solve the equations. If this second step also fails, we may vary m_2 from 0 to M. It is observed that the program only converges in the case of the real value of m_2.

In order to retrieve the thin films characteristics, we consider the four unknowns n_1, d_1, n_2 and d_2 and we varies m_1. The C_M^4 systems of four dispersion equations are solved with a Newton–Raphson algorithm. For each value of m_1, we obtain $C \leqslant C_M^4$ sets of solutions. The synchronous angles (ϕ_{calc}) corresponding to each solutions are calculated with a bisection algorithm and we compute the mean difference between these angles and the measured synchronous angles (ϕ_{meas})

$$\sigma(m_1) = \sqrt{\frac{\sum_{i=1}^{C}\sum_{j=0}^{M-1}(\phi_{ij}^{\text{calc}} - \phi_j^{\text{meas}})^2}{MC^2}} \tag{6}$$

The minimum of $\sigma(m_1)$ gives the correct indexation. Finally, the solutions are the mean values of the solutions corresponding to the right indexation.

2.3. Numerical tests

In order to estimate the accuracy of the numerical procedure described in the previous section, 10,000 guides were simulated, n_1 varying from 1.8 to 1.98 and n_2 from 2.12 to 2.30 by steps of 0.02, d_1 varying from 0.6 μm to 1.05 μm and d_2 from 0.8 μm to 1.25 μm by steps of 50 nm. These ranges correspond to the values of the layers which we process. For each waveguide $\{n_1, d_1, n_2, d_2\}$, the set of synchronous angles $\{\phi_{\text{th}}^j\}$ is calculated and a noise randomly chosen in the range $[-\delta\varphi; \delta\varphi]$ is added in order to obtain a set of noisy synchronous angles $\{\phi_{\text{noisy}}^j\}$. This set is used as input data of the numerical procedure. In order to get a statistical estimate of the accuracy, 100 sets of noisy angles were studied for each guide. The influence of noise was evaluated by varying $\delta\varphi$ between 0.01° and 0.2°.

The distributions of errors on the different parameters for one waveguide follow a normal law. So, for each waveguide we consider that the error on one parameter is the mean value of the errors over the 100 noisy sets. Highest errors arise for guides with the smallest index differences between the two layers and the smallest thicknesses. The effect of noise is shown in Fig. 3. The errors on the refractive indices are plotted in Fig. 3a and the errors on the thicknesses in Fig. 3b. The lengths of the error bars is twice the standard deviation. The error on n_2 is smaller than the error on n_1 and does not exceed 1×10^{-3} in the considered noise range, whereas the error on n_1 is of the order of a few 10^{-3}. The thicknesses are expected to be determined with a precision of the order of 10 nm.

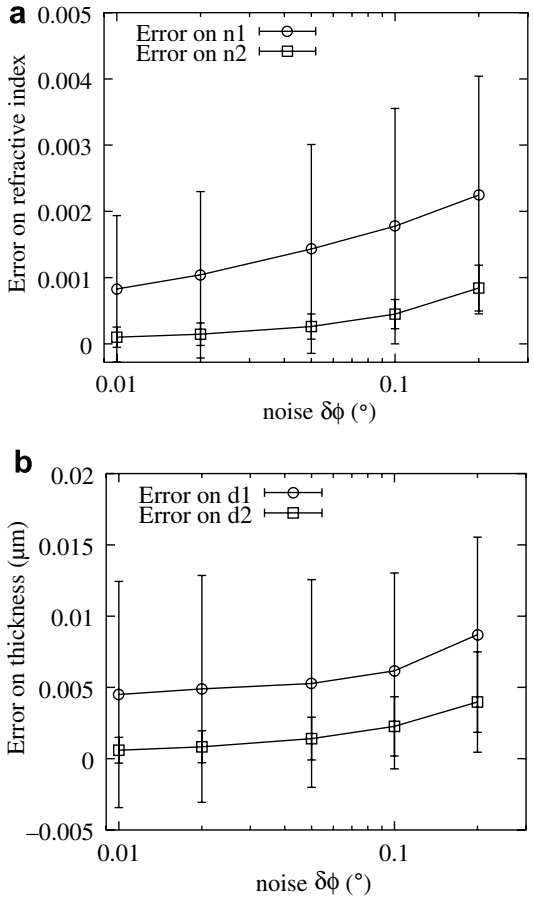

Fig. 3. Mean errors on the refractive index and the film thickness as a function of noise.

3. Characterization of PZT deposited on ZnO

3.1. Optical properties of the ZnO layer

Conducting transparent layers of Al doped ZnO in hexagonal phase were deposited by rf magnetron sputtering at room temperature. In our case, a heat treatment of 650 °C is required for PZT crystallization in the perovskite phase. In order to evaluate the possible effects of this treatment, a preliminary study on the ZnO layers deposited on 25×25 mm Corning 1737F glass substrates was performed.

The zinc oxide layers were grown by rf magnetron sputtering from a $\phi 3''$ ZnO/Al_2O_3 (98/2 wt%) ceramic target. Prior to the deposition, a base pressure lower than 5×10^{-7} mbar is reached and pure Ar is used as a sputter gas at a chamber pressure of 2×10^{-3} mbar during the deposition process. The applied rf power of 200 W results in a growth rate of approximately 100 nm/min on axis at a target–substrate distance of 7.5 cm during 10 min. As four samples were grown at the same time, the substrates were shifted from the center of symmetry of sputtering chamber, and the thickness of ZnO decreased along the diagonale of the substrate. The ZnO target contains 2 wt% of Al_2O_3, which corresponds to a [Al]/[Zn + Al] atomic ratio of about 3.3%. In order to investigate the aluminium content within the thin films, an electron dispersion spectroscopy (EDS, JEOL 5800 LV equipped with a X-ray detector) mapping was performed on thin films grown on a silicon wafer (aluminium/zinc-free substrate) with the same procedure than that used in the present work. The analysis showed that the aluminium content is homogeneous over the whole film surface and its value is $3.3\% \pm 0.5\%$.

The films were characterized with *m*-lines spectroscopy using a set-up and data analysis program described elsewhere [13]. The samples were measured as deposited at several points every 5 mm along the diagonale of the substrate. The evolutions of refractive index and thickness of sample 1 along this line are represented in the Fig. 4a and b (curves with circles). These curves reveal the inhomogeneity of the film due to the deposition technique. From one corner to another, the thickness decreases from 1.04 μm to 0.54 μm. Moreover it can be seen that the refractive index increases from 1.89 to 1.97. This implies that the crystalline structure of the ZnO is not the same across the film. The other samples show the same behavior, but sometimes, the measurements at the lower thicknesses were difficult because of the lack of modes when the thickness becomes too small.

After this first characterization, the films were annealed at 650 °C during 3 min and cooled slowly in the oven during 3 hours. The results of the index and thickness of sample 1 are also shown in the Fig. 4a and b (curves with squares). Obviously, the rapid thermal annealing does not change significantly the thickness, however, it homogenizes the refractive index of the film. Indeed, after annealing, the

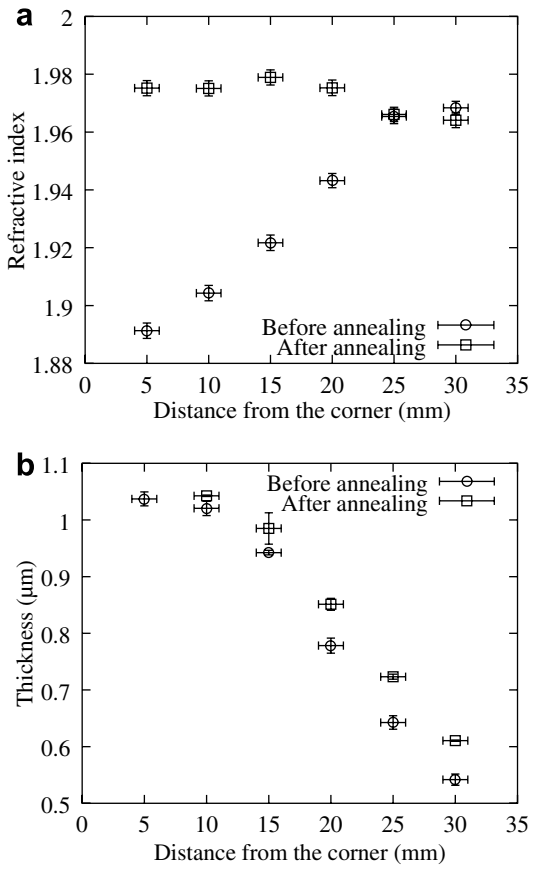

Fig. 4. Evolution of the refractive index and the film thickness along the diagonale of sample 1 before and after thermal annealing.

index ranges between $1.975 \pm 2 \times 10^{-3}$ and $1.964 \pm 1 \times 10^{-3}$. Previous studies [14–17] pointed out that the annealing improves the crystallinity of the ZnO films by promoting the formation of stoichiometric ZnO. The increase of the intensity and the decrease of the FWHM of the diffraction peak (xyz) well illustrate this phenomenon (see Fig. 5). Hence, the modification of refractive index with annealing can be related to this crystallinity improvement.

3.2. Optical properties of two layers waveguides

PZT 36/64 thin films were elaborated by Chemical Solution Deposition technique and were spin-coated on the ZnO layer at 2000 rpm for samples 1–3 and 1000 rpm for samples 4 and 5. A modified sol-gel process was used for the elaboration of the precursor solution, which consisted of lead acetate dissolved in acetic acid, zirconium and titanium *n*-propoxide; ethylene glycol was added in order to prevent from crack formation during the annealing process. The deposited films were dried on a hot plate and a Rapid Thermal Annealing procedure at 650 °C resulting in the formation of a polycrystalline perovskite phase as shown by the XRD pattern (Fig. 6). The samples were also studied with scanning electron microscopy. An example is shown in Fig. 7. The two layer structure appears clearly

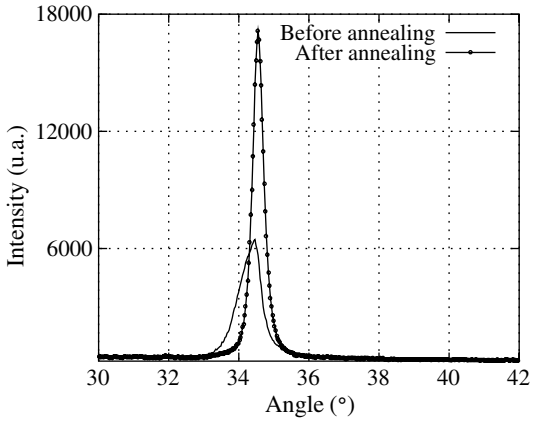

Fig. 5. X-ray diffraction diagramm of the ZnO film (sample 1) before and after annealing.

on this photography. The thickness of the ZnO layer is approximatively 1.1 μm and the thickness of the PZT layer is close to 0.7 μm. The values are in agreement with the elaboration process.

The films were measured with *m*-lines at several points along the diagonale of the sample. As an example, the spectrum of sample 5 is shown on Fig. 8. The narrow peaks correspond to the waves guided in two layers while the broad peaks correspond to waves guided in the PZT layer only. The broadening is not a peculiarity of the two layer structure, it can be also observed with PZT single layers and is probably due to the diffusion of light. The measurement given in Fig. 8 was analyzed with the previously described procedure. Only the modes 4–8 were considered which can be located with a precision of ±0.05°, while the uncertainty on the position of the first modes is of the order of 0.5° because of the broadening. From this measurement we obtain: $n_1 = 1.977 \pm 9 \times 10^{-3}$ and $d_1 = 1.11 \pm 4 \times 10^{-2}$ μm for the ZnO layer and $n_2 = 2.36 \pm 4 \times 10^{-2}$ and $d_2 = 1.01 \pm 7 \times 10^{-2}$ for the PZT. In order to verify the exactness of the results, the values may be injected in the

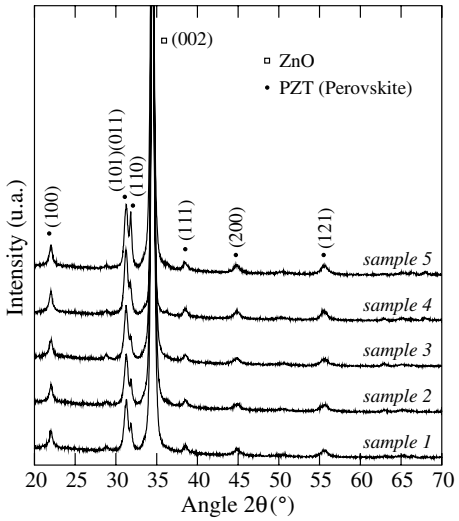

Fig. 6. X-ray diffraction diagram of the two layer films.

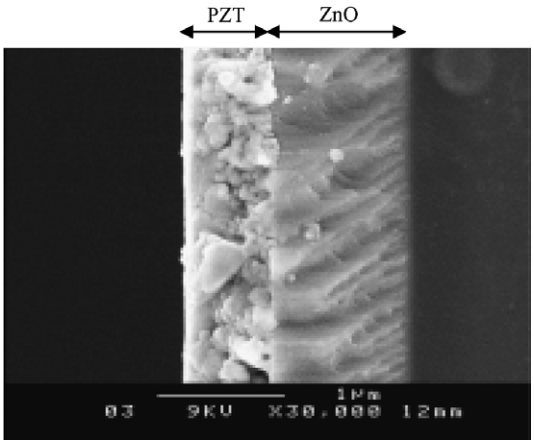

Fig. 7. SEM photography of sample 3.

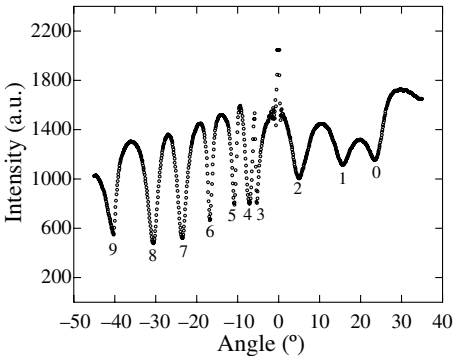

Fig. 8. *m*-Lines spectrum measured at one corner of sample 5.

dispersion Eqs. (4) and (5). Synchronous angles in very good agreement with the measured angles are found (see Table 1). The differences never exceed 0.3°, corresponding to a maximum difference between measured and calculated effective indices of the order of 10^{-3}.

The results obtained with other samples are summarized in the Fig. 9. It was not possible to analyze each measurement, especially those corresponding to points where the ZnO layer was too thin. Everywhere else a good agreement between the refractive indices and thicknesses of the ZnO determined from the single and the double layers was obtained. The variation is of the order of 10^{-2} for the index and 100 nm for the thickness in the worst case but in general remains lower than the uncertainties.

The measurement of the PZT refractive index reveals the influence resulting from the ZnO interface layer. A PZT film of the identical precursor composition, directly spin-coated on the glass substrate, has a refractive index close to 2.23, whereas the refracting index of the PZT deposited on ZnO is higher as can be seen in the Fig. 9a. Moreover, the index varies from close to 2.36 for the thicker PZT films (deposited at 1000 rpm) to close to 2.30 for the thinner films (deposited at 2000 rpm). This indicates that the structure of the film might be different. In order to verify this assumption, we compare in Fig. 10, XRD measurements

Table 1
Comparison of the measured and the calculated synchronous angles

Modes	1	2	3	4	5	6	7	8	9
Measured (°)	23.5	15.60	4.90	−5.30	−7.20	−10.80	−16.70	−23.40	−30.40
Calculated (°)	23.8	15.58	5.07	−5.28	−7.19	−10.75	−16.87	−23.54	−30.52

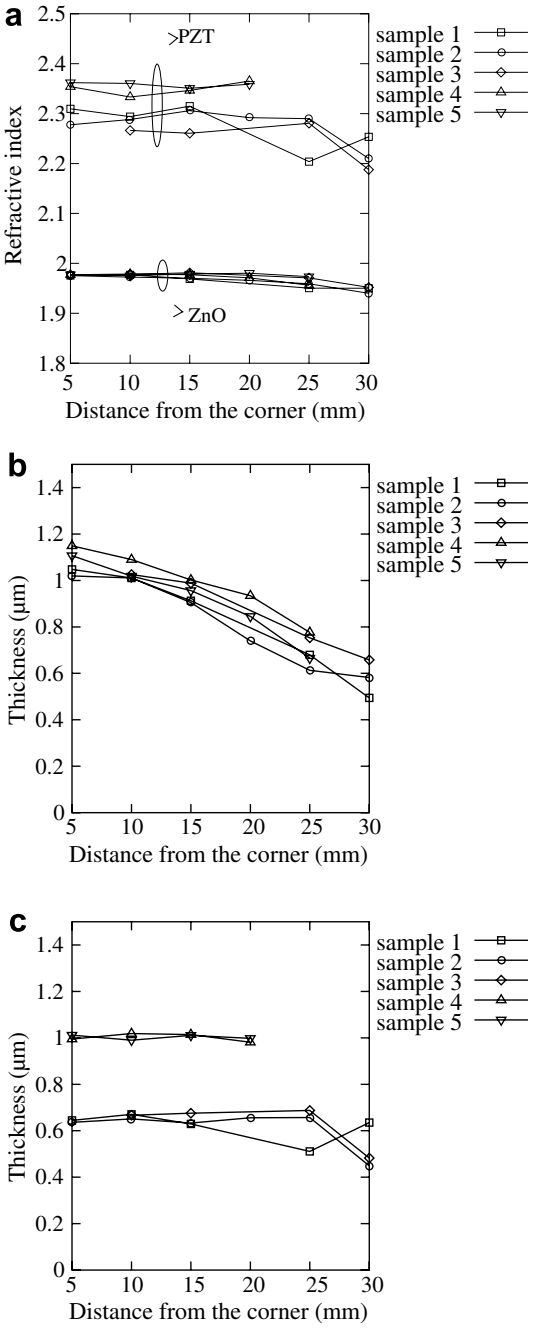

Fig. 9. Evolution of the refractive index and the film thickness along the diagonale of the two layer samples. (a) Refractive indices of the PZT and ZnO layers, (b) thicknesses of the ZnO layers, (c) thicknesses of the PZT layers.

for the two cases. The unique peak at $2\theta = 31°$ for PZT deposited on glass, corresponding to a rhomboedric structure is doubled when spin-coating the same composition

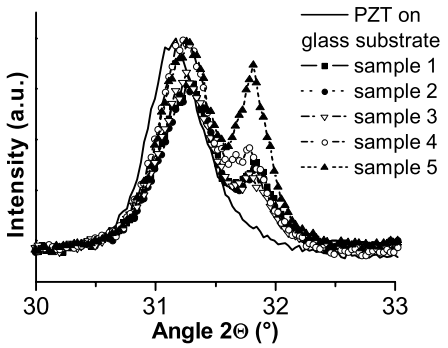

Fig. 10. X-ray diffraction diagramms.

PZT 36/64 on ZnO, indicating the appearance of a second phase corresponding to the tetragonal PZT structure.

4. Conclusions

A two-layer PZT/ZnO wave-guide structure has been elaborated by rf magnetron sputtering and chemical solution deposition technique. The numerical tools for analyzing the *m*-lines spectra obtained from this two-layer system were developed and their efficiency in the presence of noise was demonstrated. In the case of a single ZnO layer, the benefice of a heat treatment at higher temperatures in terms of homogenization of the refractive index has been shown. The study of the PZT thin films revealed the sensitivity of the *m*-lines characterization method. The different crystallization behavior of the ferroelectric resulting from the different structural properties of the underlying layers (glass or ZnO), could be observed by *m*-lines spectroscopy as a change of the PZT refractive index. This appears to be very important for the design of single mode waveguides since the thickness of the guiding layer is related to the difference between the refractive indices of the guiding and the confining layers. The presented work can be considered as a first step towards the characterization of three layer composite structures by *m*-lines spectroscopy, also resulting in the possibility to determine the refractive index as a function of an applied electric field and to deduce the electro-optical coefficient.

References

[1] R. Seveno, H.W. Gundel, S. Seifert, Applied Physics Letters 79 (2001) 4204.
[2] P.K. Tien, R. Ulrich, Journal of the Optical Society of America 60 (10) (1970) 1325.
[3] R. Ulrich, Journal of Optical Society of America 60 (10) (1970) 1337.

[4] R. Ulrich, R. Torge, Applied Optics 12 (12) (1973) 2901.
[5] J.M. White, P.F. Heidrich, Applied Optics 15 (1976) 151.
[6] K.S. Chiang, Journal of Lightwave Technology 3 (1985) 385.
[7] P.K. Tien, R.J. Martin, G. Smolinsky, Applied Optics 12 (8) (1973) 1909.
[8] W. Stutius, W. Streifer, Applied Optics 16 (12) (1977) 3218.
[9] M. Matyáš, J. Bok, T. Sikora, Physica Status Solidi (a) 126 (1991) 533.
[10] J. Aarnio, P. Kersten, J. Lauckner, IEE Proceedings—Optoelectronics 142 (5) (1995) 241.
[11] E. Auguściuk, M. Roszko, Proceedings of SPIE 5451 (2004) 495.
[12] J. Chilwell, I. Hodgkinson, Optical Society of America Journal A 1 (1984) 742.
[13] J. Cardin, D. Leduc, T. Schneider, C. Lupi, D. Averty, H.W. Gundel, Journal of the European Ceramic Society 25 (12) (2005) 2913.
[14] X.W. Sun, H.S. Kwok, Journal of Applied Physics 86 (1) (1999) 408.
[15] Y. Ohya, H. Saiki, Y. Takahashi, Journal of Materials Science 29 (1994) 4099.
[16] N. Mehan, M. Tomar, V. Gupta, A. Mansingh, Optical Materials 27 (2004) 241.
[17] R. Al Asmar, G. Ferblantier, F. Mailly, P. Gallborrut, A. Foucaran, Thin Solid Films 473 (2005) 49.

A method to retrieve optical and geometrical characteristics of three layer waveguides from *m*-lines measurements

T. Schneider,[1] D. Leduc,[1,a)] C. Lupi,[1] J. Cardin,[2] H. Gundel,[1] and C. Boisrobert[1]
[1]*Faculté des Sciences et des Techniques, Université de Nantes, Nantes Atlantique Universités, IREENA, EA1770, 2 rue de la Houssinière, BP 9208, Nantes, F-44000 France*
[2]*SIFCOM, CNRS UMR 6176, ENSICAEN, 6 Boulevard du Maréchal-Juin, F-14050 Caen Cedex, France*

(Received 8 November 2007; accepted 17 December 2007; published online 31 March 2008)

We consider three layer optical waveguides and present a method to measure simultaneously the refractive index and the thickness of each layer with *m*-lines spectroscopy. We establish the three layer waveguide modal dispersion equations and describe a numerical method to solve these equations. The accuracy of the method is evaluated by numerical simulations with noisy data and experimentally demonstrated using a PZT thin film placed between two ZnO layers. © *2008 American Institute of Physics*. [DOI: 10.1063/1.2885147]

I. INTRODUCTION

The considerable progress in thin film etching allows today the realization of almost any waveguide structure requiring submicron resolution. For example, the fabrication of single mode optical waveguides, couplers, interferometers, or ring resonators is well controlled. Whatever their function, these structures are made of a superposition of several thin layers and they have to guide light. Therefore it is essential to accurately characterize the optical and geometrical properties of each layer of the stack. Several techniques exist to perform such a characterization in the case of a single layer film, such as those based on the measurements of the reflection and transmission coefficients of the sample,[1–3] the ellipsometry,[4] and the *m*-lines spectroscopy.[5–7] The case of multilayer waveguides has been much less investigated, although the assumption that a layer in a stack shows the same properties as it has when measured individually can become wrong. The characterization of the whole structure then becomes necessary. Some work was done on the case of two layers[8–13] (sometimes denoted as a "four layer film" since the stack is deposited on a substrate and the air is considered as a top layer), however, no literature is available for three layer structures. These structures are of special interest since they consist of the minimum number of layers required in order to obtain a single mode waveguide that is thick enough to enable efficient coupling of the light. In this paper we will focus on three layer waveguides and show how the refractive indices and thicknesses of the individual layers can be retrieved simultaneously from *m*-lines spectroscopy measurements.

In classical *m*-lines devices, the sample is pressed against a face of a prism. The prism and the film are mounted on a rotating stage in order to allow the variation of the light incidence angle. A thin air gap between the sample and the prism face is maintained whose thickness should be approximately a fourth of the light probe wavelength. The incoming light is refracted inside the prism and reaches the interface between the prism and the sample. Since the refractive index of the prism is higher than that of the sample, the light is totally reflected at this interface, for a given range of incidence angles, and then emerges from the prism to be detected. For some angles, called "synchronous angles," however, part of the light is coupled into the waveguide, and hence is subtracted from the detected light. Therefore, a typical *m*-lines spectrum consists in several absorptionlike peaks, centered on the synchronous angles. From the positions of the synchronous angles, it is possible to deduce the propagation constants of the guided modes of the sample under test and derive the optical and geometrical properties of the structure (refractive index and thickness) by solving the modal dispersion equations.

The first part of this paper is devoted to the determination of the explicit form of modal dispersion equations of the three layer waveguide. We will then describe the numerical method used in order to solve these equations and present numerical tests that prove its accuracy. The validity of the method will be finally demonstrated experimentally by the analysis of *m*-lines spectra produced by three layer ZnO/PZT/ZnO waveguides.

II. THREE LAYER DISPERSION EQUATIONS

The studied structure is a stack of five transparent homogeneous layers shown in Fig. 1. The substrate (layer 0) and

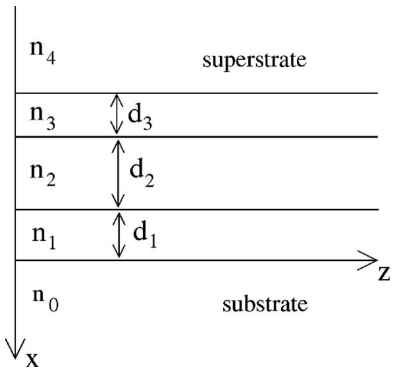

FIG. 1. Three layer waveguide.

a)Author to whom correspondence should be addressed. Electronic mail: dominique.leduc@univ-nantes.fr.

the superstrate (layer 5) are considered as semi-infinite since their thicknesses are several orders of magnitude greater than those of layers 1, 2, and 3. The light is confined only in these three central layers and presents an evanescent decay in the substrate and the superstrate. We call this structure a "three layer waveguide," whereas in the nomenclature of other authors[10] it would be called a "five layer waveguide." The central layer (layer 2) is the core of the structure and layers 1 and 3 are the claddings (true waveguide[14]). As a consequence, we assume for the refractive indices of the different layers that

$$n_2 > n_1, n_3 > n_0, n_4. \tag{1}$$

In the following, we will restrict ourselves to the case of TE modes; the extension to the case of TM modes is straightforward. The only component of the electrical field of the TE modes is along the (Oy) axis, so the electric field in the layer j can be written as $E_{yj}(x,z)=A_j \exp[i(\gamma_j x+\beta_m z)] + B_j \exp[i(-\gamma_j x+\beta_m z)]$ and the tangential component of the magnetic field is $H_{zj}(x,z)=i(\omega\mu_0)^{-1}\partial E_{yj}/\partial x$. In these expressions, ω is the angular frequency and β_m is the propagation constant of the mth guided mode. It is usually written as $\beta_m=kN_m$, where k is the wave vector modulus in vacuum and N_m is the effective index of the mth mode. Using the condensed notation $a_j=k|n_j^2-N^2|^{1/2}$, the x component of the wave vector, γ_j, which gives the nature of the wave in the layer j, becomes $\gamma_j=(\omega\mu_0)^{-1}a_j$ for a traveling wave and $\gamma_j=i(\omega\mu_0)^{-1}a_j$ for an evanescent wave. A transfer matrix M_j, which binds the electromagnetic fields at the backplane of the layer to the fields at its front plane, can be associated to each layer:[15]

$$M_j=\begin{pmatrix} \cos(\omega\mu_0\gamma_j d_j) & \dfrac{i}{\gamma_j}\sin(\omega\mu_0\gamma_j d_j) \\ i\gamma_j \sin(\omega\mu_0\gamma_j d_j) & \cos(\omega\mu_0\gamma_j d_j) \end{pmatrix}. \tag{2}$$

The boundary conditions imply that the tangential components of the magnetic and electrical fields must be continuous at the interface of the layers. These conditions together with the condition for obtaining guiding lead to

$$\begin{pmatrix} 1 \\ -\gamma_4 \end{pmatrix} E_{4y} = M_3 M_2 M_1 \begin{pmatrix} 1 \\ \gamma_0 \end{pmatrix} E_{0y} = M \begin{pmatrix} 1 \\ \gamma_0 \end{pmatrix} E_{0y}, \tag{3}$$

which has solutions only for

$$\gamma_4 m_{11} + \gamma_4\gamma_0 m_{12} + m_{21} + \gamma_0 m_{22} = 0, \tag{4}$$

where m_{ij} are the components of the matrix M. With the definition (2) of the transfer matrix, this equation can be written as[16]

$$a_2 d_2 + \arctan\left[\frac{i\gamma_0\gamma_1 - \gamma_1^2\tan(\omega\mu_0\gamma_1 d_1)}{\gamma_1\gamma_2 - i\gamma_0\gamma_2\tan(\omega\mu_0\gamma_1 d_1)}\right] + \arctan\left[\frac{i\gamma_3\gamma_4 + \gamma_3^2\tan(\omega\mu_0\gamma_3 d_3)}{\gamma_2\gamma_3 - i\gamma_2\gamma_4\tan(\omega\mu_0\gamma_3 d_3)}\right] - m\pi = 0, \tag{5}$$

which is the general modal dispersion equation for the true three layer waveguides.

As stated above, the γ_j terms are either real or imaginary depending on the nature of the waves in the jth layer. As a consequence, an analysis in the complex plane is required in order to directly solve Eq. (5). It is better to take advantage of physical arguments to split the problem into several simpler ones. Under the condition of Eq. (1), three kinds of guided waves can exist:

•The lowest order modes can only propagate in layer 2. Then γ_2 only is real and Eq. (5) becomes

$$a_2 d_2 - \arctan\left[\frac{a_0 a_1 + a_1^2\tanh(a_1 d_1)}{a_1 a_2 + a_0 a_2\tanh(a_1 d_1)}\right] - \arctan\left[\frac{a_3 a_4 + a_3^2\tanh(a_3 d_3)}{a_2 a_3 + a_2 a_4\tanh(a_3 d_3)}\right] - m\pi = 0. \tag{6}$$

•As the order of the mode increases, the wave vector approaches the normal of the interfaces. For a given mode m_2, the incidence angle on the interface between the central layer and one cladding layer becomes smaller than the limit angle for total internal reflection and the light propagates inside these two layers. If $n_3 > n_1$, then the light is guided in layers 2 and 3 and Eq. (5) becomes

$$a_2 d_2 - \arctan\left[\frac{a_0 a_1 + a_1^2\tanh(a_1 d_1)}{a_1 a_2 + a_0 a_2\tanh(a_1 d_1)}\right] - \arctan\left[\frac{a_3 a_4 - a_3^2\tan(a_3 d_3)}{a_2 a_3 + a_2 a_4\tan(a_3 d_3)}\right] - m\pi = 0. \tag{7}$$

Otherwise, the light propagates in layers 1 and 2. The corresponding modal dispersion equation is obtained by inverting the functions tan and tanh in Eq. (7).

•Finally, highest order modes can propagate in the three layers. The dispersion equation for these modes is

$$a_2 d_2 - \arctan\left[\frac{a_0 a_1 - a_1^2\tan(a_1 d_1)}{a_1 a_2 + a_0 a_2\tan(a_1 d_1)}\right] - \arctan\left[\frac{a_3 a_4 - a_3^2\tan(a_3 d_3)}{a_2 a_3 + a_2 a_4\tan(a_3 d_3)}\right] - m\pi = 0. \tag{8}$$

III. DATA ANALYSIS: ALGORITHM AND NUMERICAL TESTS

At a first glance, the problem contains six unknown parameters which are the refractive indices and thicknesses of layers 1, 2, and 3. However, depending on the guiding regime, one has to associate correctly the dispersion equation to each measured synchronous angle. Consequently, further parameters have to be determined:

- m_1, the order of the first measured mode. It is often equal to 0, but the lower order modes are sometimes difficult to excite, and hence may not be visible in the m-lines spectrum. There is no evidence on the value of m_1 in practice.
- m_2, the order of the first mode guided by two layers. Numerical simulations with noisy data showed that m_2 is the value of m such that $|N_m - N_{m-1}| > |N_{m+1} - N_m|$.

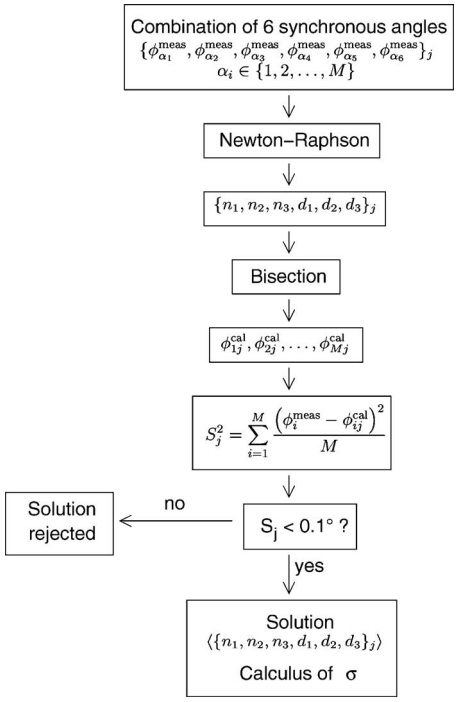

FIG. 2. Algorithm of the resolution of the system of six equations in six unknowns and M measured modes.

This criterion results in a correct value of m_2 or with a mismatch of +1.[17] In the following we will call m_2^{th} the value given by this criterion.

- m_3, the order of the first mode guided by three layers.
- Finally, the modal dispersion equation in the case of two guiding layers is not the same according to whether n_1 is smaller or greater than n_3. Hence it is also necessary to make an initial hypothesis on the relative values of n_1 and n_3 and to verify this assumption during the resolution.

The analysis of a m-lines spectrum thus requires a somewhat complicated algorithm. For clarity reasons, we split the presentation of this algorithm into two parts (Figs. 2 and 3).

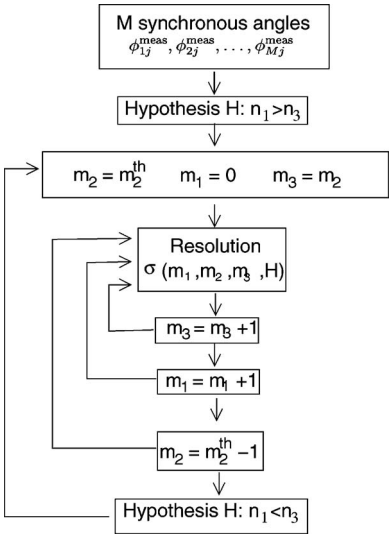

FIG. 3. Algorithm of the m-lines spectra analysis.

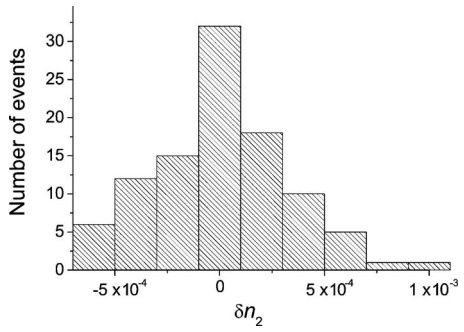

FIG. 4. Distribution of errors on the parameter n_2.

The details of the "resolution" box of the full algorithm (shown in Fig. 3) are presented in Fig. 2, aiming to solve a system of six equations in six unknowns for m_1, m_2, m_3 given and for an assumption on the relative values of n_1 and n_3. Obviously, this problem can be solved only if the m-lines spectrum contains more than six modes. Let us call M the number of measured synchronous angles. There are C_6^M combinations of six modes. For a given combination j, we first use a Newton-Raphson method to get a solution $\{n_1, n_2, n_3, d_1, d_2, d_3\}_j$. Then, we start from this solution and use a bisection algorithm to calculate the set of M corresponding synchronous angles: $\{\phi_{ij}^{\text{cal}}\}$, $i \in \{1, 2, \ldots, M\}$. The validity of the solution is evaluated by the standard deviation of the differences between the values of the calculated synchronous angles and the measured ones:

$$S_j^2 = \sum_{i=1}^{M} \frac{(\phi_i^{\text{meas}} - \phi_{ij}^{\text{cal}})^2}{M}. \tag{9}$$

If S_j is smaller than 0.1° (upper limit of experimental uncertainty), the solution is considered as correct. This procedure is used for the C_6^M combinations, but it does not find roots in all cases. Let us call Γ the number of combinations for which the procedure succeeds. The solution we finally retain is the mean value of these Γ solutions and we associate a fitness σ to this solution defined by

$$\sigma^2 = \sum_{j=1}^{\Gamma} \frac{S_j^2}{\Gamma^2}. \tag{10}$$

Γ^2 was used rather than Γ, in order to give more weight to the configurations that lead to a high number of acceptable solutions.

The parameters m_1, m_2, and m_3 are obtained with an iterative procedure schematized on Fig. 3. We start with the M measured synchronous angles and under the hypothesis $H: n_1 > n_3$. The value of m_2 is set to m_2^{th}, m_1 to 0, and m_3 to m_2, and the procedure of resolution described above is used in order to get a solution and its associated fitness σ_{H,m_1,m_2,m_3}. This procedure is repeated with first an increment of m_3 from m_2 to M, second with an incrementation of m_1 from 0 to 5 (which in general is sufficient), and third by setting m_2 to $m_2^{\text{th}} - 1$. For the case where no solution was obtained at the end of these iterations, the whole procedure is repeated with the opposite hypothesis ($n_1 < n_3$). The refractive indices and

TABLE I. Range of parameters explored with the statistical study.

	Start	End	Step
n_1, n_3	1.6	$n_2-0.1$	0.1
n_2	1.7	2.4	0.1
d_1, d_2	1.0 μm	2.0 μm	0.1 μm
d_3		100 nm	

thicknesses finally selected are those which are associated to the lowest value of σ, thus defining the values m_1, m_2, m_3, and H.

The validity of the method was verified by numerical simulations. Starting from a theoretical waveguide defined by the parameters $\{n_1^{\text{th}}, n_2^{\text{th}}, n_3^{\text{th}}, d_1^{\text{th}}, d_2^{\text{th}}, d_3^{\text{th}}\}$, we calculated the corresponding set of synchronous angles $\{\phi_i^{\text{th}}\}$, $0 \le i \le 8$. In order to test the sensitivity to the noise, this set was used for building 100 sets of noisy data $\{\phi_i^{\text{noisy}}\}$ by adding to each theoretical synchronous angle, ϕ_i^{th}, a random value, ε_i, standing in the interval $[-\delta\phi, \delta\phi]$ with a uniform probability density. The values of $\delta\phi$ used in the simulations were chosen in order to correspond to the experimentally observed noise.

The 100 noisy data sets were analyzed, giving rise to a number Λ of sets of solutions $\{n_1^{\text{sol}}, n_2^{\text{sol}}, n_3^{\text{sol}}, d_1^{\text{sol}}, d_2^{\text{sol}}, d_3^{\text{sol}}\}$. Λ depends on the magnitude of the noise; it is very close to 100 for $\delta\phi=0.01°$ and about 80 for $\delta\phi=0.1°$. Each value $p_{j,1\le j\le\Lambda}^{\text{sol}}$ of the parameter p ($p=n_1, n_2, n_3, d_1, d_2$, or d_3) differed from the theoretical value p_j^{th}. The distribution of errors $\delta p_j = p_j^{\text{sol}} - p_j^{\text{th}}$ followed a normal law for all parameters p and all noises,[16] as shown in Fig. 4 for the example of n_2. Finally, we defined the uncertainty Δp on the parameter p as three times the standard deviation of the distribution, in order to be in the confidence interval of 99%: $\Delta p = 3[\Sigma_{j=1}^{\Lambda} \Lambda^{-1} (\delta p_j - \langle \delta p \rangle)^2]^{1/2}$.

A total of 8000 waveguides were simulated, whose characteristics are summarized in Table I. The thickness of the upper layer, d_3, was constant and smaller than the penetration depth of the light, in order to make possible the evanescent coupling between the prism and the central layer. In order to get global estimators, we studied the distribution of uncertainties Δp of each parameter for p for all the simulated guides and for each noise. It was always possible to fit the distribution with a log-normal law (see Fig. 5):

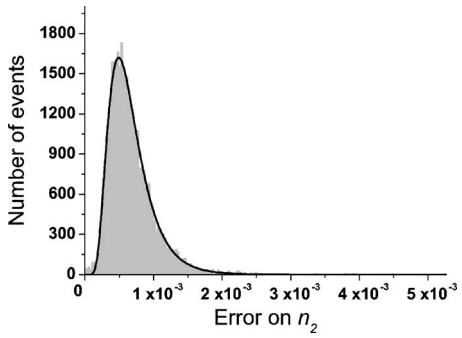

FIG. 5. Distribution of the uncertainties Δn_2 over all the simulated guides, fitted by a lognormal law.

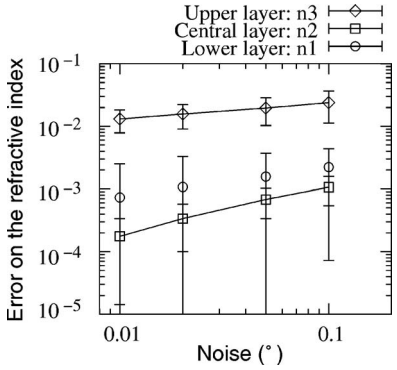

FIG. 6. Evolution of the error on the refractive indices as a function of the noise on the synchronous angles.

$$f(\Delta p) = \frac{1}{w\Delta p\sqrt{2\pi}} e^{-(\ln \Delta p - \mu)^2/2w^2}, \tag{11}$$

where w and μ are the free parameters of the model. Hence, the mean error was $\langle \Delta p \rangle = \exp(\mu + w^2/2)$ and the standard deviation of the distribution was $\sigma_{\Delta p}^2 = [\exp(w^2) - 1]\exp(2\mu + w^2)$. It followed that 85% of the errors were in the range $\langle \Delta p \rangle \pm \sigma_{\Delta p}$. We then used $\langle \Delta p \rangle$ as an estimate of the error on the parameter p with an uncertainty $\sigma_{\Delta p}$.

The results of the simulations are summarized in the graphics of Figs. 6 and 7. For the central layer, the error on the refractive index is lower than 1×10^{-3} and the error on the thickness remains lower than 10 nm for a noise on the synchronous angles below 0.1°. For the other layers the errors on the refractive indices remain acceptable. They are smaller than 1×10^{-3} for layer 1 and of the order of 1×10^{-2} for the upper layer. Nevertheless, the errors on the thicknesses can reach large values, especially for d_3. However, it should be emphasized that the number of synchronous angles used for the statistical study was limited to nine in order to limit the computation time. A closer inspection of the guides leading to inaccurate results showed that the accuracy can be considerably enhanced when increasing the number of modes taken into account. As an example, Figs. 8 and 9 show the evolution of the errors on the different parameters as a function of the number of modes for a noise of 0.01° and a guide defined by $n_1=1.9$, $n_2=2.3$, $n_3=2.2$, $d_1=1.1$ μm, $d_2=1.9$ μm, and $d_3=100$ nm. The errors on d_1 and n_1 can be reduced by two orders of magnitude while the

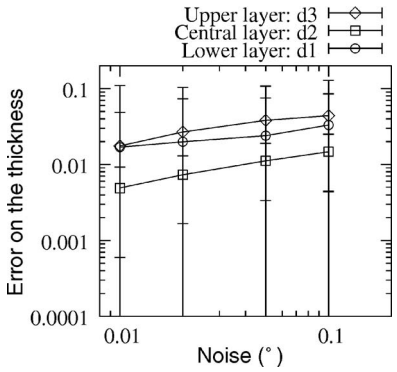

FIG. 7. Evolution of the error on the thicknesses as a function of the noise on the synchronous angles.

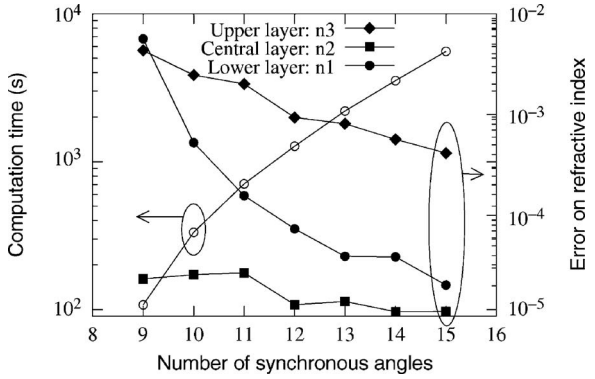

FIG. 8. Evolution of the error on the refractive indices as a function of the number of synchronous angles used in the resolution.

error on d_3 and n_3 is divided by 2 when the number of modes used in the calculation is increased from 9 to 15. This means that one should always use the maximum number of modes in order to reach the best accuracy. However, the computation time also increases.

IV. EXPERIMENTAL RESULTS

In order to experimentally validate the method, several multilayer structures were elaborated. They were deposited on glass substrates and were composed of lead zirconate titanate (PZT) for the core layer and Al doped zinc oxide (ZnO) for the claddings. A SEM picture of one of these samples is shown in Fig. 10.

The zinc oxide layers were grown by rf magnetron sputtering at room temperature from a 3 in. diameter $ZnO/Al_2O_3(98/2$ wt. %) ceramic target. Prior to the deposition, a pressure lower than 5×10^{-7} mbar was reached and pure argon was used as a sputter gas at a partial pressure of 2×10^{-3} mbar during the deposition process. An on-axis growth rate of approximately 100 nm/min was achieved at a rf power of 200 W at a target-substrate distance of 7.5 cm. The films were annealed at 650 °C for 3 min and cooled down to room temperature for 3 h. Four substrates were placed side by side under the ZnO target, resulting in a nonhomogeneous thickness of the films. In the following we will call "A_ℓ" and "A_r" the samples directly on the left and right sides of the center of deposition, "B_ℓ" the sample on the left

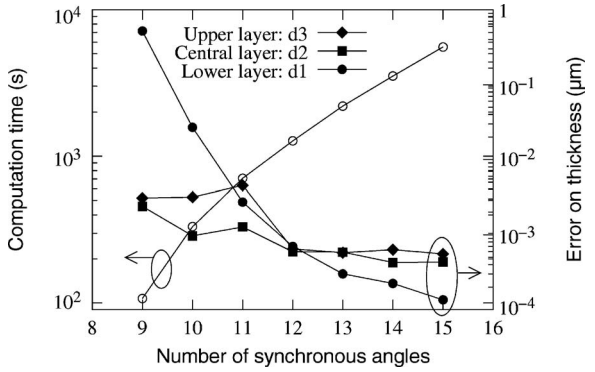

FIG. 9. Evolution of the error on the thicknesses as a function of the number of synchronous angles used in the resolution.

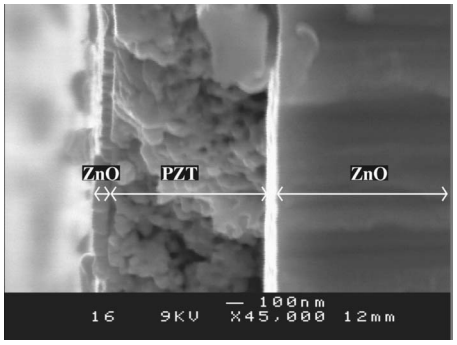

FIG. 10. SEM photograph of a three layer waveguide.

of A_ℓ, and "B_r" the sample on the right of A_r. For symmetry reasons, we expect ZnO layers A_ℓ and A_r, as well as B_ℓ and B_r, to be identical.

The PZT 36/64 layers were elaborated by chemical solution deposition technique.[18] A modified sol-gel process was used for the elaboration of the PZT precursor solution, which consisted of lead acetate dissolved in acetic acid, zirconium, and titanium n-propoxide; ethylene glycol was added in order to prevent crack formation during the annealing process. The final solution was spin-coated on the ZnO layer at 1000 rpm and a rapid thermal annealing procedure at 650 °C resulted in the formation of a polycrystalline perovskite without remaining pyrochlore phases. A layer of PZT was spin-coated individually on samples A_ℓ, A_r, B_ℓ, and B_r. After crystallization, we expect a repeatability of 8×10^{-3} on the refractive index and of 20 nm on the thickness.[18]

The upper ZnO cladding layer was only deposited on samples A_r and B_r with a thickness smaller than the penetration depth of the light. These two samples were not characterized, neither with *m*-lines nor with another technique, until the third layer was deposited, in order to avoid pollution or any other deterioration of the structure. The two layers waveguides A_ℓ and B_ℓ were used as control samples.

Another three layer sample, called "*C*" in the following, was elaborated in the same way as the samples *A* and *B*, but it was characterized by *m*-lines after each deposition step.

We first consider the samples *A* and *B*. An example of *m*-lines spectrum, obtained with sample B_r, is shown on Fig. 11. The transition from the single guiding layer to the two guiding layer regime appears clearly in the spectrum. Indeed, the broad peaks correspond to the waves guided in the PZT layer only, while the narrow peaks are associated to the waves also guided in the ZnO. This broadening is not a peculiarity of the three layer structure; it can be also observed for PZT single layers and may be due to light diffusion re-

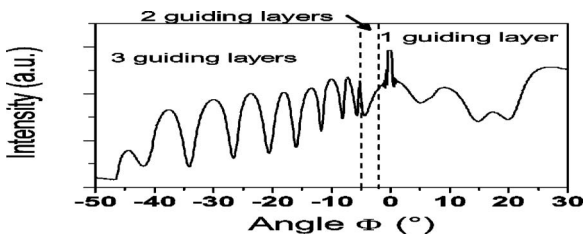

FIG. 11. *m*-lines spectrum obtained with sample B_r measured at 29 mm from the center of deposition.

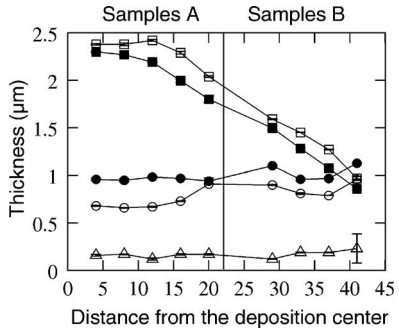

FIG. 12. Evolution of the thicknesses of the different layers of the three layer samples A_r, B_r (d_1: □, d_2: ◯, d_3: △) and the two layer samples A_ℓ, B_ℓ (d_1: ■, d_2: ●).

sulting in a loss along the direction of propagation.[14] The transition from the two guiding layer regime to the three guiding layer regime cannot be inferred from the spectrum and has to be determined by numerical computation. The spectrum of Fig. 11 was analyzed with the numerical method described in Sec. II, resulting in the following characteristics:

- Layer 1: $n_1 = 1.9701 \pm 6 \times 10^{-4}$, $d_1 = 1.588 \pm 3 \times 10^{-3}$ μm.
- Layer 2: $n_2 = 2.2702 \pm 6 \times 10^{-4}$, $d_2 = 0.894 \pm 6 \times 10^{-3}$ μm.
- Layer 3: $n_3 = 2.037 \pm 9 \times 10^{-3}$, $d_3 = 0.122 \pm 3 \times 10^{-3}$ μm.

Due to the complexity of the system to solve, the uncertainties were estimated with Monte Carlo simulations, in a similar way to what is described in Sec. III. Starting from the solution $\{n_1, n_2, n_3, d_1, d_2, d_3\}$, we calculated the associated synchronous angles $\{\phi_i\}$ and built 100 sets of noisy angles by adding a random value in the range of the experimental uncertainties. We then computed the solutions corresponding to the different noisy sets and considered their distributions. The uncertainty on each parameter is defined as three times the standard deviation of the distribution of the values of this parameter.

We performed *m*-lines measurements every 4 mm from the center of the ZnO deposition. Figures 12 and 13 show, respectively, the evolution of the thickness and the refractive indices of the different layers of the samples *A* and *B*. If we except the point located at 41 mm from the deposition center, where few modes were available due to the low thickness of

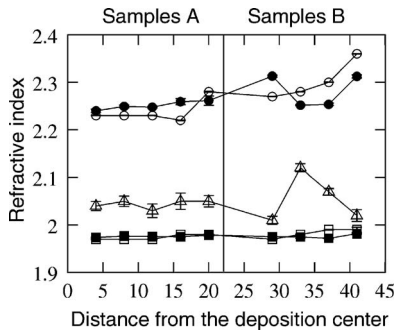

FIG. 13. Evolution of the refractive indices of the different layers of the three layer samples A_r, B_r (n_1: □, n_2: ◯, n_3: △) and the two layer samples A_ℓ, B_ℓ (n_1: ■, n_2: ●).

TABLE II. Comparison of the measured characteristics of a waveguide (sample *C*), before and after the deposition of the upper cladding layer.

	n_1	$d_1(\mu m)$	n_2	$d_2(\mu m)$	n_3	$d_3(\mu m)$
Two layers	1.978	1.11	2.360	1.02		
Three layers	1.979	1.09	2.368	0.96	1.987	0.13

the lower ZnO layer, the error bars do not clearly appear since the uncertainties are small. They are of the order of 5×10^{-4} for n_1 and n_2, and 1×10^{-2} for n_3. The uncertainties on the thicknesses are of the order of 10 nm, which corresponds to a relative accuracy of 0.5% for d_1 and d_2, and 10% for d_3. As expected, the thickness of the lower ZnO layers decreases with the distance from the ZnO deposition center (Fig. 12). The thickness of the PZT films is rather constant, except at the border of the samples where a slight increase can be observed which is typical for the spin-coating process.

The refractive index of the PZT layer varies from $2.2227 \pm 5 \times 10^{-4}$ to $2.3610 \pm 5 \times 10^{-4}$. It is slightly higher than the refractive index of the PZT deposited on glass under the same conditions.[18] This may be due to a structural change of the PZT thin film induced by the ZnO buffer layer, which acts as a diffusion barrier, thus hindering diffusion of the lead from the PZT into the glass substrate. The index of the ZnO lower layer is rather constant; it oscillates between $1.9667 \pm 6 \times 10^{-4}$ and $1.991 \pm 5 \times 10^{-3}$. On the contrary, the index of the upper ZnO layer exhibits strong variations from $2.015 \pm 8 \times 10^{-3}$ to $2.123 \pm 8 \times 10^{-3}$. This may be explained by the existence of two different crystalline structures arising when the thickness of the ZnO film is below 500 nm.[19]

The differences between the thicknesses and refractive indices obtained for the three layer waveguides (A_r, B_r) and the two layer waveguides (A_ℓ, B_ℓ) essentially stay in the range of the repeatability of the elaboration procedure and the measurement techniques. So the method of analysis of three layer guides *m*-lines spectra gives results in accordance to those obtained with two layer guides. This is confirmed by the measurements realized from sample *C*, where the refractive index and the thickness of the layers were measured before and after deposition of the upper cladding layer. The results are summarized in Table II showing that the differences between the values obtained before and after the third deposition remain always smaller than the uncertainty and the repeatability of the elaboration procedure and the measurement techniques. This good agreement proves the validity of our method.

V. CONCLUSION

In this paper, the general modal dispersion equation for a three layer planar waveguide is shown, from which the modal dispersion equations that hold for different guiding regimes are derived. A method to solve these equations is proposed, where the input data are the synchronous angles measured by *m*-lines spectroscopy. Monte Carlo simulations show that the values of the refractive indices and the thicknesses of the central layer given by this method are as accurate as those obtained for a single layer. The accuracy is not

so good for the upper layer, however the error remains smaller than 2×10^{-2} for the index and below 30 nm for the thickness when the uncertainty on the measured angles remains smaller than 0.1°. The method was applied to the characterization of real three layer planar waveguide structures made of one PZT layer embedded between two ZnO cladding layers deposited on glass substrate. The agreement between the results obtained with three layer structures and those obtained with two layer structures ensures the validity of our method. Moreover, the three layer analysis revealed changes in material properties, such as an increase of the refractive index of PZT deposited on ZnO in comparison to deposition on glass and an increase of the refractive index of ZnO deposited on PZT in comparison to deposition on glass.

The proposed method allows us to simultaneously characterize the optical and geometrical properties of each layer of three layer waveguides. Consequently, it is a very interesting instrument in order to verify whether the three layer structures are matching the parameters defined during the design process of the waveguide.

[1]F. Abelès, *Progress in Optics, Vol. 2*, edited by E. Wolf (North-Holland, Amsterdam, 1963).
[2]J. C. Manifacier, J. Gasiot, and J. P. Fillard, J. Phys. E **9**, 1002 (1976).
[3]J. C. Martínez-Antón, Appl. Opt. **39**, 4557 (2000).
[4]R. Azzam and N. Bashara, *Ellipsometry and Polarized Light* (North-Holland, Amsterdam, 1977).
[5]P. K. Tien and R. Ulrich, J. Opt. Soc. Am. **60**, 1325 (1970).
[6]R. Ulrich, J. Opt. Soc. Am. **60**, 1337 (1970).
[7]R. Ulrich and R. Torge, Appl. Opt. **12**, 2901 (1973).
[8]P. Tien, R. Martin, and G. Smolinsky, Appl. Opt. **12**, 1909 (1973).
[9]W. Stutius and W. Streifer, Appl. Opt. **16**, 3218 (1977).
[10]D. W. Hewak and J. W. Y. Lit, Appl. Opt. **26**, 833 (1987).
[11]M. Matyás, J. Bok, and T. Sikora, Phys. Status Solidi A **126**, 533 (1991).
[12]J. Aarnio, P. Kersten, and J. Lauckner, IEE Proc.-J: Optoelectron. **142**, 241 (1995).
[13]J. Kubica, J. Lightwave Technol. **20**, 114 (2002).
[14]X.-J. Zhang, X.-Z. Fan, J. Liao, H.-T. Wang, N. B. Ming, L. Qiu, and Y.-Q. Shen, J. Appl. Phys. **92**, 5647 (2002).
[15]J. Chilwell and I. Hodgkinson, J. Opt. Soc. Am. A **1**, 742 (1984).
[16]T. Schneider, Ph.D. thesis, Université de Nantes, 2006.
[17]T. Schneider, D. Leduc, J. Cardin, C. Lupi, N. Barreau, and H. Gundel, Opt. Mater. **29**, 1871 (2007).
[18]J. Cardin, D. Leduc, T. Schneider, C. Lupi, D. Averty, and H. Gundel, J. Eur. Ceram. Soc. **25**, 2913 (2005).
[19]S. Lin and J. Huang, Surf. Coat. Technol. **185**, 222 (2004).

Determination of refractive index, thickness, and the optical losses of thin films from prism-film coupling measurements

Julien Cardin, Dominique Leduc

Determination of refractive index, thickness, and the optical losses of thin films from prism–film coupling measurements

Julien Cardin[1,*] and Dominique Leduc[2]

[1]SIFCOM, CNRS UMR 6176, ENSICAEN, 6 Boulevard du Maréchal-Juin, F-14050 Caen Cedex, France

[2]Université de Nantes, Nantes Atlantique Universités, IREENA, EA1770, Faculté des Sciences et des Techniques, 2 rue de la Houssinière–BP 9208, Nantes F-44000, France

*Corresponding author: julien.cardin@ensicaen.fr

Received 4 September 2007; revised 17 December 2007; accepted 3 January 2008; posted 11 January 2008 (Doc. ID 87215); published 28 February 2008

We present a method of analysis of prism–film coupler spectroscopy based on the use of transfer matrix and genetic algorithm, which allows the simultaneous determination of refractive index, thickness, and optical losses of the measured layer. © 2008 Optical Society of America

OCIS codes: 130.3130, 120.3940, 160.4760, 300.1030.

1. Introduction

Transparent thin films find wide applications in optics: coating, sensors, integrated components for telecommunications, solar cell, etc. For all these applications, it is necessary to perform an accurate characterization of the optical properties, which include refractive index and optical losses. The optical losses of a thin film have three different origins: surface scattering due to the surface roughness, volume scattering due to volume defects such as inhomogeneity, and volume absorption due to intrinsic absorption [1,2]. From a practical point of view, this characteristic is of particular importance since it can severely degrade or modify the performances of a component.

Several techniques exist which allow the characterization of the optical parameters of thin films. For example, the measurement of reflection and transmission coefficients [3–6] and the spectroscopic ellipsometry [7–9] lead to refractive index, thickness, and extinction factor measurement.

On the other hand, since the 1970s, a prism–film coupler based method, also called *m*-lines spectroscopy has been developed to characterize thin films. Full-accuracy index and thickness measurements are obtained, for nonbirefringent films [10] and in the absence of nonlinear effects [11], once film thickness exceeds a certain minimum threshold value (typically 300 nm, depending on the film/substrate type) [12,13]. This technique is based on a selective excitation, through an evanescent field, of guided modes of a film. The total reflection at the upper boundary of the film is frustrated by the presence of the prism and allows the light to go back into the prism. Since this reflected light carries information on the film, it can be used to determine the parameters of the film. Classically, this method was restricted to the determination of the thickness and the refractive index of the films. The scope of this paper is to present a method of analysis, which allows retrieving the optical losses also from classical prism–film coupler measurements, for films of negligible roughness.

2. Prism–Film Coupler Angular Reflectivity

In *m*-lines devices, the sample is pressed against a face of a prism in such a way that it is separated from the prism by a thin air gap with a thickness about a quarter of wavelength of the measurement light. The prism and the film are mounted onto a rotating stage

0003-6935/08/070894-07$15.00/0

that varies the incidence angle. The incoming light is refracted inside the prism and reaches the interface between the prism and the sample. As the refractive index of the prism is higher than that of the sample, for a given range of incidence angles, the light is totally reflected by this interface and then emerges from the prism. However, for some angles, called "synchronous angles," a part of the light is coupled in the waveguide. Depending on refractive indices of layer and cladding, one obtains guided or leaky modes. For both cases, the light coupled inside the film is subtracted to the detected light. Thus, a typical m-lines spectrum is made of several absorption-like peaks, centered around the synchronous angles.

In classical analysis, the propagation constants of the guided modes are deduced from the positions of the synchronous angles, and then the refractive index and thickness are determined by solving the modal dispersion equations. A previous paper [14] on the analysis of m-lines spectroscopy with genetic algorithm was also done in the framework of the modal dispersion equations with the synchronous angles as input data. In our case, we are performing a fit on the whole recorded spectrum by using the transfer matrix theory to simulate the angular reflectivity of the prism–film coupler.

Consider the schematic of the m-lines prism coupler in Fig. 1. In our model, the prism positioned on the top part of the drawing is considered as a nonabsorbing medium. The optical film is surrounded by a thin air gap and a semi-infinite substrate. The complex refractive indexes, $\tilde{n} = n + ik$, including extinction factor k, are used for each layer. We cannot separate the contributions of surface, volume scattering, and volume absorption only from the m-lines spectrum. Thus, in our case we consider this extinction factor as an effective extinction factor, which represents *a priori* the three types of contribution to optical losses. The extinction factors of the air and of the prism were assumed to be zero.

A transfer matrix M_j, which binds the electromagnetic fields at the backplane of the layer to the fields at its front plane, is associated with both film and air layers [15,16]:

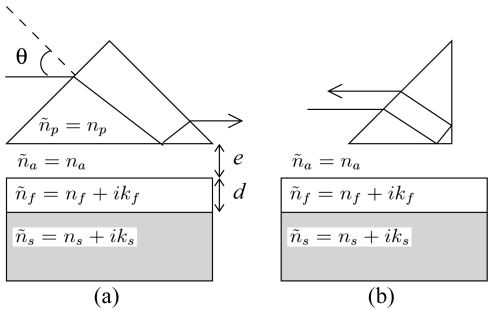

Fig. 1. Prism coupler configuration: (a) transmission configuration, and (b) reflection configuration.

$$M_j = \begin{pmatrix} \cos\phi_j & -i\gamma_j^{-1}\sin\phi_j \\ -i\gamma_j \sin\phi_j & \cos\phi_j \end{pmatrix}, \tag{1}$$

with phase factor $\phi_j = d_j[(\tilde{n}_j k_0)^2 - \beta^2]^{1/2}$, where d_j is the thickness of the jth layer, k_0 is the wave vector, and β is the propagation constant in the direction parallel to the interface. The transversal component in the direction perpendicular to the interface of the wave vector is $\gamma_j = (d_j k_0)^{-1}\phi_j$ for TE waves and $\gamma_j = k_0 \tilde{n}_j^2 \phi_j^{-1}$ for TM waves.

The global transfer matrix M of the system formed by the two layer stack (air gap + thin film) is the product of the individual transfer matrices: $M = M_a \cdot M_f$ and the power reflection coefficient $R(\theta)$ of the stack surrounded by the prism and the substrate is given by

$$R(\theta) = \left| \frac{(m_{11} + m_{12}\gamma_s)\gamma_p - m_{21} - m_{22}\gamma_s}{(m_{11} + m_{12}\gamma_s)\gamma_p + m_{21} + m_{22}\gamma_s} \right|^2, \tag{2}$$

where θ is the incidence angle of the incoming wave, m_{ij} are the elements of M, and γ_s and γ_p are, respectively, the transversal component of the wave vector (γ_j factor) in the substrate and in the prism.

Measurements were performed with two different kinds of m-lines setups at 632.8 nm and in TE mode: one commercial setup from Metricon Corporation [17] in transmission configuration (see Fig. 1(a)) and one homemade setup in reflection configuration [18] (see Fig. 1(b)). However, since there is a total internal reflection on both faces of the prism in the latter device (see Fig. 1(b)), the two cases are identical. The incident wave is first refracted inside the prism, then reflected by the two layer stack, and finally refracted in the air before reaching the detector. Hence, the global reflectivity of the prism/film coupler is $T(\theta)_{a/p} R(\theta) T(\theta)_{p/a}$, where $T(\theta)_{a/p}$ and $T(\theta)_{p/a}$ are the classical transmittivity of the prism/air diopter:

$$\begin{cases} T(\theta)_{a/p} &= \frac{\sqrt{n_p^2 - n_a^2 \sin^2\theta}}{n_a \cos\theta} |t_{\mathrm{ap}}|^2 \\ T(\theta)_{p/a} &= \frac{n_a \cos\theta}{\sqrt{n_p^2 - n_a^2 \sin^2\theta}} |t_{\mathrm{pa}}|^2 \end{cases}, \tag{3}$$

where t_{ap} (respectively, t_{pa}) is the Fresnel transmission coefficient [19] of the air/prism diopter (respectively, prism/air), and n_p and n_a are the refractive index of prism and air.

To analyze real measurements, it is necessary to add a transfer function of the apparatus $H(\theta)$ to the calculated reflectivity:

$$R_{\mathrm{calc}}(\theta) = H(\theta) T(\theta)_{a/p} R(\theta) T(\theta)_{p/a}. \tag{4}$$

This transfer function contains all the variations of the detected intensity related to the measurement device; it is the ratio of the theoretical and experimental reflectivity without the loaded sample. $H(\theta)$ is determined by measuring the angular

reflectivity $R_0^{\text{meas}}(\theta)$ of the m-lines device when no sample is pressed against the prism. The theoretical angular reflectivity without sample $R_0^{\text{calc}}(\theta)$ is equal to $T(\theta)_{a/p}T(\theta)_{p/a}$. The transfer function is then $H(\theta) = R_0^{\text{calc}}(\theta)/R_0^{\text{meas}}(\theta)$. An example of transfer function and of a raw measured reflectivity and a reflectivity corrected by the transfer function is presented in Figs. 2(a) and 2(b).

3. Fitting by Genetic Algorithm of the Prism–Film Coupler Angular Reflectivity

Once the theoretical reflection function is calculated, one has to use a numerical procedure to adjust this function to the measured reflectivity. The free parameters of the model are the refractive index n, the extinction factor k, the thickness d of the film, and the thickness e of the air gap. The genetic algorithms are very well suited to solve this problem since they perform a random search in the parameters space with a weak dependency on initial values and their ability to find global minima. This is a key feature because most of the time one has very imprecise initial guesses on the thickness of the air gap and on the extinction coefficient.

Our fitting process uses a real coded genetic algorithm written by Yedder [20] based on a limited number of classical and efficient well-established operators for genetic algorithms [21]. Let us give an outline of its principle. First the searching space is framed for each parameter; bounds are arbitrarily chosen so that the parameters remain inside physically acceptable limits. To accelerate the convergence of the algorithm, it is possible to determine approximate values $\{n_0, d_0\}$ of the refractive index and the thickness of the film by solving the modal dispersion equation and by defining a narrower searching range for these parameters centered around n_0 and d_0. Once the searching space is defined, the algorithm works in three steps:

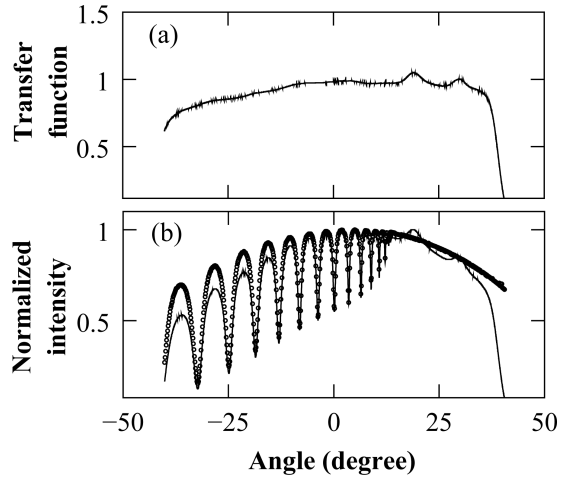

Fig. 2. (a) Transfer function of the Metricon prism-coupler, and (b) m-lines spectrum (TE mode) of a photoresist S1818 film: raw data (—) and corrected spectrum (○).

1. A starting population of two layers (thin film +air gap) is initialized; a population size of 10 is randomly created in the framed searching space.
2. An evaluation of the starting population is performed, the reflectivity R_{calc} of each individual is calculated, and its similarity to the measured reflectivity R_{meas} is evaluated with a least square estimator:

$$\sigma_m^2 = \sum_{i=1}^{N} N^{-1}[R_{\text{calc}}(\theta_i) - R_{\text{meas}}(\theta_i)]^2, \tag{5}$$

where N is the number of samples in the measured spectrum. The smallest is σ_m, the best is the individual, so this sigma is taken as the fitness of the fit.
3. A new population is created from the previous offspring by the following operators:

- Selection: a part of the best individuals are chosen, but some individuals with bad performance (i.e., high value of σ_m) can be kept; the selection is made by stochastic roulette [22,23].
- An elitism function was used to choose the best of two consecutive generations [24].
- A niching function was used to promote the full searching range exploration [25].
- A sigma scaling technique was used to avoid the selection of a single very good solution and consequently convergence of the algorithm was too rapid [26].
- A mutation operator, which is from a nonuniform type, and with a "simulated binary crossover" (SBX) type crossing [27].

Steps 2 and 3 are iterated until the fitness σ_m becomes smaller than a given value, and the maximum number of offspring is limited to 50,000 to limit the calculation time. A detailed description of all these procedures can be found in [20].

To test the efficiency of the method, numerical tests were realized. A score of m-lines spectra were simulated using the transfer matrix method by varying each parameter one after another around the configuration $n = 2.15$, $k = 0.005$, $d = 1.25\mu$m, and $e = 125$ nm. The refractive indexes of the prism and the substrate were, respectively, equal to 2.9 and 1.5. The simulated spectra were used as input data for the genetic algorithm. The program was stopped as soon as σ_m became smaller than 10^{-4}. The relative differences between the values obtained with the genetic algorithm and the theoretical one are summarized in Table 1.

A good agreement was found between the initial starting values of simulation and the results given by the genetic algorithm program. The parameters n and d are better reconstructed than the air gap thickness e and the extinction factor k, because they have a dominating influence on the shape of the angular reflectivity $R_{\text{calc}}(\theta)$. The errors on these parameters, respectively, Δn and Δd, are of the same

Table 1. Errors on Paramaters Retrieved by the Genetic Algorithm for the Simulated Spectra; Subscript th Denotes the Theoretical Values

	Δn ($\times 10^{-4}$)	Δk ($\times 10^{-4}$)	Δd (nm)	Δe (nm)	σ_m ($\times 10^{-5}$)
n_{th}					
1.900	0.9	0.1	0.1	0.1	2.8
2.025	0.9	0.1	0.1	0.0	3.5
2.150	1.1	0.3	0.2	0.3	9.0
2.275	0.7	0.6	0.1	0.0	7.0
2.400	0.2	0.0	0.0	0.2	6.0
k_{th}					
0.0010	0.0	0.1	0.0	0.3	6.2
0.0125	4.2	4.1	0.7	0.4	9.9
0.0250	25.8	1.3	4.3	0.2	9.5
0.0370	19.3	4.1	2.8	0.0	1.1
0.0500	53.9	5.1	8.5	0.4	8.8
d_{th}					
0.500	0.6	0.2	0.0	0.3	6.0
0.875	1.5	0.1	0.2	0.2	5.8
1.250	1.7	1.1	0.2	0.2	7.0
1.625	2.8	0.6	0.6	0.2	6.3
2.000	3.1	0.2	0.9	0.0	8.1
e_{th}					
50.00	0.2	0.0	0.0	0.0	9.0
87.50	0.2	0.1	0.0	0.1	9.0
125.00	0.4	0.3	0.1	0.1	9.0
162.50	0.3	0.3	0.2	0.3	2.0
200.00	0.5	0.6	0.1	0.2	3.0

order as σ_m; Δn remains smaller than 10^{-4} and Δd smaller than 1 nm. However, for $k > 0.025$: Δn reaches $5.4\,10^{-3}$ and Δd is about 9 nm. This can be explained by the fact that spectra become flatter when the k values increase. The reconstructed k and e are less accurate; however the error on e remains smaller than 0.5% in relative value, and the error on k is generally smaller than 0.5% and never exceeds 3.3%. These results demonstrate that the genetic algorithm is able to retrieve the characteristics of a thin film with a remarkable accuracy.

4. Results and Discussion

To validate our procedure experimentally, we measured the m-lines spectrum of different samples: films of photoresist S1818 [28] spin coated on silicon substrates ($\tilde{n}_{\text{silicon}} = 3.9190 + i0.0123$ [29]), films of ZnO:Al deposited by rf magnetron sputtering on glass substrates Corning 1737F ($\tilde{n}_{1737\text{F}} = 1.5172 + i0.0$), and an indium tin oxide (ITO) layer on glass substrate ($\tilde{n}_{\text{glass}} = 1.5157 + i0.0$) from Präzisions Glas & Optik GmbH [30]. Atomic force microscope (AFM) measurements showed that the samples have a small roughness (≤ 4 nm) and no correlation length at the scale of the wavelength of measurement. Using the theory of light scattering by rough surface developed by Bennet and Porteus [31] and Davies [32] and taking into account our experimental roughness we have calculated that the total scattered light by surface is $< 1\%$ of total reflected light. We conclude that the losses due to surface scattering can then be neglected in the following given results.

The measured spectra and the fits obtained with the genetic algorithm are shown in Figs. 4–6. The reconstructed parameters with uncertainties in confidence limits of 95% are summarized in Tables 2 and 3. Because of the fitting procedure with the genetic algorithm, a classical certainty calculation by differentiation of a modal equation was not possible. The certainty analysis was performed by Monte Carlo simulations. First the experimental noise distribution (Fig. 3) was measured. This distribution follows a normal law with a standard deviation of 1%. Then, for each measurement, a Gaussian noise with standard deviation corresponding to the experimental one was added to several hundreds of spectra simulated with parameters given by the fit. All noisy spectra were fitted with the genetic algorithm leading to the distributions of values of the parameters. As these distributions followed normal laws, we used twice the standard deviation (confidence interval of 95%) as the uncertainty for each parameter.

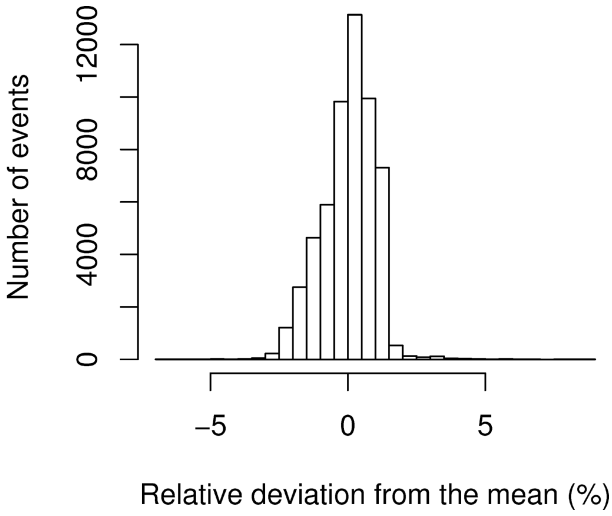

Fig. 3. Distribution of experimental noise.

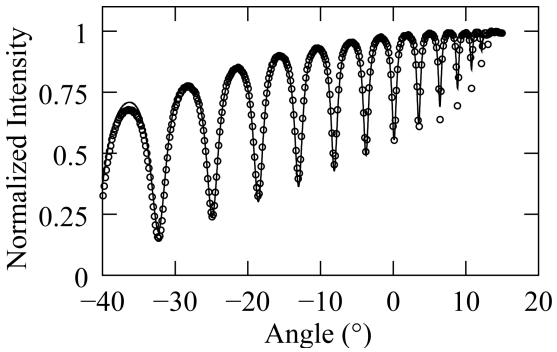

Fig. 4. Measured (○) and fitted (—) m-lines spectra of an S1818 film on silicon in TE mode.

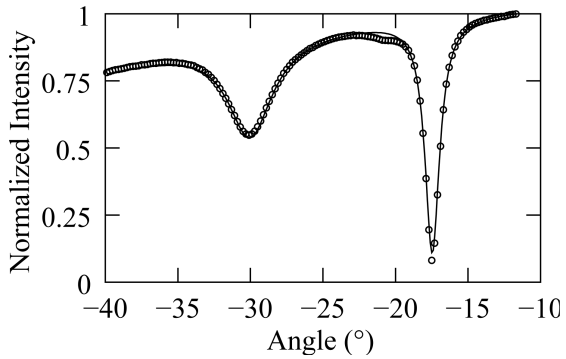

Fig. 5. Measured (○) and fitted (—) m-lines spectra of different ZnO film on glass in TE mode.

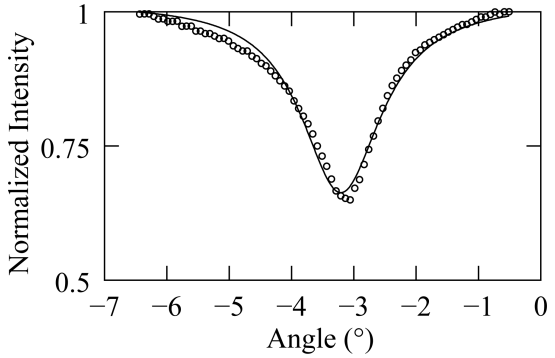

Fig. 6. Measured (○) and fitted (—) m-lines spectra of different ITO film on glass in TE mode.

The S1818 spectra (Fig. 4) were obtained with the Metricon setup and contain leaky modes, whereas the ZnO spectra (Fig. 5) were obtained with the homemade m-lines setup and are composed of guided modes. Both kinds of spectra are very well reproduced by the genetic algorithm; the fitness σ_m is of the order of 10^{-3}. There is also a good agreement between the refractive indices and the thicknesses given by the genetic algorithm and the classical m-lines analysis based on the resolution of the modal dispersion equations. The differences on the refractive index are of the order of 10^{-3}, and the differences on the thickness are generally close to 50 nm but can reach 400 nm. Let us emphasize that we do not expect a perfect matching between the values given by the two methods since the classical analysis makes the assumption that there is no absorption inside the film. So, taking into account the uncertainties of both methods, the observed differences are in the acceptable range. The effective extinction factor of the resist S1818 was found to be close to 2.10^{-3} and in the case of the ZnO between 7.10^{-4} and 3.10^{-3} depending on the sample. These effective extinction factors of ZnO are in accordance with published values [33,34].

The third kind of sample, ITO layer on glass substrate, reveals another advantage of the method: it is also available when only one mode is measured, which is the case in a thin layer or in a small difference of refractive indexes between the layer and substrate. To calculate the two researched values n and d from the spectrum of Fig. 6 using the classical m-lines analysis, one has to use *a priori* information. In the present case, the thickness was assumed equal to 180 nm from the provider data to determine the refractive index. Such an *a priori* statement was not necessary with the genetic algorithm procedure. The fitted curve obtained in this way is plotted in Figs. 2(a) and 2(b) together with the measured spectrum, and a small fitness of 6.10^{-4} was found. There is a good agreement between the refractive index found by the classical method and the refractive index given by the genetic algorithm (GA) method. The effective extinction factor $k = 0.015$ is in accordance with values commonly found for commercially available ITO [35].

5. Conclusion

In this paper, we have presented a method based on the transfer matrix formalism and a genetic algorithm to retrieve the optical and geometrical characteristics of a thin film from its m-lines spectrum and have shown its accuracy. The main interest of this method is that it not only gives the refractive index and the thickness of the film but also its effective extinction factor or optical losses. We restricted ourselves to layers with a negligible surface roughness to be able to compare the measurement of extinction factors with values found in literature; the investigation on the surface roughness effect will be the purpose of another paper. This technique does

Table 2. Characteristics of Different Thin Films Obtained with the GA and a Resolution of the Modal Dispersion Equations (MDE)

	n		d (μm)	
Sample	GA	MDE	GA	MDE
S1818 #1	1.640 ± 2.10^{-3}	1.6401 ± 1.10^{-4}	3.407 ± 9.10^{-3}	3.80 ± 2.10^{-2}
S1818 #2	1.638 ± 2.10^{-3}	1.6381 ± 1.10^{-4}	3.408 ± 9.10^{-3}	3.41 ± 2.10^{-2}
S1818 #3	1.639 ± 2.10^{-3}	1.6387 ± 1.10^{-4}	3.281 ± 9.10^{-3}	3.28 ± 2.10^{-2}
ZnO #1	1.9310 ± 4.10^{-4}	1.934 ± 1.10^{-3}	0.870 ± 3.10^{-3}	0.839 ± 3.10^{-3}
ZnO #2	1.920 ± 4.10^{-4}	1.930 ± 1.10^{-3}	0.904 ± 3.10^{-3}	0.832 ± 3.10^{-3}
ZnO #3	1.8600 ± 4.10^{-4}	1.861 ± 1.10^{-3}	0.587 ± 3.10^{-3}	0.554 ± 3.10^{-3}
ITO	1.80 ± 3.10^{-2}	1.78 ± 3.10^{-2}	0.17 ± 2.10^{-2}	$0.180.18 \pm 2.10^{-2}$

Table 3. Characteristics of Different Thin Films Obtained with the GA and a Resolution of the MDE

Sample	k	e (μm)	σ_m
S1818 #1	$0.0028 \pm 7\,10^{-4}$	$0.105 \pm 5\,10^{-3}$	$8\,10^{-4}$
S1818 #2	$0.0012 \pm 7\,10^{-4}$	$0.145 \pm 5\,10^{-3}$	$3\,10^{-4}$
S1818 #3	$0.0021 \pm 7\,10^{-4}$	$0.152 \pm 5\,10^{-3}$	$3\,10^{-4}$
ZnO #1	$0.00067 \pm 6\,10^{-5}$	$3.3\,10^{-2} \pm 2\,10^{-3}$	$2\,10^{-3}$
ZnO #2	$0.00071 \pm 6\,10^{-5}$	$1.7\,10^{-3} \pm 2\,10^{-3}$	$2\,10^{-3}$
ZnO #3	$0.00260 \pm 6\,10^{-5}$	$2.7\,10^{-2} \pm 2\,10^{-3}$	$1\,10^{-3}$
ITO	$0.015 + 1\,10^{-2}$	$0.19 + 0.17$	$6\,10^{-4}$

not allow us to distinguish the physical origin of optical losses between surface or volume scattering or intrinsic absorption, but it is efficient to determine which layers are more or less lossy and then to qualify films with low losses for development of advanced photonic devices. Moreover, this determination can be done in the same manner for either guided or leaky modes, and it can even be performed if only one mode is present in the spectrum. Last, since the matrix formalism allows calculating reflectivity of more complex stacks of layers, our genetic algorithm method could be easily extended to the case of bilayer or trilayer systems, which are of special interest in the fabrication of photonic components.

The authors thank John Jackson from Metricon Corporation for setup support and to Anand Srinivasan for AFM measurements.

References

1. X. J. Zhang, X. Z. Fan, J. Liao, H. T. Wang, N. B. Ming, L. Qiu, and Y. Q. Shen, "Propagation properties of a light wave in a film quasiwaveguide structure," J. Appl. Phys. **92**, 5647–5657 (2002).
2. H. Wang, T. Aruga, and P. Ye, "Theory and properties of quasiwaveguide modes," Appl. Phys. Lett. **69**, 611–613 (1996).
3. F. Abeles, "Methods for determining optical parameters of thin films," Prog. Opt. **2**, 248–288 (1963).
4. J. C. Manifacier, J. Gasiot, and J. P. Fillard, "A simple method for the determination of the optical constants n, k and the thickness of a weakly absorbing thin film,". J. Phys. E **9**, 1002–1004 (1976).
5. J. C. Martínez-Antón, "Determination of optical parameters in general film substrate systems: a reformulation based on the concepts of envelope extremes and local magnitudes," Appl. Opt **39**, 4557–4568 (2000).
6. J. M. Bennett, E. Pelletier, G. Albrand, J.-P. Borgogno, B. Lazarides, C. K. Carniglia, R. A. Schmell, T. H. Allen, T. Tuttle-Hart, K. H. Guenther, and A. Saxer, "Comparison of the properties of titanium dioxide films prepared by various techniques," Appl. Opt. **28** 3303–3317 (1989).
7. R. M. A. Azzam, "Return-path ellipsometry and a novel normal-incidence null ellipsometer (NINE)," J. Mod. Opt. **24**, 1039–1049 (1977).
8. A. Bashara, *Ellipsometry and Polarized Light* (Academic, 1977).
9. H. G. Tompkins and W. A. McGahan, *Spectroscopic Ellipsometry and Reflectometry: A User's Guide* (Academic, 1999).
10. F. Flory, D. Endelema, E. Pelletier, and I. J. Hodgkinson, "Anisotropy in thin films: modeling and measurement of guided and nonguided optical properties: application to TiO 2 films," Appl. Opt **32**, 5649–5659 (1993).
11. H. Rigneault, F. Flory, and S. Monneret, "Nonlinear totally reflecting prism coupler: thermomechanic effects and intensity-dependent refractive index of thin films," Appl. Opt **34**, 4358–4369 (1995).
12. P. K. Tien and R. Ulrich, "Theory of prism-film coupler and thin-film light guides," J. Opt. Soc. Am **60**, 1325–1337 (1970).
13. R. Ulrich, "Theory of the prism-film coupler by plane-wave analysis," J. Opt. Soc. Am **60**, 1337–1350 (1970).
14. S. Garcia-Blanco, E. Alfaro-Cid, R. M. De La Rue, and J. S. Aitchison, "Genetic algorithm-based characterization of the optical properties of flame-hydrolysis deposited silica waveguides," J. Lightwave Technol. **22**, 2801–2807 (2004).
15. J. Chilwell and I. Hodgkinson, "Thin-films field-transfer matrix theory of planar multilayer waveguides and reflection from prism-loaded waveguides," J. Opt. Soc. Am. A **1**, 742–753 (1984).
16. M. Born and E. Wolf, *Principles of Optics* (Academic, 1980).
17. Metricon Corporation, http://www.metricon.com/.
18. J. Cardin, D. Leduc, T. Schneider, C. Lupi, D. Averty, and H. W. Gundel, "Optical characterization of PZT thin films for waveguide applications," J. Eur. Ceram. Soc. **25**, 2913–2916 (2005).
19. P. Yeh, *Optical Waves in Layered Media* (Academic, 1988).
20. A. B. H. Yedder, "Optimisation numerique et controle optimal: (applications en chimie moleculaire)," Ph.D. dissertation (Ecole Nationale des Ponts et Chaussees 2002).
21. Z. Michalewicz, *Genetic Algorithms+ Data Structures= Evolution Programs* (Academic, 1996).
22. K. Deb, "Genetic algorithm in search and optimization: the technique and applications," in *Proceedings of International Workshop on Soft Computing and Intelligent Systems* (Academic, 1998), pp. 58–87.
23. K. Deb, Genetic Algorithms for Optimization, KanGAL Report No. 2001002, (KanGal, 2001).
24. V. S. Gordon and D. Whitley, "Serial and parallel genetic algorithms as function optimizers," in *Proceedings of the Fifth International Conference on Genetic Algorithms* (Academic, 1993), pp. 177–183.
25. S. W. Mahfoud, "Niching methods for genetic algorithms," Ph. D. dissertation (University of Urbana, 1995).
26. P. J. B. Hancock, "An empirical comparison of selection methods in evolutionary algorithms," in *Evolutionary Computing: AISB Workshop, Leeds, UK*, (Academic, 1994), selected papers.
27. K. Deb and R. B. Agrawal, "Simulated binary crossover for continuous search space," in *Complex Systems* (Academic, 1995), pp. 115–148.
28. Microchem Corporation, http://www.microchem.com/products/su_eight.htm.
29. S. Adachi, "Model dielectric constants of Si and Ge," Phys. Rev. B **38**, 12966–12976 (1988).
30. Präzisions Glas & Optik GmbH, http://www.pgo-online.com/.

31. H. E. Bennett and J. O. Porteus, "Relation between surface roughness and specular reflectance at normal incidence," J. Opt. Soc. Am, **51**, 123–129 (1961).
32. H. Davies, "The reflection of electromagnetic waves from a rough surface," in *Proceedings of the Institution of Electrical Engineers* (Academic, 1954), 209–214.
33. E. Dumont, B. Dugnoille, and S. Bienfait, "Simultaneous determination of the optical properties and of the structure of rf-sputtered ZnO thin films," Thin Solid Films **353**, 93–99 (1999).
34. M. Rebien, W. Henrion, M. Bär, and C. H. Fischer, "Optical properties of ZnO thin films: ion layer gas reaction compared to sputter deposition," Appl. Phys. Lett. **80**, 3518–3520 (2002).
35. S. Laux, N. Kaiser, A. Zöller, R. Götzelmann, H. Lauth, and H. Bernitzki, "Room-temperature deposition of indium tin oxide thin films with plasma ion-assisted evaporation," Thin Solid Films **335**, 1–5 (1998).

Towards an optimum coupling between Er ions and Si-based sensitizers for integrated active photonics

K. Hijazi, R. Rizk,[a] J. Cardin, L. Khomenkova, and F. Gourbilleau
Centre de Recherches sur les Ions Matériaux et Photonique (CIMAP), Unité Mixte de Recherche CNRS/CEA/ENSICAEN/Université de Caen, 6 Boulevard du Maréchal-Juin, 14050 Caen Cedex, France

(Received 16 February 2009; accepted 19 June 2009; published online 27 July 2009)

Series of Er-doped Si-rich silicon oxide layers were studied with the aim of optimizing the coupling between Er ions and the Si-based sensitizers. The layers were grown at substrate temperature between 400 and 600 °C by the cosputtering of three confocal targets: Si, SiO_2, and Er_2O_3. The influence of Si excess (5–15 at. %) and annealing temperature (500–1100 °C) was examined for two concentrations of Er ions (3.5×10^{20} and $\sim10^{21}$ cm^{-3}). We report the first observation of significant Er photoluminescence (PL) from as-grown samples excited by a nonresonant 476 nm line, with a lifetime in the range of 1.3–4 ms. This suggests the occurrence of an indirect excitation of Er through Si-based entities formed during the deposition. A notable improvement was observed for both Er PL intensity and lifetime after annealing at 600 °C. This temperature is lower than that required for phase separation, suggesting the formation of "atomic scale" sensitizers (Si agglomerates, for example) considered in recent work. For high Er doping ($\sim10^{21}$ cm^{-3}), an optimum Er PL was obtained for the sample grown at 500 °C, annealed at 600 °C, and containing ~13 at. % of Si excess. This high PL should correspond to an optimum fraction of coupled Er for this series, which was roughly estimated to about 11% of the total Er content for an excitation photon flux of few 10^{19} ph cm^{-2} s^{-1}. For the moderately Er-doped series (3.5×10^{20} cm^{-3}) grown at 500 °C, the optimum Er PL was found for the samples containing about 9 at. % silicon and annealed in the 600–900 °C range. The time decay reached a value as high as 9 ms for low Si excess (<6 at. %) and 6–7.5 ms for high values of Si excess. The fraction of Er ions coupled to sensitizers was similarly estimated for the best sample of this series and found to be as high as 22% of the total Er content. © *2009 American Institute of Physics*. [DOI: 10.1063/1.3177243]

I. INTRODUCTION

Silicon-based nanostructured materials have been investigated for a number years with the aim of providing silicon compatible light sources operating at room temperature for optoelectronic and photonic applications.[1,2] Two main approaches have been explored during the past two decades: visible emission from porous silicon or silicon nanocrystals (Si-nc) and infrared emission (at 1.5 μm) from Er-doped silica-based compounds. For the former, a broad emission is usually observed around 700–800 nm that is generally attributed to the recombination of excitons confined within the nanocrystals subject to quantum size effects,[3] with some contribution from interface states.[4] The 1.5 μm emission corresponding to the $^4I_{13/2}\rightarrow{}^4I_{15/2}$ transition of the Er ions corresponds to the low-loss window in silica optical fibers and has therefore been adopted as a standard wavelength for the optical communications. Consequently, special interest has been paid since many years to the indirect excitation of the Er ions through the Si nanoclusters (Si-nc).[5–11] Indeed, the large absorption cross section of Si-nc has been found to be highly beneficial to the enhancement of the *effective* excitation of Er ions by three to four orders of magnitude[8,11] with respect to that for the direct excitation of Er in silica ($\sim10^{-20}$–10^{-21} cm^2).[12] Additional advantages can be gained from the incorporation of Si-nc into Er-doped silica, such as an increase in the refractive index with respect to the silica cladding for better confinement of light and the ability of the Si-rich system to enable injection and transport of carriers for electrical excitation. These advantages pave the way to the development of compact Si-based photonic devices such as erbium-doped waveguide amplifiers which might be excited either electrically or optically by broad-band low-cost source instead of the expensive high pump laser required for Er-doped silica materials.

The sensitizing effect has been found to be efficient for both crystalline and amorphous Si-nc, provided that their diameter is less than 4 nm,[13] and the nanocluster-erbium separation is less than 0.5–1 nm.[13,14] This very short interaction distance is considered as the main limiting factor for the fraction of Er ions coupled to Si-nc, which was estimated recently to be below 2%.[15] Earlier works[16] reported similar low values for the proportion of coupled Er. Recent studies[17,18] claimed, however, that such a low fraction concerns only those ions benefiting from an energy transfer via interband transitions in the silicon nanoclusters. According to these studies, other Er ions representing about 50% of the total Er content are also coupled but are excited by an energy transfer via intraband transitions in the silicon nanoclusters to the first excited state of Er ions. These ions can therefore suffer from Auger backtransfer. We have reported recently[19] careful analyses of these detrimental effects, which were

[a]Author to whom correspondence should be addressed. Electronic mail: richard.rizk@ensicaen.fr.

found not to be significant in our samples.

The purpose of this study is to optimize the material with the aim of maximizing the fraction of Er ions coupled to Si-based sensitizers. This requires some nanoengineering of the layer composition through the growth of a high density of very small Si-based sensitizer entities to enhance the probability of their coupling with the Er ions. Series of layers were grown by magnetron cosputtering and subsequently annealed before being submitted to various structural and optical characterizations. The effects of Si excess, annealing temperature, substrate temperature and, to some extent, Er content have been examined.

II. EXPERIMENTAL DETAILS

Er-doped Si-rich silicon oxide (Er-SRSO) layers were grown onto *p*-type (100) Czochralski grown silicon substrates (5–15 Ω cm) by magnetron cosputtering of three confocal cathodes: Si, SiO_2, and Er_2O_3. The Er content and Si excess in the layers were finely controlled by individual and separate tuning of the power applied to each cathode. The rf power density applied to the Si cathode (P_{Si}^{rf}) was, therefore, varied between 0.75 and 2.07 W cm^{-2}, while that applied to the Er_2O_3 target ($P_{Er_2O_3}^{rf}$) was tuned either at 0.45 or 0.75 W cm^{-2}. For good homogeneity of both composition and thickness (1–1.5 μm), the depositions were made on a rotating substrate maintained at a temperature (T_S) between 400 and 600 °C, under a plasma of pure argon kept at a pressure of 3 mTorr. After deposition, the samples were annealed for a typical duration of 1 h in flowing nitrogen, at different annealing temperatures T_a between 500 and 1100 °C. For the sake of comparison, a reference sample (labeled R) is also considered in this study, obtained earlier by the reactive sputtering of a single SiO_2 cathode topped by Er_2O_3 chips, as described elsewhere.[11,15] This sample R contains about 7 at. % of Si excess and $\sim 4\times10^{20}$ cm^{-3} of Er and was annealed at 900 °C under similar conditions to the other samples (1 h in N_2 flux).

To investigate the structural properties and get a rough estimate of the Si excess, Fourier transform infrared (FTIR) spectra were recorded under Brewster (65°) and normal incidence, using a Nicolet Nexus spectrometer. The Er content was determined by energy dispersive x-ray spectroscopy (EDX) using an Er-implanted sample as a reference. The refractive index (n) and thickness of the layers were obtained by M-line measurements performed in reflection configuration.[20–22] These measurements were made by means of a He–Ne laser operating at 632.8 nm (1.95 eV) polarized in transverse electric (TE) mode. The photoluminescence (PL) properties of Er ions were examined using the nonresonant 476 nm excitation line delivered by an Ar^+ laser. The pumping at 476 nm was always used to ensure that Er excitation was mediated by the Si-based sensitizers. The Er PL was measured by means of a Jobin Yvon 1 m single grating monochromator coupled to a Northcoast germanium detector cooled with liquid nitrogen. The PL signal was recorded through a SRS lock-in amplifier (SP830 DPS) referenced to the chopping frequency of light of 20 Hz. The time-resolved Er PL was measured with the PL system already described, the signal being displayed on a Tektronix oscilloscope (TDS 3012B).

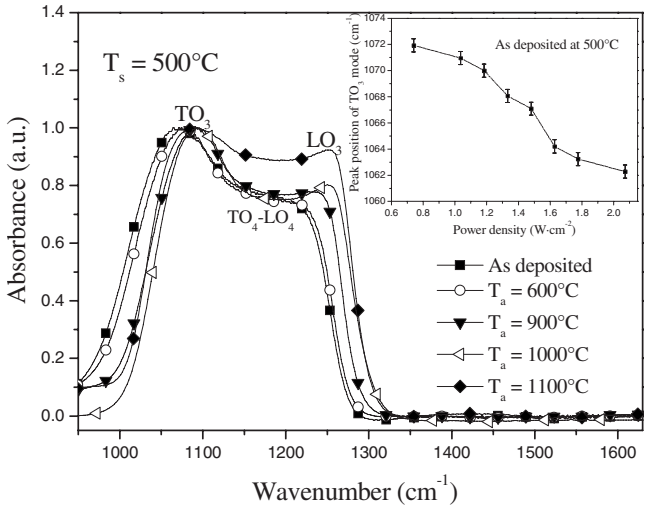

FIG. 1. Infrared absorption spectra of the layers deposited at T_S=500 °C, before and after annealing at the indicated annealing temperature T_a, as recorded at Brewster angle. The inset shows a typical shift of the TO_3 peak position for the as-grown sample at 500 °C, in function of the power density applied on the Si target.

III. RESULTS AND DISCUSSION

After a rough estimate of the Si excess in our films which will be briefly commented on, we will describe and discuss successively the influence of the Si excess, annealing temperature, substrate temperature, and, to some extent, the impact of the Er concentration on the Er PL properties. The evaluation of the fraction of Er coupled to Si-based sensitizers will follow for the two concentrations of Er considered in this study.

A. Estimate of the Si excess

Figure 1 shows a typical evolution of the FTIR spectra with the annealing temperature for the sample deposited at 500 °C with the power densities P_{Si}^{rf}=1.77 W/cm^2 and $P_{Er_2O_3}^{rf}$=0.74 W cm^{-2}. These spectra were recorded at Brewster incidence to avoid any reflection and detect the longitudinal optical mode (LO_3) associated with the Si–O–Si 180° bond around 1250 cm^{-1}.[23] This mode is therefore characteristic of the Si/SiO_2 interface and may reflect some phase separation between Si and SiO_2. For the sake of clarity, the amplitude of the LO_3 mode is normalized in the figure with respect to that of the transverse optical (TO_3) mode at about 1080 cm^{-1}. The LO_3 mode appears as an increasing function of the annealing temperature, showing a gradual evolution toward some phase separation with the appearance of pure silicon in the SiO_2 matrix. The as-deposited film and that annealed at 600 °C show similar spectra and do not contain detectable amounts of the pure silicon phase. The phase separation starts to take place after annealing at 900 °C and becomes quite pronounced after the thermal treatment at 1100 °C. In this latter case, *crystallized* Si-ncs have been observed in our previous works by conventional electron

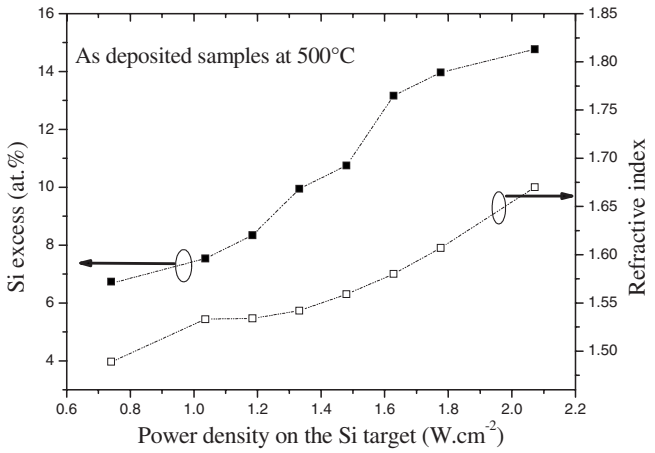

FIG. 2. Typical evolution of both Si excess and refractive index in function of the power density applied on the Si target, for the sample deposited at 500 °C.

transmission microscopy,[11] while the formation of amorphous Si-nc within SiO_2 matrices at $T_a \sim 900$ °C has been demonstrated by other groups.[9,10] On the other hand, the doublet TO_4-LO_4 appears to be still overlapping, which reflects a high degree of disorder, likely due to the high amount of Si excess corresponding to $P_{Si}^{rf}=1.77$ W/cm^2.

The amount of Si excess incorporated in the film grown with a given value of P_{Si}^{rf} has been roughly estimated from the evolution of the TO_3 mode of the FTIR spectra recorded at normal incidence on the as-deposited samples. The inset of Fig. 1 shows, indeed, a gradual shift of the peak position of TO_3 mode toward lower wavenumbers when P_{Si}^{rf} increases. A specific analysis of this evolution described in Ref. 23 allows a rough estimate of the corresponding Si excess. The method adopted for the determination of Si excess is based on a linear correlation between the frequency of the TO_3 mode for a substoichiometric SiO_x $(1<x<2)$ matrix and the stoichiometric coefficient $x=2$.[24,25] The linear relation is that used by Hinds *et al.*[25]—$x=0.02\nu-19.3$—with ν representing the asymmetric stretching mode (in cm^{-1}) of Si–O–Si.[26] Thus, the gradual shift of TO_3 peak reflects an increase in the Si excess from about 7 at. % for the lowest P_{Si}^{rf} to nearly 15 at. % for $P_{Si}^{rf}=2.07$ W cm^{-2} (Fig. 2). Our FTIR approach may underestimate the amount of Si excess since it does not take into account the Si sensitizers formed during the growth process, which constitute a volume fraction of pure silicon. As will be evidenced and discussed below, such sensitizers are actually grown at relatively high temperature ($T_S=500$ °C), and an alternative technique such as x-ray photoelectron spectroscopy (not available to us) is necessary. However, regardless of the exact value of Si excess that should be considered as indicative of the corresponding P_{Si}^{rf}, there is a clear systematic increase in Si excess with P_{Si}^{rf}. This trend is corroborated by a concomitant progressive rise of the refractive index, as determined by M-line measurements (Fig. 2). The concentrations of Er content corresponding to the two values of $P_{Er_2O_3}^{rf}$ (0.44 and 0.74 W cm^{-2}) were determined by EDX measurements (confirmed by SIMS analyses made elsewhere) and were found to be close to 3.5×10^{20} and $\sim1\times10^{21}$ at./cm^3, respectively.

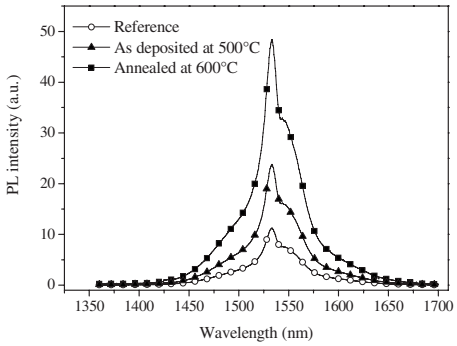

FIG. 3. Comparison of three PL spectra recorded on two samples deposited at 500 °C, before and after annealing at 600 °C, and a reference sample previously described in Refs. 11 and 15 and obtained by reactive cosputtering of a single silica layers topped by Er_2O_3 chips.

Figure 3 compares the PL spectra recorded from three samples excited by a nonresonant laser line (476 nm) at a flux of $\sim10^{19}$ ph cm^2 s^{-1}: two samples were grown at 500 °C and measured before and after annealing at T_a as low as 600 °C; the third sample is the reference sample R (described above). The first two samples contain relatively high concentrations of Si excess (13 at. %) and Er ($\sim1\times10^{21}$ at/cm^3); almost the double that of the reference sample (7 at. % and 4×10^{20} Er/cm^3) that was annealed at 900 °C. The heavily Er-doped samples were examined first with the aim of optimizing the concentration of the emitting centres, although their high Er content (10^{21} cm^{-3}) exceeds the threshold value ($\sim2\times10^{20}$ cm^{-3}) for upconversion.[8] Such detrimental effects were, however, minimized by using moderate excitation flux ($<10^{20}$ ph cm^2 s^{-1}). The case of lower Er concentration will be examined below.

From Fig. 3, we note that a significant Er PL is detected from the as-deposited sample, 50% higher than that from the R sample, with a lifetime of 1.3 ms. To our knowledge, such high PL induced by a nonresonant excitation, as well as such a long lifetime, has never been reported earlier from nonannealed samples. The Er PL is most likely stimulated by some sensitizers formed during the growth at relatively high temperature (400–600 °C). At this temperature, one should not expect the formation of large Si nanoclusters (even amorphous), but rather some Si agglomerates that could be compared to the "atomic scaled" sensitizers described recently by Savchyn *et al.*[27] for similarly sputtered samples annealed between 600 and 1100 °C. Such suggestions are supported by the fact that the FTIR spectrum of the as-deposited layer remains almost unchanged after annealing at 600 °C (see Fig. 1), indicating the absence of phase separation between amorphous Si domains and silica. This observation is corroborated by earlier studies[28,29] demonstrating that phase separation starts in these systems when T_a exceeds 650 °C. However, our annealing at 600 °C improves the Er emission by a factor of 2 (see Fig. 3) and also the lifetime (to 1.7 ms), likely due to the formation of additional atomic scale sensitizers and reduction of nonradiative channels (i.e., improvement of the matrix), respectively.

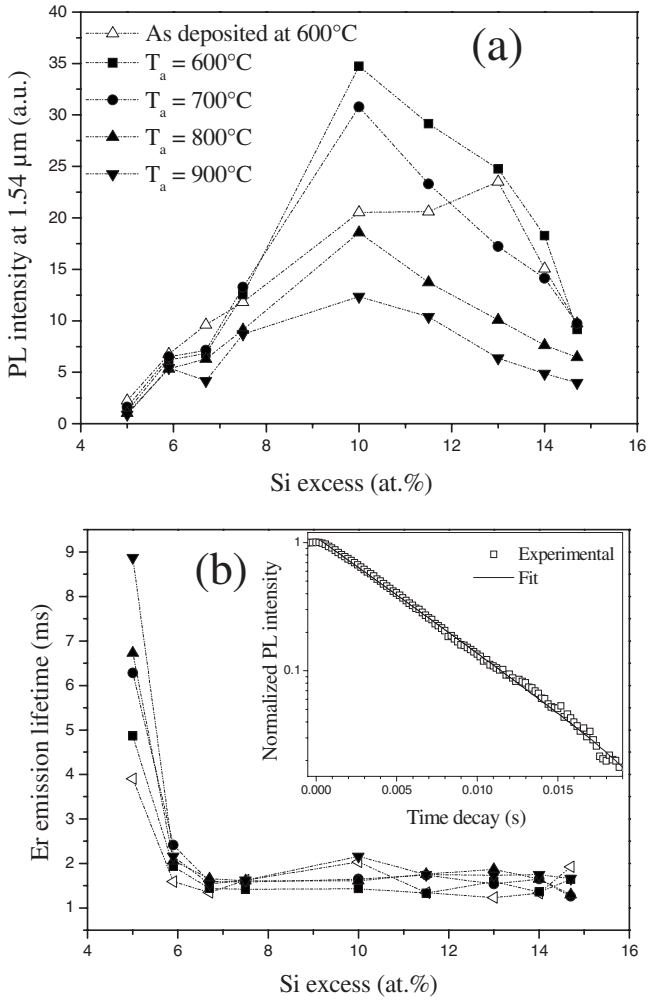

FIG. 4. (a) Variation of the Er PL intensity at 1.54 μm in function of the Si excess, for the as-deposited at 600 °C and annealing samples at the indicated temperatures T_a. (b) Evolution of the Er emission lifetime in function of Si excess, for the same samples described in (a). The inset shows typical decay of normalized Er PL. The full line is the single exponential fit of the experimental data.

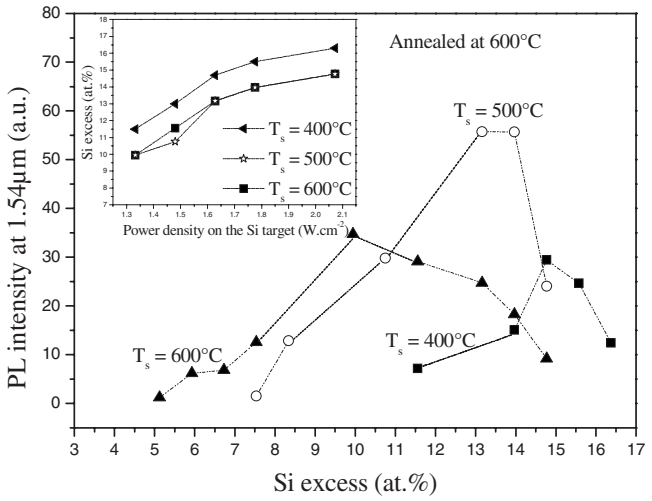

FIG. 5. Comparison of the variations of the Er PL intensity at 1.54 μm in function of Si excess, for the samples deposited at the indicated substrate temperatures and then annealed at 600 °C.

B. Effects of the Si excess and annealing temperature

Figure 4(a) shows a typical evolution of the PL intensity at 1.54 μm, I_{PL}, for the samples deposited at T_s=600 °C and annealed at the indicated temperatures, as a function of the Si excess. These spectra were recorded for nonresonant excitation (476 nm) with a photon flux of some 10^{19} ph cm^{-2} s^{-1}. The Er PL shows first an increase with the Si excess for all as-deposited and annealed samples, up to a maximum corresponding to about 10 at. % of Si excess, and then a decrease for higher values of Si excess. The highest I_{PL} is given by the sample annealed at 600 °C, for all values of Si excess. Since we are dealing with a concentration of Er ions of $\sim 10^{21}$ cm^{-3} in all these samples, this observation suggests that the fraction of Er coupled Si-nc is the highest after annealing at T_a=600 °C, in comparison with other T_a values. The proportion of coupled Er reaches a maximum for a Si excess of about 10 at. %, likely due to the formation of an optimum density of Si-based sensitizers that might consist either of atomic scale Si-based sensitizers for moderate T_a or Si-nc for high T_a. The atomic scale sensitizers can be compared to the luminescent centers (LCs) of Savchyn *et al.*[27] who consider these LCs as dominant sensitizer generators of excitons in Si-nc.[30] In our case, these sensitizers would start their growth during the deposition process on seeds available at the surface or near-surface region of the growing layer, with a density increasing with the Si excess until the seeds are saturated. When the value of Si excess is further increased, and/or T_a is raised, a coalescence phenomenon can be proposed that increases the average size of the sensitizers at the expense of their coupling with the Er ions.

The time-resolved studies of the above-described samples showed that the decay traces exhibit an exponential behavior. Within the experimental uncertainties, the typical plot shown in the inset of Fig. 4(b) is well fitted with a pure exponential function. The Er lifetime τ_{dec} showed a steep decrease from a value higher than 6 ms for a Si excess of about 5 at. % to 1–2 ms when the Si excess is higher than 7 at. %, as displayed in Fig. 4(b).

C. Influence of the substrate temperature

Similar effects of Si excess and annealing temperature were found for the series of samples deposited at T_S=500 and 400 °C. Using the same nonresonant excitation and photon flux as for Fig. 4(a), I_{PL} of these two series (T_S=400 and 500 °C) shows, similarly, an initial increase up to a maximum corresponding to a specific value of Si excess and then a decrease for high values of Si excess. The lifetime τ_{dec} ranges again between 1 and 2 ms when the Si excess exceeds 7 at. %, similarly to the set of samples deposited at T_S =600 °C. Again, the highest I_{PL} was observed for both series (T_S=400 and 500 °C) for the samples annealed at 600 °C, over the full range of Si excess. The unique difference lies in the shift of I_{PL} maximum toward high values of Si excess when T_S is decreased: from 10 at. % for T_S=600 °C to ~13 at. % for T_S=500 °C and to about 14.7 at. % for T_S =400 °C. This is shown in Fig. 5 which compares the evolution of I_{PL} as a function of Si excess for the samples deposited at the indicated T_S before being annealed at 600 °C. To explain this shift of maximum I_{PL}, we have looked for an

origin lying in the formation of different volume fractions of sensitizers (pure silicon phase) during the growth process at different T_S values. This should induce a T_S dependence for the FTIR-related Si excess and then accentuate the underestimate, as already mentioned. To shed some light on this aspect, we compare in the inset of Fig. 5 the amounts of the Si excess for the three T_S values. The highest values are those relating to T_S=400 °C, exceeding their counterparts for T_S=500 °C and T_S=600 °C by about 1.5 at. %, for all $P_{\mathrm{Si}}^{\mathrm{rf}}$. This observation is consistent with the expected formation of the lowest volume of Si sensitizers during the growth at the lowest T_S (400 °C). It could explain the shift of the 400 °C curve, whereas the quasiequivalent values of Si excess obtained for the T_S=500 and 600 °C cannot explain the shift of about 3 at. % between the curves. Other effects of T_S and Si excess should be therefore considered to explain the behavior of I_{PL} and describe the way of ensuring the highest proportion of coupled and optically active Er ions. The surface mobility of the adatoms and the growth of sensitizers on the seeds available at the surface are expected to be T_S dependent, in addition to their obvious dependence on the amount of Si excess. As already mentioned, these entities might be compared to the "atomic" scale sensitizers and their size and density are expected to evolve with the annealing.[27] The observation of the highest I_{PL} from the samples deposited at 500 °C, whether as-grown or annealed is the signature of optimum conditions allowing the achievement of a high proportion of coupled Er for a concentration as high as 10^{21} Er/cm^3.

D. Influence of the Er concentration

In this section we will examine the impact of lower concentrations of Er ions. An additional series of layers was grown with lower $P_{\mathrm{Er_2O_3}}^{\mathrm{rf}}$ value (0.44 W cm^{-2} instead of 0.75 W cm^{-2}) and slightly higher $P_{\mathrm{SiO_2}}^{\mathrm{rf}}$ (8.9 W cm^{-2} instead of 7.4 W cm^{-2}). This increase in silica sputtering aims to limit the Si excess to minimize loss due to confined carriers absorption.[31] A series of samples were deposited at T_s =500 °C and annealed between 600 and 1100 °C. Their Er content was $\sim 3.5\times 10^{20}$ cm^{-3}. The evolution of their I_{PL} as a function of Si excess for the as-deposited sample and those annealed at the indicated T_a values is shown in Fig. 6(a), similar to the plots displayed in Fig. 4(a) for the previous series (high Er content). The behavior of I_{PL} is generally analogous to that shown in Fig. 4(a), disregarding the values of T_a and Si excess corresponding to maximum I_{PL}: an initial increase until a maximum corresponding to a Si excess of about 9 at. % and then a decrease for higher values of Si excess. Within the measurement uncertainties, the samples annealed between 600 and 900 °C show almost the same I_{PL} with a slight increase at T_a=900 °C, with a sharp drop after annealing at 1100 °C. The earlier suggested explanations are still valid for this series: (i) the density of sensitizers (or their coupling rate with Er) increases first with the Si excess until the available seeds are saturated—which corresponds to maximum I_{PL}; (ii) then, for higher Si excess and/or T_a >900 °C, a coalescence phenomenon is expected to take place, as demonstrated elsewhere.[32] This should reduce the

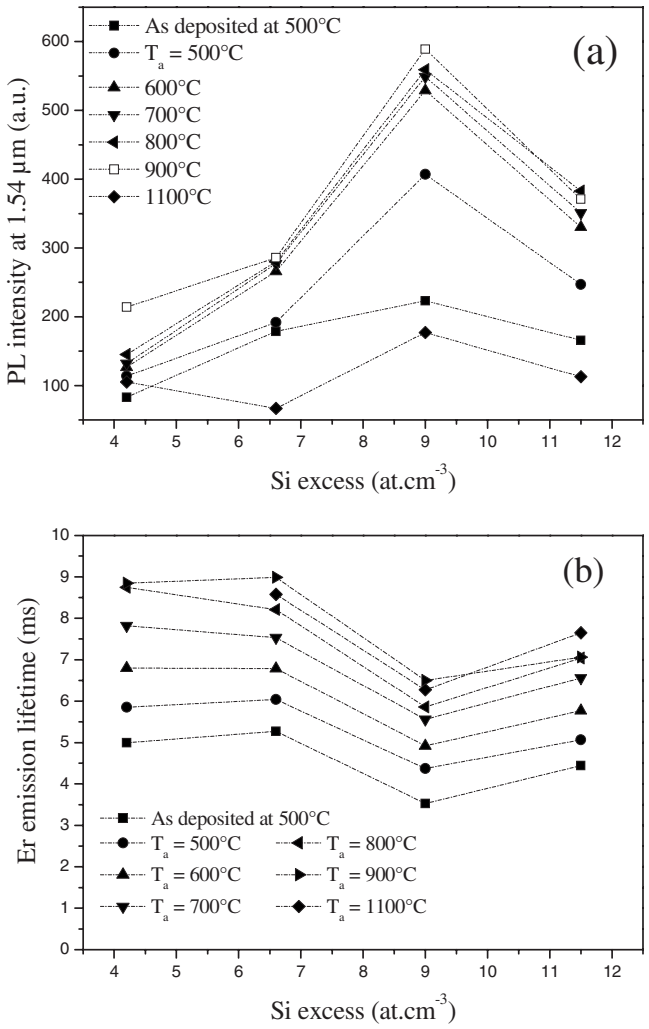

FIG. 6. (a) Variation of the Er PL intensity at 1.54 μm in function of Si excess, for the samples doped with 3.5×10^{20} Er/cm^3: as-deposited at 500 °C and annealing samples at the indicated temperatures T_a. (b) Variation of the Er emission lifetime in function of Si excess, for the samples of (a) as-deposited at 500 °C and annealed between 500 and 1100 °C.

density of the sensitizers (or their coupling rate with Er) and then explain the decrease in I_{PL}. The lower Si excess corresponding to the maximum of I_{PL} for this series can be understood as less Si is needed to couple to the lower Er content. On the other hand, the quasiconstant I_{PL} behavior for T_a between 600 and 900 °C can be attributed to the unchanged density of the sensitizer for this range of T_a, since further growth of the sensitizers by coalescence is expected to occur when T_a exceeds 900 °C. Only the matrix quality and consequently the emission lifetime are improved when T_a increases. Figure 6(b) shows the variation of the lifetime versus the Si excess for the indicated values of T_a. First, the improvement of the lifetime is confirmed for all amounts of Si excess, reaching a value as high as ~9 ms for Si excess <7 at. % and T_a=900. Second, for any T_a, the lifetime shows a certain decrease with the Si excess, which is clearly much smoother than the counterpart behavior of τ_{dec} shown in Fig. 4(b) for the heavily doped samples. Thus, for Si excess >7 at. % and T_a>600 °C, the values of the lifetime are still at a high level, between 6 and 7.5 ms, reflecting the fact that the nonradiative de-excitation processes are less than

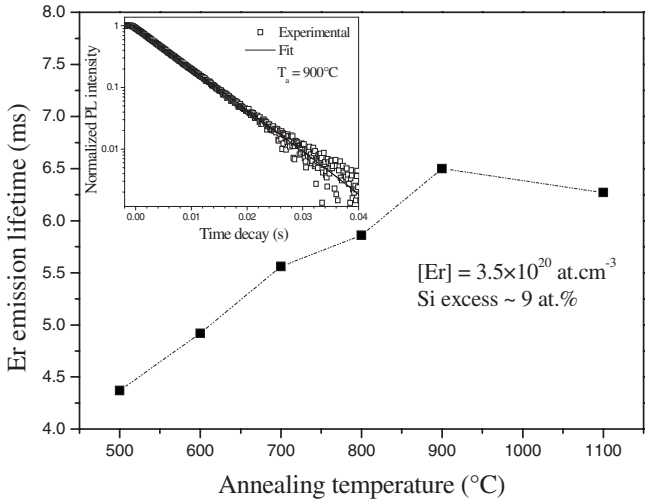

FIG. 7. Evolution of the Er emission lifetime in function of the annealing temperature for the sample deposited at 500 °C and containing 9 at. % of Si excess and 3.5×10^{20} Er/cm^3. The inset shows typical decay of normalized Er PL. The full line is the single exponential fit of the experimental data.

those in the highly Er-doped samples. Figure 7 displays a typical evolution of the lifetime with T_a for a given Si excess (9 at. %). The curve shows an improved lifetime when T_a increases from 500–600 to 900 °C, reaching a maximum of 6.5 ms, and then a slight decrease to 6.2 ms for T_a =1100 °C. The decay traces exhibited a pure exponential behavior, as shown by the typical plot reported in the inset of Fig. 7.

E. Evaluation of the fraction of Er coupled to sensitizers

We propose to estimate the fraction of Er coupled to the sensitizers for the best sample in each of the heavily and moderately Er-doped samples, labeled HD and MD, respectively. Their characteristics are reported in Table I, together with those of the already described sample R. We start by comparing the I_{PL} of the HD sample to that of sample R (see Fig. 3), both normalized to the excited volume by using the following equation:

$$I_{PL} \approx \sigma_{eff}\frac{\tau_{dec}}{\tau_{rad}}N_{Er,c}\varphi, \quad (1)$$

where σ_{eff} is the effective cross section of Er ions, $N_{Er,c}$ is the concentration of Er coupled to the sensitizers, φ is the photon flux, τ_{dec} is the decay time of Er ions, and τ_{rad} is the erbium radiative lifetime. As only 1.7% of Er ions were found coupled to sensitizers for the reference sample excited with a flux of few 10^{19} ph cm^{-2} s^{-1},[15] the value of its $N_{Er,c}$ is about 6.8×10^{18} cm^{-3}. The spectra were recorded with the same photon flux and we assume that τ_{rad} is $\propto n^2$ (n is the refractive index) owing to the importance of the local field effects in our nanocomposite material, as demonstrated in Ref. 33. In previous work,[34] the decay rate was found to increase with the refractive index n of the embedding medium where only variations in the mean field (instead of the local field) have been considered. Thus, using the n values reported in Table I for the HD and R samples, the values of τ_{rad} deduced from Ref. 33 are 9 and 12 ms, respectively (see Table I). By comparing their I_{PL} (3.7 times higher for the HD layer) and their characteristic data (Table I) in Eq. (1), one could estimate $N_{Er,c}$ for our HD sample to about 1.1×10^{20} cm^{-3}, i.e., nearly 11% of the total Er content ($\sim10^{21}$ cm^{-3}). This fraction is more than seven times higher than that of the R sample. It is also comparable to the fraction (11%–12%) reported for our other category of samples obtained by reactive sputtering of two confocal cathodes,[35] in spite of the detrimental effects expected from the high concentrations of both Er content and excess Si.

The high Er content ($\sim10^{21}$ at cm^{-3}) would produce prejudicial effects such as upconversion and concentration quenching phenomena, which become significant under photon fluxes much higher than that used here. This would lead, therefore, to a reduction of the gain, as was established in Ref. 36. On the other hand, the high Si excess needed to couple the maximum amount of the 10^{21} Er/cm^3 induces two main detrimental effects: (i) losses due to confined carrier absorption, as evidenced elsewhere for our samples[31] and which obviously increases with the Si excess and size of Si nanoclusters, (ii) an inherent increase in the density of defects, as reflected by the low lifetime (1.5–2 ms for Si excess >7 at. %) and the persistent disorder for any T_a value (TO_4-LO_4 doublet in Fig. 1).

Further comparisons were made for the two HD and MD samples of Table I: the best layers of the series of heavily ($\sim10^{21}$ cm^{-3}) and moderately (3.5×10^{20} cm^{-3}) doped with Er ions. Figure 8 shows the evolution of their I_{PL} as a function of the excitation photon flux φ. The Er PL shows the same intensity for both samples over all the range of φ, with an almost linear evolution. This is indicative of limited effects of concentration -related effects, although one may suspect some slight tendency toward saturation for HD sample. Nevertheless, the I_{PL} ratio as appears to be close to 1 when applying Eq. (1) for a rough estimate of the fraction of Er coupled to sensitizers in the MD sample. Using the values

TABLE I. Characteristics of the best samples in the heavily doped and moderaly Er-doped samples, labeled HD and MD, respectively. The reference R sample was obtained earlier by the reactive sputtering of a single SiO_2 cathode topped by Er_2O_3 chips, as described in Refs. 11 and 15. T_S: substrate temperature; n: refractive index; T_a: annealing temperature; τ_{dec}: time decay; τ_{rad}: radiative lifetime; σ_{eff}: effective excitation cross section.

Sample	Si excess (at. %)	Er content (10^{20} cm^{-3})	T_S (°C)	T_a (°C)	n	τ_{dec} (ms)	τ_{rad} (ms)	σ_{eff} (10^{-17} cm^2)
R	7	4	100	900	1.52	3.5	9	1
HD	13	~10	500	600	1.56	2	12	0.5–0.6
MD	9	3.5	500	900	1.54	6.5	10	1

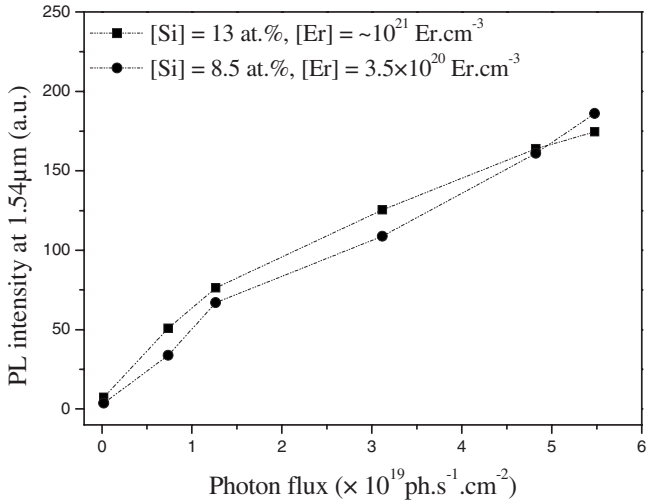

FIG. 8. Comparison of the variations of Er PL at 1.54 μm against the excitation photon flux for the two best samples of the two series: the heavily doped ($\sim 10^{21}$ Er/cm^3) sample annealed at 600 °C and the moderately doped (3.5×10^{20} Er/cm^3) layer annealed at 900 °C. Both samples were originally grown at 500 °C.

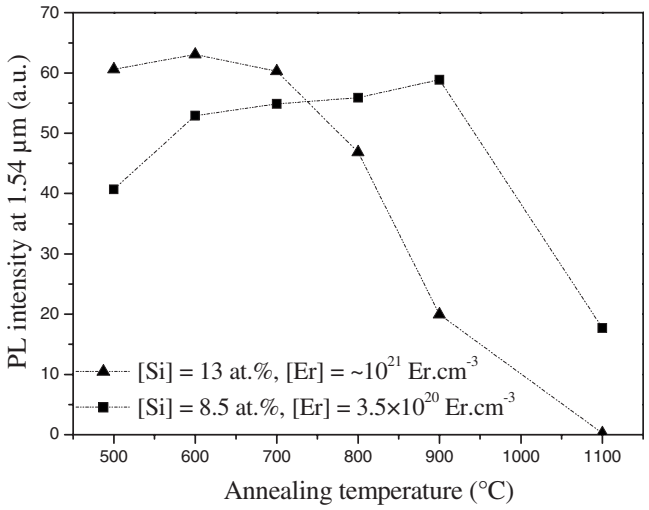

FIG. 9. Evolution of the 1.54 μm PL as a function of the annealing temperature for the two concentrations of Er content and for the two optimum values of Si excess.

reported in Table I, for both HD and MD samples in Eq. (1), one can estimate $N_{\mathrm{Er},c}$ for our MD layer to about 7.8×10^{19} cm^{-3}, i.e., 21%–22% of the total Er content (3.5×10^{20} cm^{-3}). This fraction is almost double that of the heavily doped samples. It is also more than one order of magnitude higher than that of the earlier-described reference sample R.[15]

F. Concentration-related effects

The effects related to the concentration of Er ions and/or excess Si deserve to be identified. Some induce de-excitation processes that govern the emission lifetime τ_{dec} and may explain the reduced values of τ_{dec} in the heavily Er-doped samples. They are, however, much more limited for the moderately Er-doped layers that show high τ_{dec}. This is likely to be due to the reasonable amounts of both Er content (three times lower) and Si excess, which should induce much fewer defects than their counterparts for the HD samples. The other aspect of the concentration effects is related to the optimal T_a corresponding to maximum I_{PL}. For example, the optimal T_a for the high Er concentration which was found lower than that for the moderate Er content [500–700 versus 800–900 °C, see Figs. 4(a) and 6(a)] might be mainly explained by the diffusion and segregation of Er occurring at lower temperatures for higher Er contents. This leads to the decrease in the Er PL intensity I_{PL} at $T_a>600$ °C, instead of $T_a>900$ °C for the moderate Er doping, as evidenced in Fig. 9. Similar observations of T_a variation with the Er content have been reported and similarly explained in Ref. 29. The difference of Si excess in our two samples has not apparently produced a significant influence on the optimal annealing temperature, which is the same (around 600 °C) for all heavily Er-doped samples. While the Si excess changes by tens of percent, the concentration of Er varies by a factor of about 3 and thus should have a prominent impact on the optimal annealing temperature and the decay time, which decreases from an average value of 6.5 ms to about 1.5 ms when the Er concentration is increased.

IV. CONCLUSION

In summary, this work provides a significant contribution to the optimization of coupling of Er ions and Si-based sensitizers. The influences of Si excess and annealing temperature T_a on the optical properties of Er-doped SRSO films were examined for two concentrations of Er: high ($\sim 10^{21}$ cm^{-3}) and moderate (3.5×10^{20} cm^{-3}). It was found that the samples as grown at 400–600 °C emit a notable Er PL under nonresonant excitation (476 nm), suggesting an indirect excitation of Er ions via small Si-based sensitizers formed during growth. An annealing at T_a as low as 600 °C was found to improve both Er PL and lifetime, without inducing structural changes—as evidenced by a comparison of FTIR spectra. This suggests the increasing formation of atomic scale sensitizers. For the heavily Er-doped samples ($\sim 10^{21}$ cm^{-3}), the optimum annealing temperature was found to be lower (600 °C) than that prevailing for the moderate Er doping (900 °C). Such an optimum annealing appears to be mainly governed by the concentration of Er, which varies by a factor of 3—much more so than by the corresponding 35% variation of Si excess in the best two samples of the two series. A higher Er content induces a lower temperature diffusion and segregation of Er, leading to the observed downward shift of the optimal annealing temperature. Moreover, the increasing Er–Er interaction generated by the three times increase in the Er concentration is apparently responsible for the appearance of nonradiative excitation processes that reduce drastically the decay time from an average of about 6.5 ms to about 1.5 ms.

The fraction of Er ions coupled to the Si-based sensitizers has been roughly estimated for the two best samples of the two Er concentration series. It was found that about 11% of the total Er content is coupled for the heavily Er-doped sample, and nearly 22% of the 3.5×10^{20} Er/cm^3 is coupled

for the moderately doped samples. Such a high fraction has not been observed before and might correspond to a higher percentage with respect to the optically active Er ions. Further optimization is still needed to ensure a population inversion and then an optical gain.

ACKNOWLEDGMENTS

This work is supported by the European Community through the LANCER Project (FP6-IST-033574).

[1]K. D. Hirschman, L. Tsybeskov, and S. P. Duttagupta, Nature (London) **384**, 338 (1996).
[2]L. Dal Negro, P. Fauchet, F. Iacona, eds., *E-MRS Proceedings Symposium on Frontiers in Si-based Photonics* [Physica E (Amsterdam) 41 (2009)].
[3]C. Delerue, G. Allan, and M. Lannoo, Phys. Rev. B **48**, 11024 (1993).
[4]M. V. Wölkin, J. Jorne, P. M. Fauchet, G. Allan, and C. Delerue, Phys. Rev. Lett. **82**, 197 (1999).
[5]A. J. Kenyon, P. F. Trwoga, M. Federighi, and C. W. Pitt, J. Phys.: Condens. Matter **6**, L319 (1994).
[6]M. Fujii, M. Yoshida, Y. Kanzawa, S. Hayashi, and K. Yamamoto, Appl. Phys. Lett. **71**, 1198 (1997).
[7]K. Watanabe, M. Fujii, and S. Hayashi, J. Appl. Phys. **90**, 4761 (2001).
[8]D. Pacifici, G. Franzò, F. Priolo, F. Iacona, and L. Dal Negro, Phys. Rev. B **67**, 245301 (2003).
[9]G. Franzò, S. Bonitelli, D. Pacifici, F. Priolo, F. Iacona, and C. Bongiorno, Appl. Phys. Lett. **82**, 3871 (2003).
[10]P. Pellegrino, B. Garrido, J. Arbiol, C. García, Y. Lebour, and J. R. Morante, Appl. Phys. Lett. **88**, 121915 (2006).
[11]F. Gourbilleau, L. Levalois, C. Dufour, J. Vicens, and R. Rizk, J. Appl. Phys. **95**, 3717 (2004).
[12]J. Miniscalco, J. Lightwave Technol. **9**, 234 (1991).
[13]F. Gourbilleau, R. Madelon, C. Dufour, and R. Rizk, Opt. Mater. (Amsterdam, Neth.) **27**, 868 (2005).
[14]J. H. Jhe, J. H. Shin, K. J. Kim, and D. W. Moon, Appl. Phys. Lett. **82**, 4489 (2003).
[15]B. Garrido, C. García, S.-Y. Seo, P. Pellegrino, D. Navarro-Urrios, N. Daldosso, L. Pavesi, F. Gourbilleau, and R. Rizk, Phys. Rev. B **76**, 245308 (2007).
[16]M. Wojdak, M. Klik, M. Forcales, O. B. Gusev, T. Gregorkiewicz, D. Pacifici, G. Franzò, F. Priolo, and F. Iacona, Phys. Rev. B **69**, 233315 (2004).
[17]I. Izeddin, A. S. Moskalenko, I. N. Yassievich, M. Fujii, and T. Gregorkiewicz, Phys. Rev. Lett. **97**, 207401 (2006).
[18]I. Izeddin, D. Timmerman, T. Gregorkiewicz, A. S. Moskalenko, A. A. Prokfiev, I. N. Yassievich, and M. Fujii, Phys. Rev. B **78**, 035327 (2008).
[19]D. Navarro-Urrios, A. Pitanti, N. Daldosso, F. Gourbilleau, R. Rizk, B. Garrido, and L. Pavesi, Phys. Rev. B **79**, 193312 (2009).
[20]R. T. H. Kersten, Opt. Acta **22**, 503 (1975).
[21]R. Ulrich and R. Torge, Appl. Opt. **12**, 2901 (1973).
[22]J. Cardin and D. Leduc, Appl. Opt. **47**, 894 (2008).
[23]J. E. Olsen and F. Shimura, J. Appl. Phys. **66**, 1353 (1989).
[24]P. G. Pai, S. S. Chao, Y. Takagi, and G. Lucovsky, J. Vac. Sci. Technol. A **4**, 689 (1986); N. Tomozeiu, Appl. Surf. Sci. **25**, 376 (2006).
[25]B. J. Hinds, F. Wang, D. M. Wolfe, C. L. Hinkle, and G. Lucovsky, J. Non-Cryst. Solids **227–230**, 507 (1998).
[26]D. V. Tsu, G. Lukovsky, and B. N. Davidson, Phys. Rev. B **40**, 1795 (1989).
[27]O. Savchyn, F. R. Ruhge, P. Kik, R. M. Todi, K. R. Coffey, H. Nukala, and H. Heinrich, Phys. Rev. B **76**, 195419 (2007).
[28]H. Rinnert, M. Vergnat, and A. Burneau, J. Appl. Phys. **89**, 237 (2001).
[29]G. Wora Adeola, H. Rinnert, P. Miska, and M. Vergnat, J. Appl. Phys. **102**, 053515 (2007).
[30]O. Savchyn, P. Kik, R. M. Todi, and K. R. Coffey, Phys. Rev. B **77**, 205438 (2008).
[31]N. Daldosso, D. Navarro-Urrios, M. Melchiorri, L. Pavesi, F. Gourbilleau, M. Carrada, R. Rizk, C. Garcia, P. Pellegrino, B. Garrido, and L. Cognolato, Appl. Phys. Lett. **86**, 261103 (2005).
[32]O. Jambois, H. Rinnert, X. Devaux, and M. Vergnat, J. Appl. Phys. **100**, 123504 (2006).
[33]N. Daldosso, D. Navarro-Urrios, M. Melchiorri, L. Pavesi, C. Sada, F. Gourbilleau, and R. Rizk, Appl. Phys. Lett. **88**, 161901 (2006).
[34]E. Snoeks, A. Lagendijk, and A. Polman, Phys. Rev. Lett. **74**, 2459 (1995).
[35]D. Navarro-Urrios, A. Pitanti, N. Daldosso, F. Gourbilleau, L. Khomenkova, R. Rizk, and L. Pavesi, Physica E (Amsterdam) **41**, 1029 (2009).
[36]G. N. van den Hoven, E. Snoeks, A. Polman, C. Van Dam, J. W. M. van Uffelen, and M. K. Smit, J. Appl. Phys. **79**, 1258 (1996).

Optically active Er^{3+} ions in SiO_2 codoped with Si nanoclusters

D. Navarro-Urrios,[1,a] Y. Lebour,[1] O. Jambois,[1] B. Garrido,[1] A. Pitanti,[2] N. Daldosso,[2] L. Pavesi,[2] J. Cardin,[3] K. Hijazi,[3] L. Khomenkova,[3] F. Gourbilleau,[3] and R. Rizk[3]
[1]*MIND-IN2UB, Dept. Electrònica, Universitat de Barcelona, Martí i Franquès 1, 08028 Barcelona, CAT, Spain*
[2]*Dipartimento di Fisica, Laboratorio di Nanoscienze, Università di Trento, Via Sommarive 14, I-38100 Povo (Trento), Italy*
[3]*CIMAP, UMR CEA/CNRS 6252, 6 Boulevard Maréchal Juin, 14050 CAEN Cedex 4, France*

(Received 27 May 2009; accepted 29 September 2009; published online 6 November 2009)

Optical properties of directly excited erbium (Er^{3+}) ions have been studied in silicon rich silicon oxide materials codoped with Er^{3+}. The spectral dependence of the direct excitation cross section (σ_{dir}) of the Er^{3+} atomic $^4I_{15/2} \rightarrow {}^4I_{11/2}$ transition (around 0.98 μm) has been measured by time resolved μ-photoluminescence measurements. We have determined that σ_{dir} is $9.0 \pm 1.5 \times 10^{-21}$ cm^2 at 983 nm, at least twice larger than the value determined on a stoichiometric SiO_2 matrix. This result, in combination with a measurement of the population of excited Er^{3+} as a function of the pumping flux, has allowed quantifying accurately the amount of optically active Er^{3+}. This concentration is, in the best of the cases, 26% of the total Er population measured by secondary ion mass spectrometry, which means that only this percentage could provide optical gain in an eventual optical amplifier based on this material. © *2009 American Institute of Physics*. [doi:10.1063/1.3253753]

I. INTRODUCTION

Er doped materials have been subject of an extensive research on the last decades, principally since they are used as the active media for fiber optical amplifiers and lasers operating at 1.55 μm in long-haul communications technology. In planar optical amplifiers or lasers integrated in photonic circuits, where small overall sizes are required, the presence of Er^{3+} sensitizers allows achieving high degrees of population inversion for low pumping fluxes even if reasonably high Er^{3+} concentrations are present.[1] During the last years, Si nanoclusters (Si-nc) embedded in a SiO_2 matrix have become one of the most promising Er^{3+} sensitizers. In fact, the presence of Si-nc significantly enhances and broadens in energy the effective excitation cross section (σ_{eff}) of the Er^{3+} ions as a result of an efficient energy transfer mechanism.[2,3] The restrictive conditions to be fulfilled for a pumping source could be thus relaxed, and either electrical[4] or low-power broadband light sources[5] would be possible. In addition, this composite material is fabricated using standard silicon complementary metal-oxide semiconductor processes. Great efforts have been dedicated by a broad scientific community during the last years toward understanding the physics of the system and overcoming the small percentages of the total Er population that can take advantage of the indirect excitation mechanism.[6–9] However, the complete understanding of the indirect excitation mechanism is still under debate. Recently, even the role of the Si-nc in the indirect transfer has been questioned[10] and it has been postulated that luminescent centers could play the main sensitization role instead of the Si-nc. In any case, although it seems clear that the low percentages are mainly related with the short range interaction distance of the energy transfer process and could be progressively improved,[11] it has been additionally proposed that up to several tens percent of the remaining Er content could not be even optically active,[6,12] i.e., not able to emit light even if pumped directly. In samples with a significant Er^{3+} coupled content, the inactive population starts to be a pressing issue to address a further optimization of the material. Hence, it turns essential to study the optical properties of the optically active Er^{3+} content and quantify accurately its concentration (N_{Er}), which is proportional to the maximum potential internal gain that the material would provide. The coupled Er^{3+} content should be thus compared to N_{Er} and not to the total content.

In this work we have assessed N_{Er} in samples with high coupled Er^{3+} content by performing quantitative measurements of the Er^{3+} population found in the $^4I_{13/2}$ state (N_2) as a function of the photon flux (Φ) when pumping the ions at 0.98 μm (resonant to the direct $^4I_{15/2} \rightarrow {}^4I_{11/2}$ transition). Such a pumping wavelength only allows direct excitation of Er^{3+} ions, since exciton formation within the Si-nc is very improbable. This is a key point of the present work because it both prevents indirect excitation and ensures no energetic exchange from directly excited Er^{3+} to the Si-nc. In fact, when pumping resonantly with Er^{3+} transitions at wavelengths in the UV-visible region, excitons are created within the Si-nc. Under these pumping conditions, it has been postulated the possibility that excited ions relax nonradiatively by transferring the energy to the confined carriers, producing an allowed carrier excitation among intraband levels.[9] This effect would not distinguish if the excitation has been done by direct or indirect excitation and would reduce the excited state population with respect to a case where no excitons are present.

[a]Electronic mail: dnavarro@el.ub.es.

The saturation value of N_2 gives the total erbium content that can actually be inverted, i.e., N_{Er}, among the total one,

$$N_2 = \frac{\sigma_{dir} N_{Er} \Phi}{\sigma_{dir}\Phi + 1/\tau_d}, \quad (1)$$

where τ_d is the total decay lifetime of the transition and σ_{dir} is the direct excitation cross section at 0.98 μm. It is worth to note that if the pumping flux is low enough to neglect the product $\sigma_{dir}\Phi$ with respect to the inverse of τ_d a linear approximation with Φ of Eq. (1) is valid ($N_2 \approx \sigma_{dir}\tau_d N_{Er}\Phi$). In any case, in order to apply Eq. (1) accurately, the exact values of τ_d and σ_{dir} should be determined independently for each sample under study. However, the direct quantification of σ_{dir} for these purposes is generally skipped and its value is assumed to be that of Er in a stoichiometric SiO_2 matrix, giving rise to an important uncertainty in the N_{Er} extracted values.[12,13] The main reason for the lack of σ_{dir} values in the UV-visible region is the mentioned enhancement of σ_{eff}, which, in addition, is a magnitude that depends on the distance of the particular ion with respect to the Si-nc surface.[8] In the spectral region of the $^4I_{15/2} \rightarrow {}^4I_{13/2}$, $^4I_{11/2}$ transitions, the accurate determination of σ_{dir} is also not straightforward. In fact, with the absorption techniques used in Refs. 13 and 14, it is only possible to extract the optical losses of the material that are given by the product $\sigma_{dir}N_{Er}^{ab}$, where N_{Er}^{ab} is the Er^{3+} content able to absorb light. N_{Er}^{ab} is an unknown quantity that could be lower than the total content and greater than N_{Er}. In this work we present a different approach based on time resolved μ-photoluminescence (μ-PL) measurements that has allowed the first direct assessment of the spectral dependence of σ_{dir} around 0.98 μm for this material.

II. EXPERIMENTAL DETAILS

Two layers have been fabricated with the magnetron sputtering technique. Sample A was grown at 500 °C under argon pressure by the cosputtering of three targets (SiO_2, Er_2O_3, and Si),[15] while sample B was deposited at 100 °C under argon-hydrogen mixture by the cosputtering of pure SiO_2 and Er_2O_3 targets.[16] These samples are the result of an optimization process until achieving maximum PL signal and total lifetime under 476 nm excitation, which is not resonant with an Er^{3+} direct transition. The compositions of the samples were measured x-ray photoelectron spectroscopy and secondary ions mass spectroscopy: 8.5 at. % of Si excess and 3.6×10^{20} Er/cm^{-3} for sample A and 5 at. % of Si excess and 3.4×10^{20} Er/cm^{-3} for sample B.[16] Both layers were annealed at 910 °C during 60 min in pure nitrogen flow and have a refractive index of about 1.51 at 1.55 μm, while the thicknesses were 1.36 and 1.22 μm for samples A and B, respectively. In particular, in sample B it was determined an absolute Er^{3+} concentration efficiently coupled to the Si-nc of 3.6×10^{19} cm^{-3}, i.e., 11% of the total Er content.[17] A soda-lime 1.3 mm thick sample supplied by Corning, doped with Er to a density of 0.7×10^{20} at/cm^3, was used as a reference.

Quantitative continuous wave PL experiments were performed by pumping with a 975 nm semiconductor laser (~0.2 W maximum power) focused with a 15 cm focal length lens onto a surface of 5×10^{-4} cm^2 over the samples, which allowed achieving pumping photon fluxes (Φ) as high as 10^{21} ph/cm^2 s. Since the depth of focus of the lens is much longer than the studied samples thicknesses, the pump spot surface can be assumed as constant along them. The PL emission was analyzed with a monochromator and detected with an InGaAs photomultiplier tube. The quantification of N_2 was accomplished by calibrating our detection system with the reference sample, in which the Er^{3+} concentration is fully active and whose cross sections and radiative and total lifetimes are known. The theoretical photon flux emitted (Φ_{em}) by this sample at a certain pumping photon flux is calculated and used to calibrate the detection system. After this calibration procedure, the emitted flux from any sample can be directly calculated from a PL measurement.

N_2 can be related with Φ_{em} in the following way:

$$N_2 = \frac{\Phi_{em}\tau_{rad}}{V}, \quad (2)$$

where V is the pumped volume. The radiative lifetime (τ_{rad}) was estimated to be 16 ms in the studied samples taking into account the change in the refractive index with respect to the pure SiO_2 case (τ_{rad}=18 ms) in accordance with Ref. 18.

For determining σ_{dir} we have done time resolved μ-PL measurements, where the pump laser has been modulated externally. The rise and decay lifetimes (τ_r, τ_d) of the 1.55 μm PL signal were determined as a function of Φ in a high Φ regime ($\Phi > 10^{22}$ ph/cm^2 s). For a quasitwo level system under these experimental conditions it is possible to demonstrate that[8]

$$\frac{1}{\tau_r} - \frac{1}{\tau_d} = \sigma_{dir}\Phi. \quad (3)$$

It is worth noting that, since the expected cross section is very low (~10^{-21} cm^2) very high fluxes are required to observe non-negligible differences between the rise and decay lifetimes.

The setup scheme used for performing these measurements is shown in Fig. 1(c). The laser beam was passed through a beam splitter while a charge-coupled-device (CCD) camera was placed on the remaining free optical line. For achieving the required high Φ it was focused into a micrometric spot (3×10^{-7} cm^2 area) by a microscope objective. It is worth noting that the spot surface is more than three orders of magnitude smaller than in the case of the standard PL measurements reported before. The CCD camera allows observing the dimensions of the pumping spot on the sample when the latter is on the focus of the objective. Figure 1(b) shows the real image of the laser spot on the top of a reference structure that is 32 μm wide. This setup has been also used for performing PL measurements at high Φ.

III. EXPERIMENTAL RESULTS AND DISCUSSION

In Fig. 1(a) we show the actual time-resolved (TR)-PL measurement. The 1.55 μm PL signal temporal behavior of sample A when the pump is switched on (rise) and off (decay) is presented. The rise PL signals have been measured

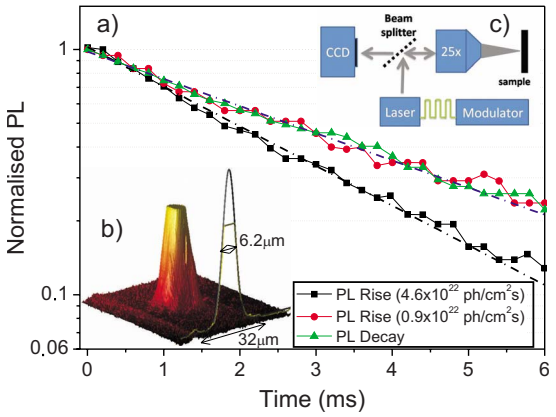

FIG. 1. (Color online) (a) Experimental PL rise for high (squares) and low (circles) Φ inverted and normalized for clarity, and PL decay (triangles). The dashed lines are the single exponential fits of the experimental data. (b) Analysis of the spatial energy distribution of the pumping spot on the surface of a 32 μm waveguide. (c) Scheme of the experimental setup built for the μ-PL time resolved experiments.

for minimum (circles) and maximum (squares) photon flux. The lifetime of the rising signal noticeably increases by lowering Φ, converging to the PL decay lifetime (triangles) at low Φ. All the set of decaying and rising signals fit very well to a single exponential law (dashed-dotted lines), thus allowing the determination of τ_r and τ_d. The decay lifetimes were determined to be 4.2 ms for sample A and 4.8 ms for sample B independently of Φ.

In the inset of Fig. 2 we represent the left part of Eq. (3) as a function of Φ for both samples. The slope of the linear fit, which has been forced to pass by zero, gives $\sigma_{\mathrm{dir}}(975\ \mathrm{nm}) = 3.1 \pm 0.5 \times 10^{-21}\ \mathrm{cm}^2$, which is roughly the same for the two samples under study.

The PL signal corresponding to the $^4I_{11/2} \rightarrow {}^4I_{15/2}$ transition observed in those samples (Fig. 2, dashed curve) is, in a first approximation, proportional to the emission cross section σ_{em}. Thus, it is possible to relate the latter with σ_{dir} by using McCumber theory,[19] which results in

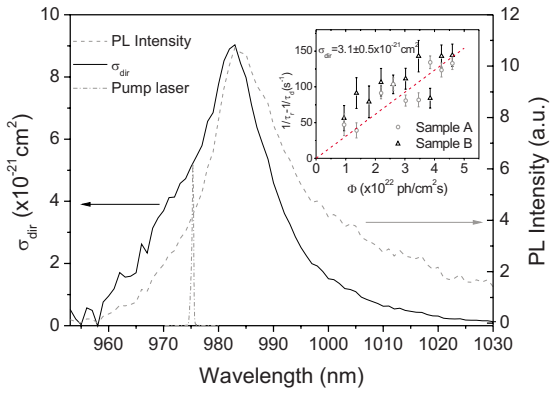

FIG. 2. (Color online) PL emission (dashed line) corresponding to the $^4I_{11/2} \rightarrow {}^4I_{15/2}$ transition. It has been obtained by pumping at low Φ at 488 nm. The solid curve shows the extracted spectrum for the excitation cross section of the $^4I_{15/2} \rightarrow {}^4I_{11/2}$ transition. The dashed-dotted gray curve shows the spectrum of the pump laser used in the present study. (Inset panel) Difference of the inverses of the rise and decay lifetimes as a function of Φ for samples A (gray circles) and B (black triangles). The dashed curve corresponds to the fit using Eq. (2).

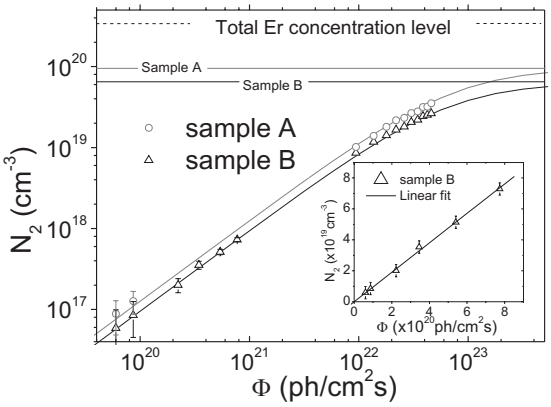

FIG. 3. N_2 as a function of Φ (in log-log scale) for samples A (gray circles) and B (black triangles) together with their respective fits using Eq. (1). The different achievable concentration levels are also represented as horizontal lines. The inset represents the low Φ set of data for sample B in a linear scale together with a linear fit using the low flux approximation of Eq. (1).

$$\sigma_{\mathrm{dir}}(\lambda) = \sigma_{\mathrm{em}}(\lambda)\exp\left[\frac{hc}{kT}(1/\lambda - 1/\lambda_m)\right], \tag{4}$$

where λ_m is defined as the wavelength of the transition between the lowest levels of the two manifolds involved. We have applied Eq. (4) to the PL spectrum to extract the spectral shape of σ_{dir} and then normalized the resulting curve by using the measured value at 975 nm in order to have the actual values. The result is the spectral dependence of the σ_{dir} for the $^4I_{15/2} \rightarrow {}^4I_{11/2}$ transition (Fig. 2, solid curve, left axis).

At the maximum of the transition the extracted σ_{dir} is $9.0 \pm 1.5 \times 10^{-21}\ \mathrm{cm}^2$, whereas the values found in the literature for Er^{3+} doped silicate glasses without Si excess are all about $2-5 \times 10^{-21}\ \mathrm{cm}^2$ at the peak wavelength.[20] The observed twofold enhancement in the material under study is associated to differences in the effective crystal field potential at the ion site,[20] since the refractive index difference with respect to the silicate cases is too small (less than 3%) to have a significant effect. This small enhancement is quite consistent with the one recently reported for the $^4I_{15/2} \rightarrow {}^4I_{13/2}$ transition,[13,14] although the determination of those values have the limitations described previously.

In Fig. 3 we show the quantitative determination of N_2 for both samples as a function of Φ. Two ranges of Φ are reported: low $\Phi(10^{20}-10^{21}\ \mathrm{ph/cm^2\ s})$ obtained with the standard PL setup (calibrated as described previously) and high $\Phi(10^{22}-10^{23}\ \mathrm{ph/cm^2\ s})$ obtained with the μ-PL setup. Since the linear approximation of Eq. (1) is valid in the low Φ range and τ_d and σ_{dir} are already known, it is possible to extract N_{Er} from the slope of the linear fit. This is reported in the inset of Fig. 3 for the case of sample B and the extracted value is $N_{\mathrm{Er}} = 0.64 \times 10^{20}\ \mathrm{cm}^{-3}$, which is only 19% of the total Er^{3+} content present in this sample $(3.4 \times 10^{20}\ \mathrm{cm}^{-3})$.

The PL data obtained at high Φ showed for both samples a sublinear behavior, which indicates that the linear approximation made for low fluxes is no longer valid and the saturation of N_2 is starting to be achieved. In order to extract the quantitative data of N_2 at high Φ it is not possible to use the reference sample for calibrating the μ-PL setup since the

depth of focus of the objective (tens of micrometers) is significantly smaller than the reference sample thickness (1.3 mm). This makes Φ vary significantly along this sample as the beam spot changes its surface so that the determination of Φ_{em} requires the resolution of a complex integral. This is not an issue on samples A and B since the thickness of the active layer is small enough with respect to the depth of focus, so Φ (and, thus, N_2) can be considered constant.

Therefore, in order to determine the total flux emitted by a sample (and thus extract N_2 from the high Φ PL signals taken) we have used the N_2 data taken at low Φ for sample B and then normalized the high Φ data by a factor that optimizes the fitting using Eq. (1) (after introducing the measured values of τ_d and σ_{dir}). This procedure has allowed us to extract a value of $N_{Er}=0.64\times10^{20}$ cm^{-3} for sample B, which is the very same value obtained by using only the points at low Φ, demonstrating the reliability of the followed procedure for calibrating the μ-PL setup.

The high flux N_2 data of sample A have been represented together with the low flux data and fitted afterwards using Eq. (1). A further demonstration of the accurate calibration of the μ-PL setup is that the fitted curve reproduces quite well both set of data obtained with different setups.

Although it has already been stated that σ_{dir} and the total Er^{3+} content are roughly the same for both samples, N_2 is visibly higher for sample A. Indeed, for sample A we have obtained $N_{Er}=0.97\times10^{20}$ cm^{-3} (26% of the total Er^{3+} content, i.e., 3.6×10^{20} cm^{-3}), slightly greater than what is obtained for sample B. These values are compatible with those reported for example in Ref. 6, although in that case the data were extracted by pumping in the visible and assuming a direct cross section equal to that of Er^{3+} in stoichiometric SiO_2.

With the determined values for N_{Er} the potential gain in an amplifier will be reduced by at least a factor of 3 with respect to what would be given by the total Er^{3+} content. For sample B, this quantity can be compared with the indirectly excitable concentration that is able to emit light, revealing that about 53% of the optically active content (11% of the total content) is coupled to the Si-nc and thus invertible by indirect excitation. This means that in principle it is possible to invert the population of optically active Er^{3+} by exploiting the indirect excitation of Si-nc.

If the remaining erbium content that is not emitting light is either (i) totally inactive or (ii) unable to efficiently emit light (although being able to absorb it) remains an open issue out of the scope of this paper. Further spectral quantitative measurements of the direct absorption coefficient would be required for determining the Er^{3+} concentration able to absorb light, which is not possible to be extracted from PL measurements. In our opinion hypothesis (ii) is more reasonable since various possible configurations of Er^{3+} within the matrix could efficiently quench the radiative recombination paths. At this stage, we can only speculate that, since experimentally the PL single exponential decays are independent on Φ with a quite long lifetime the emitting Er^{3+} population does not suffer from strong cooperative up-conversion mechanisms (otherwise the PL lifetime would be reduced as a function of Φ as the initial value of N_2 becomes higher).[17] Therefore, the hypothesis (ii) would imply the existence of two completely different kinds of Er^{3+} ions populations: one able to recombine radiatively with roughly the same probability and another surrounded by quenching centers where the radiative recombination probability is negligible with respect to the nonradiative one. A compatible scenario with the previous statement would be that the nonemitting Er^{3+} population is placed within the Si-nc or that it suffers from local concentration quenching effects (in a way that the excitation can migrate from one ion to another until it encounters a quenching center where a local phonon or deformation can deactivate the excitation). Indeed, it has already been reported in bulk glass that the local structure of the material can vary, such that clusters of ions can form in one region whereas another region might have isolated ions.[21,22] A similar observation has been reported for ion implanted Si rich SiO_2 codoped with Er^{3+}, which could contribute to the low percentages of indirectly excitable Er^{3+} content reported.[23] It is possible that further annealing would improve the optically active Er^{3+} content as reported for example in Ref. 24 in Er^{3+} doped stoichiometric SiO_2 samples. However, following this procedure, we have observed a decreasing in the Er^{3+} content that can be excited indirectly.[25]

IV. CONCLUSIONS

In conclusion, we have made a novel study on the optical properties of the directly excited Er^{3+} ions in an Er^{3+} doped SiO_2 sensitized by Si nanoclusters material, quantifying both the spectral dependence of the direct excitation cross section of the $^4I_{15/2}\rightarrow{}^4I_{11/2}$ transition and the optically active Er^{3+} concentration. We have observed a twofold enhancement of the direct cross section with respect to the values reported in the literature for silicate glasses. On the other hand, it has been demonstrated that, in the best of the studied samples, 26% of the total Er^{3+} concentration is able to emit light at 1.55 μm when directly excited, result that may impact in the potential performances of this material for amplification purposes.

ACKNOWLEDGMENTS

The authors thank the financial support by EC through the LANCER Project (Grant No. FP6-IST 033574) and kindly acknowledge Dr. C. J. Oton for fruitful discussions. One of the authors thanks the Spanish Ministry of Education and Science through the Juan de la Cierva program.

[1] A. Polman and F. C. J. M. van Veggel, J. Opt. Soc. Am. B **21**, 871 (2004).
[2] A. J. Kenyon, P. F. Trwoga, M. Federighi, and C. W. Pitt, J. Phys.: Condens. Matter **6**, L319 (1994).
[3] F. Priolo, G. Franzò, D. Pacifici, V. Vinciguerra, F. Iacona, and A. Irrera, J. Appl. Phys. **89**, 264 (2001).
[4] F. Iacona, D. Pacifici, A. Irrera, M. Miritello, G. Franzò, and F. Priolo, Appl. Phys. Lett. **81**, 3242 (2002).
[5] J. Lee, J. H. Shin, and N. Park, J. Lightwave Technol. **23**, 19 (2005).
[6] M. Wojdak, M. Klik, M. Forcales, O. B. Gusev, T. Gregorkiewicz, D. Pacifici, G. Franzò, F. Priolo, and F. Iacona, Phys. Rev. B **69**, 233315 (2004).
[7] P. G. Kik and A. Polman, J. Appl. Phys. **88**, 1992 (2000).
[8] B. Garrido, C. García, S.-Y. Seo, P. Pellegrino, D. Navarro-Urrios, N. Daldosso, L. Pavesi, F. Gourbilleau, and R. Rizk, Phys. Rev. B **76**, 245308 (2007).

[9]I. Izeddin, A. S. Moskalenko, I. N. Yassievich, M. Fujii, and T. Gregorkiewicz, Phys. Rev. Lett. **97**, 207401 (2006).
[10]O. Savchyn, F. R. Ruhge, P. G. Kik, R. M. Todi, K. R. Coffey, H. Nukala, and H. Heinrich, Phys. Rev. B **76**, 195419 (2007).
[11]D. Navarro-Urrios, A. Pitanti, N. Daldosso, F. Gourbilleau, R. Rizk, B. Garrido, and L. Pavesi, Phys. Rev. B **79**, 193312 (2009).
[12]S. Minissale, T. Gregorkiewicz, M. Forcales, and R. G. Elliman, Appl. Phys. Lett. **89**, 171908 (2006).
[13]N. Daldosso, D. Navarro-Urrios, M. Melchiorri, L. Pavesi, C. Sada, F. Gourbilleau, and R. Rizk, Appl. Phys. Lett. **88**, 161901 (2006).
[14]H. Mertens, A. Polman, I. M. P. Aarts, W. M. M. Kessels, and M. C. M. van de Sanden, Appl. Phys. Lett. **86**, 241109 (2005).
[15]K. Hijazi, L. Khomenkova, J. Cardin, F. Gourbilleau, and R. Rizk, Physica E **41**, 1067 (2009).
[16]L. Khomenkova, F. Gourbilleau, J. Cardin, and R. Rizk, Physica E **41**, 1048 (2009).
[17]D. Navarro-Urrios, A. Pitanti, N. Daldosso, F. Gourbilleau, L. Khomenkova, R. Rizk, and L. Pavesi, Physica E **41**, 1029 (2009).
[18]M. J. A. de Dood, L. H. Slooff, A. Polman, A. Moroz, and A. van Blaaderen, Phys. Rev. A **64**, 033807 (2001).
[19]D. E. McCumber, Phys. Rev. **136**, A954 (1964).
[20]W. J. Miniscalco, J. Lightwave Technol. **9**, 234 (1991).
[21]B. J. Ainslie, S. P. Craig-Ryan, S. T. Davey, J. R. Armitage, C. G. Atkins, J. F. Massicott, and R. Wyatt, IEE Proc.-J: Optoelectron. **137**, 205 (1990).
[22]B. J. Ainslie, J. Lightwave Technol. **9**, 220 (1991).
[23]P. Pellegrino, B. Garrido, J. Arbiol, C. Garcia, Y. Lebour, and J. R. Morante, Appl. Phys. Lett. **88**, 121915 (2006).
[24]J. S. Chang, J.-H. Jhe, M.-S. Yang, J. H. Shin, K. J. Kim, and D. W. Moon, Appl. Phys. Lett. **89**, 181909 (2006).
[25]F. Gourbilleau, M. Levalois, C. Dufour, J. Vicens, and A. Rizk, J. Appl. Phys. **95**, 3717 (2004).

Efficient energy transfer from Si-nanoclusters to Er ions in silica induced by substrate heating during deposition

Sébastien Cueff,[1] Christophe Labbé,[1,a)] Julien Cardin,[1] Jean-Louis Doualan,[1] Larysa Khomenkova,[1] Khalil Hijazi,[1] Olivier Jambois,[2] Blas Garrido,[2] and Richard Rizk[1]
[1]*Centre de Recherche sur les Ions, les Matériaux et la Photonique (CIMAP), ENSICAEN, CNRS, CEA/IRAMIS, Université de Caen, 14050 CAEN Cedex, France*
[2]*Dept. Electrònica, MIND-IN2UB, Universitat de Barcelona, Martí i Fanquès 1, 08028 Barcelona, CAT, Spain*

(Received 14 May 2010; accepted 22 July 2010; published online 17 September 2010)

This study investigates the influence of the deposition temperature T_d on the Si-mediated excitation of Er ions within silicon-rich silicon oxide layers obtained by magnetron cosputtering. For T_d exceeding 200 °C, an efficient indirect excitation of Er ions is observed for all as-deposited samples. The photoluminescence intensity improves gradually up to a maximum at T_d=600 °C before decreasing for higher T_d values. The effects of this "growth-induced annealing" are compared to those resulting from the same thermal budget used for the "classical" approach of postdeposition annealing performed after a room temperature deposition. It is demonstrated that the former approach is highly beneficial, not only in terms of saving time but also in the fourfold enhancement of the Er photoluminescence efficiency. © *2010 American Institute of Physics*. [doi:10.1063/1.3481375]

I. INTRODUCTION

Silicon-rich silicon oxide matrix doped with Er^{3+} ions (SRSO:Er) is now a well-known material investigated for Si-based photonics.[1] This system can take advantage of the energy transfer from Si-nanoclusters (Si-nc) to erbium ions and then benefits from the high absorption cross section of Si-nc, which is nearly three orders of magnitude higher than the direct excitation cross section of Er ions.[2,3] Such a material should, therefore, allow the fabrication of low-cost and silicon-compatible photonic devices (LEDs, planar optical amplifiers, laser, etc.). To achieve an amplifying medium, the coupling between Si-nc and Er ions must ensure the population inversion, and this requires in turn a careful optimization of the material. The fabrication process appears, therefore, as a crucial step regarding the distance-dependent interactions between the Er^{3+} ions and the Si-based sensitizers.[4–8] It is then essential to nanoengineer the density and distribution of both Er^{3+} ions and Si-based sensitizers within the silica matrix. In this regard, several groups have analyzed the influence of different annealing treatments on the optical performance of SRSO:Er layers[9–13] usually deposited at room temperature (RT) before being subsequently annealed at different temperatures. Such a process allowed the formation of Si-nc sensitizers and then the observation of Er photoluminescence (PL) under nonresonant optical excitation. However, our group has recently observed an Er-PL under these indirect excitation conditions on the as-deposited samples at about 500 °C.[13,14] The Er emission was improved after annealing at about 500–600 °C, and this aspect was also confirmed by another team on similarly sputtered layers.[15] We have assigned such an observation to the *formation of Si-based sensitizers during the deposition process* that are expected to be very small and dense, ensuring a noticeable coupling with the Er ions. Nevertheless, a careful and systematic examination of the influence of the deposition temperature (T_d) on SRSO:Er thin films is still lacking. In the present study, we demonstrate that the deposition temperature governs, on the one hand, the formation of Si-sensitizers in the as-deposited layers, and influences, on the other hand, the composition and density of sensitized Er ions. The relevance of such a "growth-induced annealing" is further evidenced through a comparison with a standard postdeposition annealing bringing into operation the same thermal budget.

II. EXPERIMENTAL DETAILS

Series of SRSO:Er samples were deposited onto a p-type, 250-μm-thick silicon wafer, thanks to the magnetron cosputtering of three confocal cathodes (SiO_2, Si, and Er_2O_3) under a plasma of pure Argon at a pressure of 2 mTorr. The deposition temperature (T_d) was varied from RT to 700 °C, being the maximal temperature that can be applied. The duration of all depositions were set to two hours. The power densities applied on the three confocals targets $P_{SiO_2} \approx 8.88$ W/cm^2, $P_{Si} \approx 1.63$ W/cm^2, $P_{Er_2O_3} \approx 0.44$ W/cm^2 were kept constant for all depositions.

The Er content was measured by time-of-flight secondary ion mass spectroscopy (TOF-SIMS) measurements. This TOF-SIMS technique was calibrated by a reference SRSO:Er sample in which the Er concentration was accurately measured by Rutherford backscattering. surfaces of deposited layers were analyzed by atomic force microscope (AFM) provided by Digital Instruments (Nanoscope), operating in tapping mode at RT. The Si excess was estimated by a Fourier transform infrared (FTIR) spectroscopy approach detailed elsewhere.[14] The refractive index and the thickness were measured using spectroscopic ellipsometry (SE).

a)Electronic mail: christophe.labbe@ensicaen.fr.

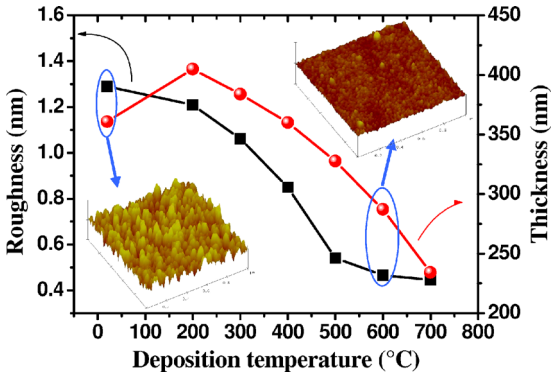

FIG. 1. (Color online) rms roughness measured by AFM and layer thickness measured by SE as a function of deposition temperature T_d. Two typical AFM micrographs (scan area: 1 μm^2) are also shown for the depositions at RT and at 600 °C.

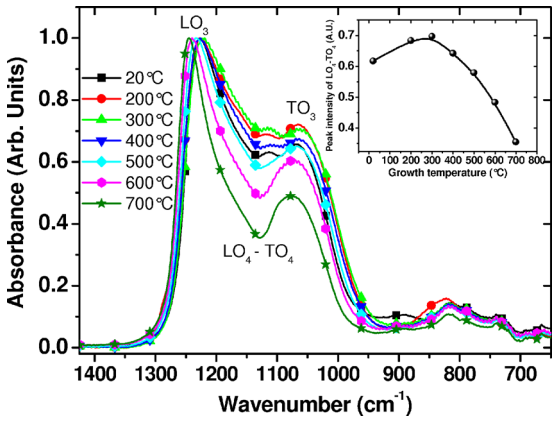

FIG. 2. (Color online) Infrared absorption spectra normalized for as-deposited samples, collected at Brewster angle (65°). Inset: relative evolution of LO_4–TO_4 peaks intensity according to the deposition temperature T_d.

Visible and IR PL spectra were obtained using the 476 nm excitation wavelength from an Ar^+ laser which is a non-resonant wavelength for the erbium ion. The spot size of the laser beam was measured by a "moving knife-edge" method and was found to be around 1 mm at $1/e^2$ of the maximum intensity. A 1 m single grating monochromator (Jobin Yvon) and a liquid-nitrogen-cooled germanium detector (Northcoast) were used to collect the Er-PL while the visible spectra were collected with a photomultiplier tube. These measurements were made by using the standard lock-in techniques (SP830 DPS) referenced with a chopping frequency of 9 Hz. Time-resolved measurements were obtained by the 435 nm excitation wavelength of a pulsed Optical Parametric Oscillator (OPO). The pulse duration was ~5 ns and the spot size 0.8 mm at $1/e^2$ of the maximum intensity. The PL signal of the time-resolved measurements was collected by an InGaAs detector.

III. RESULTS AND DISCUSSION

A. Structural analyses

The deposition temperature T_d is expected to have an influence on several structural parameters. We have first analyzed the evolution of the surface quality of the deposited layers by AFM techniques. Figure 1 shows the variation in the surface roughness in terms of root mean square (rms) as a function of T_d, as well as two typical AFM images for two T_d values (RT and 600 °C). The roughness (rms) continuously softens from 1.6 to 0.3 nm when T_d increases, with a steep decrease for T_d between 300 and 600 °C.

A similar behavior is observed for the thickness (Fig. 1) which also decreases with T_d, from about 380 to 240 nm, i.e., a reduction in about 35%. The surface roughness is generally correlated with both mobility and growth rate of the deposited atoms, especially in this specific layer-by-layer deposition technique. Indeed, the surface roughness reflects some balance between the deposition rate and the surface mobility of the sticking elements. For example, a high surface roughness is expected to result, either from a limited surface mobility at a given sputtering rate, or from a high surface mobility at a faster sputtering rate. Besides, a high surface mobility should lead to a progressive relaxation of the network through lower distortion of the atomic bond angles and an improved atomic rearrangement, together with better compactness. Thus, the decrease in both thickness and roughness can be explained by the increasing surface mobility of the deposited elements when T_d is increased. This latter statement would be further confirmed by a concomitant decrease in the atomic disorder within the film material. We have collected the FTIR spectra on the various films, in order to examine the evolution of the so-called LO_4–TO_4 doublet that is known to be indicative of the disorder within the SiO_2 matrix.[16]

Figure 2 compares the corresponding FTIR spectra obtained at the Brewster incidence angle (65°) after being normalized on the LO_3 peak. One can observe that the intensity and structure of LO_4–TO_4 doublet are slightly affected when T_d increases from RT to 400 °C. However, a gradual and significant decrease in the intensity is observed for T_d >400 °C, hence allowing an increasingly better separation between the LO_3 and TO_3 peaks. This decrease demonstrates that a strong reduction in the disorder occurs within the SiO_2 matrix when T_d increases up to 700 °C. Such a phenomenon confirms the above-mentioned increasing mobility of the deposited elements. This leads, therefore, to the following straightforward conclusion: the higher is the deposition temperature, the better is the atomic arrangement within the matrix.

An optimum reduction in the disorder should result in an improvement of the compactness, together with a more relaxed network. However, such suggestions explain only partly the decrease in the thickness of the deposited films. Indeed, the expected improvement of the compactness, combined to the reduction in the structural disorder, is not sufficient to explain the 35% decrease in the thickness. A significant part of this thickness lowering may be due to a temperature-dependent sticking/desorption rate of the sputtered elements, already demonstrated for elemental oxygen on Si substrate,[17] and/or the creation of volatiles species. Thus, the composition of the thin film may change according to the deposition temperature. The concentrations of the deposited elements and especially those of the silicon excess and Er ions are important parameters that must be determined.

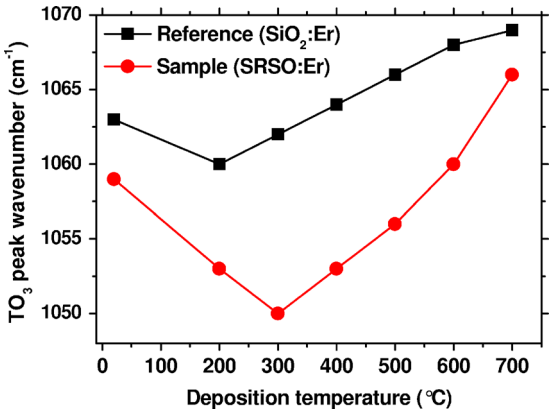

FIG. 3. (Color online) Evolution of the wave number of SiO_2:Er references and SRSO:Er samples for each deposition temperature.

The silicon excess is defined here as the percentage of elemental silicon present inside the sample in addition to the proportion of Si in stoichiometric SiO_2. For the as-deposited SRSO:Er thin films, the estimate of the Si excess is not straightforward, considering that the transmission electronic microscopy (TEM) observations are unable to detect either the formation of Si-nc or their evolution with T_d. This is due to the lack of contrast between the amorphous Si-nc and the silica matrix, as stated by previous studies.[9,18] Moreover, the smallness of Si-nc in our as-deposited films makes difficult their observation by energy filtered TEM approach.[18] Nevertheless, a rough estimate of the Si excess content is possible from the analysis of the TO_3-peak energy shift evolution in the FTIR spectra of our SRSO:Er film, as described elsewhere[19] and adopted in our previous work.[14] However, the above-described atomic disorder induces some shift in the TO_3 peak that can be misinterpreted as being due to some Si excess. To overcome this issue, a reference SiO_2 sample doped with Er was deposited for each T_d value. Such a reference sample is *considered as free from silicon excess* and its TO_3 peak is compared to that of the SRSO:Er sample deposited at the same T_d (see Fig. 3).

It can be seen in Fig. 3 that for both SRSO:Er sample and SiO_2:Er reference, the TO_3 peak position decreases when T_d changes from RT to 300 °C (200 °C for the reference), then increases for higher values of T_d. The evolution of the TO_3 peak for the SiO_2:Er reference is considered as reflecting an evolution of the atomic arrangement rather than any Si excess. On the basis of these considerations, the Si excess in the SRSO layer has been estimated from the following linear relation:

$$\%\mathrm{Si}_{\mathrm{excess}} = \frac{\upsilon_{\mathrm{TO}_3}^{\mathrm{ref\ SiO_2}} - \upsilon_{\mathrm{TO}_3}^{\mathrm{SRSO:Er}}}{\upsilon_{\mathrm{TO}_3}^{\mathrm{ref\ SiO_2}} - \upsilon_{\mathrm{TO}_3}^{\mathrm{Si}}} \times 100, \quad (1)$$

where $\upsilon_{\mathrm{TO}_3}^{\mathrm{ref\ SiO_2}}$ and $\upsilon_{\mathrm{TO}_3}^{\mathrm{SRSO:Er}}$ are, respectively, the TO_3 peak wavenumbers of SiO_2:Er and SRSO:Er, while $\upsilon_{\mathrm{TO}_3}^{\mathrm{Si}}$ is the TO_3 peak wavenumber of Si taken constant for all T_d (960 cm^{-1}).

This approach allowed us to subtract the "background disorder" of the sputtered SiO_2:Er and hence determine the corresponding Si excess for SRSO:Er. To note that the FTIR approach underestimates the amount of Si excess because the Si–Si links within the Si-nc formed during the growth are not detected and then not taken into account. Nevertheless, regardless of the absolute value of Si excess, their evolution is considered as reliably described by the FTIR-related estimate, as attested by an earlier comparison with our X-ray Photoelectron Spectroscopy (XPS) analyses done on similar samples.[20]

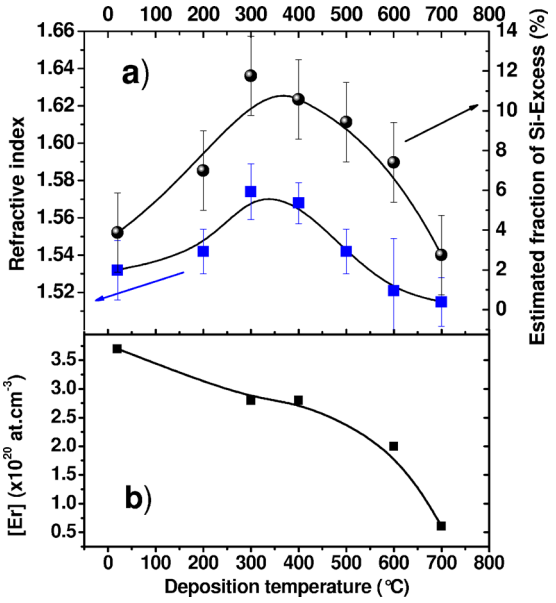

FIG. 4. (Color online) (a) Ellipsometry measurements of the refractive index at 633 nm and Si excess as estimated by FTIR techniques and the formula (1) in function of T_d (the curves are just a guide for the eyes). (b) SIMS measurements of the erbium concentration according to the deposition temperature.

Figure 4(a) displays the evolution of the Si excess, as estimated from Eq. (1), in function of T_d. A first increase in Si excess is observed when T_d is raised from RT to 300 °C, which indicates that the deposition of Si is favored by the rise of T_d up to 300 °C. This increase is followed by a "symmetric" decrease for higher T_d values. This behavior of Si excess is consistent with a similar evolution of the refractive index, n, as determined by SE measurements. To note that n of the SiO_2:Er references remains almost constant for all T_d at about 1.46 (not shown), i.e., very close to that of stoichiometric SiO_2 (1.45). This corroborates the assignment of the evolution of n for SRSO:Er samples to that of the Si excess. In particular, the decrease in n for $T_d > 300$ °C, concomitant to a decrease in Si excess as estimated by FTIR, reflects an *effective* lowering of the Si excess. Thus, the estimated decrease in Si excess is not only due to an increasing underestimate originated from further and further formation of Si-nc. In this regards, the Si excess lowering can be provoked by some increasing interactions/reactions between the deposited species, inducing the formation of volatile elements such as SiO for $T_d \geq 300$ °C, as supported by earlier studies.[21–23] Such processes are temperature-dependent, and T_d can have also some influence on the concentration N_{Er} of incorporated Er. Indeed, N_{Er} was found to decrease gradually from 3.7×10^{20} atom cm^{-3} to 6.1×10^{19} atom cm^{-3} when T_d increases from RT to 700 °C [see Fig. 4(b)]. The origin of this

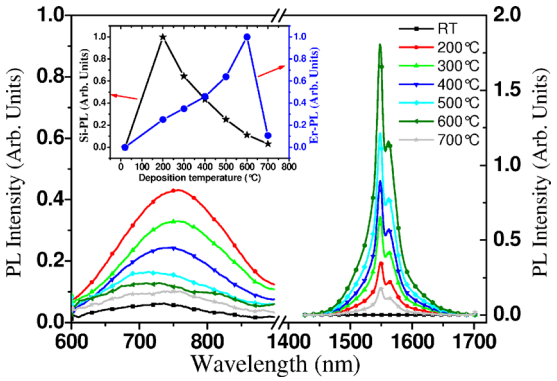

FIG. 5. (Color online) PL spectra (normalized to the thickness) at a flux of 5×10^{18} photons cm^2/s of both Si-nc (range 600–900 nm) and of Er^{3+} ions (range 1400–1700 nm) for all deposition temperatures. Inset: Si-nc PL intensities compared to the Er-PL intensities according to the deposition temperature (both normalized to unity).

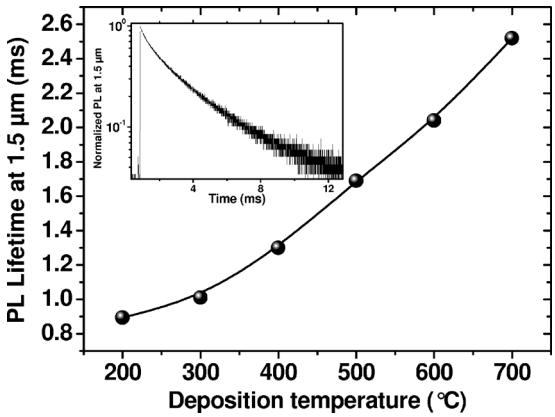

FIG. 6. Behavior of the lifetime values of Er^{3+} at 1.53 μm according to the deposited temperature detectable at the lower excitation photon flux. Inset: a typical PL decay trace of SRSO:Er collected for sample deposited at 600 °C. Note the PL decay dynamics is biexponential as described in Ref. 28.

gradual decrease is difficult to identify but might be correlated with the increasing reactive character of the sticking mechanism of the sputtered elements when T_d is increased.

B. PL properties

Figure 5 shows the evolution of the PL spectra recorded on all samples along two main wavelength ranges: the Si-PL feature from 600 to 900 nm range and the Er-PL contribution around 1540 nm. This latter corresponds to the $^4I_{13/2} \rightarrow {}^4I_{15/2}$ Er^{3+} transition. The visible emission that peaks at 750 nm for T_d=200 °C gradually shifts toward 720 nm when T_d is increased to 600–700 °C. This visible emission is assigned to quantum confinement within Si-nc (Ref. 24) that do not transfer their energy to Er^{3+} ions.[3,25] The slight shift to higher energies, in spite of T_d increase, reflects some lowering in the average size of Si-nc which is quite compatible with the above-commented decrease in Si excess. It is also worth noting that this visible emission was similarly observed and attributed to Si-nc by Savchyn *et al.*[9,26,27] for their samples annealed at 1000 °C during only 100 s. On the contrary, no contribution is detected in our samples of the so-called luminescent centers (LCs) emitting at around 500 nm.[9]

The presence of a significant Er-PL in our as-deposited samples (for $T_d \geq 200$ °C) excited with a nonresonant wavelength reveals the occurrence of an efficient energy transfer from Si-nc to Er^{3+}. When T_d is raised from 200 to 600 °C, the Er-PL shows a systematic increase at the expense of the Si-nc-PL, hence indicating an increase in sensitized Er ions (see inset of Fig. 2) through Si-nc sensitizers. The sample deposited at RT is suspected to be free from Si-sensitizers, since no Er-PL is detected. Such sensitizers start apparently to form when T_d reaches and exceeds 200 °C. It is worth noting that the Er-PL intensity increases by a factor of almost 5, in spite of the N_{Er} lowering, when T_d is increased from 200 to 600 °C, before showing an abrupt decrease for T_d =700 °C [Fig. 4(b)]. The increase in T_d improves also the quality of the matrix, as demonstrated by the systematic increase in the Er emission lifetime, for the longer time decay, from ~1 ms at 200 °C to 2.5 ms at 700 °C, (Fig. 6) which is almost one order of magnitude higher than the lifetime reported for similar layers containing LCs.[9,26]

The increase in the Er-PL intensity with T_d may originate from the formation of small Si-sensitizers, as already mentioned, and also from the improvement of the environment of Er^{3+} ions which is expected to increase the number of optically active Er^{3+} ions. Indeed, under the resonant wavelength of 980 nm corresponding to a resonant direct excitation of Er (i.e., without the Si-nc relays) from the ground state $^4I_{15/2}$ to the second excited level $^4I_{11/2}$, the Er-PL increases systematically up to T_d=600 °C (see Fig. 7), reflecting a concomitant enhancement of the number of the optically active ions. On the other hand, the sudden abrupt decrease in the Er PL at 700 °C for both nonresonant 476 nm and resonant 980 nm excitation lines, suggests some agglomeration of the Er ions at this deposition temperature (700 °C), which reduces the number of optically active Er ions,[29] and consequently the PL intensity.

The deposition temperature thus governs three different phenomena occurring during the growth process: (i) the formation and growth of Si-based sensitizers, (ii) the variation in both Si excess and Er content, and (iii) the improvement

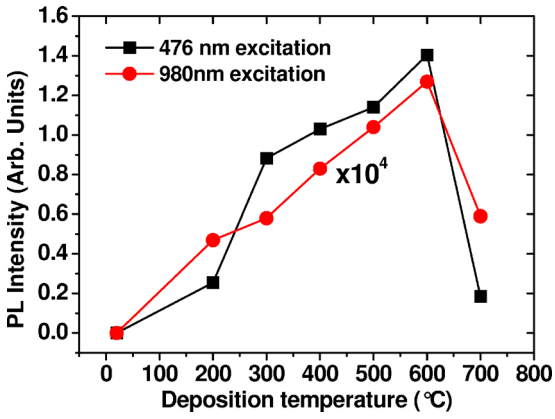

FIG. 7. (Color online) Comparison of PL intensity of as-deposited samples recorded at 1.53 μm and obtained after indirect excitation (476 nm) and direct excitation (980 nm). Note that the results corresponding to the 980 nm excitation are multiplied by 10^4.

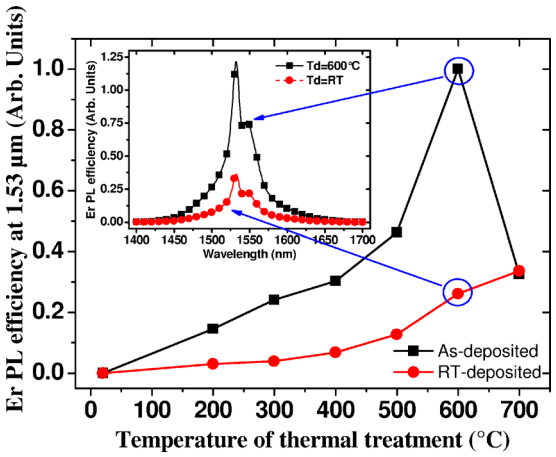

FIG. 8. (Color online) Comparison of the evolution of the Er-PL efficiency of the as-deposited samples to that obtained from their counterparts deposited at RT and annealed for 2 h at $T=T_d$. The inset compares two normalized Er-PL efficiency spectra of two SRSO: Er thin films: (i) deposited at 600 °C for 2 h (full squares) and (ii) deposited at RT and annealed at 600 °C for 2 h (full circles).

of the quality of the matrix as demonstrated by the decrease in atomic disorder and the increase in the Er emission lifetime. Those concomitant effects lead to a positive paradox when the deposition temperature is raised from 200 to 600 °C: *the PL of* Er^{3+} still increases whereas both the Si excess and the Er concentration get lower. Indeed, the improvement of the Er-PL up to a maximum for $T_d=600$ °C corresponds to a moderate value of Si excess and almost the lowest N_{Er}. Such an improvement of the PL intensity is, therefore, arising from the influence of the deposition temperature on the growth mechanisms. This leads to some optimum density and distribution of both sensitizers and Er ions, resulting in better luminescence of Er^{3+} for the used growth parameters. Two relevant parameters also compete for this enhancement: the number of optically active Er^{3+} ions which evolves similarly against T_d (Fig. 7) and the reduction in nonradiative recombination, as attested by the raise of the lifetime by a factor of ~3 (Fig. 6).

To give further insight on the influence of the growth-induced annealing, we compare the optical emission of each as-deposited sample grown at a given T_d to that recorded from its counterpart film deposited at RT and then annealed for 2 h (i.e., equivalent to the deposition duration) at $T=T_d$. This approach allows one to compare the samples having been submitted to the same "thermal budget," either during deposition or after deposition. The main difference between the intrinsically heated samples during the deposition process and those annealed after RT deposition, lies in the composition evolution: for the former, both N_{Er} value and Si excess are varying with T_d, whereas these concentrations remain constant for the latter. To take into account this aspect and accurately compare the two kinds of samples, we define the Er-PL efficiency as the ratio I_{PL}^{Er}/N_{Er}, depending on T_d. Figure 8 compares the Er-PL efficiency according to the temperature of thermal treatment, for both as-deposited and post-deposition annealed samples. For the as-deposited films, the Er-PL efficiency increases by a factor of 6–7 when T_d raises from 200 to 600 °C. When compared to their counterparts annealed after RT deposition, their Er-PL efficiency is systematically higher by a factor that reaches a maximum of about 4 for $T_d=600$ °C (see inset).

This result demonstrates the relevance of layer deposited at a temperature as high as 600 °C which favors the surface mobility of the sticking elements that can diffuse with relatively low activation energy. By comparison, the volume diffusion of the elements occurring during the postdeposition annealing requires higher activation energy and result apparently in the formation of much less Si-based sensitizers and optically active Er^{3+} ions. One can therefore infer that the growth-induced annealing is not only a "time-saving" approach but it is also a way to enhance the optical performance of SRSO:Er thin films. On the other hand, the matrix of the as-deposited samples could be further improved by an additional postdeposition annealing treatment which can be the object of a specific work beyond the scope of this study.

IV. CONCLUSION

In conclusion, the influence of the deposition temperature on the optical properties of SRSO:Er thin films was carefully investigated. The concentration of Er^{3+} ions and the amount of Si excess were found to change with the deposition temperature. It was also demonstrated that an efficient energy transfer from Si-nc to Er^{3+} can be obtained for as-deposited samples at a deposition temperature exceeding 200 °C, without any annealing. When the deposition temperature is further raised to 600 °C, the Er-PL efficiency is enhanced by a factor of 6–7, compared to 200 °C, originating from optimum density and distribution of both Si-sensitizers and optically active Er ions, as well as from the matrix improvement. The emission lifetime shows a consistent improvement with T_d, up to about 2.5 ms. For comparable thermal budget, the growth-induced annealing at $T_d=600$ °C was found to favor the Er-PL efficiency by a factor of about 4, in comparison with the classical annealing performed on layer deposited at RT.

[1] L. Pavesi and D. J. Lockwood, Top. Appl. Phys. **94**, 1 (2004).
[2] A. J. Kenyon, P. F. Trwoga, M. Federighi, and C. W. Pitt, J. Phys.: Condens. Matter **6**, L319 (1994).
[3] M. Fujii, M. Yoshida, Y. Kanzawa, S. Hayashi, and K. Yamamoto, Appl. Phys. Lett. **71**, 1198 (1997).
[4] J. H. Jhe, J. H. Shin, K. J. Kim, and D. W. Moon, Appl. Phys. Lett. **82**, 4489 (2003).
[5] B. Garrido, C. Garcia, P. Pellegrino, D. Navarro-Urrios, N. Daldosso, L. Pavesi, F. Gourbilleau, and R. Rizk, Appl. Phys. Lett. **89**, 163103 (2006).
[6] F. Gourbilleau, C. Dufour, R. Madelon, and R. Rizk, J. Lumin. **126**, 581 (2007).
[7] K. Choy, F. Lenz, X. X. Liang, F. Marsiglio, and A. Meldrum, Appl. Phys. Lett. **93**, 261109 (2008).
[8] F. Gourbilleau, M. Levalois, C. Dufour, J. Vicens, and R. Rizk, J. Appl. Phys. **95**, 3717 (2004).
[9] O. Savchyn, F. R. Ruhge, P. G. Kik, R. M. Todi, K. R. Coffey, H. Nukala, and H. Heinrich, Phys. Rev. B **76**, 195419 (2007).
[10] G. Wora Adeola, H. Rinnert, P. Miska, and M. Vergnat, J. Appl. Phys. **102**, 053515 (2007).
[11] A. Kanjilal, L. Rebohle, M. Voelskow, W. Skorupa, and M. Helm, J. Appl. Phys. **104**, 103522 (2008).
[12] A. R. Wilkinson and R. G. Elliman, J. Appl. Phys. **96**, 4018 (2004).
[13] S. Cueff, C. Labbé, J. Cardin, and R. Rizk, IOP Conf. Ser.: Mater. Sci. Eng. **6**, 012021 (2009).
[14] K. Hijazi, R. Rizk, J. Cardin, L. Khomenkova, and F. Gourbilleau, J. Appl. Phys. **106**, 024311 (2009).

[15]O. Savchyn, R. M. Todi, K. R. Coffey, L. K. Ono, B. R. Cuenya, and P. G. Kik, Appl. Phys. Lett. **95**, 231109 (2009).
[16]T. Kirk, Phys. Rev. B **38**, 1255 (1988).
[17]M. P. D'evelyn, M. M. Nelson, and T. Engel, Surf. Sci. **186**, 75 (1987).
[18]G. Franzò, S. Boninelli, D. Pacifici, F. Priolo, F. Iacona, and C. Bongiorno, Appl. Phys. Lett. **82**, 3871 (2003).
[19]P. G. Pai, S. S. Chao, Y. Takagi, and G. Lukovsky, J. Vac. Sci. Technol. **A4**, 689 (1986).
[20]S. Charvet, R. Madelon, F. Gourbilleau, and R. Rizk, J. Appl. Phys. **85**, 4032 (1999).
[21]P. Wickboldt, H. M. Cheong, D. Pang, J. H. Chen, and W. Paul, Mater. Res. Soc. Symp. Proc. 358 (1995).
[22]Y. Takakuwa, M. Nihei, and N. Miyamoto, Jpn. J. Appl. Phys., Part 2 **32**, L480 (1993).
[23]D. Gautam, E. Koyanagi, and T. Uchino, J. Appl. Phys. **105**, 073517 (2009).
[24]R. Lockwood, A. Hryciw, and A. Meldrum, Appl. Phys. Lett. **89**, 263112 (2006).
[25]F. Priolo, G. Franzò, D. Pacifici, V. Vinciguerra, F. Iacona, and A. Irrera, J. Appl. Phys. **89**, 264 (2001).
[26]O. Savchyn, R. M. Todi, K. R. Coffey, L. K. Ono, B. R. Cuenya, and P. G. Kik, Appl. Phys. Lett. **94**, 241115 (2009).
[27]O. Savchyn, P. G. Kik, R. M. Todi, and K. R. Coffey, Phys. Rev. B **77**, 205438 (2008).
[28]A. Al Choueiry, A. M. Jurdyc, B. Jacquier, F. Gourbilleau, and R. Rizk, J. Appl. Phys. **106**, 053107 (2009).
[29]A. Polman, D. C. Jacobson, D. J. Eaglesham, F. C. Kistler, and J. M. Poate, J. Appl. Phys. **70**, 3778 (1991).

Thermal stability of high-k Si-rich HfO2 layers grown by RF magnetron sputtering

ARTICLE *in* NANOTECHNOLOGY · JULY 2010

Impact Factor: 3.82 · DOI: 10.1088/0957-4484/21/28/285707 · Source: PubMed

4 AUTHORS:

L. Khomenkova
National Academy of Sciences of Ukraine
129 PUBLICATIONS **683** CITATIONS
SEE PROFILE

Xavier Portier
National Graduate School of Engineering a…
137 PUBLICATIONS **907** CITATIONS
SEE PROFILE

Julien Cardin
Université de Caen Basse-Normandie
67 PUBLICATIONS **271** CITATIONS
SEE PROFILE

Fabrice Gourbilleau
French National Centre for Scientific Resea…
206 PUBLICATIONS **1,897** CITATIONS
SEE PROFILE

Thermal stability of high-*k* Si-rich HfO_2 layers grown by RF magnetron sputtering

2010 Nanotechnology 21 285707

(http://iopscience.iop.org/0957-4484/21/28/285707)

Nanotechnology **21** (2010) 285707 (12pp) doi:10.1088/0957-4484/21/28/285707

Thermal stability of high-*k* Si-rich HfO_2 layers grown by RF magnetron sputtering

L Khomenkova[1,2], X Portier, J Cardin and F Gourbilleau[2]

CIMAP, CEA/CNRS/ENSICAEN/UCBN, 6 Boulevard Maréchal Juin, 14050 Caen Cedex 4, France

E-mail: khomenkova@rambler.ru, larysa.khomenkova@ensicaen.fr and fabrice.gourbilleau@ensicaen.fr

Received 8 April 2010, in final form 18 May 2010
Published 28 June 2010
Online at stacks.iop.org/Nano/21/285707

Abstract

The microstructure and optical properties of HfSiO films fabricated by RF magnetron sputtering were studied by means of x-ray diffraction, transmission electron microscopy, spectroscopic ellipsometry and attenuated total reflection infrared spectroscopy versus annealing treatment. It was shown that silicon incorporation in the HfO_2 matrix plays an important role in the structure stability of the layers. Thus, the increase of the annealing temperature up to 1000 °C did not lead to the crystallization of the films. The evolution of the chemical composition as well as a decrease of the density of the films was attributed to the phase separation of HfSiO on HfO_2 and SiO_2 phases in the film. An annealing at 1000–1100 °C results in the formation of the multilayer Si-rich/Hf-rich structure and was explained by a surface-directed spinodal decomposition. The formation of the stable tetragonal structure of HfO_2 phase was shown upon annealing treatment at 1100 °C.

(Some figures in this article are in colour only in the electronic version)

1. Introduction

Transition metal oxides and silicates with dielectric constants higher than that of SiO_2 have been considered to replace the silicon dioxide employed in gate dielectric systems of microelectronic devices [1, 2]. In principle, high-*k* dielectrics allow the reduction of the leakage current and demonstrate good thermal stability, as well as high transparency.

One of the goals for high-*k* materials is to attain a sufficiently high-quality interface with the Si channel coupled with a stability of the amorphous structure of the gate oxide during deposition. Such a requirement comes from the fact that grain boundaries act as diffusion paths for dopants or oxygen towards the film/substrate interface. Thus, it was observed that post-growth oxidation of pure HfO_2 layers in a $^{18}O_2$ atmosphere at 490–950 °C results in oxygen exchange without increasing the oxygen content in the films [3]. The atomic diffusion of oxygen via oxygen lattice exchange was found to be the predominant diffusion mechanism. When pure HfO_2 films are amorphous and/or nanocrystalline, the diffusion of oxygen is minimized and the excess of oxygen atoms is stabilized as interstitials. The exchange rate increases with temperature due to crystallization of the films [3].

It is known that the dielectric properties of HfO_2 depend significantly on its structure. Amorphous and monoclinic phases exhibit a dielectric constant of about 16–20, but cubic and tetragonal phases have higher relative permittivity (about 28 [4]). From the device application point of view, these latter phases are preferable to the monoclinic one. It was demonstrated both theoretically [5–7] and experimentally [8–10] that the incorporation of cationic dopants in the HfO_2 matrix favors the formation and the stabilization of the tetragonal or cubic phase. At the same time, the dopants have to be chosen to avoid a significant decrease of the band gap energy and dielectric constant of the high-*k* materials.

The most promising candidate to fulfil these conditions is silicon. For instance, for HfSiO layers grown by atomic vapor deposition [3] it was observed that the Si incorporation in HfO_2 matrix allows the oxygen diffusion from the environment into the films to be controlled. This diffusion was minimized due to the formation of covalent Si–O bonds in comparison with ionic

[1] Permanent address: V Lashkaryov Institute of Semiconductor Physics, 45 Prospekt Nauky, Kyiv 03028, Ukraine.
[2] Authors to whom any correspondence should be addressed.

Hf–O ones and, depending on the Si content, it was completely suppressed. Besides, it was shown that the annealing treatment of such HfSiO films at 490–950 °C results in the formation of SiO_2 close to the film surface that significantly decreases the oxygen diffusion at high temperatures and completely blocks it at low temperatures [3]. On the other hand, the Si incorporation minimizes oxygen exchange inside the film and controls the formation of the SiO_x interfacial layer during the deposition process and post-deposition treatment [3, 11, 12]. Thus, for HfSiO layers grown by atomic vapor deposition, the formation of a SiO_2 interfacial layer was observed at temperatures higher than 600 °C [3], whereas for HfSiO layers grown by RF magnetron sputtering it started at 900 °C [12].

Taking advantage of this Si incorporation in such a matrix, let us turn to consideration of multilayer applications of HfO-based layers. It is known that they can be used as gate and/or control oxides [2]. Besides, HfO_2-based materials with different embedded nanoparticles can be used widely for nanomemory applications [13]. However, the formation of Si nanoparticles usually requires high temperature annealing [14] that can lead to total crystallization of high-*k* oxide. For example, for HfO_2/Si-rich SiO_2/HfO_2 structures it was shown that the formation of Si nanoparticles was achieved upon annealing at 1100 °C for 1 h, when HfO_2 gate and control oxides were completely crystallized in the monoclinic phase [14]. However, for such structures one can expect that it is possible to use a rapid thermal annealing process to form Si seeds at high temperature in a short time (less than 1 min), and then to decrease the annealing temperature down to the critical temperature value to prevent the crystallization of high-*k* material during the formation of Si nanoparticles. The latter does not require temperatures as high as 1100 °C (usually 800–900 °C is sufficient), but longer annealing time (about 15–30 min) is necessary. In such a case, the gate material has to be stable during such a treatment.

As we showed earlier [11, 12], hafnium silicate thin films grown by the RF magnetron sputtering approach are homogeneous, amorphous and the thickness of the interfacial SiO_x layer between the high-*k* layer and the Si substrate does not exceed 1 nm. Moreover, they demonstrate their thermal stability by conserving the amorphous structure after an annealing at temperatures as high as 800–1000 °C for 15 min. Thus, they can be considered as promising candidates for gate materials, especially when higher temperature annealing is required for processing of the device, for example for nanomemory applications.

In addition to the thermal stability of the amorphous phase, the stability of the chemical composition of the high-*k* silicates is also required. This condition comes from the fact that during the growth process and/or annealing treatment the formation of high-*k* and low-*k* regions can occur [15–17]. Most of the studies were performed for Zr silicates. The formation of ZrO_2-rich and SiO_2-rich regions during the growth process was observed whereas the films were found to be amorphous. The alternation of ZrO_2-rich layers with SiO_2-rich layers in the normal direction to the film surface was governed by a driving force that was normal to the film surface. A similar effect was also found for ZrSiO films upon annealing [16].

A similar phenomenon was observed for HfSiO films grown by the atomic vapor deposition technique [17, 18]. The effect of the formation of HfO_2-rich and SiO_2-rich regions in HfSiO materials was explained similarly to that observed for ZrSiO [15, 17]. Unfortunately, no analysis of the crystalline structure of the films versus annealing treatment was reported.

The evolution of the microstructure and chemical composition, as well as the optical properties of the HfSiO materials under annealing treatment is the issue of the present study. The layers, fabricated by RF magnetron co-sputtering of a pure HfO_2 cathode topped by Si chips in a pure argon plasma, were analyzed by means of x-ray diffraction, infrared absorption spectroscopy, spectroscopic ellipsometry and high resolution transmission electron microscopy.

This paper is organized as follows. First, the optical properties of as-deposited and annealed films will be analyzed. The refractive index, thickness and density of as-deposited and annealed films will be extracted from analysis of the spectroscopic ellipsometry data. Next, the obtained results will be compared with the chemical composition and structure of the as-deposited and annealed films. The phase separation stimulated by annealing treatment will be described and a mechanism of this phenomenon will be proposed.

2. Experimental procedure

The HfSiO films were deposited on B-doped Si substrates with a resistivity of 15 Ω cm and the (100) orientation. To remove native oxide the substrates were cleaned in a diluted hydrofluoric solution (10%) and after drying in a nitrogen flow they were immediately placed into the vacuum preparation chamber of the deposition setup. The layers were grown by RF magnetron sputtering of a 4 inch HfO_2 target (99.9%) topped with Si chips in a pure argon plasma. The RF power density, total plasma pressure and substrate temperature were 0.74 W cm^{-2}, 40 μbar and 100 °C, respectively. The Si chips covered 12% of the total surface of the HfO_2 target.

To study the effect of annealing treatment on the layer properties, the samples were annealed under a nitrogen flow in a conventional furnace at different temperatures, T_A = 800–1100 °C, during t_A = 10–30 min.

The combination of non-destructive methods allows information about microstructural and optical properties of the films to be obtained. Thus, infrared attenuated total reflectance (ATR), usually used for thin film investigation, will provide information about the structure and chemical composition of the films. ATR-FTIR spectra were measured in the range 600–4000 cm^{-1} by means of a 60° Ge Smart Ark accessory inserted in a Nicolet Nexus spectrometer. Microstructure properties were analyzed by an x-ray diffraction method using a Phillips XPERT HPD Pro device with Cu Kα radiation (λ = 0.1514 nm) at a fixed grazing incidence angle of 0.5°. An asymmetric grazing geometry was chosen to increase the volume of material interacting with x-ray beam, as well as to eliminate the contribution from the Si substrate.

Spectroscopic ellipsometry was used to determine different parameters of the samples such as optical constants, thickness and surface roughness. The data were collected

by means of a Jobin-Yvon ellipsometer (UVISEL) where the incident light was scanned in the range 1.5–4.5 eV with an incidence angle of 66.3°. The fitting of the experimental data was performed using DeltaPsi2 software [19].

The analysis of film structure versus annealing treatment was completed by TEM observation. Cross-sectional specimens were prepared by a standard procedure involving grinding, dimpling and Ar^+ ion beam thinning until they were electron transparent. The samples were examined by conventional (CTEM) and high resolution electron microscopy (HRTEM) using a FEG 2010 JEOL instrument, operated at 200 kV. Image processing was done with the commercial Digital micrograph GATAN software.

3. Results and discussion

3.1. Spectroscopic ellipsometry analysis

It is known that spectroscopic ellipsometry is a fast, sensitive and non-destructive method for thin film characterization. It requires no special environment and can be easily integrated into semiconductor processing [20, 21].

The spectra consist of the measured Ψ and Δ ellipsometric angles defined from the fundamental equation of ellipsometry

$$\overline{r_p}/\overline{r_s} = \tan\Psi \exp \mathrm{i}\Delta, \tag{1}$$

where $\overline{r_p}$ and $\overline{r_s}$ are the complex reflection coefficients for the parallel and perpendicular polarization of light, respectively. The spectral dependencies of Ψ and Δ can be fitted with appropriate modeling approaches to extract the film thickness and optical constants (refractive index, n, and extinction coefficient, k) based on the best fit between the experimental and simulated spectra [20]. Besides the optical dielectric constant, the surface roughness and film density can also be obtained [21].

Before describing the model used for extraction of the different parameters of the layers, let us recall that the HfSiO layers investigated in the present study were found to be amorphous and homogeneous, in terms of their structural properties and chemical composition, by energy filtered TEM analysis [12]. Moreover, for the as-grown films it was shown that they had a very thin (no more than 1 nm) interfacial SiO_2 layer. This allowed us to consider the as-grown films as a homogeneous medium and to apply the effective medium approximation (EMA) [20, 22] to fit the experimental spectra.

Such an approximation supposes that the macroscopic properties of a medium are based on the properties and the relative fractions of its components. There are several EMA models (Bruggeman, Maxwell–Garnet, etc). They all assume that the macroscopic system is homogeneous (with correlation length below the Lorentz cavity radius) and typical of all mean field theories; they fail to predict the properties of a multiphase medium close to the percolation threshold due to its long-range correlation length. The most frequently considered parameters are conductivity or/and dielectric constant. The Bruggeman effective medium approximation (BEMA) used in this work is defined by the following two equations:

$$\sum_i v_i \frac{\varepsilon_i - \varepsilon}{\varepsilon_i + 2\varepsilon} = 0, \tag{2}$$

and

$$\sum_i v_i = 1, \tag{3}$$

where ε_i and v_i are the complex optical dielectric function and volume fraction for the ith component, respectively. ε is the effective dielectric function corresponding to the measured value for the film.

A four-phase optical model was used to investigate the as-deposited and annealed layers. It consists of the silicon substrate, a SiO_2 interfacial layer, an amorphous HfSiO layer, and a surface rough layer composed of a mixture of void space and HfSiO. It is worth noting that the roughness of the films was estimated to be less than 1.5 nm, as confirmed by film surface observations using atomic-force microscopy. The model structures and optical properties of the films were optimized by least-square refinements (χ^2) from the fit of the experimental data.

To fit spectroscopic ellipsometry data, a dispersion law was chosen based on the Forouhi–Bloomer model (FBM) modified for amorphous semiconductor and insulating materials [23] using an improved parameterization [24]. The dispersion formulae for n and k were given as follows

$$n(\omega) = n_\infty + \frac{B_i(\omega - \omega_i) + C}{(\omega - \omega_i)^2 + \Gamma_i^2},$$

$$k(\omega) = \begin{cases} \dfrac{f_i(\omega - \omega_g)^2}{(\omega - \omega_i)^2 + \Gamma_i^2}, & \omega > \omega_g \\ 0, & \omega \leqslant \omega_g, \end{cases}$$

where

$$B_i = \frac{f_i}{\Gamma_i}(\Gamma_i^2 - (\omega_i - \omega_g)^2),$$

$$C = 2 f_i \Gamma_i (\omega_i - \omega_g)$$

where n_∞ is the refractive index at high frequency, f_i is an oscillator strength, Γ_j is an amortization factor, and ω_i and ω_g are the frequencies of free oscillator.

Two dependencies, $I_s = I \sin 2\Psi \sin\Delta$ and $I_c = I \sin 2\Psi \cos\Delta$, where $I = \frac{E_0}{4}(|r_p|^2 + |r_s|^2)$ and E_0 is the amplitude of electric field of incident light, were fitted. The obtained values of n and k of the as-deposited films are shown in figure 1(a) and (b), respectively. The experimental data and their best fitting are presented in the inset of figure 1(b). n and k values of HfO_2, SiO_2, SiO and bulk Si are also included in figure 1(a) and (b) for comparison.

Usually, Hf silicates are considered as being composed of pure HfO_2 and pure SiO_2 structural units as $(HfO_2)_x(SiO_2)_{1-x}$ and the relative contributions determine the composition of the films [4, 16, 21, 25]. Of HfO_2 and SiO_2, the first has the higher refractive index (figure 1(a)). It is obvious that the n value of HfSiO material must increase with an increase of the HfO_2 fraction, f_{HfO_2}, up to a limit value corresponding to pure HfO_2 (figure 1(a)). In such a case, one can suppose that the k value has to follow this rule too. As one can see in figure 1(b), both oxides are completely transparent in the spectral range of our interest. However, the as-deposited HfSiO sample demonstrates some absorption ability in the 1.5–4.5 eV spectral range, contrary to the data reported in [26]. The

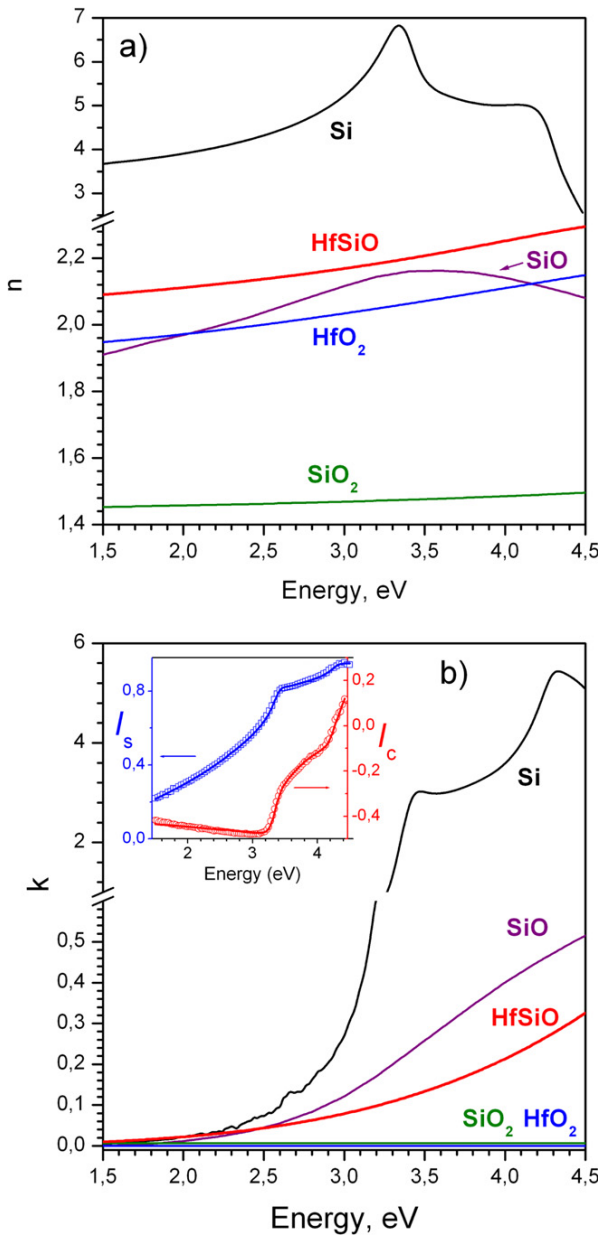

Figure 1. The estimated refractive index, n (a) and absorption coefficient, k (b) of the as-grown HfSiO layer. The inset in figure (b) represents experimental ellipsometry data (symbols) and the fitting curve (solid line) for the as-deposited HfSiO samples. $I_s = I \sin 2\Psi \sin \Delta$ and $I_c = I \sin 2\Psi \cos \Delta$ (Ψ and Δ are the measured ellipsometry parameters). The $n(E)$ and $k(E)$ dependencies for pure HfO_2, SiO_2, SiO and bulk Si are also presented.

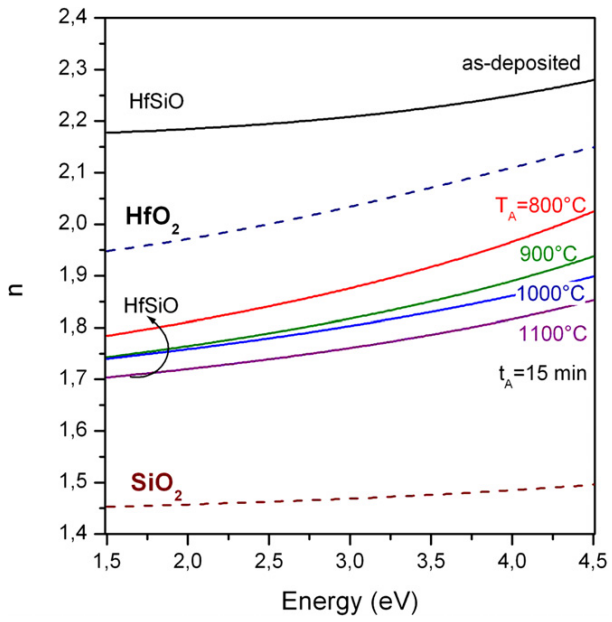

Figure 2. The calculated refractive index, n, for as-deposited films and those annealed at 900–1100 °C for 15 min, grown at RFP = 0.74 W cm^{-2}. The n variation for both pure HfO_2 and pure SiO_2 materials are also shown by dashed lines.

comparison of the absorption properties of SiO_2, SiO and bulk Si reveals that SiO_2 is transparent in this spectral range, while Si suboxides and bulk Si demonstrate high enough absorption (figure 1(b)). Thus, one can speculate that the absorption in the as-deposited HfSiO films occurs due to a presence of the SiO_x phase instead of SiO_2. On the other hand, it is possible to assume that the absorption could be due to the formation of a HfSiO network which cannot be considered as a mixture of HfO_2 and SiO_2 phases alone. However, since Hf ions are less electronegative than Si ones, it is obvious that the formation of HfO_2 structural units is preferable to SiO_2 ones and consequently, the formation of the SiO_x phase is possible. This could explain the behavior of the extinction coefficient k in the as-deposited layers (figure 1(b)).

The analysis of the annealed films shows a gradual decrease of n with annealing temperature (figure 2). Furthermore, k decreases and a shift of the 'absorption edge' to higher energy was observed, which could be evidence of the increased transparency of the films after the annealing treatment (not shown here). The data obtained can be explained by the difference in the structure and in the composition of the as-deposited and annealed films.

It is known that the refractive index of pure HfO_2 increases with the annealing temperature due to the crystallization process [27]. In our case, the n decrease could be explained by the formation of pores and/or by the increasing contribution of the SiO_2 phase. The latter could be due to oxygen diffusion into the films during the annealing treatment resulting in the formation of a thicker interfacial SiO_2 layer. Both these facts would be a reason for the decrease of n and k values.

However, as we showed earlier [11, 12], after annealing at 800 °C for 15 min, the films kept their amorphous structure without any pore formation. Moreover, the thickness of the interfacial SiO_2 layer did not exceed 2 nm; so they cannot be the only reasons for such a decrease of the refractive index. Thus, another fact has to be taken into consideration, for example a higher contribution of SiO_2 phase in the film due to phase separation and formation of HfO_2 and SiO_2 phases.

Further increasing the annealing temperature up to 1100 °C results in a decrease of the n and k values (figure 2).

Table 1. The physical and optical parameters of HfSiO samples versus annealing treatment.

Parameters		Annealing temperature (°C)				
		25	800	900	1000	1100
Thickness (nm)	HfSiO layer	17.15	17.3	20.46	21.05	22.54
	SiO_2 interfacial layer	1.03	1.06	2.73	3.32	5.0
Refractive index, n	at 1.5 eV	2.081	1.790	1.743	1.740	1.704
Polarizability, α (bohr^3)	α_{HfO_2} for HfO_6 units			35.28 [4]		
	α_{HfO_2} for HfO_8 units			32.21 [4]		
	α_{SiO_2} for SiO_4 units			19.68 [4]		
	α_{HfSiO} for HfO_6/SiO_4	33.25	30.61	29.82	29.04	28.26
	α_{HfSiO} for HfO_8/SiO_4	30.58	28.45	27.82	27.20	26.57
Fraction of HfO_2	f_{HfO_2}	0.87	0.70	0.64	0.60	0.55
Density for (g cm^{-3})	ρ_{HfSiO} for HfO_6/SiO_4	8.02	6.08	5.56	5.55	5.21
	ρ_{HfSiO} for HfO_8/SiO_4	8.72	6.54	5.94	5.92	5.54

At the same time, if HfO_2 crystallization occurs at higher temperatures, the n and k decreases will be due to the more important contribution of the SiO_2 phase. As one can see from table 1, an annealing treatment leads not only to the increase of the interfacial layer thickness but also to the increase of the thickness of the HfSiO layer itself. Such an expansion can be caused by a further increase of the contribution of the SiO_2 phase which has higher lattice parameter than HfO_2 and must affect the density of the films.

3.2. Effect of annealing treatment of the density of the films

The density of the films can be estimated using the Clausius–Mossotti relationship between optical dielectric constant and film density, ρ, given by equation (4)

$$\frac{\varepsilon - 1}{\varepsilon + 2} = \frac{4\pi}{3}\frac{\bar{\alpha}}{\bar{V}}, \tag{4}$$

where $\bar{V}$ is the average structure unit volume and polarizability $\bar{\alpha}$ can be considered as a local and additive quantity in the contrast with ε. The film being composed by different phases, its density, ρ, can be considered as $\sum_i v_i \rho_i = \rho$, where ρ_i is the density of the ith component, one can extract the ρ value, using equation (4) rewritten as

$$\frac{n^2 - 1}{n^2 + 2} = \frac{4\pi}{3}\left(\frac{N_A \rho}{M}\right)\bar{\alpha}, \tag{5}$$

where M is the molar mass and N_A is Avogadro's constant, taking into account that $\varepsilon = n^2$. In such a case, the refractive index is taken from the fitted parameters, while the polarizability was estimated based on the values available for Hf silicate materials [4].

To estimate the value of ρ, we have to use an appropriate value of the polarizability, α. This is an important parameter for mixed media. It has additive properties, contrary to the dielectric constant, that allow it to be estimated using the known polarizabilities of HfO_2 and SiO_2 phases and their contribution to the HfSiO film following the equation (6)

$$\bar{\alpha}_{HfSiO} = f_{HfO_2}\alpha_{HfO_2} + f_{SiO_2}\alpha_{SiO_2} \tag{6}$$

where f_{HfO_2} and f_{SiO_2} are the volume fractions of HfO_2 and SiO_2, α_{HfO_2} and α_{SiO_2} are the corresponding polarizabilities. The α_{HfSiO} values can be calculated for different HfO_2 contents in the matrix. We have also to know f_{HfO_2} and f_{SiO_2} for our films. One possibility to get information about the contribution of both phases is to examine the theoretical dispersion of the refractive index of HfSiO materials versus HfO_2 content and to compare these results with the experimental ones presented above. After getting both parameters, n and α_{HfSiO}, we can estimate the density of the films, ρ.

3.2.1. Dispersion of the refractive index for HfO_2-based systems. First of all, we estimate the f_{HfO_2} value. We consider HfSiO material as a two-phase system. One of them is HfO_2. The other one is often assumed to be SiO_2. However, we can assume that incorporation of Si into the HfO_2 matrix can occur as SiO_x and/or Si itself since the layers investigated were grown by sputtering of a HfO_2 target topped by pure Si chips. Thus, the Si-based phase was assumed to be SiO_2, or SiO, or Si to simplify the modeling. The dispersion of the refractive index in 1.5–6 eV spectral range was estimated for three different Si-rich HfO_2 media versus the contribution of each phase. The results versus HfO_2 content are shown in figure 3(a) and (b) only at 2 eV since they are representative over the whole spectral range.

As one can see, n values increase with f_{HfO_2} for the case of the HfO_2/SiO_2 medium, while it decreases for the HfO_2/SiO and HfO_2/Si media. To compare these results with experimental n values obtained for as-deposited films, we added the latter to the figure 3(a). Since it was only one value $n = 2.21$, we added it as a straight line. The intersection of this line with the calculated curves gives the possibility to estimate the f_{HfO_2} value for the as-deposited films. As one can see, the experimental n value exceeds the values calculated for HfO_2/SiO_2 and for HfO_2/SiO media. In such a case, it should be possible to consider that the Si-based phase is incorporated as amorphous Si itself. However, comparing the electronegativity of elements present in HfSiO material, it is obvious that the formation of Hf–O and Si–O bonds is more likely to occur than Hf–Si and Si–Si bonds, whereas Si–O bonds are more probable than Si–Si bonds. As a consequence, the Si-based phase is presented as SiO_x with $0 < x < 1$. Such an assumption could explain the high n value obtained for the as-deposited films (figure 3(a)).

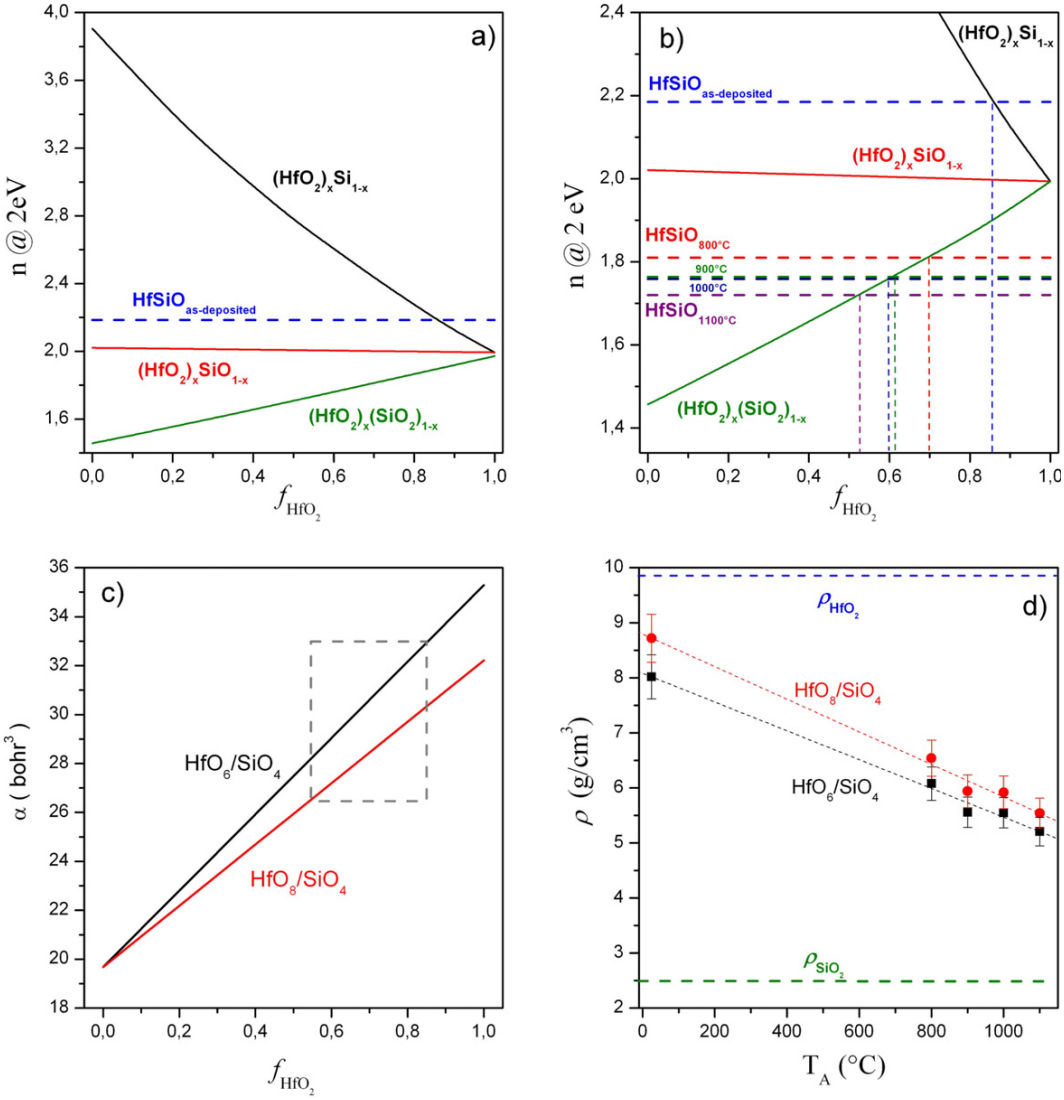

Figure 3. (a) Calculated refractive index for $(HfO_2)_x(Si)_{1-x}$, $(HfO_2)_x(SiO)_{1-x}$ and $(HfO_2)_x(SiO_2)_{1-x}$ versus HfO_2 content, f_{HfO_2}, using the Bruggemann EMA model. The refractive index for as-deposited samples is shown by the dashed line. All the data are taken for 2 eV light energy. (b) Comparison of calculated refractive indexes for $(HfO_2)_x(Si)_{1-x}$, (1), $(HfO_2)_x(SiO)_{1-x}$ (2) and $(HfO_2)_x(SiO_2)_{1-x}$ with experimental values obtained for as-deposited ($HfSiO_{AD}$) and annealed films (from $HfSiO_{800\,°C}$ to $HfSiO_{1100\,°C}$) represented by straight lines. The horizontal dashed lines represent the experimental n values whereas the corresponding vertical dashed lines show the possible volume fraction of HfO_2 in the films, considering results for the n and chemical composition obtained by the ATR method. All the data are taken for 2 eV light energy. (c) The polarizability, α, calculated using equation (6) for different HfO_2 content in HfSiO films using the approach described in [4]. The dashed line frames the range of the polarizability for the films versus HfO_2 content estimated from the corresponding refractive index data. (d) The estimated density of as-deposited films and films annealed at 800–1100 °C for 15 min (for the film composed by HfO_6/SiO_4 and HfO_8/SiO_4 structure units). The densities of SiO_2 and HfO_2 are also presented for comparison.

The experimental data obtained for annealed films are presented similarly in figure 3(b) that is a frame of figure 3(a). It is seen that the refractive index of the annealed films is less than that calculated for the HfO_2/SiO medium. This means that for the annealed samples, the Si-based phase can be considered as SiO_x with $x > 1$ for any f_{HfO_2} values. Since the best modeling results were found for the HfO_2/SiO_2 medium (figure 3(b)), we estimate the f_{HfO_2} based on this dependence. One can see that f_{HfO_2} decreases with annealing treatment from 0.7 ($T_A = 800\,°C$) to 0.55 ($T_A = 1100\,°C$). For the as-deposited films, $f_{HfO_2} \leqslant 0.86$ (figure 3(b)) and the upper limit can be overestimated, but its lower limit was not less than 0.7. To calculate the maximum density of the as-deposited films we used $f_{HfO_2} = 0.86$.

We obtained information about the refractive index and the contribution of the HfO_2 phase. To finalize the estimation of the density of as-deposited and annealed films, we have to determine the polarizability of the films.

3.2.2. Polarizability of HfSiO films. It is known that HfO_2 can be presented by HfO_4, HfO_6 and HfO_8 structure units [4], but the most probable ones are HfO_6 and HfO_8. Among these, the

highest value of α_{HfO_2} is 35.28 bohr^3 corresponding to HfO_6 structure units. However, in the case of HfSiO materials, it was shown that HfO_8 units prevail, giving $\alpha_{HfO_2} = 32.21$ bohr^3 [4]. Since both types of structure units can compose HfSiO films, we will consider that the HfO_2 phase is built by HfO_6 or HfO_8 units that will give us the lower and upper limits of the density of the films. For the case of the SiO_2 phase, it is usually composed of SiO_4 and SiO_6 units [4]. At the same time, it was shown that for the case of high-k silicates, SiO_4 units are the most probable structural elements [4] corresponding to $\alpha_{SiO_2} = 19.68$ bohr^3.

Thus, based on the assumption that our films are composed of HfO_8/SiO_4 or of HfO_6/SiO_4 structure units, we calculated the values of polarizability versus HfO_2 content for HfSiO films using equation (6). The results are presented in table 1 and in figure 3(c). As one can see, α_{HfSiO} decreases with the annealing treatment (table 1) from 33.25 down to 28.26 bohr^3 for the case of HfO_6/SiO_4 and from 30.58 to 26.57 bohr^3 for HfO_8/SiO_4.

Thus, we can turn now to the estimation of the density of the films.

3.2.3. Density of the films. Taking into account equation (5) and using the α_{HfSiO} and n values, we estimated the density of the films. The results are given in table 1 and in figure 3(d). The decrease of the film density is clearly seen. Using both types of media we found that the density of the as-deposited films is in the range of 8–8.7 g cm^{-3}. This value can be overestimated due to uncertainties in the estimation of the HfO_2 fraction in the as-deposited films based on the refractive index data. At the same time, they demonstrate an agreement with the data of [21]. The density of the films decreases from 6.1–6.5 to 5.2–5.5 g cm^{-3} when the annealing temperature increases from 800 up to 1100 °C (figure 3(d)).

It is worth noting that the film density was obtained for the HfSiO layer itself. The model used for the fitting of ellipsometry spectra allowed us to eliminate the contribution of the interfacial SiO_2 layer in the optical parameters of annealed films. In this case, the decrease of the density of the films can be explained by the increasing contribution of a low density phase. The SiO_2 phase is one of the most probable candidates to explain the decrease of the density of the films annealed at 800 °C since, as shown earlier, such an annealing did not lead to a significant transformation of the film structure [12]. However, the decrease of the film density at higher annealing temperatures could be due to a gradual increase of the contribution of the SiO_2 phase as well as pore formation. Note that even if the HfO_2 phase formed under annealing, its density increases usually [27] due to its crystallization. To discriminate the reasons responsible for the variation of the film density, the analysis of the chemical composition as well as structure properties of the films was performed for the same samples by ATR and XRD methods, whereas the TEM study was used to obtain information, not only about the presence of pores, but also to get an answer as to whether the phase separation occurs over the film thickness.

3.3. ATR spectra of as-deposited and annealed layers

Among non-destructive methods to study thin films, the ATR technique holds an important place, since it allows very thin layers to be analyzed. Unfortunately, referenced ATR data for HfSiO materials are not so numerous. The only known data are those regarding the monoclinic HfO_2 phase, while for tetragonal and cubic phases of HfO_2 and, moreover, for $HfSiO_4$ they are not available in the case of ultrathin films.

The interpretation of experimental data obtained for high-k silicate materials is usually based on the comparison of infrared spectra obtained for amorphous SiO_2 and HfO_2, and their transformation due to an increase of the high-k material contribution.

The continuous random network of SiO_2 consists of corner-coordinated SiO_4 tetrahedra, and the disorder of the amorphous structures comes from the Si–O–Si bond angle changes. Usually, SiO_2 demonstrates three main peaks in the mid-infrared range, coming mainly from the motion of oxygen atoms, and under specific conditions several LO and TO phonons of the Si–O bond can be detected in the 450–1350 cm^{-1} spectral range: at 1076 cm^{-1} (TO_3) and 1256 cm^{-1} (LO_3), at 1160 cm^{-1} (TO_4) and 1200 cm^{-1} (LO_4), at 810 cm^{-1} (TO_2) and 820 cm^{-1} (LO_2), as well as at 457 cm^{-1} (TO_1) and 507 cm^{-1} (LO_1) [28, 29]. It is known that the decrease of SiO_2 layer thickness to nanometer scale is accompanied by a shift of the peak positions of all vibration bands to lower wavenumbers, as well as a decrease of the intensity of TO_4–LO_4 phonons that are usually considered as a feature of the disordering of the SiO_2 matrix [29]. In the case of LO_3 and TO_3 phonons this shift is about 25–30 cm^{-1} [30]. However, the detection of the LO_3 phonon is usually considered as evidence of the formation of a perfect Si/SiO_2 interface [31].

The typical ATR spectrum of SiO_2 film, having a similar thickness to the studied HfSiO films, is presented in figure 4(a). Two Si–O vibration bands, peaked at about 1060 cm^{-1} (TO_3 phonon) and at about 815 cm^{-1} (TO_2 phonon), are revealed in the 600–1350 cm^{-1} spectral range. The difference in the observed peak positions for Si–O bands in comparison with the corresponding values mentioned above is due to the film thickness [29].

ATR spectra of as-deposited HfSiO layers demonstrate the presence of a broad band peaked at 1050 cm^{-1} with a shoulder at about 900 cm^{-1} with a tail up to 600 cm^{-1} (figures 4(a) and (b)). The broadening of Si–O vibration bands as well as the shift of their peak positions to lower wavenumbers is due to the Hf incorporation into the SiO_2 matrix. The latter modifies the SiO_2 network due to the higher Hf–O bond length (1.96–2 Å) in comparison to the Si–O one (1.6 Å). The shape of the ATR spectrum (figure 4) gives evidence of the formation of an amorphous network of a binary compound in the as-deposited films.

An annealing of the layers at $T_A = 800$ °C for 15 min leads to an increase of the intensity as well as to the slight narrowing and to the shift of the broad ATR peak from 1050 to 1070 cm^{-1}. By contrast, the lower wavenumber part of the ATR spectrum is featureless (figure 4). A further increase of the temperature up to $T_A = 1000$ °C results in a continuous

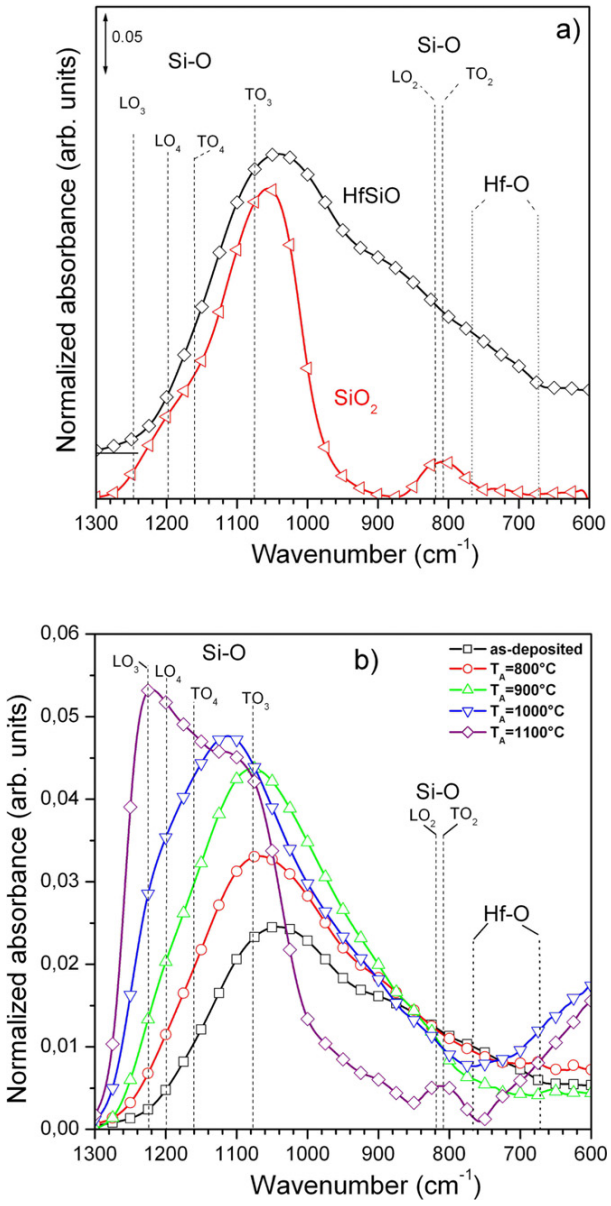

Figure 4. (a) Comparison of ATR spectra of HfSiO and SiO_2 thin films. The thickness of both films is about 18 nm. The vertical dashed lines show the peak positions of all vibration bands observed for the SiO_2 and HfSiO layers. (b) Evolution of ATR spectra with annealing treatment of the HfSiO layer at 800–1100 °C. The annealing time is 15 min.

increase of the peak intensity, to the shift of the peak position to 1120 cm^{-1} and to the appearance of a shoulder at about 1220 cm^{-1}. A treatment at $T_A = 1100$ °C causes the narrowing of this vibration band, a redistribution of the intensities of its components and the appearance of a band at about 820 cm^{-1}.

All these three bands can be ascribed to the SiO_2 phase, as observed for the SiO_2 film (figure 4(a)). The intensity increase and the peak shift to higher wavenumbers can be explained by the increasing contribution of the SiO_2 phase in the film structure as well as by a realignment of the Si–O bonds followed the SiO_2 phase formation. The latter could be due to the formation of an interfacial SiO_2 layer confirmed by the higher intensity of the LO_3 phonon exceeding the TO_3 one (figure 4(b)). At the same time, the contribution of TO_3 and TO_4–LO_4 phonons to the ATR spectrum enables us to assume the presence of a SiO_2 phase in the film due to the phase separation inside the HfSiO film into SiO_2 and HfO_2 phases.

The phase separation under annealing at $T_A = 1000$ and 1100 °C is confirmed by an increase of the ATR intensity in the range of 780–600 cm^{-1}, corresponding to Hf–O vibrations. Usually, two vibration bands peaked at 770–780 cm^{-1} and 680 cm^{-1}, and coming from the HfO_2 monoclinic phase, can be found in this spectral range [32–34], whereas a broad and featureless band is ascribed to amorphous HfO_2 [11, 12]. We suppose that this increase of the ATR band intensity corresponds to the HfO_2 phase formation. However, it is hardly believable that such a high annealing temperature (1100 °C) could lead to an amorphous HfO_2 phase. To get more information about the structure of the HfO_2 phase, we performed a XRD study for these samples.

It is worth noting that the absence of any transformation of the ATR band in the range 780–600 cm^{-1} during annealing at T_A up to 900 °C gives evidence that the incorporation of silicon into an HfO_2 matrix improves the thermal stability of the layers. The most probable reason is that the high flexibility of the Si–O bonds allows the amorphous nature of fused silica to be conserved. However, even if HfSiO could be stable at such an annealing temperatures, the transformation of the Si–O vibration band might be due to a better silicon oxide structure and/or due to the formation of a SiO_2 interfacial layer. Such a transformation occurs at lower temperatures (less than 900 °C) than the phase separation in the HfSiO film (1000–1100 °C). To clarify this issue, we performed TEM observations of cross sections of the samples which we will present below.

3.4. XRD study of HfSiO films

To obtain information about the phase separation caused by high temperature annealing and about the HfO_2 structure, an XRD study has been performed on the samples described above.

It is worth noting that most of the crystallographic data for HfO_2-based materials found in the literature are for monoclinic HfO_2 and tetragonal $HfSiO_4$ phases. The data for other HfSiO compounds are rare and in most cases they were interpreted based on results obtained for bulk HfO_2 and $HfSiO_4$ materials.

In figure 5, the XRD pattern for as-deposited films shows a broad peak in the range of $2\Theta \approx 25°$–$35°$ with a maximum intensity located at $2\Theta \approx 32°$. This result demonstrates the amorphous nature of as-deposited layers. An annealing at temperatures as high as $T_A = 800$–900 °C for 15 min does not lead to a transformation of the shape of this broad peak. The appearance of two overlapped peaks at $2\Theta \approx 30.3°$ and 35.3° occurs after annealing at $T_A = 1000$ °C. The increase of annealing temperature results in an increase in the intensity of these peaks with their concomitant narrowing, as well as the appearance of other peaks in the range of $2\Theta = 40°$–$65°$ at $2\Theta \approx 50.6°$ and 59.8°. Note that the peak at $2\Theta \approx 55°$

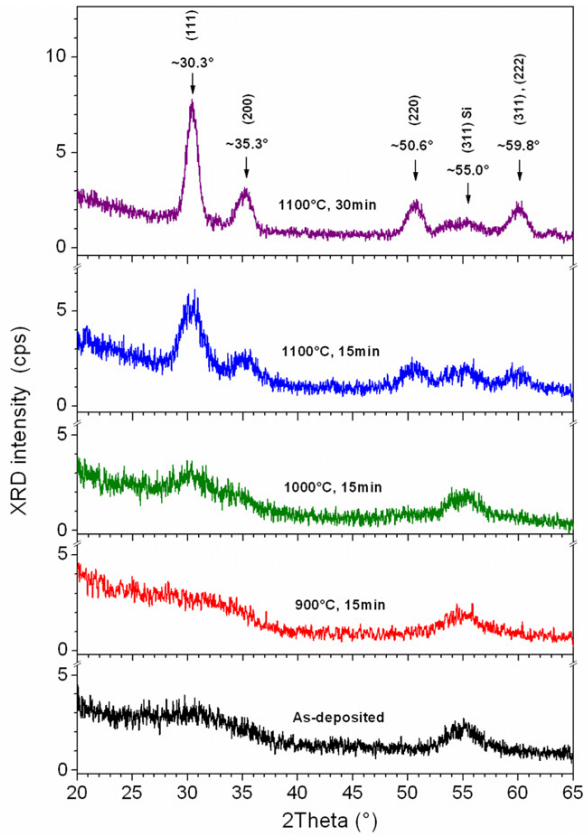

Figure 5. XRD patterns of as-deposited and annealed HfSiO layers. Annealing parameters are mentioned for each spectrum in the figure.

observed for all the samples is due to the Si substrate. The layer annealed at $T_A = 1100\,°C$ for 15 min shows the most intense XRD peaks at $2\Theta \approx 30.3°$, $2\Theta \approx 35.3°$ and $2\Theta \approx 50.6°$ corresponding to the (111), (200) and (220) planes of the tetragonal HfO_2 phase, respectively. The peak at $2\Theta \approx 59.8°$ can be considered as a overlapping of the reflections from the (311) and (222) planes of the same phase.

Usually the tetragonal phase of HfO_2 is observed for ultrathin films, while the annealing treatment at temperatures as high as 800 °C favors its transformation to the monoclinic phase [35]. However, in our case, a longer annealing treatment (up to 30 min) at $T_A = 1100\,°C$ results in an increase of the intensities of only the observed XRD peaks and does not lead to the appearance of other peaks. This could be evidence of the thermal stability of the tetragonal HfO_2 phase in our samples. Since it has higher dielectric constant in comparison with that of the monoclinic phase, such a film can be used as a gate material for structures needing a high temperature annealing process, for example, for some nanomemory structures with embedded Si nanoparticles [14].

One of the important results obtained from comparison of our XRD data with ATR spectra measured for the same samples, is the fact that the increase of intensity of ATR band in the spectral range of 600–780 cm^{-1} is due to the HfO_2 phase formation, which begins mostly at $T_A \geqslant 1000\,°C$. However, the absence of a well-defined peak at 770–780 cm^{-1} demonstrates that our samples do not contain the monoclinic HfO_2 phase, while they cannot be considered as amorphous only. As we showed above, the formation of the tetragonal HfO_2 phase is also possible, leaving the low wavenumber part of the ATR spectra as featureless. In such a case, a combination of both techniques is required to obtain the information about the structure of the HfSiO films.

The analysis of the optical properties of the layers showed a decrease of their refractive index with annealing treatment. Regarding the structural properties, the phase separation is confirmed by ATR spectra, whereas the crystallization of the HfO_2 phase is demonstrated by the XRD data. Since an increase of refractive index is expected with HfO_2 crystallization, one can conclude that the continuous n decrease occurs due to an increasing contribution of the SiO_2 phase. At the same time, neither ATR nor XRD studies can reveal unambiguously where this SiO_2 phase is located, i.e. at film/substrate interface or embedded in the film itself. However, based on these results and on the estimation of the film density, we can assume the presence of the SiO_2 phase inside the volume of the HfSiO layer. The latter will be confirmed by TEM analysis of the as-deposited and annealed films.

3.5. TEM analysis of the structural properties of the films

TEM images of the cross sections of as-deposited and annealed samples are shown in figure 6. As-deposited samples are homogeneous, smooth enough and do not have a thick interfacial layer (its thickness not higher than 1 nm). These observations corroborate the results obtained by fitting of ellipsometry spectra. The increase of the annealing temperature up to 900 °C leads to an increase of total film thickness. However not only an increase of the interfacial SiO_2 layer thickness, but also an expansion of the HfSiO film itself occurs (figure 6(b)). The appearance of bright and dark alternate lines parallel to the film/substrate interface is seen and can be explained by the Hf segregation process, whereas the film stays amorphous (figure 6(b)). A further increase of annealing temperature up to 1000 °C results in the formation of a thicker SiO_2 interfacial layer as well as in a greater contrast between the bright and dark regions (figure 6(c)). They correspond to SiO_2-rich and HfO_2-rich phases that are evidence of the HfSiO phase separation. Also, the crystallization of a HfO_2 phase begins to appear. Upon annealing at 1100 °C, an increase of the SiO_2 interfacial layer thickness (up to 5 nm) is seen. The crystallization of the HfO_2 phase is more pronounced (figure 6(d) and (e)). The crystallites are mainly located in the dark regions as demonstrated by figure 6(e) which is an enlargement of the squared region shown in figure 6(d).

The evolution of the interfacial SiO_2 layer thickness as well as that of the entire film confirm the values obtained by fitting of ellipsometry spectra (table 1).

Figure 6(f) represents a typical selected area electron diffraction (SAED) pattern corresponding to the film and a part of the [110] oriented silicon substrate. Apart from the well-defined dots coming from the silicon substrate, four weak

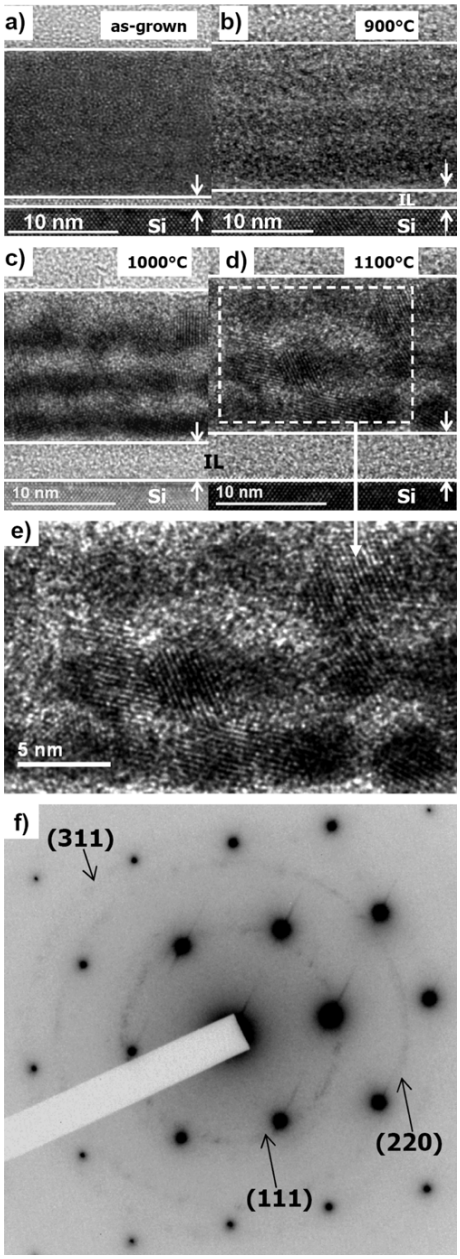

Figure 6. TEM cross sections of the HfSiO layer taken for as-deposited (a), annealed at 900 °C (b), 1000 °C (c) and 1100 °C (d) in N_2 flow for 15 min. The electron diffraction pattern is shown for the sample annealed at 1100 °C. IL is the interfacial layer.

rings appeared, as marked in figure 6(e). The lattice plane distances estimated from SAED were 2.95, 1.80 and 1.53 Å. These distances are compatible with lattice planes of the HfO_2 tetragonal phase: $d_{[111]} = 2.95$ Å, $d_{[220]} = 1.82$ Å and $d_{[311]} = 1.59$ Å.

It is known that thick pure HfO_2 usually has the monoclinic phase, whereas tetragonal and cubic phases appear at 1670–2200 °C [35]. When the thickness of the layer decreases to the nanometer scale, the presence of the tetragonal phase can be observed in pure HfO_2 layers [36]. However, it transforms easily to the monoclinic phase at moderate temperatures [36]. TEM observations of HfSiO films show that the tetragonal phase is stable in such films under annealing at 1100 °C and such films can be used for applications that need high temperature annealing [14].

The appearance of bright (SiO_2-rich) and dark (HfO_2-rich) regions without crystallization of the films (at 900 °C, figure 6(b)) can be explained by a diffusional spinodal decomposition [16, 17] that requires an external field or sources. The latter could be the difference in free energies between the film volume and the film/substrate interface or film surface. For ultrathin films, both of them play an important role in the film decomposition and surface-directed spinodal decomposition was predicted for thin silicate films.

It is known that the Si–O bond is covalent, whereas the M–O (M = Ti, Zr, Hf) is ionic, giving rise to a metastable miscibility gap in high-*k* silicates. They are usually strained, and a decrease of their free energy is predicted through a phase separation process [37]. The appearance of SiO_2 and MO_2 phases occurs due to lowering of the coordination of silicon and metal cations. The reduction of the Si–Si and Si–O distances and the lowering of Si coordination occur faster than the lowering of metal cation coordination and an optimization of the M–M distance. This is due to an energetic barrier for movement of metal cations through the O sub-lattice caused by the ionic behavior of M–O bonds [37]. At the same time, this barrier is lowered at elevated temperatures and favors the formation of MO_2 nuclei followed by the growth of crystallites around them [37].

A similar film decomposition was observed in previous works for ZrSiO films [15, 25]. It was shown that $(ZrO_2)_x(SiO_2)_{1-x}$ films with $x = 0.1$–0.6 decompose into ZrO_2-rich and SiO_2-rich phases under annealing at 900 °C. The alternation of ZrO_2-rich layers with SiO_2-rich ones was formed in the direction normal to the surface. The nature of the layer closest to the film/substrate interface (i.e. ZrO_2 rich layer or SiO_2 one) depends on the total thickness of the film [25]. Above a critical thickness, the ZrO_2 layer can be localized at the film/substrate interface as well as near the film surface, leading to the formation of a multilayer structure.

It was shown that the mechanism of phase separation of HfSiO films is also a *surface-directed* spinodal decomposition. This effect was demonstrated in films fabricated by the atomic-layer deposition technique [16, 17]. It was shown that, usually, a very thin SiO_2 layer (about monolayer of SiO_2) is located near the film surface, whereas beneath it a Hf-rich layer was observed. For films thinner than 5 nm, a Hf-enrichment of the top layer of the film occurs during the growth process due to the diffusion of Hf towards the film surface, while a Si-rich layer forms close to the film/substrate interface. For thicker films, the formation of an alternating Si-rich/Hf-rich structure was found and explained by the diffusion of Hf ions towards the substrate. However, films thicker than 10 nm lose their layered structure in the middle of the film [16, 17]. It was shown that rapid thermal annealing of such films results in the formation of a layer structure, while longer annealing time led to the formation and crystallization of the HfO_2 phase. Unfortunately, this study was performed only for

$(HfO_2)_{0.25}(SiO_2)_{0.75}$ films [16, 17] without detailed analysis of the crystalline HfO_2 structure.

Considering the fact that the decomposition of $(ZrO_2)_x(SiO_2)_{1-x}$ films was studied for $x = 0.1$–0.6 and the properties of $(HfO_2)_{0.25}(SiO_2)_{0.75}$ were found to be similar to Zr silicates with a close composition, one can admit that Hf and Zr silicates have similar properties over a wide range of x. In such a case, the mechanisms responsible for the phase separation in both silicates have to be the same.

Based on the results presented above, we can assume that the formation of HfO_2-rich and SiO_2-rich layers in our films during the annealing treatment is also governed by a surface-directed spinodal decomposition. Annealing at moderate temperatures results in a diffusion transformation of the layer composition leading to the formation of HfO_2-rich and SiO_2-rich regions without crystallization of the films. This was observed at $T_A = 800\,^{\circ}C$ in [14] and demonstrated in figure 6(b) for $T_A = 900\,^{\circ}C$. The further increase of the annealing temperature and/or time governs the HfO_2 phase crystallization, as is demonstrated by figures 5 and 6(c) and (d).

TEM study showed also the increase of the total thickness of the film stimulated by annealing treatment (figure 6), confirming the results obtained by fitting of ellipsometry data (table 1). The increase of film thickness occurs not only due to the increase of the interfacial layer thickness. Since no formation of pores in the layers was observed in the TEM experiment, the expansion of the HfSiO film itself takes place due to the SiO_2 phase formation. The latter has a lower density than the HfO_2 one and can be considered as the only reason for the decrease of the density of the annealed films.

It is worth noting that the use of high-k silicate as a gate material supposes that the thickness of the gate layer can be increased in comparison with the SiO_2 gate. At the same time, as shown above, the annealing of HfSiO films at specific temperatures enables them to keep their amorphous structure without major transformation of their chemical composition. Post-deposition treatment at 1000–1100 °C results in the formation of a stable HfO_2 tetragonal phase that favors the increase of the film permittivity. The latter is considered as an advantage of the high-k gate material [5]. However, the formation of the alternating HfO_2/SiO_2 multilayer structure at 1100 °C demonstrated above could be a reason for the worsening of the dielectric properties of the films. In such a case, the use of the appropriate thickness of HfSiO material could be a solution.

4. Conclusion

Si-rich HfO_2 layers have been fabricated by RF magnetron sputtering of a HfO_2 target topped by Si chips in a pure argon plasma. The effect of the annealing treatment on the properties of the layers had been investigated by means of spectroscopic ellipsometry, x-ray diffraction, infrared absorption spectroscopy and high resolution transmission electron microscopy. It was demonstrated that annealing treatment results in the formation of an interfacial SiO_2 layer as well as in the increase of the HfSiO film thickness itself. The latter was explained by a phase separation of HfSiO into HfO_2 and SiO_2 phases over its volume. The density of the films versus annealing temperature was estimated. Its decrease with an increase of annealing temperature is explained only by a formation of SiO_2 phase over the film volume and the increase of its contribution with annealing. The formation of a HfO_2 phase was also revealed. It is shown that annealing at temperatures less than 900 °C results only in phase separation, without crystallization of the films. The higher temperature annealing favors HfO_2 crystallization into the tetragonal phase. The latter was found to be stable, offering a possibility to use such HfSiO materials for microelectronic applications, for example, for nanomemory structures with embedded Si nanoparticles requiring high temperature annealing. The formation of the multilayer Si-rich/Hf-rich structure after annealing treatment was observed and explained by surface-directed spinodal decomposition.

Acknowledgments

This work is supported by the French National Research Agency (ANR) through the Nanoscience and Nanotechnology Program (NOMAD Project no ANR-07-NANO-022-02) and, for one of the authors (LK), by the Conseil Régional de Basse Normandie through the CPER project—Nanoscience axe (2007-2013).

References

[1] Wilk G D, Wallace R M and Anthony J M 2000 *J. Appl. Phys.* **87** 484
[2] Wilk G D, Wallace R M and Anthony J M 2001 *J. Appl. Phys.* **89** 5243
[3] Goncharova L V, Dalponte M, Starodub D G, Gustafsson T, Garfunkel E, Lysaght P S, Foran B, Barnett J and Bersuker G 2006 *Appl. Phys. Lett.* **89** 044108
[4] Rignanese G-M 2005 *J. Phys.: Condens. Matter* **17** R357
[5] Fischer D and Kersch A 2008 *Appl. Phys. Lett.* **92** 012908
[6] Lee Ch-K, Lee H-S, Hwang Ch S and Han S 2008 *Phys. Rev.* B **78** 012102
[7] Cockayne A 2008 *J. Appl. Phys.* **103** 084103
[8] Tsoutsou D *et al* 2009 *J. Appl. Phys.* **106** 024107
[9] Majumder P, Jursich G and Takoudis C 2009 *J. Appl. Phys.* **105** 104106
[10] Tomida K, Kita K and Toriumi A 2006 *Appl. Phys. Lett.* **89** 142902
[11] Gourbilleau F, Khomenkova L, Dufour C, Coulon P-E and Bonafos C 2009 HfO_2-based thin films deposited by magnetron sputtering *Materials and Physics for Nonvolatile Memories* (*Mater. Res. Soc. Symp. Proc.* vol 1160) ed Y Fujisaki, R Waser, T Li and C Bonafos (Warrendale, PA: Material Research Society) pp 69–72
[12] Khomenkova L, Dufour C, Coulon P-E, Bonafos C and Gourbilleau F 2010 *Nanotechnology* **21** 095704
[13] Li W, Jia R, Chen C, Liu M, Zhu C and Long S 2009 *ECS Trans.* **18** 1071
[14] Perego M, Seguini G, Wiemer C, Fanciulli M, Coulon P-E and Bonafos C 2010 *Nanotechnology* **21** 055606
[15] Lucovsky G and Rayner G B 2000 *Appl. Phys. Lett.* **77** 2912
[16] Liu J, Wu X, Lennard W N and Landheer D 2009 *Phys. Rev.* B **80** 041403
[17] Liu J, Wu X, Lennard W N and Landheer D 2009 *ECS Trans.* **25** 163
[18] Cho M-H, Kim C Y, Moon K, Chung K B, Yim C J, Ko D-H, Sohn H C and Jeon H 2008 *J. Chem. Phys.* **129** 034705
[19] http://www.horiba.com/scientific/products/ellipsometers/software/

[20] Charvet S, Madelon R, Gourbilleau F and Rizk R 1999 *J. Appl. Phys.* **85** 4032
[21] Buiu O, Davey W, Lu Y, Mitrovic I Z and Hall S 2008 *Thin Solid Films* **517** 453
[22] Bruggeman D A G 1935 *Ann. Phys.* **416** 636
[23] Forouhi A R and Bloomer I 1986 *Phys. Rev.* B **34** 7018
[24] Jelisson G E Jr and Modine F A 1996 *Appl. Phys. Lett.* **69** 371
[25] Neumayer D A and Cartier E 2001 *J. Appl. Phys.* **90** 1801
[26] Mitrovic I Z, Buiu O, Hall S, Bungey C, Wagner T, Davey W and Lu Y 2007 *Microelectron. Reliab.* **47** 645
[27] Tan T, Liu Zh, Lu H, Liu W and Tian H 2010 *Opt. Mater.* **32** 432
[28] Kirk C T 1988 *Phys. Rev.* B **38** 1255
[29] Lange P 1989 *J. Appl. Phys.* **66** 201
[30] Ono H, Ikarashi T, Ando K and Kitano T 1998 *J. Appl. Phys.* **84** 6064
[31] Olsen J E and Shimura F 1989 *J. Appl. Phys.* **66** 1353
[32] Maunoury C *et al* 2007 *J. Appl. Phys.* **101** 034112
[33] Frank M M, Sayan S, Dörmann S, Emge T J, Wielunski L S, Garfunkel E and Chabal Y J 2004 *Mater. Sci. Eng.* B **109** 6
[34] Nguyen N V, Davydov A V, Chandler-Horowitz D and Frank M F 2005 *Appl. Phys. Lett.* **87** 192903
[35] Tang J, Zhang F, Zoogman P, Fabbri J, Chan S-W, Zhu Y, Brus L E and Steigerwald L 2005 *Adv. Funct. Mater.* **15** 1595
[36] Ho M-Y *et al* 2003 *J. Appl. Phys.* **93** 1477
[37] Monaghan S, Greer J C and Elliott S D 2005 *J. Appl. Phys.* **97** 114911

Influence of neodymium concentration on excitation and emission properties of Nd doped gallium oxide nanocrystalline films

A. Podhorodecki,[1,a)] M. Banski,[1] J. Misiewicz,[1] C. Lecerf,[2] P. Marie,[2] J. Cardin,[2] and X. Portier[2]
[1]*Institute of Physics, Wroclaw University of Technology, Wybrzeze Wyspianskiego 27, 50-370 Wroclaw, Poland*
[2]*CIMAP, CEA/UMR CNRS 6252/ENSICAEN, Université de Caen Basse Normandie, 6 Boulevard Maréchal Juin, 14050 Caen, France*

(Received 2 July 2010; accepted 29 July 2010; published online 24 September 2010)

Gallium oxide and more particularly β-Ga_2O_3 matrix is an excellent material for new generation of devices electrically or optically driven as it is known as the widest band gap transparent conductive oxide. In this paper, the optical properties of neodymium doped gallium oxide films grown by magnetron sputtering have been analyzed. The influence of the Nd ions concentration on the excitation/emission mechanisms of Nd ions and the role of gallium oxide matrix have been investigated. The grain size reduction into gallium oxide films have been observed when concentration of Nd increases. It has been found for all samples that the charge transfer is the main excitation mechanism for Nd ions where defect states play an important role as intermediate states. As a consequence Nd emission efficiency increases with temperature giving rise to most intensive emission at 1087 nm at room temperature. © *2010 American Institute of Physics*. [doi:10.1063/1.3484039]

I. INTRODUCTION

Light emitting diodes or laser sources working in the near infrared region are under extensive investigation due to a wide range of their potential applications. Among many different solutions like quantum wells,[1] quantum dashes,[2] or quantum dots,[3] and doping or codoping of semiconductors by rare earth (RE), i.e., Nd, Er ions[4,5] gives many new opportunities for infrared light sources. Their exceptional properties arise from the fact that their optical transitions take place among internal 4*f* orbitals, which are shielded from the environment by 5*d*-orbital electrons. It results in an emission with a narrow band and extremely stable wavelength, regardless in some extent of the external conditions in matrix transparent in the wide spectral range. In addition, this concept gives many other new possibilities since this kind of matrices can be easily codoped by other ions covering a spectral range from 400–2000 nm.[6]

However, the main limitation of RE ions is their small absorption cross section due to electric dipole transitions which are forbidden according to Laporte's rule. In addition, their low solubility in the matrix is reflected as ions clustering which quenches their emission above critical, often very low (less then 0.1%), RE content. Thus, in order to increase their emission efficiency, crucial for practical applications, their excitation should be sensitized by an additional donor center, i.e., matrix,[7] defects states,[8] nanocrystals,[4] or other molecules, i.e., molecular oxygen.[9] At these limited conditions for using RE ions as emitters in real devices, a better understanding of the excitation and quenching mechanisms should be investigated in details to optimize their optical properties.

The other important issue, to overcome for this kind of "discrete" light emitters is the poor electrical properties of matrices used as a RE ions host. Thus, even if optical pumping of RE ions via the energy transfer gives promising results, electrical pumping became very difficult to realize in practice.

In the following, gallium oxide films were used as a host matrix of Nd^{3+} ions. This material is well known as a transparent conductive oxide with the widest band gap (4.9 eV), which can exhibit n-type semiconductor properties in case of some oxygen deficiency.[10] Thus, this material is a promising matrix for next generation optoelectronic devices working in a longer wavelength. Due to its low maximum phonon energy ($\sim$793 cm^{-1}) (Ref. 11) as compared to silicate glasses ($\sim$1100 cm^{-1}), and its high refractive index (n=1.96 at 1.06 μm) (Ref. 12) it is expected to provide significantly high radiative decay rates and low nonradiative relaxation rates of RE excited-state levels. RE-doped gallium oxide is also a promising material for electroluminescent based devices.[13–16] Additionally, this matrix can exhibit good electrical properties when doped within.[17]

In the present work, gallium oxide films doped with various Nd^{3+} concentrations have been investigated to determine their excitation mechanism and its evolution versus Nd content in the matrix. The absorption, photoluminescence (PL) and photoluminescence excitation (PLE) measurements in the wide temperature range of 10–300 K have been performed for all the samples.

II. EXPERIMENTAL DETAILS

The neodymium doped gallium oxide films have been elaborated by magnetron sputtering of a Ga_2O_3 target (99.99% purity) partially covered by Nd_2O_3 (99.99% purity)

a)Electronic mail: artur.p.podhorodecki@pwr.wroc.pl.

pellets of calibrated shapes. Nd^{3+} concentration varies with the r parameter, corresponding to the Nd_2O_3 pellets-to-Ga_2O_3 target surface ratio. The samples investigated in our study had r in the range 0%–38.8%. The layers were grown on p doped and (100)-oriented Si substrates. During all the growth process, the 100 °C temperature was kept constant. Post annealing treatments were carried out at 1000 °C during 1 h under a continuous flow of nitrogen. A more detailed description of the sample preparation was already presented in a previous article.[18]

Rutherford backscattering spectroscopy (RBS) experiments were performed using a $^4He^+$ ion beam with a 2.5 MeV Van de Graaff accelerator of the "Institut des Nanosciences de Paris."

Transmission electron microscope (TEM) observations of the films were carried out using a JEOL 2010F TEM operated at 200 kV. Dark field images and high resolution TEM images were taken along the [110] direction of the Si substrate. This direction allows a cross sectional view of the samples with the beam parallel to the film/substrate interface.

Regarding the optical properties of the films, for PLE spectroscopy, samples were excited by a xenon lamp (450 W) coupled with a monochromator (Jobin Yvon TRIAX 180) and for absorbance measurements, a tungsten–deuterium halogen lamp was used. The visible PL, absorbance, and PLE signals were collected and transmitted by an optical fiber to the spectrometer (HR4000 Ocean Optics) and divided by the light source characteristic. The PL spectra in the infrared spectral range were obtained by cooled linear InGaAs array detector of 512 pixels coupled to the monochromator (Jobin Yvon TRIAX 550).

III. RESULTS AND DISCUSSION

The relationship between r values and Nd contents in the films has been established thanks to RBS measurements from as-deposited films, in which the Nd distribution is supposed to be homogeneous. Obtained in this way values are equal to 0.08 at. %, 0.94 at. %, 1.56 at. %, and 1.79 at. % of Nd for r=24.2, 29.1, 33.9 and 38.8, respectively. Also, secondary ion mass spectroscopy experiments are in progress and complementary results will be published in a forthcoming publication.[19]

As it has been already shown in previous works,[20] all as-grown films are amorphous. Upon annealing treatment at 1000 °C, the films become mostly crystalline. TEM images of cross-section views of annealed gallium oxide films are shown in Fig. 1. Figures 1(a) and 1(c) correspond to a film grown with r=9.7%, which is equivalent to a Nd^{3+} atomic concentration lower than 0.08%. The images show a rather good crystallinity of the film with a columnar growth more particularly in the upper part of the film [Fig. 1(c)]. In the bottom part of the film [Fig. 1(a)], relatively large grains are visible with no texture or columnar structure. The average grain size is approximately 55 nm, but the size distribution is large (from 10 up to 100 nm). It is worth noting that voids (brightest regions in the image) are also present in the film as well as amorphous regions (gray regions). Figure 1(b) presents a bright field TEM image of a sample prepared with

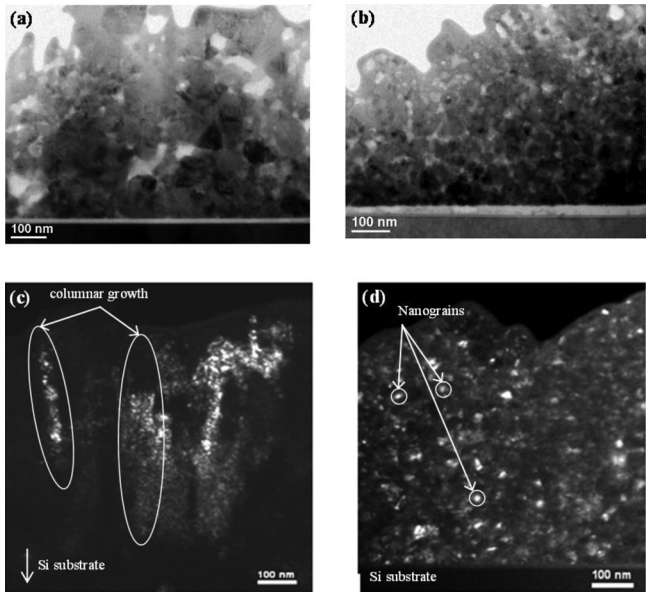

FIG. 1. Bright field TEM images of annealed samples elaborated with (a) r=9.7% and (b) r=38.8%. Dark field TEM images of the corresponding r values (c) and (d), respectively. In the first case, columnar growth and relatively large grains are observed whereas in the latter case, a random growth prevails with a concomitant nanostructuration of the film.

1.79% of Nd ions. A dark field image of this sample is also reported in Fig. 1(d). In this case, the average grain size is about 10 nm and then much smaller than the previous case. It is also interesting to notice that the grain size is more uniform.

In our previous article,[20] x-ray diffraction experiments demonstrated the formation of the stable β-Ga_2O_3 phase for all r values upon annealing. This result was confirmed by high resolution TEM (HREM) observations of well oriented grains whose patterns were consistent with the above mentioned structure. However, RBS experiments have revealed that, for low r values, the expected gallium oxide stoichiometry (Ga_2O_3) is not reached and this was observed for both as-deposited and annealed films. Indeed, the stoichiometry evolves from $Ga_2O_{2.7}$ for low r values and tends to the expected Ga_2O_3 alloy for higher r values.

These results mean that, despite the formation of the β-Ga_2O_3 phase in all cases, a more pronounced oxygen deficiency is observed for low r values. Furthermore, a high degree of Nd doping favors the formation of β-Ga_2O_3 nanoparticles.

Regarding Nd localization in the film, local energy dispersive x-ray diffraction (EDX) experiments have been tempted for both samples of Fig. 1. No variation in the Nd concentration has been noticed for the lowest r value (9.7%). A more particular attention has been paid to grain boundaries but the Nd concentration remained lower than the detection limit of the spectrometer. Concerning the highest r value, significant Nd concentrations (up to 7%) have been noticed around the β-Ga_2O_3 nanoparticles confirming a nonuniform distribution of the RE in the film and a pronounced presence of Nd in the surrounding of the β-Ga_2O_3 nanoparticles. By contrast, local composition measurements in the grains lead to a Nd concentration varying from 1.5 up to 2%.

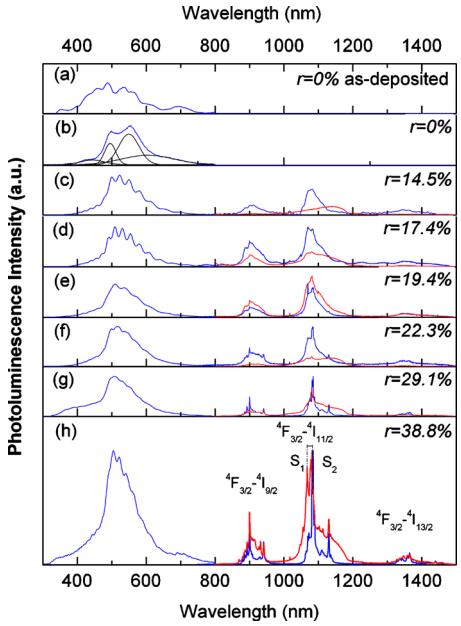

FIG. 2. (Color online) PL spectra obtained for Nd doped gallium oxide films at two different excitation wavelengths: 266 (blue line) and 787 nm (red line). All films have been annealed, excluded the one related to the (a) spectra. (Scales have been adapted for better view).

Figure 2 shows the PL spectra obtained for gallium oxide films with different Nd contents at two different excitation wavelengths, resonantly through the Nd^{3+} levels ($^4I_{9/2} \rightarrow {}^4F_{5/2}$) at 787 nm (thick red line) and nonresonantly at 266 nm (thin blue line). As we can see, for all samples excited by the UV light, a strong and complex green emission (GE) band centered at 500 nm is clearly observed with subbands at ~440, 500, 550, and 600 nm [see Fig. 2(b)]. This band is also present for undoped annealed sample. Moreover, emission band covering a very similar energy range appears also for undoped but also not annealed sample [Fig. 2(a)]. However, its intensity is much lower than for the annealed one (factor ~40). Based on our observations, where the emission intensity for this GE band strongly increases with the annealing, the energy levels responsible for this emission could be related to Ga_2O_3 nanoclusters (Ga_2O_3-nc), whose formation is strongly enhanced by the annealing. These levels can be related to cluster's core but more probable to energy levels (defects or surface states) related to nanoclusters boundaries formation.

The blue side of observed emission bands in Ga_2O_3 can be explained as originating from Ga vacancies (V_{Ga}), O vacancies (V_O),[21] and Ga–O vacancy pairs in Ga_2O_3.[22] In β-Ga_2O_3, the donors (V_O) were found to be gathered in clusters that form a donor band 40 meV below the conduction band where gallium–oxygen vacancy pair clusters form an acceptor band 420 meV above the valence band. These levels are responsible for the formation of an exciton bound as donor-acceptor pair giving rise to a blue-GE band. In addition, red band centered at about 706 nm has been already observed in β-Ga_2O_3 originating from the recombination of an electron trapped by (V_O) donor and a hole trapped by acceptor due to the nitrogen doping, presumably replacing oxygen in the lattice.[23,24]

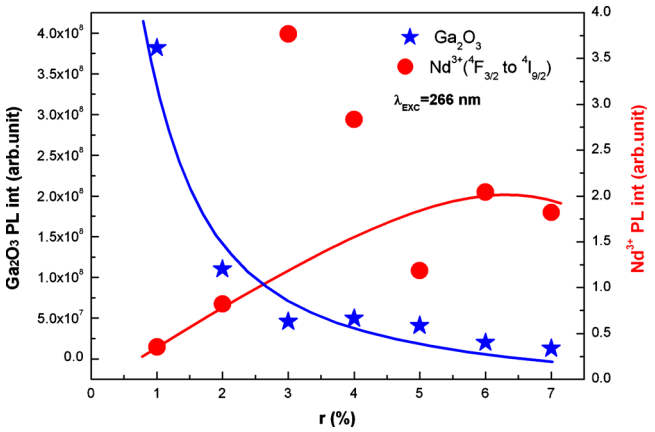

FIG. 3. (Color online) PL intensities for Nd ions and VIS emission vs surface ratio (r).

Additionally, it has been found that the emission intensity of the GE band depends on the Nd content what can be seen in more details in Fig. 3. This feature could be a consequence of more efficient coupling between the Ga_2O_3-nc and Nd ions when the Nd content increases. In consequence, the averaged intensity of the Ga_2O_3-nc is reduced since part of absorbed carriers is lost for Nd excitation. Unfortunately, when the Nd content increases, the shape of the emission band also changes and well resolved interference patterns are observed [see Fig. 2(c) for instance]. Despite this thickness effect, a more detailed analysis of the effect of Nd doping on the visible emission intensities has been tempted and the integrated PL intensities have been extracted and shown in Fig. 3. This figure will be discussed in the next paragraphs.

Moving to Nd related emission, at this nonresonant excitation (266 nm) emission appears only for samples with r values higher than 17.4%. Three main emission bands related to Nd ions have been observed for these samples centered at 900 nm, 1087 nm, and 1362 nm and related to transitions from $^4F_{3/2}$ to $^4I_{9/2}$, $^4I_{11/2}$, $^4I_{15/2}$ energy levels of Nd^{3+} ions, respectively, while the most intense band is at 1087 nm, which band is the most interesting from the application point of view. Above this concentration, Nd related emission strongly increases and the shape of Nd emission lines becomes narrower and characterized by a Stark effect leading to at least two sets of emission lines at characteristic energies S_1=1.1462 eV (1081 nm) and S_2=1.1419 eV (1085 nm).

On the other hand, when the samples are excited resonantly, unwanted emission band centered at 1100 nm can be observed for all Nd concentrations which band overlaps with the emission from Nd ions. We associated this band to a recombination process from the silicon substrate.[25] Second, as for nonresonant excitation, emission from Nd ions appears clearly when r is above 17.4% and also characterized by the evolution of the emission line shape.

When comparing both PL spectra related to the emission from the Nd ions obtained at resonant and nonresonant excitations, two phenomena are observed with the increase in Nd content. First, in both cases, the Stark splitted lines become stronger and the peaks are well separated with a spectral narrowing. This implies that with the r increase, Nd sites distribution goes from a broad one (amorphous environment)

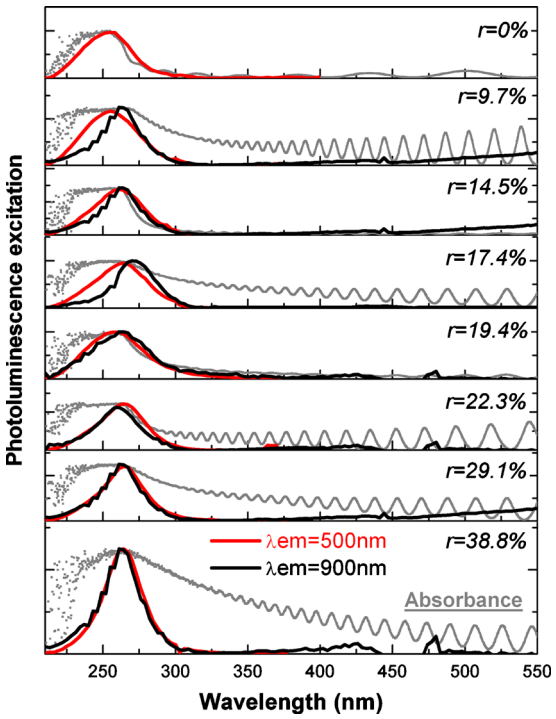

FIG. 4. (Color online) PLE spectra obtained both for emission at 500 nm (red line) and emission related to Nd ions at 900 nm (dark line) for samples containing different amount of Nd ions. Additionally, absorbance spectra have been given (dotted line).

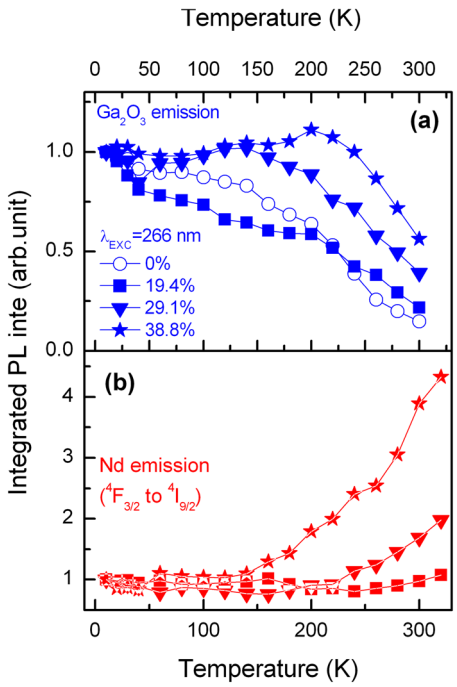

FIG. 5. (Color online) Normalized at 10K integrated PL intensities of the 500 nm (a) and 900 nm (b) bands, measured at different temperatures and obtained for samples with different Nd contents at 266 nm excitation wavelength.

to a sharper one (crystalline environment). Second, we deal with different contributions of the Stark splitted lines grouped at two different spectral positions, which is clearly observed for the highest r value. These results suggest that there are two main sites of Nd ions, where the ions at site-S_2 are mostly excited during a nonresonant process.

Based on these observations, we can conclude that when the gallium oxide matrix is excited resonantly (787 nm), Nd ions placed at two averaged sites (S_1 and S_2) are excited equally but when the matrix is excited nonresonantly (266 nm) most of the ions which are excited are Nd ions "coupled to element" responsible for their high energy sensitization, i.e., energy levels related to Ga_2O_3-nc. Moreover, the improvement in emission line shapes is in agreement with our structural data which indicates that with Nd content the stoichiometry of the matrix became improved thus ions are placed in more crystalline environment.

First of all, to confirm this coupling between the sensitizing element and the Nd ions, the integrated emission intensity has been calculated for both emission bands. An evident correlation for these two emission bands (~500 and 900 nm) can be observed indicating that we deal with the "medium-coupling regime" since the element sensitizing the Nd ions is also responsible for the emission observed at 500 nm and only a part of excited carriers sensitizes the Nd ions.

In the second step, to define the "sensitizing element" and to confirm the excitation energy transfer from it to the Nd ions, the excitation spectra have been measured for Nd emissions at 900 and 500 nm. Figure 4 shows the excitation and the absorbance spectra obtained from the reflectance data corrected by the Si substrate reflectance. As it can be seen for each sample, the excitation spectra overlap each other and their maxima agree with the maxima of the absorbance bands centered at 250 nm (4.95 eV). These observations indicate that the excitation mechanism responsible for the emission band at 500 nm is the same as for the emission at 900 nm.

In addition, it can be seen that the excitation band position, within the experimental errors, is approximately the same for all samples. Moreover, from the absorbance spectra, evident interference patterns are clearly resolved, confirming also our previous conclusions related to the origin of multipeaks structure of the emission band centered at 500 nm. The obtained excitation (absorption) band position is in good agreement with the values reported by other authors for the band gap of Ga_2O_3 in β phase. This indicates that the main excitation mechanism of Nd ions is through the Ga_2O_3 matrix which plays the role of a sensitizer for the Nd ions. Since we know that the Ga_2O_3-matrix plays a crucial role in the excitation of the Nd ions, the question is to know what kind of physical process is responsible for the excitation energy transfer after the carriers are absorbed by the matrix. Is this a direct excitation energy transfer from the grains to the lanthanide ions[4] or is this a defect mediated process?[8] For the latter one, two main processes can be responsible for the energy transfer mediated by the defect states, namely nonradiative dipole-dipole energy transfer (Förster–Dexter) (Ref. 26) or charge (electron/hole) transfer from donor/acceptor states to Nd ions.[9]

To verify these hypotheses, the emission intensities for both emission bands at 500 and 900 nm have been recorded at different temperatures and at nonresonant excitation (266 nm). Results are shown in Fig. 5. The PL integrated intensity of the visible emission band [Fig. 5(a)] obtained for undoped

and doped with r=19.4% samples decreases with temperature and can be well fitted with a simple model describing a thermal quenching with one thermal deactivation energy equals to 43 meV and 44 meV, respectively. For doped samples with r=29.1% and 38.8%, the behavior with temperature is a bit different but the main quenching mechanism seems to be similar to the ones observed in a previous samples and can be characterized by deactivation energies equal to 54 meV and 65 meV for samples with r=29.1 and 38.8, respectively.

Surprisingly, emission intensity of Nd ions has a much more different behavior when the temperature is changing [Fig. 5(b)]. In this case, the emission does not change at all until the temperature exceed approximately 150 K, which temperature corresponding to deactivation energy responsible for the quenching in emission intensities related to Ga_2O_3 grains. Based on this temperature behavior, it has been concluded that the main excitation path of Nd ions must include the charge transfer (CT) process, either the charge is directly transferred to Nd ions or via an intermediate defect states.

Taking all these results into account, excitation mechanisms of the Nd ions can be discussed in details. When the free electron will appear in the conduction band and a hole in the valence band after the 266 nm excitation (or after electrical pumping) the carriers quickly relax to the lowest levels within the energy gap of Ga_2O_3 nanocrystalline matrix (surface or defect states related to Ga_2O_3-nc). For all temperatures, these carriers recombine radiatively giving rise to a complex emission band centered at 500–550 nm. However, when the temperature increases (above corresponding energy of 40 meV), the recombination states become thermally depopulated to: (i) conduction band, (ii) over the potential barrier directly to Nd^{+3} ions in CT process, or (iii) over the potential barrier to the other defects energy levels which are in close spatial vicinity of Ga_2O_3-nc. However, based on the fact that observed Nd emission is characteristic of +3 oxidation state and direct CT from GE related donor levels to Nd requires also CT of hole to keep Nd ions optically active, we believe that the main excitation mechanism of Nd ions can be explained by two steps process via defects states. Thus, in the first step, absorbed by Ga_2O_3 matrix carriers are thermally depopulated and form an exciton localized at the energy levels related to defect states spatially close to Nd ions. In the second step, localized in this way exciton transfer its energy to Nd ion via nonradiative dipole-dipole interaction. After such a nonradiative excitation, the upper $4f$ state of Nd ions may then decay via a variety of radiative and nonradiative pathways giving rise to emission bands at 900, 1087, and 1362 nm.

Moreover, deactivation energy of 40 meV agrees very well with reported value of 40 meV below the conduction band for the oxygen vacancies related subband.[10] This process decreases the number of carriers captured on nanoclusters related energy levels, what will be directly reflected in a decrease in GE band intensity and accompanied by an increase in energy transfer efficiency to Nd ions as observed in Fig. 5 and finally to increase in Nd related emission.

IV. CONCLUSIONS

Nd doped gallium oxide films of micron scale thick have been grown by magnetron sputtering. Nd concentration plays an important role in the film structure since the grain size is at least five times lower when the Nd concentration reaches 1.79%. For high Nd concentrations, Nd ions are mainly located in the surrounding of the nanoparticles of β-Ga_2O_3. The films are nonhomogeneous and contain empty cavities and small amorphous regions where the Nd content is higher than that in the grains. The optical properties have shown that a maximum intensity of Nd^{3+} emission upon optical excitation source is observed for r=19.4% corresponding to a Nd concentration slightly lower than 0.08%.

Based on the results presented above, we can conclude that there are at least two main Nd ions sites in the Ga_2O_3 film: ions being coupled to Ga_2O_3 nanoclusters, which are responsible for their sensitization and ions not coupled to any sensitizating center, which can only be excited resonantly through the Nd energy levels. Moreover, it has been shown that the main excitation mechanism of Nd ions involves a thermally activated CT process, where electrons localized in the vicinity of Ga_2O_3 nanoclusters are transferred to other states from which nonradiative dipole-dipole energy transfer to Nd ions appears. This indicates that even if Ga_2O_3 nanoclusters are the main sensitization center for Nd ions, the defect states play a crucial role in transferring excitation energy to Nd ions.

ACKNOWLEDGMENTS

The authors want to thank Jacques Perrière from the "Institut des Nanosciences de Paris" for the RBS experiments results and Łukasz Gołacki from Wroclaw University of Technology for writing the software for excitation spectra analysis. This work has been supported by the Polonium project.

[1]A. Podhorodecki, J. Andrzejewski, R. Kudrawiec, J. Misiewicz, J. Wojcik, B. J. Robinson, T. Roschuk, D. A. Thompson, and P. Mascher, J. Appl. Phys. **100**, 013111 (2006).
[2]G. Sęk, P. Podemski, J. Andrzejewski, J. Misiewicz, S. Hein, S. Höfling, and A. Forchel, Appl. Phys. Express **2**, 061102 (2009).
[3]W. Rudno-Rudziński, G. Sęk, J. Misiewicz, T. E. Lamas, and A. A. Quivy, J. Appl. Phys. **101**, 073518 (2007).
[4]A. Podhorodecki, J. Misiewicz, F. Gourbilleau, and C. Dufour, Electrochem. Solid-State Lett. **13**, K26 (2010).
[5]A. Podhorodecki, J. Misiewicz, J. Wójcik, E. Irvin, and P. Masher, J. Lumin. **121**, 230 (2006).
[6]A. J. Kenyon, Prog. Quantum Electron. **26**, 225 (2002).
[7]A. Podhorodecki, M. Bański, J. Misiewicz, J. Serafińczuk, and N. V. Gaponenko, J. Electrochem. Soc. **157**, H628 (2010).
[8]A. Podhorodecki, G. Zatryb, J. Misiewicz, D. Kaczmarek, J. Domaradzki, and A. Borkowska, J. Electrochem. Soc. **156**, H214 (2009).
[9]A. Podhorodecki, R. Kudrawiec, M. Nyk, J. Misiewicz, and W. Strek, Opt. Mater. **31**, 1252 (2009).
[10]L. Binet and D. Gourier, J. Phys. Chem. Solids **59**, 1241 (1998).
[11]B. Liu, M. Gu, and X. Liu, Appl. Phys. Lett. **91**, 172102 (2007).
[12]R. Adair, L. L. Chase, and S. A. Payne, Phys. Rev. B **39**, 3337 (1989).
[13]T. Miyata, T. Nakatani, and T. Minami, J. Lumin. **87**, 1183 (2000).
[14]T. Xiao, A. H. Kitai, G. Liu, A. Nakua, and J. Barbier, Appl. Phys. Lett. **72**, 3356 (1998).
[15]P. Wellenius, A. Suresh, and J. F. Muth, Appl. Phys. Lett. **92**, 021111 (2008).
[16]E. Nogales, B. Méndez, J. Piqueras, and J. A. García, Nanotechnology **20**,

115201 (2009).
[17]S. Ohira, N. Suzuki, N. Arai, M. Tanaka, T. Sugawara, K. Nakajima, and T. Shishido, Thin Solid Films **516**, 5763 (2008).
[18]C. Lecerf, P. Marie, C. Frilay, J. Cardin, and X. Portier, Mater. Res. Soc. Symp. Proc. **1111**, 259 (2009).
[19]C. Lecerf, P. Marie, J. Cardin, A. Podhorodecki, M. banski, J. Misiewicz, and X. Portier (unpublished).
[20]P. Marie, X. Portier, and J. Cardin, Phys. Status Solidi A **205**, 1943 (2008).
[21]T. Harwig and F. Kellendouk, J. Solid State Chem. **24**, 255 (1978).
[22]V. I. Vasil'tasiv, Ya. M. Zakharko, and Ya. I. Prim, Ukr. Fiz. Zh. **33**, 1320 (1998).
[23]Y. P. Song, H. Z. Zhang, C. Lin, Y. W. Zhu, G. H. Li, F. H. Yang, and D. P. Yu, Phys. Rev. B **69**, 075304 (2004).
[24]H. W. Kim and S. H. Shim, Thin Solid Films **515**, 5158 (2007).
[25]R. Ahrenkiel, S. Johnston, W. Metzger, and P. Dippo, J. Electron. Mater. **37**, 396 (2008).
[26]D. L. Dexter, T. Förster, and R. S. Knox, Phys. Status Solidi **34**, K159 (1969).

Electrochemical and Solid-State Letters, **13** (3) K26-K28 (2010)
1099-0062/2010/13(3)/K26/3/$28.00 © The Electrochemical Society

High Energy Excitation Transfer from Silicon Nanocrystals to Neodymium Ions in Silicon-Rich Oxide Film

A. Podhorodecki,[a,z] J. Misiewicz,[b] F. Gourbilleau,[b] J. Cardin,[b] and C. Dufour[b]

[a]*Institute of Physics, Wroclaw University of Technology, 50-370 Wroclaw, Poland*
[b]*Center of Research on Ions Materials and Photonics, UMR CNRS 6252, 14050 Caen Cedex 4, France*

In this work, direct experimental evidence of the excitation energy transfer from silicon quantum dots (Si-QDs) to Nd ions has been given based on photoluminescence (PL) and PL excitation measurements in a wide spectral range. The indirect excitation of Nd ions by transfer from excited Si-QDs is possible and even more efficient at higher energy levels ($^4I_{9/2} \rightarrow {}^4D_{3/2}$, $^4D_{5/2}$) than the indirect excitation reported up to now at lower energy ($^4I_{9/2} \rightarrow {}^4F_{3/2} - {}^4F_{7/2}$) levels.
 [DOI: 10.1149/1.3279688]

Manuscript submitted October 28, 2009; revised manuscript received December 4, 2009. Published January 5, 2010.

The recent discovery of efficient luminescent emission from silicon nanoclusters[1] and their sensitizing action toward rare-earth (RE) ions[2] has opened the field of important applications for integrated optoelectronic devices using the complementary metal oxide semiconductor technology. For example, in the fields of optical telecommunications, the erbium ion that emits at 1.54 μm has become attractive because this wavelength corresponds to the minimum absorption of the optic silica fiber. For this reason, silica-based matrices co-doped with erbium ions and silicon quantum dots (Si-QDs) have been extensively investigated.[3-9] However, up to now, among all the teams working on that domain, only one group has reported net gain in an Er-doped structure.[10] One of the main reasons lies in the nature of the three-level electronic 4f structure of the Er^{3+} ions so that the de-excitation from $^4I_{13/2}$ to $^4I_{15/2}$ may lead to a reabsorption of the photon emitted by the neighboring Er^{3+} ions. Among the other RE ions that can benefit from the sensitizing effect of Si-QDs described by Kenyon et al.,[2] Nd^{3+} offers the $^4F_{13/2}$–$^4I_{11/2}$ emission at about 1060 nm, which corresponds to an operating mode based on four levels. The relaxation toward the fundamental state $^4I_{9/2}$ takes place by nonradiative de-excitation. Consequently, the signal emitted by the Nd^{3+} ions is not reabsorbed by another Nd^{3+} ion. This confers to the Nd-doped material the possibility of reaching a net gain. Therefore, such a Nd-doped system appears to be more favorable than its Er-doped counterpart for the achievement of a significant population inversion. It would consequently be the "preferred material" to obtain a net gain in structures containing Si nanoclusters even if the fiber absorption is higher at this emission wavelength than at 1.54 μm. The possible sensitizing role of Si-QDs toward Nd^{3+} in such a dielectric matrix has been reported so far by only a few studies.[11-14] However, Seo et al.[11] claimed that only films with Si content lower than 44 atom % show significant Nd^{3+} luminescence because low Si excess is needed to precipitate small Si nanoclusters. Similar results were also reported by Franzo et al.,[3] who investigated Nd-implanted Si-rich silicon oxide (SRSO).

In this article, we discuss the indirect excitation of Nd^{3+} ions embedded in SRSO thin films produced by reactive magnetron cosputtering. We propose an excitation channel describing the energy transfer from the high energy levels of Si-QDs to the high energy levels of the Nd^{3+} ions.

Thin RE-doped layers were deposited by reactive magnetron cosputtering of a pure SiO_2 target topped with Nd_2O_3 chips. The silicon excess in the layer was obtained through the monitoring of the hydrogen partial pressure mixed to the Ar plasma in the chamber. This reactive deposition approach was based on the ability of hydrogen to reduce the oxygen species originating from the sputtered SiO_2 target. This allowed the control of Si incorporation in the growing thin films.[15] The RE content was controlled through the number of the Nd_2O_3 chips placed on the SiO_2 target. For this study, Si excess was kept constant at about 7 atom %, while Nd concentration was fixed at 0.08 atom %. These parameters have been chosen based on our previous investigation[16] and have led to an optimal Nd emission intensity. The Nd-doped SRSO (Nd-SRSO) layers were deposited at a power density of 0.76 W cm^{-2} on (1 0 0) p-type Si wafers and were annealed at 1100°C for 1 h under a N_2 flow.

Photoluminescence (PL) experiments have been obtained using a 266 nm excitation wavelength. The UV-visible spectral range has been detected by an HR4000 Ocean Optics spectrophotometer, while the near-IR visible emission has been collected by an InGaAs charge-coupled device camera after dispersing through a Triax 550 Jobin Yvon monochromator. For the total photoluminescence excitation (TPLE) measurements, a 450 W xenon lamp has been used as the excitation source. The configuration (Triax 180, Jobin Yvon monochromator and HR4000 Ocean Optics spectrophotometer) gives an averaged excitation flux lower than $\sim 10^{19}$ photons/s cm^2 in the whole excitation range. The TPLE spectrum has been built from PL spectra corrected by the power wavelength dependency, integrated (hachured areas, Fig. 1) and plotted as a function of the excitation wavelength.

Figure 1a shows the PL spectrum obtained at 266 nm excitation wavelength for the SRSO matrix doped with 0.08% of Nd ions and annealed at 1100°C. The emission band centered at ~650 nm (1.9 eV) has been related to Si-QDs. Additionally, PL lines centered at 920, 1100, and 1400 nm correspond, respectively, to transitions originating from the $^4F_{3/2}$ state to the $^4I_{9/2}$, $^4I_{11/2}$, and $^4I_{13/2}$ levels of Nd ions. At nonresonant excitation, these strong Nd-related emissions suggest an efficient energy transfer from excited Si-QDs (or defect states) to Nd ions.

To further analyze this effect, TPLE spectra of Si-QDs and Nd ions recorded at $\sim 10^{19}$ photons/s cm^2 are shown in Fig. 1b and normalized to the maximum value. It can be observed that the strongest signal for both emission bands has been detected in the 250–450 nm range. We observed a similar shape of both excitation spectra obtained for Nd and Si-QDs, suggesting a common mechanism of the excitation for both elements. Additionally, except for the signal in the UV-vis range, there is no evidence of resonant excitation of Nd^{3+} ions or indirect excitation through Si-QDs at 488 nm at this low excitation flux.

Contrary to this result, the reference TPLE spectrum recorded for the Si-free Nd-doped commercial glass, using the same excitation flux shown in Fig. 1c, proves that the lack of resonant excitation bands for the SRSO-doped sample (Fig. 1b) is due to its very low excitation cross section (compared to indirect excitation) rather than due to the setup limitations. Such a result suggests that (*i*) the direct excitation of Nd ions is not efficient for SRSO films, (*ii*) a high energy excitation followed by the energy transfer from Si-QDs to Nd^{3+} ions is observed, and (*iii*) this excitation mechanism is much more efficient than the indirect one reported up to now.[11,14] This latter point is observed using the 488 nm argon laser excitation line, which allows us to populate lower energy states in the vicinity of

[z] E-mail: artur.p.podhorodecki@pwr.wroc.pl

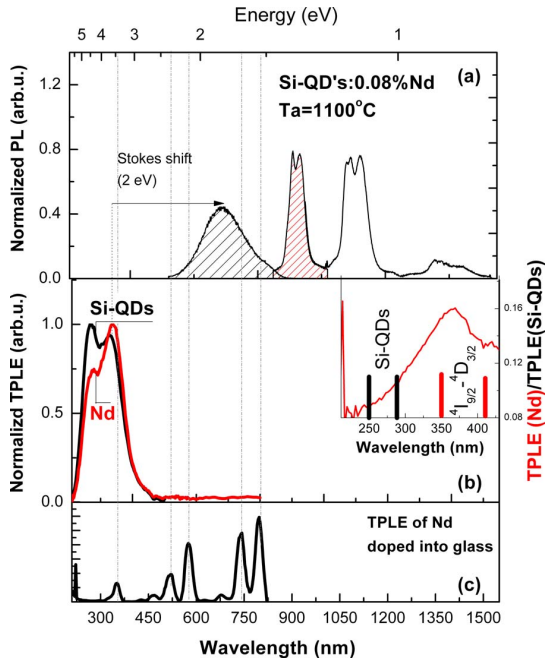

Figure 1. (Color online) (a) PL spectrum of SRSO:Nd sample annealed at 1100°C obtained at 266 nm excitation wavelength, (b) excitation spectra obtained for the emission band related to recombination in the vicinity of Si-QDs and for the emission band related to $^4F_{3/2} \rightarrow {}^4I_{9/2}$ transition of Nd ion, and (c) reference excitation spectrum obtained for the emission band related to $^4F_{3/2} \rightarrow {}^4I_{9/2}$ transition of Nd ion embedded inside the commercial glass matrix. Inset: Ratio of the excitation signal obtained for the Nd ion and for the Si-QD reflecting the excitation wavelength dependency of the energy-transfer efficiency from Si-QDs to Nd ions.

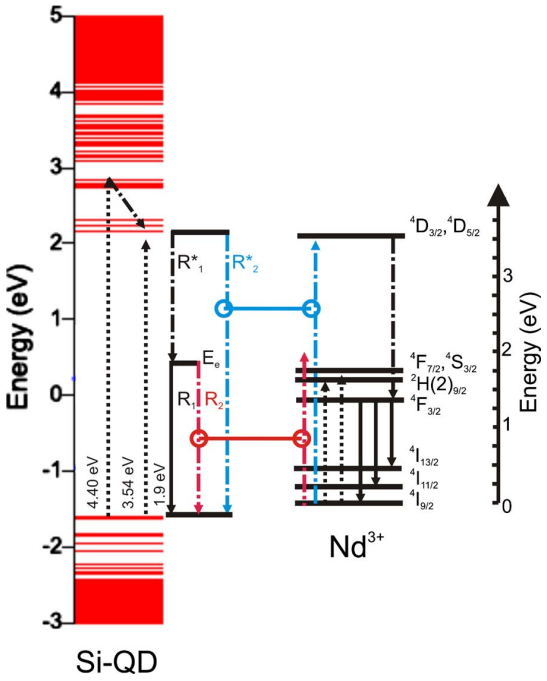

Figure 2. (Color online) Schematic presentation of possible excitation mechanisms of a silica matrix co-doped with Nd ions and Si-QDs. The energy levels for Si-QDs, with a size of 1.36 nm, have been redrawn after Bulutay.[21]

Si-QDs from which the energy is transferred to the $^4F_{3/2}$ Nd level, but only at a much higher excitation flux.

To investigate the wavelength-dependent excitation mechanism, we focus on the 250–425 nm range. The observed emission intensity related to Nd ions is a combination of the probability of several processes: $P_{\mathrm{PL_{Nd}}}(E_{\mathrm{exc}})\alpha P_{\mathrm{abs_{Si\text{-}Qds}}}(E_{\mathrm{exc}})P_{\mathrm{tran}}(E_{\mathrm{exc}},E_{\mathrm{em}})P_{\mathrm{em_{Nd}}}(E_{\mathrm{em}})$, where the first term describes the probability of Si-QD light absorption dependent on the excitation energy E_{exc}, the second term is the probability of the energy transfer from Si-QD to Nd ions dependent on the excitation and emission energies, E_{exc} and E_{em}, and the last one is the probability of the Nd ion emission, which can be assumed to be excitation energy independent of indirect excitation via Si-QDs. Thus, assuming that $P_{\mathrm{em_{Nd}}}$ is constant, the ratio $(P_{\mathrm{PL_{Nd}}}/P_{\mathrm{abs_{Si\text{-}Qds}}})$ is a signature of the excitation wavelength dependency of the energy transfer between Si-QDs and Nd ions. This ratio is shown in the inset to Fig. 1b. The inset shows that the excitation process of the Nd ions is the most efficient at the 350 nm excitation wavelength, which is typical of the $^4I_{9/2} \rightarrow {}^4D_{3/2}$ and $^4D_{5/2}$ absorption bands of Nd ions and thus at an energy in which the resonant energy transfer takes place.

Such an energetically high process, which is more efficient than the energy transfer from the lower energy states, can be due to two facts. First, from the point of view of the silicon dot, the relaxation from the higher excited states is inhibited due to the discreteness of the states.[17] Second, the relaxation process from the higher excited energy levels to the lowest ones can be strongly reduced due to the formation of charge-separated complexes as it has been evidenced for CdSe nanocrystals.[18] Those two facts may increase the carrier's lifetime at higher energy levels, making energy transfer from these higher levels very efficient.

This finding can have important applicative consequences because in most cases, researchers choose the RE ions based on the correspondence of their energy levels to the Si-QD bandgap (~1.5 to 2.0 eV), evaluated from its emission band position. However, our result shows that the excitation energy can be transferred from the Si-QDs to the Nd ions at much higher energies (~3 to 5 eV) than usually assumed so that channels of excitation of the RE ions may open.

The last issue arising from Fig. 1b concerns the shape and the position of the excitation band related to Si-QDs, which is composed of two bands centered at 280 nm (4.40 eV) and 350 nm (3.54 eV). The double-peak nature and the sharp edge of the excitation band suggest the presence of well-crystallized nanocrystals, which can be expected at such high annealing temperatures. Moreover, such a high value of the Si-QD bandgap is characteristic of very small Si-QDs, with a diameter close to 2 nm. For example, a very similar spectrum was obtained theoretically by Trani et al.[19] for Si:H nanocrystals with sizes close to 2 nm, or by Wilcox et al.[20] Similar absorption bands were also observed by Bulutay[21] for Si nanocrystals with a size of 1.36 nm. The result obtained in his work has been schematically redrawn in Fig. 2.

These results enable us to provide a schematic representation of the energy levels of the Si-QD and Nd ions and a possible energy-transfer process, which has been shown in Fig. 2. Thus, two main energy-transfer processes are possible in our system: the most efficient nonradiative energy transfer from higher energy levels of Si-QDs (R_2^*) and the weak nonradiative energy transfer from the lowest energy levels (most probably surface/defect states) described as (R_2) and preceded by a carrier relaxation (R_1^*) from higher energy levels (confined states of Si-QDs).

In summary, it has been shown that the excitation energy transfer from the Si-QDs to Nd ions is possible. Moreover, an excitation channel of Nd ions has been proposed and discussed. It has been shown that the excitation of Nd ions through the $^4I_{9/2}$

$\rightarrow {}^4D_{3/2}, {}^4D_{5/2}$ transition from the higher energy levels of Si-QDs through the nonradiative energy-transfer process is very efficient and seems to be much more efficient than the excitation through the lower energy absorption transitions of Nd ion (i.e., ${}^4I_{9/2} \rightarrow {}^4F_{5/2}$). This opens possibilities for sensitizing a wide range of RE ions and thus paves the way to promising photovoltaic or photonic applications.

Acknowledgments

The work was supported by the Polish Ministry of Education and Scientific Research through grant no. N515 074 31/3896 and by the Polonium project. Moreover, A.P. acknowledges the financial support from the Foundation for Polish Science under the START program. F.G., J.C., and C.D. thank the French National Agency (ANR), which supported this work through the Nanoscience and Nanotechnology program (DAPHNES project no. ANR-08-NANO-005).

Wroclaw University of Technology assisted in meeting the publication costs of this article.

References

1. L. T. Canham, *Appl. Phys. Lett.*, **57**, 1046 (1990).
2. A. J. Kenyon, P. F. Trwoga, M. Federighi, and C. W. Pitt, *J. Phys.: Condens. Matter*, **6**, L319 (1994).
3. G. Franzò, V. Vinciguerra, and F. Priolo, *Appl. Phys. A: Mater. Sci. Process.*, **69**, 3 (1999).
4. A. J. Kenyon, C. E. Chryssou, C. W. Pitt, T. Shimizu-Iwayama, D. E. Hole, N. Sharma, and C. J. Humphreys, *J. Appl. Phys.*, **91**, 367 (2002).
5. D. Pacifici, G. Franzo, F. Priolo, F. Iacona, and L. Dal Negro, *Phys. Rev. B*, **67**, 245301 (2003).
6. I. Izeddin, D. Timmerman, T. Gregorkiewicz, A. S. Moskalenko, A. A. Prokofiev, I. N. Yassievich, and M. Fujii, *Phys. Rev. B*, **78**, 035327 (2008).
7. A. Podhorodecki, J. Misiewicz, J. Wójcik, E. Irvin, and P. Masher, *J. Lumin.*, **121**, 230 (2006).
8. F. Gourbilleau, C. Dufour, M. Levalois, J. Vicens, R. Rizk, C. Sada, F. Enrichi, and G. Battaglin, *J. Appl. Phys.*, **94**, 3869 (2003).
9. K. Imakita, M. Fujii, Y. Yamaguchi, and S. Hayashi, *Phys. Rev. B*, **71**, 115440 (2005).
10. H. S. Han, S. Y. Seo, and J. H. Shin, *Appl. Phys. Lett.*, **79**, 4568 (2001).
11. S.-Y. Seo, M.-J. Kim, and J. Shin, *Appl. Phys. Lett.*, **83**, 2778 (2003).
12. K. Watanabe, H. Tamaoka, and M. Fujii, *Physica E*, **13**, 1038 (2002).
13. A. N. MacDonald, A. Hryciw, F. Lenz, and A. Meldrum, *Appl. Phys. Lett.*, **89**, 173132 (2006).
14. D. Bréard, F. Gourbilleau, A. Belarouci, C. Dufour, and R. Rizk, *J. Lumin.*, **121**, 209 (2006).
15. C. Ternon, F. Gourbilleau, X. Portier, P. Voivenel, and C. Dufour, *Thin Solid Films*, **419**, 5 (2002).
16. F. Gourbilleau, D. Bréard, C. Dufour, and R. Rizk, *Opt. Mater. (Amsterdam, Neth.)*, **31**, 479 (2009).
17. U. Bockelmann and G. Bastard, *Phys. Rev. B*, **42**, 8947 (1990).
18. P. Guyot-Sionnest, M. Shim, C. Matranga, and M. Hines, *Phys. Rev. B*, **60**, R2181 (1999).
19. F. Trani, G. Cantele, D. Ninno, and G. Iadonisi, *Phys. Rev. B*, **72**, 075423 (2005).
20. J. P. Wilcoxon, G. A. Samara, and P. N. Provencio, *Phys. Rev. B*, **60**, 2704 (1999).
21. C. Bulutay, *Phys. Rev. B*, **76**, 205321 (2007).

Nanoscale Research Letters
a SpringerOpen Journal

NANO EXPRESS Open Access

Effect of the Nd content on the structural and photoluminescence properties of silicon-rich silicon dioxide thin films

Olivier Debieu, Julien Cardin, Xavier Portier, Fabrice Gourbilleau*

Abstract

In this article, the microstructure and photoluminescence (PL) properties of Nd-doped silicon-rich silicon oxide (SRSO) are reported as a function of the annealing temperature and the Nd concentration. The thin films, which were grown on Si substrates by reactive magnetron co-sputtering, contain the same Si excess as determined by Rutherford backscattering spectrometry. Fourier transform infrared (FTIR) spectra show that a phase separation occurs during the annealing because of the condensation of the Si excess resulting in the formation of silicon nanoparticles (Si-np) as detected by high-resolution transmission electron microscopy and X-ray diffraction (XRD) measurements. Under non-resonant excitation at 488 nm, our Nd-doped SRSO films simultaneously exhibited PL from Si-np and Nd^{3+} demonstrating the efficient energy transfer between Si-np and Nd^{3+} and the sensitizing effect of Si-np. Upon increasing the Nd concentration from 0.08 to 4.9 at.%, our samples revealed a progressive quenching of the Nd^{3+} PL which can be correlated with the concomitant increase of disorder within the host matrix as shown by FTIR experiments. Moreover, the presence of Nd-oxide nanocrystals in the highest Nd-doped sample was established by XRD. It is, therefore, suggested that the Nd clustering, as well as disorder, are responsible for the concentration quenching of the PL of Nd^{3+}.

Introduction

Over the last decade, there has been an increasing interest toward nanomaterials for novel applications. One of the challenging fields concerns silicon-compatible light sources which are getting more and more attractive since they can be integrated to microelectronics devices [1]. Amorphous SiO_2 is an inefficient host matrix for the photoluminescence (PL) of Nd^{3+} ions since, on the one hand, the absorption cross section of Nd is low (1×10^{-20} cm^2) and, on the other hand, the Nd solubility in silica is limited by clustering [2 ,3], which quenches the PL of the rare earth (RE) ions [4,5]. However, since the discovery of the sensitizing effect of silicon nanoparticles (Si-np) toward the RE ions [6], RE-doped a-SiO_2 films containing Si-np are promising candidates for the achievement of future photonic devices. In such nanocomposites, Nd^{3+} ions benefit from the high absorption cross section of Si-np (1-100 $\times$ 10^{-17} cm^2) by an efficient energy transfer mechanism, which enables the PL efficiency of RE ions to be enhanced by 3-4 orders of magnitude offering interesting opportunities for the achievement of future practical devices optically excited. In contrast to Er^{3+} ions [6-8], such materials doped with Nd have not been widely investigated and, accordingly, the energy transfer mechanism between Si-np and Nd^{3+} ions, and its limitation [9-16]. Several authors have demonstrated that the energy transfer is more effective with small Si-np [10,11]. Seo et al. [11] have observed a decrease of the PL intensity of Nd^{3+} ions upon increasing the Si excess, i.e., increasing the Si-np average size. They concluded that only small Si-np which present excitonic states with a sufficient energy band-gap can excite the $^4F_{3/2}$ level of Nd^{3+} ions. Several groups, which studied the effect of the Nd concentration in the PL properties of Nd-doped Si-np/SiO_2 demonstrated that the PL of Nd^{3+} ions is more efficient at low Nd concentration [12,13].

The object of the present investigation is therefore to characterize the PL properties of nanostructured thin films containing a low concentration of Si excess as a

* Correspondence: fabrice.gourbilleau@ensicaen.fr
CIMAP, UMR CNRS/CEA/ENSICAEN/UCBN, Ensicaen 6 Bd Maréchal Juin, 14050 Caen Cedex 4, France

function of the Nd concentration and the annealing temperature in relation with their microstructures. The Nd-doped silicon-rich silicon oxide (SRSO) thin layers were synthesized by reactive magnetron co-sputtering. Their microstructures were examined using high-resolution transmission electron microscopy (HRTEM), X-ray diffraction (XRD), and Fourier transform infrared (FTIR) spectroscopy. We could notably establish the proper conditions to obtain efficient PL of Nd^{3+} but also describe its limitations.

Experiment

In this study, Nd-doped SRSO thin layers were deposited at room temperature on *p*-type Si wafers by a reactive magnetron RF co-sputtering method that consists in sputtering simultaneously a pure SiO_2 target topped with Nd_2O_3 chips. The Nd content was monitored by the surface ratio between the Nd_2O_3 chips and the SiO_2 target. The sputtering gas was a mixture of argon and hydrogen; the latter enables us to control the Si excess of the deposited layers by reacting with oxide species in the plasma [17]. The samples were subsequently annealed at high temperature ranging from 900 to 1100 °C in a dry nitrogen flow.

The composition of the deposited layers was determined by Rutherford backscattering spectrometry, while microstructural analyses were performed using of XRD and HRTEM on samples prepared in the cross-sectional configuration using a JEOL 2010F (200 kV). The infrared absorption properties were investigated unsing a Nicolet Nexus FTIR spectrometer at Brewster's incidence.

Room temperature PL measurements were performed using an argon ion laser operating at 488 nm (7.6 W/cm^2) as excitation source. This excitation wavelength is non-resonant with Nd^{3+} ions so that only an indirect excitation of Nd can occur [13,15]. The visible spectra were recorded using a fast photomultiplier (Hamamatsu) after dispersion of the PL with a Jobin-Yvon TRIAX 180 monochromator, while the infrared PL was measured using a Jobin-Yvon THR 1000 monochromator mounted with a cooled Ge detector and a lock-in amplifier to record the near-infrared spectra up to 1.5 μm.

Results

In this study, we were interested in four Nd-doped SRSO thin films containing the same excess of Si (7 at.%) with various Nd contents ranging from 0.08 to 4.9 at.%.

Microstructure

Figure 1 shows the FTIR spectrum of the lowest Nd-doped sample as-deposited and a fit with eight Gaussian peaks. Several bands characteristic of amorphous SiO_2 are observed. The two prominent bands at 1236 (red), and 1052 cm^{-1} (blue) are assigned to longitudinal optical

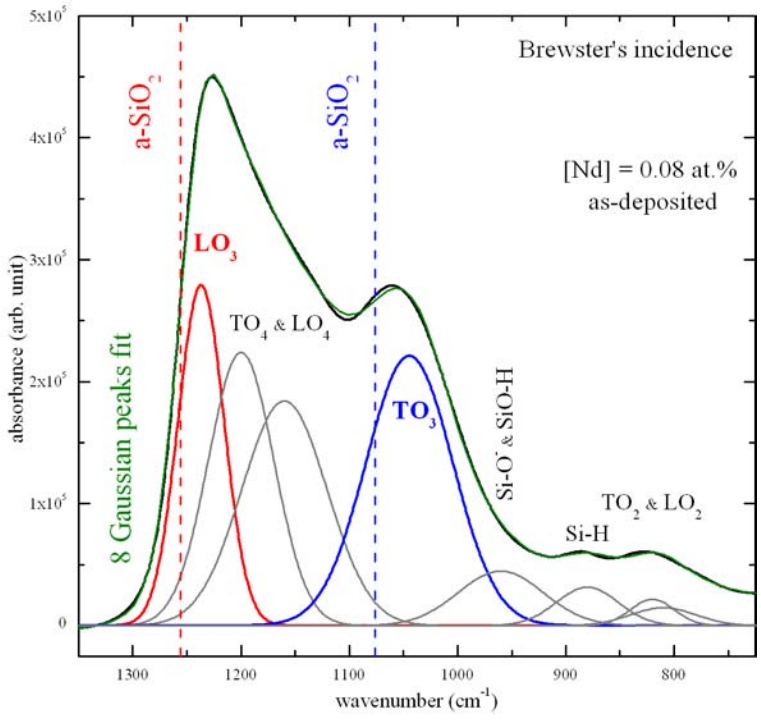

Figure 1 FTIR spectrum of the lowest Nd-doped sample as-deposited.

(LO_3) and transverse optical (TO_3) phonons of Si-O bonds, respectively. One can notice that these two bands are slightly shifted to lower wavenumbers compared to the stoichiometric positions of a-SiO_2 at 1256 and 1076 cm^{-1}, respectively. The TO_2, LO_2, LO_4, and TO_4 vibration modes are also present at 810, 820, 1160, and 1200 cm^{-1}, respectively. In addition to Si-O vibration modes, a weak absorption band centered at 880 cm^{-1} is observed. This peak, which is assigned to Si-H bonds, disappears after annealing because of the hydrogen desorption.

Figure 2a shows the evolution of the positions of the LO_3 and TO_3 vibration modes, and the LO_3/TO_3 intensity ratio, as a function of the annealing temperature. One can observe that, while the annealing temperature was increased, the TO_3 and LO_3 peaks' positions progressively shifted to higher wavenumbers toward their respective stoichiometric positions. It is explained by the phase separation that results in the formation of Si-np [18,19]. The increase of the LO_3 band intensity (see Figure 2b) is related to the increase of the number of Si-O-Si bonds at the SiO_x/Si-np interface [19,20], i.e., the increase of the density of Si-np [21].

Figure 3 presents the evolution of the FTIR spectra of samples annealed at 1100 °C as a function of the Nd concentration. One can observe that the LO_3 band intensity, which is constant at low Nd concentrations of 0.08 and 0.27 at.%, significantly decreased while the Nd content was increased from 1.68 to 4.9 at.%. This evolution contrasts with the one of the TO_4-LO_4 pair modes. Indeed, the TO_4-LO_4 intensity remains constant at low Nd concentrations of 0.08 and 0.27 at.%, and then, it progressively increases with increasing Nd content. This demonstrates that the incorporation of Nd in the thin films generates disorder in the host SiO_2 matrix.

Moreover, one can notice, in the spectrum of the highest Nd-doped sample, the emergence of two weak absorption peaks centered at 910 and 950 cm^{-1} which are assigned to asymmetric mode of Si-O-Nd bonds [22]. These peaks are located above a shoulder which can originate from Si-O^- and Si-OH phonons [23,24]. However, one can exclude the existence of the Si-OH vibration mode after annealing because of the hydrogen desorption. The emergence of these two absorption peaks suggests that other phonons are also optically active in this spectral range.

In Figure 4 is depicted the XRD spectra of the lowest and highest Nd-doped samples. In the former sample, one broad band corresponding to a-SiO_2 is observed, while the pattern of the latter sample indicates the presence of additional phases. In the 27-32° range, it shows various sharp peaks that are located above a broad band

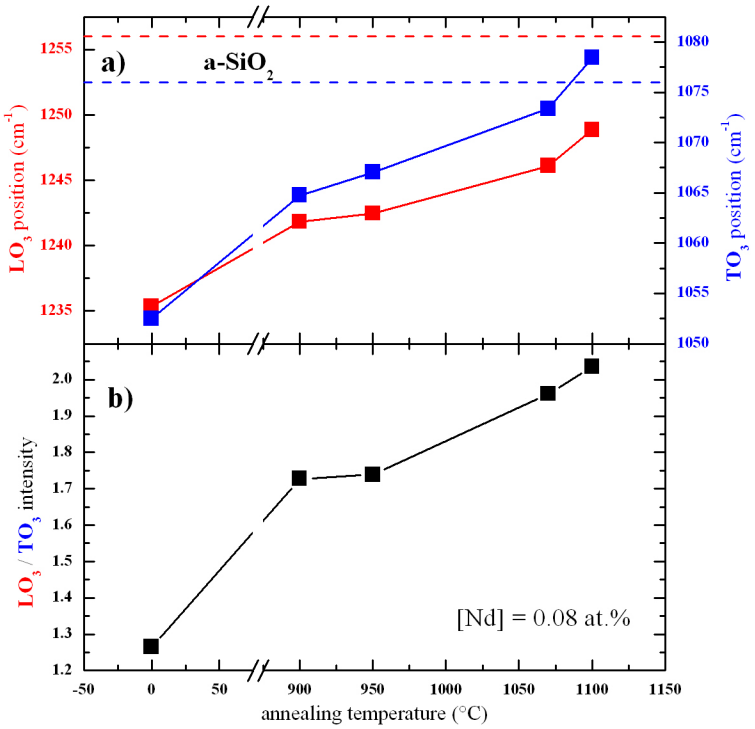

Figure 2 Evolutions of the positions of the LO_3 and TO_3 peaks, and the LO_3/TO_3 intensity ratio, as a function of the annealing temperature.

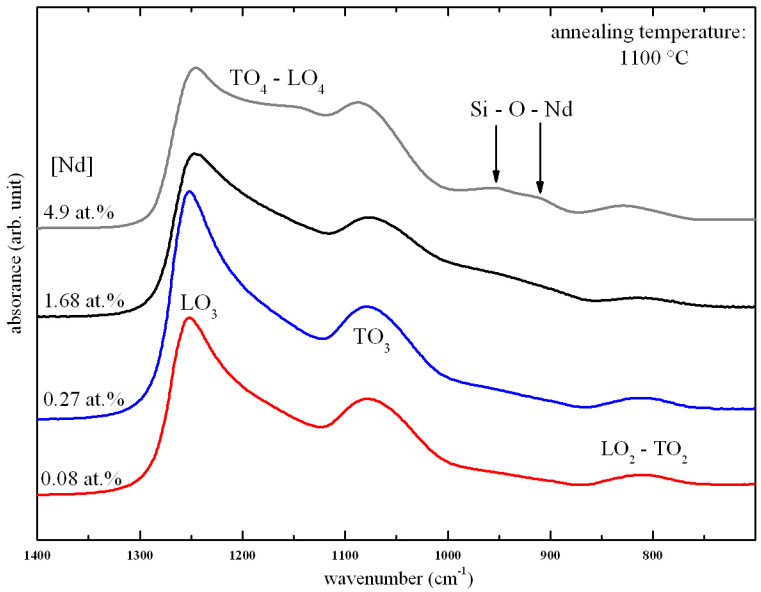

Figure 3 Evolution of the FTIR spectra as a function of the Nd concentration.

centered at 29°. This peak, and the 48° one, indicate the presence of nanocrystalline Si [21,25], while the sharp and intense peaks located at 27.6°, 28.8°, and 30.7° are assigned to Nd_2O_3 crystals. However, the 28.8° peak may result from both crystalline Si and Nd_2O_3. It is interesting to note that the 27.6° and 30.7° peaks fairly concur with the ones observed in neodymia-silica composites containing Nd_2O_3 nanocrystals by several groups [2,3]. As a consequence, the presence of Nd_2O_3 and Si nanocrystals in the highest Nd-doped sample is established, while no crystalline phases are detected in the low Nd-doped one.

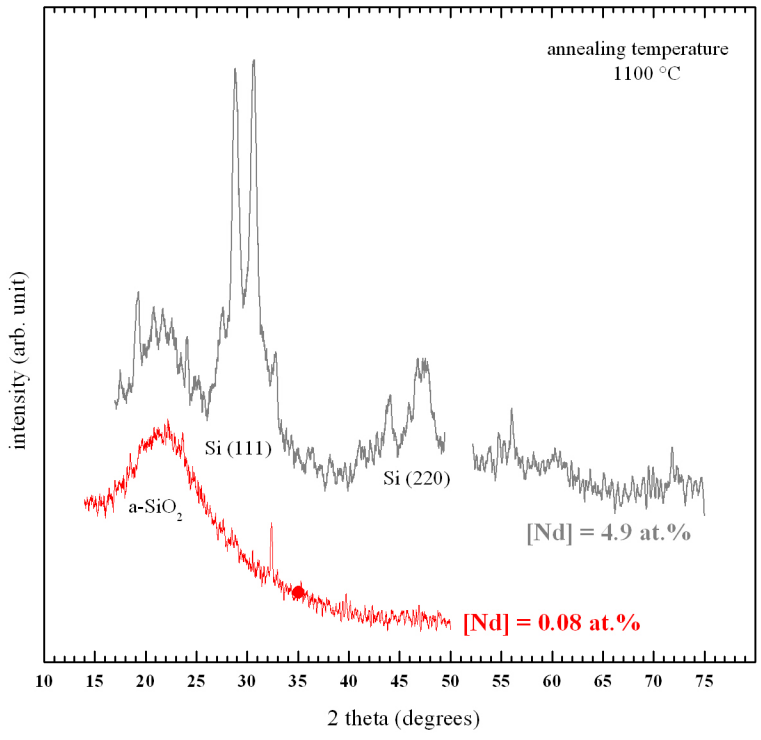

Figure 4 XRD patterns of the highest and lowest Nd-doped samples annealed at 1100 °C.

Figure 5 shows the HRTEM images of the two latter samples investigated by XRD after annealing at 1100 °C. In the image of the sample with the highest Nd concentration of 4.9 at.% (Figure 5a), one can recognize small Si nanocrystals because of the lattice fringes corresponding to the Si crystalline feature, while no crystalline structure was observed in the images of the film containing the lowest Nd concentration of 0.08 at.% (Figure 5b). These two images are in accordance with the XRD results (see Figure 4). However, one cannot exclude that the lowest Nd-doped sample could small contain amorphous Si-np.

PL spectroscopy

Figure 6 shows the PL spectrum of the lowest Nd-doped sample after annealing at 1100 °C. In the visible domain, one can observe a broad PL band that is originating from quantum-confined excitonic states in small Si-np, while in the infrared domain, three peaks centered at around 920, 1100, and 1350 nm are distinguishable and

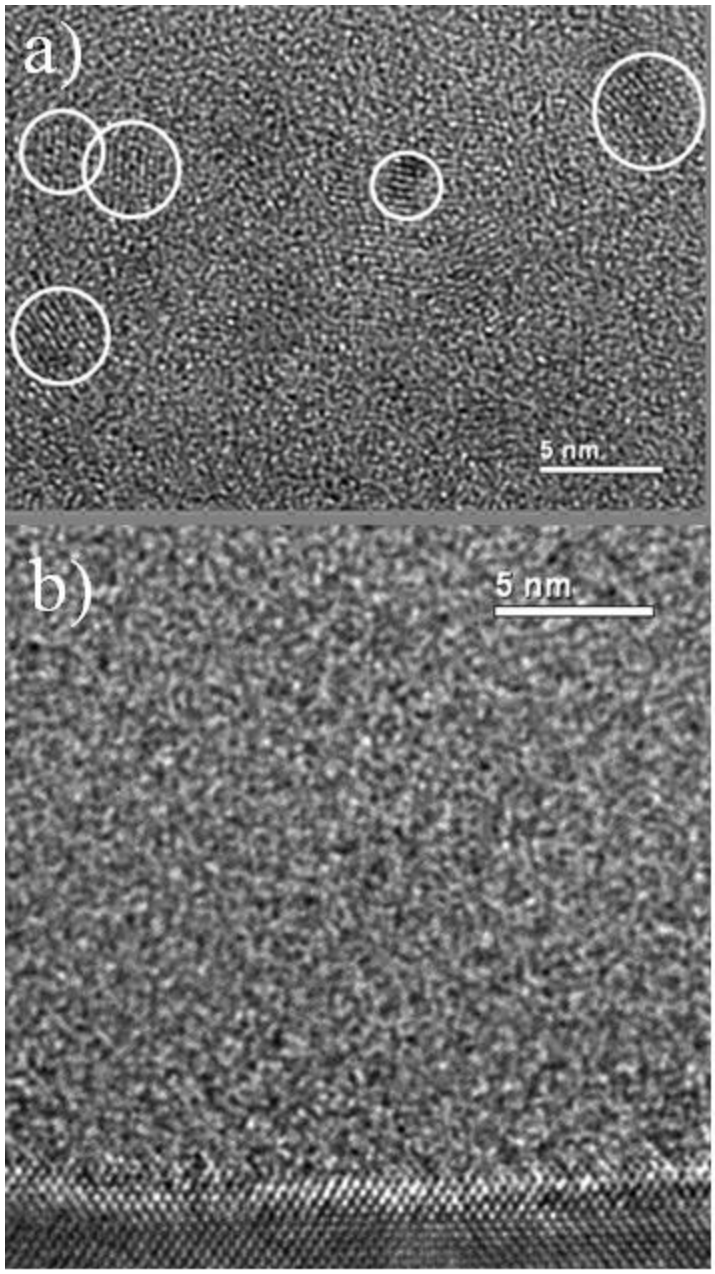

Figure 5 HRTEM images of the highest (a) and lowest (b) Nd-doped samples annealed at 1100 °C.

are attributed to the infra-4*f* shell transitions of Nd^{3+} ions from the $^4F_{3/2}$ level to the $^4I_{9/2}$, $^4I_{11/2}$, and $^4I_{13/2}$ levels, respectively. The presence of the PL of Nd^{3+} ions after non-resonant excitation brings to light the sensitizing effect of Si-np towards Nd^{3+} ions.

The evolution of the integrated PL intensity of the Si-np PL band and the 920-nm PL peak is shown in the inset of Figure 6. The enhancement of the PL intensity of the broad visible PL band with the annealing temperature is characteristic for Si-np embedded in SiO_2. It is due to the increase of the Si-np density, as shown by the increase of the LO_3 band intensity in the FTIR spectra (see Figure 2) [21], as well as the improvement of their passivation [26] and the decrease of disorder in the host matrix. The latter is a source of non-radiative recombination channels. Interestingly, one can observe that the evolution of the PL intensity of Nd^{3+} ions as a function of the annealing temperature is manifestly correlated with the one of Si-np. Reminding that the PL measurements were done under non-resonant excitation, this behavior underlines the strong coupling between Si-np and Nd^{3+} ions, and, accordingly, the potential of sensitizing of Si-np. The increase of the PL intensity of Nd^{3+} is then explained by the increase of the Si-np density as well as the increase of non-radiative de-excitation channels of both Si-np and Nd^{3+}. The Nd^{3+} PL intensity is then maximal after annealing at 1100 °C which is generally admitted as the optimal annealing temperature for the PL of Si-np.

Figure 7 shows the behavior of the PL spectra of the thin films annealed at 1100 °C as a function of the Nd concentration. As the Nd content increases from 0.08 to 0.27 at.%, the PL intensity of Si-np drastically drops and disappears at 1.68 at.%. Then, PL of Si-np surprisingly reappears at the highest Nd concentration of 4.9 at.%. Interestingly, one can observe that the positions and widths of the PL peaks of the two lowest Nd-doped samples remain identical (see the inset); whereas the PL peak of the highest Nd-doped film is manifestly shifted to longer wavelengths. According to the quantum confinement model, the PL of the latter sample therefore emanates from Si-np that are sensibly larger than the ones present in the two former samples. In the infrared spectral domain, one can observe that the PL intensity of Nd^{3+} ions drops progressively with increasing Nd concentration.

Discussion

During the annealing, a phase separation occurs as demonstrated in the FTIR spectra in Figure 1, leading to the condensation of Si-np that were detected by XRD (see Figure 4) and HRTEM (see Figure 5). Besides, the presence of Si-np in the films was confirmed by the occurrence after annealing of a 740-nm broad PL band that is characteristic for Si-np.

The presence of PL of Nd^{3+} ions under non-resonant excitation evidenced the efficient energy transfer between Si-np and Nd^{3+} ions (Figure 6). The concentration quenching of the PL of Nd^{3+} ions that was observed in Figure 7 is partly explained by cross relaxation processes between Nd^{3+} ions and neighboring Nd^{3+} ions and/or Nd_2O_3 nanocrystals as reported in glass matrices [4,5]. This is supported by the existence of Nd_2O_3 nanocrystals in the highest Nd-doped sample

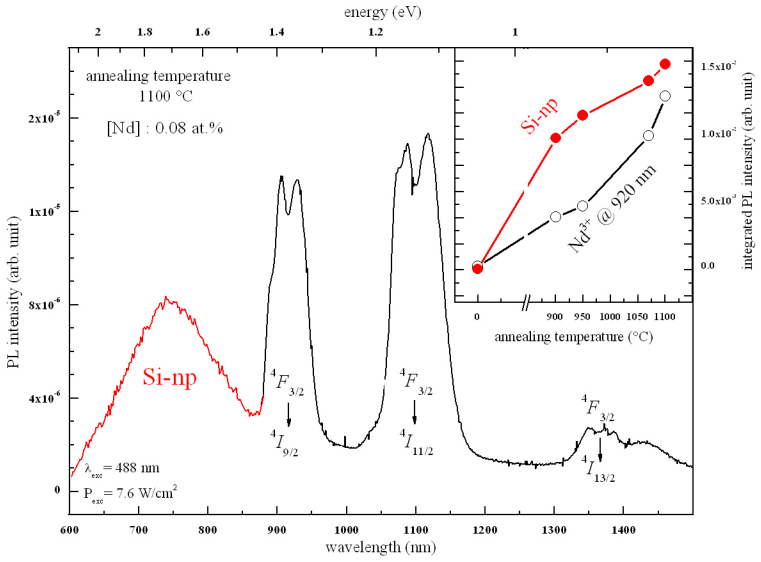

Figure 6 PL spectrum of the lowest Nd-doped sample annealed at 1100 °C. (Inset) Evolutions of the integrated PL intensity of the Si-np PL band and the first Nd^{3+} ions PL peak as a function of the annealing temperature.

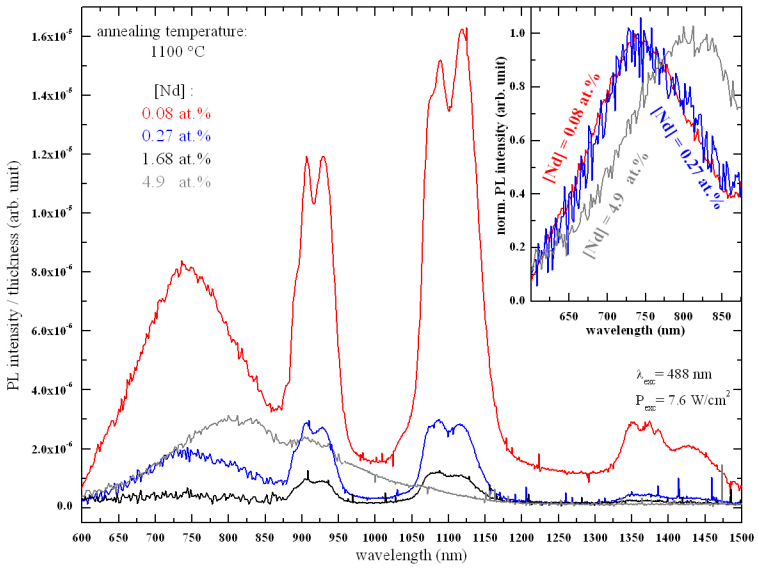

Figure 7 Evolution of the PL spectra as a function of the Nd concentration.

(see Figure 4). Besides, non-radiative channels inherent to disorder induced by the Nd incorporation (see Figure 3) can be in competition with the energy transfer mechanism between Si-np and Nd^{3+} ions in such nanocomposite systems leading to the common decrease of the PL intensity of Nd^{3+} and Si-np. As a consequence, the emission of Nd^{3+} ions is more efficient while Si-np are formed, and while the Nd content is low (0.08 at.%). In such conditions, Nd^{3+} ions benefit from the sensitizing effect of Si-np and from the weak competition of non-radiative recombinations in the host matrix. The decrease of the PL of Si-np with increasing Nd content ranging from 0.08 to 4.9 at.% (Figure 7) is explained by the raise of energy transfer between Si-np and Nd^{3+} ions (which can be luminescent or not), and by the increase of non-radiative recombinations provided by the increase of disorder as shown in Figure 3. Besides, the presence of a Nd_2O_3 phase in the host matrix at the highest Nd content significantly modifies the number of oxygen atoms available to form the silicon oxide host matrix consequently leading to the formation of larger Si-np with a higher density. Besides, the formation of Nd_2O_3 nanocrystals results in the rise of the average interaction distance between Si-np and Nd atoms (agglomerated or not) leading to the occurrence of not-coupled Si-np, which therefore enables emission of light in the visible range. This explains the presence of the PL peak of Si-np in the highest Nd-doped sample (Figure 7) which is significantly shifted to longer wavelengths. The fact that XRD pattern of Si nanocrystals, were detected in the latter sample and not in the lowest Nd-doped sample (Figure 4) may also be attributed to the modification of the Si-np size and density.

Conclusion

The relationships between the composition, the microstructure, and the PL properties of Nd-doped SRSO thin films that contain the same Si excess were studied. We could establish that the maximum of the PL intensity of Nd^{3+} ions was obtained after annealing at 1100 °C which corresponds to the better situation for the achievement of highly luminescent Si-np embedded in SiO_2, i.e., containing a small quantity of non-radiative recombination channels. It was demonstrated that the PL of Nd^{3+} ions was quenched at high Nd-concentration (4.9 at.%) because of the formation of Nd_2O_3 nanocrystals and the occurrence of disorder in the host matrix. The former participates in the concentration quenching mechanism because of cross relaxation processes, while the latter induces the occurrence of new non-radiative channels which are in competition with the energy transfer mechanism between Si-np and Nd^{3+} ions.

Abbreviations

FTIR: Fourier transform infrared; LO: longitudinal optical; PL: photoluminescence; RE: rare earth; Si-np: silicon nanoparticles; SRSO: silicon-rich silicon oxide; TO: transverse optical; XRD: X-ray diffraction.

Acknowledgements

The authors are grateful to the French Agence Nationale de la Recherche, which supported this study through the Nanoscience and Nanotechnology program (DAPHNES project ANR-08-NANO-005).

Authors' contributions

OD fabricated the thin films and carried out the optical and microstructural characterizations. XP investigated the films by HRTEM. JC made significant contribution to the optical properties. FG conceived of the study and participated in the coordination and writing of the manuscript. All authors read and approved the final manuscript.

Competing interests
The authors declare that they have no competing interests.

Received: 24 September 2010 Accepted: 21 February 2011
Published: 21 February 2011

References

1. Kenyon AJ: **Recent developments in rare-earth doped materials for optoelectronics.** *Prog Quant Electron* 2002, **26**:225.
2. Kępiński L, Zawadzki M, Miśta W: **Hydrothermal synthesis of precursors of neodymium oxide nanoparticles.** *Solid State Sci* 2004, **6**:1327.
3. Lal B, Kumar S, Aghamkar P, Rohilla S, Singh D: **Structural studies of annealed neodymia-silica composite synthesized by solgel technique.** *Physica B* 2009, **404**:3452.
4. Caird JA, Ramponi AJ, Staver PR: **Quantum efficiency and excited-state relaxation dynamics in neodymium-doped phosphate laser glasses.** *JOSA B* 1991, **8**:1392.
5. Jacinto C, Oliveira SL, Nunes LAO, Myers MJ, Catunda T: **Normalized-lifetime thermal-lens method for the determination of luminescence quantum efficiency and thermo-optical coefficients: Application to Nd3 +-doped glasses.** *Phys Rev B* 2006, **73**:125107.
6. Kenyon AJ, Trwoga PF, Federighi M, Pitt CW: **Optical properties of PECVD erbium-doped silicon-rich silica: evidence for energy transfer between silicon microclusters and erbium ions.** *J Phys Condens Matter* 1994, **6**:L319.
7. Franzo G, Iacona F, Vinciguerra V, Priolo F: **Enhanced rare earth luminescence in silicon nanocrystals.** *Mater Sci Eng B* 2000, **69-70**:335.
8. Gourbilleau F, Levalois M, Dufour C, Vicens J, Rizk R: **Optimized conditions for an enhanced coupling rate between Er ions and Si nanoclusters for an improved 1.54-μm emission.** *J Appl Phys* 2004, **95**:3717.
9. Franzó G, Vinciguerra G, Priolo F: **The excitationmechanism of rare-earth ions in silicon nanocrystals.** *Appl Phys A Mater Sci Process* 1999, **69**:3.
10. Watanabe K, Tamaoka H, Fujii M, Moriwaki K, Hayashi S: **Excitation of Nd3+ and Tm3+ by the energy transfer from Si nanocrystals.** *Physica E* 2002, **13**:1038.
11. Seo SY, Kim M-J, Shin J: **The Nd-nanocluster coupling strength and its effect in excitation/de-excitation of Nd3+ luminescence in Nd-doped silicon-rich silicon oxide.** *Appl Phys Lett* 2003, **83**:2778.
12. MacDonald AN, Hryciw A, Lenz F, Meldrum A: **Interaction between amorphous silicon nanoclusters and neodymium ions.** *Appl Phys Lett* 2006, **89**:173132.
13. Bréard D, Gourbilleau F, Dufour C, Rizk R, Doulan J-L, Camy P: **Spectroscopic studies of Nd3+-doped silicon-rich silicon oxide films.** *Mater Sci Eng* 2008, **146**:179.
14. Bréard D, Gourbilleau F, Belarouci A, Dufour C, Rizk R: **Nd3+ photoluminescence study of Nd-doped Si-rich silica films obtained by reactive magnetron sputtering.** *J Lumin* 2006, **121**:209.
15. Gourbilleau F, Belarouci A, Bréard D, Dufour C, Rizk R: **Active emitters based on nanostructured Si.** *Int J Nanotechnol* 2008, **5**:574.
16. Podhorodecki A, Misiewicz J, Gourbilleau F, Cardin J, Dufour C: **High Energy Excitation Transfer from Silicon Nanocrystals to Neodymium Ions in Silicon-Rich Oxide Film.** *Electrochem Solid State* 2010, **13**:K26-K28.
17. Ternon C, Gourbilleau F, Portier X, Voivenel P, Dufour C: **An original approach for the fabrication of Si/SiO2 multilayers using reactive magnetron sputtering.** *Thin Solid Films* 2002, **419**:5.
18. Hinds BJ, Wang F, Wolfe DM, Hinkle CL, Lucovsky G: **Study of SiOx decomposition kinetics and formation of Si nanocrystals in an SiO2 matrix.** *J Non-Cryst Solids* 1998, **227-230**:507.
19. Ono H, Ikarashi T, Ando K, Kitano T: **Infrared studies of transition layers at SiO2/Si interface.** *J Appl Phys* 1998, **84**:6064.
20. Charvet S, Madelon R, Gourbilleau F, Rizk R: **Spectroscopic ellipsometry analyses of sputtered Si/SiO2 nanostructures.** *J Appl Phys* 1999, **85**:4032.
21. Gourbilleau F, Dufour C, Levalois M, Vicens J, Rizk R, Sada C, Enrichi F, Battaglin G: **Room-temperature 1.54 μm photoluminescence from Er-doped Si-rich silica layers obtained by reactive magnetron sputtering.** *J Appl Phys* 2003, **94**:3869.
22. Ono H, Katsumata T: **Interfacial reactions between thin rare-earth-metal oxide films and Si substrates.** *Appl Phys Lett* 2001, **78**:1832.
23. Fidalgo A, Ilharco LM: **The defect structure of sol-gel-derived silica/polytetrahydrofuran hybrid films by FTIR.** *J Non-Cryst Solids* 2001, **283**:144.
24. Innocenzi P: **Infrared spectroscopy of sol-gel derived silica-based films: a spectra-microstructure overview.** *J Non-Cryst Solids* 2003, **316**:309.
25. Kapaklis V: **Structural characterization of silicon nanocrystals from amorphous silicon oxide materials.** *J Non-Cryst Solids* 2008, **354**:612.
26. Garrido B, López M, Pérez-Rodríguez A, García C, Pellegrino P, Ferré R, Moreno JA, Morante JR, Bonafos C, Carrada M, Claverie A, de la Torre J, Souifi A: **Optical and electrical properties of Si-nanocrystals ion beam synthesized in SiO2.** *Nucl Instrum Meth. B* 2004, **216**:213.

doi:10.1186/1556-276X-6-161
Cite this article as: Debieu *et al.*: Effect of the Nd content on the structural and photoluminescence properties of silicon-rich silicon dioxide thin films. *Nanoscale Research Letters* 2011 **6**:161.

Nanoscale Research Letters
a SpringerOpen Journal

NANO EXPRESS Open Access

Electromagnetic modeling of waveguide amplifier based on Nd^{3+} Si-rich SiO_2 layers by means of the ADE-FDTD method

Christian Dufour*, Julien Cardin, Olivier Debieu, Alexandre Fafin and Fabrice Gourbilleau

Abstract

By means of ADE-FDTD method, this paper investigates the electromagnetic modelling of a rib-loaded waveguide composed of a Nd^{3+} doped Silicon Rich Silicon Oxide active layer sandwiched between a SiO_2 bottom cladding and a SiO_2 rib. The Auxilliary Differential Equations are the rate equations which govern the levels populations. The Finite Difference Time Domain (FDTD) scheme is used to solve the space and time dependent Maxwell equations which describe the electromagnetic field in a copropagating scheme of both pumping (λ_{pump} = 488 nm) and signal (λ_{signal} = 1064 nm) waves. Such systems are characterized by extremely different specific times such as the period of electromagnetic field ~ 10^{-15} s and the lifetimes of the electronic levels between ~ 10^{-10}s and ~ 10^{-4} s. The time scaling method is used in addition to specific initial conditions in order to decrease the computational time. We show maps of the Poynting vector along the propagation direction as a function of the silicon nanograin (Si-ng) concentrations. A threshold value of 10^{24} Si-ng m^{-3} is extracted below which the pump wave can propagate so that a signal amplication is possible.

Keywords: Silicon nanograin, Silica, Neodymium, ADE-FDTD, Waveguide, amplification

Introduction

The feasibility of optical amplifying waveguide has been for almost two decades the purpose of numerous experimental works [1]. The devices under study were based on an active layer constituted of a silica film co-doped with silicon nanograins (Si-ng) and rare earth ions RE (Er^{3+} in particular) deposited on a substrate and covered by a cladding layer of pure silica. The differences in the optical indices of the three layers ensure the optical guiding. The amplification of a signal is based on an efficient population inversion of the rare earth levels whose energy difference correspond to the signal wavelength. Due to the very low RE signal absorption cross section, a solution has been found using silicon nanoparticles. The physical background lies on two major phenomena: on the one hand, the ability of Si-ng's to absorb efficiently a pumping light and, on the other hand, the effective energy transfer between Si-ng's and RE ions. In this way, a RE population inversion could have been achieved in order to fulfill the amplification function of the device. Despite all these promising features, a net gain is hardly achievable with the former Er^{3+} ions due to their great probability of signal reabsorption from the ground state. This drawback is prevented with the use of Nd^{3+} ions described by a five level scheme since the transition does not involve the ground state. The theoretical studies of the waveguide amplifiers have accounted for both rate population equations and Maxwell equations. In this paper we investigate the ADE-FDTD method applied to a rib-loaded waveguide whose active layer is composed of a silica film co doped with Nd^{3+} ions and silicon nanograins. One of the main issues to be addressed in such systems consists in dealing with extremely different time scales: the populations lifetimes (1 ms) and the electromagnetic field period (10^{-15} s). According to [2,3] we use a time scaling that allows to circumvent this issue. All the lifetimes have been shortened by a factor of 10^6, and consequently the transfer coefficient K has also been divided by the same coefficient. In this paper, we investigate the accuracy of this scaling method through longitudinal and trans-verse maps of the Poynting vector for

* Correspondence: christian.dufour@ensicaen.fr
CIMAP, CEA/CNRS/ENSICAEN/UCBN, 6 Boulevard Maréchal Juin, 14050 Caen Cedex 4, France

several Si-ng concentrations. The applicability of this method is linked to the space and time calculation steps since a reasonable computing time must not be exceeded.

Computational details

We treat the problem within a calculation box as described in Figure 1. Each axis (*x*,*y* and *z*) is divided into space steps (Δx, Δy and Δz respectively).

Four zones appear and will be described hereafter: *i*) the rib-loaded waveguide composed of the active layer (optical index n_{act} = *1.52*) stacked between the SiO_2 cladding and rib (optical index n_{siO_2} = *1.45*), *ii*) the plane containing the electromagnetic field source (z_{source} = 6 Δz), *iii*) the diaphragm (between 7Δz and 10Δz) which transforms the source into a realistic electromagnetic Gaussian field impinging on the waveguide and *iv*) the boundary zone (PML) (4Δz in thickness) characterized by appropriate values of electrical (ρ) and magnetic (σ) conductivities in order to absorb the electromagnetic field so that the box borders do not influence the field in the zone of interest [4].

Lorentz Model for the dielectric susceptibility

Considering a transition between levels *i* and *j* we use the Lorentz following relationship which makes the coupling between the polarization density $\mathbf{P}_{i\ j}$, the level populations *Ni* and N_j in m^{-3} and the total electric field **E**:

$$\frac{d^2\mathbf{P}_{ij}(t)}{dt^2} + \Delta\omega_{ij}\frac{d\mathbf{P}_{ij}(t)}{dt} + \omega_{ij}^2\mathbf{P}_{ij}(t) = \kappa\,\Delta N_{ij}(t)\mathbf{E}(t) \qquad (1)$$

$\Delta\omega_{ij}$ is the FWHM of the *ij* transition deduced from photoluminescence measurements according to [5], $\omega_{ij} = \frac{2\pi c}{\lambda_{ij}}$ is the oscillator pulsation linked to the *ij* transition wavelengh λ_{ij}, $\kappa = \frac{6\pi\varepsilon_0 c^3\gamma_{ij}}{\omega_{ij}^2}$ and γ_{ij} is the *ij* radiative transition rate in s^{-1} [6,7]. The level populations difference in m^{-3} is given by $\Delta N_{ij} = N_i - N_j$.

In the same way, we describe the polarisation density $\mathbf{P}_{si}$ linked to the silicon level populations N_{Si} (ground level) and N_{Si}^* (excited level),to the oscillator pulsation ω_{Si} and finally to the transition FWHM $\Delta\omega_{Si}$.

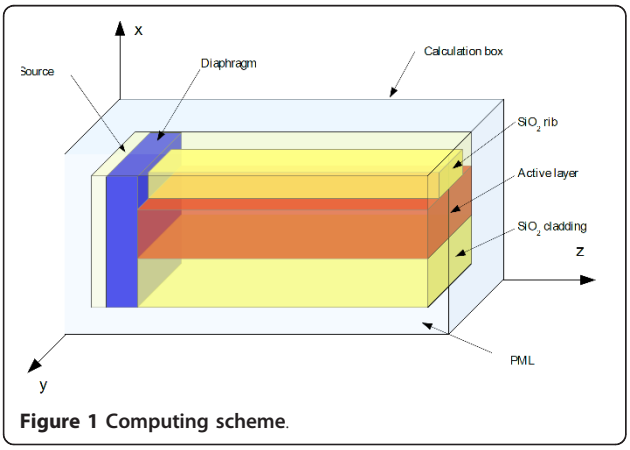

Figure 1 Computing scheme.

Maxwell equations: FDTD numerical method

We start from the Maxwell equation which links the displacement vector **D** to the magnetic excitation **H**:

$$\frac{\partial\mathbf{D}}{\partial t} = \overrightarrow{\text{curl}}\mathbf{H} - \mathbf{J}_e$$

where the current density $\mathbf{J}_e$ is related to **E** by $\mathbf{J}_e = \sigma\mathbf{E}$ where σ is the electrical conductivity. Accounting for the relationship between **D** and the total polarisation density, $\mathbf{D} = \varepsilon_0\mathbf{E} + \Sigma\,\mathbf{P_{ij}}$ we may write:

$$\frac{\partial\mathbf{E}}{\partial t} = \frac{1}{\varepsilon_0\varepsilon_r}\overrightarrow{\text{curl}}\,\mathbf{H} - \frac{\sigma}{\varepsilon_0\varepsilon_r}\mathbf{E} - \frac{1}{\varepsilon_0\varepsilon_r}\frac{\partial\left(\sum\mathbf{P}_{Si}\right)}{\partial t} \qquad (2)$$

$$\frac{\partial\mathbf{H}}{\partial t} = -\frac{1}{\mu}\overrightarrow{\text{curl}}\mathbf{E} - \frac{\rho}{\mu}\mathbf{H} \qquad (3)$$

All the calculations are performed with real variables. Hence, in order to account for absorption processes other than those due to the level transitions, we characterize (especially for the diaphragm and PML) a specific electric conductivity σ and magnetic conductivity ρ.

Both equations 2 and 3 are solved using the Yee algorithm [8]. The space steps are chosen so that: $\Delta x = \Delta y = \Delta z \ll \lambda_{min}$ (the lowest values among all the wavelengths) Hereafter: $\Delta x = \Delta y = \Delta z$ = 45 nm. The time step Δt must fulfill the condition: $\Delta t \ll \frac{\Delta z}{c}$. Finally the fields inputs (pump and signal) are known as the 'source issue'. Since no perfect source is available, we choose an *xy* plane at $z_{source} = 6\Delta z$ in which we define a polarized electric field. $\mathbf{E_{source}} = \mathrm{E_x}(\mathrm{x,y})\,\vec{i}$. This source impinges on the diaphragm so that a Gaussian beam enters the waveguide itself at $z = 11\Delta z$. The total waveguide length is $15\Delta z$ = 0.665 μm and the number of time steps is 25000, which amounts to a total simulated time of 0.3 10^{-12} s.

Rate equations

In this section, we detail the ADE part of the method which describes the time population dynamics of Si-ng and Nd^3+ levels with the following rate equations.

Silicon nanoclusters

We consider both radiative *r* and non radiative *nr* transitions. The optical pumping power (in m^{-3}) writes $\frac{1}{\hbar\omega_p}\mathbf{E}(t)\frac{d\mathbf{P}_p(t)}{dt}$. The energy transfer between Si-ng and

RE ions is described by a transfer coefficient K and equal to $KN^*_{Si}(t)\,N_0(t)$ at time t. This leads to the following rate equations:

$$\frac{dN^*_{Si}(t)}{dt} = +\frac{1}{\hbar\omega_p}\mathbf{E}(t)\frac{d\mathbf{P}_p(t)}{dt} - \frac{N^*_{Si}(t)}{\tau^*|^r_{nr}} - KN^*_{Si}(t)N_0(t), \quad (4)$$

$$\frac{dN_{Si}(t)}{dt} = -\frac{1}{\hbar\omega_p}\mathbf{E}(t)\frac{d\mathbf{P}_p(t)}{dt} + \frac{N^*_{Si}(t)}{\tau^*|^r_{nr}} + KN^*_{Si}(t)N_0(t). \quad (5)$$

Rare earth ions Nd $^{3+}$

A five level scheme is adopted for the Nd^{3+} ion in Figure 2 [9,10].

We consider three radiative transitions ($4F_{3/2} \rightarrow 4I_{9/2}$, λ_{20} = 945 nm; $4F_{3/2} \rightarrow 4I_{11/2}$, λ_{21} = 1064 nm; and $4F_{3/2} \rightarrow 4I_{13/2}$, λ_{24} = 1340 nm) and three non radiative transitions ($4F_{5/2}$ - > $4F_{3/2}$ ($N_3 \mapsto N_2$) $4I_{11/2}$ - > $4I_{9/2}$ ($N_1 \mapsto N_0$) and $4I_{13/2}$ - > $4I_{11/2}$ ($N_4 \mapsto N_1$)).

The terms $+\frac{1}{\hbar\omega_{21}}\mathbf{E}(t)\frac{d\mathbf{P}_{21}(t)}{dt}$, $+\frac{1}{\hbar\omega_{20}}\mathbf{E}(t)\frac{d\mathbf{P}_{20}(t)}{dt}$ and $+\frac{1}{\hbar\omega_{24}}\mathbf{E}(t)\frac{d\mathbf{P}_{24}(t)}{dt}$ correspond to the stimulated transitions 2 → 1, 2 → 0 and 2 → 4. The terms $-\frac{N_2(t)}{\tau_{21}|^r_{nr}}$, $-\frac{N_2(t)}{\tau_{20}|^r_{nr}}$ and $-\frac{N_2(t)}{\tau_{24}|^r_{nr}}$ correspond to the spontaneous transitions 2 → 1, 2 → 0 and 2 → 4.

The associated rate equations read:

$$\frac{dN_3(t)}{dt} = -\frac{N_3(t)}{\tau_{32}|_{nr}} + KN^*_{Si}(t)N_0(t), \quad (6)$$

$$\frac{dN_2(t)}{dt} = \frac{1}{\hbar\omega_{24}}\mathbf{E}(t)\frac{d\mathbf{P}_{24}(t)}{dt} + \frac{1}{\hbar\omega_{21}}\mathbf{E}(t)\frac{d\mathbf{P}_{21}(t)}{dt} + \frac{1}{\hbar\omega_{20}}\mathbf{E}(t)\frac{d\mathbf{P}_{20}(t)}{dt} + \frac{N_3(t)}{\tau_{32}|_{nr}} - \frac{N_2(t)}{\tau_{21}|^r_{nr}} - \frac{N_2(t)}{\tau_{20}|^r_{nr}} - \frac{N_2(t)}{\tau_{24}|^r_{nr}}, \quad (7)$$

$$\frac{dN_4(t)}{dt} = -\frac{1}{\hbar\omega_{24}}\mathbf{E}(t)\frac{d\mathbf{P}_{24}(t)}{dt} + \frac{N_2(t)}{\tau_{24}|^r_{nr}} - \frac{N_4(t)}{\tau_{41}|_{nr}}, \quad (8)$$

$$\frac{dN_1(t)}{dt} = -\frac{1}{\hbar\omega_{21}}\mathbf{E}(t)\frac{d\mathbf{P}_{21}(t)}{dt} + \frac{N_2(t)}{\tau_{21}|^r_{nr}} - \frac{N_1(t)}{\tau_{10}|_{nr}} + \frac{N_4(t)}{\tau_{41}|_{nr}}, \quad (9)$$

$$\frac{dN_0(t)}{dt} = -\frac{1}{\hbar\omega_{20}}\mathbf{E}(t)\frac{d\mathbf{P}_{20}(t)}{dt} + \frac{N_2(t)}{\tau_{20}|^r_{nr}} + \frac{N_1(t)}{\tau_{10}|_{nr}} - KN^*_{Si}(t)N_0(t). \quad (10)$$

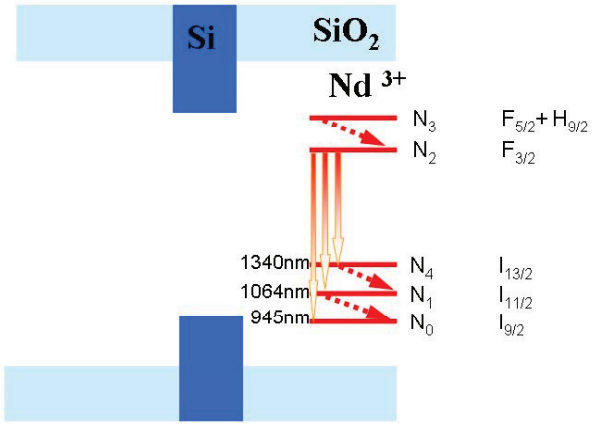

Figure 2 Five level scheme of Nd^{3+} ions.

Application to rib-loaded waveguide

In table 1, we collect the simulation parameters taken into account for the transitions. The lifetimes correspond to the experimental ones divided by the scaling factor 10^6.

The transfer coefficient K estimated to ~ 10^{-20} m^3 s^{-1} [11] has also been scaled with the same factor 10^6: K = 10^{-14} $m^3.s^{-1}$. The amplitudes of the input pumping and signal electric fields have been taken equal to E_{pump} = 10^7 $V.m^{-1}$ and E_{signal} = 100 $V.m^{-1}$.

After the time Fourier transform of both **E** and **H** fields, we deduce the z component of the pump (R_z^{pump}) and signal (R_z^{signal}) Poynting vectors (in $W.m.^{-2}$)

Three Si-ng concentrations have been investigated (N_{si} = 10^{25}, 10^{24} and 10^{23} m^{-3}). In the initial states, only the ground level is populated. The corresponding (xz) maps (R_z^{pump}) are plotted in Figures 3, 4 and 5.

In these figures, the different calculation box zones may be recognized: *i*) the Perfectly Matched Layer (PML) which lies in the area from the lefthand side between z = 0 nm and z = 180 nm, and from the

Table 1 Simulation parameters of the Si-ng and Nd^{3+} transitions

Transition	lifetime(s)	type	ω_{ij} (s^{-1})	$\Delta\omega_{ij}$ (s^{-1})
Si →Si *	4 10^{-11}	R	3.86 10^{15}	4.4 10^{14}
3 → 2	2.3 10^{-16}	NR		
2 → 0	3 10^{-10}	R	2.07 10^{15}	1.38 10^{14}
2 → 1	3 10^{-10}	R	1.7 10^{15}	1.39 10^{14}
2 → 4	3 10^{-10}	R	1.3 10^{15}	1.33 10^{14}
4 → 1	9.7 10^{-16}	NR		
1 → 0	5.1 10^{-16}	NR		

R and NR stand for radiative and non-radiative transitions respectively.

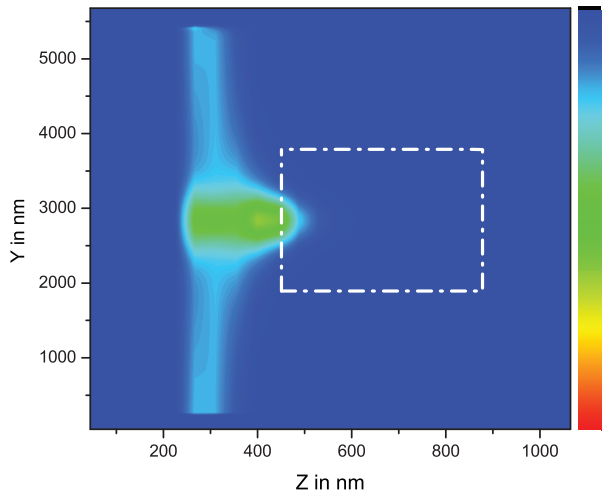

Figure 3 (*yz*) maps of R_z^{pump} in W.m^{-2} for [Si-ng] = 10^{25} m^{-3}, the dashed-dot rectangle represents the waveguide rib.

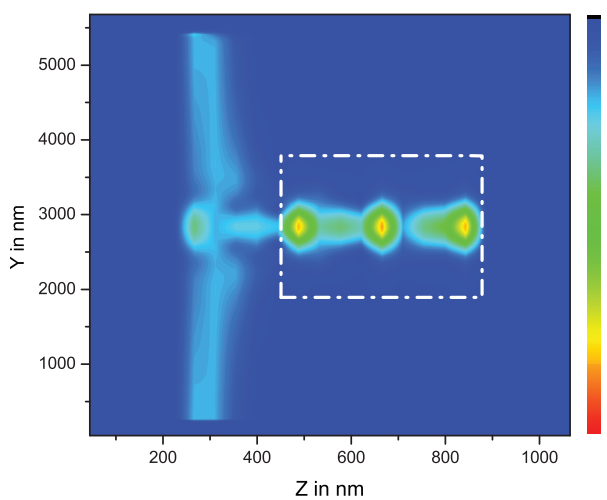

Figure 5 (*yz*) maps of R_z^{pump} in W.m^{-2} for [Si-ng] = 10^{23} m^{-3}, the dashed-dot rectangle represents the waveguide rib.

righthand side between z = 890 nm and z = 1000 nm, *ii*) the plane containing the electromagnetic field source at z ~ 300 nm, *iii*) the FDTD zone which is located at about 180 nm from border of plot, the Gaussian beam impinging in the waveguide at z ~ 500 nm and the intensity propagating in waveguide from z ~ 500 nm to z ~ 900 nm.

On the basis of the parameters taken from experiments, these plots evidence the fact that for Si-ng concentrations above 10^{24} m^{-3}, the pumping wave does not reach the end of the waveguide. This concentration threshold corresponds to high experimental values [12], and is above the lower values leading to minimal optical losses [1].

In order to reduce the computing time, in addition to the scaling method, we start the calculations with Si-ng levels already populated at the maximum inversion rate, $N_{Si} = N_{Si}^* = 5\ 10^{22}$ m^{-3}. Hence, for a given total Si-ng concentration of 10^{23} m^{-3}, this result (Figure 6) can be compared to the preceding one where $N_{Si} = 10^{23}$ m^{-3} and $N_{Si}^* = 0$ (Figure 5). The propagation of the pump power within the waveguide seems to be similarly attenuated in both cases. The main difference occurs in the N_3 level concentration which is directly populated from the excited N_{Si}^* level. In case of maximum inversion rate, the stationary regime is reached and the concentration becomes equal to $N_3 = \tau_{32}.K.N_{Si}^*.N_0 \approx 1.1\ 10^{18}$ m^{-3}. In case of $N_{Si} = 10^{23}$ m^{-3} and $N_{Si}^* = 0$ starting

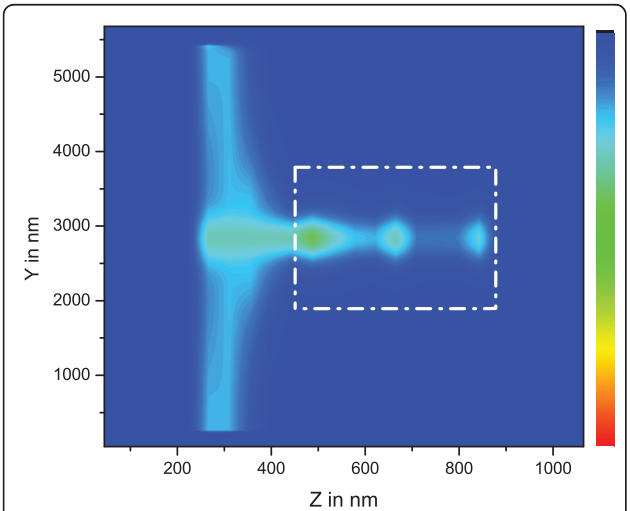

Figure 4 (*yz*) maps of R_z^{pump} in W.m^{-2} for [Si-ng] = 10^{24} m^{-3}, the dashed-dot rectangle represents the waveguide rib.

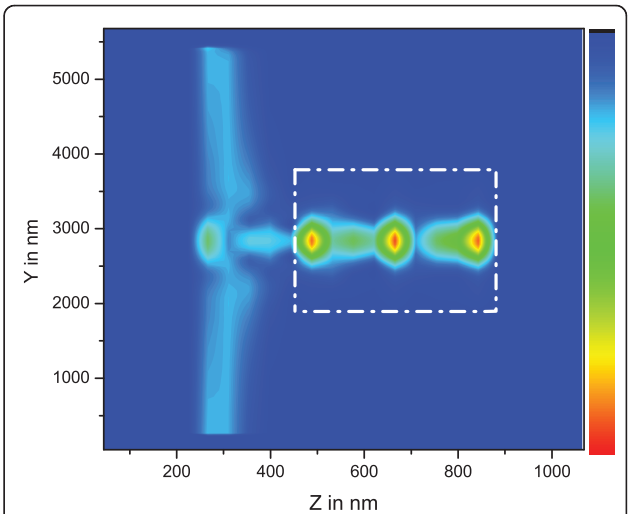

Figure 6 (*yz*) map of R_z^{pump} in W.m^{-2} N_{Si} 5 10^{22} m^{-3}/N_{Si}^* = 5 10^{22} m^{-3}.

concentration, the N_3 concentration does not reach a stationary regime and stays below several 10^{17} m^{-3}.

Conclusion

We have investigated by means of ADE-FDTD method the electromagnetic field propagation in rib-loaded waveguides constituted of an active layer of Nd^{3+} doped silicon rich silica stacked between pure silica bottom cladding and rib. This numerical method treats Nd^{3+} and Si-ng levels rate equations (ADE) coupled to the Maxwell equations (FDTD). The extremely different specific times involved in the ADE (levels lifetimes ≈ 10 μs) and in FDTD (electromagnetic wave periods ≈ 10^{-15} s) have required the use of the scaling time method which allows reasonable computing time: the number of time iterations has been reduced by six orders of magnitude. In addition to this method, we have proposed to start the calculations with steady state Si-ng ground and excited populations. The numerical computation has been performed for several Si-ng concentrations. Therefore we can infer that the pumping wave propagation (λ_{pump} = 488 nm) is possible for [Si-ng] ≤ 10^{24} m^{-3} in agreement with experimental loss measurements. The upper Nd^{3+} level reaches its stationary value predicted with the analytical solution of the steady state rate equations.

Acknowledgements

The authors are grateful to the French Agence Nationale de la Recherche, which supported this work through the Nanoscience and Nanotechnology program (DAPHNES project ANR-08-NANO-005).

Authors' contributions

CD and JC conceived the calculation code, AF carried out most of the calculations, OD performed the optical measurements on our samples and FG conceived the whole project. All authors read and approved the final manuscript.

Competing interests

The authors declare that they have no competing interests.

Received: 27 September 2010 Accepted: 4 April 2011
Published: 4 April 2011

References

1. Navarro-Urrios D, Melchiorri M, Daldosso N, Pavesi L, García C, Pellegrino P, Garrido B, Pucker G, Gourbilleau F, Rizk R: **Optical losses and gain in silicon-rich Silica waveguides containing Er ions.** *Journal of Luminescence* 2006, **121**:249-255.
2. Shi S, Prather DW: **Lasing dynamics of a silicon photonic crystal microcavity.** *Opt Express* 2007, **15(16)**:10294-10302.
3. Redding B, Shi S, Creazzo T, Prather DW: **Electromagnetic modeling of active silicon nanocrystal waveguides.** *Opt Express* 2008, **16**:8792-8799.
4. Berenger JP: **A perfectly matched layer for the absorption of electromagnetic waves.** *J of Computational Physics* 1994, **114(2)**:185-200.
5. Biallo D, De Sario M, Petruzzelli V, Prudenzano F: **Time domain analysis of optical amplification in Er3+ doped SiO2-TiO2 planar waveguide.** *Opt Express* 2005, **13(12)**:4683-4692.
6. Taflove A, Hagness SC, *et al*: **Computational electrodynamics: the finite-difference time-domain method.** *Artech House Norwood, MA* 1995.
7. Zhukovsky SV, Chigrin DN: **Numerical modelling of lasing in microstructures.** *Phys Status Solidi (b)* 2007, **244(10)**:3515-3527.
8. Yee K: **Numerical solution of inital boundary value problems involving Maxwell's equations in isotropic media IEEE Transactions on antennas and propagation.** 1966, **14(3)**:302-307.
9. Serqueira EO, Dantas NO, Monte AFG, Bell MJV: **Judd Ofelt calculation of quantum efficiencies and branching ratios of Nd3+ doped glasses.** *J of Non-Crystalline Solids* 2006, **352(32-35)**:3628-3632.
10. Pecoraro E, Sampaio JA, Nunes LAO, Gama S, Baesso ML: **Spectroscopic properties of water free Nd2O3-doped low silica calcium aluminosilicate glasses.** *J of Non-Crystalline Solids* 2000, **277(2-3)**:73-81.
11. Pacifici Domenico, Franzò Giorgia, Priolo Francesco, Iacona Fabio, Dal Negro Luca: **Modeling and perspectives of the Si nanocrystals-Er interaction for optical amplification.** *Phys Rev B* 2003, **67(24)**:245301.
12. Gourbilleau F, Levalois M, Dufour C, Vicens J, Rizk R: **Optimized conditions for an enhanced coupling rate between Er ions and Si nanoclusters for an improved 1.54-μm emission.** *J Appl Phys* 2004, **95**:3717.

doi:10.1186/1556-276X-6-278
Cite this article as: Dufour *et al.*: Electromagnetic modeling of waveguide amplifier based on Nd^{3+} Si-rich SiO_2 layers by means of the ADE-FDTD method. *Nanoscale Research Letters* 2011 **6**:278.

Nanoscale Research Letters
a SpringerOpen Journal

NANO EXPRESS Open Access

SiO_x/SiN_y multilayers for photovoltaic and photonic applications

Ramesh Pratibha Nalini[1*], Larysa Khomenkova[1], Olivier Debieu[1], Julien Cardin[1], Christian Dufour[1], Marzia Carrada[2] and Fabrice Gourbilleau[1]

Abstract

Microstructural, electrical, and optical properties of undoped and Nd^{3+}-doped SiO_x/SiN_y multilayers fabricated by reactive radio frequency magnetron co-sputtering have been investigated with regard to thermal treatment. This letter demonstrates the advantages of using SiN_y as the alternating sublayer instead of SiO_2. A high density of silicon nanoclusters of the order 10^{19} nc/cm^3 is achieved in the SiO_x sublayers. Enhanced conductivity, emission, and absorption are attained at low thermal budget, which are promising for photovoltaic applications. Furthermore, the enhancement of Nd^{3+} emission in these multilayers in comparison with the SiO_x/SiO_2 counterparts offers promising future photonic applications.

PACS: 88.40.fh (Advanced materials development), 81.15.cd (Deposition by sputtering), 78.67.bf (Nanocrystals, nanoparticles, and nanoclusters).

Keywords: SiO_x/SiN_y, multilayers, Nd^{3+} doping, photoluminescence, XRD, absorption coefficient, conductivity

Introduction

Silicon nanoclusters [Si-ncs] with engineered band gap [1] have attracted the photonic and the photovoltaic industries as potential light sources, optical interconnectors, and efficient light absorbers [2-5]. Multilayers [MLs] of silicon-rich silicon oxide [SiO_x] alternated with SiO_2 became increasingly popular due to the precise control on the density and size distribution of Si-ncs [6,7]. Moreover, the efficiency of light emission from SiO_x-based MLs exceeds that of the single SiO_x layers with equivalent thickness due to the narrower Si-nc size distribution. The ML approach is also a powerful tool to investigate and control the emission of rare-earth [RE] dopants, for example, Er-doped SiO_x/SiO_2 MLs [8]. It also allows us to control the excitation mechanism of the RE ions by adjusting the optimal interaction distance between the Si-ncs and the RE ions. However, achieving electroluminescence and hence extending its usage for photovoltaic applications are problematic due to the high resistivity caused by SiO_2 barrier layers [9]. Hence, replacement of the SiO_2 sublayer by alternative dielectrics becomes interesting. Due to the lower potential barrier and better electrical transport properties of silicon nitride [Si_3N_4] in comparison to SiO_2, multilayers like SiO_x/Si_3N_4 [10], Si-rich Si_3N_4 (SiN_y)/Si_3N_4 [11], and Si-rich Si_3N_4/SiO_2 [12] were proposed and investigated [13] for their optical and electrical properties.

In this letter, we investigate SiO_x/SiN_y MLs and compare them with the SiO_x/SiO_2 counterparts reported earlier [9,14]. We demonstrate that an enhancement in the conductive and light-emitting properties of SiO_x/SiN_y MLs can be achieved with a reduced thermal budget. We also report a pioneering study on Nd-doped SiO_x/SiN_y MLs. A comparison between the properties of Nd^{3+}-doped SiO_x/SiO_2 and SiO_x/SiN_y MLs are presented, and we show the benefits of using SiN_y sublayers to achieve enhanced emission from Nd^{3+} ions.

Experimental details

Undoped and Nd-doped 3.5-nm SiO_x/5-nm SiN_y (50 periods) MLs were deposited at 500°C on a 2-inch p-Si substrate by radio frequency [RF] magnetron co-sputtering of Si and SiO_2 targets in hydrogen-rich plasma for the SiO_x sublayers and a pure Si target in nitrogen-rich plasma for the SiN_y sublayers. An additional Nd_2O_3 target was used to dope the SiO_x and SiN_y sublayers by

* Correspondence: pratibha-nalini.sundar@ensicaen.fr
[1]CIMAP UMR CNRS/CEA/ENSICAEN/UCBN, 6 Bd. Maréchal Juin, 14050 Caen Cedex 4, France
Full list of author information is available at the end of the article

Nd^{3+} ions. More details on the growth process can be found elsewhere [15]. The excess Si content in the corresponding SiO_x and SiN_y single layers obtained from RBS studies are calculated to be 25 and 11 at.%, respectively (i.e., $SiO_{x\ =\ 1}$ and $SiN_{y\ =\ 1.03}$). Conventional furnace annealing under nitrogen atmosphere at different temperatures, T_A = 400 to 1,100°C, and times, t_A = 1 to 60 min, was performed on the MLs. X-ray diffraction analysis was performed using a Phillips XPERT HPD Pro device (PANalytical, Almelo, The Netherlands) with CuK_α radiation (λ = 0.1514 nm) at a fixed grazing angle incidence of 0.5°. Asymmetric grazing geometry was chosen to increase the volume of material interacting with the X-ray beam and to eliminate the contribution of the Si substrate. Photoluminescence [PL] spectra were recorded in the 550- to 1,150-nm spectral range using the Triax 180 Jobin Yvon monochromator (HORIBA Jobin Yvon SAS, Longjumeau, Paris, France) with an R5108 Hamamatsu PM tube (Hamamatsu, Shizuoka, Japan). The 488-nm Ar^+ laser line served as the excitation source. All the PL spectra were corrected by the spectral response of the experimental setup. Top and rear-side gold contacts were deposited on the MLs by sputtering for electrical characterization. Current-voltage measurements were carried out using a SUSS Microtec EP4 two-probe apparatus (SUSS Microtec, Germany) equipped with Keithley devices (Keithly, Cleveland, OH, USA). Energy-filtered transmission electron microscopy [EFTEM] was carried out on a cross-sectional specimen using a TEM-FEG microscope Tecnai F20ST (FEI, Eindhoven, The Netherlands) equipped with an energy filter TRIDIEM from Gatan (Gatan, München, Germany). The EFTEM images were obtained by inserting an energy-selecting slit in the energy-dispersive plane of the filter at the Si (17 eV) and at the SiO_2 (23 eV) plasmon energy, with a width of ± 2 eV.

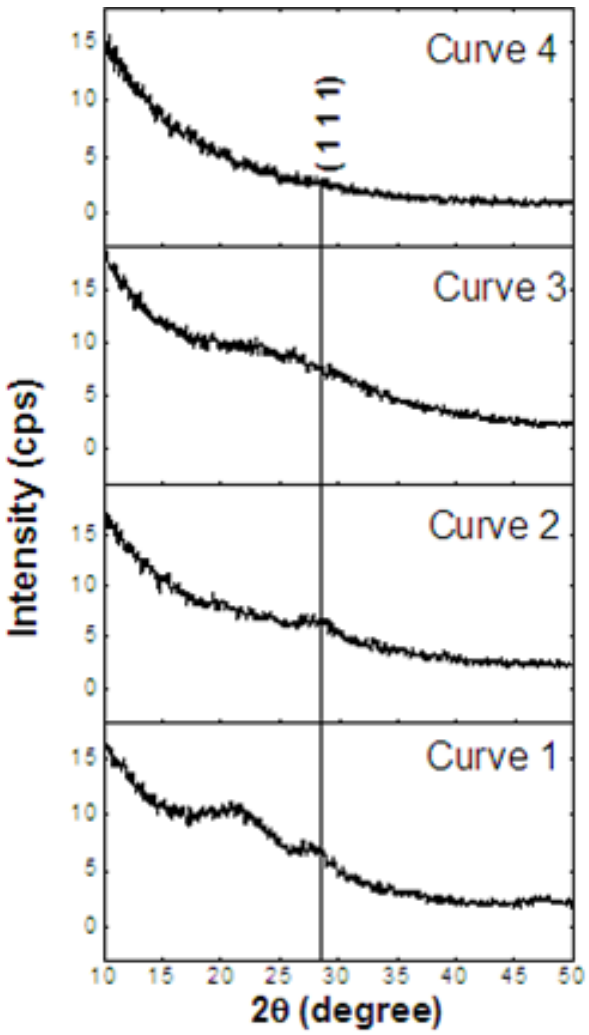

Figure 1 XRD spectra of annealed Si-based MLs. (curve 1) SiO_x/SiO_2 1 h, 1,100°C; (curve 2) SiO_x/SiN_y 1 h, 1,100°C; (curve 3) SiO_x/SiN_y 1 min, 1,000°C; and (curve 4) SiO_x/SiO_2 1 min, 1,000°C.

Results and discussions

Effect of annealing on the PL

Since an annealing at T_A = 1,100°C and t_A = 60 min is the most suitable to achieve an efficient PL from Si-ncs either in sputtered SiO_x single layers [7] or in SiO_x /SiO_2 MLs [16], such treatment was first employed on SiO_x/SiN_y MLs. The X-ray diffraction [XRD] broad peak centered around 2θ = 28° is the signature of the Si nanoclusters' formation in the SiO_x /SiO_2 (Figure 1, curve 1) and SiO_x/SiN_y MLs (Figure 1, curve 2) as already observed by means of atomic scale studies on similar multilayers [17]. However, contrary to the PL emission obtained from the SiO_x/SiO_2 MLs, no PL emission was observed in the SiO_x/SiN_y MLs after such annealing (Figure 2a). This stimulated a deeper investigation of the post-fabrication processing to achieve efficient light emission from the SiO_x/SiN_y MLs.

It was observed that the PL signals from the MLs annealed during t_A = 60 min are significant only at lower temperatures (T_A = 400°C to 700°C), and high intensities are obtained when the samples are annealed at high temperatures for a short time (T_A = 900°C to 1,000°C, t_A = 1 min). It is interesting to note that an interplay between T_A and t_A can yield similar PL efficiencies, as can be seen for T_A = 900°C and t_A = 1 min, and T_A = 700°C and t_A = 15 min (Figure 2a).

The highest PL intensity in SiO_x/SiN_y MLs was obtained with T_A = 1,000°C and t_A = 1 min (Figure 2b, c), whereas the SiO_x/SiO_2 MLs showed no emission after such short-time annealing treatment (Figure 2a). Corresponding XRD pattern of this short-time annealed [STA] (STA = 1 min, 1,000°C) SiO_x/SiN_y showed a broad peak in the range 2θ = 20° to 30° which is absent

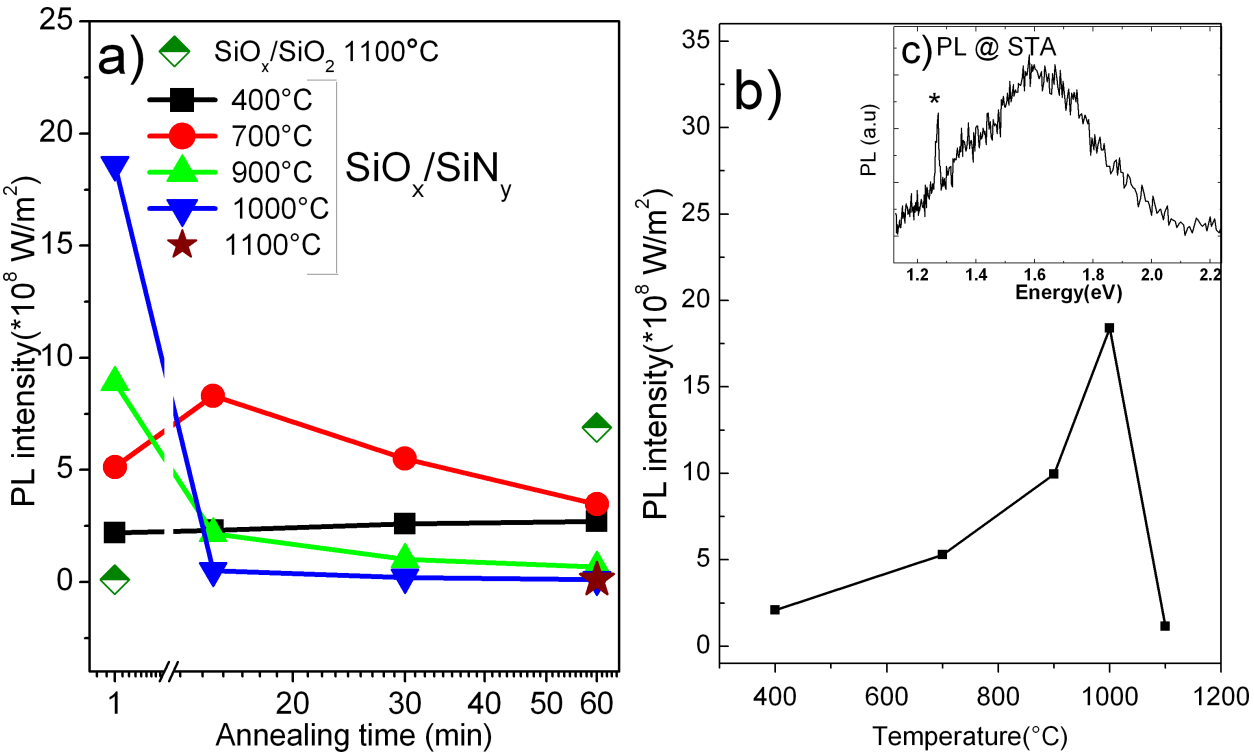

Figure 2 Photoluminescence. (**a**) Maximum PL intensity [I_{PL}] of SiO_x/SiN_y MLs vs T_A and t_A, and SiO_x/SiO_2 at 1,100°C; (**b**) PL spectra of STA SiO_x/SiN_y MLs; (**c**) I_{PL} vs T_A for t_A = 1 min. The asterisk represents the peak from second order emission of laser.

in STA SiO_x/SiO_2 MLs (Figure 1, curves 3 and 4). This suggests the presence of small Si clusters in the SiO_x/SiN_y MLs, with lower sizes (broader peak) by comparison with higher annealing temperature (1,100°C; Figure 1, curves 1 and 2). However, we cannot distinguish which of the sublayer is at the origin of the PL emission. Consequently, the recorded PL may be a combined contribution of the Si-ncs in the SiO_x sublayers and the localized bandtail defect states in the SiN_y sublayers.

Absorption and electrical studies

The absorption studies show similar absorption coefficients for as-grown and STA MLs, whereas annealing at T_A = 1,100°C and t_A = 60 min results in an absorption enhancement (Figure 3a). One can say that, at such temperature, an increase in density and size of the Si-ncs occurs due to phase separation of the SiO_x sublayers into Si and SiO_2 phases. The formation of Si nanocrystals is complete at T_A = 1,100°C and t_A = 60 min and leads to this enhancement. This reasoning is supported by the results obtained from the PL and the XRD analysis of the samples annealed at such temperature. The PL in the SiO_x/SiN_y MLs is quenched after an increase in the time and temperatures of annealing (Figure 2a), and this can be attributed to the increase in the size leading to the loss of quantum confinement effect. The formation of Si nanoclusters can be witnessed from the appearance of the XRD peak at 2θ = 28° (Figure 1, curve 2), which is not seen in the short-time annealed sample (Figure 1, curve 3).

Considering a balance between light emission and absorption for photovoltaic applications, we chose to study STA SiO_x/SiN_y MLs with a total thickness of 850 nm for electrical measurements. Figure 3b compares the dark current curves of 3.5-nm SiO_x/5-nm SiN_y with our earlier reported 3.5-nm SiO_x/3.5-nm SiO_2 (140 nm) MLs [14]. The resistivity was calculated at 7.5 V to be 2.15 and 214 MΩ·cm in the SiO_x/SiN_y and SiO_x/SiO_2 MLs, respectively. Since the thickness of the SiO_x sublayer is the same in both cases (3.5 nm), this decrease in the resistivity of the SiO_x/SiN_y MLs can be ascribed to the substitution of 3.5-nm SiO_2 by 5-nm SiN_y sublayers. This hundred-times enhanced conductivity at low voltage paves way for further improvement of the SiO_x/SiN_y MLs' conductivity, for example, by decreasing the thickness of this SiN_y sublayer.

Microstructural studies

The high-resolution transmission electron microscope [HRTEM] and EFTEM observations on STA SiO_x/SiN_y show Si-ncs in the SiO_x sublayers with an average diameter of 3.4 nm. Only a couple of Si nanocrystals were

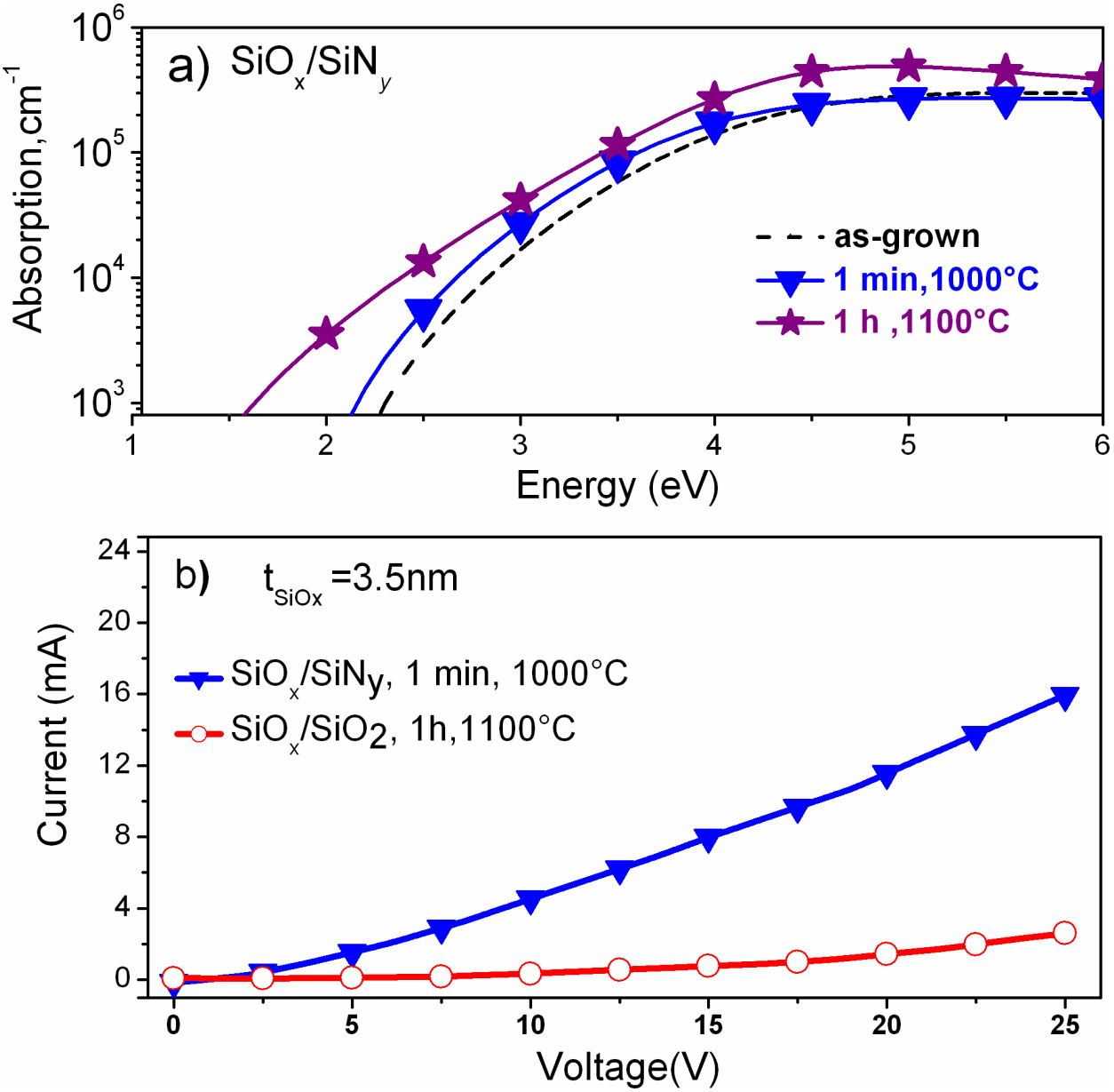

Figure 3 Absorption coefficient and current-voltage behavior. (**a**) Evolution of absorption coefficient with annealing; (**b**) Comparison of current-voltage behavior of SiO_x/SiN_y and SiO_x/SiO_2 MLs.

observed in the HRTEM (Figure 4a), whereas a high density of Si-nanoclusters of about 10^{19} nc/cm^3 can be witnessed from the EFTEM images taken at the Si plasmon energy (Figure 4c) implying that they are predominantly amorphous. Interestingly, this density of the Si-ncs in the SiO_x/SiN_y MLs is an order of magnitude higher than the Si-ncs formed in the SiO_x/SiO_2 MLs fabricated under similar conditions. The brighter SiO_x sublayers are distinguished from the darker SiN_y sublayers by filtering the SiO_2 plasmon energy (Figure 4b). No evidence of Si-ncs within the SiN_x sublayers was obtained. The STA could favor the formation of Si-ncs only in SiO_x and not in SiN_y sublayers. This could be attributed to the different mechanism of Si-ncs formation in SiO_x and SiN_y in MLs as opposed to that in single layers [18] and/or the low Si-excess content in SiN_y.

Effect of Nd^{3+}-doping

Understanding the microstructure of MLs and considering the enhancement of absorption and emission properties in SiO_x/SiN_y MLs compared to the SiO_x/SiO_2 MLs, we investigate the effect of using SiN_y sublayer on

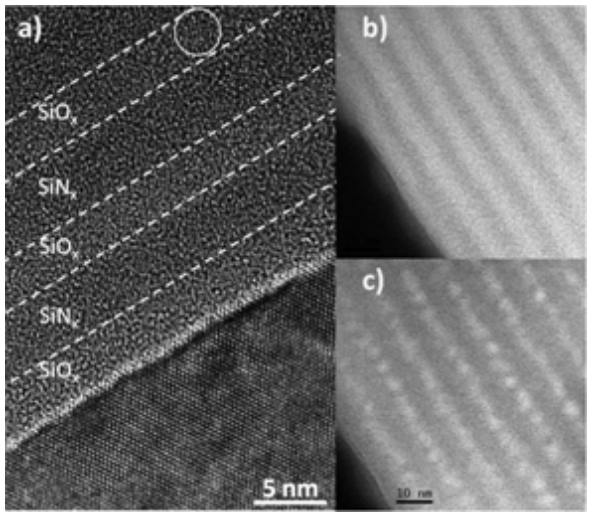

Figure 4 HRTEM (a) and EFTEM (b, c) images. SiO_x/SiN_y ML annealed at T_A = 1,000°C, t_A = 1 min by filtering the energy at SiO_2 plasmon (b) and Si plasmon (c) energies, respectively.

the PL emission from Nd^{3+} ions. For this purpose, the SiO_x-Nd/SiN_y-Nd and SiO_x-Nd/SiO_2-Nd MLs were fabricated, and their PL properties were compared. No PL emission was detected from the Nd^{3+}-doped SiN_y single layers at the different annealing treatments investigated here. Figure 5 shows the PL spectra of the Nd^{3+}-doped as-grown MLs under non-resonant excitation with peaks corresponding to the $^4F_{3/2} \rightarrow {}^4I_{9/2}$ and $^4F_{3/2} \rightarrow {}^4I_{11/2}$ transitions at 1.37 and 1.17 eV, respectively. The comparison between the PL properties of undoped (Figure 2c) and Nd^{3+}-doped MLs (Figure 5, inset) clearly shows the quenching of visible PL emission and the appearance of two Nd^{3+}-related PL peaks in the Nd-doped MLs. Moreover, the intensity of Nd^{3+} PL from the doped SiO_x/SiN_y MLs exceeds that of the SiO_x/SiO_2 MLs (Figure 5, inset). Thus, we deal with the efficient energy transfer towards Nd^{3+} ions not only in SiO_x but also in SiN_y sublayers. Since this emission is observed for as-grown MLs, when no Si-ncs were formed in these MLS, it is obvious that the emission from the Nd^{3+} ions in the SiN_x-Nd sublayers is due to an efficient energy transfer from SiN_y-localized defect states towards the Nd^{3+} ions [19,20]. PL observed from the doped MLs after STA was not intense, and it was quenched with increasing annealing time. The same behavior was observed for the 900°C annealing. This could be due to the decrease in the number of defect-related sensitizers in SiN_y and the formation of Nd_2O_3 clusters in the SiO_x sublayers [21]. On the other hand, annealing at T_A = 400°C to 700°C,

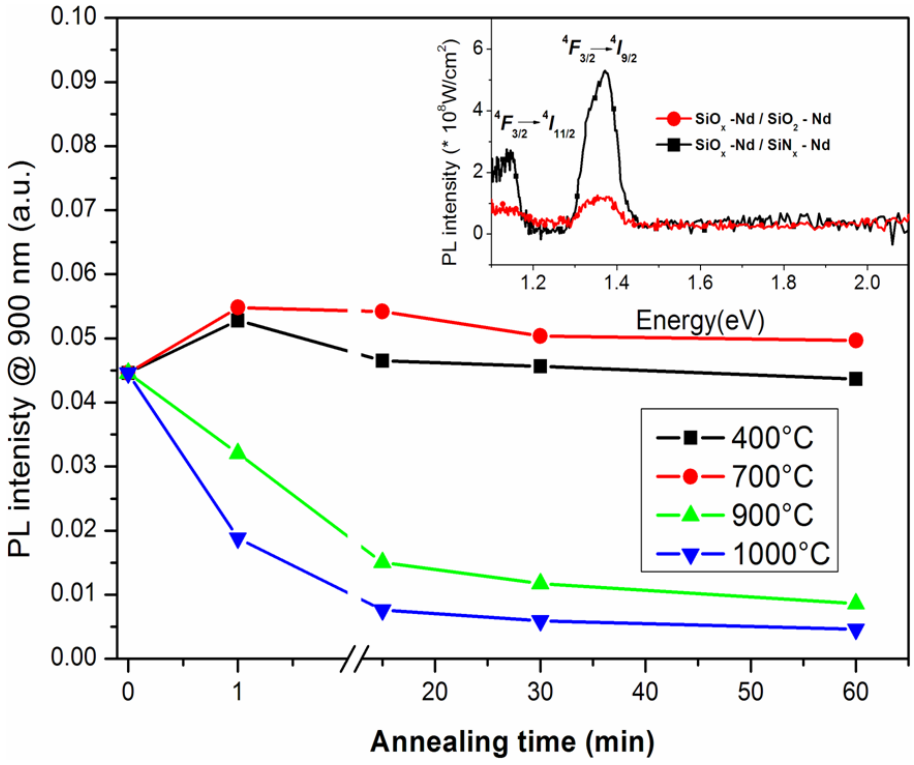

Figure 5 PL intensity with annealing time and temperature. Evolution of the Nd^{3+} PL intensity at 1.37 eV for doped SiO_x/SiN_y MLs with annealing temperature and time. (Inset) PL spectra of as-grown Nd^{3+}-doped SiO_x/SiN_y and SiO_x/SiO_2 MLs with equal number of periods. The thicknesses of the SiO_x, SiO_2, and SiN_y sublayers are 3.5, 5.0, and 5.0 nm, respectively.

discussed above for the undoped SiO_x/SiN_y MLs, enhance Nd^{3+} PL emission when applied to the doped counterparts (Figure 3). Thus, we attain intense PL at a low thermal budget with T_A (400°C to 700°C) and t_A (1 min). To optimize Nd^{3+} emission, the effect of the thickness of each sublayer in SiO_x/SiN_y MLs is under consideration now.

Conclusion

In conclusion, we show that SiO_x/SiN_y MLs fabricated by RF magnetron sputtering can be engineered as structures for photovoltaic and photonic applications. The as-grown and STA SiO_x/SiN_y MLs show enhanced optical and electrical properties than the SiO_x/SiO_2 counterparts. Besides achieving a high density of Si-ncs at a reduced thermal budget, we show that high emission and absorption efficiencies can be achieved even from amorphous Si-ncs. The Nd-doped MLs, as-grown and those annealed at lower thermal budgets, demonstrate efficient emission from rare-earth ions. We also show that our STA SiO_x/SiN_y MLs have about a hundred times higher conductivity compared to the SiO_x/SiO_2 MLs. These results show the advantages of SiO_x/SiN_y MLs as materials for photovoltaic and photonic applications and open up perspectives for a detailed study.

Abbreviations

MLs: multilayers; PL: photoluminescence; Si-nc: silicon nanoclusters; SiN_y: silicon-rich silicon nitride; SiO_x: silicon-rich silicon oxide; STA: short time annealing at 1,000°C for 1 min.

Acknowledgements

This study is supported by the DGA (Defense Procurement Agency) through the research program no. 2008.34.0031. The authors acknowledge J. Pierriére for the RBS measurements done with the SAFIR accelerator (INSP, UPMC) and X. Portier (CIMAP) for the TEM image.

Author details

[1]CIMAP UMR CNRS/CEA/ENSICAEN/UCBN, 6 Bd. Maréchal Juin, 14050 Caen Cedex 4, France [2]CEMES/CNRS, 29 rue J. Marvig, 31055 Toulouse, France

Authors' contributions

RPN fabricated the undoped multilayers under investigation and carried out the characterization studies. LK and OD fabricated the Nd-doped layers and studied the effect of Nd doping on the MLs. JC and CD made contributions to the optical studies. MC performed the EFTEM measurements. FG conceived of the study and participated in the coordination of the manuscript. All authors read and approved the final manuscript.

Competing interests

The authors declare that they have no competing interests.

Received: 11 October 2011 Accepted: 14 February 2012
Published: 14 February 2012

References

1. Canham LT: **Silicon quantum wire array fabrication by electrochemical and chemical dissolution of wafers.** *Appl Phys Lett* 1990, **57**:1046.
2. Pavesi L, Dal Negro L, Mazzoleni C, Franzo G, Priolo F: **Optical gain in silicon nanocrystals.** *Nature* 2000, **408**:440.
3. Irrera A, Franzo G, Iacona F, Canino A, Di Stefano G, Sanfilippo D, Piana A, Fallica PG, Priolo F: **Light emitting devices based on silicon nanostructures.** *Physica E* 2007, **38**:181.
4. Garrido B, Lopez M, Pérez Rodriguez A, Garcia C, Pellegrino P, Ferré R, Moreno JA, Morante JR, Bonafas C, Carrada M, Claverie A, De La Torre J, Souifi A: **Optical and electrical properties of silicon nanocrystals ion-beam synthesized in SiO_2.** *Nucl Inst Meth Phys B* 2004, **216**:231.
5. Conibeer G, Green MA, Corkish R, Cho Y, Cho EC, Jiang CW, Fangsuwannarak T, Pink E, Huang Y, Puzzer T, Trupke T, Richards B, Shalav A, Lin KL: **Silicon nanostructures for third generation photovoltaic solar cells.** *Thin Solid Films* 2006, **511**:654.
6. Zacharias M, Heitmann J, Scholz R, Kahler U, Schimdt M, Blasing J: **Size controlled highly luminescent silicon nanocrystals: a SiO/SiO_2 superlattice approach.** *Appl Phys Lett* 2002, **80**:661.
7. Gourbilleau F, Portier X, Ternon C, Voivenel V, Madelon R, Rizk R: **Si-rich/SiO_2 nanostructured multilayers by reactive magnetron sputtering.** *Appl Phys Lett* 2001, **78**:3058.
8. Gourbilleau F, Dufour C, Madelon R, Rizk R: **Effects of Si nanocluster size and carrier Er interaction distance on the efficiency of energy transfer.** *J Lumin* 2007, **126**:581.
9. Maestre D, Palais O, Barakel D, Pasquinelli M, Alfonso C, Gourbilleau F, De Laurentis M, Irace A: **Structural and optoelectronical characterization of Si-SiO_2/SiO_2 multilayers with applications in all Si tandem solar cells.** *J Appl Phys* 2010, **107**:064321.
10. Di D, Perez-Wurfl I, Conibeer G, Green MA: **Formation and photoluminescence of Si quantum dots in SiO_2/Si_3N_4 hybrid matrix for all-Si tandem solar cells.** *Solar Energy Materials & Solar Cells* 2010, **94**:2238.
11. So YH, Huang S, Conibeer G, Green MA: **Formation and photoluminescence of Si nanocrystals in controlled multilayer structure comprising of Si-rich nitride and ultrathin silicon nitride barrier layers.** *Thin Solid Films* 2011, **519**:5408.
12. Delachat F, Carrada M, Ferblantier G, Grob JJ, Slaoui A, Rinnert H: **The structural and optical properties of SiO_2/Si rich SiN_x multilayers containing Si-ncs.** *Nanotechnology* 2009, **20**:275608.
13. Conibeer G, Green MA, Perez- Wurfl I, Huang S, Hao X, Di D, Shi L, Shrestha S, Puthen-Veetil B, So Y, Zhang B, Wan Z: **Silicon quantum dot based solar cells: addressing the issues of doping, voltage and current transport.** *Prog Photovolt: Res Appl* Paper presented at the 25th EU PVSEC WCPEC-5, Spain; 2010.
14. Pratibha Nalini R, Dufour C, Cardin J, Gourbilleau F: **New Si-based multilayers for solar cell applications.** *Nanoscale Res Lett* 2011, **6**:156.
15. Ternon C, Gourbilleau F, Portier X, Voivenel P, Dufour C: **An original approach for the fabrication of Si/SiO_2 multilayers using reactive magnetron sputtering.** *Thin Solid Films* 2002, **419**:5.
16. Gourbilleau F, Ternon C, Maestre D, Palais O, Dufour C: **Silicon-rich SiO_2/SiO_2 multilayers: a promising material for the third generation of solar cell.** *J Appl Phys* 2009, **106**:013501.
17. Talbot E, Lardé M, Gourbilleau F, Dufour C, Pareige P: **Si nanoparticles in SiO2: an atomic scale observation for optimization of optical devices.** *EPL* 2009, **87**:26004.
18. Dal Negro L, Yi JH, Michel J, Kimerling MC, Chang TWF, Sukhovatkin V, Sargent EH: **Light emission efficiency and dynamics in silicon-rich silicon nitride films.** *Appl Phys Lett* 2006, **88**:233109.
19. Biggemann D, Tessler LR: **Near infra-red photoluminescence of Nd^{3+} in hydrogenated amorphous silicon sub-nitrides a-SiN_x:H <Nd>.** *Mat Sci Eng B* 2003, **105**:188.
20. Lin R, Yerci S, Kucheyev SO, Van Buuren T, Dal Negro L: **Energy transfer and stimulated emission dynamics at 1.1 μm in Nd-doped SiN_x.** *Optics Express* 2011, **19**:5379.
21. Debieu O, Bréard D, Podhorodecki A, Zatryb G, Misiewicz J, Labbé C, Cardin J, Gourbilleau F: **Effect of annealing and Nd concentration on the photoluminescence of Nd^{3+} ions coupled with silicon nanoparticles.** *J Appl Phys* 2010, **108**:113114.

doi:10.1186/1556-276X-7-124
Cite this article as: Nalini *et al.*: SiO_x/SiN_y multilayers for photovoltaic and photonic applications. *Nanoscale Research Letters* 2012 **7**:124.

Journal of Luminescence 132 (2012) 3118–3121

Contents lists available at SciVerse ScienceDirect

Journal of Luminescence

journal homepage: www.elsevier.com/locate/jlumin

Effect of the Si excess on the structure and the optical properties of Nd-doped Si-rich silicon oxide

C.-H. Liang, O. Debieu, Y.-T. An, L. Khomenkova, J. Cardin *, F. Gourbilleau

CIMAP, UMR CNRS/CEA/ENSICAEN/UCBN, Ensicaen, 6 Bd Maréchal Juin, 14050 Caen Cedex 4, France

ARTICLE INFO

Available online 3 February 2012

Keywords:
Si-rich-silicon oxide
Neodymium
Magnetron sputtering
Refractive index
Infrared absorption
Photoluminescence

ABSTRACT

Nd-doped Si-rich silicon oxide thin films were produced by radio frequency magnetron co-sputtering of three confocal cathodes: Si, SiO_2, and Nd_2O_3, in pure argon plasma at 500 °C. The microstructure and optical properties of the films were investigated versus silicon excess and post-deposition annealing treatment by means of ellipsometry and Fourier transform infrared spectrometry as well as by the photoluminescence method. A notable emission from Nd^{3+} ions was obtained for the as-deposited sample, while the films annealed at 900 °C showed the highest peak intensity. The maximum emission was observed for the films with 4.7 at% of Si excess.

1. Introduction

During last decade a great research effort has been focused on the development of the Si-based nanostructured materials for photonic application [1–5]. Among them, Si nanoclusters (Si-ncs) embedded in SiO_2 host are widely studied due to an achievement of room-temperature light emission from the blue to the infrared depending on the Si-ncs size [6,7].

Rare-earth (RE) ions possess narrow emission lines and receive more and more interest from the scientists in the world [8]. RE doped silica is a well-known medium for laser application, but its use requires high-power sources to achieve an efficient emission. Considerable attention was paid to silica co-doped with RE ions and Si-ncs since (i) such nanocomposite materials can be pumped using broadband sources due to the spectrally wide absorption of Si-ncs and (ii) Si-ncs are found to be efficient sensitizers of RE ions.

In this regard, the most studied materials are Er-doped Si-rich silicon oxide (SRSO) due to promising application as a source for optical communication. In previous works [9–15] a significant enhancement of photoluminescence (PL) intensity of the intra-4f shell transition of Er^{3+} due to the energy transfer from Si-ncs to RE ions has been demonstrated. The detailed study of the excitation mechanism of Er^{3+} ions showed that the excitation rate depends on the Si-ncs size and becomes higher for the smaller Si-ncs [16].

In the contrast of well-studied Er-SRSO system, other RE ions are not well-addressed. On the contrary to Er^{3+} ions, the doping of SRSO with Nd^{3+} ions is most promising due to overlapping of 4f-shell absorption transitions with the range of intrinsic Si-ncs PL. Moreover, Nd^{3+} ions offer very important light emission in the infrared spectral range at 1.06 and 1.32 μm in a four-level system configuration which avoid re-absorption of the emitted radiation. The benefits of Si-nc sensitizers towards Nd3+ ions was already demonstrated [17,18]. However, its improvement requires a special attention to some critical parameters as the coupling rate between Nd^{3+} ions and Si-ncs as well as the quality of the surrounded host medium aiming significant decrease of the non-radiative channels contribution. In the former case, the coupling rate can be monitored via the Nd^{3+} ions content and the Si excess (Si_{ex}) concentration. The latter has a direct influence on the number of Si-ncs embedded in SiO_2 as well as on the host quality.

In this study, both the structure and the optical properties of Nd-doped SRSO thin films were investigated versus Si_{ex} and the annealing treatment in order to obtain high efficient of Nd^{3+} light emission via energy transfer from Si-ncs toward Nd^{3+} ions.

2. Experimental techniques

The samples were deposited onto p-type silicon wafers by radio frequency magnetron co-sputtering of three confocal cathodes: Si, SiO_2, and Nd_2O_3, in a pure argon plasma. The substrate was rotated during the deposition to ensure a high homogeneity of the film. The deposition temperature and the total plasma pressure were kept at 500 °C and 3 mTorr, respectively. The power density applied on the SiO_2 and the Nd_2O_3 cathodes were fixed at 8.88 and 0.30 W/cm^2, respectively, whereas the power density applied on the Si cathode, P_{Si}, was varied from 0.74 to

* Corresponding author.
E-mail address: julien.cardin@ensicaen.fr (J. Cardin).

0022-2313/$ - see front matter © 2012 Elsevier B.V. All rights reserved.
doi:10.1016/j.jlumin.2012.01.046

2.37 W/cm^2. The deposition time was tuned to achieve the film thickness in the 250–300 nm range for avoiding the effect of the film stresses on the optical parameters [19]. An annealing treatment was performed in a conventional furnace at 900 and 1100 °C during 1 h in a nitrogen flow. Spectroscopic ellipsometry was used to determine the optical constants: thickness and refractive index n of the films. The data were collected by means of a Jobin–Yvon ellipsometer (UVISEL) where the incident light was scanned in the 1.5–4.5 eV range under an incident angle of 66.3°. The fitting of the experimental data was performed using DeltaPsi2 software [20].

The sample's infrared absorption properties were investigated by means of a Nicolet Nexus Fourier transform infrared (FTIR) spectrometer. The spectra were acquired under normal and Brewster angle incidence (65°). The PL spectra were recorded with a photomultiplier tube Hamamatsu (R5108) after dispersion of the PL signal with a Jobin–Yvon TRIAX 180 monochromator using an Ar^+ laser operated at 488 nm which is a non-resonant wavelength for Nd^{3+} excitation. For this study, we focused our PL experiment in the visible-near infrared range (600–1000 nm) to analyze the unique contribution of the RE ions in the de-excitation process [17].

3. Results and discussion

3.1. The Si_{ex} estimation

Fig. 1 displays the evolutions of the refractive index n and the TO_3 peak position of Si–O vibration bond as a function of P_{Si} for as-deposited samples. The n value increases from 1.48 to 1.70 with P_{Si}. According to the effective medium approximation (EMA) and using the Bruggeman model theory [21–23], the O/Si ratio (x) can be determined from the following equation:

$$x = \frac{-36n^4 + 691n^2 + 773}{22n^4 + 665n^2 - 472} \quad (1)$$

To note that the n value is given at 1.95 eV, and during the deducing of Eq. (1), $n_{a-Si}=4.498$ and $n_{SiO2}=1.457$ are used.

Furthermore, the peak position of the TO_3 mode in Fig. 1 decreases almost linearly with the increased P_{Si}. On the basis of the following equation [24]:

$$x = 0.02\upsilon - 19.3 \quad (2)$$

$\boldsymbol{\upsilon}$ is the TO_3 peak position of sample SiO_x, one can obtain the x value. For this pure SiO_2 layer was grown at the same conditions as SRSO-Nd layers and had the same thickness. This approach gives more accurate estimation than the comparison with the TO_3 peak position of SiO_2 ($\sim$1080 cm^{-1}) published elsewhere [25].

Thereafter, Si_{ex} (at%) was calculated from x using the following equation:

$$Si_{ex}(at\%) = \frac{2-x}{2+2x}100 \quad (3)$$

And the results of Si_{ex} estimated from both FTIR and EMA are shown in Fig. 2. It is worth to note that the Si_{ex} values obtained by the two methods are in good agreement within uncertainty.

3.2. Effect of annealing treatment on the microstructure

Fig. 3 shows a typical evolution of the FTIR spectra recorded at the Brewster incidence for films ($P_{Si}=1.33$ W/cm^2) as-deposited and annealed at 900 and 1100 °C. This film was chosen as a typical one to study for its highest emission from Nd^{3+} ions discussed later. The spectra are normalized with respect to the TO_3 phonon mode intensity. It is found that the TO_3 peak position shifts from 1050 to 1080 cm^{-1} with the increasing annealing temperature (T_A). This great shift is explained by the condensation and agglomeration of the Si_{ex} resulting in the formation of Si-ncs [26] at the expense of volumic silica. The evolution of FTIR spectra is a confirmation of the formation of SiO_2 and Si phases via phase separation in the SiO_x host [25]. Moreover, the intensity of the LO_3 peak increases and the intensity of the LO_4–TO_4 pair mode attenuates with the increase of T_A. The former is a signature of the improvement of the Si/SiO_x interface [27], whereas the latter indicates a reduction in disorder of the host.

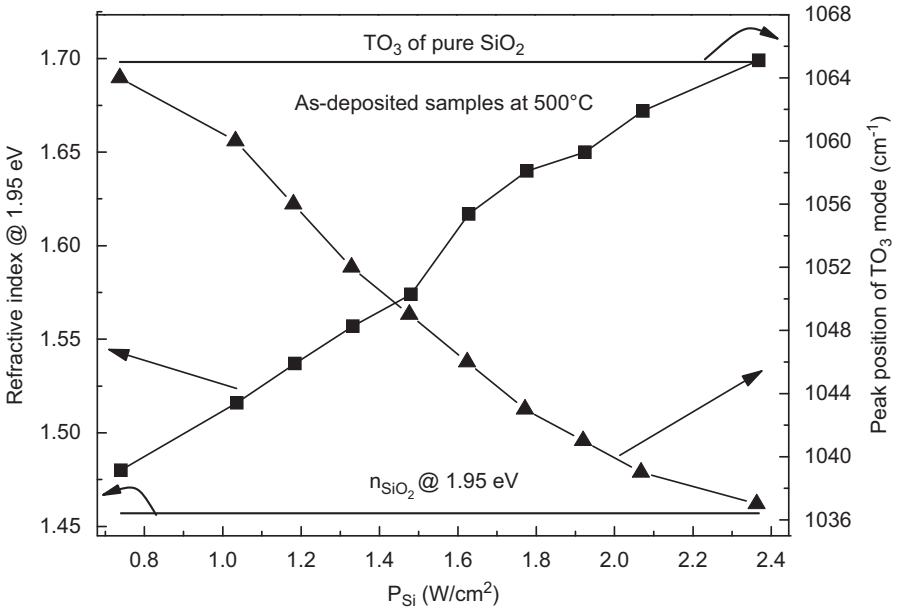

Fig. 1. Evolution of the refractive index n taken at 1.95 eV energy (left axis) and of the TO_3 Si-O peak position (right axis) versus P_{Si} for as-deposited samples. The lines on top and bottom are the TO_3 position (1065 cm^{-1}) and the refractive index n (1.457) for pure SiO_2 grown at the same conditions with the same thickness as SRSO-Nd layers, respectively.

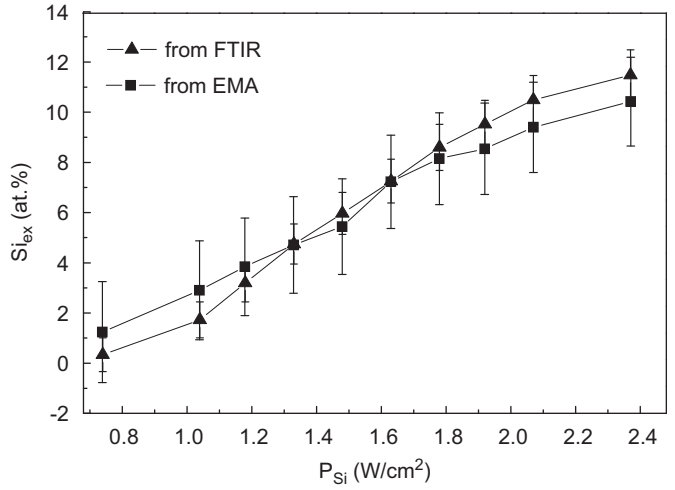

Fig. 2. Evolution of Si_{ex} (at%) as a function of P_{Si} for as-deposited samples.

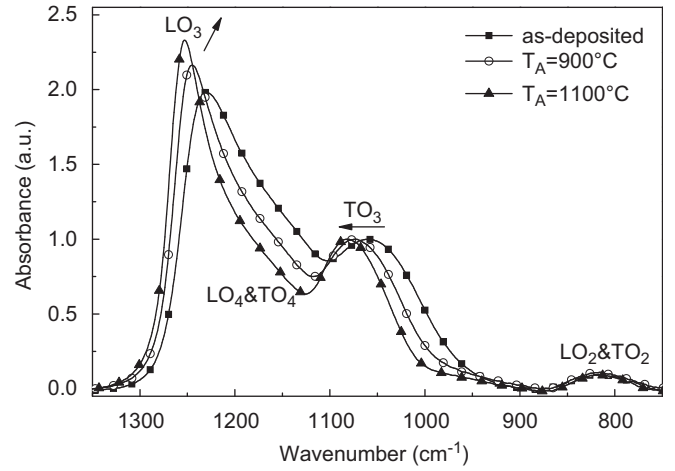

Fig. 3. Typical evolution of the FTIR spectra measured in Brewster incidence for as-deposited and annealed films.

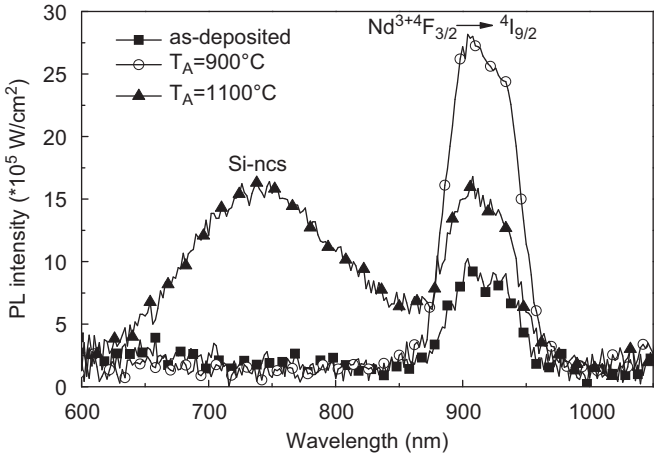

Fig. 4. Typical evolution of the PL spectra of sample with P_{Si}=1.33 W/cm^2 for as-deposited and annealed films.

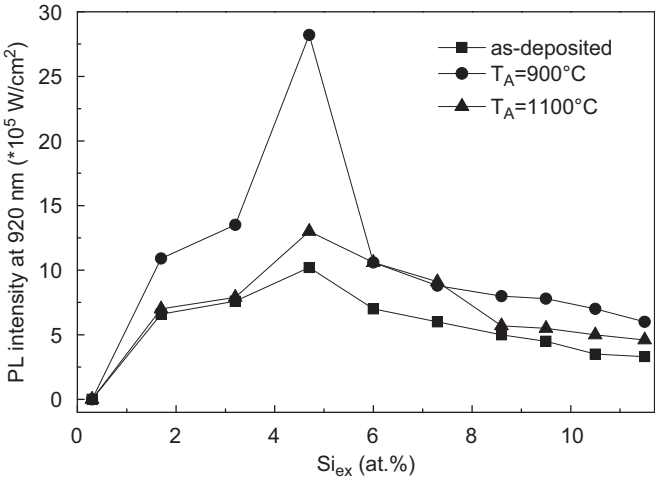

Fig. 5. Evolution of the Nd^{3+} PL intensity at 920 nm as a function of the P_{Si} for as-deposited and annealed films.

3.3. Photoluminescence properties

The film with P_{Si}=1.33 W/cm^2 was once more chosen to demonstrate the evolution of light emission properties versus an annealing treatment. The room temperature PL spectra of sample as-deposited and annealed at 900 and 1100 °C are shown in Fig. 4. It is seen that the sample annealed at 1100 °C emits a broad PL band in the visible domain that can be ascribed to radiative carrier recombination in Si-ncs.

As one can also see from Fig. 4, no emission was detected in this range for both as-deposited and 900 °C-annealed sample. However, this latter FTIR spectrum (Fig. 3) shows a phase separation process and thus the presence of Si-ncs. We conclude that the visible emission is quenched either due to energy transfer or to defect in the host [28]. This assumption is confirmed by the analysis of the Nd^{3+} PL bands (Fig. 4).

In the infrared domain, there are peaks centered at around 920 nm corresponding to the intra-4f shell transition of Nd^{3+} ions from the $^4F_{3/2}$ to the $^4I_{9/2}$ level. The presence of the PL of Nd^{3+} ions after non-resonant excitation at 488 nm confirms the sensitizing effect of Si-ncs toward Nd^{3+} ions. Moreover, the most efficient emission is observed for the sample annealed at 900 °C which corresponds to the best coupling between Si-ncs and Nd^{3+} ions. It is worth to note that a notable emission from Nd^{3+} ions was obtained for the as-deposited sample and this fact can be explained by either formation of Si-ncs during fabrication process or by energy transfer from host defects towards RE ions [19].

In the following part, the effect of Si_{ex} on Nd^{3+} PL properties will be studied as shown in Fig. 5. The Nd^{3+} PL intensity shows first an increase with Si_{ex} for all as-deposited and annealed samples, up to a maximum corresponding to sample with Si_{ex}=4.7% (P_{Si}=1.33 W/cm^2), and then decreases for higher Si_{ex}. This behavior may be explained by two reasons. On one hand, the first increase of Si_{ex} is expected to enhance the density of Si-ncs for an optimized Nd^{3+}:Si-ncs interaction. Further increase of Si_{ex} up to 11.5 at% might lead to increasing the average size of the former Si-ncs at the expense of their density and then of their coupling with Nd^{3+} ions. On the other hand, the Si incorporated into the sample may result in disorder in the host, which will favor the non-radiative channels. Besides in Fig. 5, the samples annealed at 900 °C show the highest PL intensity whatever the Si_{ex}. This observation may be ascribed to the formation of Nd_2O_3 clusters [17] for samples after annealing at high temperature (T_A=1100 °C). To note that there is no peak for sample with Si_{ex}=0.3 at%, possibly because the emission is too weak to be detected for the low Si_{ex}, the Nd^{3+}:Si-ncs distance is too high to allow the energy transfer process.

4. Conclusion

We have investigated the influences of Si_{ex} and T_A on the structure and optical properties of Nd-doped SRSO thin films fabricated by co-sputtering technique. It has been shown that the increase in Si_{ex} improves the Si-ncs coupling to Nd^{3+} ions, and that, it may raise the disorder in layer resulting in the increase of the number of non-radiative channels. In addition, it has been evidenced that the post annealing treatment at 900 and 1100 °C enhances the layer quality favoring the Nd^{3+} PL emission. However, high temperature annealing leads to a decrease of the Nd^{3+} emission due to the coalescence of Si-ncs and/or the formation of Nd_2O_3 cluster. Therefore, both moderate T_A and Si_{ex} are very important to be found with aim to optimize the emission from Nd^{3+} ions. In this study, the sample with Si_{ex}=4.7 at% (P_{Si}=1.33 W/cm^2) shows the highest Nd^{3+} peaks after annealing at 900 °C for 1 h.

Acknowledgments

The authors thank the French National Agency (ANR), which supported this work through the Nanoscience and Nanotechnology program (DAPHNES project ANR-08-NANO-005).

References

[1] A. Polman, B. Min, J. Kalkman, T.J. Kippenberg, K.J. Vahala, Appl. Phys. Lett. 84 (2004) 1037.
[2] A.J. Kenyon, Semicond. Sci. Technol. 20 (2005) R65.
[3] L. Dal Negro, J.H. Yi, J. Michel, L.C. Kimerling, S. Hamel, A. Williamson, G. Galli, IEEE J. Sel. Top. Quantum Electron. 12 (2006) 1628.
[4] M. Fujii, M. Yoshida, Y. Kanzawa, S. Hayashi, K. Yamamoto, Appl. Phys. Lett. 71 (1997) 1198.
[5] A.J. Kenyon, P.F. Trwoga, M. Federighi, C.W. Pitt, J. Phys.: Condens. Matter 6 (1994) L319.
[6] S. Charvet, R. Madelon, F. Gourbilleau, R. Rizk, J. Lumin. 80 (1998) 257.
[7] S. Cueff, C. Labbe´, B. Dierre, F. Fabbri, T. Sekiguchi, X. Portier, R. Rizk, J. Appl. Phys. 108 (2010) 113504.
[8] C.W. Thiel, T. Böttger, R.L. Cone, J. Lumin. 131 (2011) 353.
[9] K. Watanabe, M. Fujii, S. Hayashi, J. Appl. Phys. 90 (2001) 4761.
[10] G. Franzò, S. Bonitelli, D. Pacifici, F. Priolo, F. Iacona, C. Bongiorno, Appl. Phys. Lett. 82 (2003) 3871.
[11] F.D. Pacifici, G. Franzò, F. Priolo, F. Iacona, L.Dal Negro, Phys. Rev. B 67 (2003) 245301.
[12] F. Gourbilleau, M. Levalois, C. Dufour, J. Vicens, R. Rizk, J. Appl. Phys. 95 (2004) 3717.
[13] C. Garcia, P. Pellegrino, Y. Lebour, B. Garrido, F. Gourbilleau, R. Rizk, J. Lumin. 121 (2006) 204.
[14] P. Pellegrino, B. Garrido, J. Arbiol, C. García, Y. Lebour, J.R. Morante, Appl. Phys. Lett. 88 (2006) 121915.
[15] K. Hijazi, R. Rizk, J. Cardin, L. Khomenkova, F. Gourbilleau, J. Appl. Phys. 106 (2009) 024311.
[16] F. Gourbilleau, R. Madelon, C. Dufour, R. Rizk, Opt. Mater. 27 (2005) 868.
[17] O. Debieu, D. Bréard, A. Podhorodecki, G. Zatryb, J. Misiewicz, C. Labbé, J. Cardin, F. Gourbilleau, J. Appl. Phys. 108 (2010) 113114.
[18] D. Bréard, F. Gourbilleau, C. Dufour, R. Rizk, J.-L. Doualan, P. Camy, Mater. Sci. Eng. B. 146 (2008) 179.
[19] S. Cueff, C. Labbé, O. Jambois, B. Garrido, X. Portier, R. Rizk, Nanoscale Res. Lett. 6 (2011) 395.
[20] 〈http://www.horiba.com/scientific/products/ellipsometers/software/〉.
[21] D.E. Aspnes, Thin Solid Films 89 (1982) 249.
[22] E. Dehan, P. Temple-Boyer, R. Henda, J.J. Pedroviejo, E. Scheid, Thin Solid Films 266 (1995) 14.
[23] L. Khomenkova, X. Portier, J. Cardin, F. Gourbilleau, Nanotechnology 21 (2010) 285707.
[24] B.J. Hinds, F. Wang, D.M. Wolfe, C.L. Hinkle, G. Lucovsky, J. Non-Cryst. Solids 227–230 (1998) 507.
[25] S. Charvet, R. Madelon, F. Gourbilleau, R. Rizk, J. Appl. Phys. 85 (1999) 4032.
[26] H. Ono, T. Ikarashi, K. Ando, T. Kitano, J. Appl. Phys. 84 (1998) 6064.
[27] F. Gourbilleau, C. Dufour, M. Levalois, J. Vicens, R. Rizk, C. Sada, F. Enrichi, G. Battaglin, J. Appl. Phys. 94 (2003) 3869.
[28] L. Skuja, J. Non-Cryst. Solids 239 (1998) 16.

AIP Journal of Applied Physics

Evidence of two sensitization processes of Nd3+ ions in Nd-doped SiOx films

C.-H. Liang, J. Cardin, C. Labbé, and F. Gourbilleau

Citation: Journal of Applied Physics **114**, 033103 (2013); doi: 10.1063/1.4813610
View online: http://dx.doi.org/10.1063/1.4813610
View Table of Contents: http://scitation.aip.org/content/aip/journal/jap/114/3?ver=pdfcov
Published by the AIP Publishing

Evidence of two sensitization processes of Nd^{3+} ions in Nd-doped SiO_x films

C.-H. Liang,[a] J. Cardin, C. Labbé, and F. Gourbilleau[b]
CIMAP, UMR CNRS/CEA/ENSICAEN/UCBN, Ensicaen, 6 Bd Mal Juin, 14050 Caen Cedex 4, France

(Received 14 March 2013; accepted 25 June 2013; published online 16 July 2013)

This paper aims to study the excitation mechanism of Nd^{3+} ions in Nd-SiO_x ($x < 2$) films. The films were deposited by magnetron co-sputtering followed by a rapid thermal annealing at temperature T_A ranging from 600 to 1200 °C. Two different photoluminescence (PL) behaviors have been evidenced in SiO_x layers depending on the annealing temperature. For low T_A ($T_A < 1000$ °C), the recorded visible PL originates from defects energy levels while for high T_A ($T_A > 1000$ °C), the visible emission emanates from recombination of excitons in Si nanoclusters. When doped with Nd^{3+} ions, the visible PL behaviors of Nd-SiO_x films follow the same trends. Nd^{3+} PL was investigated and its decay rate was analyzed in detail. Depending on the annealing conditions, two types of sensitizers have been evidenced. Finally, maximum Nd^{3+} PL emission has been achieved at around 750 °C when the number of Nd^{3+} ions excited by the two types of sensitizers reaches a maximum. [http://dx.doi.org/10.1063/1.4813610]

I. INTRODUCTION

As a leading semiconductor material in the microelectronic industry, silicon has received significant attention on its optical functionality in these last years aiming at integrating photonics with semiconductor microelectronics.[1,2] However, suffering from the indirect nature of its band gap, bulk Si shows poor emission efficiency. Fortunately, two important results have been achieved by decreasing the Si grain size to the nanoscale range. On one hand, the nature of Si band gap changes from indirect to quasi-direct with the decrease in grain size.[3] This quasi-direct band gap allows room temperature photoluminescence (PL) of Si nanoclusters (Si-ncs) without any phonon assistance. This emission is ranging in the visible spectra from 700 to 900 nm depending on the Si-ncs size.[3–6] On the other hand, Si-ncs can play the role of sensitizer towards rare earth (RE) ions such as Er^{3+} ion[7–12] or Nd^{3+} ion.[13] Hence, the effective excitation cross section of RE ions is enhanced by several orders of magnitude and broadened spectrally in the visible range.[14,15] This result provides the possibility to manufacture less-cost and miniaturized Si-based optoelectronic devices.

To better understand the limiting factors for achievement of such optoelectronic devices, huge effort has been focused on the mechanism of energy transfer from Si-ncs towards Er^{3+} ions. It appears that the Si-ncs:Er^{3+} interaction distance should be less than 2 nm[16] for an effective coupling whose efficiency decreases exponentially with the increasing of distance.[10] Fujii *et al.*[17] observe the coexistence of two processes for Si-ncs:Er^{3+} energy transfer depending on the sizes of the sensitizers. A fast process is attributed due to the large Si-ncs sensitizer, while a slow one is found to depend on the recombination rate of excitons in small Si-ncs. In contrast, Savchyn *et al.*[12] demonstrate the existence of two excitation processes for Er^{3+} $^4I_{13/2}$ level involving multi-levels sensitization: fast direct excitation by Si-excess-related luminescence centers and slow excitation related to the fast excitation of Er^{3+} ions up to the higher energy levels such as $^4F_{9/2}$ and $^4I_{9/2}$ with subsequent slow relaxation to the $^4I_{13/2}$ level. These works agree the origin of Er^{3+} excitation from recombination of generated excitons within Si-ncs and subsequent energy transfer to the nearby Er^{3+} ions. Even though a great number of papers have been published on the Si-based matrices co-doped with Er^{3+} and Si-ncs, evidence of the achievement of net gain from such a system has been presented in only one report.[18] This is due to the nature of the three-level electronic 4f structure for the Er^{3+} ions leading to a threshold power necessary to get population inversion and to the possibility of reabsorption of photon emitted by the neighboring Er^{3+} ions. In contrast, the Nd^{3+} ions emitting in four-level configuration (1.06 μm) do not have a threshold pump power for inversing population and there is no reabsorption of the emitted light at 1.06 μm. Moreover, the up-conversion is negligible with Nd^{3+} ions[19] emitting at 1.06 μm compared to Er^{3+} ions[20] emitting at 1.53 μm. Consequently, net gain should be achievable with Nd^{3+} ions in easier way than with Er^{3+} ions.

However, the study on excitation mechanism of Nd^{3+} ions in Nd-SiO_x films is still rather rare by comparison to its Er^{3+} ions counterpart. After the discovery of energy transfer from Si-ncs to Nd^{3+} ions,[21] several groups[22–24] investigated the energy transfer with the goal of improving the Nd^{3+} emission properties. Our previous work[24] evidences that high Nd^{3+} content incorporated into the layers would form Nd_2O_3 clusters leading to the quenching of the Nd^{3+} PL. Moreover, Watanabe *et al.*[25] point out that the Si-ncs size plays an important role in the Si-ncs:Nd coupling. The authors show that the Si-ncs:Nd energy transfer is more effective with smaller Si-ncs. This is explained by a good match of energy band gap in small Si-ncs with Nd^{3+} excited energy levels (higher than $^3F_{3/2}$). Therefore, the discussion on excitation mechanism of Nd^{3+} ions should include an investigation of Si-ncs PL properties. Two main models on the origin of Si-ncs emission have been proposed on the basis of both experimental and theoretical studies. The first

[a]Electronic mail: chuan-hui.liang@ensicaen.fr
[b]Electronic mail: fabrice.gourbilleau@ensicaen.fr

model depicts the quantum confinement effect,[26] which in general explains the evolution of Si-ncs PL versus its size depending on the Si excess and/or annealing treatment.[27] The second model considers that the Si-ncs PL is correlated to the presence of defects at the interface between Si-ncs and SiO_2 matrix in SiO_x layers,[28,29] supporting the PL peak position size-independent.[30]

In this paper, we investigate the optical properties of SiO_x and Nd-SiO_x films annealed using rapid thermal annealing (RTA) process. The influence of Si-ncs PL origins on the excitation mechanism of Nd^{3+} ions is investigated depending on the annealing conditions.

II. EXPERIMENT

Undoped- and Nd-doped-SiO_x ($x < 2$) films of about 350 nm thick were deposited by magnetron co-sputtering of two (SiO_x) or three (Nd-SiO_x) confocal cathodes under a plasma of pure argon. The p-type monocrystalline Si or fused silica substrates were used and maintained at 500 °C during the growth. The plasma power density for Nd_2O_3, Si, and SiO_2 targets were fixed at 0.30, 1.48, and 8.88 W/cm^2, respectively. After deposition, the films were submitted to RTA process under N_2 for variable durations, t_A, and different temperatures, T_A, ranging from 1 min to 1 h and 600 to 1200 °C, respectively. The microstructural characteristics were obtained by RAMAN and Fourier transform infrared (FTIR) spectroscopies. The optical properties were achieved by means of PL experiments. These latter were carried out using the 488-nm-line of a CW Ar^+ laser (Innova 90C Coherent), which is a non-resonant wavelength for Nd^{3+} ions.[31] PL decay times have been recorded at the maximum PL intensity for Si-ncs peak and 920 nm for Nd^{3+} ions after short excitation pulses (5 ns) at full width at half maximum of a tunable pulsed laser (EKSPLA NT 340 OPO pumped by a YAG:Nd laser) set at 488 nm with a repetition rate of 10 Hz. The focusing beam was 500 μm with an average energy of 15 mJ. The PL decay was recorded with an appropriated electronic and detector (PM R5509-73 Hamamatsu) on a digital oscilloscope (Tiektronix tds 3012).

III. RESULTS AND DISCUSSION

The two kinds of films, SiO_x and Nd-SiO_x, object of the present study, have the same value of O/Si ratio ($x = 1.74$). The x value was calculated as shown in our previous paper[32] using the equation

$$x = 0.02v - 19.3, \quad (1)$$

where v is the transverse optical (TO_3) peak position in FTIR spectrum collected at normal incidence. As a consequence, the Si excess (Si_{ex}) is found to be 4.7 at. % using the following relation:

$$Si_{ex}(at\%) = [(2-x)/(2+2x)]100. \quad (2)$$

This silicon excess value has been confirmed by Rutherford backscattering experiments, which have given a Nd content of about 5×10^{19} Nd cm^{-3}.

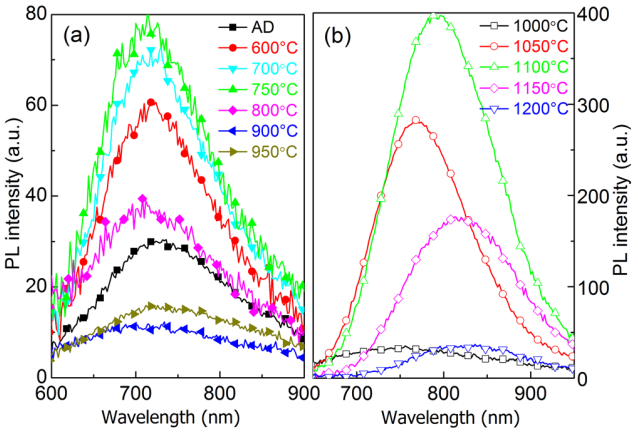

FIG. 1. The PL spectra of SiO_x films annealed at the indicative temperature with 1 min duration. The left (a) corresponds to T_A lower than 1000 °C while the right (b) to high T_A higher than 1000 °C. AD is the abbreviation of as-deposited.

A. Photoluminescence properties of SiO_x films

The PL properties of SiO_x films were investigated as a function of T_A. The spectra are separately shown in Figure 1(a) for low T_A less than 1000 °C and Figure 1(b) for high T_A more than 1000 °C. As noticed on these two graphs, the emission bands peak at different wavelengths depending on the T_A range. Thus, the emission peaks obtained for low T_A will be defined as E_L; while for high T_A, the recorded emission peaks will be called E_H. To easily catch the evolution trend, both integrated peak intensity and maximum peak position have been determined and are presented in Figure 2. The E_L peak intensity first increases to reach a maximum for $T_A = 750$ °C before decreasing for higher annealing temperatures. This could be explained by a passivation of some non-radiative centers with increasing T_A up to 750 °C and for T_A above 750 °C by a decrease of the number of emitting centers at the origin of the E_L peak emission. Its position does not change with T_A peaking at around 720 nm. The exact origin of this E_L peak is still unclear. Wang *et al.*[30] and Wora Adeola *et al.*[33] have separately observed the very similar E_L peak in their samples. The former attribute it to surface states while the latter to band tails states. Therefore, at this level of discussion, we ascribe this E_L peak to defects related radiative states which origin will be specified later in this paper. Comparatively for T_A higher than 1000 °C, the E_H peak

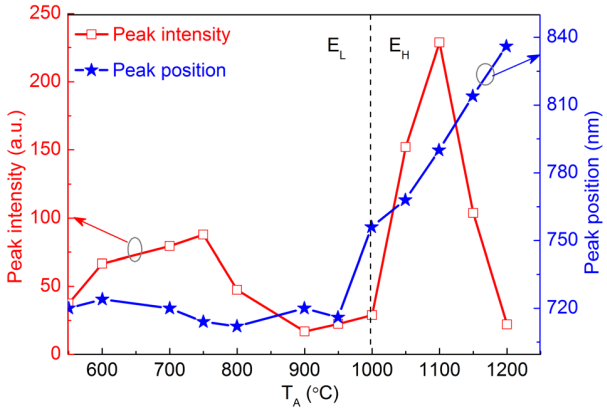

FIG. 2. Peak intensity (left scale) and position (right scale) of SiO_x films versus T_A.

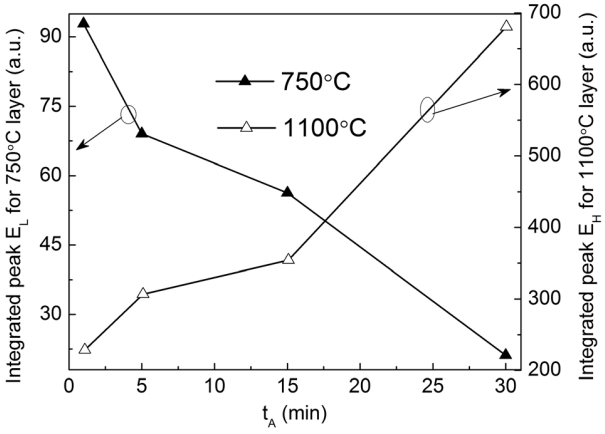

FIG. 3. E_L and E_H peak intensity versus t_A for SiO_x films annealed at 750 °C (left scale) and 1100 °C (right scale), respectively.

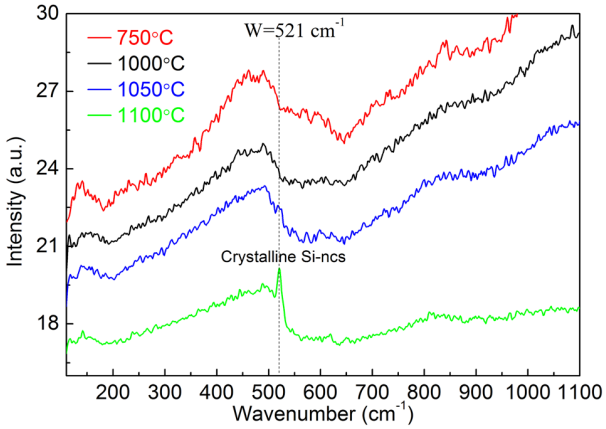

FIG. 4. RAMAN spectra of the SiO_x films deposited on quartz substrate and annealed at indicated T_A for 1 min.

intensity rises up abruptly till a maximum at $T_A = 1100$ °C and thereafter drops down to a very low value for the highest annealing temperature ($T_A = 1200$ °C). However, the maximum E_H intensity is more than three times higher than the one achieved for E_L peak after annealing at $T_A = 750$ °C. The band positions red-shift from 756 to 836 nm with increasing T_A, allowing of attributing the E_H peak to the quantum-confined excitonic states in Si-ncs.[26] This evolution of E_H intensity versus T_A is related both to the passivation of non-radiative channels and the Si-ncs density increase up to 1100 °C. If the former continues for higher annealing temperature, the latter will decrease due to a Si-ncs size growth over the quantum confinement limit. Such an oversize growth explains the quench of the PL observed for temperature as high as 1200 °C. Note that both E_L and E_H peaks are related to the Si excess incorporated in the SiO_2 matrix as no emission was observed from pure SiO_2 sputtered films annealed at any T_A.

To further analyze the different PL behaviors between low- and high-T_A layers, two typical annealing temperatures (750 and 1100 °C) corresponding to the maximum PL intensities achieved were set to study the effect of annealing time t_A. The evolutions of peak intensity as a function of t_A are presented in Figure 3. It can be noticed that the E_L peak intensity gradually decreases with time for the 750 °C-annealed samples while E_H peak significantly increases for the 1100 °C-ones, for the same range of time. This PL evolution is another evidence of different excitation-de-excitation mechanisms: radiative defects controlled at 750 °C while quantum confinement controlled at 1100 °C. When the annealing duration is increased, the radiative defects are quenched at 750 °C probably due to the rearrangement of Si and/or O atoms, while the 1100 °C-extended annealing could mainly passivate the non-radiative defects such as stressed bond angles, distorted bond length in host. In high temperature range, Garrido Fernandez *et al.*[34] have obtained the same PL behavior versus t_A. They observe that during annealing process the nucleation and growth of Si-ncs are almost completed in a few minutes and the average Si-ncs diameter remains constant for longer annealing times. Thus, increasing annealing time up to 30 min favors achievement of high Si-ncs density but remains sufficiently short to avoid the growth of large Si-ncs, which are detrimental for the quantum confinement process.[35] Moreover, such extra annealing time favors the recovering of the non-radiative channels.

B. Microstructural characterization

To understand the above PL properties, the evolution of film microstructure versus T_A has been analyzed by means of RAMAN spectroscopy (Figure 4). Each curve has a broad band peaking at $\sim 480\,cm^{-1}$ attributed to amorphous Si agglomerates. Such a result is in agreement with previous work showing that the formation of amorphous Si agglomerates in similar thin films starts to occur at about 600 °C.[36] By increasing T_A up to 1100 °C, a sharp peak at around $521\,cm^{-1}$ assigned to crystalline Si-ncs appears while, in the same time, the $480\,cm^{-1}$-band intensity decreases. This convincingly certifies that the $T_A = 1100$ °C annealing promotes the formation of Si nanocrystals. The results of RAMAN experiments on the Nd-doped SiO_x thin films (not shown here) follow the same trends as results obtained on undoped films. This is supported by the fact that the low Nd content incorporated may not affect the formation of either amorphous or crystalline Si-ncs.

Figure 5 shows the evolution of FTIR spectra for SiO_x films annealed at different temperatures. There are two main

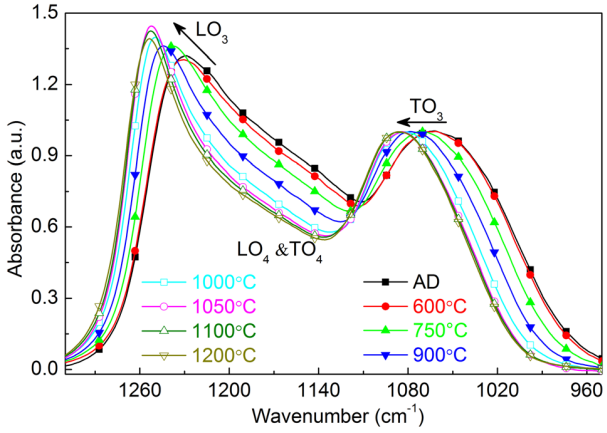

FIG. 5. FTIR spectra recorded at Brewster angle of 65° for SiO_x films deposited on a Si wafer and annealed at indicated T_A during 1 min. The spectra were normalized with respect to the TO_3 band intensity.

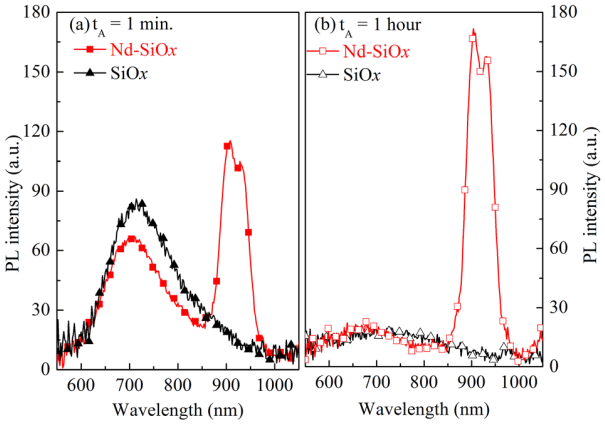

FIG. 6. PL spectra of Nd-SiO_x and SiO_x films annealed at 750 °C during (a) 1 min and (b) 1 h.

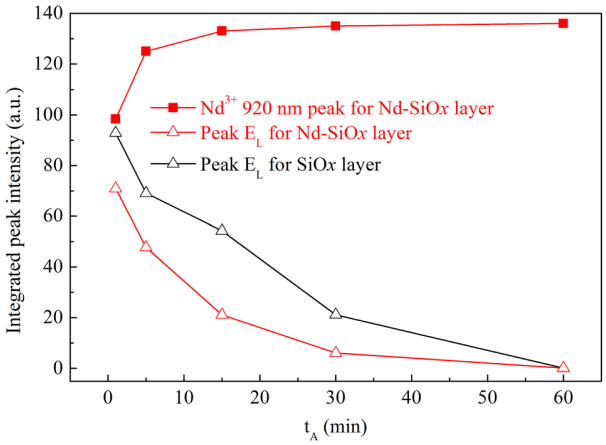

FIG. 7. Integrated peak intensities of Nd-SiO_x and SiO_x films annealed at 750 °C versus t_A.

bands attributed to longitudinal optical (LO_3) and TO_3 phonons of Si-O bonds. The relative intensity of the former peaking in the 1230–1255 cm^{-1} range increases with T_A up to 1050 °C, and then slightly decreases for higher T_A. According to the work of Olsen and Shimura,[37] LO_3 band intensity corresponds to the number of Si-O-Si bonds at 180° present at the Si/SiO_2 interface. Consequently, this is the signature of the increasing formation of Si-ncs in our film upon annealing temperature up to 1050 °C. The continuously increase of T_A will then favor the growth of Si-ncs size leading to the decrease of the Si-ncs density and thus the number of Si-O-Si bonds at the Si/SiO_2 interface. As a consequence, a slight decrease of the LO_3 mode intensity is noticed. Concerning the TO_3 mode, it blue-shifts from 1052 to about 1081 cm^{-1} with increasing T_A. This progressive shift towards the stoichiometric position of amorphous SiO_2 (1081 cm^{-1}) is indicative of the phase separation between Si and SiO_2 occurring in the film. This is confirmed by the decrease of the disorder in the matrix as evidenced by the evolution of the intensity of the LO_4 and TO_4 pair modes with T_A.

C. Comparison of Nd-SiO_x PL properties with SiO_x films

To study the excitation mechanism of Nd^{3+} ions in Nd-SiO_x system, the PL experiments are performed on Nd-doped SiO_x layers annealed at 750 and 1100 °C which correspond to the two temperatures allowing achievement of the maximum intensity for E_L and E_H peaks, respectively. Figure 6(a) shows the PL spectra of Nd-SiO_x and SiO_x films annealed at 750 °C during 1 min. The significant Nd^{3+} PL peak from the de-excitation from the $^4F_{3/2}$ to $^4I_{9/2}$ level at around 920 nm is observed for Nd-doped layer excited with the non-resonant 488 nm-Ar laser wavelength. This implies the existence of Nd^{3+} sensitizers present in the SiO_x matrix. The occurrence of an energy transfer from sensitizers to Nd^{3+} ions is evidenced by the concomitant lowering E_L peak intensity compared to that from undoped SiO_x layer.

To confirm this behavior, investigation of the visible and Nd^{3+} PL intensities as a function of annealing duration has been carried out (Figure 7). One can noticed that the visible E_L peak intensity decreases versus t_A for both SiO_x and Nd-SiO_x films. As explained above, this evolution can be ascribed to the recovering of the radiative defects. For at least $t_A \leq 30$ min, the E_L peak intensity from Nd-doped SiO_x layer annealed at 750 °C shows a lower value than that of undoped one. Such a behavior is an evidence of an efficient energy transfer from these radiative defects to Nd^{3+} ions states, playing the role as Nd^{3+} sensitizers as mentioned above. Concerning the Nd^{3+} emission evolution at 920 nm, it increases until 15 min of annealing and saturates afterward. Such saturation may be attributed to (i) the passivation of some non-radiative defect and/or (ii) the existence of another type of sensitizers. Moreover, we have observed in the Figure 3 a decrease of the low T_A type Nd^{3+} sensitizer (E_L peak) with longer annealing, which should contribute to a decrease of the Nd^{3+} PL intensity. Consequently, those trends of visible and Nd^{3+} PL intensities are a signature of the existence of another type of sensitizers that also excite efficiently the Nd^{3+} ions (Figure 6(b)). As demonstrated in our previous work,[38] such sensitizers grown at low T_A contain a few Si atoms (less than 15 atoms) and will be here named atomic scale sensitizers (ASSs). They differ from the luminescence centers proposed by Savchyn *et al.*[39] Since using also a RTA of 100 s, they observed always a PL peak position shift, which is in disagreement with our results (seen Figure 1(a)).

When annealed at higher temperature (1100 °C), the intensity of E_H peak falls down by about 8 times after Nd incorporation (Figure 8). It is thus supposed that most of emitters transfer energy to their nearby Nd. One can notice that the position of E_H peak shifts from about 790 to 730 nm after Nd incorporation. This shift is probably explained by the two Nd^{3+} absorption bands peaking at about 750 and 808 nm[31] and is a confirmation of the energy transfer process involved. Nevertheless, the Nd^{3+} PL intensity achieved at such T_A appears very low. This demonstrates the E_H peak emitters formed at this high temperature act as sensitizer of Nd^{3+} ions, but unfortunately, this efficient energy transfer process suffers from Nd_2O_3 clusters formation and/or a too large sensitizer-Nd^{3+} distance. This can explain that the drop of Si-ncs PL does not lead to a high PL emission of the Nd^{3+}

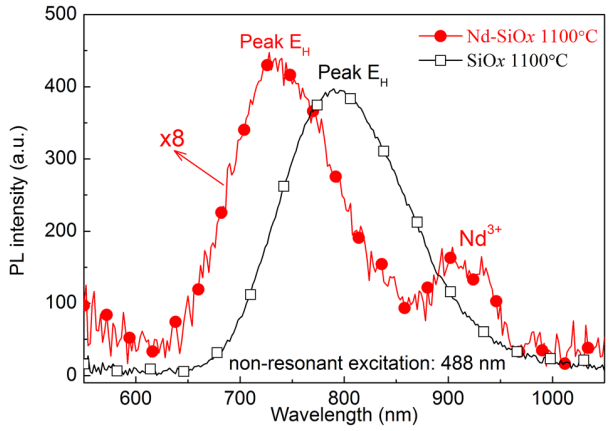

FIG. 8. PL spectra of Nd-SiO_x and SiO_x films annealed for 1 min at 1100 °C.

ions. In addition, the effect of annealing duration was investigated at 1100 °C. The E_H peak intensity of Nd-SiO_x film gradually increases with increasing t_A (data not shown here), presenting thus a similar trend to that achieved for undoped layer (Figure 3).

This paragraph will address the effect of T_A on Nd^{3+} PL properties (Figure 9). Even though the as-deposited layer clearly shows PL, the intensity increases with T_A and is enhanced by a factor 2.5 upon annealing at 750 °C before decreasing for higher T_A. The optimized temperature at 750 °C corresponding to maximum Nd^{3+} PL may be explained by the fact that both matrix ordered degree and coupled Nd^{3+} number evolve in opposite trend with annealing temperature. For the former, the FTIR spectra reported in Figure 5 have evidenced the attenuation of LO_4 and TO_4 pair mode with increasing T_A. Such an evolution implies that the film matrix gradually becomes ordered, which would favor the Nd^{3+} emission by decreasing the non-radiative paths. The concomitant increase of the LO_3 intensity with T_A up to 1050 °C suggests an increase of Si-ncs density also favoring an enhancement of Nd^{3+} emission. For the latter, the visible E_L peak (Figure 1(a)) is quenched with T_A higher than 750 °C attesting the decreasing of radiative defect. When $T_A \geq 750$ °C, the Nd^{3+} ions were consumed by the formation of Nd_2O_3 clusters decreasing the coupled Nd^{3+} ions as evidenced by lifetime measurements detailed below. Therefore, a maximum Nd^{3+} PL is reached at the moderated temperature (T_A=750 °C). Moreover, it is worth to note that the Nd^{3+} PL at T_A = 900 °C is still remarkable and only decreases by less than 1.5 times in contrast to that at T_A = 750 °C. However, the defects emission (E_L peak) almost completely quenches at about 900 °C as shown in Figure 1(a). This again evidences the existence of atomic scale sensitizers apart from the radiative defects.

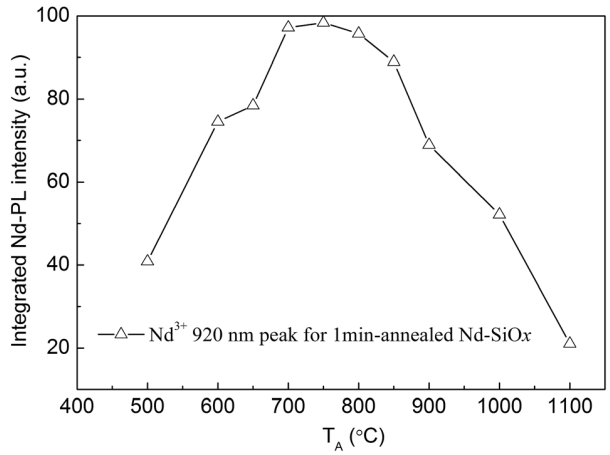

FIG. 9. Evolution of Nd^{3+} PL intensity as a function of T_A for Nd-SiO_x films annealed during 1 min.

D. Analysis of both visible PL and Nd^{3+} infrared PL decay curves

Lifetimes τ measured on E_L and E_H peaks do not show a single exponential trend, therefore as a first approach the integrated Eq. (3)[40] was used in order to fit the decay curve

$$\tau = \int \frac{I}{I_0} dt, \tag{3}$$

where I is a time dependent peak intensity while I_0 is the intensity at t = 0 s. For E_L peak, the lifetimes of both doped and non-doped films are low and invariable at about 2 μs as shown in Figure 10. This confirms that the visible E_L peak origins from the defects.[41] For E_H peak from non-doped SiO_x film, the lifetime increases dramatically and holds a value of 29 μs for 1100 °C-SiO_x film. This value is indicative that E_H peak originates from the exciton recombination confined by quantum effect inside Si-ncs.[42] In contrast for Nd-SiO_x film annealed at 1100 °C, this lifetime value decreases to 3.6 μs. This decrease is due to the energy transfer to Nd^{3+} ions as described by the effective lifetime deduced from rate equation[43] in the sensitizer:Nd system

$$\tau_{Nd-SiO_x} = \frac{\tau_{SiO_x}}{1 + KN^0_{Nd}\tau_{SiO_x}}, \tag{4}$$

where τ_{Nd-SiO_x} is the E_L or E_H peak lifetime for Nd-SiO_x film while τ_{SiO_x} corresponds to the non-doped SiO_x film lifetime; K is the coupling constant between sensitizers and

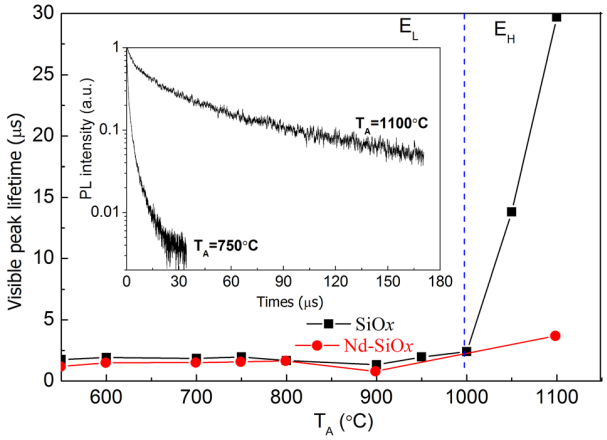

FIG. 10. Evolution of PL lifetimes measured on peak E_L and E_H versus T_A for 1 min-annealed SiO_x and Nd-SiO_x films detected at the maximum point of each peak. The inset shows the PL decay curves for SiO_x films annealed at 750 and 1100 °C.

Nd^{3+} ions; and N^0_{Nd} is the Nd^{3+} density in the fundamental state. The term $KN^0_{Nd}\tau_{SiO_x}$ describes phenomenologically[44] the coupling between sensitizers and Nd^{3+} ions. Therefore, the decrease of τ_{Nd-SiO_x} with respect to τ_{SiO_x} can be ascribe to the increasing of the coupling term $KN^0_{Nd}\tau_{SiO_x}$ and thus evidence the energy transfer to Nd^{3+} ions. In Nd-SiO_x films annealed at $T_A < 1000\,°C$, the lifetime τ_{Nd-SiO_x} is slightly lower than τ_{SiO_x} taking into account our experimental uncertainties. For layers annealed at $T_A > 1000\,°C$, the lifetime τ_{Nd-SiO_x} is 10 to 20 times lower than SiO_x lifetime (Figure 10). Consequently, for low T_A, Nd-SiO_x layers have a weaker coupling term $KN^0_{Nd}\tau_{SiO_x}$ compared to higher one. The efficiency η of energy transfer can be estimated by the following equation:[45]

$$\eta = 1 - \frac{\tau_{Nd-SiOx}}{\tau_{SiOx}}. \quad (5)$$

One can obtain that in Nd-SiO_x films annealed at $T_A < 1000\,°C$, the efficiency is lower than 10%, while η reaches about 90% for 1100 °C-annealed layer. Notwithstanding, the weaker sensitizer:Nd coupling regime and lower efficiency for the low T_A, the highest PL intensity is achieved. Such a feature can be explained by the larger number of sensitized Nd^{3+} ions due to the larger density of both radiative defects and atomic scale sensitizers (low T_A) than that of Si-ncs sensitizers (high T_A).

The decay rate of Nd^{3+} infrared PL at 920 nm has a non-exponential nature as seen from the Figure 11 inset (a). For all the films, the Nd^{3+} PL decay rate was fitted by a two-exponential decay model

$$I(t) = A_1 \exp\left(-\frac{t}{\tau_1}\right) + A_2 \exp\left(-\frac{t}{\tau_2}\right). \quad (6)$$

Fast (τ_1) and slow lifetimes (τ_2) have been reported in Figure 11, and the corresponding component of lifetime $(\frac{A_1}{A_1+A_2}, \frac{A_2}{A_1+A_2})$ is described in the inset (b). On one hand, the fast lifetime is shorter than 24 μs, while the slow one is in the 50–130 μs range. It is observed that both of them gradually increase followed by a dramatic decrease. The maximum is achieved after an annealing at $T_A = 800\,°C$. This evolution versus T_A is comparable to the results reported by Li *et al.*[46] explaining that the local environment of Nd^{3+} ions is deteriorated because of the formation of Nd_2O_3 clusters after annealing at high temperatures. Such a rare earth clusterization has been also observed in a similar sputtered system as demonstrated in our study using atom probe tomography technique.[38] On the other hand, the component of fast lifetime decreases from 0.68 to 0.51, in Figure 11 inset (b), while the slow case increases from 0.32 to 0.49. This indicates that (i) the fast lifetime dominates the Nd^{3+} emission for all the layers, and that (ii) the contribution of slow lifetime to Nd^{3+} PL gradually increases with T_A.

E. Energy transfer mechanism

The energy transfer from sensitizers present in SiO_x matrix to Nd^{3+} ions has been demonstrated using a non-resonant excitation as described above and now our purpose is to analyze this transfer process in more details (Figure 12). The absorption spectrum (Figure 12 (ii-b)) of Nd^{3+} ions in Nd-doped SiO_2 film presents four typical absorption bands peaking at about 880, 808, 750, and 585 nm. They correspond to the transitions from the ground level $^4I_{9/2}$ to the excited level $^4F_{3/2}$, $^4F_{5/2}$, $^4F_{7/2}$, and $^2G_{7/2}$, respectively.[31] Thus, from these quantified energy levels and the positions of E_L and E_H emissions, one can propose a scheme of the transfer mechanism as detailed in Figure 12.

For low T_A-annealed Nd-SiO_x layers, ASSs and radiative defects are present in the matrix. Both efficiently sensitize the Nd^{3+} ions, since the intense Nd^{3+} PL has been observed in both samples annealed at 750 °C for 1 min and 1 h (Figure 6). When the radiative defects are recovered with T_A, the atomic scale sensitizers, whose density increases with the temperature, dominate the sensitization of the rare earth ions. As a consequence, in this intermediate

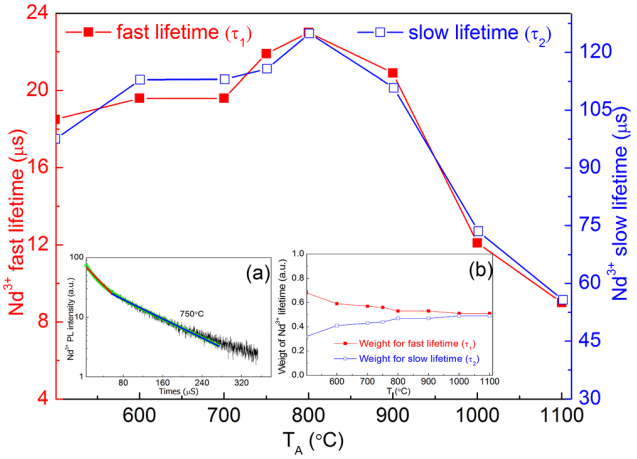

FIG. 11. Evolution of Nd^{3+} PL lifetime at 920 nm versus T_A. The inset (a) is a representative decay rate of 750 °C Nd-SiO_x PL, fitted by a two-exponential decay model, while the inset (b) is the component of Nd^{3+} fast or slow lifetime.

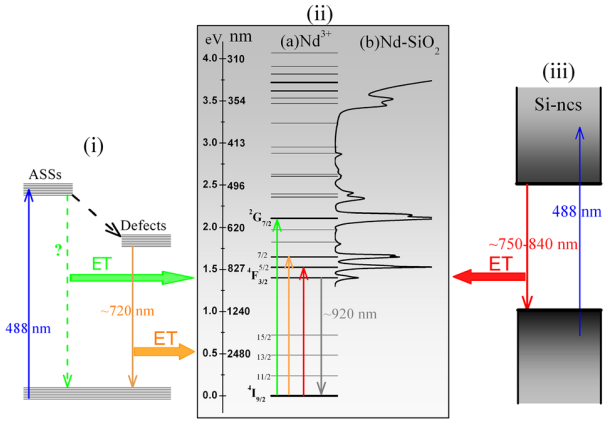

FIG. 12. Schematic illustrations of the Nd^{3+} ions excitation. (i) Energy diagrams of ASSs and defects within the films annealed at $T_A < 1000\,°C$, (ii) (a) energy diagram of Nd^{3+} ions and (b) absorption spectrum of Nd^{3+} ions doped in SiO_2 film, and (iii) energy diagram of Si-ncs within the films annealed at $T_A > 1000\,°C$. ET is the abbreviation of energy transfer.

temperature range, two paths of sensitization of Nd^{3+} ions will coexist and are at the origin of the radiative recombination from the $^4F_{3/2}$ to the ground state $^4I_{9/2}$ level with an emission at about 920 nm.

In the case of high T_A-annealed Nd-SiO_x layers, the formed Si-ncs have a smaller band gap than in the case of atomic scale sensitizers. These Si-ncs can also transfer their energy to Nd^{3+} ions as demonstrated by the decreasing of Si-ncs PL intensity (Figure 8) as well as its lifetime (Figure 10). But the PL intensity of Nd^{3+} ions achieved after such a treatment is low. Such a feature can be attributed to two phenomena: (i) a cross relaxation process among Nd^{3+} ions occurs due to the formation of Nd_2O_3 clusters as witnessed by its lifetimes (Figure 11), (ii) the formation of Si-ncs as already observed in similar sample doped with Er ions[47] will lead to an increase of the sensitizer:Nd distance.

For all the Nd-SiO_x layers, a Nd^{3+} ions PL decay with a non-exponential nature was observed and fitted using a double exponential decay model leading to the determination of a fast and a slow components. They present an opposite behavior with the annealing temperature (inset (b) in Figure 11): the former decreases while the latter increases. Horak *et al.*[48] have attributed the shortening of the decay time to a modification of local density of states (LDOS) brought by the Si interface. This is consequently a signature of the distance between rare earth ions and sensitizer. Considering that the annealing temperature favors the phase separation in our layers,[35] higher the temperature is, higher the Sensitizer:Nd^{3+} distance. Thus, one can explain the two components of the PL decay to the different environment of Nd^{3+} ions, which is modified by the annealing treatment. This would explain the observed increase of the ratio of slow over fast components of PL decay with temperature.

IV. CONCLUSION

The microstructure and PL properties were investigated as a function of annealing conditions for SiO_x and Nd-SiO_x layers. It has been demonstrated that for the low T_A-($T_A < 1000\,^\circ C$) annealed layers, the visible E_L peak origins from the defects levels, while quantum confinement effect rules the visible E_H peak for the layers annealed at higher temperature. For the Nd^{3+} emission in Nd-SiO_x layers, the former low T_A-layers present high intensity while the latter high T_A-layers have low one. The high PL intensity achieved at 920 nm has been attributed to the high density of sensitizers present in the layers that are able to transfer efficiently their energy to the rare earth ions. For increasing annealing temperatures, this 920 nm-emission decreases. It has been ascribed to both the formation of Nd_2O_3 clusters and the increasing sensitizer:Nd^{3+} distance. As studied on the mechanism of excitation towards Nd^{3+} ions, two kinds of sensitizers (radiative defects and atomic scale entities) would coexist for low T_A-annealed Nd-SiO_x films, while Si-ncs were grown acting as sensitizer for high T_A films. This would allow one to obtain high content of Nd^{3+} ions sensitized, which is the key parameter to achieve future photonic component.

ACKNOWLEDGMENTS

The authors thank the French National Agency (ANR) and Chinese Scholarship Council (CSC), which supported this work through the Nanoscience and Nanotechnology Program (DAPHNES Project ANR-08-NANO-005).

[1]L. Khriachtchev, *Silicon Nanophotonics: Basic Principles, Present Status and Perspectives* (Pan Stanford Publishing, Singapore, 2008), Chap. 1.
[2]L. Pavesi and R. Turan, *Silicon Nanocrystals: Fundamentals, Synthesis and Applications* (Wiley, New York, 2010), Chap. 2.
[3]J. P. Proot, C. Delerue, and G. Allan, Appl. Phys. Lett. **61**, 1948 (1992).
[4]T. Inokuma, Y. Wakayama, T. Muramoto, R. Aoki, Y. Kurata, and S. Hasegawa, J. Appl. Phys. **83**, 2228 (1998).
[5]F. Iacona, G. Franzò, and C. Spinella, J. Appl. Phys. **87**, 1295 (2000).
[6]C. Dufour, S. Chausserie, and F. Gourbilleau, J. Lumin. **129**, 73 (2009).
[7]A. J. Kenyon, P. F. Trwoga, M. Federighi, and C. W. Pitt, J. Phys.:Condens. Matter **6**, L319 (1994).
[8]A. J. Kenyon, C. E. Chryssou, C. W. Pitt, T. Shimizu-Iwayama, D. E. Hole, N. Sharma, and C. J. Humphreys, J. Appl. Phys. **91**, 367 (2002).
[9]I. Izeddin, A. S. Moskalenko, I. N. Yassievich, M. Fujii, and T. Gregorkiewicz, Phys. Rev. Lett. **97**, 207401 (2006).
[10]A. Pitanti, D. Navarro-Urrios, N. Prtljaga, N. Daldosso, F. Gourbilleau, R. Rizk, B. Garrido, and L. Pavesi, J. Appl. Phys. **108**, 053518 (2010).
[11]J. M. Ramírez, F. F. Lupi, O. Jambois, Y. Berencén, D. Navarro-Urrios, A. Anopchenko, A. Marconi, N. Prtljaga, A. Tengattini, L. Pavesi, J. P. Colonna, J. M. Fedeli, and B. Garrido, Nanotechnology **23**, 125203 (2012).
[12]O. Savchyn, R. M. Todi, K. R. Coffey, and P. G. Kik, Appl. Phys. Lett. **93**, 233120 (2008).
[13]A. N. MacDonald, A. Hryciw, F. Lenz, and A. Meldrum, Appl. Phys. Lett. **89**, 173132 (2006).
[14]J. S. Chang, J. H. Jhe, M. S. Yang, J. H. Shin, K. J. Kim, and D. W. Moon, Appl. Phys. Lett. **89**, 181909 (2006).
[15]F. Priolo, G. Franzò, D. Pacifici, V. Vinciguerra, F. Iacona, and A. Irrera, J. Appl. Phys. **89**, 264 (2001).
[16]J. H. Jhe, J. H. Shin, K. J. Kim, and D. W. Moon, Appl. Phys. Lett. **82**, 4489 (2003).
[17]M. Fujii, K. Imakita, K. Watanabe, and S. Hayashi, J. Appl. Phys. **95**, 272 (2004).
[18]H. S. Han, S. Y. Seo, and J. H. Shin, Appl. Phys. Lett. **79**, 4568 (2001).
[19]S. L. Oliveira, D. F. de Sousa, A. A. Andrade, L. A. O. Nunes, and T. Catunda, J. Appl. Phys. **103**, 023103 (2008).
[20]D. Navarro-Urrios, A. Pitanti, N. Daldosso, F. Gourbilleau, L. Khomenkova, R. Rizk, and L. Pavesi, Physica E **41**, 1029 (2009).
[21]S. Y. Seo, M.-J. Kim, and J. H. Shin, Appl. Phys. Lett. **83**, 2778 (2003).
[22]E. Steveler, H. Rinnert, and M. Vergnat, J. Appl. Phys. **110**, 113518 (2011).
[23]A. Podhorodecki, J. Misiewicz, F. Gourbilleau, J. Cardin, and C. Dufour, Electrochem. Solid State **13**, K26 (2010).
[24]O. Debieu, D. Bréard, A. Podhorodecki, G. Zatryb, J. Misiewicz, C. Labbé, J. Cardin, and F. Gourbilleau, J. Appl. Phys. **108**, 113114 (2010).
[25]K. Watanabe, H. Tamaoka, M. Fujii, K. Moriwaki, and S. Hayashi, Physica E **13**, 1038 (2002).
[26]N. M. Park, C. J. Choi, T. Y. Seong, and S. J. Park, Phys. Rev. Lett. **86**, 1355 (2001).
[27]A. Podhorodecki, G. Zatryb, J. Misiewicz, J. Wojcik, and P. Mascher, J. Appl. Phys. **102**, 043104 (2007).
[28]F. Koch, V. Petrova-Koch, and T. Muschik, J. Lumin. **57**, 271 (1993).
[29]S. M. Prokes, Appl. Phys. Lett. **62**, 3244 (1993).
[30]M. Wang, D. Yang, D. Li, Z. Yuan, and D. Que, J. Appl. Phys. **101**, 103504 (2007).
[31]D. Bréard, F. Gourbilleau, A. Belarouci, C. Dufour, and R. Rizk, J. Lumin. **121**, 209 (2006).
[32]C.-H. Liang, O. Debieu, Y.-T. An, L. Khomenkova, J. Cardin, and F. Gourbilleau, J. Lumin. **132**, 3118 (2012).
[33]G. Wora Adeola, H. Rinnert, P. Miska, and M. Vergnat, J. Appl. Phys. **102**, 053515 (2007).
[34]B. Garrido Fernandez, M. Lopez, C. Garcia, A. Perez-Rodriguez, J. R. Morante, C. Bonafos, M. Carrada, and A. Claverie, J. Appl. Phys. **91**, 798 (2002).

[35]M. Roussel, E. Talbot, P. Pareige, and F. Gourbilleau, J. Appl. Phys. **113**, 063519 (2013).
[36]C. H. Liang, J. Cardin, L. Khomenkova, and F. Gourbilleau, Proc. SPIE **8431**, 84311Y (2012).
[37]J. E. Olsen and F. Shimura, J. Appl. Phys. **66**, 1353 (1989).
[38]E. Talbot, R. Larde, P. Pareige, L. Khomenkova, K. Hijazi, and F. Gourbilleau, Nanoscale Res. Lett. **8**, 39 (2013).
[39]O. Savchyn, F. R. Ruhge, P. G. Kik, R. M. Todi, K. R. Coffey, H. Nukala, and H. Heinrich, Phys. Rev. B **76**, 195419 (2007).
[40]Y. H. Xie, M. S. Hybertsen, W. L. Wilson, S. A. Ipri, G. E. Carver, W. L. Brown, E. Dons, B. E. Weir, A. R. Kortan, G. P. Watson, and A. J. Liddle, Phys. Rev. B **49**, 5386 (1994).
[41]L. N. Dinh, L. L. Chase, M. Balooch, W. J. Siekhaus, and F. Wooten, Phys. Rev. B **54**, 5029 (1996).
[42]M. L. Brongersma, A. Polman, K. S. Min, E. Boer, T. Tambo, and H. A. Atwater, Appl. Phys. Lett. **72**, 2577 (1998).
[43]B. Garrido, C. García, S. Y. Seo, P. Pellegrino, D. Navarro-Urrios, N. Daldosso, L. Pavesi, F. Gourbilleau, and R. Rizk, Phys. Rev. B **76**, 245308 (2007).
[44]D. Pacifici, G. Franzò, F. Priolo, F. Iacona, and L. Dal Negro, Phys. Rev. B **67**, 245301 (2003).
[45]P. Vergeer, T. J. H. Vlugt, M. H. F. Kox, M. I. den Hertog, J. P. J. M. van der Eerden, and A. Meijerink, Phys. Rev. B **71**, 014119 (2005).
[46]R. Li, S. Yerci, S. O. Kucheyev, T. van Buuren, and L. Dal Negro, Opt. Express **19**, 5379 (2011).
[47]F. Gourbilleau, M. Levalois, C. Dufour, J. Vicens, and R. Rizk, J. Appl. Phys. **95**, 3717 (2004).
[48]P. Horak, W. H. Loh, and A. J. Kenyon, Opt. Express **17**, 906 (2009).

Nanoscale Research Letters
a SpringerOpen Journal

NANO EXPRESS Open Access

Correlation between matrix structural order and compressive stress exerted on silicon nanocrystals embedded in silicon-rich silicon oxide

Grzegorz Zatryb[1], Artur Podhorodecki[1*], Jan Misiewicz[1], Julien Cardin[2] and Fabrice Gourbilleau[2]

Abstract

Silicon nanocrystals embedded in a silicon oxide matrix were deposited by radio frequency reactive magnetron sputtering. By means of Raman spectroscopy, we have found that a compressive stress is exerted on the silicon nanocrystal cores. The stress varies as a function of silicon concentration in the silicon-rich silicon oxide layers varies, which can be attributed to changes of nanocrystal environment. By conducting the Fourier transform infrared absorption experiments, we have correlated the stresses exerted on the nanocrystal core to the degree of matrix structural order.

Keywords: Silicon, Nanocrystals, Stress, Raman, Phonon, Confinement, Order, Disorder, Matrix

PACS: 78.67.Bf, 78.67.Pt, 73.63.Bd, 78.47.D, 74.25.Nd

Background

Silicon nanocrystals (Si-NCs) embedded in a silicon-rich silicon oxide (SRSO) have been extensively studied due to their promising applications in the third generation tandem solar cells [1], light-emitting diodes [2], or silicon-based lasers [3]. These SRSO structures may be successfully deposited by magnetron sputtering technique. After deposition, during annealing in a N_2 atmosphere and 1,100°C temperature, the excess silicon in SRSO layer precipitates to form Si nanocrystals in nearly stoichiometric silicon dioxide matrix.

The structural quality of the matrix surrounding Si-NCs is very important since it influences the optical properties of Si-NCs [4]. For example, it has been shown that various defects present in the matrix may quench the emission originated from Si-NCs due to non-radiative recombination [5]. This is a serious problem from the point of view of applications, especially in the case of light-emitting devices. Besides the optical properties, due to differences in Si-NCs and SiO_2 crystal structure, the matrix structural ordering may affect also the Si-NCs crystallinity and shape. It has been shown by first-principles calculations that the surrounding matrix always produces a strain on the nanocrystals, especially at the Si-NCs/SiO_2 interface. According to theory, the amount of stress exerted on the nanocrystal is connected to the Si-NCs size [6] as well as to the number of oxygen per interface silicon [7]. These structural parameters can be controlled during deposition process by varying the excess silicon concentration in the SRSO matrix [8]. The structural properties of the Si-NCs may be then experimentally examined by means of the Raman spectroscopy, since the Si-Si bonding is Raman active. On the other hand, Si-O-Si bonds are active in the infrared (IR) region and therefore the matrix properties can be examined by means of the Fourier transform IR (FTIR) spectroscopy. In this work, we investigate the correlation between short-range structural order of the matrix and stress exerted on the Si-NCs by means of the Raman and FTIR spectroscopy. Our results indicate that there is a strong dependence of stress on the Si-NCs size and on the degree of short-range structural order of the matrix. We conclude that from the point of view of applications, a compromise has to be considered between good structural quality of the matrix and Si-NCs size.

* Correspondence: artur.p.podhorodecki@pwr.wroc.pl
[1]Institute of Physics, Wroclaw University of Technology, Wybrzeze Wyspianskiego 27, Wroclaw 50-370, Poland
Full list of author information is available at the end of the article

Methods

The SRSO films with a nominal thickness of 500 nm used for this study were deposited onto the quartz substrates by radio frequency reactive magnetron sputtering. The incorporation of Si excess was monitored through the variation of the hydrogen rate $r_H = P_{H2} / (P_{Ar} + P_{H2})$. In this work we examined three samples deposited with r_H value equal to 10%, 30%, and 50%. The films were deposited without any intentional heating of the substrates and with a power density of 0.75 W/cm^2. More details on the process can be found elsewhere [9]. All samples were subsequently annealed at 1,100°C for 1 h under N_2 flux in order to favor the precipitation of Si excess and to induce Si-NCs formation.

The room temperature micro-Raman scattering was measured in vertical transmit, horizontal receive polarization, using single-stage spectrometer (T64000 Horiba Jobin Yvon, Longjumeau, France) equipped with a silicon charge-coupled device camera. An Ar^+ laser (λ = 514.5 nm) was used as the excitation source. The lack of noticeable heating of the samples was assured by determination of the Stokes/anti-Stokes ratio. The FTIR spectra were collected using Nicolet iS10 spectrometer (Thermo Fisher Scientific Instruments, PA, USA). These measurements were conducted in attenuated total reflectance mode (ATR) using VariGATR accessory (Harrick Scientific Products Inc, NY, USA).

Results and discussion

In our previous papers [9,10] we have reported results of structural investigations (including atomic force microscopy, X-ray diffraction, high-resolution electron microscopy or Rutherford backscattering) of SRSO films fabricated with the same technological parameters as the samples examined in the present study. The main conclusion of these investigations is that the deposition with r_H = 10% favors the formation of well-crystallized Si-NCs with average size of about 3 nm, whereas deposition with r_H = 50% favors formation of Si-NCs with size less than 2 nm. We have also shown that an increase of r_H results in a drop of the crystalline fraction of nanoclusters.

The samples examined in the present study were previously investigated by means of absorption spectroscopy [11]. The Tauc formula $(\alpha E) = A\,(E - E_g)^m$ was used to estimate the optical band gap (E_g) of these structures. The best fit to the experimental absorption data was obtained for m = 1/2, which corresponds to the directly allowed transition. It was found that the absorption edge is significantly blue-shifted from 3.76 eV for r_H = 10% to 4.21 eV for r_H = 50%, due to quantum confinement effect [12]. Moreover, it was found that below the optical band gap, the absorption spectra reveal long, exponentially decreasing absorption tails which can be described by Urbach equation: $\alpha = C \exp(E / E_U)$, where E_U is the characteristic Urbach energy. It was found that E_U increases as a function of r_H also increases from 73 meV (r_H = 10%) to 90 meV (r_H = 50%). For clarity, these results are summarized in Table 1.

Figure 1 shows Raman spectra measured for samples deposited with r_H equal to 10%, 30%, and 50%. The spectra consist mainly of two bands: a broad low-frequency band (LF) with maximum at around 480 cm^{-1} and a narrower, asymmetrically broadened high-frequency (HF) peak centered between 518 and 519 cm^{-1}. The LF band may be attributed to the amorphous silicon (a-Si) [13], whereas the HF originates from Si-NCs [14]. To compare we also show the reference spectrum of bulk Si with peak centered at ω_{Si} = 520 cm^{-1}. Interestingly, despite the fact that the Si-NCs size decreases as a function of r_H, the Raman line related to Si-NCs does not shift to the lower frequencies according to the predictions of the phonon confinement (PC) model [15]. Quite the contrary, it can be seen in Figure 1 that the Raman line slightly upshifts as a function of r_H. In order to explore this rather surprising effect in more details, we have analyzed the HF Raman band using the PC model, following the approach proposed by Paillard et al. [16]:

$$I_{Si-NC}(\omega) = C \int_0^{0.5} \frac{\sin^2[(\mathrm{q}d/a_0)\pi]}{\left[1-(\mathrm{q}d/a_0)^2\right]^2} \frac{d\mathrm{q}}{\left[\omega-\omega(\mathrm{q})\right]^2 + (\Gamma_0/2)^2}, \quad (1)$$

where d is the Si-NC diameter, a_0 = 0.543 nm is the Si lattice constant, q is the phonon wave vector expressed in $2\pi/a_0$ units and Γ_0 is the natural line width. As shown by Zi et al. [17], for small Si-NCs, the phonon confinement model can give a relatively good description of Raman frequency shifts, comparable to the predictions of the bond polarizability model. The high anisotropy of the phonon dispersion curves in silicon was also taken into account, using the averaged dispersion relation for the optical phonons, as proposed by Paillard et al.:

$$\omega(\mathrm{q}) = \sqrt{\omega_c^2 - \frac{126,100 \times \mathrm{q}^2}{\mathrm{q} + 0.53}} \quad (2)$$

In the equation (2), the $\omega_c = \omega_{Si}$ = 520 cm^{-1} is the optical phonon frequency at the Γ point of the Brillouin

Table 1 The optical band gap (E_g) and Urbach energy (E_U) determined for the investigated samples

r_H (%)	E_g (eV) (m = 1/2)	E_u (meV)
10	3.75	73
30	3.97	75
50	4.22	90

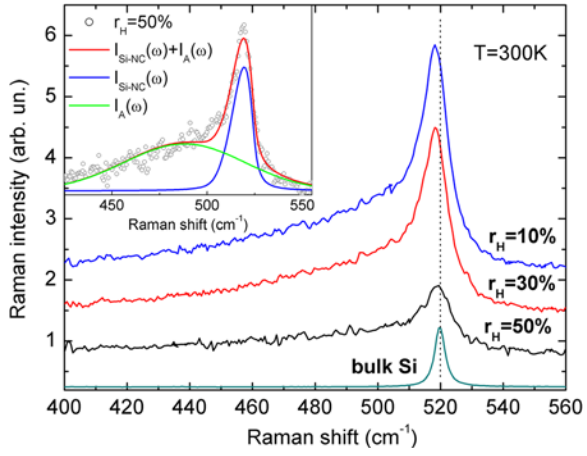

Figure 1 Raman spectra measured for samples deposited with r_H equal to 10%, 30%, and 50%. To compare, a reference spectrum of bulk Si is also shown. The spectra have been upshifted for clarity reasons. The inset shows fit of the phonon confinement model to the spectrum measured for r_H = 50% sample.

zone of an unstressed bulk Si crystal. However, if stress is present in the material, the ω_c value changes [18]. Therefore, to retain all the information, during fitting procedure, we left ω_c as a free parameter together with d. Additionally, a Gaussian function was used to fit the LF band:

$$I_A(\omega) = A_A \exp\left(-\frac{[\omega - \omega_A]^2}{2\delta_A^2}\right) \quad (3)$$

where ω_A is the LF band frequency, A_A denotes amplitude, and δ_A is related to Gaussian width. The overall model used to fit the Raman data is a sum of the amorphous and crystalline components:

$$I(\omega) = I_{Si-NC}(\omega) + I_A(\omega). \quad (4)$$

Inset in Figure 1 shows an example of the fit obtained for r_H = 50% sample. It can be seen that the PC model accounts for the asymmetric shape of the Raman band of Si-NCs. This asymmetric shape is a result of a finite nanocrystals volume, which allows phonons away from the Brillouin zone center to contribute to the Raman scattering. Therefore, during the fitting procedure, we rely on two factors that directly depend on the Si-NCs size: the line-shape of the Raman band and the expected frequency of this band.

From the fit of Equation 4 to the Raman data, we obtained that the Si-NCs diameter d increases from about 2.4 nm for r_H = 50% to about 2.7 nm for r_H = 10% (the statistical error from the fitting procedure is less than 0.05 nm). The obtained results are in agreement with our expectations based on the structural data measured for similar samples. This result also confirms that the model given by Equation 1 can be used to estimate the Si-NCs size based on the Raman data.

The second important result obtained from the fit is ω_c. For the unstressed Si crystal, this value equals to 520 cm^{-1}. However, we obtained that ω_c increases as a function of r_H increases, from ω_c = 523 cm^{-1} for r_H = 10% to ω_c = 525 cm^{-1} for r_H = 50%. The obtained values strongly indicate that we deal with a compressive stress exerted on the Si-NCs which shifts the observed Raman lines towards higher wavenumbers [4]. Similar effect has been observed for Si-NCs obtained by chemical vapor deposition technique and annealed at 1,250°C [19]. Moreover, the observed rise of ω_c indicates that the stress increases as a function of r_H. Assuming that the hydrostatic pressure of about 1 GPa results in approximately 1.88 cm^{-1} shift of the Raman line [20], we may estimate the maximum stress to be about 2.6 GPa for r_H = 50% sample. The obtained results also explain why we do not observe a clear downshift of the Raman frequency related to PC effect. Namely, the compressive stress increases as a function of r_H and compensates for the downshift due to the finite crystallite size. It is worth to note that PC effect has been actually observed for Si-NCs synthesized in the form of free-standing powder [21]. Therefore, the difficulties related to the observation of this effect in our case seem to be matrix-related. It should be also noted here that the obtained values of ω_c do not strongly depend on the PC model selection. To check this, we fitted the HF Raman band with another PC model proposed by Campbell et al. [15] (with a Gaussian weighting function instead of sinc). Although this model predicted overestimated Si-NCs sizes (4 nm for r_H = 50% and 5 nm for r_H = 10%), the obtained values of ω_c were similar (ω_c = 523 cm^{-1} for r_H = 10% and ω_c = 524 cm^{-1} for r_H = 50%). It should also be mentioned that both models are simplified since they do not take into account such effects as stress distribution or Si-NCs size distribution. Therefore, the estimated stress values should be treated as estimation.

In the next step, the Raman results were used to calculate the relative contribution of the HF (Si-NCs) and LF (a-Si) bands to the total Raman scattering, according to the following equations:

$$f_{HF} = \frac{I_{Si-NC}}{I_A + I_{Si-NC}}$$
$$f_{LF} = \frac{I_A}{I_A + I_{Si-NC}}, \quad (5)$$

where the intensities I_{Si-NC} and I_A are defined as integrals over ω of Equations 1 and 3, respectively. We prefer to calculate the relative contributions instead of the absolute amorphous and crystalline fractions since, as shown by Ossadnik et al. [22], the Raman-based estimates of the latter can be very inaccurate.

Figure 2a shows the relative contributions of the HF (Si-NCs) and LF (a-Si) bands to the total Raman scattering intensity as a function of r_H. It can be seen that the relative contribution from Si-NCs drops with r_H, which we believe reflects a relative drop of the crystalline fraction. Simultaneously, we observe a relative increase of the amorphous fraction with r_H. These results are in agreement with our previous structural investigations for similar structures, where it has been shown that increase of r_H results in the increase of the amount of a-Si in the structures.

Figure 2b shows the integrated Raman intensities of Si-NCs and a-Si bands as a function of absorption coefficient (α). The absorption coefficient was determined at 4 eV (high-energy part of the absorption spectra). It can be seen that there is a linear correlation between α and the Raman intensity for Si-NCs as well as a-Si, with correlation coefficient equal to 0.98 and 0.97, respectively. Since both the Raman intensity and α depend linearly on the number of nanoparticles (e.g., Si-NCs), the obtained correlation indicates that the high-energy absorption is related to both: Si-NCs and a-Si. It should be also noted here that we obtained a strong correlation for the whole high-energy part of the absorption spectra (between 3 and 5 eV). Moreover, the correlation coefficient calculated for Si-NCs was always slightly higher than for a-Si. On the other hand, when energy drops approximately below 2.5 eV, the correlation coefficient also drops below 0.7. This result can be expected if we bear in mind that the estimated optical band gap exceeds 2.5 eV for all of the investigated structures (see Table 1). This result may also indicate that the low-energy part of the absorption spectra is (at least partially) related to some different structures e.g., defects in the matrix.

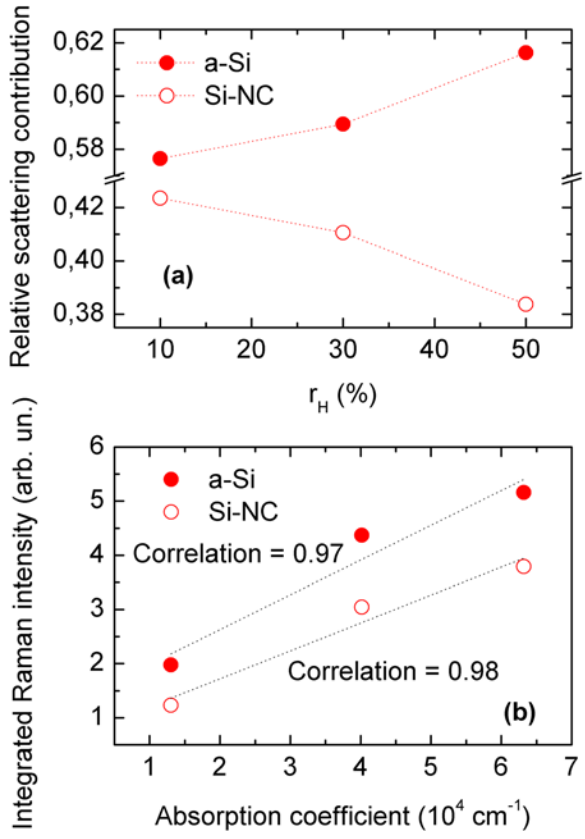

Figure 2 Relative contribution of the HF (Si-NC) and LF (a-Si) Raman bands and their integrated Raman intensities. (**a**) Relative contribution of the HF (Si-NC) and LF (a-Si) Raman bands to the total scattering intensity is shown as a function of r_H. (**b**) Integrated Raman intensities of HF (Si-NC) and LF (a-Si) bands are shown as a function of absorption coefficient. Pearson's correlation coefficients have been also shown for a-Si and Si-NC.

In order to explore the matrix properties for more details, we conducted FTIR measurements in ATR mode. Figure 3 shows normalized IR spectra obtained for the samples deposited with different r_H. To compare, Figure 3 also contains a reference spectrum measured for pure quartz. In each case, the main band located in the range 1,000 to 1,300 cm^{-1} is associated with the asymmetric stretching Si-O-Si mode [23], where the bridging oxygen atoms move in the direction opposite to their Si neighbors and roughly parallel to the Si-Si lines. Moreover, the band around 800 cm^{-1} is identified as the bending Si-O-Si vibration [23] in which the oxygen move approximately at right angles to the Si-Si lines and in the Si-O-Si planes.

Figure 3 one can also see that the spectra of the samples deposited with excess silicon are much broader in comparison with the IR spectra of pure quartz. Moreover, the decrease of the r_H used during deposition leads to a significant broadening of the IR spectra. This effect can be related to the lowering of the degree of matrix structural order. It should be emphasized here that we consider a short-range order since the matrix is non-

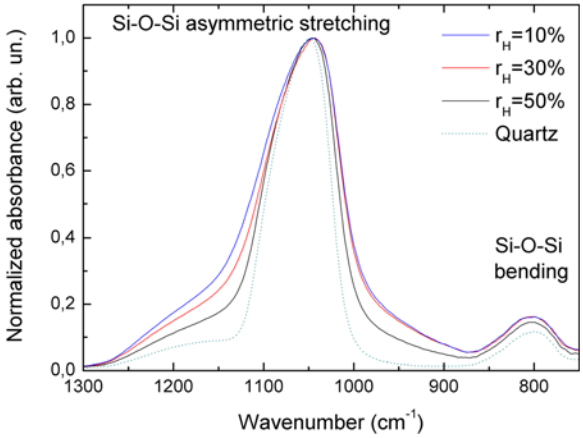

Figure 3 Normalized FTIR spectra measured in ATR mode for samples deposited with different r_H. The quartz reference spectrum is also shown for comparison (dotted line).

crystalline. A more quantitative definition of the matrix structural disorder is discussed below.

Recently, it has been well established that amorphous silica (a-SiO_2) contains ring structures with different sizes [24]. The structure of a-SiO_2 is a network of SiO_4 tetrahedra containing irregular rings of order $n < 6$, where n is the number of Si atoms in a ring. In other words, the n-fold ring implies n Si atoms and n O atoms alternately connected in a loop. The irregularity of these rings is associated with the number of atoms in a loop (n-fold rings) as well as with the broad distribution of the Si-O-Si intertetrahedral bond angles θ [25]. In the framework of central-force network model, the distribution of θ can be ascribed entirely to the width of an IR or Raman mode [26]. This is because the mode angular frequency ω_i is related to θ by the following equation [26]:

$$\omega_i \Delta\omega_i = \gamma_i(\alpha/2m_X)\sin\theta\Delta\theta \quad (6)$$

where $\Delta\omega_i$ is the change of the ω_i mode angular frequency, $\Delta\theta$ is the variation of the angle θ, γ is a constant, α is a bond force constant and m_x denotes element mass. In this work we relate the structural disorder to a spread in θ and a wide distribution of n in the n-fold rings. This approach is clearly oversimplified since it does not account for the appearance of new modes induced by the disorder [27], which actually exist in an amorphous SiO_2. Nevertheless, the above model enables us to understand the obtained results at least qualitatively and relate the observed broadening of the IR spectra to increase structural disorder of the matrix. This means that the siloxane rings structure is more diversified in the case of r_H = 10% samples, with various ring orders n and a large spread in the intertetrahedral angle θ.

We would like to note that there is a correlation between the structural order of the matrix and the magnitude of the compressive stress exerted on Si-NCs. Namely, the stress is higher when the structural order of the matrix increases. Although several explanations of the compressive stress exerted on Si-NCs in SRSO matrix have been proposed [19,28], we have not found any explanation which takes this effect into consideration. Here, we would like to suggest another possible origin of the compressive stress that accounts also for the observed correlation of the compressive stress magnitude on the structural order of the matrix.

Before we discuss this effect, we would like to note that after crystallization of a melted silicon nanoparticle, its volume increases by about 10% [29]. This is rather not typical behavior, related to the fact that silicon has greater density in the liquid state than in the solid state. Therefore, the phase-transition from liquid to crystalline state should lead to a compressive stress, when Si-NCs are embedded in a SiO_2 matrix, despite the different thermal expansion coefficients of Si and SiO_2. This also means that the compressive stress observed in our experiment may be indicative of the crystallization process, which proceeds through melting. This kind of process has been suggested by Hirasawa et al. [30] for Si nanoparticles synthesized by pulsed laser ablation, where the determined crystallization temperatures were in the range of 800 to 1,300 K (depending on the nanoparticle size). These temperatures are far below the melting point of bulk Si (1,683 K). In our case, the annealing temperature of 1,373 K is also well below the melting point of bulk Si and only slightly below the melting point of a-Si (1,420 K for relaxed a-Si [31]). However, it is well known that the melting temperature of a nanoparticle decreases significantly with size, as a consequence of the additional free energy contribution of the surface to the overall Gibbs free energy [32]. For example, it has been shown that free-standing Si nanoparticles with a size of 20 nm melt at around 1,000 K [32]. On the other hand, nanoparticles embedded in a matrix can exhibit both melting-point depression and enhancement [33], and the actual melting behavior depends on the nature of the interface between the nanoparticle and the matrix. It has been found that when the interface between the nanoparticle and the matrix is coherent, the thermal vibration of the surface (interface) atoms of the nanoparticle is suppressed. This suppression may prevent the melting of the nanocrystals' surface and lead to an increase of the melting temperature. This kind of behavior has been found for lead nanocrystals in an aluminum matrix and was attributed to the lattice structures of the two crystals 'locking up', suppressing the vibration of the nanoparticles' surface atoms [34]. Contrary to this, irregularly shaped and incoherent interfaces can be directly correlated with lowering of melting temperature of a nanoparticle [35].

In the investigated case, we expect that directly after deposition we deal with amorphous Si nanoparticles embedded in a disordered oxide matrix. Moreover, it is improbable that the sputtering technique allows deposit of coherent (epitaxial) interfaces between the amorphous nanoparticles and the matrix. Due to a large density gradient of the Si nanoparticles and the oxide host, when merged at their interface, the network topologies in either side deform in order to accommodate the transition [36]. Therefore, we expect the interfaces between Si nanoparticles and the matrix to be incoherent. This can be further supported by the latest findings of molecular dynamics simulations which have shown that the interface structure between Si-NCs and the matrix is generally highly porous on the silica side, making the contact with the Si-NCs discontinuous [37]. Taking this into account, we expect that the melting temperature of small, amorphous Si nanoparticles embedded in SRSO matrix

might be depressed below the melting point of a-Si. If this is the case, melting of the nanoparticles may be possible at 1,100°C.

Having this in mind, we suggest the following origin of the compressive stress observed in our experiment. First of all, it should be emphasized that the matrix structure before and after annealing is not the same. Annealing at 1,100°C leads to phase separation on Si and SiO_2 and the structural order of the matrix increases. Secondly, the crystallization of small a-Si nanoparticles takes place simultaneously to the matrix ordering. We suggest that for non-uniform structures obtained by sputtering, the crystallization may proceed through melting which in turn leads to volume expansion and compressive stress exerted on the Si-NC. Moreover, we may expect that the ability of Si-NCs to expand after crystallization should depend on the environment - particularly, on the degree of the structural order of the matrix (since expansion of the nanocrystal leads to matrix deformation). In other words, the matrix structure determines its ability to accommodate to the expanding Si-NCs. In this way, formation of a well-ordered matrix does not allow Si-NCs to expand freely, leading to a stronger compressive stress exerted on the Si-NCs. We deal with this situation for r_H = 50%, where the compressive stress is the strongest and the FTIR spectra are quite narrow, suggesting a higher structural order of the matrix than for the other samples. On the other hand, for larger Si-NCs (r_H = 10%), the structural order of the matrix is the lowest, resulting in a broad IR spectrum. This structural disorder indicates that the matrix can accommodate to the Si-NCs size/shape; therefore, compressive stress exerted on the Si-NCs is lowered.

Remarkably, the IR spectrum of pure quartz is much narrower than the spectra of the samples containing Si-NCs. It means that Si-NCs always introduce a large amount of the structural disorder to the matrix which may influence also the optical properties. This problem should be taken into account while designing structures for a particular application.

Conclusions

In conclusion, we have shown that compressive stress is exerted on Si-NCs in SRSO samples deposited by radio frequency reactive magnetron sputtering. This stress may completely compensate for the phonon quantum confinement effects, resulting in the lack of a clear dependence of the Si-NCs-originated Raman line on the Si-NCs size. The compressive stress increases with the increasing r_H used during deposition. We relate the observed strong stress dependence on r_H to the changes of structural order of the matrix surrounding Si-NCs induced by r_H variation. The formation of an ordered matrix structure clearly competes with the formation of unstressed Si-NCs.

Competing interests
The authors declare that they have no competing interests.

Authors' contributions
GZ, AP, and JM carried out the spectroscopic measurements as well as calculations. JC and FG designed and deposited the investigated samples. All authors read and approved the final manuscript.

Acknowledgments
GZ would like to acknowledge for financial support to Program Iuventus Plus (no. IP2011 063471). In this work, the Raman spectra measurements were conducted as a part of the NLTK project (POIG. 02.02.00-00-003/08-00). This research was conducted as part of the Polonium program.

Author details
[1]Institute of Physics, Wroclaw University of Technology, Wybrzeze Wyspianskiego 27, Wroclaw 50-370, Poland. [2]CIMAP, UMR CNRS/CEA/ENSICAEN/UCBN, Ensicaen 6 Blvd Maréchal Juin, Caen Cedex 4 14050, France.

Received: 8 October 2012 Accepted: 19 November 2012
Published: 21 January 2013

References

1. Cho EC, Green MA, Conibeer G, Song D, Cho YH, Scardera G, Huang S, Park S, Hao XJ, Huang Y, Van Dao L: **Silicon quantum dots in a dielectric matrix for all-silicon tandem solar cells.** *Adv Optoelectron* 2007, **2007:**1–11.
2. Huh C, Kim K, Kim BK, Kim W, Ko H, Choi C, Sung GY: **Enhancement in light emission efficiency of a silicon nanocrystal light emitting diode by multiple luminescent structures.** *Adv Mater* 2010, **22:**5058–5062.
3. Pavesi L, Dal Negro L, Mazzoleni C, Franzo G, Priolo F: **Optical gain in silicon nanocrystals.** *Nature* 2000, **408:**440–444.
4. Zatryb G, Podhorodecki A, Hao XJ, Misiewicz J, Shen YS, Green MA: **Correlation between stress and carrier nonradiative recombination for silicon nanocrystals in an oxide matrix.** *Nanotechnology* 2011, **22:**335703.
5. Zatryb G, Podhorodecki A, Hao XJ, Misiewicz J, Shen YS, Green MA: **Quantitative evaluation of boron-induced disorder in multilayers containing silicon nanocrystals in an oxide matrix designed for photovoltaic applications.** *Opt Express* 2010, **18:**22004–22009.
6. Hadjisavvas G, Remediakis IN, Kelires PC: **Shape and faceting of Si nanocrystals embedded in a-SiO2: a Monte Carlo study.** *Phys Rev B* 2006, **74:**165419.
7. Guerra R, Degoli E, Ossicini S: **Size, oxidation, and strain in small Si/SiO nanocrystals.** *Phys Rev B* 2009, **80:**155332.
8. Podhorodecki A, Zatryb G, Misiewicz J, Wojcik J, Mascher P: **Influence of the annealing temperature and silicon concentration on the absorption and emission properties of Si nanocrystals.** *J Appl Phys* 2007, **102:**043104–043105.
9. Ternon C, Gourbilleau F, Portier X, Voivenel P, Dufour C: **An original approach for the fabrication of Si/SiO2 multilayers using reactive magnetron sputtering.** *Thin Sol Film* 2002, **419:**5–10.
10. Gourbilleau F, Levalois M, Dufour C, Vicens J, Rizk R: **Optimized conditions for an enhanced coupling rate between Er ions and Si nanoclusters for an improved 1.54-μm emission.** *J Appl Phys* 2004, **95:**3717–3722.
11. Zatryb G, Podhorodecki A, Misiewicz J, Cardin J, Gourbilleau F: **On the nature of the stretched exponential photoluminescence decay for silicon nanocrystals.** *Nanoscale Res Lett* 2011, **6:**106.
12. Podhorodecki A, Misiewicz J, Gourbilleau F, Rizk R: **Absorption mechanisms of silicon nanocrystals in cosputtered silicon-rich-silicon oxide films.** *Electrochem Solid-State Lett* 2008, **11:**K31–K33.
13. Khriachtchev L, Kilpelä O, Karirinne S, Keränen J, Lepisto T: **Substrate-dependent crystallization and enhancement of visible photoluminescence in thermal annealing of Si/SiO2 superlattices.** *Appl Phys Lett* 2001, **78:**323.
14. Khriachtchev L, Räsänen M, Novikov S, Pavesi L: **Systematic correlation between Raman spectra, photoluminescence intensity, and absorption coefficient of silica layers containing Si nanocrystals.** *Appl Phys Lett* 2004, **85:**1511.
15. Campbell IH, Fauchet PM: **The effects of microcrystal size and shape on the one phonon Raman spectra of crystalline semiconductors.** *Solid State Commun* 1986, **58:**739–741.

16. Paillard V, Puech P, Laguna MA, Carles R, Kohn B, Huisken F: **Improved one-phonon confinement model for an accurate size determination of silicon nanocrystals.** *J Appl Phys* 1999, **86:**1921–1924.
17. Zi J, Zhang K, Xie X: **Comparison of models for Raman spectra of Si nanocrystals.** *Phys Rev B* 1997, **55:**9263.
18. Manotas S, Agulló-Rueda F, Moreno JD, Ben-Hander F, Martínez-Duart JM: **Lattice-mismatch induced-stress in porous silicon films.** *Thin Sol Film* 2001, **401:**306–309.
19. Hernández S, Martínez A, Pellegrino P, Lebour Y, Garrido B, Jordana E, Fedeli JM: **Silicon nanocluster crystallization in SiO*x* films studied by Raman scattering.** *J Appl Phys* 2008, **104:**044304.
20. Anastassakis E, Cantarero A, Cardona M: **Piezo-Raman measurements and anharmonic parameters in silicon and diamond.** *Phys Rev B* 1990, **41:**7529–7535.
21. Hessel CM, Wei J, Reid D, Fujii H, Downer MC, Korgel BA: **Raman spectroscopy of oxide-embedded and ligand-stabilized silicon nanocrystals.** *J Phys Chem Lett* 2012, **3:**1089–1093.
22. Ossadnik C, Vepřek S, Gregora I: **Applicability of Raman scattering for the characterization of nanocrystalline silicon.** *Thin Sol Film* 1999, **337:**148–151.
23. Aguiar H, Serra J, González P, León B: **Structural study of sol–gel silicate glasses by IR and Raman spectroscopies.** *J Non-Cryst Solids* 2009, **355:**475–480.
24. Awazu K, Kawazoe H: **Strained Si-O-Si bonds in amorphous SiO2 materials: a family member of active centers in radio, photo, and chemical responses.** *J Appl Phys* 2003, **94:**6243–6262.
25. Galeener FL, Thorpe MF: **Rings in central-force network dynamics.** *Phys Rev B* 1983, **28:**5802–5813.
26. Galeener FL: **Band limits and the vibrational spectra of tetrahedral glasses.** *Phys Rev B* 1979, **19:**4292–4297.
27. Kirk CT: **Quantitative analysis of the effect of disorder-induced mode coupling on infrared absorption in silica.** *Phys Rev B* 1988, **38:**1255.
28. Crowe IF, Halsall MP, Hulko O, Knights AP, Gwilliam RM, Wojdak M, Kenyon AJ: **Probing the phonon confinement in ultrasmall silicon nanocrystals reveals a size-dependent surface energy.** *J Appl Phys* 2011, **109:**083534–083538.
29. Ujihara T, Sazaki G, Fujiwara K, Usami N, Nakajima K: **Physical model for the evaluation of solid–liquid interfacial tension in silicon.** *J Appl Phys* 2001, **90:**750–755.
30. Hirasawa M, Orii T, Seto T: **Size-dependent crystallization of Si nanoparticles.** *Appl Phys Lett* 2006, **88:**093119.
31. Grimaldi MG, Baeri P, Malvezzi MA: **Melting temperature of unrelaxed amorphous silicon.** *Phys Rev B* 1991, **44:**1546–1553.
32. Schierning G, Theissmann R, Wiggers H, Sudfeld D, Ebbers A, Franke D, Witusiewicz VT, Apel M: **Microcrystalline silicon formation by silicon nanoparticles.** *J Appl Phys* 2008, **103:**084305.
33. Jiang Q, Zhang Z, Li J: **Melting thermodynamics of nanocrystals embedded in a matrix.** *Acta Mater* 2000, **48:**4791–4795.
34. Xu Q, Sharp ID, Yuan CW, Yi DO, Liao CY, Glaeser AM, Minor AM, Beeman JW, Ridgway MC, Kluth P, Ager JW, Chrzan DC, Haller EE: **Large melting-point hysteresis of Ge nanocrystals embedded in SiO2.** *Phys Rev Lett* 2006, **97:**155701.
35. Singh A, Tsai AP: **Melting behaviour of lead and bismuth nano-particles in quasicrystalline matrix - the role of interfaces.** *Sadhana* 2003, **28:**63–80.
36. Hadjisavvas G, Kelires PC: **Structure and energetics of Si nanocrystals embedded in a-SiO2.** *Phys Rev Lett* 2004, **93:**226104.
37. Soulairol R, Cleri F: **Interface structure of silicon nanocrystals embedded in an amorphous silica matrix.** *Solid State Sci* 2010, **12:**163–171.

doi:10.1186/1556-276X-8-40
Cite this article as: Zatryb *et al.*: Correlation between matrix structural order and compressive stress exerted on silicon nanocrystals embedded in silicon-rich silicon oxide. *Nanoscale Research Letters* 2013 **8**:40.

Modeling of the electromagnetic field and level populations in a waveguide amplifier: a multi-scale time problem

Alexandre Fafin,* Julien Cardin,[1] Christian Dufour, and Fabrice Gourbilleau

CIMAP, CNRS/CEA/ENSICAEN/UCBN
6 boulevard Maréchal Juin, 14050 Caen cedex 4, France
[1]*julien.cardin@ensicaen.fr*
**alexandre.fafin@ensicaen.fr*

Abstract: A new algorithm based on auxiliary differential equation and finite difference time domain method (ADE-FDTD method) is presented to model a waveguide whose active layer is constituted of a silica matrix doped with rare-earth and silicon nanograins. The typical lifetime of rare-earth can be as large as some ms, whereas the electromagnetic field in a visible range and near-infrared is characterized by a period of the order of fs. Due to the large difference between these two characteristic times, the conventional ADE-FDTD method is not suited to treat such systems. A new algorithm is presented so that the steady state of rare earth and silicon nanograins electronic levels populations along with the electromagnetic field can be fully described. This algorithm is stable and applicable to a wide range of optical gain materials in which large differences of characteristic lifetimes are present.

OCIS codes: (050.1755) Computational electromagnetic methods; (160.5690) Rare-earth-doped materials; (230.4480) Optical amplifiers; (230.7370) Waveguides; (230.5590) Quantum-well, -wire and -dot devices.

References and links

1. K. Yee, "Numerical solution of initial boundary value problems involving maxwell's equations in isotropic media," IEEE Trans. Antennas Propag. **14**, 302–307 (1966).
2. A. Taflove and S. C. Hagness, *Computational Electrodynamics: the Finite-Difference Time-Domain Method* (Artech House, 1995).
3. W. Miniscalco, "Erbium-doped glasses for fiber amplifiers at 1500 nm," J. Lightwave Techno. **9**, 234 –250 (1991).
4. P. Kik and A. Polman, "Erbium-doped optical-waveguide amplifiers on silicon," Mater. Res. Bull. **23**, 48–54 (1998).
5. A. Polman and F. C. J. M. van Veggel, "Broadband sensitizers for erbium-doped planar optical amplifiers: review," J. Opt. Soc. Am. B **21**, 871–892 (2004).
6. A. J. Kenyon, P. F. Trwoga, M. Federighi, and C. W. Pitt, "Optical properties of PECVD erbium-doped silicon-rich silica: evidence for energy transfer between silicon microclusters and erbium ions," J. Phys.: Condens. Matter **6**, 319–324 (1994).
7. M. Fujii, M. Yoshida, Y. Kanzawa, S. Hayashi, and K. Yamamoto, "1.54 m photoluminescence of Er3+ doped into SiO2 films containing Si nanocrystals: Evidence for energy transfer from Si nanocrystals to Er3+," Appl. Phys. Lett. **71**, 1198 –1200 (1997).
8. C. Dufour, J. Cardin, O. Debieu, A. Fafin, and F. Gourbilleau, "Electromagnetic modeling of waveguide amplifier based on Nd3+ Si-rich SiO2 layers by means of the ADE-FDTD method," Nanoscale Res. Lett. **6**, 1–5 (2011).
9. S. C. Hagness, R. M. Joseph, and A. Taflove, "Subpicosecond electrodynamics of distributed Bragg reflector microlasers: Results from finite difference time domain simulations," Radio Sci. **31**, 931–941 (1996).

#194030 - $15.00 USD Received 22 Jul 2013; revised 16 Sep 2013; accepted 17 Sep 2013; published 2 Oct 2013

10. J. Berenger, "A perfectly matched layer for the absorption of electromagnetic waves," J. comput. phys. **114**, 185–200 (1994).
11. A. Taflove and M. E. Brodwin, "Numerical solution of steady-state electromagnetic scattering problems using the time-dependent Maxwell's equations," IEEE Trans. Microwave Theory Tech. **23**, 623–630 (1975).
12. S.-H. Chang and A. Taflove, "Finite-difference time-domain model of lasing action in a four-level two-electron atomic system," Opt. Express **12**, 3827–3833 (2004).
13. A. E. Siegman, *Lasers* (University Science Books, 1986).
14. P.G. Petropoulos, "Stability and phase error analysis of FD-TD in dispersive dielectrics," IEEE Trans. Antennas Propag. **42**, 62–69 (1994).
15. A. Nagra and R. York, "FDTD analysis of wave propagation in nonlinear absorbing and gain media," IEEE Trans. Antennas Propag. **46**, 334–340 (1998).
16. D. Pacifici, G. Franzo, F. Priolo, F. Iacona, and L. Dal Negro, "Modeling and perspectives of the Si nanocrystals-Er interaction for optical amplification," Phys. Rev. B **67**, 245301(2003).
17. H. Lee, J. Shin, and N. Park, "Performance analysis of nanocluster-Si sensitized Er doped waveguide amplifier using top-pumped 470nm LED," Opt. Express **13**, 9881–9889 (2005).
18. V. Toccafondo, S. Faralli, and F. Di Pasquale, "Evanescent Multimode Longitudinal Pumping Scheme for Si-Nanocluster Sensitized Er^{3+} Doped Waveguide Amplifiers," J. Lightwave Techno. **26**, 3584–3591 (2008).
19. C. Oubre and P. Nordlander, "Optical properties of metallodielectric nanostructures calculated using the finite difference time domain method," J. Phys. Chem. B **108**, 17740–17747 (2004).
20. D. Biallo, A. D'Orazio, and V. Petruzzelli, "Enhanced light extraction in Er^{3+} doped SiO2-TiO2 microcavity embedded in one-dimensional photonic crystal," J. Non-Cryst. Solids **352**, 3823–3828 (2006).
21. A. Fallahkhair, K. Li, and T. Murphy, "Vector finite difference modesolver for anisotropic dielectric waveguides," J. Lightwave Techno. **26**, 1423–1431 (2008).
22. P. R. Amestoy, I. S. Duff, J. Koster, and J.-Y. L'Excellent, "A Fully Asynchronous Multifrontal Solver Using Distributed Dynamic Scheduling," SIAM. J. Matrix Anal. & Appl. **23**, 15–41 (2001).
23. P. R. Amestoy, A. Guermouche, J.-Y. L'Excellent, and S. Pralet, "Hybrid scheduling for the parallel solution of linear systems," Parallel Computing **32**, 136–156 (2006).
24. O. Debieu, J. Cardin, X. Portier, and F. Gourbilleau, "Effect of the Nd content on the structural and photoluminescence properties of silicon-rich silicon dioxide thin films," Nanoscale Res. Lett. **6**, 1–8 (2011).
25. M. Govoni, . Marri, and S. Ossicini, "Carrier multiplication between interacting nanocrystals for fostering silicon-based photovoltaics," Nat. Photonics **6**, 672–679 (2012).
26. F. Priolo, G. Franzo, D. Pacifici, V. Vinciguerra, F. Iacona, and A. Irrera, "Role of the energy transfer in the optical properties of undoped and Er-doped interacting Si nanocrystals," J. Appl. Phys. **89**, 264–272 (2001).
27. P. Pirasteh, J. Charrier, Y. Dumeige, Y. G. Boucher, O. Debieu, and F. Gourbilleau, "Study of optical losses of Nd^{3+} doped silicon rich silicon oxide for laser cavity," Thin Solid Films **520**, 4026–4030 (2012).

1. Introduction

The aim of this paper is to model the propagation of an electromagnetic field into an active optical waveguide. K. Yee in 1966 [1] presents the initial algorithm based on the finite difference time domain method (FDTD) used to discretize Maxwell's equations. in time and space so that it is suited to calculate the propagation of an electromagnetic field into dielectric media. In the past two decades, as computers have become more and more powerful, the FDTD method has met a growing success and has been extended to model antennas, periodic structures, dielectric materials exhibiting non linear dispersion *etc*. [2]. One of the improvements to the basic FDTD method was to account for active dielectric materials which can absorb or emit the electromagnetic field. This improvement has been made by coupling Maxwell's equations to auxiliary differential eqations (ADE) describing the polarization densities linked to the authorized transitions and electronic level populations.

For many years, rare earth ions have been used in silica-based optical amplifiers such as Erbium Doped Fibre Amplifier (EDFA) [3]. In these systems, the low gain value requires to employ significant length (10 to 15 m) of doped fiber to achieve a workable power operation. In more compact system such as erbium-doped waveguide amplifier (EDWA) a higher gain has to be reach in order to shorten the operating length of the amplifier [4]. One limiting factor of the gain is the low absorption cross section σ_{abs} of rare earth ions. In order to increase this σ_{abs}, absorption sensitizers have been used such as ytterbium, semiconductor nanograins, metallic ions or organic complexes [5]. Several studies have pointed out that silicon nanograins are effi-

#194030 - $15.00 USD Received 22 Jul 2013; revised 16 Sep 2013; accepted 17 Sep 2013; published 2 Oct 2013

cient sensitizers and can increase by a factor of 10^4 the effective absorption cross section of rare earth ions [6, 7]. Erbium (Er^{3+}) has been the first rare earth studied due to the emission wavelength of 1.5 μm, adapted to the telecommunications window in optical fibers [3]. However, there are three major gain limiting factors for the erbium ions: up-conversion, the excited state absorption and the re-absorption of the signal from the fundamental level. This last drawback is characteristic of a three levels system. More recently, neodymium ion has been proposed instead of erbium ion since its four levels configuration prevent signal re-absorption from the fundamental level.

Our goal is to model the propagation of an electromagnetic field into a waveguide with a layer containing absorbing and emitting centers as for example Nd^{3+} ions and silicon nanograins. More particularly, we want to determine the system characteristics as Fields, level populations, and gain in a steady state regime as a function of initial parameters such as concentration of emitting center, geometry, pumping configuration and pump and signal powers. Moreover, to model those steady states regime in a waveguide with a layer containing absorbing and emitting centers, we must take into account the time evolution of electromagnetic field and electronic levels populations of absorbing/emitting centers. In a waveguide containing silicon nanograins and neodymium ions, the typical lifetime of the electronic levels is about some ms, whereas the characteristic period of the electromagnetic field is of the order of fs. The choice of a common time step to treat such different time scales would require prohibitively long computation times (about 10^{15} iterations). One possible solution to overcome this multi-scale times issue was proposed in 2011 [8], by applying the so-called time scaling method which consists in multiplying the population rate differential equations by a scaling factor (10^6) so that the convergence of levels population is accelerated. Despite the number of required time iterations that has been reduced by 6 order of magnitude, this technique does not sufficiently decrease the computation time and may lead to numerical instabilities for higher scaling factors.

In section 2, we present the classical ADE-FDTD method and show that, within a reasonable computation time, the steady state of the system cannot be reached with such a difference between absorbing and emitting centers lifetimes and electromagnetic field period. Consequently, in section 3, we propose a new algorithm based on the ADE-FDTD method which allows to compute the electromagnetic field distribution, the gain, and the electronic levels populations in the waveguide in the steady state regime. Finally, we show in section 4 the results of a calculation performed on a waveguide composed of silicon rich silicon oxide (SRSO) matrix containing silicon nanograins and neodymium ions.

2. Classical ADE-FDTD method

The FDTD is based on time and space discretization scheme of Maxwell equations proposed by Yee [1] which allows to calculate the propagation of electromagnetic field (**E**,**H**) in time domain [2]. The ADE method consists in the use of extra terms such as current density **J** or polarization density **P** which are solutions of a differential equation with the aim to model some non linear optical behavior such as dispersive or gain media [9]. The fields **E**, **H** are treated by Maxwell equations rewritten as following:

$$\begin{cases} \nabla \wedge \mathbf{E} = -\mu \dfrac{\partial \mathbf{H}}{\partial t} - \rho \mathbf{H} \\ \nabla \wedge \mathbf{H} = \varepsilon_0 \varepsilon_r \dfrac{\partial \mathbf{E}}{\partial t} + \dfrac{\partial \mathbf{P}_{tot}}{\partial t} + \sigma \mathbf{E} \end{cases} \tag{1}$$

where $\varepsilon_0\varepsilon_r$ and μ are respectively the static permittivity and magnetic permeability. σ is the usual electrical conductivity and ρ is a fictitious magnetic resistivity used for boundary conditions of the calculation box. Berenger's perflectly matched layers (PML) [10] have been

#194030 - $15.00 USD Received 22 Jul 2013; revised 16 Sep 2013; accepted 17 Sep 2013; published 2 Oct 2013

implemented as boundary conditions. Both σ and ρ have been chosen so that PML boundary conditions can minimize electromagnetic reflection and maximize absorption. $\mathbf{P}_{tot} = \sum \mathbf{P}_{ij}$ is the sum of all polarizations corresponding to each transition of the absorbing/emitting centers (hereafter: silicon nanograins and rare earth ions). The use of one polarization density $\mathbf{P}_{ij}$ per optical transition between levels i and j allows the description of the global dynamic permittivity $\varepsilon(\omega)$ of the matrix arising from the dipole moment densities induced by optical transitions in emitting centers.

The time and space steps must fulfill the classical stability conditions of FDTD calculation [11]:

- Space step $\Delta < \frac{\lambda}{10}$, where λ is the smaller wavelength in the calculation.
- Time step $\Delta t = S_c \frac{\Delta}{c\sqrt{d}}$, where c is the speed of light, $d = 1,2,3$ depending on the dimensionality of the problem and S_c is the Courant number between 0 and 1 whose choice is empirical.

Neglecting the Rabi oscillation term [12], for a transition between levels i and j the polarization density $\mathbf{P}_{ij}$ is linked to the instantaneous electric field $\mathbf{E}(t)$ and to the population difference $\Delta N_{ij} = N_i - N_j$ through the Lorentz type polarization density differential equation ([13]):

$$\frac{d^2\mathbf{P}_{ij}(t)}{dt^2} + \Delta\omega_{ij}\frac{d\mathbf{P}_{ij}(t)}{dt} + \omega_{ij}^2\mathbf{P}_{ij}(t) = \kappa_{ij}\Delta N_{ij}(t)\mathbf{E}(t) \tag{2}$$

where $\Delta\omega_{ij}$ is the linewidth including radiative, non-radiative and dephasing processes of the transition [8], and ω_{ij} is the resonance frequency of this transition. κ_{ij} defined in [13] depends on the transition lifetime τ_{ij} and on the optical index n:

$$\kappa_{ij} = \frac{6\pi\varepsilon_0 c^3}{\omega_{ij}^2\tau_{ij}n} \tag{3}$$

from Eq. (2) and the stability conditions in Lorentz media obtained by P. G. Petropoulos [14] another numerical stability condition appears:

$$\Delta t \leq \frac{2\pi}{100\omega_{ij}} \tag{4}$$

Finally, the time evolution of the electronic level populations N_i is modelled by usual rate equations. For example in the case of a two level system, where N_1 is the fundamental level and N_2 the excited level, the rate equation. of the fundamental level is [15]:

$$\frac{dN_1(t)}{dt} = -\frac{1}{\hbar\omega_{12}}\mathbf{E}(t)\frac{d\mathbf{P}_{21}(t)}{dt} + \frac{N_2(t)}{\tau_{21}|_{nr}^{r}} \tag{5}$$

The term $\frac{1}{\hbar\omega_{12}}\mathbf{E}(t)\frac{d\mathbf{P}_{21}(t)}{dt}$ (in ph.cm^{-3}.s^{-1}) is the induced radiation rate (resp. excitation rate) if it is negative (resp. positive). The terms N_i (i=1,2) (in cm^{-3}) are the population densities of different atomic levels, and $\tau_{21}|_{nr}^{r}$corresponds to the lifetime of spontaneous emission from the level 2 to the level 1. In principle, Eqs. (1), (2) and (5) must be solved simultaneously. As explained above, in the visible and near infrared spectra the electromagnetic field has a characteristic time of the order of 10^{-15} s. Furthermore, the excited levels have characteristic lifetimes as long as a few ms [16–18]. Accordingly, due to the time step imposed by the ADE-FDTD method lower than 10^{-17} s [19, 20], the number of iteration must be as huge as 10^{15} in order to reach the steady states of the levels populations. So, a conventional calculation with the classical ADE-FDTD method where the equations of populations are calculated at the same time of the electromagnetic field is impossible in reasonable time.

#194030 - $15.00 USD Received 22 Jul 2013; revised 16 Sep 2013; accepted 17 Sep 2013; published 2 Oct 2013

3. Development of the new algorithm

In order to reduce the computational time, we developed a new algorithm based on the ADE-FDTD method diagrammed in Fig. 1. The choice of the linewidth $\Delta\omega_{ij}$, its link to the absorption cross section of emitting center and its consequence on the calculation duration will also be discussed.

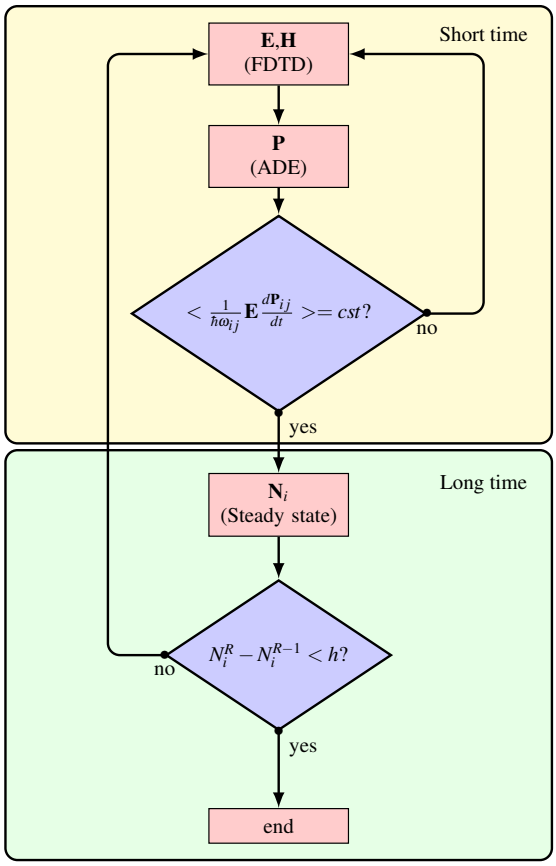

Fig. 1. The new algorithm flowchart showing the alternation of the short time loop calculating electromagnetic field and polarizations and the long time loop including calculation of levels populations.

3.1. Explanation of the new algorithm

Considering the timescale difference between the fields **E, H**, $\mathbf{P}_{ij}$ on the one hand and populations N_i on the other hand, we propose to decouple Eqs. (1), (2) and (5) into two sets of equations, solved one after the other: (i) the electromagnetic field and polarization Eqs. (1) and (2) and (ii) calculation of steady state populations (eq 5). By analyzing the time evolution of volumic density of photon $I_{ij}(t) = \frac{1}{\hbar\omega_{ij}} \mathbf{E} \frac{d\mathbf{P}_{ij}}{dt}$ obtained with classical ADE-FDTD method, we notice that $I_{ij}(t)$ is a "quickly variable" function with a "slowly variable" envelope which reaches a stationary value after 10^5 iterations. Moreover, it has been noticed that the time evolution of populations $N_i(t)$, in Eq. (5), is governed by the "slowly variable" evolution of the volumic density of photon I_{ij} envelope. Based on these two observations, we propose a new

#194030 - $15.00 USD Received 22 Jul 2013; revised 16 Sep 2013; accepted 17 Sep 2013; published 2 Oct 2013

ADE-FDTD algorithm divided in short and long time loops:

- In the short time loop, electromagnetic fields and polarizations are calculated Eqs. (1) and (2) assuming that all the levels populations are constant. Thus, for each transition, ΔN_{ij} in Eq. (2) are constant and the current average value of photon volumic density $< I_{ij} > (t)$ is calculated. This latter follows the temporal evolution of the "slowly variable" envelope of $I_{ij}(t)$. We exit from this short time loop of the algorithm when a stationary value $< I_{ij} >^{stat}$ is reached. This occurs when the relative difference between successive iterations becomes lower than a threshold value η

$$\frac{< I_{ij} > (t^{n+1}) - < I_{ij} > (t^{n-1})}{< I_{ij} > (t^n)} < \eta \tag{6}$$

where t^{n-1}, t^n, and t^{n+1} are three successive maxima as shown in Fig. 2.

$$< I_{ij} > (t) = \frac{1}{t} \int_0^t I_{ij}(t')dt' \tag{7}$$

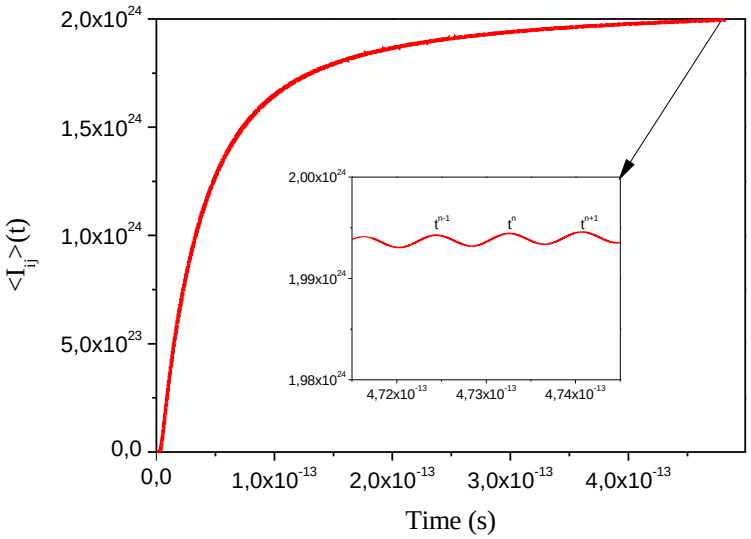

Fig. 2. The typical evolution of $< I_{ij} > (t)$ when the populations do not vary and $\Delta N_{ij} > 0$

- In the long time loop of the algorithm, the levels population are calculated with Eq. (5) by replacing the term $\frac{1}{\hbar\omega_{12}}\mathbf{E}(t)\frac{d\mathbf{P}_{21}(t)}{dt}$ by its current average value in steady state $< I_{12} >^{steady}$ determined in the short time loop. More generally, referring to equations in sect. 4.2, all $\frac{1}{\hbar\omega_{ij}}\mathbf{E}(t)\frac{d\mathbf{P}_{ij}(t)}{dt}$ terms will be replaced by their current average value $< I_{ij} >^{steady}$. In the long time loop, levels population are calculated by seeking the analytic solution solutions of rate equations in steady states ($\frac{dN_i}{dt} = 0$). Until the difference of levels population $N_i^R - N_i^{R-1}$ for all levels populations between two consecutive long time iterations $R-1$ and R is greater than a threshold value h, we return to short time loop, otherwise the overall calculation is stopped.

#194030 - $15.00 USD Received 22 Jul 2013; revised 16 Sep 2013; accepted 17 Sep 2013; published 2 Oct 2013

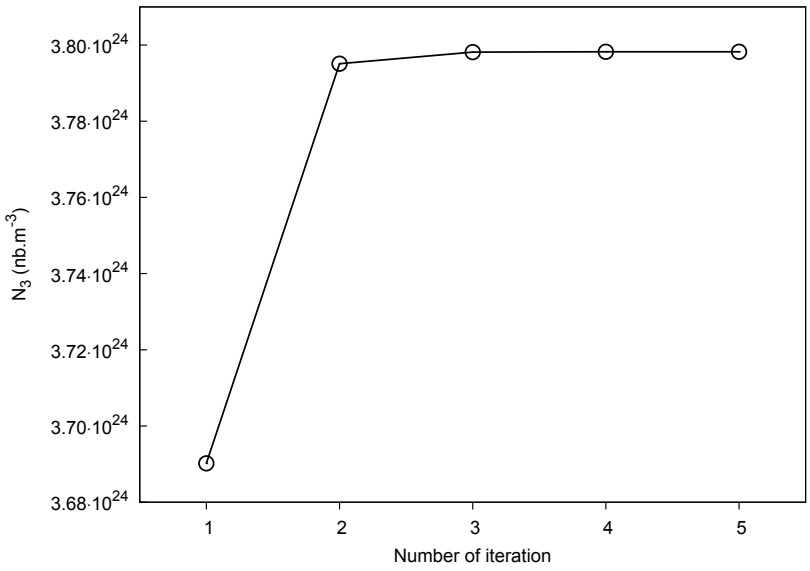

Fig. 3. Evolution of the level N_i according to the number of long time iteration R

On Fig. 3 it can be noticed that the level population reaches a constant value in very few iterations. The overall number of iterations of the new algorithm is reduced from 10^{15} with the classical ADE-FDTD method to only 10^5 resulting in a considerable reduction of calculation duration. The new algorithm is summarized in Fig. 1.

3.2. Choice of linewidth $\Delta\omega$

The description of an absorption or an emission process occurring during a transition i to j by the Lorentz oscillator polarization density Eq. (2) implies the equality of absorption and emission cross sections and that there is no inhomogeneous broadening. In order to calibrate the proper linewidth $\Delta\omega_{ij}$ of this Lorentz oscillator with respect to the absorption cross section, the Eq. (2) is solved in forced harmonic regime resulting in a solution in the $\mathbf{P} = \varepsilon_0 (\varepsilon_r(\omega) - 1)\mathbf{E}$ form. This solution leads to the relationship between $\sigma(\omega)$ and $\Delta\omega_{ij}$:

$$\sigma(\omega) = \frac{\kappa_{ij}\omega_{ij}}{\varepsilon_0 c}\left(\frac{\omega\Delta\omega_{ij}}{\left(\omega_{ij}^2 - \omega^2\right)^2 + \omega^2\Delta\omega_{ij}^2}\right) \tag{8}$$

If the linewidth $\Delta\omega_{ij}$ is chosen at the resonance frequency $\omega = \omega_{ij}$, the Eq. (8) is reduced to:

$$\sigma(\omega_{ij}) = \frac{\kappa_{ij}}{\varepsilon_0 c}\frac{1}{\Delta\omega_{ij}} \tag{9}$$

According to Eq. (9), high absorption cross sections σ (typically greater than 10^{-17} cm^2) lead to small linewidths $\Delta\omega_{ij}$ (of the order of 10^{11} rad.s^{-1}) which imposes a large number of iterations to reach a steady state. In order to calibrate the proper absorption cross section while keeping the number of iterations as small as possible, we exploit the superposition property of the polarization densities by using a number N_p of identical polarization densities with larger $\Delta\omega_{ij}$. Despite, the fact that off-resonance cross sections ($\sigma(\omega)$ with $\omega \neq \omega_{ij}$) becomes wrong, its fast decreases off-resonance leads to a negligible effect. Fig. 4 shows the absorption cross sections as a function of ω for both cases: (i) $\Delta\omega = 10^{11}$ rad.s^{-1}

#194030 - $15.00 USD Received 22 Jul 2013; revised 16 Sep 2013; accepted 17 Sep 2013; published 2 Oct 2013

with only one polarization ($N_P = 1$), and (ii) $\Delta\omega = 10^{14}$ rad.s^{-1} with 1000 polarizations ($N_P = 1000$). At resonance for $\omega_{ij} = 3.8 \times 10^{15}$ rad.s^{-1}, the two methods lead to identical cross sections: $\sigma(\omega_{ij})_{(N_P=1)} = \sigma(\omega_{ij})_{(N_P=1000)}$.

Eq. (9) becomes into Eq. (10):

$$\sigma = \frac{\kappa_{ij}}{\varepsilon_0 c} \frac{1}{N_p \Delta\omega_{ij}} \tag{10}$$

With this method, the calibration of the cross section is made by choosing appropriate values of the number N_p of polarizations and linewidths $\Delta\omega_{ij}$.

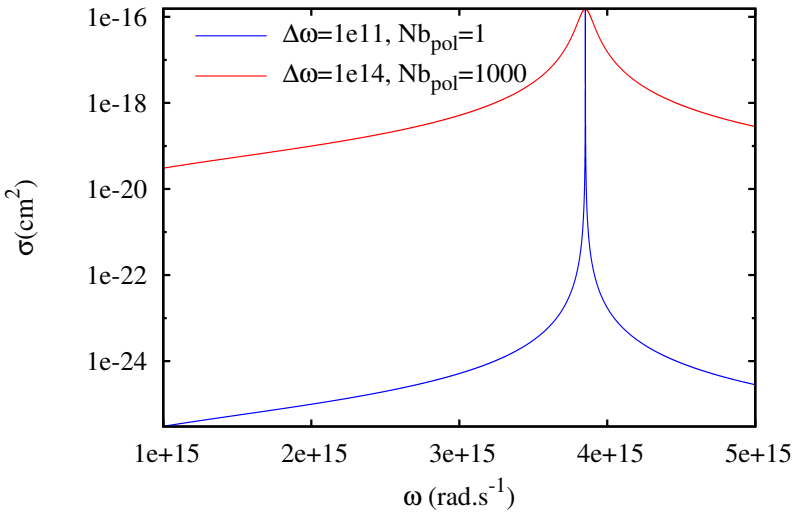

Fig. 4. Cross section as a function of the pulsation with a transition at 3.8×10^{15} rad.s^{-1}

4. Results

The present algorithm is applied to a waveguide composed of three layers as shown in Fig. 5. Finite difference frequency domain method (FDFD) proposed by Fallakhair et al [21] has been used to compute the electromagnetic mode profile. This eigenvalue problem of large sparse matrix has been solved using Fortran MUMPS library [22, 23]. The dimensions of the waveguide have been investigated so that the waveguide is monomode at the signal wavelength whereas obviously it is multimode at the pumping wavelength. We choose to inject the fundamental transverse electric (TE) mode related to the pumping field, in accordance with the experimental conditions. Moreover the FDTD algorithm was set up with the parameters reported in Table 1.

Table 1. FDTD algorithm parameters

Parameter	Δ	Δ_t	S_c	box length x	box length y	box length z
Value	50 nm	10^{-17} s	1	169Δ	321Δ	161Δ

With these parameters, the maximum physical phase velocity error is -1.68% and the maximum velocity-anisotropy error is 0.847% [2]. Since we propagate single modes at the same wavelength and the wavefront distortion is small with respect to the wavefront of modes, we assume that this numerical dispersion is negligible in the results and conclusion that we will present in the paper.

#194030 - $15.00 USD Received 22 Jul 2013; revised 16 Sep 2013; accepted 17 Sep 2013; published 2 Oct 2013

4.1. *Description of the waveguide*

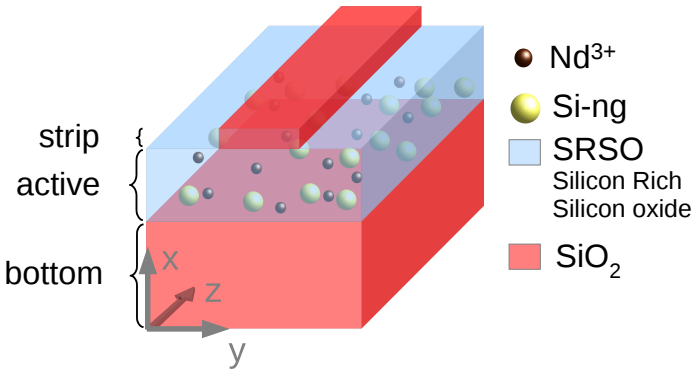

Fig. 5. General view of the waveguide constituted by a bottom and strip cladding layers of silica surrounding the active layer constituted by silicon rich silicon oxide (SRSO) matrix doped with silicon nanograins (Si-ng) and Nd^{3+} ions.

The bottom cladding layer is composed of pure silica with a thickness of 3.5 μm. The active layer constituted of Silicon Rich Silicon Oxide (SRSO) contains silicon nanograins (Si-ng) and rare earth ions with a thickness of 2μm. A pure silica strip layer is stacked on the top of the SRSO layer. The width of the strip is 2 μm and the thickness is 400 nm. The static refractive index of the active layer has been chosen greater (1.5) than the one of the strip and bottom cladding layers (1.448) to ensure the guiding conditions.

4.2. *Description of the active layer*

The SRSO active layer contains silicon nanograins (Si-ng) and Nd^{3+} that are modeled respectively by two levels and five levels systems as schematized in Fig. 6. The excitation

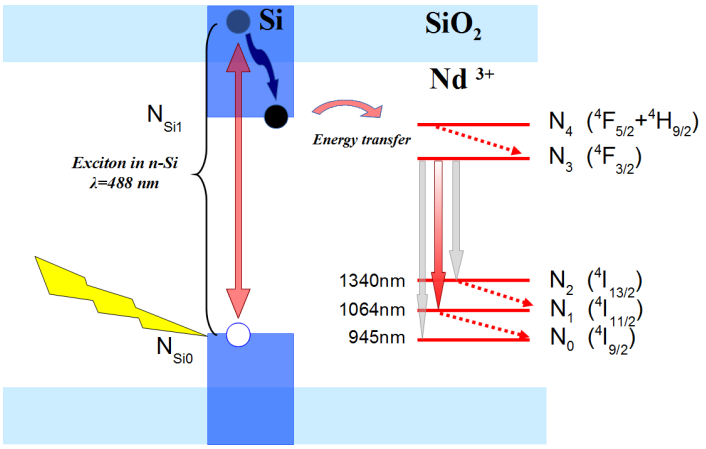

Fig. 6. Excitation mechanism of rare earth

mechanism of the Nd^{3+} ions is presented in Fig. 6. According to our experimental investigations [24] we pump the SRSO layer with an electromagnetic wave at 488 nm. The excitation mechanism leads to excitons generation in Si-ngs. Due to a low probability of multi-

exciton generation in a single Si-ng [25], we assume a single exciton per Si-ng and therefore the Si-ng population will correspond to the exciton population. After non-radiative de-excitations, the exciton energy corresponds to the gap between the Nd^{3+} levels N_0 ($^4I_{9/2}$) and N_4 ($^4F_{5/2} + {}^4H_{9/2}$). Exciton can either transfer its energy to the Nd^{3+} ions by dipole-dipole interaction and excites an electron from N_0 to N_4 or recombines radiatively or not to Si-ng ground level. After a fast non-radiative de-excitations from the level N_4 to the level N_3 ($^4F_{3/2}$), we consider only the following three radiative transitions (we neglect the $^4F_{3/2} \rightarrow {}^4I_{15/2}$ transition) : $N_3 \rightarrow N_0(^4F_{3/2} \rightarrow {}^4I_{9/2}, \lambda_{30} = 945nm)$, $N_3 \rightarrow N_1(^4F_{3/2} \rightarrow {}^4I_{11/2}, \lambda_{31} = 1064nm)$ and $N_3 \rightarrow N_2(^4F_{3/2} \rightarrow {}^4I_{13/2}, \lambda_{32} = 1340nm)$. De-excitations from level N_2 to level N_1 and from level N_1 to level N_0 are fast non-radiative transitions. Since the branching ratio of $N_3 \rightarrow N_1$ transition is high ($> 50\%$) and the probability of re-absorption by N_1 level is low, it is advantageous to use the $N_3 \rightarrow N_1(^4F_{3/2} \rightarrow {}^4I_{11/2})$ transition emitting at 1064 nm as a signal wavelength. We describe hereafter the full set of rate equations governing the levels populations.

Silicon nanograins We consider a two level system where N_{Si_0} and N_{Si_1} are respectively the ground level and excited level populations.

$$\frac{dN_{Si_1}(t)}{dt} = +\frac{1}{\hbar\omega_{Si_{10}}}\mathbf{E}(t)\frac{d\mathbf{P}_{Si_{10}}(t)}{dt} - \frac{N_{Si_1}(t)}{\tau_{Si_{10}}|_{nr}^{r}} - KN_{Si_1}(t)N_0(t) \tag{11}$$

$$\frac{dN_{Si_0}(t)}{dt} = -\frac{1}{\hbar\omega_{Si_{10}}}\mathbf{E}(t)\frac{d\mathbf{P}_{Si_{10}}(t)}{dt} + \frac{N_{Si_1}(t)}{\tau_{Si_{10}}|_{nr}^{r}} + KN_{Si_1}(t)N_0(t) \tag{12}$$

The term $\frac{1}{\hbar\omega_{Si_{10}}}\mathbf{E}(t)\frac{d\mathbf{P}_{Si_{10}}(t)}{dt}$ is the photon density rate. The transfer coefficient between silicon nanograins and rare earth ions K is chosen equal to 10^{-14} cm^3.s^{-1} according to Toccafondo et al. [18]. Based on Pacifici et al. [16], the decay time of the level N_{Si_1} including radiative and non-radiative recombinations is fixed at $\tau_{Si_{10}}|_{nr}^{r} = 50\ \mu s$. The Si-ng absorption cross section σ_{Si} is taken equal to 10^{-16} cm^2 [26]. From Eq. (10) this leads to a linewidth of $\Delta\omega_{Si} = 1.5 \times 10^{11}$ rad.s^{-1} with one polarization density($N_P = 1$). According to the discussion in sect. 3.2, in order to reduce the number of iterations, we choose a superposition of $N_p = 1000$ polarization densities with a linewidth of $\Delta\omega_{Si} = 1.5 \times 10^{14}$ rad.s^{-1} (see Table 2). The Si-ng concentration is fixed at 10^{19} cm^{-3}.

Neodymium ions The levels populations of Nd^{3+} are described by the following rate equations:

$$\frac{dN_4(t)}{dt} = -\frac{N_4(t)}{\tau_{43}|_{nr}} + KN_{Si_1}(t)N_0(t) \tag{13}$$

$$\begin{aligned}\frac{dN_3(t)}{dt} = &+\frac{1}{\hbar\omega_{30}}\mathbf{E}(t)\frac{d\mathbf{P}_{30}(t)}{dt} + \frac{1}{\hbar\omega_{31}}\mathbf{E}(t)\frac{d\mathbf{P}_{31}(t)}{dt} + \frac{1}{\hbar\omega_{32}}\mathbf{E}(t)\frac{d\mathbf{P}_{32}(t)}{dt} \\ &+\frac{N_4(t)}{\tau_{43}|_{nr}} - \frac{N_3(t)}{\tau_{30}|_{nr}^{r}} - \frac{N_3(t)}{\tau_{31}|_{nr}^{r}} - \frac{N_3(t)}{\tau_{32}|_{nr}^{r}}\end{aligned} \tag{14}$$

$$\frac{dN_2(t)}{dt} = -\frac{1}{\hbar\omega_{32}}\mathbf{E}(t)\frac{d\mathbf{P}_{32}(t)}{dt} + \frac{N_3(t)}{\tau_{32}|_{nr}^{r}} - \frac{N_2(t)}{\tau_{21}|_{nr}} \tag{15}$$

$$\frac{dN_1(t)}{dt} = -\frac{1}{\hbar\omega_{31}}\mathbf{E}(t)\frac{d\mathbf{P}_{31}(t)}{dt} + \frac{N_3(t)}{\tau_{31}|_{nr}^{r}} - \frac{N_1(t)}{\tau_{10}|_{nr}} + \frac{N_2(t)}{\tau_{21}|_{nr}} \tag{16}$$

#194030 - $15.00 USD Received 22 Jul 2013; revised 16 Sep 2013; accepted 17 Sep 2013; published 2 Oct 2013

7 October 2013 | Vol. 21, No. 20 | DOI:10.1364/OE.21.024171 | OPTICS EXPRESS 24180

$$\frac{dN_0(t)}{dt} = -\frac{1}{\hbar\omega_{30}}\mathbf{E}(t)\frac{d\mathbf{P}_{30}(t)}{dt} + \frac{N_3(t)}{\tau_{30}|_{nr}^{r}} + \frac{N_1(t)}{\tau_{10}|_{nr}} - KN_{Si_1}(t)N_0(t) \quad (17)$$

Similar to the case of silicon nanograins, we calculate the linewidth $\Delta\omega_{ij}$ for the different Nd^{3+} transitions by Eq. (10). Since in literature, depending of the host matrix [13], the emission cross section of Nd^{3+} at 1064 nm varies from 3×10^{-20}cm^2 to 4.6×10^{-19}cm^2, we choose to test two extreme values of Nd^{3+} ions emission cross section equal to $\sigma = 10^{-19}$ cm^2 and $\sigma = 10^{-20}$ cm^2. For each transition, the corresponding linewidth values are high enough with regard to the number of iterations to reach steady state with one polarization density ($N_P = 1$). All the parameters discussed here are gathered in tables 2 and 3. The concentration of Nd^{3+} is fixed at 10^{19} cm^3.

Table 2. Pulsation, linewidth and number of polarizations chosen of radiative transitions

Transition	Pulsation (rad.s^{-1})	Linewidth (rad.s^{-1})	Nb of polarizations
$N_{Si_1} \rightarrow N_{Si_0}$	$\omega_{Si_{10}} = 3.86\times10^{15}$	$\Delta\omega_{Si} = 1.5\times10^{14}$	1000
$N_3 \rightarrow N_2$	$\omega_{32} = 1.34\times10^{15}$	$\Delta\omega_{32} = 6.683\times10^{15}$	1
$N_3 \rightarrow N_1$	$\omega_{31} = 1.77\times10^{15}$	$\Delta\omega_{31} = 1.786\times10^{15}$ ($\sigma = 10^{-20}$ cm^2)	1
$N_3 \rightarrow N_1$	$\omega_{31} = 1.77\times10^{15}$	$\Delta\omega_{31} = 1.786\times10^{14}$ ($\sigma = 10^{-19}$ cm^2)	1
$N_3 \rightarrow N_0$	$\omega_{31} = 1.99\times10^{15}$	$\Delta\omega_{30} = 1.054\times10^{15}$	1

Table 3. Lifetimes of different transitions for Si-ng and Nd^{3+}

Transition	$N_{Si_1} \rightarrow N_{Si_0}$	$N_4 \rightarrow N_3$	$N_3 \rightarrow N_2$	$N_3 \rightarrow N_1$	$N_3 \rightarrow N_0$	$N_2 \rightarrow N_1$	$N_1 \rightarrow N_0$
Lifetime (μs)	50	230×10^{-6}	1000	200	250	970×10^{-6}	510×10^{-6}

4.3. Field map

Poynting vector ($\mathbf{R} = \mathbf{E}\times\mathbf{H}$) expressed in W.mm^{-2} has been calculated from electromagnetic field ($\mathbf{E}$, $\mathbf{H}$) compute by ADE-FDTD method. After a time Fourier transform of $\mathbf{R}(t)$, we determine the main z component of the pump (488nm) and signal (1064nm) intensities of $\mathbf{R}$ in longitudinal section view [Fig. 7]. We can notice that, for both wavelengths, the electromagnetic field is well guided within the SRSO active layer of the waveguide. Due to the absorption at 488 nm by the silicon nanograins, a decrease of the pump intensity $R_{z,pump}$ along the waveguide is observed. However, the signal intensity $R_{z,signal}$ at 1064 nm does not appear absorbed over the 7μm length of the waveguide.

Figure 8 shows a transverse view of the $R_{z,pump}$ (left) and $R_{z,signal}$ (right) in the center of the active layer. We can notice that both pump and signal wavelengths are well guided all along the waveguide.

4.4. Population map

The ADE-FDTD method allows to compute tridimensional population distributions in different states. We present the population ratio distributions in the waveguide in a longitudinal section view along the propagation axis in the Fig. 9. On the left, the ratio between the excited level population (N_{Si_1}) and the total number of Si-ng ($N_{Si} = N_{Si_0} + N_{Si_1}$) and, on the right, the ratio between the level population N_3 and the total number of Nd^{3+} ions for a pump power equal to 10^3 mW.mm^{-2}. The maximum percentage of the excited Si-ng is 10%, and the maximum percentage of the excited Nd^{3+} is 50%. With a transfer coefficient taken K is equal to 0, the

#194030 - $15.00 USD Received 22 Jul 2013; revised 16 Sep 2013; accepted 17 Sep 2013; published 2 Oct 2013

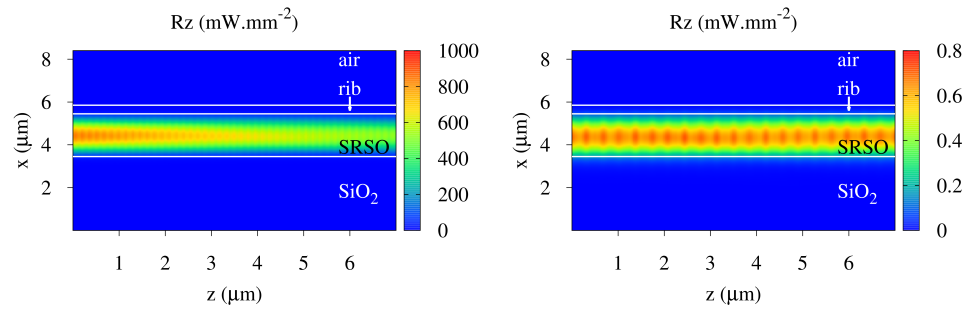

Fig. 7. Longitudinal section view of Z-component of the Poynting vector of the pump (on the left) and of the signal (on the right). The pump ($\lambda_s = 488$ nm) and the signal ($\lambda_p = 1064$ nm) power injected are respectively 1 W.mm^{-2} and 1 mW.mm^{-2}

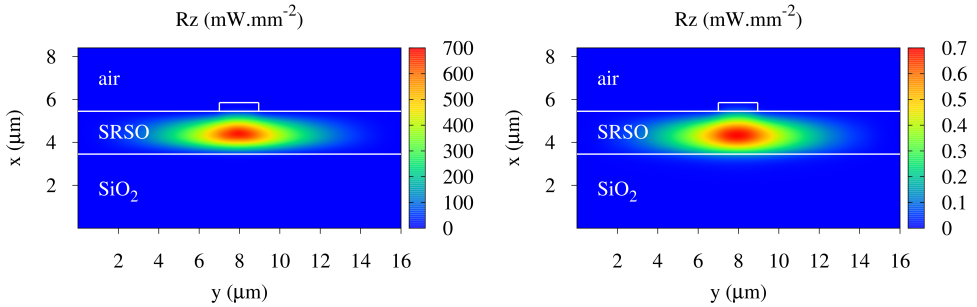

Fig. 8. Transverse section view of Z-component of the Poynting vector of the pump (on the left) and of the signal (on the right) in the middle of the waveguide. The pump ($\lambda_s = 488$ nm) and the signal ($\lambda_p = 1064$ nm) power injected are respectively 1 W.mm^{-2} and 1 mW.mm^{-2}

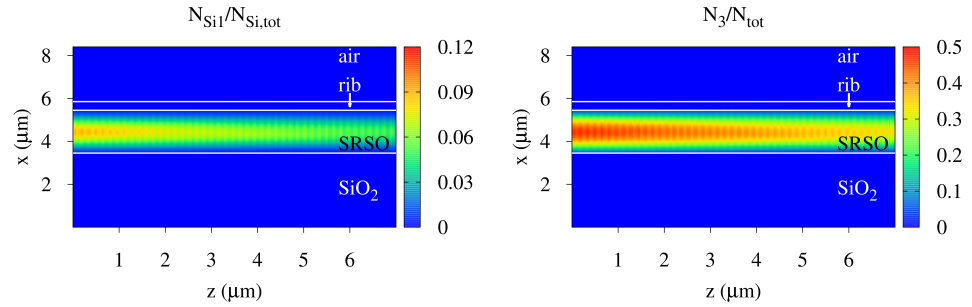

Fig. 9. Longitudinal section view of $N^*_{Si}/N_{Si_{tot}}$ (on the left) and N_3/N_{tot} (on the right)

percentage of the excited Nd^{3+} is close to 0%. This confirms the major role of energy transfer in the exciting process of neodymium ions.

The decreasing profile $N_{Si_1}(z)$ of the excited Si-ng is consistent with the pump profile $R_{z,pump}(z)$ decrease in Fig. 7 due to the absorption of the pump field by the Si-ng. Hence, the excited level population N_3 decreases by 30 % over the 7 μm length of the waveguide. This imply that co-propagation pumping scheme is not a good method in order to reach a uniformly pump longer waveguide. A top pumping configuration along the waveguide length would prob-

#194030 - $15.00 USD Received 22 Jul 2013; revised 16 Sep 2013; accepted 17 Sep 2013; published 2 Oct 2013

ably lead to a more uniformly pumped active layer but is not the purpose of the present paper.

4.5. *Calculation of the gain*

From population distributions, we calculate the gross gain of the transition of our interest $N_3 \rightarrow N_1(^4F_{3/2} \rightarrow ^4I_{11/2}, \lambda_{31} = 1064nm)$. The local gross gain per unit length at 1064 nm is given by:

$$g_{\mathrm{dB.cm}^{-1}}(x,y,z) = \frac{10}{\ln 10}\left(\sigma_{em}N_3(x,y,z) - \sigma_{abs}N_1(x,y,z)\right)) \tag{18}$$

where σ_{abs} and σ_{em} are respectively the absorption and the emission cross sections. Due to the short decay lifetime (τ_{10}) from level 1 to the ground level 0, we observe that: $N_1 \ll N_3$. Moreover, we consider that σ_{em} is comparable to σ_{abs} thus Eq. (18) becomes:

$$g_{\mathrm{dB.cm}^{-1}}(x,y,z) \simeq \frac{10}{\ln 10}\left(\sigma_{em}N_3(x,y,z)\right) \tag{19}$$

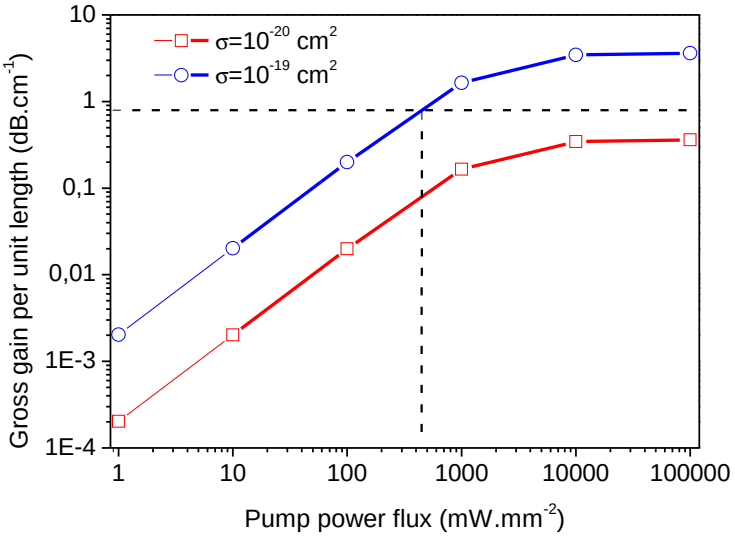

Fig. 10. Local gross gain per unit length at the center of the active layer as a function of the pumping power, (horizontal dashed line) Losses of 0.8 dB.cm^{-1} found by Pirastesh et al [27].

For two extreme values of the emission cross section ($\sigma_{em} = 10^{-20}$ cm^2 and $\sigma_{em} = 10^{-19}$ cm^2), we calculate the local gross gain per unit length versus different values of pump intensity in Fig. 10 at the point (x_c, y_c, z_c), where x_c, y_c are the coordinates of the center of the active layer and z_c is the middle of the waveguide. We can notice that the local gross gain per unit length saturates for pumping powers higher than 10^5 mW.mm^{-2} and reach 0.36 dB.cm^{-1} for $\sigma_{em} = 10^{-20}$ cm^2 and 3.6 dB.cm^{-1} for $\sigma_{em} = 10^{-19}$ cm^2 respectively. In a similar waveguide, Pirasteh et al [27] determined experimentally losses equal to $\alpha = 0.8$ dB.cm^{-1}, represented by a horizontal dashed line on Fig. 10. For the lower emission cross section $\sigma_{em} = 10^{-20}$ cm^2 the local gross gain cannot compensate the experimentally determined losses of 0.8 dB cm^{-1}. For the highest emission cross section $\sigma_{em} = 10^{-19}$ cm^2, it is necessary to pump the waveguide with power higher than a threshold value of 450 mW.mm^{-2} to obtain internal net gain. By linear extrapolation and with a high pump power equal to 10^5 mW.mm^{-2} we can estimate a

#194030 - $15.00 USD Received 22 Jul 2013; revised 16 Sep 2013; accepted 17 Sep 2013; published 2 Oct 2013

threshold value of cross section $\sigma_{em} = 2.2 \times 10^{-20}$ cm^2 at which positive internal net gain is reached. Despite, more accurate measurement of the emission cross section will lead to better estimation of the possible internal net gain with such a waveguide. This study shows that to increase the gain, several ways may be explore: (i) An increase of the neodymium and Si-ng concentration may lead to higher gain, however some limits to concentration may occurs above some 10^{20} dopants.cm^{-3}(ii) An increase of the coupling efficiency or of the fraction of excited rare earth may lead to higher gain (iii) A top pumping configuration may result in a more uniformly pumped active layer and consequently in more uniform distribution of gain along the waveguide length. These will be the object of further experimental and theoretical studies.

5. Conclusion

A new algorithm based on ADE-FDTD method has been presented that allow to describe the spatial distribution of the eletromagnetic field and levels population in steady state in an active optical waveguide. The multi-scale times issue of such a system has been overcome by the development of this algorithm leading a drastic reduction of number of iterations to reach steady states values of fields and levels population (from 10^{15} to 10^5 iterations). Moreover, we proposed a method to calibrate the $i \rightarrow j$ transition linewidth $\Delta\omega_{ij}$ according to the experimental absorption cross section, making a possible comparison between experimental and theoretical studies. We apply our new algorithm to a strip loaded waveguide whose active layer is constituted of a silicon rich silicon oxide (SRSO) layer doped with silicon nanograin and neodymium ions. Using physical parameters such as absorption cross section ranging from 10^{-20} cm^2 to 10^{-19} cm^2 and concentrations in accordance with the literature, we found a gross gain ranging from 0.36 dB.cm^{-1} to 3.6 dB.cm^{-1}, based on experimental losses we found a threshold pump power value of 450 mW.mm^{-2} necessary to have a positive net gain. We would like to emphasize the point that the method developed here is generalizable to other systems presenting very different characteristic times resulting in a drastic reduction of the calculation time for reaching steady states.

Acknowledgments

The authors are grateful to the French Nation Research Agency, which supported this work through the Nanoscience and Nanotechnology program (DAPHNES project ANR-08-NANO-005).

#194030 - $15.00 USD Received 22 Jul 2013; revised 16 Sep 2013; accepted 17 Sep 2013; published 2 Oct 2013

Sensitization of Er3+ Infrared Photoluminescence Embedded in a Hybrid Organic–Inorganic Copolymer containing Octahedral Molybdenum Clusters

ARTICLE *in* ADVANCED FUNCTIONAL MATERIALS · APRIL 2013

Impact Factor: 11.81 · DOI: 10.1002/adfm.201300417

4 AUTHORS, INCLUDING:

Yann Molard
Université de Rennes 1
81 PUBLICATIONS **711** CITATIONS
SEE PROFILE

Julien Cardin
Université de Caen Basse-Normandie
67 PUBLICATIONS **265** CITATIONS
SEE PROFILE

Stéphane Cordier
Université de Rennes 1
180 PUBLICATIONS **1,269** CITATIONS
SEE PROFILE

ADVANCED FUNCTIONAL MATERIALS
www.afm-journal.de

Sensitization of Er^{3+} Infrared Photoluminescence Embedded in a Hybrid Organic-Inorganic Copolymer containing Octahedral Molybdenum Clusters

Yann Molard, Christophe Labbé, Julien Cardin, and Stéphane Cordier*

Luminescent hybrid copolymers are obtained by copolymerizing in bulk methylmethacrylate with a methacrylic acid (MAC) solution containing $[n\text{-}Bu_4N]_2[Mo_6Br_8(MAC)_6]$, and aliquots of an $Er(TMHD)_3$ complex (TMHD for 2,2,6,6-tetramethyl-3,5-heptanedione) solution. This leads to novel homogeneous and transparent hybrid materials in which the Er^{3+} infrared luminescence at 1.55 μm, a standard wavelength for telecommunication applications, is up to six time more intense in the presence of Mo_6 clusters when samples are irradiated at 476.5 nm. This work demonstrates the outstanding potential of Mo_6 clusters, compounds obtained by high-temperature solid-state synthesis, in the design of functional hybrid materials via soft chemistry routes.

1. Introduction

As the needs for both information throughput and user densities are constantly increasing, significant efforts have to be devoted toward the design of innovative, robust, and cost-effective transmission systems able to rapidly transport information between users. So far the *C*-band (1530–1565 nm) has been the standard wavelength in telecommunication applications owing to its very favorable attenuation (0.2 dB km^{-1}) in optical fibers.[1] Trivalent rare-earth ions, such as erbium, which is able to emit at 1550 nm (4f–4f transitions), are elements of major importance in optical telecommunication technologies.[2] In particular, Er^{3+} doped silica-based fiber amplifiers (EDFA) and Er^{3+} doped silica-based waveguide amplifiers (EDWA) compensating for the dispersion of the working optical signal centered around 1550 nm have emerged as key devices for telecommunication applications due to their high (photo)chemical and thermal stability.[3] However, further extension of the scope of such materials is now limited by the high cost of their multiple-step preparation and their very small absorption cross-sections, leading to inefficient emission from the rare earth 4f levels under direct excitation. One strategy to overcome the limitation of this class of materials is the design of organic/inorganic polymer-based devices. In this frame, Slooff et al.[4] and Kuriki et al.[5] pointed out that, beside improving production cost, fabrication processing, and generating polymers which possess high mechanical and thermal stability, special attention should be drawn to improving the fluorescence of lanthanide ions. Two approaches can be developed to meet these needs: the first one consists of the coordination of highly absorbing organic antenna groups around the rare earth trivalent cation to increase the pump efficiency, while the second involves using a SiO_2 matrix as host for rare-earth ions. This last strategy can be achieved by introducing Er^{3+}-doped silica colloidal spheres in organic polymers. A severe limitation to the first approach is that organic antennas are highly sensitive to premature aging under irradiation, whereas the second approach is negatively impacted by the fact that an efficient rare-earth cross-section absorption in the colloid cannot be obtained without sensitizers.

We propose in this manuscript an alternative and innovative approach to obtain an easily processable material containing Er^{3+} and having luminescence which is sensitized by phosphorescent octahedral metal atom clusters incorporated in a host organic matrix.

Metal atom clusters are inorganic molecular species obtained via solid-state chemistry routes containing metal atoms linked together by metal–metal bonds. Many routes[6] now afford soluble discrete $[M_6Q^i{}_8X^a{}_6]^{2-}$ units (X = halogen) that exhibit, either in the liquid or solid state, specific electronic, magnetic, and photophysical properties related to the number of metallic electrons available for metal–metal bonds.[7] In particular, they are highly emissive in the red–near infrared (NIR) region, have photoluminescence quantum yields of up to 0.23, and display long excited-state lifetimes.[8] Owing to the stronger covalent nature of the M–Q^i bond relative to the M–X^a one, halogen apical atoms can be replaced by inorganic or organic ligands without any alteration of the $(M_6Q^i{}_8)^{m+}$ core, leading to functional building blocks usable for the design of liquid crystalline material,[9] supramolecular architectures,[10] polymeric frameworks,[11] or nanomaterials[12] with unique properties. In order to obtain M_6 clusters containing material suitable for realistic applications, we incorporated them in a poly(methyl methacrylate) (PMMA) matrix

Dr. Y. Molard, Dr. S. Cordier
UMR, Institut des Sciences Chimiques de Rennes
UR1-CNRS 6226, Université de Rennes 1
Campus de Beaulieu, CS 74205, F-35042
Rennes Cedex, France
E-mail: yann.molard@univ-rennes1.fr
Dr. C. Labbé, Dr. J. Cardin
Université de Caen
Centre de Recherche sur les Ions
les Matériaux et la Photonique (CIMAP)
ENSICAEN, CNRS, CEA/IRAMIS, 14050 CAEN cedex, France

DOI: 10.1002/adfm.201300417

and investigated the optical properties of the resulting hybrid material. PMMA was chosen for its excellent optical properties (i.e., transparency from the near-UV to the near-IR regions), damage resistance in the range needed for optical applications, good mechanical properties, thermal stability, and easy shaping. A major challenge in the preparation of such hybrid materials is the prevention of phase separation and aggregation of the inorganic species in the host matrix. A few examples are found in the literature where polymers showing stable luminescence properties are obtained by incorporation of octahedral clusters. Shriver et al.[13] coordinated $[Mo_6Cl_8(OTf)_6]^{2-}$ and $[Mo_6Cl_8{}^{i}Cl_4{}^{a}(EtOH)^{a}{}_2]$ to poly(vinylpyridine) (PVP) to produce crosslinked materials. Transient emission spectroscopy revealed that polymer bound hexatriflate cluster lacks the luminescence properties characteristic of many $[Mo_6Cl_8]^{4+}$ -based clusters while the other one displays luminescence. A similar result was obtained by Jackson et al.[11b] who showed that the PVP-Mo_6Cl_{12} system could be employed for oxygen sensing or photo-oxidation applications. Here, we develop a simple technique for the synthesis of transparent PMMA-Mo_6 hybrids with stable luminescence properties, and their analogues containing Er^{3+} complexes. We demonstrate for the first time an effective transfer between transition metal clusters and Er^{3+} complexes within the polymer that will allow the development of new families of optical amplifiers using low-cost excitation sources.

2. Results and Discussion

The choice of Mo_6 clusters was driven by their superior luminescence properties, in terms of quantum yield, as compared to their Re_6 analogues.[8b,14] The synthetic approach is based on our recent studies developed for the design of clustomesogen[9a,9b] and on the solvent as monomer approach described by Golden et al.[11a] It consists of the preparation of a mother liquor containing a $[n\text{-}Bu_4N]_2[Mo_6Br_8F_6]$ cluster precursor and methacrylic acid, aliquots of which are mixed with methylmethacrylate (MMA) and subsequently copolymerized by a radical process using AIBN (0.02 wt%) as initiator. Several samples containing from 0 to 0.36 wt% of cluster (Ref_1, A1-5) were synthesized by this bulk polymerization process. The full dissolution of $[n\text{-}Bu_4N]_2[Mo_6Br_8F_6]$ in methacrylic acid is obtained by a gentle heating of the mixture, giving a high-concentration cluster mother solution ($c = 0.015$ M). ^{19}F NMR in d^6-acetone of this solution revealed the complete disappearance of the signal assigned to the starting cluster located around −188 ppm. Thus, heating the cluster mother solution induces an acid–base reaction between methacrylic acid molecules and the fluorinated clusters, leading to grafting in the apical position and, via covalent Mo–O bond formation, six methacrylate moieties with liberation of HF.[9a,9b] As shown in **Figure 1**, the resulting hybrid polymers are fully optically transparent materials, indicating the absence of macroscopic segregation of the inorganic moieties in the organic matrices. Note that this segregation was observed when $[n\text{-}Bu_4N]_2[Mo_6Br_{14}]$ was used instead of $[n\text{-}Bu_4N]_2[Mo_6Br_8F_6]$, meaning that strong interactions (in our case a covalent linking) between clusters and the organic matrix are mandatory to prevent phase separation.

Figure 1. Digital photographs of the Mo_6-PMMA hybrid copolymer pellets under visible (top) and UV light (bottom); $\lambda_{exc} = 365$ nm; cluster concentrations range from 0 to 0.36 wt% from left to right.

The hybrid materials thermal behavior was examined by thermogravimetric analysis (TGA) and differential scanning calorimetry (DSC) under N_2 atmosphere. Size exclusion chromatography (SEC) was also used to further characterize the doped polymers (see the Supporting Information, Figures S1–3). **Table 1** summarizes the thermal data and molecular weight calculations obtained by these techniques for all samples. While the obtained pure PMMA has a glass transition temperature (T_g) comparable to that of commercial PMMA, the introduction of small amounts of clusters drops it dramatically. This phenomenon is attributed to a plasticizing effect induced by an increase in the distance between the polymer chains.[15] By increasing the cluster amount within the copolymer, the T_g and M_w increase, showing that the clusters are covalently linked to the polymer strands and act as cross-linking agents. Moreover, if pure PMMA and pellets from A1 to A3 were completely soluble in tetrahydrofuran (THF), pellet A4 could not be entirely dissolved while pellet A5 was not soluble and started

Table 1. Thermal data for copolymer samples.

	Amount of cluster [wt%]	[Cluster] [molecules cm^{-3}]	T_g [°C][a)]	T_d [°C][b)]	M_w [g mol^{-1}][c)]
Ref_1	0	0	123.8	377	495 000
A1	0.018	0.56×10^{17}	92.5	387	705 500
A2	0.044	1.36×10^{17}	100.8	391	981 000
A3	0.09	2.79×10^{17}	123.6	395	987 000
A4	0.18	5.57×10^{17}	110.5	400	456 500
A5	0.36	11.14×10^{17}	109.5	412	–

[a)]Glass transition temperature; [b)]decomposition temperature; [c)]average molecular weight.

Adv. Funct. Mater. **2013**,
DOI: 10.1002/adfm.201300417

to swell in this solvent, confirming the clusters cross-linking ability as well as the chemical stability of the cluster–polymer bonds in solution.

The influence of the cluster concentration on the Mo_6-PMMA copolymer thermal stability was studied by comparing the degradation temperatures of all samples under N_2 atmosphere (see the Supporting Information for TGA and differential thermal analysis (DTA) thermograms). A small weight loss (<2.5%) starting around 80 °C due to the evaporation of unreacted monomers was observed for all samples, meaning that the polymerization process is not complete under our conditions. This point is corroborated by the detection of traces of monomers during the SEC experiments (see the Supporting Information). The main reaction stage corresponding to the maximum weight loss is located at 377 °C for pure PMMA. This maximum is shifted to higher temperature for higher cluster content, showing that the thermal stability of hybrid copolymers is significantly improved as compared to pure PMMA and evidencing once again the cross-linking ability of the modified cluster as well as its stability within the polymer matrix.

Optical properties determinations were investigated directly on the 5 mm thick copolymer pellets. Transmittance measurements (see the Supporting Information) showed the typical cut off of PMMA in the UV region under 300 nm, while the doped polymer pellets transmittance spectra revealed a shoulder around 400 nm increasing with the cluster amount present in the pellets (Supporting Information, Figure S4a). Luminescence measurements were realized in the solid state directly on the doped polymer pellets and revealed the apparition of a broad and structure-less emission band extending from 560 to more than 900 nm and centered around λ_{em} = 710 nm (Supporting Information, Figure S4b). For all pellets, the emission maximum is slightly shifted to lower wavelength ($\Delta\lambda$ = 35 nm) when compared to the $[n\text{-}Bu_4N]_2[Mo_6Br_8F_6]$ emission spectrum, as observed in a previous case when carboxylate derivatives were grafted on the six apical positions of the inorganic core.[9a] A luminescence absolute quantum yield of 0.15 at λ_{exc} = 360 nm was calculated by using a Hamamatsu Quantaurus-QY system, which is nearly double the previous reported value for M_6 clusters embedded in a PMMA matrix.[11d] At this stage we must emphasize that these properties are kept after 72 months of aging, attesting to the outstanding stability of the copolymer that is a prerequisite for the design of functional devices, and validating our approach.

Taking into consideration that stability and processability of the hybrid copolymers are prerequisites for the design of optical amplifiers, we synthesized Er^{3+}-Mo_6-PMMA materials containing various amount of Er^{3+} complexes (0.5, 0.90, or 1.3 wt%) with (P_{xC}) or without (P_x) 0.25 wt% of clusters. Several samples were thus prepared, using the same bulk copolymerization process as previously described but adding aliquots of a concentrated dichloromethane solution of $Er(TMHD)_3$ complex (TMHD for 2,2,6,6-tetramethyl-3,5-heptanedione) in the monomer mixtures prior to copolymerization. A pellet of pure PMMA (Ref_2) was also synthesized for comparison purposes. Compositions of prepared samples are summarized in **Table 2**.

TGA measurements (see the Supporting Information) showed that the integration of Er complexes has little influence on the copolymer samples' thermal stability. Indeed, only weak

Table 2. Summary of the prepared copolymer samples composition.

	Er^{3+} [wt%]	[Er^{3+}][molecules cm^{-3}]	Clusters [wt%]	[Cluster] [molecules cm^{-3}]	T_d [°C]
$P_{0.5}$	0.50	4.2×10^{18}	0	0	390
$P_{0.9}$	0.90	7.1×10^{18}	0	0	390
$P_{1.3}$	1.30	10.1×10^{18}	0	0	390
$P_{0.5C}$	0.50	4.2×10^{18}	0.25	7.74×10^{17}	410
$P_{0.9C}$	0.90	7.1×10^{18}	0.25	7.74×10^{17}	410
$P_{1.3C}$	1.30	10.1×10^{18}	0.25	7.74×10^{17}	410
Ref_2	0	0	0	0	380

interactions exist between the Er^{3+} complexes and the organic matrix whereas clusters are covalently bonded to PMMA. Therefore Er^{3+} -containing polymers keep the processability of PMMA.

Optical properties were measured in this case on 1.90 ± 0.03 mm thick pellets (**Figure 2** shows pellets $P_{1.3}$, $P_{0.5C}$, and $P_{1.3C}$ under normal and UV light). At first sight, one can notice a difference in the red luminescence upon UV excitation of $P_{0.5C}$ and $P_{1.3C}$ pellets, illustrating the influence of Er^{3+} content on the visible emission properties of Mo_6 clusters.

Figure 3 presents absorption spectra of pure PMMA, Er^{3+} containing, and, Er^{3+} and Mo_6 cluster-containing samples. If these pellets have similar absorption behaviours in the IR and NIR area, they keep the particularities of their individual components in the UV-vis region. Emission measurements were realized at room temperature using an Argon Laser as the excitation source with a 476.5 nm irradiation wavelength. Thought this wavelength is not the optimum one to observe an intense cluster luminescence. It was chosen because it overlaps only very weakly with Er^{3+} absorption bands.

As depicted in **Figure 4**a, irradiation of P_x pellets induces a very weak and broad emission with a maximum centered around 1530 nm characteristic of the $^4I_{13/2} \rightarrow {}^4I_{15/2}$ Er^{3+} transition. This emission could either be due to a weak absorption of the excitation wavelength by the $^4I_{15/2} \rightarrow {}^4F_{7/2}$ transition located

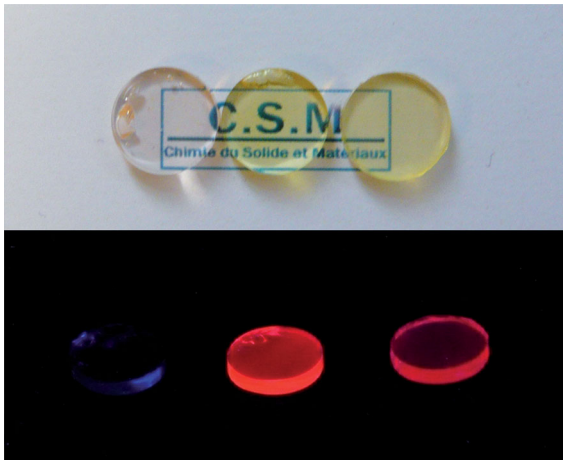

Figure 2. Digital photographs of hybrid copolymer pellets $P_{1.3}$, $P_{0.5C}$, and $P_{1.3C}$ under visible (top) and UV (λ_{exc} = 365 nm) irradiation (bottom).

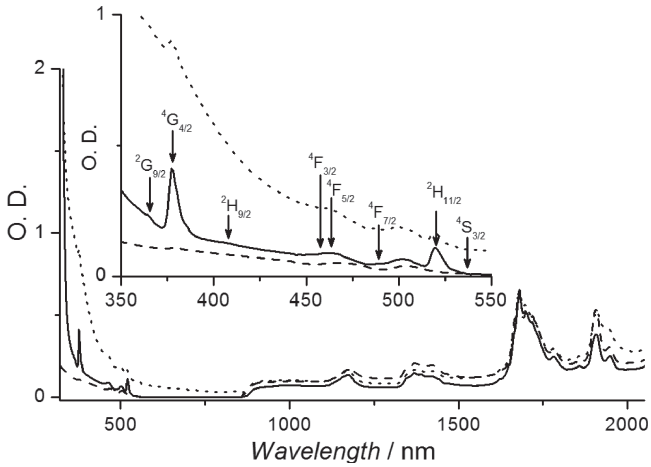

Figure 3. Solid state absorption spectra of $P_{1.3}$ (plain line), $P_{1.3C}$ (dotted line), and Ref_2 (dashed line) pellets.

around 483 nm or by an energy transfer from the organic matrix to the Er^{3+} ion.[16] The broadening of the emission is associated to the coupling of f–f electronic transition of erbium with vibrational modes of the PMMA matrix.

One can notice that if the observed emission intensities seem proportional to the Er^{3+} content in $P_{0.5}$ and $P_{0.9}$, $P_{1.3}$ emits approximately the same amount of photons as $P_{0.9}$. As our Er^{3+} working concentration is low compared to previous reported results, we attribute this phenomenon to a self aggregation process of Er^{3+} complexes within the host matrix instead of some quenching phenomena induced by cooperative up-conversion and resonant energy transfer which should occur for higher concentrations.[17] It confirms the existence of an optimum concentration of Er^{3+} complexes within the polymer matrix that was not determined in the scope of these investigations. Figures 4c,d represent the emission spectra of P_{xC} pellets either in the visible (4c) or IR (4d) area. Increasing the Er^{3+} complex concentration induces a decrease of the cluster emission together with a large increase of Er^{3+} complex in the IR region, showing the existence of an effective transfer between the two species. This phenomenon is best seen on Figure 4b, where the IR Er^{3+} complex emissions without ($P_{1.3}$) or with ($P_{1.3C}$) cluster are superimposed. Indeed the emission in the IR is enhanced because of cluster Er^{3+} sensitization. This sensitization allows an emission improvement by a factor 4 to 6 depending on the samples (inset Figure 4b). Even though this improvement is still weak for application purposes, it demonstrates for the first time the possibility to sensitize IR emission of trivalent rare-earth metal complexes with transition metal clusters within a transparent and easily processable organic matrix.

3. Conclusions

We have described in this manuscript a simple method to obtain Mo_6-PMMA copolymer samples within which Mo_6 clusters keep their intrinsic luminescence properties. These emissive properties have been used successfully to sensitize trivalent Er^{3+} complex emission in the infrared region and within the polymer matrix. Indeed, introduction of 0.25 wt% of metallic

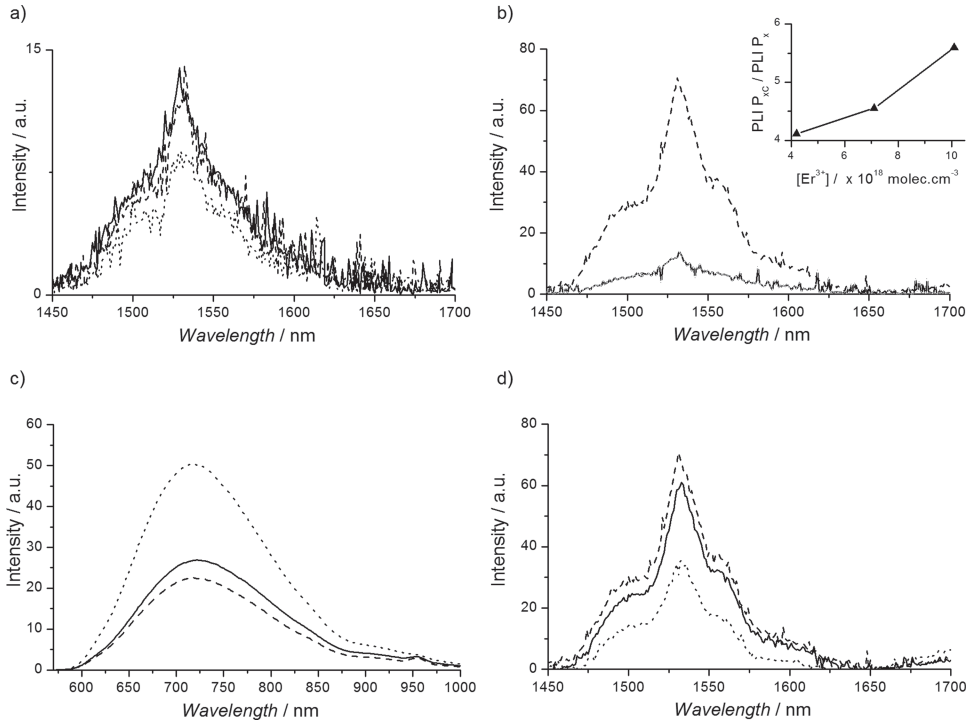

Figure 4. Solid state luminescence properties at 25 °C upon excitation at λ_{exc} = 476.5 nm of: a) pellets $P_{0.5}$ (dotted line), $P_{0.9}$ (solid line), and $P_{1.3}$ (dashed line); b) pellets $P_{1.3}$ (solid line) and $P_{1.3C}$ (dotted line) (inset: photoluminescence intensity ratio between P_{xC} and P_x samples); c,d) pellets $P_{0.5C}$ (dotted line), $P_{0.9C}$ (solid line), and $P_{1.3C}$ (dashed line).

Adv. Funct. Mater. 2013,
DOI: 10.1002/adfm.201300417

cluster induces increases by factors from 4 to 6 of the Er^{3+} transition at 1.5 µm wavelength, thus validating the concept of trivalent rare-earth metal infrared luminescence sensitization by transition metal clusters. Although further investigations are ongoing to maximize this sensitization, this first study offers promising perspectives in the design of easy-to-handle Er^{3+} -containing materials suitable for excitation using cheap optical illumination systems directed towards telecom applications.

4. Experimental Section

Starting materials were purchased from Alfa Aesar or Aldrich. Methacrylic acid and methyl methacrylate were distilled before use. Azobisizobutyronitryle (AIBN) was purified via recrystallization in ether prior to use. (*n*-Bu4N)2[Mo6Br8F6] precursor was obtained by a procedure reported elsewhere.[18] The full dissolution of [n-Bu4N]2[Mo6Br8F6] in methacrylic acid was obtained by a gentle heating of the mixture, giving a high-concentration cluster solution ($c = 0.015$ M).

A Series: Aliquots of the cluster mother liquor and methyl methacrylate monomers were poured into a test tube to give a mixture weighing 1.5 g. After addition of the radical initiator (AIBN, 0.02 wt%), the homogeneous solution was kept at 60 °C in an ultrasonic bath for 3 h and allowed to stand at 60 °C for 72 h.

Px and PxC Series: Er(TMHD)3 complex (TMHD for 2,2,6,6-tetramethyl-3,5-heptanedione; 10, 17, or 24 mg) was placed in a sample tube and solubilized with a few drops of distilled CH_2Cl_2. Methyl methacrylate, clusters dissolved in methacrylic acid, and AIBN (0.02 wt%) were added to the test tubes to reach a total weight of 2 g. The homogeneous solutions were kept at 60 °C in an ultrasonic bath for 3 h and allowed to stand at 60 °C for 72 h.

Supporting Information

Supporting Information is available from the Wiley Online Library or from the author.

Acknowledgements

The authors thank Dr. R. Rizk from CIMAP Caen for useful discussions and Dr. Jocelyne Galy From LIMP UMR CNRS 5223 Insa Lyon for SEC measurements. This work was financially supported by the Fondation Langlois and GDR2975-C'Nano Nord Ouest.

Received: February 1, 2013
Published online:

[1] R. Noé, *Essentials of Modern Optical Fiber Communication*, Springer, Berlin/Heidelberg **2010**.
[2] K. Binnemans, *Chem. Rev.* **2009**, *109*, 4283.
[3] a) D. Bayart, *C. R. Phys.* **2003**, *4*, 65; b) S. Frolov, S. Tek-Ming, A. J. Bruce, *Proc. SPIE* **2003**, *47*, 4990.
[4] L. H. Slooff, A. van Blaaderen, A. Polman, G. A. Hebbink, S. I. Klink, F. C. J. M. Van Veggel, D. N. Reinhoudt, J. W. Hofstraat, *J. Appl. Phys.* **2002**, *91*, 3955.
[5] K. Kuriki, Y. Koike, Y. Okamoto, *Chem. Rev.* **2002**, *102*, 2347.
[6] a) J. R. Long, L. S. McCarty, R. H. Holm, *J. Am. Chem. Soc.* **1996**, *118*, 4603; b) K. Kirakci, S. Cordier, C. Perrin, Z. Anorg. *Allg. Chem.* **2005**, *631*, 411.
[7] a) R. Chevrel, M. Sergent, in *Topics in Current Physics* (Eds.: O. Fischer, M. P. Maple), Springer Verlag, Berlin, **1982**; b) D. G. Nocera, H. B. Gray, *J. Am. Chem. Soc.* **1984**, *106*, 824; c) J. M. Tarascon, F. J. Disalvo, D. W. Murphy, G. W. Hull, E. A. Rietman, J. V. Waszczak, *J. Solid State Chem.* **1984**, *54*, 204.
[8] a) A. W. Maverick, H. B. Gray, *J. Am. Chem. Soc.* **1981**, *103*, 1298; b) A. W. Maverick, J. S. Najdzionek, D. MacKenzie, D. G. Nocera, H. B. Gray, *J. Am. Chem. Soc.* **1983**, *105*, 1878.
[9] a) Y. Molard, F. Dorson, V. Circu, T. Roisnel, F. Artzner, S. Cordier, *Angew. Chem., Int. Ed.* **2010**, *49*, 3351; b) A. S. Mocanu, M. Amela-Cortes, Y. Molard, V. Circu, S. Cordier, *Chem. Commun.* **2011**, *47*, 2056; c) Y. Molard, A. Ledneva, M. Amela-Cortes, V. Circu, N. G. Naumov, C. Meriadec, F. Artzner, S. Cordier, *Chem. Mater.* **2011**, *23*, 5122.
[10] a) Z. N. Chen, T. Yoshimura, M. Abe, Y. Sasaki, S. Ishizaka, H. B. Kim, N. Kitamura, *Angew. Chem., Int. Ed.* **2001**, *40*, 239; b) H. D. Selby, B. K. Roland, Z. Zheng, *Acc. Chem. Res.* **2003**, *36*, 933; c) D. Mery, C. Ornelas, M.-C. Daniel, J. Ruiz, J. Rodrigues, D. Astruc, S. Cordier, K. Kirakci, C. Perrin, *C. R. Chim.* **2005**, *8*, 1789; d) G. Prabusankar, Y. Molard, S. Cordier, S. Golhen, Y. Le Gal, C. Perrin, L. Ouahab, S. Kahlal, J. F. Halet, *Eur. J. Inorg. Chem.* **2009**, 2153; e) F. Dorson, Y. Molard, S. Cordier, B. Fabre, O. Efremova, D. Rondeau, Y. Mironov, V. Circu, N. Naumov, C. Perrin, *Dalton Trans.* **2009**, 1297.
[11] a) J. H. Golden, H. B. Deng, F. J. Disalvo, J. M. J. Frechet, P. M. Thompson, *Science* **1995**, *268*, 1463; b) J. A. Jackson, M. D. Newsham, C. Worsham, D. G. Nocera, *Chem. Mater.* **1996**, *8*, 558; c) M. A. Shestopalov, S. Cordier, O. Hernandez, Y. Molard, C. Perrin, A. Perrin, V. E. Fedorov, Y. V. Mironov, *Inorg. Chem.* **2009**, *48*, 1482; d) Y. Molard, F. Dorson, K. A. Brylev, M. A. Shestopalov, Y. Le Gal, S. Cordier, Y. V. Mironov, N. Kitamura, C. Perrin, *Chem. Eur. J.* **2010**, *16*, 5613.
[12] a) S. Ababou-Girard, S. Cordier, B. Fabre, Y. Molard, C. Perrin, *ChemPhysChem* **2007**, *8*, 2086; b) F. Grasset, F. Dorson, S. Cordier, Y. Molard, C. Perrin, A.-M. Marie, T. Sasaki, H. Haneda, Y. Bando, M. Mortier, *Adv. Mater.* **2008**, *20*, 143; c) F. Grasset, F. Dorson, Y. Molard, S. Cordier, V. Demange, C. Perrin, V. Marchi-Artzner, H. Haneda, *Chem. Commun.* **2008**, 4729; d) F. Grasset, Y. Molard, S. Cordier, F. Dorson, M. Mortier, C. Perrin, M. Guilloux-Viry, T. Sasaki, H. Haneda, *Adv. Mater.* **2008**, *20*, 1710; e) S. Cordier, F. Dorson, F. Grasset, Y. Molard, B. Fabre, H. Haneda, T. Sasaki, M. Mortier, S. Ababou-Girard, C. Perrin, *J. Clust. Sci.* **2009**, *20*, 9; f) B. Fabre, S. Cordier, Y. Molard, C. Perrin, S. Ababou-Girard, C. Godet, *J. Phys. Chem. C* **2009**, *113*, 17437; g) T. Aubert, F. Grasset, S. Mornet, E. Duguet, O. Cador, S. Cordier, Y. Molard, V. Demange, M. Mortier, H. Haneda, *J. Colloid Interface Sci.* **2010**, *341*, 201; h) T. Aubert, A. Y. Ledneva, F. Grasset, K. Kimoto, N. G. Naumov, Y. Molard, N. Saito, H. Haneda, S. Cordier, *Langmuir* **2010**, *26*, 18512; i) D. Dybtsev, C. Serre, B. Schmitz, B. Panella, M. Hirscher, M. Latroche, P. L. Llewellyn, S. Cordier, Y. Molard, M. Haouas, F. Taulelle, G. Ferey, *Langmuir* **2010**, *26*, 11283; j) V. Roullier, V. Marchi-Artzner, O. Cador, F. Dorson, T. Aubert, S. Cordier, Y. Molard, F. Grasset, S. Mornet, H. Haneda, *Int. J. Nanotechnol.* **2010**, *7*, 46.
[13] L. M. Robinson, D. F. Shriver, *J. Coord. Chem.* **1996**, *37*, 119.
[14] T. G. Gray, C. M. Rudzinski, E. E. Meyer, R. H. Holm, D. G. Nocera, *J. Am. Chem. Soc.* **2003**, *125*, 4755.
[15] F. Girardi, F. Graziola, P. Aldighieri, L. Fedrizzi, S. Gross, R. Di Maggio, *Prog. Org. Coat.* **2008**, *62*, 376.
[16] R. S. Fonseca, M. Flores, R. Rodriguez, J. Hernandez, A. Munoz, *J. Lumin.* **2001**, *93*, 327.
[17] A. Q. Le Quang, E. Besson, R. Hierle, A. Mehdi, C. Reye, R. Corriu, I. Ledoux-Rak, *Opt. Mater.* **2007**, *29*, 941.
[18] W. Preetz, D. Bublitz, H. G. Vonschnering, J. Sassmannshausen, *Z. Anorg. Allg. Chem.* **1994**, *620*, 234.

ADVANCED OPTICAL MATERIALS
www.advopticalmat.de

Highly Efficient Infrared Quantum Cutting in Tb^{3+}–Yb^{3+} Codoped Silicon Oxynitride for Solar Cell Applications

Yong-Tao An, Christophe Labbé, Julien Cardin, Magali Morales, and Fabrice Gourbilleau*

A high efficiency infrared quantum cutting effect in a Tb^{3+}–Yb^{3+} codoped silicon oxynitride system is demonstrated. The thin films are deposited on Si substrates by reactive magnetron co-sputtering of a Si target topped with Tb_4O_7 and Yb_2O_3 chips under pure nitrogen plasma. The photoluminescence dynamics are investigated, revealing a quantum efficiency of this system at 980 nm up to 197% for the higher Yb^{3+} concentration. Thus, via a cooperative transfer mechanism between Tb^{3+} and Yb^{3+}, an absorbed UV–visible photon gives rise to almost two emitted IR photons. Such a down-conversion effect is demonstrated upon indirect excitation of energy donors, via defect states in the host matrix. These down-converter films could be directly and easily integrated on top of the Si-based solar cell to improve the photoelectric conversion efficiency at a lower cost. An evaluation of the additional external quantum efficiency is deduced from this optical system and found to be almost 2%.

1. Introduction

Among the different approaches to improve the solar cells efficiency, the quantum cutting (QC) is one of the interesting ways proposed since the thermalization effect of the electrons is limited for the energetic photons.[1–3] Placed on top of a solar cell, a QC layer consists in dividing the absorbed UV-Visible photon energy to emit two IR photons absorbed by the classical Si solar cell below. This down-conversion (DC) process leads to a quantum efficiency (η_{QE}) higher than 100% as theoretically predicted by Dexter et al.[4] and experimentally seen by different authors on Pr^{3+}-, Tm^{3+}-, or Gd^{3+}-doped host matrices.[5]. Almost 15 years ago, a high η_{QE} was achieved close to 200% by Wegh et al.[6] on a $LiGdF_4$:Eu^{3+}–Gd^{3+} phosphor system. This result has relaunched the research activity on the development of efficient QC layers.[2,7,8] Another system based on double co-doping Er^{3+}–Gd^{3+}–Tb^{3+} was studied in such a matrix,[9] but a system associating a donor to Yb^{3+} ion seems to be more promising. Indeed, the Yb^{3+} ion has a single excited state, reducing the harmful effect of up-conversion and harvesting the energy corresponding to a photon emission of 1 μm wavelength, just above the gap of c-Si thus limiting the thermalization.[10]

In this regard, the scientific community makes great effort to enhance the η_{QE} of Yb^{3+} doped materials. The first report on efficient DC material containing Yb^{3+} ions was on Tb^{3+}-Yb^{3+} system in phosphor matrix with the achievement of a 188% internal η_{QE}.[11] This has been followed by several studies on the same system in different host matrices such as borate (η_{QE} = 196% and 152%),[12,13] hafnia glass ceramic (η_{QE} = 138%),[14] oxyfluoride glass (η_{QE} = 120% and 166%).[15,16] High η_{QE} were also demonstrated in system associating Yb^{3+} with other absorber-donor rare earth ions such as Ce^{3+} (η_{QE} = 174%) in a borate glasses,[17] Pr^{3+} (η_{QE} = 197%) in a fluoride,[18] and Er^{3+} ion (η_{QE} = 196–199%) in a glass ceramic and a bromide matrix respectively.[19,20] Unfortunately, most of these rare earth-doped hosts are not easily compatible with the fabrication process of conventional crystalline silicon solar cells. Consequently, the gain achieved in terms of photon is lost by the cost required to adapt the fabrication line and/or to design a new solar cell structure. This is the reason why some investigations are now focusing on silicon integration: Zn_2SiO_4:Tb^{3+}–Yb^{3+},[21] silicon nanocrystals,[22] Er^{3+} in SiO_2.[23]

In order to obtain both a host environment based on silicon to offer an industrial compatibility and a very high down-conversion η_{QE}, we propose to investigate a silicon oxynitride matrix codoped with Tb^{3+}–Yb^{3+} system. To perform this study, the photoluminescence (PL), PL excitation (PLE) as well as the decay lifetimes were investigated as a function of the Yb^{3+} concentration. The latter allowed us to calculate the η_{QE} which has been enhanced up to almost 197% in such host matrix. By considering the non-radiative losses, a rough correction, never taken into account in previous similar studies, gives a η_{QE} of 183%. Our work demonstrates the feasibility of a high η_{QE} down-converter thin film easily deposited on a common solar cell to improve its external quantum efficiency. This additional external quantum efficiency due to this DC effect is evaluated to almost 2%.

Y.-T. An, Dr. C. Labbé, Dr. J. Cardin, Dr. M. Morales, Dr. F. Gourbilleau
Centre de Recherche sur les Ions les Matériaux et la Photonique (CIMAP)
UMR 6252 CNRS/CEA/Ensicaen/UCBN
6 Boulevard Maréchal Juin, Cedex 4, 14050 Caen, France
E-mail: christophe.labbe@ensicaen.fr

DOI: 10.1002/adom.201300186

Table 1. Atomic composition measured by RBS technique an d the excess of nitrogen (N_{excess}) deduced.

Sample name based on the Yb_2O_3 chip number	Si [at%]	N [at%]	O [at%]	N_{excess}	Tb [at%]	Yb [at%]
0Yb	32.98	46.00	20.28	14.90	0.74	0
10Yb	31.53	34.11	32.54	12.23	1.34	0.48
20Yb	30.45	38.28	27.46	12.90	1.84	1.97
30Yb	28.89	26.06	39.68	9.73	1.86	3.51

2. Results and Discussion

2.1. Samples

The thicknesses of the deposited films were measured 201 to 245 nm (±10 nm). The refractive index is constant of about 1.73. The concentrations of different elements deduced from the RBS experiments are displayed on the **Table 1**.

As shown, the silicon content is almost constant of about 30 at% whereas the nitrogen content tends to decrease with the Yb^{3+} concentration in favor of the oxygen element. The amount of oxygen contained only in the Tb_4O_7 and Yb_2O_3 chips could contribute to the formation of SiO_2 phase detected by the presence of Si-O bond in FTIR spectrum as previously reported.[24] The refractive index measured is consequently the signature of a composite layer containing SiO_2 (n = 1.55) and Si_3N_4 (n = 2.00) phases. Moreover, the lower 1.73 value could also be ascribed to the excess of nitrogen incorporated with respect to the stoichiometric Si_3N_4 matrix. Indeed the nitrogen excess (N_{excess}), responsible for the deviation from a perfect SiO_2+Si_3N_4 mixture is calculated with help of the equation (1):

$$N_{excess} = \frac{[N]-(4/3)[Si]+(2/3)[O]-(7/6)[Tb]-(1/4)[Yb]}{[N]+[Si]+[O]+[Tb]+[Yb]} \quad (1)$$

where the term [element] represents the atomic concentration (at%) of the aforesaid element.[25] On the basis of Kistner et al.[26] study, this excess of nitrogen explains the value of 1.73 measured. So our deposited thin film is a nitrogen-rich silicon oxynitride (NRSON). Note that even if the number of Tb_4O_7 chips is constant during the deposition run, the Tb^{3+} concentration is multiplied by 2.5 with the increasing number of the Yb_2O_3 chips.

2.2. Photoluminescence

The PL spectrum of the Tb^{3+} monodoped sample is displayed in **Figure 1** with a 239 nm excitation wavelength, corresponding to the best PL signal taking account our experimental set up response.

In the visible range, the peaks of the Tb^{3+} at 545, 590 and 624 nm were identified as the transitions $^5D_4 \rightarrow {}^7F_j$ (j = 5, 4, 3) respectively. In our previous study,[24] a non-resonant excitation wavelength with the Tb^{3+} ion at 325 nm, allow us to see also the transition at 490 nm, like Jeong et al. with the same matrix,[27]

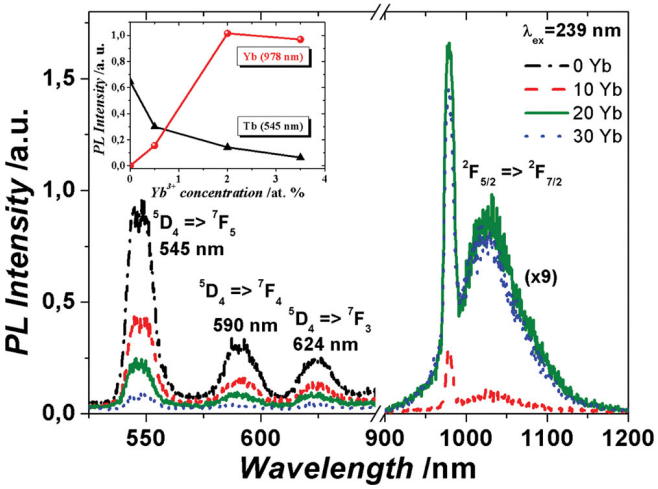

Figure 1. PL spectra under 239 nm excitation wavelength as a function of Yb^{3+} concentration. In inset, the variation of the Tb^{3+} and Yb^{3+} PL intensities with the Yb^{3+} concentration. Note that each Yb^{3+} intensity is multiplied by a factor of 9 for a best readability.

corresponding to the transition $^5D_4 \rightarrow {}^7F_6$, hidden by the second-order grating with a 239 nm excitation wavelength. These four transitions are depicted in **Figure 2**.

On the Figure 1, when a small content of Yb^{3+} ions is added (10Yb curve), we note a remarkable decreasing Tb^{3+} PL intensity and concomitantly in the IR range emerging two typical Yb^{3+} peaks located at 976 and 1026 nm coming from $^2F_{5/2} \rightarrow {}^2F_{7/2}$ transition. The variation of these visible and IR PL peaks intensities versus the Yb^{3+} concentration are shown in the inset of Figure 1. The PL intensity of the Tb^{3+} ion at 545 nm decreases, with the Yb^{3+} concentration, while that of Yb^{3+} PL increases. This opposite behavior is the sign of cooperative DC energy transfer (ET) as shown on the Figure 2. The $^5D_4$–$^7F_6$ Tb^{3+} energy transition (490 nm ≈ 2.53 eV) is divided

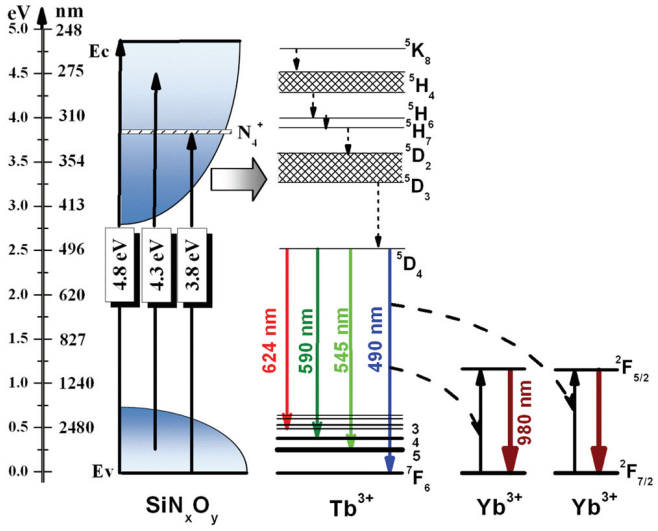

Figure 2. Scheme of the Tb^{3+} and Yb^{3+} energy diagram depicting the QC effect. Note that in this diagram we have supposed for the legibility that the top of the valence band (E_v) is at the same energy than the rare earths' ground states.

Adv. Optical Mater. 2013,
DOI: 10.1002/adom.201300186

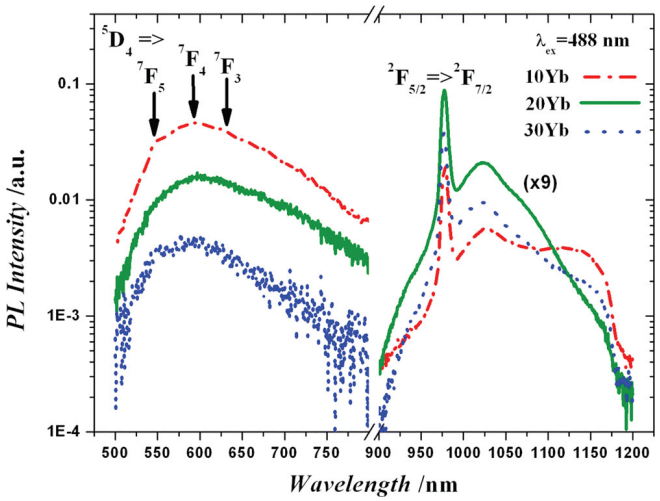

Figure 3. PL spectra of the codoped Tb^{3+}–Yb^{3+} samples excited at 488 nm wavelength. Note that each the Yb^{3+} intensity is multiplied by a factor of 9 for a best readability.

into two IR photons coming from two $^2F_{5/2}$–$^2F_{7/2}$ Yb^{3+} energy transitions (980 nm ≈ 1.26 eV).[11,28] We also observe a saturation and a slight decrease of the Yb^{3+} PL intensity for the 30Yb curve, when we almost have one Tb^{3+} ion (1.86 at%) for two Yb^{3+} ions (3.51 at%) (see Table 1). This could be the expression of the usual quenching effect observed for high concentration corresponding to a migration between the Yb^{3+} ions into non-radiative defects. But the self-quenching effect is ruled out here because it has been observed for system containing more than 10 at% concentration.[29,30] So this saturation could be explained by the beginning of the formation of Yb^{3+} clusters due to the annealing of the samples at 700 °C, reducing de facto the active numbers of Yb^{3+} ions.[31]

One may argue that, depending on the used host matrix, the 239 nm excitation wavelength (5.2 eV) could induce charge transfer energy on the Yb ion (Yb^{3+}→Yb^{2+}) and thus directly excite the Yb^{3+} ion without sensitizing the Tb^{3+}.[32] To avoid this drawback, we have excited the three Yb^{3+} samples at 488 nm which is clearly non resonant with the Yb^{3+} ion, but resonant with the Tb^{3+} ion.[21,29]

The **Figure 3** depicts clearly the Yb^{3+} PL spectra in the IR range suggesting an ET via the Tb^{3+} ion is possible. The visible range shows this time a broad band of almost 200 nm width and centered at 600 nm. This broad emission band is attributed to the band tail states of the matrix.[24,27,33] Indeed this band tail comes from localized states associated with defects such as dangling bonds in the host matrix. Its PL spectrum is strongly blue-shifted with the decrease of the excitation wavelength (see Figure S1) due to the occupancy of the density of states. This visible band finally disappear when we use an excitation (239 nm ≈ 5.2 eV) higher to the band gap (4.8 eV),[24] due to the trapping of the electron (Figure 1 and drawing in Figure 2). This effect is also seen by Kistner et al.[26] but in their case the excitation wavelength is constant while the gap changes with the composition.

We also distinguish on Figure 3 a weak PL intensity of the Tb^{3+} peaks at 545, 590, and 624 nm identified as the transitions $^5D_4$→^7F_j (j = 5, 4, 3) respectively (Figure 2). In our previous study without Yb doping,[24] we mentioned two energy transfer mechanisms producing these four transitions coming from the $^5D_4$ level of the Tb^{3+} ion: (i) one coming from the carriers across the optical gap into the extended states-carriers that could be captured directly by Tb^{3+} related states, (ii) the second when excitation energy is lower than the gap, carriers trapped in the band tail states can transfer energy to Tb^{3+} ions. So with the 488 nm (and also 457 nm and 476 nm not shown) excitation wavelength, which is non resonant with the Yb^{3+} ion, the last mechanism is involved, and gives a significant Yb^{3+} PL intensity with the help of a DC effect. The best PL intensity is again obtained for the 20Yb sample.

2.3. Photoluminescence Excitation

To investigate in more details the excitation range of the Tb^{3+} ion to get ET towards Yb^{3+}, we perform the PLE spectra of the samples with and without Yb^{3+} ions normalized to the thickness (**Figure 4**).

The PLE measurements are carried out by setting the detection at 545 nm attributed to the $^5D_4$→$^7F_5$ transition of Tb^{3+}, also including the band tail. The PLE spectra range is extended from about 250 to 550 nm (≈2.2–5.0 eV), corresponding to the solar spectra range available for the DC effect.[1] The PLE intensities behaviors following the lowering of the Tb^{3+} PL intensity with the Yb^{3+} content attest that the transfer mechanism involved in this system is efficient in a wide range of wavelengths. The PLE spectra comprise three peaks centered at almost 3.8 eV, 4.3 eV, and 4.8 eV. These three peaks are also identified in a sample without any rare earth (not shown) respectively centered at 3.3 eV, 3.8 eV, and 4.3 eV. The first peak at 3.3e V is identified as a nitrogen defect state (N_4^+).[34] The second at 3.8 eV with a very broad band (almost 1.5 eV width) is linked to the band tail,[35] while the third one at 4.3 eV is due to the gap of the NRSON host matrix. Indeed the refractive index of the undoped sample is found to be 1.80 corresponding to a tauc gap of 4.3 eV based

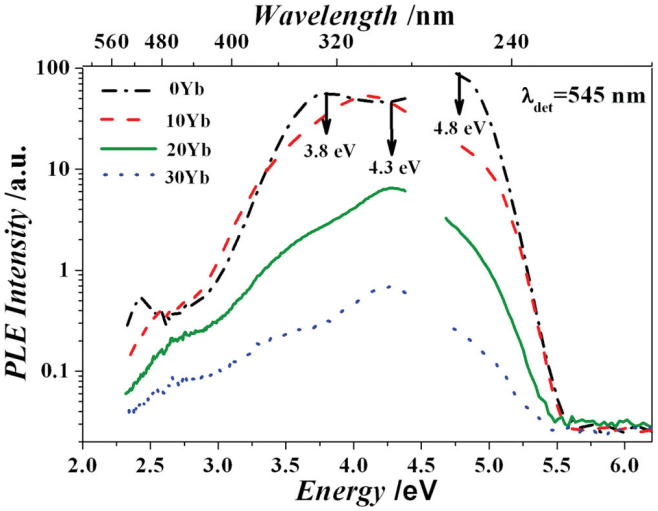

Figure 4. PLE spectra detected at a 545 nm wavelength corresponding to the $^5D_4$→$^7F_5$ transition of Tb^{3+} for three different Yb^{3+} concentrations.

to the average results reported by Kistner et al.[26] and Wang et al.[36] The four rare earth-doped samples in this study have a refractive index of 1.73 resulting in a slightly higher gap which explains the energy position shift of almost 0.5 eV of their three peaks compared to their undoped counterparts. Therefore the three peaks at 3.8 eV, 4.3 eV, and 4.8 eV of the doped samples on the Figure 4, are attributed also to the nitrogen defect state (N_4^+), band tail and band gap respectively, and are represented schematically in the diagram of Figure 2. The excitation of Tb^{3+} in such thin films was previously studied and has proved the involvement of these energy states in the excitation mechanism, confirming our results of the PLE spectra.[27,35] Thus the excitation of the Tb^{3+} ions in a large spectral range in order to obtain a DC effect with an Yb^{3+} ion is possible, upon indirect excitation of energy donors, via defect states in the NRSON host matrix.

2.4. Time-Resolved Photoluminescence

Figure 5 depicts the decay times of the Tb^{3+} at 545 nm ($^5D_4 \rightarrow {}^7F_5$) under 239 nm excitation wavelength with different concentrations of Yb^{3+}.

The lifetime curves present a biexponential decay. For example, the Yb^{3+}-free sample displays fast (151 µs) and slow (627 µs) components. Note that the lifetime linked to the band tail is a nanosecond time scale and is not detectable here.[36,37] The slow decay value is comparable to that obtained in similar matrix with a Tb^{3+} concentration four times lower.[27] These two decays could correspond to the Tb^{3+} ions linked to the Tb cluster (fast component) and the "isolated" Tb ions (slow component).[38] To overcome such non exponential decays, a mean decay time (τ_m) is calculated by the formula (2):

$$\tau_m = \int_0^\infty \left(\frac{I(t)}{I_0} \right) dt \tag{2}$$

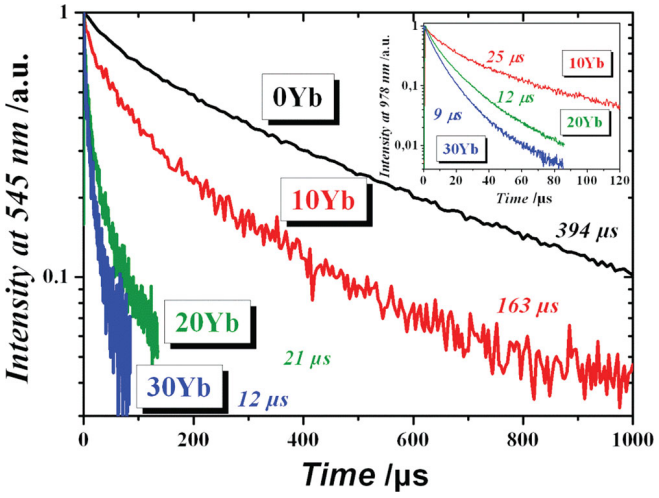

Figure 5. Tb^{3+} decay times at 545 nm under a 239 nm excitation wavelength with different concentrations of Yb^{3+}. In inset: Yb^{3+} decay times at 980 nm under a 239 nm excitation wavelength with different concentrations of Yb^{3+}.

where I(t) is the decay intensity and I_0 the maximum of the I(t).[39] The values of the different samples are presented on Figure 5. The τ_m of the Tb^{3+} falls down drastically with the increase of the Yb^{3+}concentrations showing a reduction by a factor of more than 30. Such an evolution with the Yb^{3+} concentration was also observed in previous studies,[3,13,15,16,21,29,40] but in a lower proportion of a factor 4 at maximum whatever the Yb^{3+} concentration. The decrease was identified as the consequence of the cooperative ET from one Tb^{3+} to two Yb^{3+} ions acting as quantum cutting mechanism, and the factor 30 presuppose a very high efficiency transfer.

2.5. Quantum Efficiency

To quantify such cooperative ET, we calculate the energy transfer efficiency (η_{ETE}) at 545 nm ($^5D_4 \rightarrow {}^7F_5$) described in the formula (3):

$$\eta_{ETE} = 1 - \frac{\tau_{Tb-Yb}}{\tau_{Tb}} \tag{3}$$

where $\tau_{Tb\text{-}Yb}$ and τ_{Tb} are the decay times of the Tb^{3+} with and without Yb^{3+}, respectively. Thus the quantum efficiency (η_{QE}) usually defined as the ratio between the total number of emitted photons and the total number of absorbed photons, is described by the formula (4):

$$\eta_{QE} = \eta_{Tb}\left(1 - \eta_{ETE}\right) + 2\eta_{ETE} = 2 - \frac{\tau_{Tb-Yb}}{\tau_{Tb}} \tag{4}$$

assuming that the quantum efficiency of Tb^{3+} is 1.[6,11]

The **Figure 6** shows the η_{QE} of the transfer according to the Yb^{3+} concentration. To calculate the η_{QE}, it is always supposed implicitly that τ_{Tb} is constant in order to compare the different Yb^{3+} concentrations. During the increase of the Yb^{3+} concentration, we note an increase of the Tb^{3+} content by a factor of 2.5, from 0.74 at% to 1.86 at%, mentioned previously in the Table 1, although the number of the Tb^{3+} chips is kept constant during the deposition process. This increase of the Tb^{3+} concentration could contribute to a variation of its own lifetime by two different effects (cross relaxation or

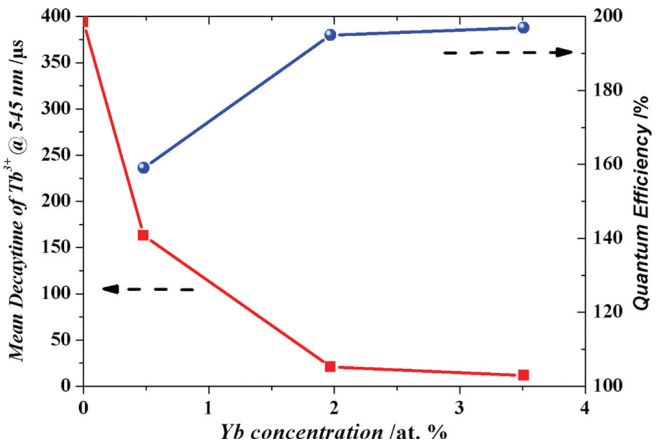

Figure 6. Tb^{3+} decay times at 545 nm under a 239 nm excitation wavelength with different concentrations of Yb^{3+}.

DOI: 10.1002/adom.201300186

migration) and affect the comparison. In the first effect, the known cross relaxation is defined by ($^5D_3 \rightarrow {}^5D_4$)/($^7F_6 \rightarrow {}^7F_0$) transitions, which contributes to extend the $^5D_4$ experimental lifetime and consequently underestimates the η_{QE} obtained.[41] On the contrary, the self-quenching process, caused by the migration of the excitation energy of the Tb^{3+} to non-radiative defects could reduce the $\tau_{Tb}(^5D_4)$ and overestimate the η_{QE}. But the decrease of the intensity linked to the migration is usually observed for very high concentration of Tb^{3+}, which has not been studied in this work.[42] So the $\tau_{Tb}(^5D_4)$ is not affected by Tb^{3+} concentration used. On Figure 6, we observe an increasing of the η_{QE} following by a plateau at 197%. This plateau is due to weak variation of the $\tau_{Tb\text{-}Yb}$ values (21 µs to 12 µs) compare to the τ_{Tb} (394 µs). Note that the behaviors of the variation with the Yb^{3+} concentration of the fast and slow Tb^{3+} decay times are the same as the τ_m, which represents an average of these two components. So for the fast and slow components, the η_{QE} limits are almost the same, 198% and 195% respectively. This means that almost two Yb^{3+} ions are excited for one excited Tb^{3+} ion attesting a highly efficient quantum cutting mechanism. This limit has been approached for a Tb^{3+}-Yb^{3+} system in phosphor matrix (η_{QE} = 188%)[11] or borate (η_{QE} = 196%)[12] and with other rare earth with Yb^{3+} like Pr^{3+} (η_{QE} = 197%)[18], or Er^{3+} (η_{QE} = 196–199%).[19,20]

Usually, the η_{QE} calculations suppose that the decrease of the Tb^{3+} lifetime with the Yb^{3+} content is completely attributed to the ET.[13] But the increase of the Yb^{3+} concentration could introduce some non-radiative (NR) losses, by inclusion of defects or impurities, contributing to the fall of the decay time and overestimate the η_{QE}. To investigate this point, we have measured the Yb^{3+} lifetime at 980 nm wavelength (inset Figure 5). The Yb^{3+} decay time is reduced from 25 µs to 9 µs with the increase of the concentration, revealing the NR losses, because the self-quenching effect is not expected as mentioned above.[29] In spite of the Yb^{3+} lifetime diminution, we observe that its PL intensity is constantly increasing (inset Figure 1) with the Yb content. This is due to the growing number of excited Yb^{3+} ions and the efficient ET that counterbalances this weak decrease linked to the NR losses. To take into account this effect, and see how this decrease could affect the η_{QE}, we have estimated the nonradiative rate ($1/\tau_{NR}$) considering that τ_{Tb} is affected by the ET and NR losses and can be described by the following equation (5):

$$\frac{1}{\tau_{Tb-Yb}} = \frac{1}{\tau_{Tb}} + \frac{1}{\tau_{ET}} + \frac{1}{\tau_{NR}} \quad (5)$$

So we can define in equation (6), a new lifetime by $\tau'_{Tb\text{-}Yb}$ to calculate the new quantum efficiency η'_{QE} taking into account the NR part.

$$\frac{1}{\tau'_{Tb-Yb}} = \frac{1}{\tau_{Tb-Yb}} - \frac{1}{\tau_{NR}} = \frac{1}{\tau_{Tb}} + \frac{1}{\tau_{ET}} \quad (6)$$

To roughly estimate the non-radiative rate ($1/\tau_{NR}$) for the Tb^{3+}, we use the Yb^{3+} decay measurements considering that the lowering of the quality approximately affects the decay times of the rare earth in the same proportion (see inset Figure 5). Based on the fact that we assume there are no NR losses for the decay time (τ_{Yb} = 25 µs) of the lower Yb^{3+} concentration sample, the non-radiative rate is described by the equation (7):

$$\frac{1}{\tau_{NR}} = \frac{1}{\tau_{Yb}} - \frac{1}{\tau'_{Yb}} \quad (7)$$

where τ'_{Yb} is the decay time of the higher Yb^{3+} concentration sample (9 µs). The τ'_{Tb-Yb} is found to be almost 66 µs, then giving a new quantum efficiency η'_{QE} of 183%, compared to the 197% found, without taking into account these NR losses. Of course the component $1/\tau_{NR}$ is not exactly the same for Tb^{3+} and Yb^{3+}, but this method could give a rapid proportion of the overestimated η_{QE}, never made in the literature.

3. Additional External Quantum Efficiency Evaluation

The additional external quantum efficiency (η^{add}_{EQE}) induced by this DC layer has been estimated. An external quantum efficiency of a conventional solar cell (*sc*) with a DC film is noted η^{with}_{EQE}. To extract the additional external quantum efficiency cause by the DC layer, we have to take into account a possible loss of the external quantum efficiency (η^{loss}_{EQE}) of the *sc* due to its partial occultation by this converting frequency layer. Then the additional external quantum efficiency (η^{add}_{EQE}) can thus be obtained in according to the equation (8):

$$\eta^{add}_{EQE} = \eta^{with}_{EQE} - \eta^{loss}_{EQE} \quad (8)$$

The η^{with}_{EQE} is defined by the ratio between the charge carriers generated by the *sc* and the incident photons on the *sc* in the DC wavelength range (ϕ_{sun}), i.e. ,between 250 nm and 550 nm as mentioned above.[1] The efficiency of the *sc* for a corresponding wavelength λ is called (η^{λ}_{sc}). Thus the charge carriers generated by the *sc* are obtained by the product of the η^{980}_{sc} and the incident photons flux on the *sc* at 980 nm wavelength coming from the conversion performed by the DC layer (ϕ'_{sc}). The η^{with}_{EQE} is well defined by the equation (9):

$$\eta^{with}_{EQE} = \eta^{980}_{sc} \frac{\phi'_{sc}}{\phi_{sun}} \quad (9)$$

To separate each efficiency, corresponding at each step of the conversion, we define $\Delta\phi_{DC}$ representing the absorbed photon flux inside the DC layer. After the DC process, ϕ'_{DC} describes the emitted photon flux at the 980 nm wavelength inside the DC layer (**Figure 7**).

Therefore the η^{with}_{EQE} can be rewritten by the equations (10) and (11):

$$\eta^{with}_{EQE} = \eta^{980}_{sc} \left(\frac{\phi_{DC}}{\phi_{sun}}\right)\left(\frac{\phi'_{DC}}{\phi_{DC}}\right)\left(\frac{\phi'_{sc}}{\phi'_{DC}}\right) \quad (10)$$

$$\eta^{with}_{EQE} = \eta^{980}_{sc}.\eta^{DC}_{abs}.\eta^{DC\rightarrow 980}_{conv}.\eta^{980}_{extrac} \quad (11)$$

where, η^{DC}_{abs}, $\eta^{DC\rightarrow 980}_{conv}$, and η^{980}_{extrac} are the different efficiencies linked respectively to the different terms of the equation (10).

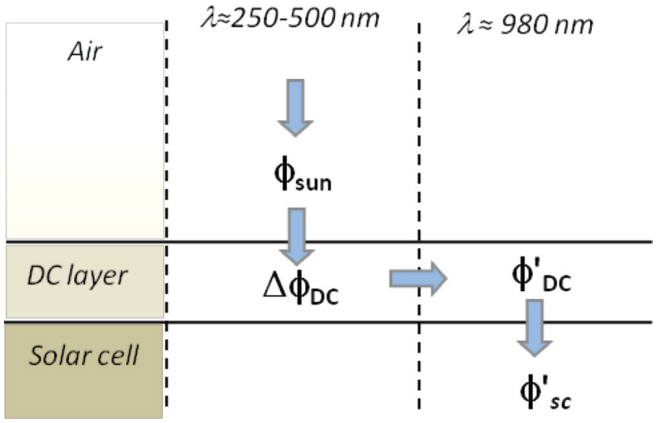

Figure 7. Schematic diagram of the down-converter system.

These four efficiencies can be estimated using the following approach:

i. The efficiency η_{sc}^{980}

This efficiency can be obtained at 980 nm (1.26 eV) using the efficiency versus band gap calculated for the AM1.5G spectra in the extended Shockley–Queisser approach.[43] At 980 nm, the η_{sc}^{980} is found to be equal to 32.9%.

ii. The efficiency η_{abs}^{DC}

Coming from the ellipsometry measurement at each wavelength, the absorption coefficient spectrum of the host matrix is determined using the imaginary part of the refractive index. This spectrum is used with the help of the solar spectral irradiance AM1.5G (equal to ϕ_{sun} at each DC range wavelength) to calculate the transmitted photon flux after the DC layer ($\phi_{after\ DC}$) at the normal incident angle (**Figure 8**).

The integrated photon flux of ϕ_{sun} on the spectral range is equal to 6.05×10^{12} ph s^{-1} m^{-2} while the integrated photon flux of $\phi_{after\ DC}$ is equal to 5.20×10^{12} ph s^{-1} m^{-2}. The number of absorbed photons in the DC layer is then equal to 0.85×10^{12} ph s^{-1} m^{-2}. Consequently, the η_{abs}^{DC} is equal to 14% of the incident solar photons, on the DC range.

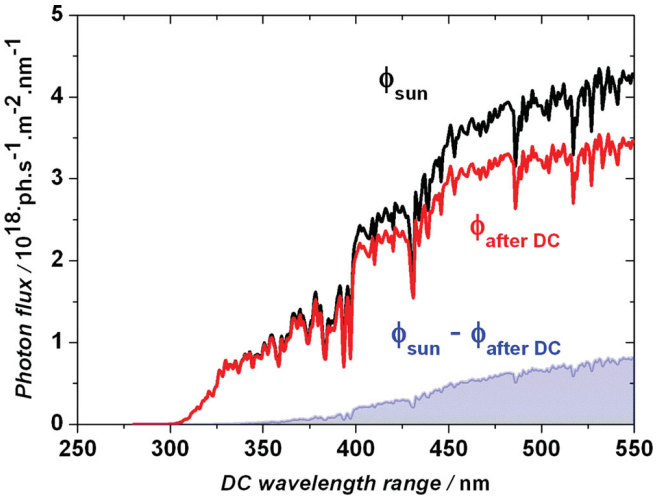

Figure 8. Photon flux of the solar spectral irradiance AM1.5G on the DC range (ϕ_{sun}), transmitted photon flux after the DC layer ($\phi_{after\ DC}$), and the photon flux absorbed by the DC layer ($\Delta\phi_{DC} = \phi_{sun} - \phi_{after\ DC}$)

iii. The efficiency $\eta_{conv}^{DC \to 980}$

The energy transfer demonstrated above between the host matrix and the Tb^{3+} ion ($\eta_{matrix \to Tb}$) is supposed here equal to 100%. It means that all the absorbed photons by the host matrix are transferred to the Tb^{3+} ion and contributed to the DC conversion process. Note that the photon flux is less than the common densities of the rare earth ions usually used and consequently the efficiency is not limited by an eventual saturation. So the $\eta_{conv}^{DC \to 980}$ efficiency is defined by the product of ($\eta_{matrix \to Tb}$ = 100%) and the η'_{QE} found in Section 2.5 at 183% taking account the NR losses, i.e., a $\eta_{conv}^{DC \to 980}$ equal to 183%.

iv. The efficiency η_{extrac}^{980}

The PL emission is omnidirectional. So, in this part, we have to take into account the extraction of the down-converted low-energy photons in the *sc* which are confined in a layered media formed by the DC layer stack on the *sc*.[7] Based on a transfer matrix formalism and electric dipole source terms,[44] a method of modeling light emission in layered media has been developed. This method leads us to the distribution modeling of emitted intensities versus emission angle in each considered medium (**Figure 9**a) and versus wavelength i.e. around 980 nm for the Yb^{3+} ion in this case. We consider an average DC layer thickness of 225 nm, with refractive index describe by a new amorphous model.[45] The emission of Yb^{3+} ions was modelized by a Lorentzian function centered at 980nm and with a FWHM of 50nm. So we obtained the PL spectra by the integration over emission angles in DC and *sc* materials (**Figure 9**b). This numerical calculation shows that the efficiency η_{extrac}^{980} is equal to 30%.

Therefore the external quantum efficiency induced by the DC layer (η_{EQE}^{with}) is found to be 2.53%, using the equation (12).

$$\eta_{EQE}^{with} = \eta_{sc}^{980} . \eta_{abs}^{DC} . \eta_{conv}^{DC \to 980} . \eta_{extrac}^{980}$$
$$= 32.9\% \times 14\% \times 183\% \times 30\% = 2.53\% \quad (12)$$

To calculate the loss due to the occultation by DC layer (η_{EQE}^{loss}) of 14% of the incident energy on the *sc*, we assume no DC effect ($\eta_{conv}^{DC \to 980} = 100\%$) and full extraction ($\eta_{extrac}^{980} = 100\%$) for the *sc*. The efficiency calculated for the AM1.5G spectra in the extended Shockley–Queisser approach,[43] gives a η_{sc}^{400} of 3.5%. at a 400 nm (3.1 eV) wavelength, corresponding to the middle of the DC range. Then the external quantum efficiency of the *sc* (η_{EQE}^{loss}) is equal to 0.49% following the equation (13):

$$\eta_{EQE}^{loss} = \eta_{sc}^{400} . \eta_{abs}^{DC} . \eta_{conv}^{DC \to 980} . \eta_{extrac}^{980}$$
$$= 3.5\% \times 14\% \times 100\% \times 100\% = 0.49\% \quad (13)$$

So using the equation (8), the additional external quantum efficiency (η_{EQE}^{add}) is equal to almost 2% (η_{EQE}^{add} = 2.53–0.49%). It means that the stacking of a DC layer gives 2% more external quantum efficiency compare to a bare *sc*. However, it's interesting to calculate also the maximum η_{EQE}^{loss} with the η_{sc}^{550} (17.5%), obtained at the 550 nm (2.25 eV) giving a value of

Adv. Optical Mater. **2013**,
DOI: 10.1002/adom.201300186

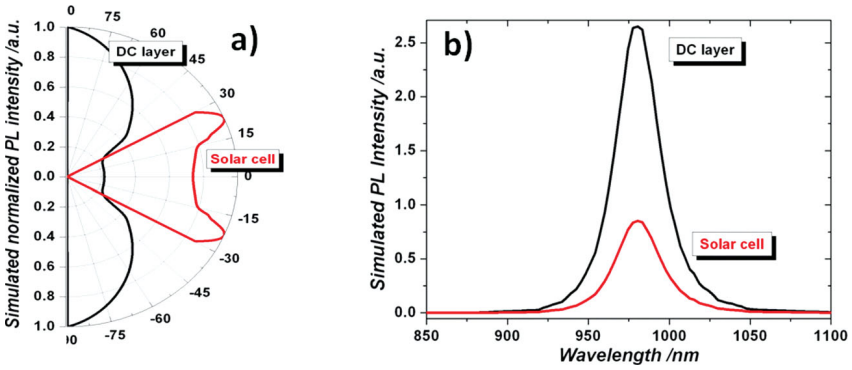

Figure 9. a) Emission pattern normalized of the Yb^{3+} ion emission in the DC layer (black) and in the *sc* (red) at a 980 nm wavelength. b) PL spectra obtained by the integration over emission angles in DC and *sc* material, centered at 980 nm.

2.45%. In this case the η_{EQE}^{add} is close to zero (η_{EQE}^{add} = 2.53–2.45%), indicating that is not interesting to use a DC layer. But on the DC range, the η_{sc}^{λ} decreases with the wavelength witnessing the thermalization effect. So, at least the η_{EQE}^{add} is positive. This is the reason, why we choose the middle wavelength of the DC range to estimate additional external efficiency value of 2%.

This latter has to be compared with theoretical results obtained in the literature. Trupke et al.[7] have estimated a maximum η_{EQE}^{add} of about 9%, while Abrams et al.[46] found 7%. We are almost 4 times lower than these theoretical estimations. The η_{EQE}^{with} could however be improved, and consequently the η_{EQE}^{add} also, by different technical processes. Indeed, in playing in particular with the nitrogen excess, the refractive index would increase, as well as the absorption. In addition the increasing of the DC layer refractive index should increase the efficient of the *sc* as mentioned by Trupke et al.[7]. Furthermore, this deposit process opens the possibility of designing Bragg mirror to have a good optical confinement in playing with the excess of silicon and/or nitrogen[47] and to increase the low extraction part found to be only 30% in the *sc*. Such process might give some improvement of an external quantum efficiency photovoltaic cell.

4. Conclusion

In summary, a Tb^{3+}–Yb^{3+} codoped silicon oxynitride system was deposited on Si substrate by magnetron cosputtering for different Yb^{3+} concentrations. RBS measurements were investigated to confirm the element composition and the excess of nitrogen. PL spectra and decay times were performed to point out a cooperative energy transfer between the Tb^{3+} and the Yb^{3+}. Indeed a down-conversion effect is established upon indirect excitation of energy donors, via defect states in the host matrix. It was found this down-conversion process leads to quantum efficiency equal to 183% taking into account the nonradiative losses for the higher Yb^{3+} concentration with a rough estimation. Without taking into account these losses and in order to compare to the literature, this corresponds to a quantum efficiency of 197%, leading to almost one photon energy into two emitted IR photon energies. In addition, these thin films are easily integrated on the top of c-Si solar cell, compatible with solar spectra range which is available for the down-conversion effect and its additional external quantum efficiency coming from this down-conversion process is estimated to almost 2%.

5. Experimental Section

Samples Preparation: The films were deposited on p-type 250 µm-thick [001] 2" Si substrates by means of a reactive magnetron co-sputtering setup, using pure Si target topped with Tb_4O_7 and Yb_2O_3 chips. The deposition temperature and radio frequency power density were fixed at 200 °C and 1.23 W cm^{-2} respectively, while the nitrogen plasma used was set at a pressure of 23 µbar.[24] The Si target was covered with five Tb_4O_7 chips and different numbers of Yb_2O_3 chips going from 0, to 10, 20, or 30 in order to increase the Yb^{3+} concentration. After deposition, the samples were annealed at 700 °C during 1h in a conventional furnace under a dry nitrogen flow.

Sample Composition Analysis: The compositions of the deposited layers were determined by Rutherford backscattering spectrometry (RBS) using the 2.5 MeV Van de Graaff-type accelerator located at the Institute of NanoSciences in Paris(INSP). The RBS data were obtained using a 1.5 MeV $^4He^+$ ions incident along the direction normal to the sample surface and a scattering angle of 165°. In this work, a standard sample consisting on Bi implanted in Si layer with $N_{SiBi} = 5.6 \times 10^{15}$ at cm^{-2} is used as a reference in order to calibrate the detector channel and the ion energy, as well as to determine the solid angle of the detector. The chemical composition of the films was determined through the simulation of the corresponding RBS spectrum using the SIMNRA program.

Ellipsometry: The thickness and the refractive index at 632 nm wavelength were deduced from spectroscopic ellipsometry experiments. The uncertainty of thickness is ±10 nm and for the refractive index ±0.01.

Photoluminescence Spectra: All the PL spectra of this study were performed at room temperature (RT). Two techniques were used to obtain these spectra. Continuous PL spectra were obtained using the 488 nm excitation wavelength from an Ar^+ laser with a power of 270 mW on the sample and a chopping frequency of 60 Hz. The spot size of the laser beam was measured by a "moving knife-edge" method and was found to be around 1 mm at $1/e^2$ of the maximum intensity. For UV excitation at a 239 nm excitation wavelength, time-integrated PL spectra were carried out using an optical parametric oscillator (OPO) having a pulse of 5 ns at full width at half maximum and a repetition rate of 10 Hz. The focusing beam was 500 µm at $1/e^2$ of the maximum intensity with an average energy of 15 mJ. For these two techniques, a 1 m single grating monochromator (Jobin Yvon) and a liquid-nitrogen-cooled germanium detector (Hamamatsu-R5509–73) were used. These measurements were made by using the standard lock-in techniques (SP830 DPS). All the PL spectra were corrected for the response of the experimental setup and systematically normalized to the film thickness. In order to carefully compare the PL intensities between each sample, a mechanical system was built to place each sample in the same focusing plan of the collected PL.

Time-resolved Photoluminescence: The decay times were carried out by means of the OPO at 239 nm excitation wavelength at RT and in using the same experimental set up of the PL spectra. The decay times' data were acquired by a Labview system and an oscilloscope.

Photoluminescence Excitation: A 450 W Xenon arc lamp as excitation source was used to carry out the PLE measurements at RT with help of Jobin-Yvon Fluorolog spectrophotometer. All the PLE spectra were corrected by the response of the experimental setup.

Supporting Information

This work is supported by the CEA/DSM/ENERGY contract (Project HOFELI) and the Chinese Scholarship Council (CSC) program.

Acknowledgements

The authors would like to thank Dr. Ian Vickridge from SAFIR, "Institut des NanoSciences de Paris" for the RBS data, Dr. Sophie Boudin from CRISMAT Lab for her technical support on the PLE spectra, and Dr. Sébastien Cueff from the "School of Engineering" (Providence, USA) for his careful re-reading.

Received: April 25, 2013
Revised: July 19, 2013
Published online:

[1] B. S. Richards, *Sol. Energ. Mat. Sol. C.* **2006**, *90*, 2329.
[2] C. Strümpel, M. McCann, G. Beaucarne, V. Arkhipov, A. Slaoui, V. Svrcek, C. del Canizo, I. Tobias, *Sol. Energ. Mat. Sol. C.* **2007**, *91*, 238.
[3] Q. Y. Zhang, X. Y. Huang, *Prog. Mater. Sci.* **2010**, *55*, 353.
[4] D. L. Dexter, *Phys. Rev.* **1957**, *108*, 630.
[5] a) J. L. Sommerdijk, A. Bril, A. W. de Jager, *J. Lumin.* **1974**, *8*, 341; b) W. W. Piper, J. A. DeLuca, F. S. Ham, *J. Lumin.* **1974**, *8*, 344; c) R. Pappalardo, *J. Lumin.* **1976**, *14*, 159; d) R. T. Wegh, H. Donker, A. Meijerink, R. J. Lamminmäki, J. Hölsä, *Phys. Rev. B* **1997**, *56*, 13841.
[6] R. T. Wegh, H. Donker, K. D. Oskam, A. Meijerink, *Science* **1999**, *283*, 663.
[7] T. Trupke, M. A. Green, P. Wurfel, *J. Appl. Phys.* **2002**, *92*, 1668.
[8] K. D. Oskam, R. T. Wegh, H. Donker, E. V. D. van Loef, A. Meijerink, *J. Alloys Compd.* **2000**, *300–301*, 421.
[9] R. T. Wegh, E. V. D. van Loef, A. Meijerink, *J. Lumin.* **2000**, *90*, 111.
[10] W. G. J. H. M. van Sark, A. Meijerink, R. E. I. Schropp in Solar Spectrum Conversion for Photovoltaics Using Nanoparticles,Third Generation Photovoltaics (Ed: V. Fthenakis), InTech Europe, Croatia **2012**.
[11] P. Vergeer, T. J. H. Vlugt, M. H. F. Kox, M. I. den Hertog, J. P. J. M. van der Eerden, A. Meijerink, *Phys. Rev. B* **2005**, *71*, 014119.
[12] Q. Y. Zhang, C. H. Yang, Y. X. Pan, *App. Phys. Lett.* **2007**, *90*, 021107.
[13] Y. Wang, L. Xie, H. Zhang, *J. Appl. Phys.* **2009**, *105*, 023528.
[14] G. Alombert-Goget, C. Armellini, S. Berneschi, A. Chiappini, A. Chiasera, M. Ferrari, S. Guddala, E. Moser, S. Pelli, D. N. Rao, G. C. Righini, *Opt. Mater.* **2010**, *33*, 227.
[15] Q. Duan, F. Qin, D. Wang, W. Xu, J. Cheng, Z. Zhang, W. Cao, *J. Appl. Phys.* **2011**, *110*, 113503.
[16] G. Lakshminarayana, J. Qiu, *J. Alloys Compd.* **2009**, *481*, 582.
[17] D. Chen, Y. Wang, Y. Yu, P. Huang, F. Weng, *J. Appl. Phys.* **2008**, *104*, 116105.
[18] D. Serrano, A. Braud, J.-L. Doualan, P. Camy, R. Moncorgé, *J. Opt. Soc. Am. B* **2011**, *28*, 1760.
[19] V. D. Rodriguez, V. K. Tikhomirov, J. Méndez-Ramos, A. C. Yanes, V. V. Moshchalkov, *Sol. Energ. Mat. Sol. C.* **2010**, *94*, 1612.
[20] J. J. Eilers, D. Biner, J. T. van Wijngaarden, K. Kramer, H. U. Gudel, A. Meijerink, *App. Phys. Lett.* **2010**, *96*, 151106.
[21] X. Y. Huang, Q. Y. Zhang, *J. Appl. Phys.* **2009**, *105*, 053521.
[22] D. Timmerman, I. Izeddin, P. Stallinga, I. N. Yassievich, T. Gregorkiewicz, *Nat. Photonics* **2008**, *2*, 105.
[23] N. N. Ha, S. Cueff, K. Dohnalova, M. T. Trinh, C. Labbé, R. Rizk, I. N. Yassievich, T. Gregorkievwicz, *Phys. Rev. B* **2011**, *84*, 241308(R).
[24] Y.-T. An, C. Labbé, M. Morales, P. Marie, F. Gourbilleau, *Phys. Stat. Solidi C* **2012**, *9*, 2207.
[25] S. Cueff, C. Labbé, L. Khomenkova, O. Jambois, P. Pellegrino, B. Garrido, C. Frilay, R. Rizk, *Mater. Sci. Eng. B* **2012**, *177*, 725.
[26] J. Kistner, X. Chen, Y. Weng, H. P. Strunk, M. B. Schubert, J. H. Werner, *J. Appl. Phys.* **2011**, *110*, 023520.
[27] H. Jeong, S.-Y. Seo, J. H. Shin, *App. Phys. Lett.* **2006**, *88*, 161910.
[28] F. Auzel, *Chem. Rev.* **2004**, *104*, 139.
[29] Q. Y. Zhang, C. H. Yang, Z. H. Jiang, X. H. Ji, *App. Phys. Lett.* **2007**, *90*, 061914.
[30] A. Bensalah, M. Ito, Y. Guyot, C. Goutaudier, A. Jouini, A. Brenier, H. Sato, T. Fukuda, G. Boulon, *J. Lumin.* **2007**, *122–123*, 444.
[31] S. Cueff, C. Labbé, O. Jambois, B. Garrido, X. Portier, R. Rizk, *Nanoscale Res. Lett.* **2011**, *6*, 395.
[32] P. Dorenbos, *J. Phys.: Condens. Matter.* **2003**, *15*, 8417.
[33] H. Kato, N. Kashio, Y. Ohki, K. S. Seol, T. Noma, *J. Appl. Phys.* **2003**, *93*, 239.
[34] L. Zhang, H. Jin, W. Yang, Z. Xie, H. Miao, L. An, *App. Phys. Lett.* **2005**, *86*, 061908.
[35] Z. Yuan, D. Li, M. Wang, P. Chen, D. Gong, L. Wang, D. Yang, *J. Appl. Phys.* **2006**, *100*, 083106.
[36] M. Wang, M. Xie, L. Ferraioli, Z. Yuan, D. Li, D. Yang, L. Pavesi, *J. Appl. Phys.* **2008**, *104*, 083504.
[37] S. Yerci, R. Li, S. O. Kucheyev, T. van Buuren, S. N. Basu, N. Soumendra, L. D. Negro, *IEEE J. Sel. Topics Quantum Electron.* **2010**, *16*, 114.
[38] M. Shah, M. Wojdak, A. J. Kenyon, M. P. Halsall, H. Li, I. Crowe, *J. Lumin.* **2012**, *132*, 3103.
[39] J. C. Vial, A. Bsiesy, F. Gaspard, R. Hérino, M. Ligeon, F. Muller, R. Romestain, R. M. Macfarlane, *Phys. Rev. B* **1992**, *45*, 14171.
[40] a) I. A. A. Terra, L. J. Borrero-González, T. R. Figueredo, J. M. P. Almeida, A. C. Hernandes, L. A. O. Nunes, O. L. Malta, *J. Lumin.* **2012**, *132*, 1678; b) P. Molina, V. Vasyliev, E. G. Villora, K. Shimamura, *J. Appl. Phys.* **2011**, *110*, 123527; c) S. Ye, B. Zhu, J. Chen, J. Luo, J. R. Qiu, *App. Phys. Lett.* **2008**, *92*, 141112.
[41] D. J. Robbins, B. Cockayne, B. Lent, J. L. Glasper, *Solid State Commun.* **1976**, *20*, 673.
[42] a) N. Duhamel-Henry, J. L. Adam, B. Jacquier, C. Linarès, *Opt. Mater.* **1996**, *5*, 197; b) F. Auzel, J. Dexpert-Ghys, C. Gautier, *J. Lumin.* **1982**, *27*, 1.
[43] a) M. A. Green, *Prog. Photovolt.: Res. Appl.* **2012**, *20*, 954; b) W. Shockley, H. J. Queisser, *J. Appl. Phys.* **1961**, *32*, 510.
[44] a) J. P. Weber, S. Wang, *IEEE J. Quantum Electron.* **1991**, *27*, 2256; b) H. Benisty, R. Stanley, M. Mayer, *J. Opt. Soc. Am. A* **1998**, *15*, 1192;
[45] A. R. Forouhi, I. Bloomer, *Phys. Rev. B* **1988**, *38*, 1865.
[46] Z. R. Abrams, A. Niv, X. Zhang, *J. Appl. Phys.* **2011**, *109*, 114905.
[47] W. R. Taube, A. Kumar, R. Saravanan, P. B. Agarwal, P. Kothari, B. C. Joshi, D. Kumar, *Sol. Energ. Mat. Sol. C.* **2012**, *101*, 32.

Theoretical investigation of the more suitable rare earth to achieve high gain in waveguide based on silica containing silicon nanograins doped with either Nd^{3+} or Er^{3+} ions

Alexandre Fafin,* Julien Cardin,[1] Christian Dufour, and Fabrice Gourbilleau

CIMAP, CNRS/CEA/ENSICAEN/UCBN
6 boulevard Maréchal Juin, 14050 Caen cedex 4, France
[1]*julien.cardin@ensicaen.fr*
**alexandre.fafin@ensicaen.fr*

Abstract: We present a comparative study of the gain achievement in a waveguide whose active layer is constituted by a silica matrix containing silicon nanograins acting as sensitizer of either neodymium ions (Nd^{3+}) or erbium ions (Er^{3+}). By means of an auxiliary differential equation and finite difference time domain (ADE-FDTD) approach that we developed, we investigate the steady states regime of both rare earths ions and silicon nanograins levels populations as well as the electromagnetic field for different pumping powers ranging from 1 to 10^4 mW/mm^2. Moreover, the achievable gain has been estimated in this pumping range. The Nd^{3+}doped waveguide shows a higher gross gain per unit length at 1064 nm (up to 30 dB/cm) than the one with Er^{3+}doped active layer at 1532 nm (up to 2 dB/cm). Taking into account the experimental background losses we demonstrate that a significant positive net gain can only be achieved with the Nd^{3+}doped waveguide.

OCIS codes: (050.1755) Computational electromagnetic methods; (160.5690) Rare-earth-doped materials; (230.4480) Optical amplifiers; (230.7370) Waveguides; (230.5590) Quantum-well, -wire and -dot devices.

References and links

1. N. Daldosso and L. Pavesi, "Nanosilicon photonics," Laser Photonics Rev. **3**, 508–534 (2009).
2. G. P. Agrawal, *Fiber-optic communication systems* (John Wiley & Sons, 2010).
3. O. Lumholt, A. Bjarklev, T. Rasmussen, and C. Lester, "Rare earth-doped integrated glass components: modeling and optimization," J. Lightwave Technol. **13**, 275–282 (1995).
4. A. Podhorodecki, J. Misiewicz, F. Gourbilleau, J. Cardin, and C. Dufour, "High energy excitation transfer from silicon nanocrystals to neodymium ions in silicon-rich oxide film," Electrochem. Solid-State Lett. **13**, K26–K28 (2010).
5. A. Polman and F. C. J. M. van Veggel, "Broadband sensitizers for erbium-doped planar optical amplifiers: review," J. Opt. Soc. Am. B **21**, 871–892 (2004).
6. A. N. MacDonald, A. Hryciw, Quan Li, and A. Meldrum, "Luminescence of Nd-enriched silicon nanoparticle glasses," Opt. Mater. **28**, 820–824 (2006).
7. A. Fafin, J. Cardin, C. Dufour, and F. Gourbilleau, "Modeling of the electromagnetic field and level populations in a waveguide amplifier: a multi-scale time problem," Opt. Express **21**, 24171–24184 (2013).

#208737 - $15.00 USD Received 24 Mar 2014; revised 5 May 2014; accepted 5 May 2014; published 13 May 2014

8. P. Pirasteh, J. Charrier, Y. Dumeige, Y. G. Boucher, O. Debieu, and F. Gourbilleau, "Study of optical losses of Nd^{3+} doped silicon rich silicon oxide for laser cavity," Thin Solid Films **520**, 4026–4030 (2012).
9. N. Daldosso, D. Navarro-Urrios, M. Melchiorri, C. Garcia, P. Pellegrino, B. Garrido, C. Sada, G. Battaglin, F. Gourbilleau, R. Rizk, and L. Pavesi, "Er-Coupled Si Nanocluster Waveguide," IEEE J. Sel. Topics Quantum Electron. **12**, 1607–1617 (2006).
10. W. L. Barnes, R. Laming, E. J. Tarbox, and P. R. Morkel, "Absorption and emission cross section of Er3+ doped silica fibers," IEEE J. Quantum. Electron. **27**, 1004–1010 (1991).
11. E. O. Serqueira, N. O. Dantas, A. F. G. Monte, and M. J. V. Bell, "Judd ofelt calculation of quantum efficiencies and branching ratios of Nd3+ doped glasses," J. Non-Cryst. Solids **352**, 3628–3632 (2006).
12. A. Taflove, *Computational electrodynamics: The finite-difference time-domain method*. (Artech House, Boston, 1995).
13. K. Yee, "Numerical solution of initial boundary value problems involving Maxwell's equations in isotropic media," IEEE Trans. Antennas Propag. **14**, 302–307 (1966).
14. A. S. Nagra and R. A. York, "FDTD analysis of wave propagation in nonlinear absorbing and gain media," IEEE Trans. Antennas Propag. **46**, 334–340 (1998).
15. C. Dufour, J. Cardin, O. Debieu, A. Fafin, and F. Gourbilleau, "Electromagnetic modeling of waveguide amplifier based on Nd^{3+} Si-rich SiO2 layers by means of the ADE-FDTD method," Nanoscale Res. Lett. **6**, 1–5 (2011).
16. A. J. Kenyon, C. E. Chryssou, C. W. Pitt, T. Shimizu-Iwayama, D. E. Hole, N. Sharma, and C. J. Humphreys, "Luminescence from erbium-doped silicon nanocrystals in silica: Excitation mechanisms," J. Appl. Phys. **91**, 367–374 (2002).
17. B. J. Ainslie, S. P. Craig, R. Wyatt, and K. Moulding, "Optical and structural analysis of neodymium-doped silica-based optical fibre," Matter. Lett. **8**, 204–208 (1989).
18. M. Govoni, I. Marri, and S. Ossicini, "Carrier multiplication between interacting nanocrystals for fostering silicon-based photovoltaics," Nat. Photonics **6**, 672–679 (2012).
19. F. Priolo, G. Franzo, D. Pacifici, V. Vinciguerra, F. Iacona, and A. Irrera, "Role of the energy transfer in the optical properties of undoped and Er-doped interacting Si nanocrystals," J. Appl. Phys. **89**, 264–272 (2001).
20. D. Pacifici, G. Franzo, F. Priolo, F. Iacona, and L. Dal Negro, "Modeling and perspectives of the Si nanocrystals-Er interaction for optical amplification," Phys. Rev. B **67**, 245301 (2003).
21. V. Toccafondo, S. Faralli, and F. Di Pasquale, "Evanescent multimode longitudinal pumping scheme for si-nanocluster sensitized Er^3+ doped waveguide amplifiers," J. Lightwave Technol. **26**, 3584–3591 (2008).
22. S. L. Oliveira, D. F. de Sousa, A. A. Andrade, L. A. O. Nunes, and T. Catunda, "Upconversion in Nd^{3+}-doped glasses: Microscopic theory and spectroscopic measurements," J. Appl. Phys. **103**, 023103 (2008).
23. J. Yang, K. van Dalfsen, F. Ay and M. Pollnau, "High-gain Al2O3: Nd3+ channel waveguide amplifiers at 880 nm, 1060 nm, and 1330 nm," Appl. Phys. B **101**, 119–127 (2010).
24. A. E. Siegman. *Lasers. Mill Valley*. (University Science Books, 1986).
25. H.-S. Han, S.-Y. Seo, J. H. Shin, and N. Park, "Coefficient determination related to optical gain in erbium-doped silicon-rich silicon oxide waveguide amplifier," Appl. Phys. Lett. **81**, 3720–3722 (2002).
26. N. Daldosso, D. Navarro-Urrios, M. Melchiorri, L. Pavesi, F. Gourbilleau, M. Carrada, R. Rizk, C. Garcia, P. Pellegrino, B. Garrido, and L. Cognolato, "Absorption cross section and signal enhancement in er-doped si nanocluster rib-loaded waveguides," Appl. Phys. Lett. **86**, 261103 (2005).
27. D. Navarro-Urrios, F. Ferrarese Lupi, N. Prtljaga, A. Pitanti, O. Jambois, J. M. Ramirez, Y. Berencen, N. Daldosso, B. Garrido, and L. Pavesi, "Copropagating pump and probe experiments on Si-nc in SiO_2 rib waveguides doped with er: The optical role of non-emitting ions," Appl. Phys. Lett. **99**, 231114 (2011).
28. D. R. Zimmerman and L. H. Spiekman "Amplifiers for the masses: EDFA, EDWA, and SOA amplets for metro and access applications," J. Lightwave Technol. **22**, 63 (2004).

1. Introduction

The development of waveguide optical amplifiers based on rare earth (RE) doped silicon based matrix is of great interest for the semiconductor research community [1]. Erbium ions are particularly interesting due to an optical transition at 1532 nm which coincides with the maximum of transmission in optical glass fiber [2]. However, in the case of erbium this transition involves the ground level, which may limit the achievable gain due to reabsorption mechanisms [3]. To overcome this critical issue, neodymium ion has been recently proposed because its emission scheme makes it more suitable for achieving higher gain [4]. In such a system, the amplification is commonly achieved through RE level population inversion by an appropriate optical pumping. One main drawback of RE ions is their low absorption cross section. However this can be overcome by the use of sensitizers that are characterized by a larger absorption cross section. Those sensitizers have shown an efficient transfer of energy to RE ions in their vicinity.

#208737 - $15.00 USD Received 24 Mar 2014; revised 5 May 2014; accepted 5 May 2014; published 13 May 2014

Several sensitizers of RE have been proposed in literature. Polman *et al* [5] shows the sensitization of Er^{3+}ions by different kinds of sensitizers such as ytterbium ions, metal ions and silicon nanograins (Si-ng). The work of MacDonald *et al* [6] presents the sensitization of Nd^{3+}ions by Si-ng.

In this paper we present a comparative study of waveguides with an active layer containing Si-ng and doped either with erbium or neodymium ions. The typical composition and structure of such waveguides is presented in section 1.1. The electromagnetic field and level populations of Si-ng and RE ions have been computed using an algorithm published in a previous paper [7] and briefly detailed in section 1.2.

In section 2, we describe levels populations equations associated with Si-ng, erbium ions and neodymium ions. For the two RE ions, due to their different transition time properties, two particular ways of calculation will be detailed. In section 3, we present for both RE population inversions, population map and optical gain as a function of optical pump power. We conclude by the comparison of the optical gain of two waveguides doped either with erbium or neodymium ions as a function of the pump power.

1.1. General description of the waveguide

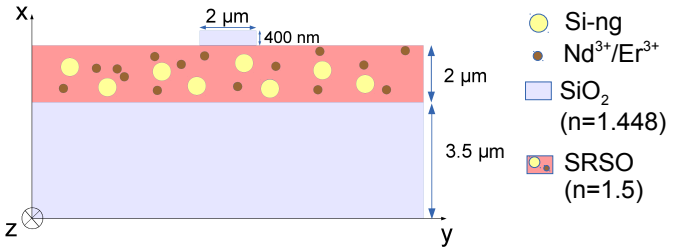

Fig. 1. Transverse section view of the waveguide constituted by bottom and strip cladding layers of silica surrouding the active layer constituted by silicon rich silicon oxide (SRSO) matrix doped with silicon nanograins (Si-ng) and Nd^{3+}or Er^{3+}ions.

The waveguide is composed of three layers (Fig. 1). The bottom cladding layer is composed of pure silica. In order to ensure optical confinement of modes, this layer is about 5 to 8 μm thick in a typical experimental waveguide doped either with Nd^{3+}ions [8] or Er^{3+}ions [9]. In this modeling method the thickness of bottom cladding layer was taken equal to 3.5 μm in order to limit the use of memory. The 2 μm active layer constituted of silicon rich silicon oxide (SRSO) contains Si-ng and RE ions. A pure silica strip layer is stacked on the top of the SRSO layer. The static refractive index (*i.e.* refractive index which remains constant with wavelength) of the active layer (1.5) has been chosen greater than the one of the strip and bottom cladding layers (1.448) to ensure the guiding conditions.

In order to investigate which is the most suitable RE between $Nd^{3+}$and $Er^{3+}$for achieving high gain, both waveguides are pumped continuously (CW) by the propagation in the active layer of a pump mode at 488 nm. A signal mode is co-propagated in the active layer in order to investigate the achievability of amplification by stimulated emission. This signal corresponds to a transition occurring between electronics levels of RE, either at 1532 nm for erbium ions or at 1064 nm for neodymium ions [10,11]. The waveguide dimensions are identical for erbium or neodymium ions and according to the experimental conditions we propagate the fundamental transverse electric mode (TE_{00}) for the pump and signal along z direction. The calculation and the injection of mode profiles in ADE-FDTD method for all wavelengths considered here are described in our previous paper [7].

#208737 - $15.00 USD Received 24 Mar 2014; revised 5 May 2014; accepted 5 May 2014; published 13 May 2014

1.2. Calculation method

The electromagnetic fields ($\mathbf{E},\mathbf{H}$) and Poynting vector ($\mathbf{R}=\mathbf{E}\times\mathbf{H}$) as well as RE and Si-ng populations in steady state are computed by the algorithm described by Fafin et al [7]. This algorithm is based on finite-difference time-domain method (FDTD) and auxiliary differential equations (ADE). The FDTD method consists in the discretization in time and space of the electromagnetic fields [12] according to the K. Yee algorithm [13]. The ADE makes the link between electromagnetic fields and absorption and emission processes by the use of a set of polarisation densities $\mathbf{P}_{ij}$ following a Lorentz electronic oscillator model [12, 14]. A typical polarisation equation (Eq. (1)) between two level populations i and j is described below:

$$\frac{\partial^2\mathbf{P}_{ij}}{\partial t^2}+\Delta\omega_{ij}\frac{\partial\mathbf{P}_{ij}}{\partial t}+\omega_{ij}^2\mathbf{P}_{ij}=\kappa_{ij}(N_i-N_j)\mathbf{E} \tag{1}$$

where $\Delta\omega_{ij}$ is the transition linewidth including radiative, non-radiative and de-phasing processes [15], and ω_{ij} is the resonance frequency of this transition. κ_{ij} used in [7] depends on the transition lifetime τ_{ij} and on the optical index n.

The time evolution of levels populations for each emitter (RE, Si-ng) is described by a rate equation which depends on polarisation densities of considered transitions, lifetimes, transfer coefficient and levels populations. Since in visible wavelength range, the electromagnetic field has a characteristic time of the order of 10^{-15} s and the levels populations of emitters have characteristic lifetimes as long as a few milliseconds [16, 17], a classical ADE-FDTD calculation is impossible in a reasonable time [7]. Indeed with the classical ADE-FDTD method the equations of populations are calculated simultaneously with the electromagnetic field leading to about 10^{15} iterations. We have recently overcome this multiscale issue [7] after splitting the classical ADE-FDTD single loop into two interconnected loops separating short time and long time processes. The electromagnetic fields and polarisation densities are calculated in the short time loop and the rate equations in the long time one. This method allows us to reduce drastically the number of iterations from 10^{15} to 10^5 and consequently reduces the calculation time to more reasonable duration (7 days for the present waveguide at bi-processors quad-core Intel Nehalem EP @ 2.8 GHz). Moreover, in order to minimize phase velocity error and velocity anisotropy errors inherent to the FDTD method, the algorithm was set up with the time and space steps introduced in our previous paper [7].

2. Description of populations

In this section we describe the excitation mechanism of the erbium and neodymium ions and the numerical calculation of the levels populations at the steady state.

2.1. Silicon nanograins

We model silicon nanograins (Si-ng) as a two levels system (Fig. 2) where the ground and excited levels populations (respectively N_{Si0} and N_{Si1}) are given by the rate equations Eq. (2) and Eq. (3). Due to a low probability of multi-exciton generation in a single Si-ng [18], we assume the excitation of one single exciton by Si-ng, therefore the Si-ng population will correspond to the exciton population. After non-radiative transitions in the conduction band, the exciton may either radiatively recombine or excite an emitter in its vicinity. This energy transfer may occur if the energy gap between conduction and valence band of Si-ng matches the energy gap between the RE fundamental level and an upper level leading to a possible emission. According to literature [19] the lifetime of excited level N_{Si1} is chosen at $\tau_{Si_{10}}|_{nr}^{r}=50\ \mu$s. Since few papers studied the energy transfer coefficient in Si-ng and erbium ions [20, 21] and to our knowledge no study was made on this coefficient in Si-ng and neodymium, this energy transfer coefficient

#208737 - $15.00 USD Received 24 Mar 2014; revised 5 May 2014; accepted 5 May 2014; published 13 May 2014

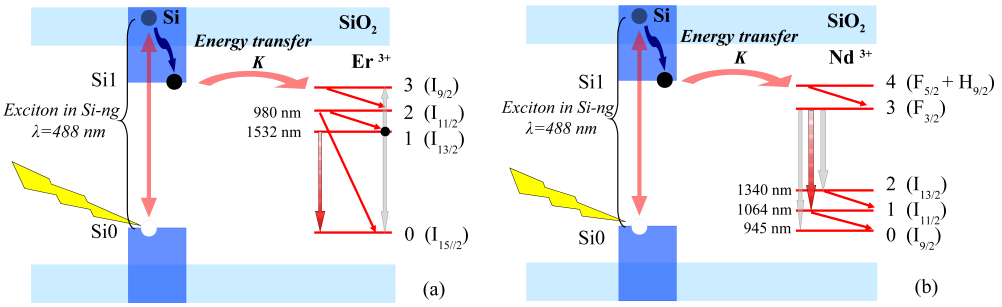

Fig. 2. Excitation mechanism of (a) erbium ions and (b) neodymium ions

between Si-ng and both RE is assumed identical and taken equal to $K = 10^{-14}$ cm^3/s. We took the same concentration of Si-ng equal to 10^{19} cm^{-3} for both active layers doped either with Er^{3+}or Nd^{3+}ions. In order to simulate a realistic absorption and emission cross section equal to 10^{-16} cm^2 the linewidth $\Delta\omega_{ij}$ and the number of polarizations N_p are respectively fixed to 10^{14} rad/s and 2756 according to the method explained in [7]. These parameters are reported in Table 1.

$$\frac{dN_{Si_1}(t)}{dt} = +\frac{1}{\hbar\omega_{Si_{10}}}\mathbf{E}(t)\frac{d\mathbf{P}_{Si_{10}}(t)}{dt} - \frac{N_{Si_1}(t)}{\tau_{Si_{10}}|_{nr}^{r}} - KN_{Si_1}(t)N_0(t) \tag{2}$$

$$\frac{dN_{Si_0}(t)}{dt} = -\frac{1}{\hbar\omega_{Si_{10}}}\mathbf{E}(t)\frac{d\mathbf{P}_{Si_{10}}(t)}{dt} + \frac{N_{Si_1}(t)}{\tau_{Si_{10}}|_{nr}^{r}} + KN_{Si_1}(t)N_0(t) \tag{3}$$

Table 1. Parameters levels of silicon nanograins

$j \to i$	Lifetime (s)	$\omega_{ij}(10^{15}$ rad/s)	$\Delta\omega_{ij}(10^{14}$ rad/s)	N_p
$1 \to 0$	50.10^{-6}	3.682	1	2756

2.2. *Erbium ions*

Erbium ions are modelled by four levels: 0 ($^4I_{15/2}$), 1 ($^4I_{13/2}$), 2 ($^4I_{11/2}$) and 3 ($^4I_{9/2}$). We consider two non-radiative transitions 3→2, 2→1 and one radiative transition from level 1 to level 0 at 1532 nm. The emission cross section of this transition is equal to 6×10^{-21}cm^{-2} [20, 21] and corresponds to a linewidth $\Delta\omega_{10}$ equal to 0.15×10^{15} rad/s with one polarisation ($N_p = 1$) [7]. Moreover there is an up-conversion process from level 1 to level 0 and 3 which can be modelled by a coefficient $C_{up} = 5 \times 10^{-17}$ cm^3/s. The concentration of erbium ions is equal to 10^{20} cm^{-3}. The time evolution of Er^{3+}levels populations is described by the rate equations Eq. (4) to Eq. (7). All parameters of erbium ions transitions are taken from [20, 21] and reported in Table 2.

#208737 - $15.00 USD Received 24 Mar 2014; revised 5 May 2014; accepted 5 May 2014; published 13 May 2014

$$\frac{dN_3(t)}{dt} = -\frac{N_3(t)}{\tau_{32}|_{nr}} + KN_{Si_1}(t)N_0(t) + C_{up}N_1^2 \tag{4}$$

$$\frac{dN_2(t)}{dt} = +\frac{N_3(t)}{\tau_{32}|_{nr}} - \frac{N_2(t)}{\tau_{21}|_{nr}} - \frac{N_2(t)}{\tau_{20}|_{nr}} \tag{5}$$

$$\frac{dN_1(t)}{dt} = +\frac{1}{\hbar\omega_{10}}\mathbf{E}(t)\frac{d\mathbf{P}_{10}(t)}{dt} + \frac{N_2(t)}{\tau_{21}|_{nr}} - \frac{N_1(t)}{\tau_{10}|_{nr}^{r}} - 2C_{up}N_1^2 \tag{6}$$

$$\begin{aligned}\frac{dN_0(t)}{dt} = &-\frac{1}{\hbar\omega_{10}}\mathbf{E}(t)\frac{d\mathbf{P}_{10}(t)}{dt} \\ &+\frac{N_2(t)}{\tau_{20}|_{nr}} + \frac{N_1(t)}{\tau_{10}|_{nr}^{r}} - KN_{Si_1}(t)N_0(t) + C_{up}N_1^2\end{aligned} \tag{7}$$

Table 2. Parameters levels of erbium ions

$j \to i$	3→2	2→1	2→0	1→0
Lifetime (s)	0.1×10^{-6}	2.4×10^{-6}	710×10^{-6}	8.5×10^{-3}
ω_{ij} (10^{15} rad/s)		1.23		
$\Delta\omega_{ij}$ (10^{15} rad/s)		0.15		
N_p		1		

2.3. Neodymium ions

Neodymium ions are modelled by five levels: 0 ($^4I_{9/2}$), 1 ($^4I_{11/2}$), 2 ($^4I_{13/2}$), 3 ($^4F_{3/2}$) and 4 ($^4F_{5/2} +^2 H_{9/2}$). We consider three non-radiative transitions 4→3, 2→1, 1→0 and three radiative transitions 3→2 at 1340 nm, 3→1 at 1064 nm and 3→0 at 945 nm. The emission cross section of these transitions is equal to 10^{-19}cm^{-2} [24] and correspond to linewidths $\Delta\omega_{ij}$ reported in Table 3. The up-conversion coefficient C_{up} ranging from 1×10^{-17} to 5×10^{-17} cm^3/s was found in [22, 23]. This value leads to an equivalent lifetime $\tau_{up} = \frac{1}{C_{up}N_1}$ that remains 10 times larger than the longest level lifetime of Nd^{3+}ions which allows neglecting the up-conversion process [7]. The concentration of neodymium ions is equal to 10^{20} cm^{-3}. The time evolution of Nd^{3+}levels populations is described by the rate equations Eq. (8) to Eq. (12). Parameters of neodymium ions transitions are taken from [11, 24] and reported in Table 3.

$$\frac{dN_4(t)}{dt} = -\frac{N_4(t)}{\tau_{43}|_{nr}} + KN_{Si_1}(t)N_0(t) \tag{8}$$

$$\begin{aligned}\frac{dN_3(t)}{dt} = &+\frac{1}{\hbar\omega_{30}}\mathbf{E}(t)\frac{d\mathbf{P}_{30}(t)}{dt} + \frac{1}{\hbar\omega_{31}}\mathbf{E}(t)\frac{d\mathbf{P}_{31}(t)}{dt} + \frac{1}{\hbar\omega_{32}}\mathbf{E}(t)\frac{d\mathbf{P}_{32}(t)}{dt} \\ &+\frac{N_4(t)}{\tau_{43}|_{nr}} - \frac{N_3(t)}{\tau_{30}|_{nr}^{r}} - \frac{N_3(t)}{\tau_{31}|_{nr}^{r}} - \frac{N_3(t)}{\tau_{32}|_{nr}^{r}}\end{aligned} \tag{9}$$

$$\frac{dN_2(t)}{dt} = -\frac{1}{\hbar\omega_{32}}\mathbf{E}(t)\frac{d\mathbf{P}_{32}(t)}{dt} + \frac{N_3(t)}{\tau_{32}|_{nr}^{r}} - \frac{N_2(t)}{\tau_{21}|_{nr}} \tag{10}$$

$$\frac{dN_1(t)}{dt} = -\frac{1}{\hbar\omega_{31}}\mathbf{E}(t)\frac{d\mathbf{P}_{31}(t)}{dt} + \frac{N_3(t)}{\tau_{31}|_{nr}^{r}} - \frac{N_1(t)}{\tau_{10}|_{nr}} + \frac{N_2(t)}{\tau_{21}|_{nr}} \tag{11}$$

$$\frac{dN_0(t)}{dt} = -\frac{1}{\hbar\omega_{30}}\mathbf{E}(t)\frac{d\mathbf{P}_{30}(t)}{dt} + \frac{N_3(t)}{\tau_{30}|_{nr}^{r}} + \frac{N_1(t)}{\tau_{10}|_{nr}} - KN_{Si_1}(t)N_0(t) \tag{12}$$

#208737 - $15.00 USD Received 24 Mar 2014; revised 5 May 2014; accepted 5 May 2014; published 13 May 2014

Table 3. Parameters levels of neodymium ions

$j \rightarrow i$	4→3	3→2	3→1	3→0	2→1	1→0
Lifetime (s)	230×10^{-12}	1000×10^{-6}	200×10^{-6}	250×10^{-6}	970×10^{-12}	510×10^{-12}
ω_{ij} (10^{15} rad/s)		1.34	1.77	1.99		
$\Delta\omega_{ij}$ (10^{15} rad/s)		0.67	0.18	0.11		
N_p		1	1	1		

2.4. Difference in calculation method of populations

We aim at calculating levels populations in steady states in a fast and convenient manner. Consequently, the preferred method would be an analytical calculation of populations by setting $dN_i/dt = 0$. However, this is only applicable in case of neodymium levels equations. Moreover, the up-conversion term in erbium rate equations leads to equations that are hardly analytically solvable. In that case, the steady states of population levels are reached by a finite difference method. This calculation was possible using a reasonable time step of 0.01 μs ten times lower than the shortest lifetime (0.1 μs) considered in this model. The calculation time is then no longer negligible but does not rise up significantly the global calculation time of our ADE-FDTD method.

3. Results and discussion

The solution of Eq. (2) to Eq. (12) gives the levels populations in their steady states. We define for $i \rightarrow j$ transition the population inversion (section 3.1) as the ratio $(N_i - N_j)$ over the total population number ($N_{tot} = 10^{20}$ at/cm^3 for RE or $N_{Si_{tot}} = 10^{19}$ at/cm^3 for Si-ng). We deduced also the optical gain (section 3.2) at 1064 nm for $Nd^{3+}$and 1532 nm for Er^{3+}. These values are computed for a pump power ranging from 1 to 10^4 mW/mm^2.

3.1. Populations inversion

We present in this section the spatial distribution of population inversion in waveguides doped either with erbium or neodymium ions for a pump power of 1000 mW/mm^2 in a longitudinal section view along the propagation axis (Fig. 3). For both waveguides the plots show a decrease of population inversion with direction of propagation which can be attributed to the coupling between rare earth ions and silicon nanograins.

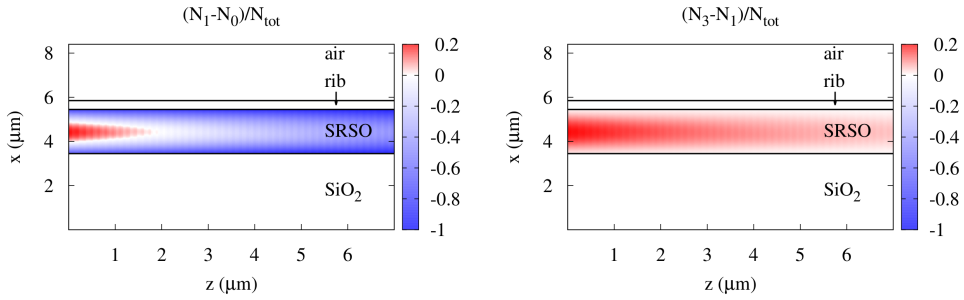

Fig. 3. Population inversion along the direction of propagation for the erbium ions (on the left) and the neodymium ions (on the right) for a pump power equal to 1000 mW/mm^2

For erbium ions, the population inversion remains positive over a length of 1.5 μm. Beyond

#208737 - $15.00 USD Received 24 Mar 2014; revised 5 May 2014; accepted 5 May 2014; published 13 May 2014

this length, the population inversion becomes negative witnessing the threshold effect occurring with three-level system.

For neodymium ions the population inversion remains positive along the whole structure. Indeed, in this four-level system, the level 1 is depopulated quickly to the ground level leading to $N_3 >> N_1$.

We now consider the population inversion distribution of Si-ng presented in longitudinal section view in Fig. 4 for both RE. This decrease of population inversion of Si-ng shows an identical behaviour with direction of propagation as the one observed with RE. This is characteristic of the pump strong absorption due to the presence of the nanograins as shown in our previous paper [7].

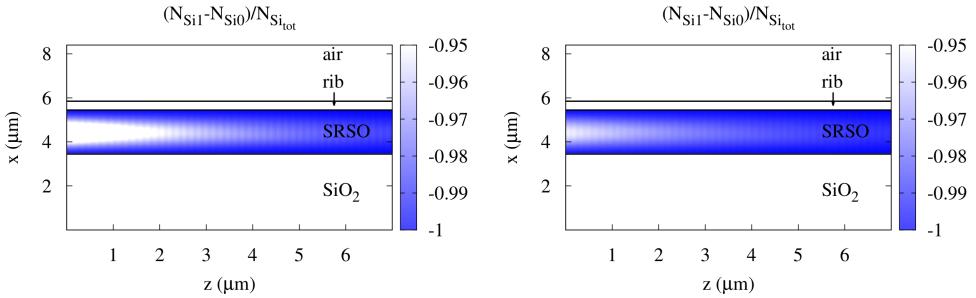

Fig. 4. Population inversion of Si-ng along the direction of propagation in the case of erbium ions (on the left) and neodymium ions (on the right) for a pump power equal to 1000 mW/mm^2

From Fig. 4 we extract a particular set of values of the population inversion of Si-ng along the direction of propagation recorded at $x = 4.5$ μm and $y = 8.55$ μm (center of the XY section of the active layer) (Fig. 5). On this figure, we observe along the whole length of the waveguide a larger Si-ng population inversion with erbium than with neodymium. Since the Si-ng modeling is the same with both RE, the population inversion difference is due to each specific Si-ng/RE interaction. This interaction is governed by the transfer coefficient K, which is the same for both RE, but also by specific transitions lifetimes of each RE. The larger population inversion observed for erbium than with neodymium is consequently due to the difference of lifetimes between these RE (Table 2 and 3). This observation leads us to the conclusion that RE excitation occurring from Si-ng is more efficient in the case of neodymium than in the case of erbium ions due to the specific time dynamics of transitions in different RE.

Figure 6 shows the influence of pump power on population inversion for the erbium and the neodymium ions as well as for the Si-ng. We observe that the population inversion occurs above a threshold pump power (600 mW/mm^2) for erbium. This behaviour is typical of a three-level system. For neodymium ions, we observe a positive population inversion for the whole pump power range which is characteristic of a four-level system. For high pump power (1000 mW/mm^2), both populations inversions reach a comparable value witnessing the saturation of the excitation mechanism.

Finally, we plot (dotted lines) the population inversion of Si-ng as a function of pump power. Whatever the pump power, this inversion is higher for erbium than for neodymium ions. This evidences a more efficient transfer from Si-ng to neodymium ions than to erbium ions.

#208737 - $15.00 USD Received 24 Mar 2014; revised 5 May 2014; accepted 5 May 2014; published 13 May 2014

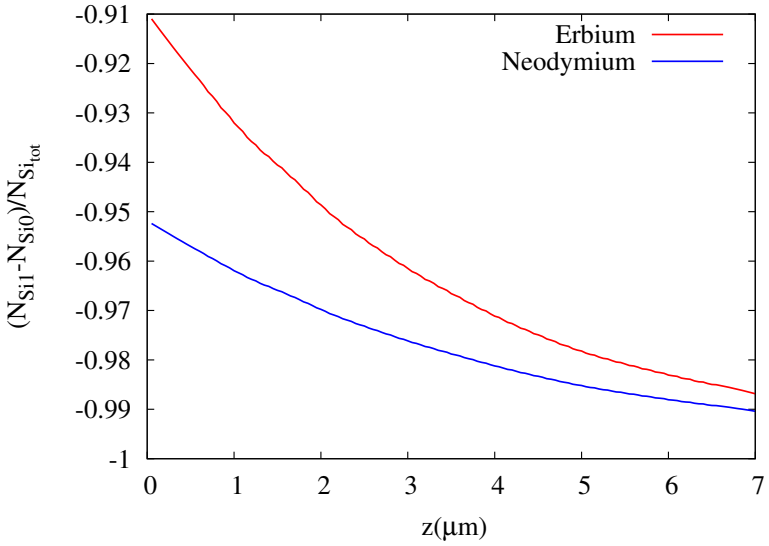

Fig. 5. Population inversion of Si-ng along the direction of propagation in the case of erbium and neodymium recorded at $x = 4.5$ μm and $y = 8.55$ μm (center of the XY section of the active layer) for a pump power equal to 1000 mW/mm^2

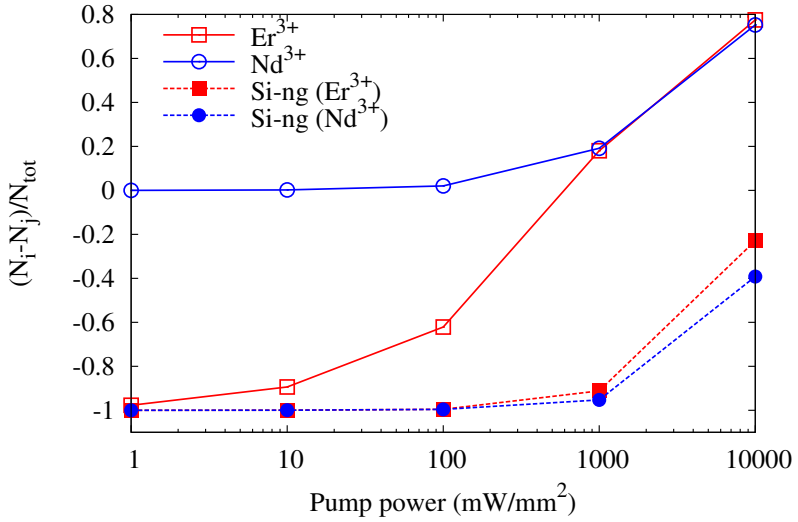

Fig. 6. Population inversion for neodymium, erbium ions and silicon nanograins divided by the rare earth ions concentration (10^{20} at/cm^3) recorded at $x = 4.5$ μm and $y = 8.55$ μm (center of the XY section of the active layer) and z=0 (beginning of the waveguide)

3.2. *Optical gain*

From population levels $N_i(x,y,z)$ we deduced the local gross gain per unit length $g_{dB/cm}$ (Eq. (13)) at the signal wavelength:

$$g_{dB/cm}(x,y,z) = \frac{10}{ln10}\left(\sigma_{em}N_{high}(x,y,z) - \sigma_{abs}N_{low}(x,y,z)\right) \tag{13}$$

#208737 - $15.00 USD Received 24 Mar 2014; revised 5 May 2014; accepted 5 May 2014; published 13 May 2014

where N_{high} and N_{low} are respectively the higher and lower levels of the considered transition and σ_{abs} and σ_{em} are absorption and emission cross sections. For erbium ions, we make the link $N_{high} = N_1$ and $N_{low} = N_0$ and for neodymium ions $N_{high} = N_3$ and $N_{low} = N_1$ and we assume equal emission and absorption cross sections for one RE. The local gross gain per unit length recorded at $x = 4.5$ μm and $y = 8.55$ μm (center of the XY section of the active layer) and $z = 0$ (beginning of the waveguide) is plotted in Fig. 7.

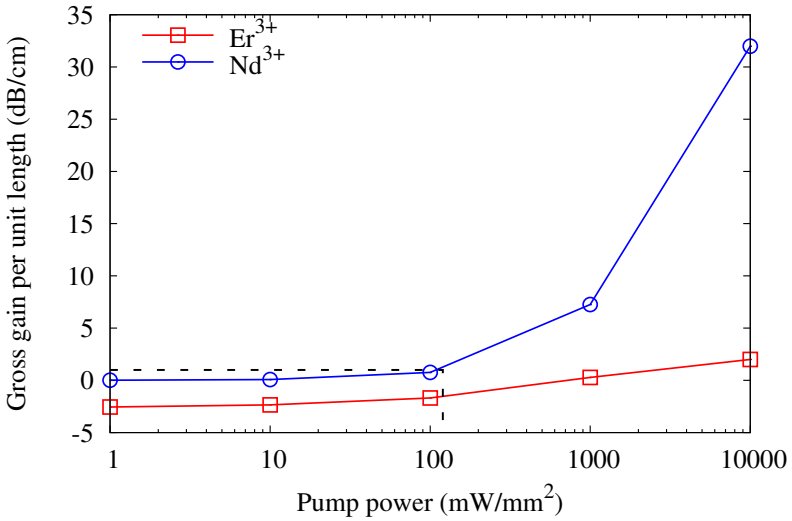

Fig. 7. Local gross gain per unit length at the center of the active layer and in the beginning of the waveguide as a function of the pumping power for a waveguide doped with Nd^{3+}(open circle) and a waveguide doped with Er^{3+}(open square) recorded at $x = 4.5$ μm and $y = 8.55$ μm (center of the XY section of the active layer) and $z = 0$ (beginning of the waveguide). Losses found by Pirasteh *et al* [8] are represented (dashed line).

For Er^{3+}doped waveguide, we find that, above a threshold pump power of 1550 mW/mm^2, a positive gross gain is reached which increases up to 2 dB/cm for the highest pump power simulated in our study. In order to estimate the net gain, we must account for the background losses such as those found by Navarro-Urrios *et al* [27] on comparable samples (3.0 dB/cm at 1532 nm). We can conclude that it is not possible to reach a positive net gain in this range of pump power. However Navarro-Urrios *et al* found a positive net gain equal to 0.3 dB/cm, this small difference with our modelling result may be explained by higher pump power that was used in the experiment (4.10^5 mW/mm^2 to 6.10^6 mW/mm^2).

For Nd^{3+}doped waveguide, we find that the optical gain remains positive over the whole power range. It increases up to 30 dB/cm for the highest pump power of 10^4 mW/mm^2. We can also estimate a net gain taking into account background losses of 0.8 dB/cm found by Pirasteh *et al* in a similar system [8]. Figure 7 shows that for a pump power above 130 mW/mm^2 the losses (dashed line) can be compensated leading to a net gain.

The gross gain per unit length obtained for Nd^{3+}remains higher that the one obtained for Er^{3+}whatever the pump power range. The gross gain per unit length difference (between $Nd^{3+}$and Er^{3+}doped waveguide) is all the higher as the pump power increases. This feature may be due to the difference in Si-ng/RE transfer efficiency (section 3.1) linked to the levels dynamics as well as to the difference in absorption/emission cross section ($\sigma_{Er} = 6 \times 10^{-21}$ cm^2 against $\sigma_{Nd} = 1 \times 10^{-19}$ cm^2). The three categories of commercially available optical amplifier

#208737 - $15.00 USD Received 24 Mar 2014; revised 5 May 2014; accepted 5 May 2014; published 13 May 2014

on C-band (EDFA, EDWA and SOA) present a gain level about 20 to 25 dB with a working length ranging from cm to few meters for EDFA and for a power consumption mainly dedicated to optical or electrical pumping of about few watts [28]. Since we found a low gain and a short length of positive population inversion by modeling of Er^{3+}doped based waveguide on the broad range of pump power. We conclude to the impossibility of achievement of an optical amplifier with this configuration of co-propagating pump and signal which would compete with commercially available systems. The gross gain per unit length reachable with Nd^{3+}, about one order of magnitude larger than the one obtained with Er^{3+}, could lead a significant amplification. To our knowledge, there is no commercially available comparable optical amplifier based on Nd3+ emission bands. However, Nd^{3+}doped Aluminum oxide channel waveguide amplifiers developed by Yang *et al* show a maximal internal gain of 6 dB/cm for a pump power of 45 mW [23].

4. Conclusion

Our algorithm based on ADE-FDTD method previously used for modeling steady states of fields, population levels and gross gain per unit length for Nd^{3+}doped waveguide has been extended with success to the case of erbium ions doped waveguide.

We have demonstrated that the neodymium ions are more suitable than the erbium ions to obtain a net positive gain per unit length in silica based waveguide containing silicon nanograins. The theoretical maximum gross gain per unit length of 2 dB/cm at 1532 nm (10^4 mW/mm^2) does not compensate background losses experimentally estimated to 3 dB/cm. On the contrary, the use of neodymium ions leads to a gross gain per unit length of 30 dB/cm at 1064 nm (10^4 mW/mm^2). Moreover the background losses are compensated above a pump power threshold of 130 mW/mm^2. This theoretical demonstration of a large gross gain per unit length for a Nd^{3+}doped active layer may justify further experimental work in order to achieve Nd^{3+}doped silicon based waveguide optical amplifier or laser.

In order to investigate the possibility of achieving larger gain further studies may be performed with other concentrations of rare earth and Si-ng, other rare earth and other pumping configurations. This method may be applied to study the electromagnetic fields and levels populations distribution in steady states of systems with other kind of emitters (quantum dots, quantum wells...) and in other configuration (VCELs, down-converting layers...).

Acknowledgments

The authors are grateful to the French Nation Research Agency, which supported this work through the Nanoscience and Nanotechnology program (DAPHNES project ANR-08-NANO-005) and Centre de ressources informatiques de Haute-Normandie, (CRIHAN France) for computing facilities.

#208737 - $15.00 USD Received 24 Mar 2014; revised 5 May 2014; accepted 5 May 2014; published 13 May 2014

Langmuir

Article

pubs.acs.org/Langmuir

Photochemical Preparation of Silver Nanoparticles Supported on Zeolite Crystals

Moussa Zaarour,[†] Mohamad El Roz,[†] Biao Dong,[†] Richard Retoux,[‡] Roy Aad,[§] Julien Cardin,[§] Christian Dufour,[§] Fabrice Gourbilleau,[§] Jean-Pierre Gilson,[†] and Svetlana Mintova*[,†]

[†]LCS, [‡]CRISMAT, and [§]CIMAP, ENSICAEN, Université de Caen, CNRS, 6 bd du Maréchal Juin, 14050 Caen, France

Supporting Information

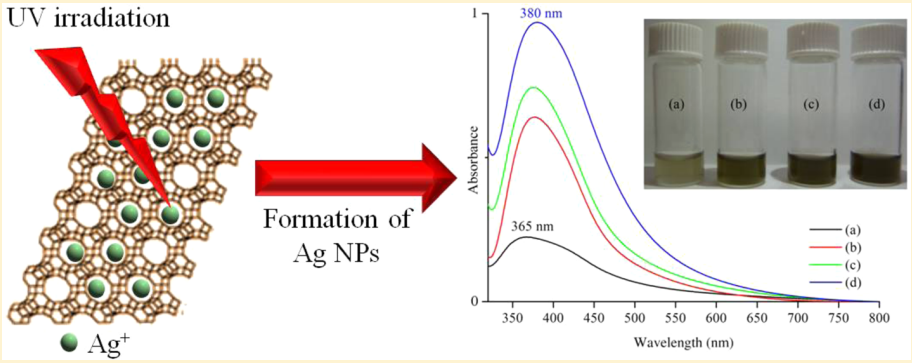

ABSTRACT: A facile and rapid photochemical method for preparing supported silver nanoparticles (Ag-NPs) in a suspension of faujasite type (FAU) zeolite nanocrystals is described. Silver cations are introduced by ion exchange into the zeolite and subsequently irradiated with a Xe−Hg lamp (200 W) in the presence of a photoactive reducing agent (2-hydroxy-2-methylpropiophenone). UV−vis characterization indicates that irradiation time and intensity (I_0) influence significantly the amount of silver cations reduced. The full reduction of silver cations takes place after 60 s of a polychromatic irradiation, and a plasmon band of Ag-NPs appears at 380 nm. Transmission electron microscopy combined with theoretical calculation of the plasmon absorbance band using Mie theory shows that the Ag-NPs, stabilized in the micropores and on the external surface of the FAU zeolite nanocrystals, have an almost spheroidal shape with diameters of 0.75 and 1.12 nm, respectively. Ag-NPs, with a homogeneous distribution of size and morphology, embedded in a suspension of FAU zeolites are very stable (~8 months), even without stabilizers or capping agents.

INTRODUCTION

Silver nanoparticles are currently the focus of intensive research because of their catalytic, antibacterial, and optical properties.[1] Their interesting optical properties, more precisely, their plasmonic properties, make them highly desirable in various applications like sensors,[2] OLEDs,[3] and photovoltaic solar cells.[4−6] Their plasmonic properties depend strongly on their size, morphology, and density.[7] Therefore, a systematic modification of these parameters allows the tuning of their plasmonic response over the whole visible spectrum.

In solution, silver nanoparticles agglomerate to form clusters or even large particles and hence lose their optical properties. To prevent this and maintain the plasmonic properties, Ag-NPs are usually charged or dispersed in media such as noble gases, organic scaffolds, or a porous matrix (zeolites).[7]

Zeolites are crystalline aluminosilicates with a framework made of SiO_4 and AlO_4 tetrahedra, in which the negatively charged Al sites are neutralized by the charge-balancing extra-framework cations, such as K^+, Li^+, Na^+, etc.[8] These charge compensating cations are noncovalently bonded to the zeolite and offer the possibility of replacing them with organic molecules or metals with interesting properties for optical applications.[9−14] In fact, the use of zeolites for optical applications has already attracted the attention of researchers because of their diverse structures, high porosity, high thermal stability, and availability in different sizes and morphologies.[10] The incorporation of zeolites into an optical device offers the possibility of stabilizing and organizing the photoactive guests as well as preventing intermolecular interactions that reduce or even quench their photophysical properties.[11] As a result, several studies reported the use of zeolites as suitable supports for Ag-NPs.[12−14]

Ag-NPs are generally prepared by either thermal reduction,[15] microwave reduction,[16] sonochemical reduction,[17] chemical reduction,[18] or photoreduction of silver cations (Ag^+) in solution.[19−21] Thermal treatment is a classical way to prepare Ag-NPs: the solution containing silver cations is heated in the presence of a reducing agent such as H_2 or CO, introduced

Received: February 19, 2014
Revised: May 7, 2014

   dx.doi.org/10.1021/la5006743 | *Langmuir* XXXX, XXX, XXX−XXX

directly into the reaction mixture, or generated *in situ*.[15] Microwave-assisted reduction presents several advantages like a more homogeneous heating, a shorter reaction time, and an easier nucleation of Ag-NPs.[16] The sonochemical process is used for the preparation of Ag-NPs when the particle size strongly depends on the type of reducing agent applied.[17] Using sodium borohydride, a strong reducing agent, results in spherical Ag-NPs 10 nm in size, while with a weak reducing agent, such as sodium citrate, the formation of Ag-NPs ~3 nm in size is observed.[17] Moreover, chemical treatment is an efficient process for preparing Ag-NPs in solution with good control of their size and shape. The key to a rational design is to find the proper combination of silver precursors, a reducing agent, stabilizers, and reaction conditions (rate and pH).[18] The drawback of these methods is the use of relatively large amounts of reducing agents and their subsequent elimination in an additional step. Furthermore, Ag-NPs are generally sensitive to heat and oxygen; the addition of capping and stabilizing agents is usually recommended to preserve their structure and prevent their aggregation in solution.

The photoassisted synthesis (photoreduction) of silver is another method used for the preparation of Ag-NPs, albeit less practiced. It allows the preparation of stable nanoparticles of Ag-NPs by irradiation of a reaction mixture with a light source (laser or lamp) in the presence of photoreducing agents without the need to introduce stabilizers or surfactants.[19−21] Their size and the time needed for their preparation are directly proportional to the irradiation power of the light source. For example, with a low-power lamp (4 W), irradiation for 9 h is needed to produce 19 nm diameter Ag-NPs,[21] while with a stronger source (150 W), the reaction takes only 45 min. However, in the latter case, the Ag-NPs are polydisperse and smaller than when they are prepared using a lower-energy lamp.[21]

In this work, we report a facile and rapid preparation of Ag-NPs, supported on FAU type zeolite crystals, using a photochemical reduction method. The silver cations are introduced into the FAU zeolite nanocrystals (Si/Al = 1.2) by ion exchange and subsequently reduced (to Ag^0) by irradiation with a Xe−Hg lamp (200 W) for 5−60 s. The irradiation intensity and time have a direct influence on the Ag nanoparticles and their plasmonic properties. The microstructure and optical properties of the Ag-NPs are monitored by high-resolution transmission electron microscopy (HRTEM) and UV−vis spectroscopy, respectively.

EXPERIMENTAL SECTION

Raw Materials. Silver nitrate ($AgNO_3$) was purchased from Alfa Aesar, and 2-hydroxy-2-methylpropiophenone [$C_6H_5COC(CH_3)_2OH$], benzophenone ($C_{13}H_{10}O$), and benzaldehyde (C_7H_6O) were purchased from Sigma-Aldrich. Aluminum hydroxide [$Al(OH)_3$, Sigma-Aldrich], sodium hydroxide (NaOH, Sigma-Aldrich, 97%), and colloidal silica (SiO_2, Ludox-HS 30, 30 wt % SiO_2, pH 9.8, Aldrich) were used to prepare FAU type zeolite crystals (zeolite X) according to the procedure below; these reagents were used without further purification.

Preparation of a FAU Type Zeolite Suspension. The FAU nanocrystals were synthesized from a clear precursor suspension with a 9:0.9:10:200 Na_2O:Al_2O_3:SiO_2:H_2O ratio. The suspension was prepared by mixing $Al(OH)_3$, NaOH, and SiO_2 with doubly distilled water and subjected to vigorous stirring at room temperature until a clear suspension was obtained. Then the resulting clear suspension was aged for 24 h at room temperature prior to the hydrothermal synthesis. The crystallization was performed at 150 °C for 45 min in a conventional oven. The zeolite nanocrystals were purified by centrifugation (25000 rpm for 4 h) and dispersed in doubly distilled water (dd H_2O) until the pH of the decanted suspension reached 7. Finally, the purified FAU zeolite sample was centrifuged and decanted; the resulting FAU slurry is further ion-exchanged as described below.

Ion Exchange of FAU Zeolites. The FAU slurry (100 mg) was sonicated in a 10 mL aqueous solution of $AgNO_3$ (0.1 M) for 6 h, and the product was purified by centrifugation and washed three times with doubly distilled water to remove any excess of silver. The ion-exchanged FAU zeolite in a water suspension will hereafter be termed FAU-Ag^+. The as-prepared suspension was freeze-dried; the color of the FAU-Ag^+ sample prior reduction is white. The FAU-Ag^+ powder sample was redispersed in water (0.25 g/L in H_2O). One milliliter of this FAU-Ag^+ suspension containing 2.64×10^{-4} mg of Ag^+ was then added to 0.1 mL of 2-hydroxy-2-methylpropiophenone (0.096 M in ethanol, 99%). This mixture was stirred while being irradiated with a Xe−Hg polychromatic lamp with an intensity varying from 20 to 100% for 5−60 s.

Preparation of Ag-NPs in FAU Zeolites. UV irradiation of the FAU-Ag^+ suspension (1 mL) was conducted with a polychromatic Xe−Hg lamp (LC8-01A spot light, Hamamatsu, L10852, 200 W) using a UV light guide (model A10014-50-0110). This device was mounted at the entrance of the reactor containing the zeolite suspensions to establish a "homogeneous" irradiation. The UV irradiation intensity (I_0) at full capacity of the lamp measured with a light power meter (from Hamamatsu) was 55 mW/cm^2 at 366 nm. All samples were stirred in the reactor during the reduction process. The Xe−Hg polychromatic lamp intensity varied from 20 to 100% for 5−60 s. The FAU suspensions containing Ag-NPs will hereafter be termed FAU-Ag.

Characterization of Ag-NPs in FAU Zeolite Suspensions. The UV−vis absorption spectra of the zeolite suspensions containing Ag-NPs were recorded on a Thermo-electron evolution 500 UV−vis spectrometer working in transmission and in quartz cuvettes with a 1 cm path length. The zeolite suspension prior to ion exchange was used as a reference for all UV−vis measurements.

Dynamic Light Scattering (DLS) Analysis. The hydrodynamic diameters of the as-prepared suspensions of zeolite nanoparticles and those containing Ag-NPs were determined with a Malvern Zetasizer Nano instrument using a backscattering geometry (scattering angle of 173°, He−Ne laser with a 3 mW output power at a wavelength of 632.8 nm). The DLS analyses were performed on samples with a solid concentration of 1 wt %.

High-Resolution Transmission Electron Microscopy (HRTEM). The crystal size, morphology, crystallinity, and chemical composition of suspensions of FAU-containing Ag-NPs were characterized using HRTEM coupled with an energy dispersive analysis (EDS) on a 200 kV JEOL 2010 FEG STEM electron microscope (tilt of ±42°) equipped with an EDS (energy dispersive spectrometer, Si/Li detector; a double tilt sample holder was used). The suspensions were sonicated for 15 min prior to their deposition on a holey carbon supported on a nickel grid.

Theoretical Modeling of the Ag Plasmon Band. The simulation of the UV−vis absorbance spectra was performed using the Mie theory.[22] Simulations were conducted using the refractive index of water taken from the IAPWS[23] or an adjustable constant refractive index for the surrounding medium. The refractive index of silver was taken from ref 24. The refractive index of silver was size-corrected to take into account the reduction of the electron mean free path in nanoparticles. The size correction was conducted by introducing an additional surface contribution into the electronic scattering to retain the Drude part of the dielectric function using the electron scattering rate given by Kriebig:[25]

$$\gamma = \gamma_0 + 2g\frac{\nu_F}{D} \quad (1)$$

where γ_0 is the bulk scattering rate and ν_F is the Fermi velocity of silver. The nanoparticle diameter (D) and a phenomenological dimensionless parameter (g) are related to the shape of the particles as well as the material properties and the surrounding dielectric host

dx.doi.org/10.1021/la5006743 | Langmuir XXXX, XXX, XXX−XXX

Scheme 1. Preparation of Ag-NPs by Photogeneration of Free Radicals in Suspension

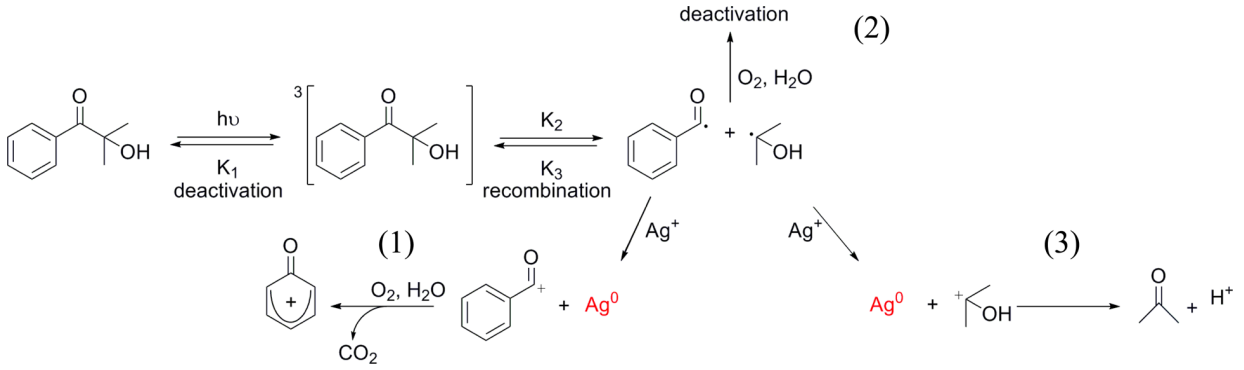

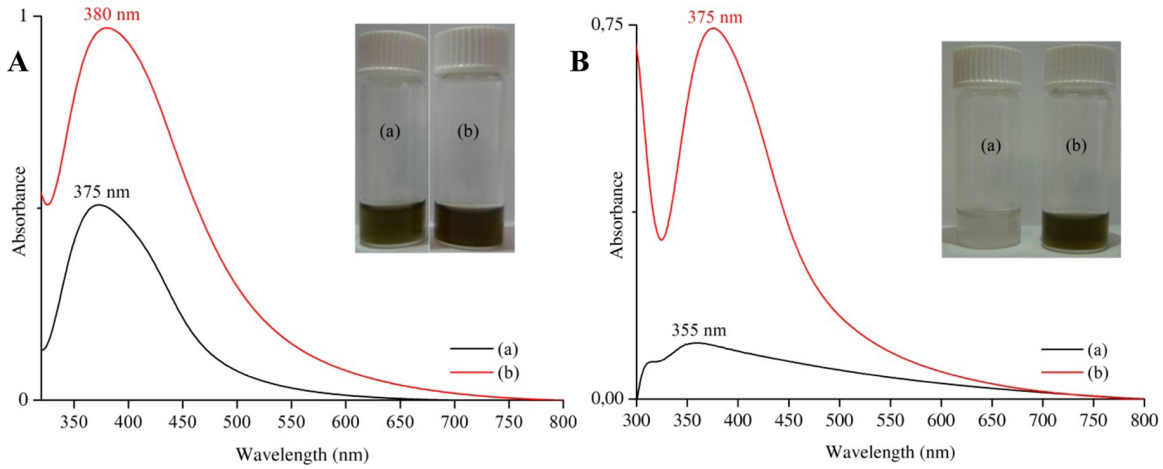

Figure 1. Evolution of the Ag plasmon band in FAU zeolite suspensions after UV treatment (H_2O suspension) (A) at 60 s at (a) an I_0 of 20% or (b) an I_0 of 100% and (B) at 15 s at (a) an I_0 of 20% or (b) an I_0 of 100%.

matrix. For spherical nanoparticles, g is estimated to be ~0.7 ± 0.1.[26] The values of γ_0 and ν_F for silver were taken from ref 27.

RESULTS AND DISCUSSION

The photochemical treatment of materials is a fast and efficient method for producing electrons. It requires the use of a photoreducing agent or a photoactive species that becomes electronically excited and rapidly transfers electrons to the Ag^+ cations (reducing them into Ag^0), upon irradiation at a specific wavelength. The compatibility between the photoreducing agent and the irradiation source is of prime importance because the catalyst should absorb in the same range as the light excitation to generate the free electrons. Besides the reducing activity, the catalyst is used as a stabilizing agent for the produced species.

In this work, three photoreducing agents, benzophenone, benzaldehyde, and 2-hydroxy-2-methylpropiophenone, are used as photocatalysts. The first two show a very low reactivity in the FAU-Ag^+ suspension, while the last one is the most compatible with the zeolite suspension and consequently used in all experiments. To ensure the miscibility between the zeolite suspension and the reducing agent, 2-hydroxy-2-methylpropiophenone was first dissolved in ethanol and subsequently added to the FAU-Ag^+ suspension (in water); the mixture was stirred vigorously during the reaction to ensure homogeneous suspensions free of sedimentation.

The photo-reducing agent used is from the family of hydroxyl-methylphenone, which is well-known to undergo a homolytic C−C bond scission (α-cleavage) upon exposure to UV irradiation giving rise to a pair of radicals[28] (Scheme 1). After the radical formation, the following processes are possible: (1) recombination of radicals going back to the original compound or (2) deactivation of radicals by dissolved oxygen present in the reaction medium (Scheme 1). (3) In the presence of silver cations, the radicals can undergo a redox process giving rise to silver nanoparticles (Ag-NPs) in addition to the cationic form of the radicals that rearrange to form their corresponding ketones. At the end of the reaction, the reducing agent is fully dissociated and will be no longer available to stabilize the produced Ag-NPs.

Influence of Irradiation Intensity on the Formation of Ag-NPs. Because the light source used is of adjustable intensity, the FAU-Ag^+ suspension is irradiated with different intensities (I_0). At I_0 values of <20%, few and nonreproducible reactions are triggered because of a nonstable irradiation at such low intensities. Upon irradiation with an I_0 of 20% for 60 s, a plasmon absorbance band at 375 nm appears in the UV−vis spectrum of the FAU-Ag^+ suspension and is associated with a green coloration, indicative of the generation of Ag-NPs. Interestingly, a further increase in I_0 induces a progressive hyperchromic shift of the plasmon absorbance band as well as a slight bathochromic (red) shift. The sample irradiated with an I_0 of 100% presents an absorbance twice that at an I_0 of 20%, and the peak position shifts from 375 to 380 nm (Figure 1A). This implies that more silver cations are reduced.[19] The reaction rate is directly proportional to the irradiation intensity

dx.doi.org/10.1021/la5006743 | Langmuir XXXX, XXX, XXX−XXX

used. At a low intensity, a small number of radicals are generated, because of the competing deactivation process (Scheme 1); only a few radicals are available for the reduction of silver cations, explaining the low intensity of the plasmon absorbance band. At a high irradiation intensity (I_0 = 100%), many free radicals are generated and are rapidly consumed. This favors the reduction of silver over the deactivation of free radicals and leads to the full reduction of silver cations after only 60 s. This assumption is confirmed by running the reaction for a shorter time (15 s) (Figure 1B). At a low irradiation intensity (I_0 = 20%), a very low intensity band appears at 355 nm with no change in the color of the suspension. This suggests that the number of free radicals generated is not enough to reduce the silver cations. With an I_0 of 100%, an intense absorption at 375 nm is associated with the appearance of a dark green color, indicating that the reaction is almost complete after irradiation for 15 s. For comparison, the UV−visible spectra of the FAU-Ag^+ suspension without and with a photoreducing agent (2-hydroxy-2-methylpropiophenone) at time zero are taken and presented in Figure S1 of the Supporting Information. It is clearly seen that after mixing, no absorption band is observed in the spectrum, while the plasmon band appears after 15 s (Figure 1). These results demonstrate that the photoreducing agent upon exposure to UV irradiation is giving rise to a pair of radicals, and the sequential processes are followed as presented in Scheme 1.

Influence of Irradiation Time on the Formation of Ag-NPs. The irradiation of a silver-containing zeolite suspension is conducted for different times while fixing the intensity of the light source at 100%. As observed in Figure 2, a plasmon band

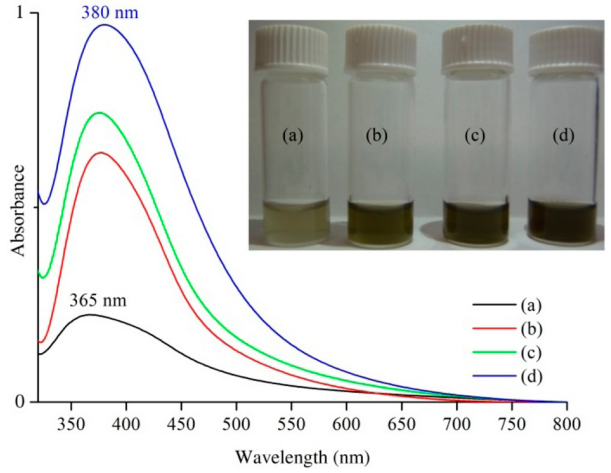

Figure 2. Evolution of the Ag plasmon band in FAU suspensions after UV treatment at 100% for (a) 5, (b) 10, (c) 15, and (d) 60 s.

appears at 365 nm, associated with a pale green coloration of the suspension after irradiation for 5 s. This highlights the high efficiency of this mode of reduction, i.e., formation of Ag-NPs after irradiation for only 5 s instead of several hours for the chemical reduction method.[21] Increasing the reaction time leads to a continuous hyperchromic shift of the plasmon band and a darkening of the zeolite suspension, indicative of the progressive formation of Ag-NPs. On the basis of the band intensity, more than 75% of the silver cations are reduced after only 15 s. Furthermore, all silver cations are reduced after irradiation for 60 s with no increase in the plasmon band intensity with longer irradiation times [2 or 3 min (Figure S2 of the Supporting Information)]. Besides, an additional amount of reducing agent is added to the samples and then subjected to irradiation. No notable change in the plasmon band is observed under these conditions; thus, we conclude that the silver cations are fully reduced after treatment for only 1 min. Instead, a decrease in plasmon band intensity takes place at a long irradiation time (5 min), probably because of a partial destruction of the zeolite nanoparticles caused by the harsh conditions used. Interestingly, no change in the absorbance wavelength is noticed; this indicates that the reaction does not occur via the formation of small Ag seeds growing into larger particles during the reaction.[21] Because of the fast reaction process, Ag-NPs of a similar size are progressively produced.

The DLS study of the FAU-Ag suspensions obtained under different irradiation conditions shows a monomodal particle size distribution of particles with an average diameter of 70 nm (Figure 3), matching the DLS from a pure FAU zeolite

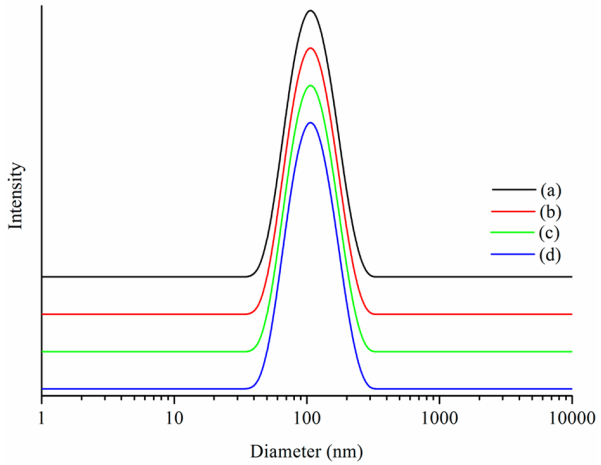

Figure 3. DLS curves of FAU-Ag suspensions after irradiation with an I_0 of 100% for (a) 5, (b) 10, (c) 15, and (d) 60 s.

suspension (Figure S3 of the Supporting Information). This indicates that the silver nanoparticles are completely associated with the zeolite crystals and no evidence of separate Ag-NPs is observed in the suspensions.

The DLS results are confirmed by a HRTEM study (Figure 4 and Figure S4 of the Supporting Information). The zeolite crystals contain silver nanoparticles predominantly located in the channels of FAU crystals; however, several Ag-NPs are seen on the zeolite surface. At high magnifications, the zeolite nanoparticles show a high degree of crystallinity and well-aligned crystal fringes. As previously mentioned, because of the short reaction period, the Ag nanoparticles are of similar size and shape and appear as spheres with a diameter in the range of 0.7−1.1 nm. More than 80% of the Ag-NPs are located in the super cages (1.1 nm) and some in the sodalite cages (0.7 nm) of the FAU zeolite crystals. The entire FAU zeolite crystal containing Ag-NPs at high magnification is shown in Figure 4C; the homogeneous distribution of Ag-NPs all over the zeolite crystal can be seen. The regular distribution of Ag-NPs in the zeolite crystals is observed at high magnifications, as shown as an inset of the enlarged selected area in Figure 4B. However, some Ag-NPs with a size of 5−6 nm can be seen on the zeolite external surface (Figure 4A).

The zeolite crystals containing Ag-NPs are further characterized by EDS-TEM (Figure 5).

dx.doi.org/10.1021/la5006743 | Langmuir XXXX, XXX, XXX−XXX

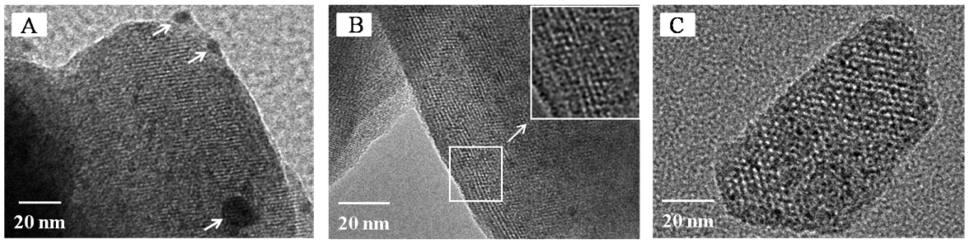

Figure 4. HRTEM images of FAU crystals containing Ag-NPs. (A) Ag-NPs within the cages and on the external surface of the zeolite crystals (arrows). (B) Ag-NPs in the zeolite cages only. The inset shows an enlarged selected area showing the silver nanoparticle in the zeolites. (C) Ag-NPs homogeneously distributed in the entire crystalline FAU zeolite particle. This sample was obtained after UV treatment at 100% for 60 s.

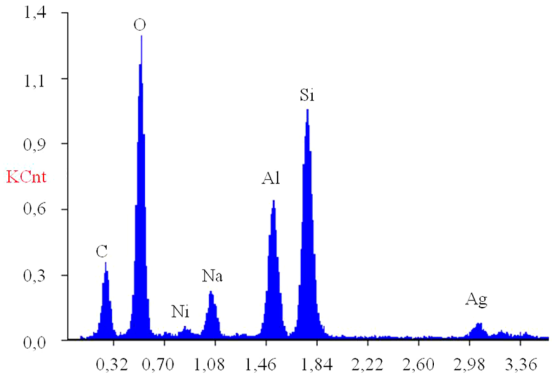

Element	Weight %	Atomic %
Na	26.7	32.6
Al	28.0	29.2
Si	35.7	35.7
Ag	9.5	2.5

Figure 5. Elemental composition of the FAU-Ag sample measured by EDX-HRTEM (C corresponds to the holey carbon film, and Ni is coming from the grid used in the TEM experiment). The inset shows the elemental analysis of the FAU-Ag sample expressed in weight and atomic percent.

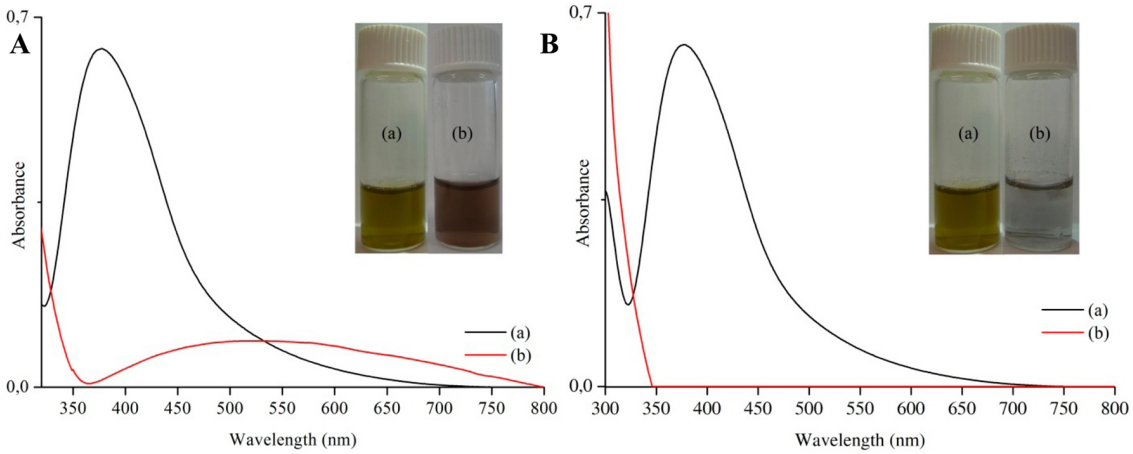

Figure 6. (A) Plasmon band of Ag-NPs in (a) a FAU-Ag suspension and (b) pure Ag-NPs in water (I_0 = 100% for 10 s). (B) Evolution of the plasmon band for (a) FAU-Ag and (b) pure Ag in water after 60 min.

The zeolite main components, i.e., Al, Si, and Na, are measured and presented in Figure 5. A Si:Al ratio of ∼1.2, which is characteristic of the FAU type zeolite (X), is measured. Additionally, the partial ion exchange of sodium for silver is evidenced. Besides, the chemical composition of the ion-exchanged (FAU-Ag^+) and reduced (FAU-Ag) zeolite samples is determined and presented in Table S1 of the Supporting Information. The results confirm that the silver content does not change; thus, only reduction of the silver cations occurred, leading to the formation of Ag-NPs, which is proven by UV−vis measurements.

Stability of Ag-NPs. The stability of Ag-NPs in the FAU zeolite is of prime importance. It is expected that the photoreductant has a dual action during the photoreduction process: (1) reducing the silver cations and simultaneously (2) stabilizing the Ag-NPs from further oxidation. However, we have already mentioned that, in our case, the reducing agent is fragmented during the reaction and so produces free radicals. Hence, it is not capable of ensuring the stability of the reaction products. The zeolite is therefore used as an inorganic matrix to stabilize the Ag-NPs.[10] In Figure 6A, the plasmon band of Ag-NPs stabilized in the FAU zeolite, and a control test with the same amount of nonsupported and reduced silver in a water solution is presented. It is clearly seen that the Ag-NPs in FAU zeolite exhibit an intense and nearly symmetrical band reflecting their high degree of monodispersity, already shown by HREM. Moreover, the Ag-NPs in a water solution have a very broad and weak band extending from 365 to 800 nm

dx.doi.org/10.1021/la5006743 | Langmuir XXXX, XXX, XXX−XXX

(Figure 6A, black line). This band indicates the presence of Ag-NPs of different sizes. Hence, the first role of the zeolite crystals is to induce a homogeneous formation of Ag-NPs with a defined location within the zeolite pores, and on the zeolite surface. One hour after irradiation, the plasmon band of Ag-NPs supported on FAU zeolite crystals is unchanged (Figure 6B), while the corresponding band for free Ag-NPs in a water solution totally disappears. This evolution is accompanied by the discoloration of the suspension, from light brown to colorless. For the FAU-Ag suspension, no change in suspension color, plasmon band position, or intensity is observed after several months, while in the absence of zeolite, the Ag-NPs start to be oxidized after reduction for only a few minutes (Figure S5 of the Supporting Information).

Theoretical Calculations of Ag-NPs Based on the Plasmon Band. A comparative study between the experimental and calculated plasmon bands for Ag-NPs stabilized in FAU zeolites is presented in Figure 7. Simulations of Ag-NPs in water are first conducted. The simulations are performed for two spheres with diameters of 0.74 nm (opening of the supercage) and 1.12 nm (diameter of the supercage, dotted blue line), using an adjustable damping parameter (g), determined using a fitting algorithm. As shown in Figure 7, the D = 0.74 nm, g = 0.55 case and the D = 1.12 nm, g = 0.85 case result in similar absorption spectra. In fact, the experimental absorption spectrum can be reproduced with various values of D and g. However, larger nanoparticle diameters would be best fit using a "g" value of >0.85, and smaller nanoparticle diameters would be best fit with a "g" value of <0.55. Thus, the values shown in Figure 7 present the best agreement between the diameters expected for the silver nanoparticles and the g value, reported in the literature for spherical particles (i.e., 0.7 ± 0.1). The fits can be improved by changing the refractive index of the surrounding medium to a value of 1.28. Again, the experimental data can be best fit with the D = 0.74 nm, g = 0.62 case and the D = 1.12 nm, g = 0.96 case, as shown in Figure 7. Although both diameters can explain the experimental absorption spectra, additional Mie theory simulations, using adjustable Gaussian distributions of nanoparticle diameters, show that the experimental results are best fit with a unique diameter. While it is difficult to ponder the relative weight of both diameters, the simulations unambiguously show that silver nanoparticles with sizes ranging between 0.74 and 1.12 nm are at the origin of the absorption peak at 380 nm. The ratio of the two sizes of Ag-NPs (D = 0.735 nm, and D = 1.124 nm) with different damping factors could be further investigated to determine the ratio of the opening of the super cage (sodalite cage) over the super cage.

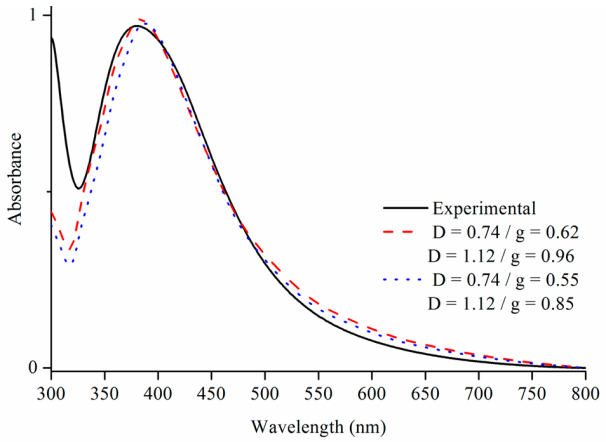

Figure 7. Experimental plasmon band of Ag-NPs in a FAU zeolite suspension irradiated with an I of 100% after 60 s (black line) and calculated plasmon band for Ag spheres with diameters (d) of 0.74 and 1.12 nm [parameter g = 0.62 and g = 0.96, N_m = 1.28 (red dotted line)] and calculated plasmon band for the Ag sphere with diameters of 0.74 and 1.12 nm (parameter g = 0.55 and g = 0.85, N_m = 1.28).

CONCLUSIONS

A facile and rapid preparation of silver nanoparticles supported on FAU zeolite crystals (zeolite X) based on UV irradiation is reported and analyzed. A silver ion-exchanged FAU zeolite suspension is irradiated with a Xe–Hg lamp (200 W) in the presence of a photoactive reducing agent (2-hydroxy-2-methylpropiophenone). Silver nanoparticles are prepared after a very short irradiation time (5–60 s), and a faster reduction is achieved after optimizing the process conditions at higher irradiation intensities. The optimal conditions for fully reducing the silver cations are a lamp intensity (I_0) of 100% for 60 s.

The size, morphology, and distribution of Ag-NPs in the FAU zeolite crystals are characterized by HRTEM. The Ag-NPs are located predominantly inside the micropores and to a lesser extent on the external surface of the FAU zeolite crystals. The Ag-NPs have an almost spheroidal shape with a diameter of 0.74–1.124 nm, which corresponds to the size of the cage opening (sodalite cage) and super cage of FAU type zeolite. This is further confirmed by a theoretical modeling of the plasmon band. The Ag-NPs in the FAU zeolite crystals without stabilizers or capping agents exhibit high stability and, after several months, do not change, again because of the stabilizing role of the zeolite nanocrystals.

ASSOCIATED CONTENT

Supporting Information

UV–vis spectra of the FAU-Ag^+ suspension without and with a photoreducing agent (2-hydroxy-2-methylpropiophenone) at time zero (Figure S1), evolution of the Ag plasmon band in the FAU-Ag suspension after UV treatment at an I_0 of 100% for 1, 2, and 3 min (Figure S2), DLS curve of the FAU zeolite suspension with a solid content of 1 wt % (Figure S3), TEM picture of the FAU-Ag sample (M = 100 nm) (Figure S4), evolution of the plasmon band of Ag-NPs with time after irradiation of $AgNO_3$ in water (Figure S5), modeling of Ag NPs based on the UV–vis spectra, and elemental analysis of the FAU-Ag sample before and after reduction expressed in weight and atomic percent (Table S1). This material is available free of charge via the Internet at http://pubs.acs.org.

AUTHOR INFORMATION

Corresponding Author

*E-mail: svetlana.mintova@ensicaen.fr.

Notes

The authors declare no competing financial interest.

ACKNOWLEDGMENTS

The financial support from the SOLAIRE Emergent Region Project of Lower Normandy and the MEET, INTERREG EC project is acknowledged. We acknowledge Hussein Awala for the preparation of FAU zeolite crystals.

REFERENCES

(1) Flores-Lopez, N. S.; Castro-Rosas, J.; Ramirez-Bon, R.; Mendoza-Cordova, A.; Larios-Rodriguez, E.; Flores-Acosta, M. Synthesis and properties of crystalline silver nanoparticles supported in natural zeolite chabazite. *J. Mol. Struct.* **2012**, *1028*, 110−115.

(2) Tung, N. H.; Chikae, M.; Ukita, Y.; Viet, P. H.; Takamura, Y. Sensing technique of silver nanoparticles as labels for immunoassay using liquid electrode plasma atomic emission spectrometry. *Anal. Chem.* **2012**, *84*, 1210−1213.

(3) Liu, F.; Rao, B. S.; Nunzi, J.-M. A dye functionalized silver−silica core−shell nanoparticle organic light emitting diode. *Org. Electron.* **2011**, *12*, 1279−1284.

(4) Noh, H. S.; Cho, E. H.; Kim, H. M.; Han, Y. D.; Joo, J. Organic solar cells using plasmonics of Ag nanoprisms. *Org. Electron.* **2013**, *14*, 278−285.

(5) Kulkarni, A. P.; Noone, K. M.; Munechika, K.; Guyer, S. R.; Ginger, D. S. Plasmon-enhanced charge carrier generation in organic photovoltaic films using silver nanoprisms. *Nano Lett.* **2010**, *10*, 1501−1505.

(6) Atwater, H. A.; Polman, A. Plasmonics for improved photovoltaic devices. *Nat. Mater.* **2010**, *3*, 205−213.

(7) Cuong, N. H.; Nguyen, H. M. T.; Nguyen, M. T. Theoretical modeling of optical properties of Ag^{8} and Ag^{14} silver clusters embedded in an LTA sodalite zeolite cavity. *Phys. Chem. Chem. Phys.* **2013**, *15*, 15404−15415.

(8) Miyanaga, T.; Suzuki, Y.; Matsumoto, N.; Narita, S.; Ainai, T.; Hoshino, H. Formation of Ag clusters in zeolite X studied by in situ EXAFS and infrared spectroscopy. *Microporous Mesoporous Mater.* **2013**, *168*, 213−220.

(9) Lee, J.-H.; Hwang, J.-H.; Nam, J.-M. DNA-tailored plasmonic nanoparticles for biosensing applications. *WIREs Nanomedicine and Nanobiotechnology* **2013**, *5*, 96−109.

(10) Zaarour, M.; Dong, B.; Naydenova, I.; Retoux, R.; Mintova, S. Progress in zeolite synthesis promotes advanced applications. *Microporous Mesoporous Mater.* **2014**, *189*, 11−21.

(11) Devaux, A.; Calzaferri, G.; Miletto, I.; Cao, P.; Belser, P.; Bruhwiler, D.; Khorev, O.; Robert Haner, R.; Kunzmann, A. Self-absorption and luminescence quantum yields of dye-zeolite L composites. *J. Phys. Chem. C* **2013**, *117*, 23034−23047.

(12) Yang, M.; Fujino, T. Silver nanoparticles on zeolite surface for laser desorption/ionization mass spectrometry of low molecular weight compounds. *Chem. Phys. Lett.* **2013**, *576*, 61−64.

(13) Guerra, R.; Lima, E.; Viniegra, M.; Guzman, A.; Lara, V. Growth of *Escherichia coli* and *Salmonella typhi* inhibited by fractal silver nanoparticles supported on zeolites. *Microporous Mesoporous Mater.* **2012**, *147*, 267−273.

(14) Liu, Y.; Zhu, Z.; Liu, G.; Xu, Z.; Kuznicki, S. M.; Zhang, H. A novel method to improve crystallinity of supported nanoparticles using low melting point metals. *J. Phys. Chem. C* **2011**, *115*, 14591−14597.

(15) Cavicchioli, M.; Varanda, L. C.; Massabni, A. C.; Melnikov, P. Silver nanoparticles synthesized by thermal reduction of a silver(I)−aspartame complex in inert atmosphere. *Mater. Lett.* **2005**, *28*, 3585−3589.

(16) Aswathy, B.; Avadhani, G. S.; Sumithra, I. S.; Suji, S.; Sony, G. Microwave assisted synthesis and UV-Vis spectroscopic studies of silver nanoparticles synthesized using vanillin as a reducing agent. *J. Mol. Liq.* **2011**, *159*, 165−169.

(17) Wani, I. A.; Ganguly, A.; Ahmed, J.; Ahmad, T. Silver nanoparticles: Ultrasonic wave assisted synthesis, optical characterization and surface area studies. *Mater. Lett.* **2011**, *65*, 520−522.

(18) Rycenga, M.; Cobley, C. M.; Zeng, J.; Li, W.; Moran, C. H.; Zhang, Q.; Qin, D.; Xia, Y. Controlling the synthesis and assembly of silver nanostructures for plasmonic applications. *Chem. Rev.* **2011**, *111*, 3669−3712.

(19) Jia, H.; Zeng, J.; Song, W.; An, J.; Zhao, B. Preparation of silver nanoparticles by photo-reduction for surface-enhanced Raman scattering. *Thin Solid Films* **2006**, *2*, 281−287.

(20) Tsuji, T.; Okazaki, Y.; Tsuji, M. Photo-induced morphological conversions of silver nanoparticles prepared using laser ablation in water-enhanced morphological conversions using halogen etching. *J. Photochem. Photobiol., A* **2008**, *194*, 247−253.

(21) Kshirsagar, P.; Sangaru, S. S.; Malvindi, M. A.; Martiradonna, L.; Cingolani, R.; Pomp, P. P. Synthesis of highly stable silver nanoparticles by photoreduction and their size fractionation by phase transfer method. *Colloids Surf., A* **2011**, *392*, 264−270.

(22) Bohren, C. F.; Huffman, D. R. *Absorption and Scattering of Light by Small Particles*; John Wiley & Sons: New York, 1998.

(23) International Association for the Properties of Water and Steam. Release on Refractive Index of Ordinary Water Substance as a Function of Wavelength, Temperature and Pressure, 1997.

(24) Johnson, P. B.; Christy, R. W. Optical Constants of the Noble Metals. *Phys. Rev.* **1972**, *B6*, 4370−4379.

(25) Kreibig, U. Electronic properties of small silver particles: The optical constants and their temperature dependence. *J. Phys. F: Met. Phys.* **1974**, *4*, 999−1014.

(26) Lermé, J.; Baida, H.; Bonnet, C.; Broyer, M.; Cottancin, E.; Crut, A.; Maioli, P.; Del Fatti, N.; Valle, F.; Pellarin, M. Size Dependence of the Surface Plasmon Resonance Damping in Metal Nanospheres. *J. Phys. Chem. Lett.* **2010**, *1*, 2922−2928.

(27) Zeman, E. J.; Schatz, G. C. An accurate electromagnetic theory study of surface enhancement factors for silver, gold, copper, lithium, sodium, aluminum, gallium, indium, zinc, and cadmium. *J. Phys. Chem.* **1987**, *91*, 634−643.

(28) Andrzejewska, E. Photopolymerization kinetics of multifunctional monomers. *Prog. Polym. Sci.* **2001**, *26*, 605−665.

Modeling of optical amplifier waveguide based on silicon nanostructures and rare earth ions doped silica matrix gain media by a finite-difference time-domain method: comparison of achievable gain with Er^{3+} or Nd^{3+} ions dopants

Julien Cardin[a], Alexandre Fafin[a,⋆], Christian Dufour[a] and Fabrice Gourbilleau[a]

[a]Centre de Recherche sur les Ions, les Matériaux et la Photonique (CIMAP), ENSICAEN, UMR 6252 CNRS, CEA/IRAMIS, Université de Caen Cedex 4, 6 boulevard Maréchal Juin, 14050 Caen, France

ABSTRACT

A comparative study of the gain achievement is performed in a waveguide optical amplifier whose active layer is constituted by a silica matrix containing silicon nanograins acting as sensitizer of either neodymium ions (Nd^{3+}) or erbium ions (Er^{3+}). Due to the large difference between population levels characteristic times (ms) and finite-difference time step (10^{-17}s), the conventional auxiliary differential equation and finite-difference time-domain (ADE-FDTD) method is not appropriate to treat such systems. Consequently, a new two loops algorithm based on ADE-FDTD method is presented in order to model this waveguide optical amplifier. We investigate the steady states regime of both rare earth ions and silicon nanograins levels populations as well as the electromagnetic field for different pumping powers ranging from 1 to 10^4 $mW.mm^{-2}$. Furthermore, the three dimensional distribution of achievable gain per unit length has been estimated in this pumping range. The Nd^{3+} doped waveguide shows a higher gross gain per unit length at 1064 nm (up to 30 $dB.cm^{-1}$) than the one with Er^{3+} doped active layer at 1532 nm (up to 2 $dB.cm^{-1}$). Considering the experimental background losses found on those waveguides we demonstrate that a significant positive net gain can only be achieved with the Nd^{3+} doped waveguide. The developed algorithm is stable and applicable to optical gain materials with emitters having a wide range of characteristic lifetimes.

Keywords: ADE-FDTD, waveguide, rare earth, Si nanostructures, Gain, Computational methods, optical amplifier, silicon photonics

1. INTRODUCTION

For many years, rare earth ions have been used in silica-based optical amplifiers. In these systems, the low gain value requires to employ significant length (10 to 15 m) of doped fiber to achieve a workable power operation. In more compact systems such as erbium-doped waveguide amplifiers (EDWA) a higher gain has to be reached in order to shorten the operating length of the amplifier.[1] Mostly trivalent erbium ions (Er^{3+}) have been studied due to their emission wavelength at 1532 nm, which is adapted to the telecommunications window in optical fibers.[2] However, there are three major gain limiting factors for the erbium ions : the up-conversion mechanism, the excited state absorption and the re-absorption of the signal from the fundamental level. This last drawback is characteristic of a three levels system. More recently, neodymium ions (Nd^{3+}) has been proposed instead of erbium ion since its four levels emission scheme prevent signal re-absorption from the fundamental level and makes it more suitable for achieving higher gain.

One main drawback of seeking gain with rare earth ions is their low absorption cross section (σ_{abs}). However this can be overcome by the use of sensitizers that are characterized by a larger absorption cross section and an efficient energy transfer to RE^{3+} ions. Several sensitizers of RE have been proposed in literature, Polman et

Further author information: (Send correspondence to Julien Cardin)
Julien Cardin: E-mail: julien.cardin@ensicaen.fr, Telephone: +33(0)2.31.45.26.64
⋆ Present address: Institut P′, Département Physique et Mécanique des Matériaux, UPR 3346 CNRS, Université de Poitiers, Bât. SP2MI, Boulevard Marie et Pierre Curie, BP 30179, 86962 Futuroscope Chasseneuil, France

Physics and Simulation of Optoelectronic Devices XXIII, edited by Bernd Witzigmann, Marek Osiński, Fritz Henneberger, Yasuhiko Arakawa, Proc. of SPIE Vol. 9357, 935709
 · doi: 10.1117/12.2077611

al[1] show the sensitization of Er^{3+} ions by different kinds of sensitizers such as ytterbium ions, metal ions and silicon nanograins (Si-ng). Several studies[3,4] have pointed out that silicon nanograins are efficient sensitizers of Er^{3+} ions and can increase its effective absorption cross section by a factor up to 10^4. MacDonald et al[5] showed a likewise efficient sensitization of Nd^{3+} ions by those Si-ng sensitizers.

We aim to model the propagation of an electromagnetic field into a waveguide with a layer containing absorbing and emitting centers as for example rare earth ions and silicon nanograins. More particularly, we want to determine the system characteristics as fields, level populations, and gain in a steady state regime as a function of initial parameters such as concentration of emitting centers, geometry, pumping configuration and pump and signal powers. Moreover, to model those steady states regimes in a waveguide with a layer containing absorbing and emitting centers, we must take into account the time evolution of electromagnetic field and electronic levels populations of these centers. In a waveguide containing silicon nanograins and rare earth ions, the typical lifetime of the electronic levels is about some ms, whereas the characteristic period of the electromagnetic field is of the order of fs. The steady state of the system cannot be reached with such a difference between absorbing and emitting centers lifetimes and electromagnetic field period by means of classical ADE-FDTD. It would require prohibitively long computation times with about 10^{15} iterations. Consequently, we developed a two loops new algorithm based on ADE-FDTD method which allows to compute the electromagnetic field distribution, the electronic levels populations, and the gain in the waveguide in the steady state regime.[6,7] In this paper we present briefly the two loops ADE-FDTD algorithm of calculation and the comparative study of waveguides with an active layer containing Si-ng and doped either with erbium or neodymium ions.

2. RARE EARTH DOPED SILICON BASED WAVEGUIDE

The system describe hereafter is an optical amplifier strip loaded waveguide, composed of three layers as presented on figure 1. Bottom and top cladding layers of pure silica of a thickness equal to 3.5 μm and 0.4 μm respectively ensure vertical guiding of modes, whereas a top silica strip stacked on the active layer ensures lateral confinement of modes. The static refractive index (i.e. refractive index which remains constant with wavelength) of the active layer is equal to 1.5 and the one of the strip and bottom cladding layers to 1.448 to ensure the guiding conditions. We inject at one end of the waveguide pump and signal guide modes in a co-propagation scheme as presented on figure 1(a). The active layer of 2 μm thick is constituted of non-stoichiometric Silicon oxide (SiO_x) containing silicon nanograins and rare earth ions (RE^{3+}).

The active layers doped with RE^{3+} are grown by magnetron sputtering technique as described in references.[8–10] Those composite layers contain silicon nanograins (Si-ng) and RE^{3+} ions dispersed in non-stoichiometric Silicon oxide (SiO_x) as schematically presented of figure 2. Those Si-ng act as sensitizers of RE^{3+} ions in their vicinity by a mechanism of energy transfer and therefore enhance their excitability by several order of magnitude. The effective absorption cross section of RE^{3+} sensitized by Si-ng is of the order of 10^{-16} cm^2 against RE^{3+} direct excitation absorption cross section which is in the 10^{-19} to 10^{-21} cm^2 range. According to our experimental investigations[11] an exciton is photogenerated in Si-ng by pumping of SiO_x :Si-ng :RE^{3+} layer with an electromagnetic wave at 488 nm. After non-radiative deexcitations, the exciton energy reaches the corresponding energy gap of RE^{3+}. Exciton can then vanish either by transfer of energy to the RE^{3+} ions by dipole-dipole interaction or by radiative or non-radiative recombination to Si-ng ground level.

Hence those active layers have typical/particular photoluminescence properties as presented on figure 3. The characteristic emission band of radiative transition occurring from excited (Si^*) to ground state (Si) in Si-ng is at 770nm. The characteristic emission bands of Er^{3+} and Nd^{3+} ions are respectively at 1532 nm and at 921, 1106 and 1395 nm.

3. TWO LOOPS ADE-FDTD METHOD

The FDTD method is based on time and space discretization scheme of Maxwell equations proposed by Yee[12] which allows to calculate the propagation of electromagnetic field (**E**,**H**) in time domain.[13] The ADE method consists in the use of extra terms such as current density **J** or polarization density **P** which are solutions of differential equations with the aim to model some non linear optical behavior such as dispersive or gain media.[14,15] The Maxwell equations describing fields **E**, **H** are rewritten in the form given in equation 1.

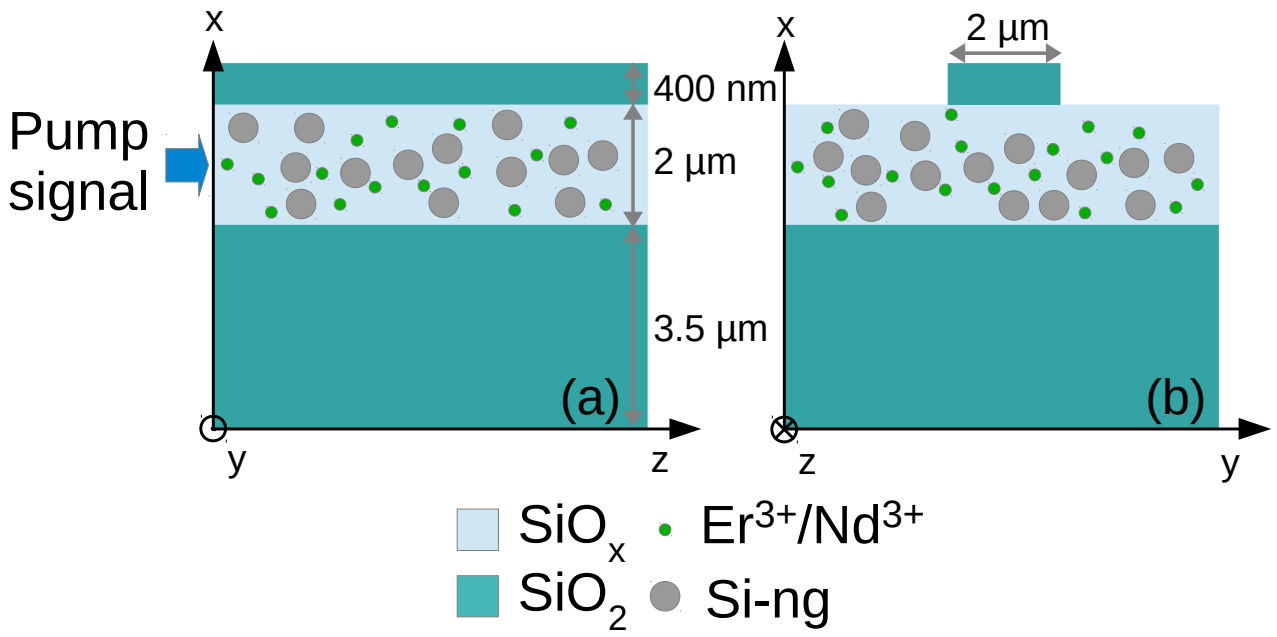

FIGURE 1. Optical amplifier waveguide based silicon rich silicon oxide doped with rare earth ions : (a)in longitudinal view with configuration of co-propagation of pump and signal and (b) in cross section view

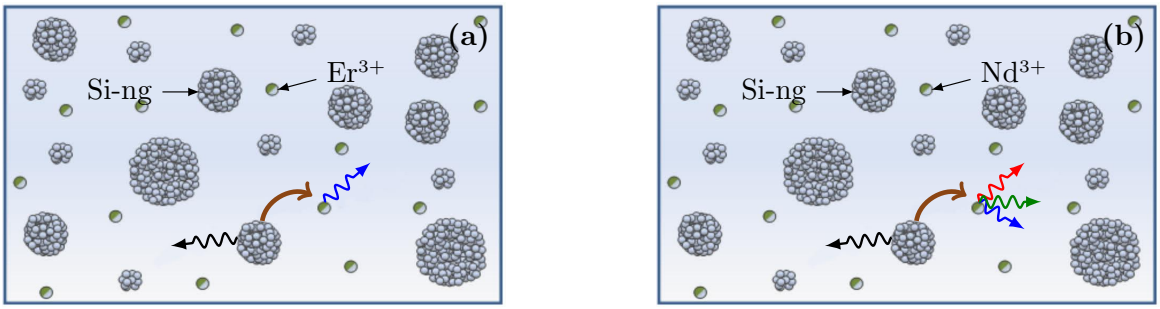

FIGURE 2. Schematic representation of the principle of optical indirect excitation of the rare earth ions via sensitization by silicon nanograin in silicon rich silicon oxide sample with silicon nanograins and doped with : (a) erbium ion (b) neodymium ion

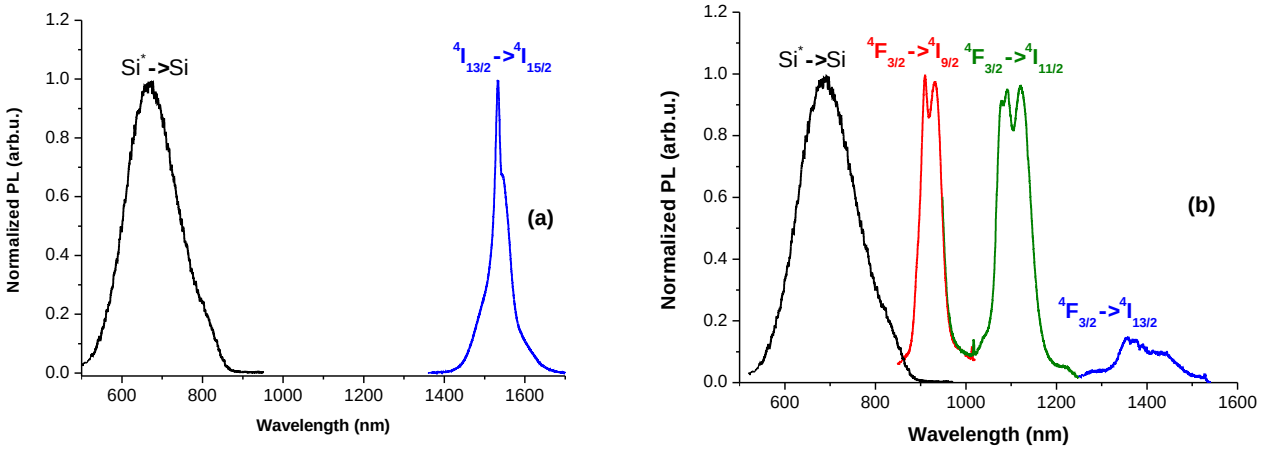

FIGURE 3. Typical photoluminescence spectra of silicon rich silicon oxide sample containing silicon nanograins and doped with rare earth ions : (a) erbium ions (b) neodymium ions

$$\begin{cases} \nabla \wedge \mathbf{E} = -\mu_0 \mu_r \dfrac{\partial \mathbf{H}}{\partial t} - \rho \mathbf{H} \\ \nabla \wedge \mathbf{H} = \epsilon_0 \epsilon_r \dfrac{\partial \mathbf{E}}{\partial t} + \dfrac{\partial \mathbf{P}_{tot}}{\partial t} + \sigma \mathbf{E} \end{cases} \tag{1}$$

In equation 1, ϵ_r and μ_r are respectively the static dielectric permittivity and magnetic permeability of different considered materials. σ is the electrical conductivity and ρ is a fictitious magnetic resistivity used for boundary conditions of the calculation box. The perflectly matched layers (PML) scheme developped by Berenger[16] have been implemented as boundary conditions. $\mathbf{P}_{tot} = \sum \mathbf{P}_{ij}$ is the sum of all polarizations corresponding to each transition of absorbing/emitting centers (hereafter : silicon nanograins and rare earth ions). The use of one polarization density $\mathbf{P}_{ij}$ per optical transition between levels i and j allows the description of the active layer dynamic permittivity $\epsilon(\omega)$ arising from the dipole moment densities induced by optical transitions in emitting centers. The FDTD space step Δ, time step Δ_t, Courant number S_c and calculation box size are reported in Table 1.

TABLE 1. FDTD algorithm parameters

Parameter	Δ	Δ_t	S_c	box length x	box length y	box length z
Value	50 nm	10^{-17} s	1	169Δ	321Δ	161Δ

Neglecting the Rabi oscillation term,[17] for a transition between levels i and j the polarization density $\mathbf{P}_{ij}$ is linked to the instantaneous electric field $\mathbf{E}$(t), to the population difference $\Delta N_{ij} = N_i - N_j$, and to a constant $\kappa_{ij} = \frac{6\pi\epsilon_0 c^3}{\omega_{ij}^2 \tau_{ij} n}$ through the Lorentz type polarization density differential equation[18] :

$$\frac{d^2\mathbf{P}_{ij}(t)}{dt^2} + \Delta\omega_{ij}\frac{d\mathbf{P}_{ij}(t)}{dt} + \omega_{ij}^2 \mathbf{P}_{ij}(t) = \kappa_{ij}\Delta N_{ij}(t)\mathbf{E}(t) \tag{2}$$

The time evolution of electronic levels population N_i is modeled by classical rate equations system. Full detailed rate equations system of considered emitters will be given thereafter. As mentioned in the introduction, some excited levels characteristic lifetimes may be as long as a few ms.[19,20] Due to the time step of ADE-FDTD classical method (figure 4a), which are lower than 10^{-17} s,[13] the number of iteration should be as huge as 10^{15} in order to reach the steady states of the levels populations. A conventional calculation is therefore impossible

in a reasonable time. Consequently a new two loops algorithm based on ADE-FDTD method (figure 4b) has been developed that overcomes the multi-scale times issue of such a system and allows to describe the spatial distribution of the electromagnetic field and levels population in steady state in an active optical waveguide.[6,7] This algorithm works with a drastic reduction of number of iterations to reach steady states values of fields and levels population from about 10^{15} to 10^5 iterations.

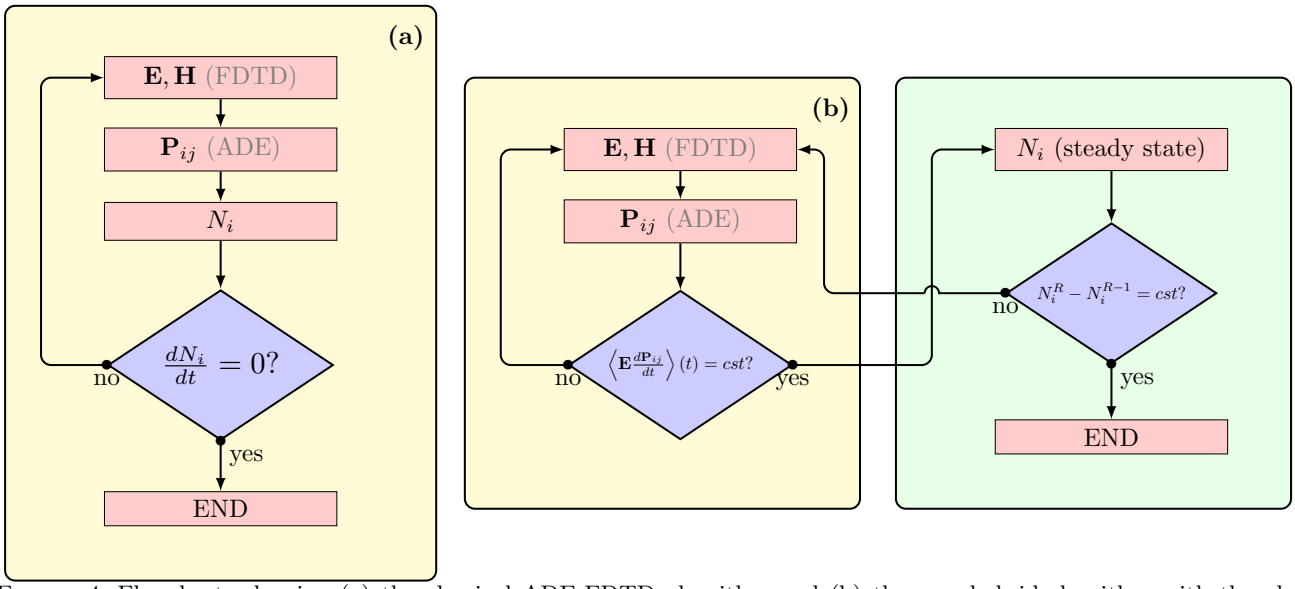

FIGURE 4. Flowcharts showing (a) the classical ADE-FDTD algorithm and (b) the new hybrid-algorithm with the alternation of the short times loop calculating electromagnetic field and polarizations and the long times loop including calculation of levels populations.

The description by the Lorentz oscillator polarization density (Equation 2) of an absorption or an emission process occurring during a transition i to j implies the equality of absorption and emission cross sections and only homogeneous broadening of the transition linewidth. At the resonance frequency, each Lorentz oscillator linewidth $\Delta\omega_{ij}$ is related to the absorption/emission cross section by the equation 3.

$$\sigma_{ij} = \frac{\kappa_{ij}}{\epsilon_0 c}\frac{1}{\Delta\omega_{ij}} \tag{3}$$

According to equation 3, high absorption cross sections σ_{ij} (typically greater than 10^{-17} cm^2) lead to a small linewidth $\Delta\omega_{ij}$ (about 10^{11} rad.s^{-1}) which impose a large number of iterations to reach a steady state. In order to calibrate the proper absorption cross section while keeping the number of iterations as small as possible, we exploit the superposition property of the polarization densities by using a number N_p of identical polarization densities with larger $\Delta\omega_{ij}$. Hence, equation (3) becomes equation (4).

$$\sigma_{ij} = \frac{\kappa_{ij}}{\epsilon_0 c}\frac{N_p}{\Delta\omega_{ij}} \tag{4}$$

At resonance frequency for $\omega_{ij} = 3.8 \times 10^{15}$ rad.s^{-1}, the two methods lead to identical cross sections : $\sigma_{ij}(N_p = 1) = \sigma_{ij}(N_p = 1000)$ as represented on figure 5. By this method, the cross section calibration is performed by choosing the appropriate value of the number of identical polarization densities N_p and the linewidth $\Delta\omega_{ij}$.

Silicon nanograins (Si-ng) are modeled as a two levels system (Figure 6) where the ground and excited levels populations (respectively N_{Si} and N_{Si^*}) are given by the rate equations (Equation 5 and 6). Due to a low probability of multi-exciton generation in a single Si-ng,[21] we assume the excitation of one single exciton by Si-ng, therefore the Si-ng population will correspond to the exciton population.

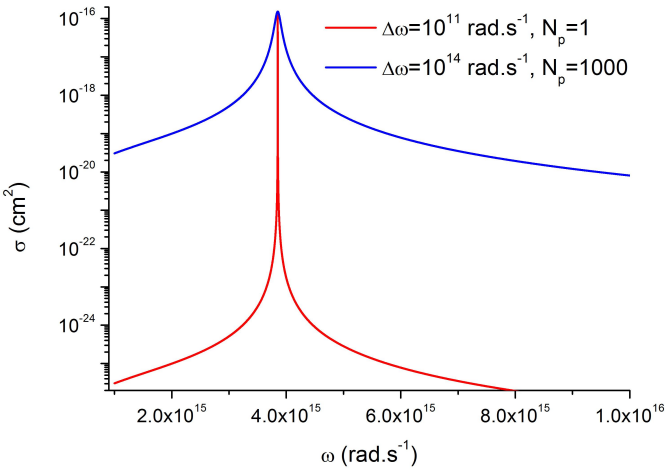

FIGURE 5. Absorption cross section as a function of the pulsation with a transition at 3.8×10^{15} rad.s^{-1} for two number of polarization densities N_p and two linewidths $\Delta\omega_{ij}$

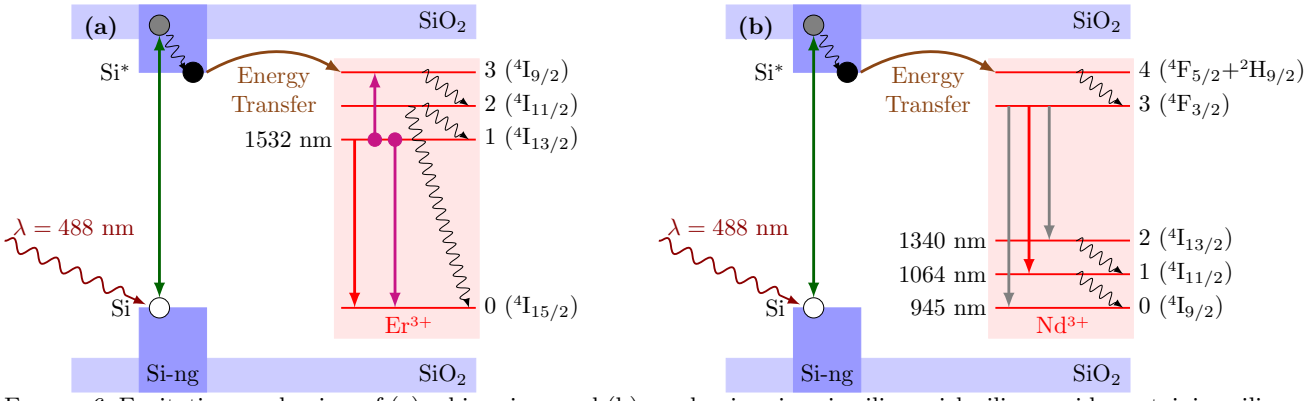

FIGURE 6. Excitation mechanism of (a) erbium ions and (b) neodymium ions in silicon rich silicon oxide containing silicon nanograins and rare earth ions. Radiative transitions are represented by straight lines and nonradiative ones by sinusoidal lines.

$$\frac{dN_{Si^*}(t)}{dt} = +\frac{1}{\hbar\omega_{Si}}\mathbf{E}(t)\frac{d\mathbf{P}_{Si}(t)}{dt} - \frac{N_{Si^*}(t)}{\tau_{Si}|_{nr}^{r}} - KN_{Si^*}(t)N_0(t) \tag{5}$$

$$\frac{dN_{Si}(t)}{dt} = -\frac{1}{\hbar\omega_{Si}}\mathbf{E}(t)\frac{d\mathbf{P}_{Si}(t)}{dt} + \frac{N_{Si^*}(t)}{\tau_{Si}|_{nr}^{r}} + KN_{Si^*}(t)N_0(t) \tag{6}$$

The Si-ng physical parameters are reported in table 2 (for further detail see references[6] and[7]).

TABLE 2. Parameters levels of silicon nanograins

$j \to i$	Lifetime (s)	$\omega_{ij}(10^{15}$ rad/s)	$\Delta\omega_{ij}(10^{14}$ rad/s)	N_p	K $(cm^{-3}.s^{-1})$	[Si-ng] (cm^{-3})
$Si^* \to Si$	50.10^{-6}	3.682	1	2756	10^{14}	10^{19}

Erbium ions levels diagram is presented on figure 6a. We consider two non-radiative transitions and one radiative transition from level 1 to level 0 at 1532 nm. Moreover an up-conversion process from level 1 to levels 0 and 3 can be modeled. The time evolution of Er^{3+} levels populations is described by the rate equations 7 to 10. The concentration of erbium ions was taken equal to 10^{20} cm^{-3}. All parameters of erbium ions transitions are taken from references[19,22] and reported in Table 3.

$$\frac{dN_3(t)}{dt} = -\frac{N_3(t)}{\tau_{32}|_{nr}} + KN_{Si^*}(t)N_0(t) + C_{up}N_1^2 \tag{7}$$

$$\frac{dN_2(t)}{dt} = +\frac{N_3(t)}{\tau_{32}|_{nr}} - \frac{N_2(t)}{\tau_{21}|_{nr}} - \frac{N_2(t)}{\tau_{20}|_{nr}} \tag{8}$$

$$\frac{dN_1(t)}{dt} = +\frac{1}{\hbar\omega_{10}}\mathbf{E}(t)\frac{d\mathbf{P}_{10}(t)}{dt} + \frac{N_2(t)}{\tau_{21}|_{nr}} - \frac{N_1(t)}{\tau_{10}|_{nr}^{r}} - 2C_{up}N_1^2 \tag{9}$$

$$\begin{aligned}\frac{dN_0(t)}{dt} = &-\frac{1}{\hbar\omega_{10}}\mathbf{E}(t)\frac{d\mathbf{P}_{10}(t)}{dt} \\ &+\frac{N_2(t)}{\tau_{20}|_{nr}} + \frac{N_1(t)}{\tau_{10}|_{nr}^{r}} - KN_{Si^*}(t)N_0(t) + C_{up}N_1^2\end{aligned} \tag{10}$$

TABLE 3. Erbium ions parameters

$j \to i$	3→2	2→1	2→0	1→0
Lifetime (s)	0.1×10^{-6}	2.4×10^{-6}	710×10^{-6}	8.5×10^{-3}
ω_{ij} $(10^{15}$ rad/s)		1.23		
$\Delta\omega_{ij}$ $(10^{15}$ rad/s)		0.15		
N_p		1		
C_{up} $(cm^3.s^{-1})$				$5{\times}10^{-17}$

Neodymium ions levels diagram is presented on figure 6b. We consider three non-radiative transitions and three radiative transitions and neglect up-conversion phenomena. The concentration of neodymium ions is taken equal to 10^{20} cm^{-3}. The time evolution of Nd^{3+} levels populations is described by the rate equations 11 to 15. Parameters of neodymium ions transitions are taken from[18,23] and reported in Table 4.

$$\frac{dN_4(t)}{dt} = -\frac{N_4(t)}{\tau_{43}|_{nr}} + KN_{Si^*}(t)\,N_0(t) \tag{11}$$

$$\frac{dN_3(t)}{dt} = +\frac{1}{\hbar\omega_{30}}\mathbf{E}(t)\frac{d\mathbf{P}_{30}(t)}{dt} + \frac{1}{\hbar\omega_{31}}\mathbf{E}(t)\frac{d\mathbf{P}_{31}(t)}{dt} + \frac{1}{\hbar\omega_{32}}\mathbf{E}(t)\frac{d\mathbf{P}_{32}(t)}{dt} + \frac{N_4(t)}{\tau_{43}|_{nr}} - \frac{N_3(t)}{\tau_{30}|^r_{nr}} - \frac{N_3(t)}{\tau_{31}|^r_{nr}} - \frac{N_3(t)}{\tau_{32}|^r_{nr}} \tag{12}$$

$$\frac{dN_2(t)}{dt} = -\frac{1}{\hbar\omega_{32}}\mathbf{E}(t)\frac{d\mathbf{P}_{32}(t)}{dt} + \frac{N_3(t)}{\tau_{32}|^r_{nr}} - \frac{N_2(t)}{\tau_{21}|_{nr}} \tag{13}$$

$$\frac{dN_1(t)}{dt} = -\frac{1}{\hbar\omega_{31}}\mathbf{E}(t)\frac{d\mathbf{P}_{31}(t)}{dt} + \frac{N_3(t)}{\tau_{31}|^r_{nr}} - \frac{N_1(t)}{\tau_{10}|_{nr}} + \frac{N_2(t)}{\tau_{21}|_{nr}} \tag{14}$$

$$\frac{dN_0(t)}{dt} = -\frac{1}{\hbar\omega_{30}}\mathbf{E}(t)\frac{d\mathbf{P}_{30}(t)}{dt} + \frac{N_3(t)}{\tau_{30}|^r_{nr}} + \frac{N_1(t)}{\tau_{10}|_{nr}} - KN_{Si^*}(t)\,N_0(t) \tag{15}$$

TABLE 4. Neodymium ion parameters

$j \to i$	4→3	3→2	3→1	3→0	2→1	1→0
Lifetime (s)	230×10^{-12}	1000×10^{-6}	200×10^{-6}	250×10^{-6}	970×10^{-12}	510×10^{-12}
ω_{ij} (10^{15} rad/s)		1.34	1.77	1.99		
$\Delta\omega_{ij}$ (10^{15} rad/s)		0.67	0.18	0.11		
N_p		1	1	1		

We aim at calculating levels populations in steady states in a faster and more convenient manner. Therefore, the preferred method would be to analytically calculate the steady state populations by setting $\frac{dN_i}{dt} = 0$ in each equation. Consequently, this method is applied in case of neodymium levels equations system. In erbium rate equations system a finite-difference method was used in order to reach the steady states of population levels. This calculation was performed using a time step ten times lower than the shortest lifetime (0.1 μs) of the rate equations system. The calculation time is then no longer negligible but does not rise up significantly the global calculation time of the two loops ADE-FDTD method.

4. RESULTS AND DISCUSSION

Poynting vector ($\mathbf{R} = \mathbf{E} \times \mathbf{H}$) has been calculated from time Fourier transform of electromagnetic field ($\mathbf{E}$, $\mathbf{H}$) computed by ADE-FDTD method. Both signal and pump were injected as guided mode in the waveguide. We determine the main component $\mathbf{R}_z$ of the guided pump (488 nm) and signal (1064 nm) power density of $\mathbf{R}$ in transverse and longitudinal section view (in W.mm^{-2}) on figures 7 and 8 respectively. A decrease of the pump $\mathbf{R}_z^{pump}$ along the waveguide is observed, which is due to the absorption at 488 nm by the silicon nanograins. Moreover, the signal $\mathbf{R}_z^{signal}$ at 1064 nm does not appear absorbed over the 7μm length of the waveguide.

The two loops ADE-FDTD algorithm allows to compute tridimensional population distributions in different states. For a transition of interest, N_{high} and N_{low} represent respectively the higher and lower levels of the transition. We present the relative population difference (RPD) $\frac{N_{high}-N_{low}}{N_{tot}}$ distributions in the waveguide in a longitudinal section view along the propagation axis for the transition in Si-ng, and the 1532 nm transition of Er^{3+} (figure 9) and the 1064 nm transition of Nd^{3+} (figure 10) for a pump power equal to 10^3 mW.mm^{-2}.

In case of Si-ng (figures 9 left, 10 left), the decreasing RPD profile with waveguide length is consistent with the pump profile $\mathbf{R}_z^{pump}$(z) decrease figure 8 due to the absorption of the pump field by the Si-ng. For erbium ions (figures 9 right), the RPD of Nd^{3+} ions shows a decrease with propagation length in the waveguide. This decrease is characteristic of the pump strong absorption due to the presence of the nanograins as shown in our previous paper.[6] The RPD of Er^{3+} ions remains positive (inversion population is realized) over a length of 1.5 μm, beyond which it becomes negative witnessing the threshold effect occurring with three-levels system. For neodymium ions (figures 10 right), the RPD of Nd^{3+} ions shows also a decrease with propagation length in the waveguide which is also due to pump strong absorption by nanograins. The RPD of Nd^{3+} ions remains positive

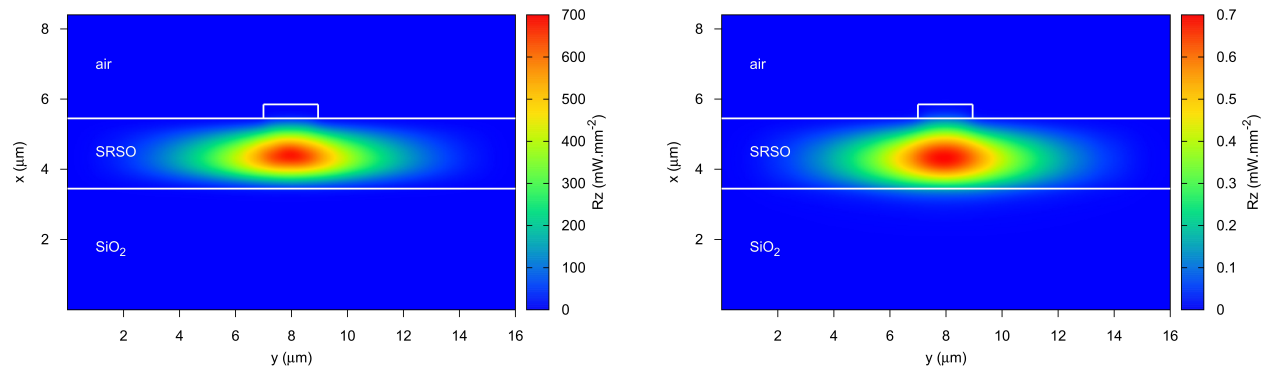

FIGURE 7. Transverse section views of Z-component of the time average Poynting vector of the pump (on the left) and of the signal (on the right) in the middle of the waveguide. The pump wavelength is λ_p=488 nm and the signal λ_s=1064 nm. Injected powers are respectively 1 $W.mm^{-2}$ and 1 mW.mm^{-2}

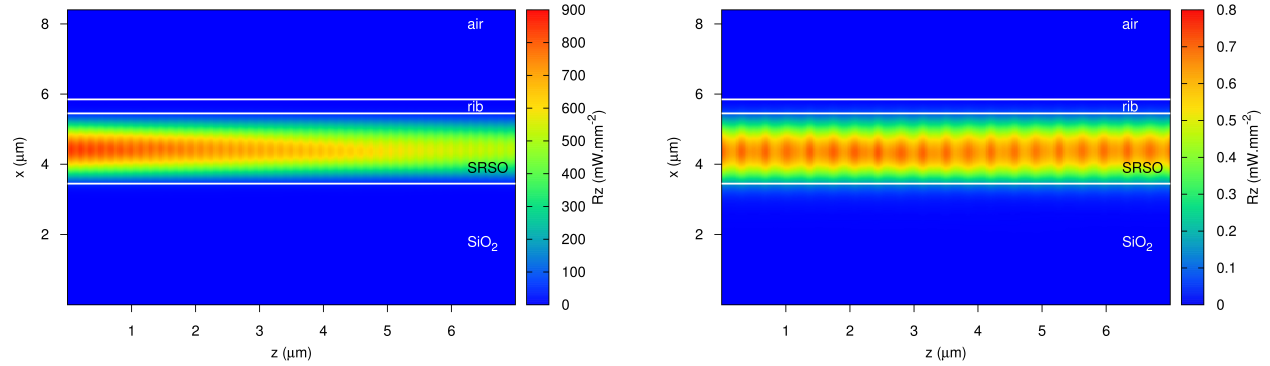

FIGURE 8. Longitudinal section views of Z-component of the time average Poynting vector of the pump (on the left) and of the signal (on the right) in the middle of the waveguide. The pump wavelength is λ_p=488 nm and the signal λ_s=1064 nm. Injected powers are respectively 1 $W.mm^{-2}$ and 1 mW.mm^{-2}

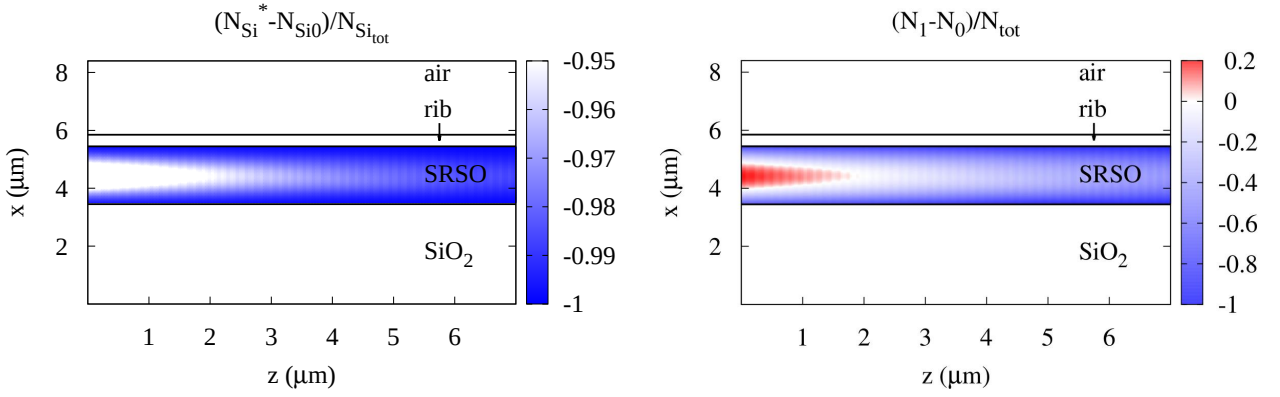

FIGURE 9. Relative population differences along the direction of propagation of Si-ng (on the left) and for the erbium ions (on the right) in SiO_x :Si-ng :Er^{3+} system for a pump power equal to 1000 mW.mm^{-2}

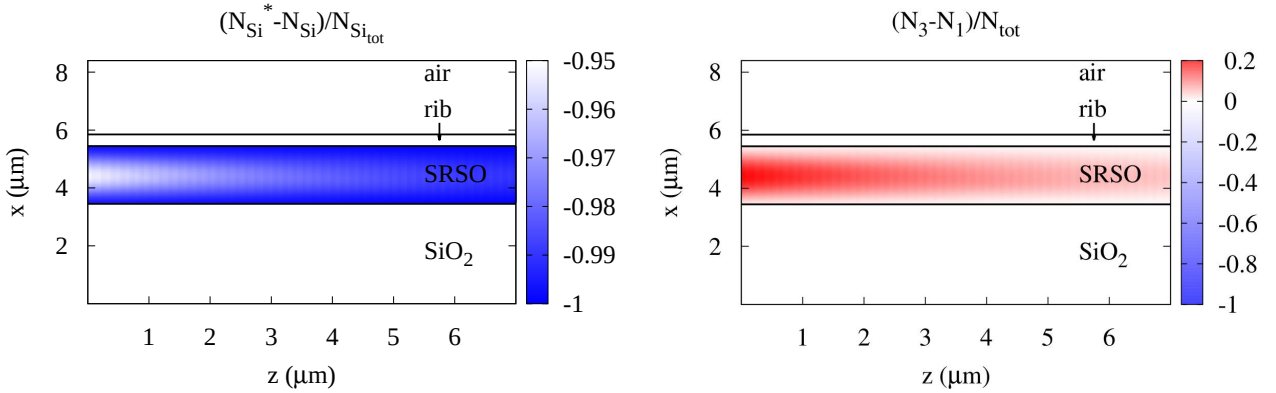

FIGURE 10. Relative population differences along the direction of propagation of Si-ng (on the left) and for the neodymium ions (on the right) in SiO_x :Si-ng :Nd^{3+} system for a pump power equal to 1000 mW.mm^{-2}

(inversion population is realized) along the whole waveguide length witnessing the four-level system behavior, where the level 1 is depopulated quickly to the ground level leading to $N_3 \gg N_1$.

This co-propagating pumping configuration allows to study locally the waveguides with various pumping values in one calculation. Indeed from population levels distribution $N_i(x,y,z)$ we can calculated the gross gain per unit length (dB.cm^{-1}) at the signal wavelength by equation 16.

$$g_{dB/cm}(x,y,z) = \frac{10}{ln10}\left(\sigma_{em}N_{high}(x,y,z) - \sigma_{abs}N_{low}(x,y,z)\right) \tag{16}$$

N_{high} and N_{low} are respectively the higher and lower levels of the considered transition and σ_{abs} and σ_{em} are respectively absorption and emission cross sections. For erbium ions, we use $N_{high} = N_1$ and $N_{low}=N_0$ and for neodymium ions $N_{high} = N_3$ and $N_{low} = N_1$ (figure 6). Assuming equal emission and absorption cross sections, the gross gain per unit length longitudinal distribution for both rare earth ions are plotted in figure 11. In case

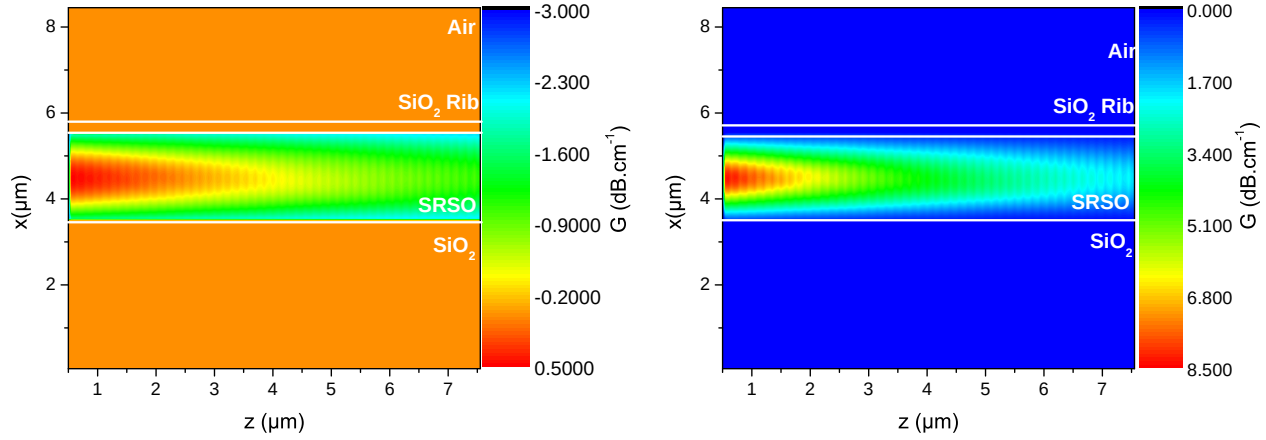

FIGURE 11. Gross gain per unit length (dB.cm^{-1}) along the direction of propagation in the case of erbium ions (on the left) and neodymium ions (on the right) for a pump power equal to 1000 mW.mm^{-2}

of erbium ions, figure 11a shows a positive (in red) gain per unit length only in the first 1.5 μm of the waveguide. Elsewhere, the gain per unit length remains negative. For neodymium ions, the figure 11b shows a positive gain per unit length that remains everywhere positive in the waveguide. On these two dimensional distributions of

the gross gain per unit length, the local gross gain per unit length can be extracted from anywhere in the active layer. We choose to take the local gross gain per unit length at the beginning of the waveguide in the center of the active layer (x = 4.5 μm and y = 8.55 μm) and in the first cell of the active layer of the waveguide where the pumping flux was recorded. We perform calculations with different pumping power densities at this extraction position and obtain the local gross gain per unit length plotted for different pumping power densities in figure 12.

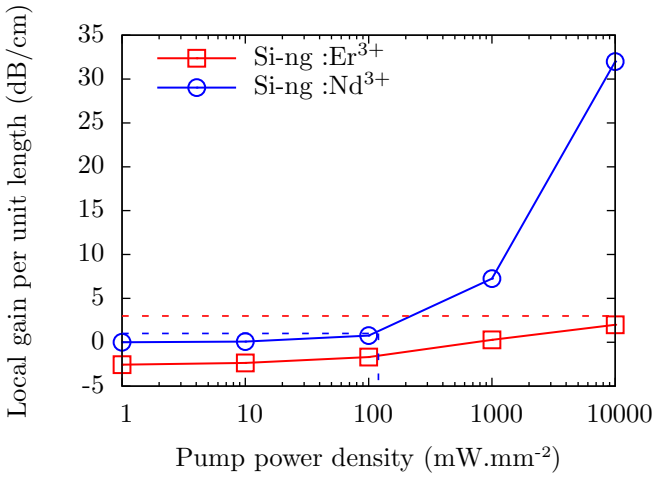

FIGURE 12. Local gross gain per unit length as a function of the pumping power density for a waveguide doped with Nd^{3+}(open circle) and a waveguide doped with Er^{3+}(open square) recorded at x = 4.5 μm and y = 8.55 μm (center of the XY section of the active layer) and z = 0 (beginning of the waveguide). Losses found by Pirasteh et al[24] and by Navarro-Urrios et al[25] are reported respectively in blue and red dashed line.

For Er^{3+} doped waveguide, above a threshold pump power of 1550 mW.mm^{-2}, a positive gross gain is reached which increases up to 2 dB.cm^{-1} for the highest pump power density simulated. In order to estimate the net gain, we must account for the background losses such as those found experimentally by Navarro-Urrios et al.[25] They found on comparable waveguide losses of about 3 dB.cm^{-1} at 1532 nm, making it impossible to reach a positive net gain in this range of pump power density. In case of Nd^{3+} doped waveguide, we find that the optical gain remains positive over the whole power range and it increases up to 30 dB.cm^{-1} for the highest pump power of 10^4 mW.mm^{-2}. Taking into account experimental background losses of 0.8 dB.cm^{-1} found by Pirasteh et al[24] in a similar system, we can estimate a net gain per unit length. Figure 12 shows that for a pump power above 130 mW.mm^{-2} the losses (dashed line) can be compensated leading to a net gain. The gross gain per unit length obtained for Nd^{3+} remains higher that the one obtained for Er^{3+} whatever the pump power density range. The gross gain per unit length difference between Nd^{3+} and Er^{3+} doped waveguides increases also with pump power density. Difference in Si-ng/RE transfer efficiency linked to the levels dynamics as well as to the difference in absorption/emission cross sections[7] (σ_{Er} =6.10^{21} cm^2 against σ_{Nd} =1.10^{19} cm^2) may explain this gross gain per unit length feature. The low gain and a short length of positive population inversion obtained by modeling of Er^{3+} doped based waveguide on the broad range of pump power make impossible the achievement of an optical amplifier with this configuration which would compete with commercially available systems. The gross gain per unit length reachable with Nd^{3+}, about one order of magnitude larger than the one obtained with Er^{3+}, could lead to a significant amplification. Nowadays, there is no commercially available comparable optical amplifier based on Nd^{3+} emission bands. However, Nd^{3+} doped Aluminum oxide channel waveguide amplifiers developed by Yang et al[26] show a maximal internal gain of 6 dB.cm^{-1} for a pump power of 45 mW.

5. CONCLUSION

A new two loops ADE-FDTD algorithm has been developed that allows to describe the spatial distribution of the electromagnetic field and steady state population levels in an active optical waveguide. The multi-scale times issue of such a system consisting in crippling calculation duration due to large difference between FDTD time step and population level lifetimes has been overcome by this algorithm. Moreover, we proposed a calibration method of the $i \rightarrow j$ transition linewidth $\Delta\omega_{ij}$ according to the experimental cross section, making a possible comparison between experimental and theoretical studies. We apply our algorithm to a strip loaded waveguide whose active layer is constituted of a silicon rich silicon oxide layer containing silicon nanograins and doped with either Er^{3+} or with Nd^{3+} ions. Our method permits to determine a three dimensional distribution of gross gain per unit length in the waveguide in steady state. We have demonstrated that, to obtain a net positive gain per unit length in SiO_x :Si-ng :RE^{3+} based waveguide, the neodymium ions are more suitable than the erbium ions. For the latter, the theoretical maximum gross gain per unit length of 2 $dB.cm^{-1}$ at 1532 nm (10^4 $mW.mm^{-2}$) does not compensate background losses experimentally estimated to 3 $dB.cm^{-1}$. On the contrary, the use of neodymium ions leads to a gross gain per unit length of 30 $dB.cm^{-1}$ at 1064 nm (10^4 $mW.mm^{-2}$). Moreover the background losses are compensated above a pump power threshold of 130 $mW.mm^{-2}$. This theoretical demonstration of a large gross gain per unit length for a Nd^{3+} doped active layer may justify further experimental work in order to achieve Nd^{3+} doped silicon based waveguide optical amplifier or laser. Further studies may be performed exploring other concentrations of rare earth ions and Si-ng, other rare earth ions and other pumping configurations in order to investigate the possibility of achieving larger gain. This method may be applied successfully to describe steady states of other kind of emitters (quantum dots, quantum wells, Dyes...) and in other configuration (VCELs, down-converting layers...).

ACKNOWLEDGMENTS

The authors are grateful to the French National Research Agency, which supported this work through the Nanoscience and Nanotechnology program (DAPHNES ANR-08-NANO-005 project), to the project EMC3 Labex ASAP and to the Centre de ressources informatiques de Haute-Normandie (CRIHAN) for computing facilities.

REFERENCES

[1] A. Polman and F. C. J. M. van Veggel, "Broadband sensitizers for erbium-doped planar optical amplifiers : review," *J. Opt. Soc. Am. B* **21**, pp. 871–892, May 2004.

[2] W. Miniscalco, "Erbium-doped glasses for fiber amplifiers at 1500 nm," *Lightwave Technology, Journal of* **9**, pp. 234 –250, feb 1991.

[3] A. J. Kenyon, P. F. Trwoga, M. Federighi, and C. W. Pitt, "Optical properties of PECVD erbium-doped silicon-rich silica : evidence for energy transfer between silicon microclusters and erbium ions," *Journal of Physics : Condensed Matter* **6**(21), p. L319, 1994.

[4] M. Fujii, M. Yoshida, Y. Kanzawa, S. Hayashi, and K. Yamamoto, "1.54 μm photoluminescence of Er^{3+} doped into Sio_2 films containing si nanocrystals : Evidence for energy transfer from Si nanocrystals to Er^{3+}," *Applied Physics Letters* **71**, pp. 1198 –1200, sep 1997.

[5] A. MacDonald, A. Hryciw, Q. Li, and A. Meldrum, "Luminescence of Nd-enriched silicon nanoparticle glasses," *Optical Materials* **28**(6), pp. 820–824, 2006.

[6] A. Fafin, J. Cardin, C. Dufour, and F. Gourbilleau, "Modeling of the electromagnetic field and level populations in a waveguide amplifier : a multi-scale time problem," *Optics express* **21**(20), pp. 24171–24184, 2013.

[7] A. Fafin, J. Cardin, C. Dufour, and F. Gourbilleau, "Theoretical investigation of the more suitable rare earth to achieve high gain in waveguide based on silica containing silicon nanograins doped with either Nd^{3+} or Er^{3+} ions," *Optics Express* **22**(10), pp. 12296–12306, 2014.

[8] K. Hijazi, L. Khomenkova, J. Cardin, F. Gourbilleau, and R. Rizk, "Structural and optical characteristics of Er-doped SRSO layers deposited by the confocal sputtering technique," *Physica E : Low-dimensional Systems and Nanostructures* **41**(6), pp. 1067–1070, 2009.

[9] S. Cueff, C. Labbé, J. Cardin, and R. Rizk, "Impact of the annealing temperature on the optical performances of Er-doped Si-rich silica systems," in *IOP Conference Series : Materials Science and Engineering*, **6**(1), p. 012021, IOP Publishing, 2009.

[10] C.-H. Liang, J. Cardin, C. Labbé, and F. Gourbilleau, "Evidence of two sensitization processes of Nd^3+ ions in Nd-doped SiOx films," *Journal of Applied Physics* **114**(3), p. 033103, 2013.
[11] O. Debieu, J. Cardin, X. Portier, and F. Gourbilleau, "Effect of the Nd content on the structural and photoluminescence properties of silicon-rich silicon dioxide thin films," *Nanoscale Research Letters* **6**(1), pp. 1–8, 2011.
[12] K. Yee, "Numerical solution of initial boundary value problems involving maxwell's equations in isotropic media," *Antennas and Propagation, IEEE Transactions on* **14**(3), pp. 302–307, 1966.
[13] A. Taflove, *Computational electrodynamics : The finite-difference time-domain method*, Artech House (Boston), 1995.
[14] A. Nagra and R. York, "Fdtd analysis of wave propagation in nonlinear absorbing and gain media," *Antennas and Propagation, IEEE Transactions on* **46**, pp. 334 –340, mar 1998.
[15] S. C. Hagness, R. M. Joseph, and A. Taflove, "Subpicosecond electrodynamics of distributed bragg reflector microlasers : Results from finite difference time domain simulations," *Radio Science* **31**(4), pp. 931–941, 1996.
[16] J. Berenger, "A perfectly matched layer for the absorption of electromagnetic waves," *Journal of computational physics* **114**(2), pp. 185–200, 1994.
[17] S.-H. Chang and A. Taflove, "Finite-difference time-domain model of lasing action in a four-level two-electron atomic system," *Optics express* **12**(16), pp. 3827–3833, 2004.
[18] A. E. Siegman, *Lasers. Mill Valley*, University Science Books, 1986.
[19] D. Pacifici, G. Franzo, F. Priolo, F. Iacona, and L. Dal Negro, "Modeling and perspectives of the Si nanocrystals-Er interaction for optical amplification," *Phys. Rev. B* **67**, p. 245301, Jun 2003.
[20] H. Lee, J. Shin, and N. Park, "Performance analysis of nanocluster-Si sensitized Er doped waveguide amplifier using top-pumped 470nm LED," *Opt. Express* **13**, pp. 9881–9889, Nov 2005.
[21] M. Govoni, I. Marri, and S. Ossicini, "Carrier multiplication between interacting nanocrystals for fostering silicon-based photovoltaics," *Nature Photonics* **6**(10), pp. 672–679, 2012.
[22] V. Toccafondo, S. Faralli, and F. Di Pasquale, "Evanescent multimode longitudinal pumping scheme for Si-nanocluster sensitized Er^{3+} doped waveguide amplifiers," *Lightwave Technology, Journal of* **26**(21), pp. 3584–3591, 2008.
[23] E. Serqueira, N. Dantas, A. Monte, and M. Bell, "Judd ofelt calculation of quantum efficiencies and branching ratios of Nd^{3+} doped glasses," *Journal of non-crystalline solids* **352**(32), pp. 3628–3632, 2006.
[24] P. Pirasteh, J. Charrier, Y. Dumeige, Y. G. Boucher, O. Debieu, and F. Gourbilleau, "Study of optical losses of Nd^{3+} doped silicon rich silicon oxide for laser cavity," *Thin Solid Films* **520**(11), pp. 4026 – 4030, 2012.
[25] D. Navarro-Urrios, F. F. Lupi, N. Prtljaga, A. Pitanti, O. Jambois, J. Ramírez, Y. Berencén, N. Daldosso, B. Garrido, and L. Pavesi, "Copropagating pump and probe experiments on Si-nc in SiO_2 rib waveguides doped with Er : The optical role of non-emitting ions," *Applied Physics Letters* **99**(23), p. 231114, 2011.
[26] J. Yang, K. van Dalfsen, F. Ay, M. Pollnau, *et al.*, "High-gain $Al_2O_3 : Nd^{3+}$ channel waveguide amplifiers at 880nm, 1060nm, and 1330nm," *Applied Physics B* **101**(1-2), pp. 119–127, 2010.